DECOVALEX-2019
Task C Final Report

Iwatsuki T.

With contributions from:
Ishibashi, M., Onoe, H., Ozaki, Y., Hadgu, T., Jove-Colon, C.F., Kalinina, E., Wang, Y
Balvin, A., Hokr, M., Landa, J., Šembera, J., Zeman, J.

October 2020

Disclaimer

This document was prepared as an account of the international research project DECOVALEX-2019 comprising participants from industry, government and academia, with funding organizations--Andra, BGR/UFZ, CNSC, U.S. DOE, ENSI, JAEA, IRSN, KAERI, NWMO, RWM, SÚRAO, SSM and Taipower. The statements made in the report are, however, solely those of the authors and do not necessarily reflect those of the Funding Organizations. While this document is believed to contain correct information, neither the United States Government nor any agency thereof, nor the Regents of the University of California, nor any of their employees, makes any warranty, express or implied, or assumes any legal responsibility for the accuracy, completeness, or usefulness of any information, apparatus, product, or process disclosed, or represents that its use would not infringe privately owned rights. Reference herein to any specific commercial product, process, or service by its trade name, trademark, manufacturer, or otherwise, does not necessarily constitute or imply its endorsement, recommendation, or favoring by the United States Government or any agency thereof, or the Regents of the University of California. The views and opinions of authors expressed herein do not necessarily state or reflect those of the United States Government or any agency thereof or the Regents of the University of California.

Copyright

DECOVALEX-2019

Task C Final Report

Lead Author: Iwatsuki, T.
Japan Atomic Energy Agency

Contributing Authors:

Ishibashi, M., Onoe, H., Ozaki, Y.
(Japan Atomic Energy Agency)

Hadgu, T., Jove-Colon, C.F., Kalinina, E., Wang, Y.
(Sandia National Laboratories)

Balvin, A., Hokr, M., Landa, J., Šembera, J., Zeman, J.
(Technical University of Liberec)

Reviewed by AE Bond

October 2020

LBNL-2001264

Preface

The DECOVALEX Project is an on-going international research collaboration, established in 1992, to advance the understanding and modeling of coupled Thermal (T), Hydrological (H), Mechanical (M) and Chemical (C) processes in geological in geological systems. DECOVALEX was initially motivated by the recognition that prediction of these coupled effects is an essential part of the performance and safety assessment of geologic disposal systems for radioactive waste and spent nuclear fuel. Later it was realized that these processes also play a critical role in other subsurface engineering activities, such as subsurface CO_2 storage, enhanced geothermal systems, and unconventional oil and gas production through hydraulic fracturing. Research teams from many countries (e.g., Canada, China, Czech Republic, Finland, France, Germany, Japan, Republic of Korea, Spain, Sweden, Switzerland, Taiwan, United Kingdom, and the United States) various institutions have participated in the DECOVALEX Project over the years, providing a wide range of perspectives and solutions to these complex problems. These institutions represent radioactive waste management organizations, national research institutes, regulatory agencies, universities, as well as industry and consulting groups.

At the core of the collaborative work with in DECOVALEX is the collaborative analysis and comparative modeling of state-of-the-art field and laboratory experiments. DECOVALEX engages model comparison in a broad and comprehensive sense, including the modelers' interpretation of experimental data, selection of boundary conditions, rock and fluid properties, etc., in addition to their choice of coupling schemes and simulator. In-depth and detailed discussions among the teams yield insight into the coupled THMC processes and stimulate development of modeling capabilities and measurement methods which would not be possible if the data were studied by only one or two groups.

Since the project initiation, DECOVALEX has been organized in several four-year phases, each phase featuring a number of modeling tasks of importance to radioactive waste disposal and other geoscience applications. Six project phases were successfully concluded between 1992 and 2015, results of which have been summarized in several overview publications (e.g., Tsang et al., 2009; Birkholzer et al., 2018; Birkholzer et al., 2019). The most recent phase, named DECOVALEX-2019, started in 2016 and ended in 2019. Seven tasks were conducted in DECOVALEX-2019, as follows:

- **Task A: ENGINEER** - Advective gas flow through low permeability materials
- **Task B: Fault Slip Test** - Fault slip processes in argillaceous rock
- **Task C: GREET** - Hydro-mechanical-chemical processes during groundwater recovery
- **Task D: INBEB** - HM and THM interactions in bentonite engineered barriers
- **Task E: Upscaling Heater Tests** - Upscaling of heater test results to repository scale
- **Task F: FINITO** - Fluid inclusions and movement in tight rock
- **Task G: EDZ Evolution** - EDZ evolution and permeability changes in crystalline rock

This document is the final report of Task C which was proposed and coordinated by the Japan Atomic Energy Agency (JAEA), presenting the technical definitions of the problems studied, approaches applied, achievements made and outstanding issues for future research.

The DECOVALEX Project would not have been possible without the support and engagement from the participating organizations who jointly support coordination of the project within a given project phase, propose and coordinate modeling tasks including the necessary experimental data, and deploy their own research team (or teams) working on a selection of the tasks conducted in the project. The partner organizations in DECOVALEX-2019 were:

- Andra, National Radioactive Waste Management Agency, *France*
- BGR, Federal Institute for Geosciences and Natural Resources, *Germany*
- CNSC, Canadian Nuclear Safety Commission, *Canada*
- DOE, Department of Energy, *USA*
- ENSI, Swiss Federal Nuclear Safety Inspectorate, *Switzerland*
- IRSN, Institut de Radioprotection et de Sûreté Nucléaire, *France*
- JAEA, Japan Atomic Energy Agency, *Japan*
- KAERI, Korea Atomic Energy Research Institute, Republic of Korea
- NWMO, Nuclear Waste Management Organization, *Canada*
- RWM, Radioactive Waste Management, *United Kingdom*
- SSM, Swedish Radiation Safety Authority, *Sweden*
- SÚRAO, Radioactive Waste Repository Authority, *Czech Republic*
- Taipower, Taiwan Power Company, *Taiwan*
- UFZ, Helmholtz Centre for Environmental Research, *Germany*

We are extremely grateful to these organizations for their financial and technical support of DECOVALEX-2019.

Jens Birkholzer (Chairman of the DECOVALEX project) and Alex Bond (Technical Coordinator of the DECOVALEX Project)

Berkeley, California, USA

June 2020

References:

Birkholzer, J.T., Bond, A.E., Hudson, J.A., Jing, L., Tsang, C.-F., Shao, H., Kolditz, O. (2018): DECOVALEX-2015 - An International Collaboration for Advancing the Understanding and Modeling of Coupled Thermo-Hydro-Mechanical-Chemical (THMC) Processes in Geological Systems, Environmental Earth Sciences, 77(14).

Birkholzer, J.T., Tsang, C.-F., Bond, A.E., Hudson, J.A., Jing, L., and Stephansson, O. (2019): 25 Years of DECOVALEX - Scientific Advances and Lessons Learned from an International Research Collaboration in Coupled Subsurface Processes, Invited Review, International Journal and Rock Mechanics and Mining Sciences, 122.

Tsang, C.-F., Stephansson, O., Jing, L., and Kautsky, F. (2009): DECOVALEX Project: from 1992 to 2007. Environmental Geology, 57(6).

Executive Summary

The construction of underground facilities for the geological disposal of radioactive waste will change the environmental conditions which are identified at the surface-based investigations before the construction of the facility. However, it is still unclear whether the disturbed environment will recover after the facility is closed.

GREET (Groundwater REcovery Experiment in Tunnel) project was conducted at the Mizunami Underground Research Laboratory of the Japan Atomic Energy Agency (JAEA) to evaluate the environmental recovery process around research galleries in fractured crystalline rock. The experiment has been planned to observe any environmental changes following water refilling the Closure Test Drift (CTD). The baseline hydro-mechanical-chemical (H-M-C) condition was identified before the excavation of CTD. Then excavation of the CTD and isolation by a water-tight plug, and subsequent flooding with groundwater was conducted. Environmental disturbance and recovery were observed for more than 6 years. In the experiment, hydraulic and chemical changes of groundwater were obviously dependent on the fracture distribution in the granite. During the tunnel closure experiment, the water pressure in the intact rock mass zone showed less of a response, while those in the fracture connected to the CTD directly reflected the change of the water pressure in the CTD. These observations indicated that the rock mass around the CTD has a high heterogeneity. Cl concentrations in the fractures varied through different mixing with groundwater derived from shallow or deep depths. The groundwater in the CTD evolved to alkaline and reducing conditions. The collected data was made available for DECOVALEX-2019 Task C.

DECOVALEX-2019 Task C aims to develop modelling and prediction methods using numerical simulation based on the water-filling experiment to examine the post-drift-closure environment recovery processes. Three research teams, JAEA, Sandia National Laboratories in the United States (SNL), and the Technical University of Liberec in the Czech Republic (TUL) were challenged to simulate the observed environmental changes. The Task consisted of following three main steps. The simulation targets were the water pressure drawdown/recovery and the variation of water chemistry during the tunnel excavation and closure, as observed in the monitoring boreholes and the CTD.

Step1: Modelling and prediction of environmental disturbance by CTD excavation

Step2: Modelling and prediction of environmental recovery by CTD isolation

Step3: Modelling and prediction of the long-term environmental condition after CTD isolation

In the simulation trials, a stochastic approach using a discrete fracture network (DFN) model, an equivalent continuum porous media (ECPM) model, and deterministic approach based on mixed-hybrid finite element methods were applied by the JAEA, SNL and TUL teams respectively. Furthermore, reactive transport modelling and basic thermodynamic analysis were examined to capture the chemical evolution of isolated groundwater in the CTD. The JAEA team constructed a reference model to check the viability of the original simulation code "COUPLYS", and then examined the sensitivity of the various parameters to the simulation results. The target parameters were estimated by using a DFN model with 100 realizations based on the fracture data (size distributions, orientation, volumetric intensity, the relationship between the aperture and permeability and the radius) and the ECPM model converted from the best reasonable DFN model. SNL team also developed a DFN model with 10 realizations and ECPM models converted from each DFN model. The simulations were conducted using the coupled "DAKOTA-PFLOTRAN" codes. The TUL team applied a deterministic approach based on a multi-dimensional concept (discrete fractures + equivalent continuum) using the code "Flow123d" for modelling.

As a result of the work by each team, the methodology for modelling and simulation achieved the following technical outcomes. The combination of a stochastic and deterministic approach with an iterative calibration considering high permeability fractures is successful in representing the range of groundwater inflow rates into the tunnel, hydraulic drawdown and the recovery. Using the ECPM models converted from the DFN models, with a deterministic approach and inverse modelling, the variation of Cl concentration in each monitoring point around the tunnel could not be simultaneously reproduced. This suggests the importance to model the channelization formed by the connection of water-conducting fractures in the heterogeneous fracture distribution. Currently, it is possible to represent the general range of Cl concentration variation using the current modelling methodology.

For modelling and simulation of the isolated groundwater evolution, thermodynamic analysis can identify dominant water-mineral interactions that affect the future chemistry of isolated groundwater in the tunnel. Reactive transport modelling including these minerals has not yet been completed, but the spread of alkaline groundwater from CTD to rock was inferred to be retained in the vicinity of the shotcrete. Further checks of the applicability of the reactive transport modelling methodology is required to estimate the long-term advection or diffusion of chemically distinct water around the tunnel in the future.

The developed modelling and simulation methods can be applied to all phases of the HLW geological disposal project.

Contents

1 Introduction

The geological disposal of radioactive wastes for a given facility is expected to extend over a period of around 100 years to repository closure. Geological environments are likely be influenced for several decades due to the construction and operation of a large underground facility. In particular, groundwater flows into an underground facility would likely lead to significant changes in hydraulic pressure distribution and hydrochemical conditions. However, knowledge about the process of recovery from such environmental disturbance after the closure of the facility is limited at the moment (Dixon et al., 2009).

Japan Atomic Energy Agency (JAEA) is performing GREET (Groundwater REcovery Experiment in Tunnel) project for an understanding of the post-closure recovery of the geological environment in and around the Mizunami Underground Research Laboratory (MIU) construction site. In the GREET project, a part of research tunnel at 500 m depth is being filled with in-situ groundwater prior to the backfilling test with burial materials. These drift closure tests are preliminary studies for the facility closure of the MIU in future. Drift closure experiments without backfilling are rare when compared with previous international studies where the focus has been on backfilled drifts. The un-backfilled condition is suitable to carry out a repetitive drift-scale hydraulic tests and to understand simple hydrochemical process regarding cementing materials, amongst other processes.

The project aims to understand the relevant recovery processes of the geological environment during facility closure, to verify the hydro-mechanical-chemical (H-M-C) simulation methods for recovery processes in fractured granite and to develop monitoring techniques for the facility closure phase and appropriate closure methodologies taking recovery processes into account.

In the experiments, the baseline H-M-C-B (B: Biology) condition was identified prior to the excavation of closure test drift (CTD). Then excavation of CTD and isolation by the water-tight plug, and subsequent flooding with groundwater were conducted. Environmental disturbance and recovery were observed for more than 6 years. The collected data was used for the DECOVALEX-2019 Task C (reported here), which aimed to develop a modelling and simulation methodology for the environmental recovery process.

In Task C, three research teams, JAEA, Sandia National Laboratories in the United States (SNL), and Technical University of Liberec in the Czech Republic (TUL) were challenged to simulate the observed environmental changes. The simulation targets are the water pressure drawdown/recovery and the variation of water chemistry during the tunnel excavation and closure, as observed in the monitoring boreholes and in the CTD. In these simulation trials, a stochastic approach using a discrete fracture network (DFN) model and an equivalent continuum porous media (ECPM) model, and deterministic approach based on mixed-hybrid finite element methods were applied by each team to reproduce the hydraulic changes and Cl concentration in groundwater around the CTD. Furthermore, the reactive transport modelling and basic thermodynamic analysis were examined to capture the chemical evolution of isolated groundwater in the CTD.

1.1 Overview of Mizunami Underground Research Laboratory (MIU)

The Mizunami Underground Research Laboratory (MIU) is operated by the Japan Atomic Energy Agency (JAEA), in the Cretaceous Toki Granite in the Tono area, Central Japan. The MIU project is a broad-based, multi-disciplinary study of the deep geological environment, providing a scientific basis for the research and development of technologies needed for geological disposal. The MIU design consists of two shafts, and several horizontal research galleries (Figure 1).

1.1.1 Hydrogeological condition in the experiment site

Figure 2 shows the geological structures in and around the MIU construction site. In this site, Pliocene to Pleistocene rocks of the Seto Group (5 to 0.7 Ma) unconformably overlies Miocene sedimentary rocks of the Mizunami Group (20 to 15 Ma). The Mizunami Group in turn unconformably overlies a basement of Cretaceous granitic rocks, the Toki Granite (72.3 Ma; Shibata and Ishihara, 1979; Shikazono and Nakata, 1999). The middle and upper parts of the Mizunami Group, the Akeyo Formation and Oidawara Formation respectively (18 to 15 Ma), are composed of alternating shallow marine siltstone-sandstone. In contrast, the lower part of the Mizunami Group, the Toki Lignite-Bearing Formation (ca. 20 Ma) consists of lignite-bearing fluvial deposits.

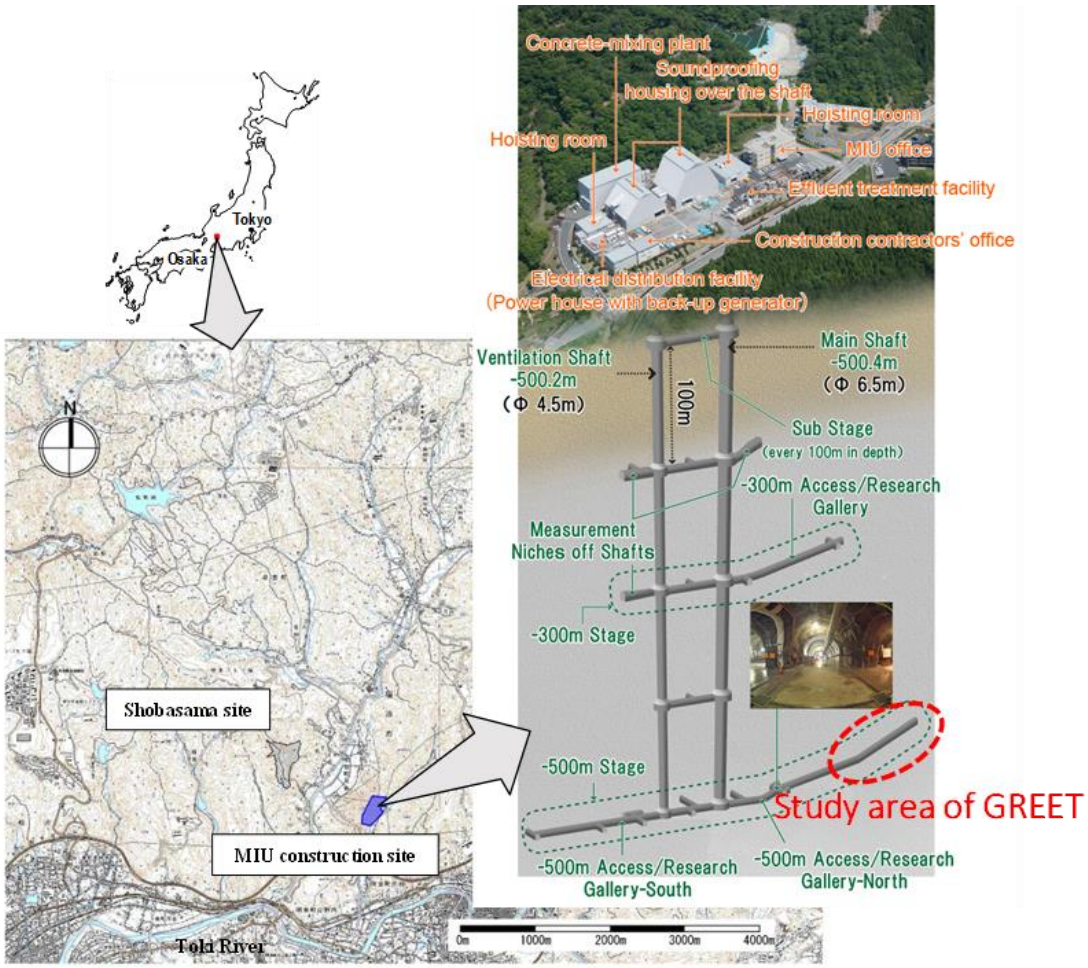

Figure 1. Location and layout of the MIU

The vertical shafts of the MIU facility penetrate through the Mizunami Group into the Toki granite at the unconformity, which is at about 170 m below ground level (GL) (Figure 2). The Toki granite of the Tono district, Central Japan, is a Late Cretaceous plutonic intrusive in the Sanyo Belt. The Toki granitic rocks consist of medium- to coarse-grained biotite granite and medium-grained hornblende-biotite porphyry, and are partly intruded by quartz porphyry and aplite dikes.

Toki granite can be divided into two structural domains, an upper highly fractured domain (UHFD) and a lower sparsely fractured domain (LSFD), based on the distribution of fracture frequency. In addition, a low-angle fracture zone (LAFZ) which is a significant water conducting feature has been identified in the UHFD, which zone distributed approximately GL-200 m. GREET experiment is being conducted in a part of the deepest stage of at the GL -500m in LAFZ. In addition, the presence of several faults has been confirmed and their geometry determined (Figure 2).

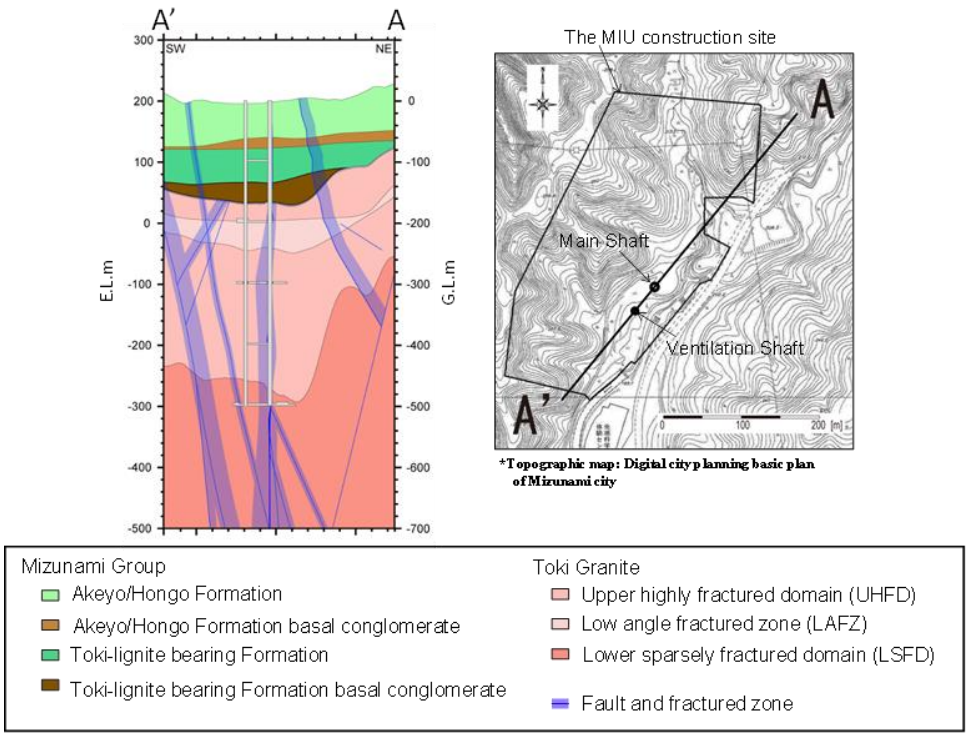

Figure 2. Estimated geological structures around the MIU construction site

Figure 3 shows the layout of shafts and galleries of the MIU and several monitoring boreholes drilled from the galleries. The design of the underground facility consists of a Main Shaft and Ventilation Shaft, two Access/Research galleries at 300 m and 500 m below ground level, and sub-stages at 100 m depths between two shafts. The length of 300 m Access/Research Gallery and 500 m Access/Research Gallery (North) is about 100 m. The shafts have been excavated by two 1.3 m blasting and mucking cycles followed by emplacement of a concrete liner in every 2.6 m section of shaft (Shimono et al., 2004). Pre-excavation grouting of a water-conducting fracture zone was carried out in both shafts and gallery. The construction of the shafts commenced in July 2003. The construction of the -500 m Stage was completed by the end of February 2014. GREET is being conducted in the deepest part of the -500m Stage.

Long-term hydrochemical monitoring was conducted in the boreholes in and around the MIU construction site in the Surface-based Investigations Phase to determine baseline conditions before the MIU facility was constructed (Figure 3). This monitoring has provided the basis on which to assess hydraulic and hydrochemical disturbances in response to the construction of the MIU.

From the results of various monitoring in the MIU, it is estimated that shallow groundwater infiltrated into deep parts of the granite, accompanying the changes in

hydraulic pressure distributions during construction and operation of the facility (Figure 4 and Figure 5). Changes of hydraulic and hydrochemical conditions from the baseline conditions are influenced by hydrogeological heterogeneities such as faults. It is important to understand the recovery process of the geological environment during underground facility closure.

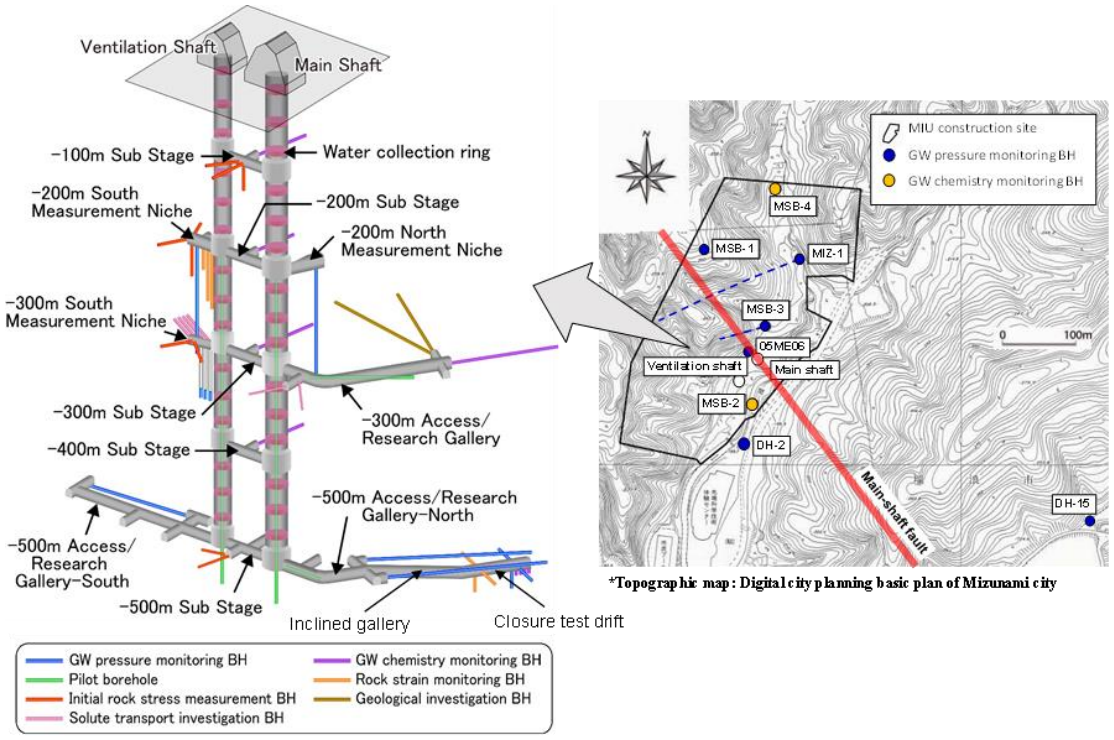

Figure 3. Layout of the MIU facility and monitoring boreholes

1.1.2 Groundwater REcovery Experiment in Tunnel (GREET)

The experiment gallery locates 500 m below ground level. The length of the experiment gallery is 46.5 m, the width is 5 m and height are 4.5 m (approx. 900m^3). The fracture distribution around the test drift, hydraulic and hydrochemical baseline have been identified by monitoring boreholes (Figure 6).

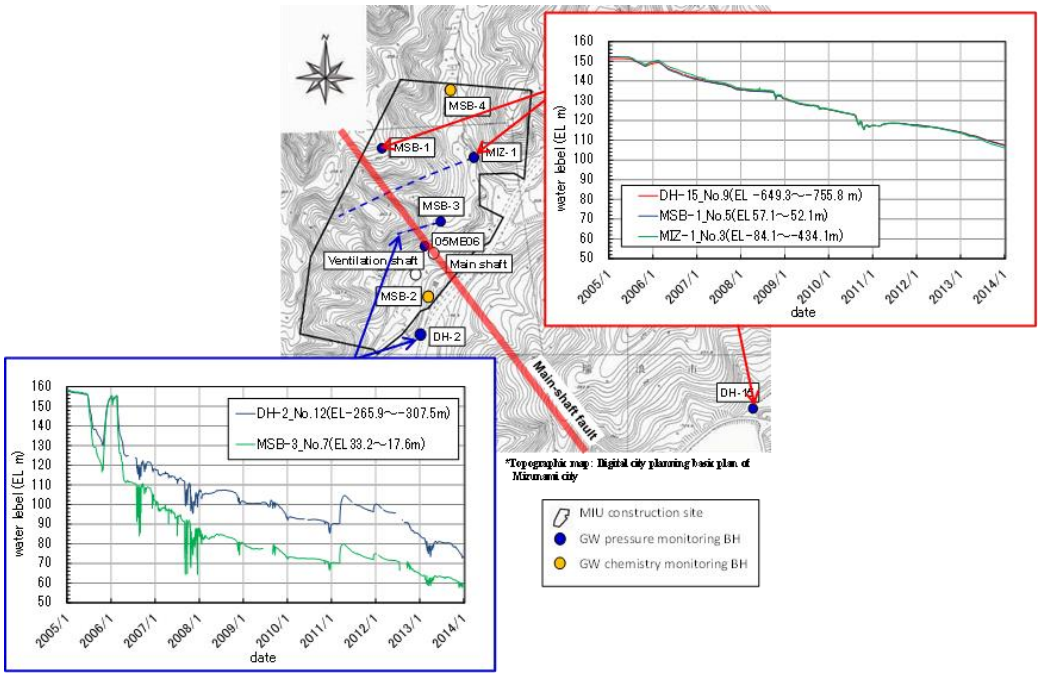

Figure 4. Pressure response in the granite due to construction of the MIU facility

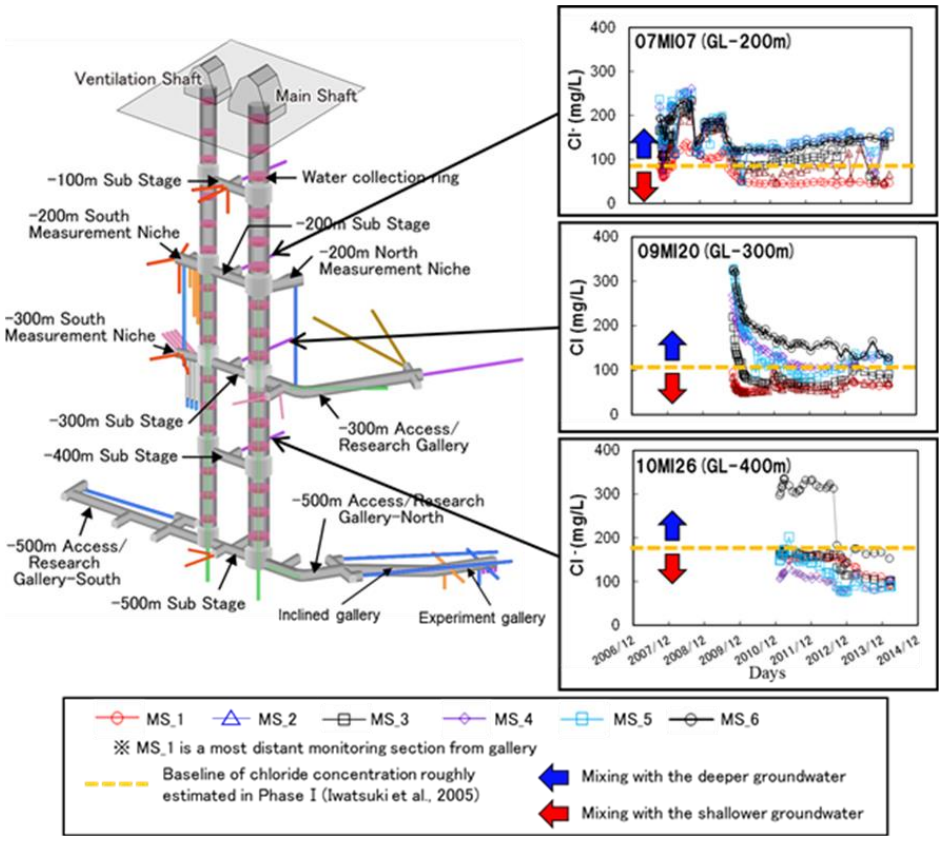

Figure 5. Long-term changes in salinity of groundwater at each Sub-stage

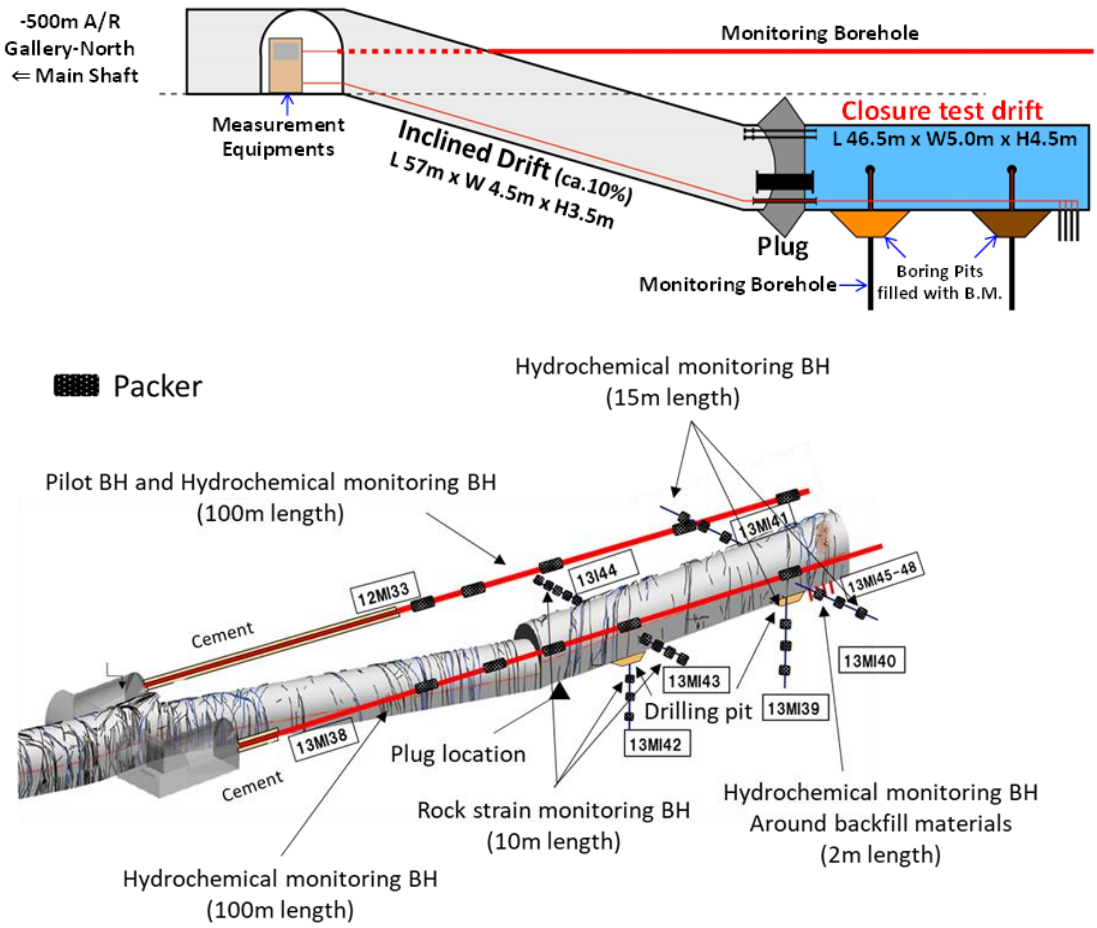

Figure 6. Preparing the experiment area for GREET

The experimental steps of the groundwater recovery experiment are shown in Figure 7. The overall approach was as follows; prior to construction of the experiment gallery, a pilot borehole, adjacent and parallel to the gallery, was drilled to estimate a baseline of hydraulic and hydrochemical conditions. Hydraulic and hydrochemical conditions and any changes during gallery construction were monitored in the borehole. Geological mapping of the gallery was conducted to characterize the fracture distribution.

Additional monitoring boreholes were drilled and an impervious plug installed at the entrance to the experiment gallery in order to understand and assess the recovery process in terms of hydraulic pressure changes, changes in hydrochemical conditions and in rock stress distribution around the experiment gallery during water filling and draining events. A backfill material test was then carried out using pit bored into the experiment gallery floor in order to accumulate data on saturation phenomenon of the backfill material and its influence on the hydrochemical environment in the rock mass.

Applicability of monitoring techniques and plug performance during a facility closure phase was validated based on the result. The simulations carried out in Task C were evaluated against the results of the experiment.

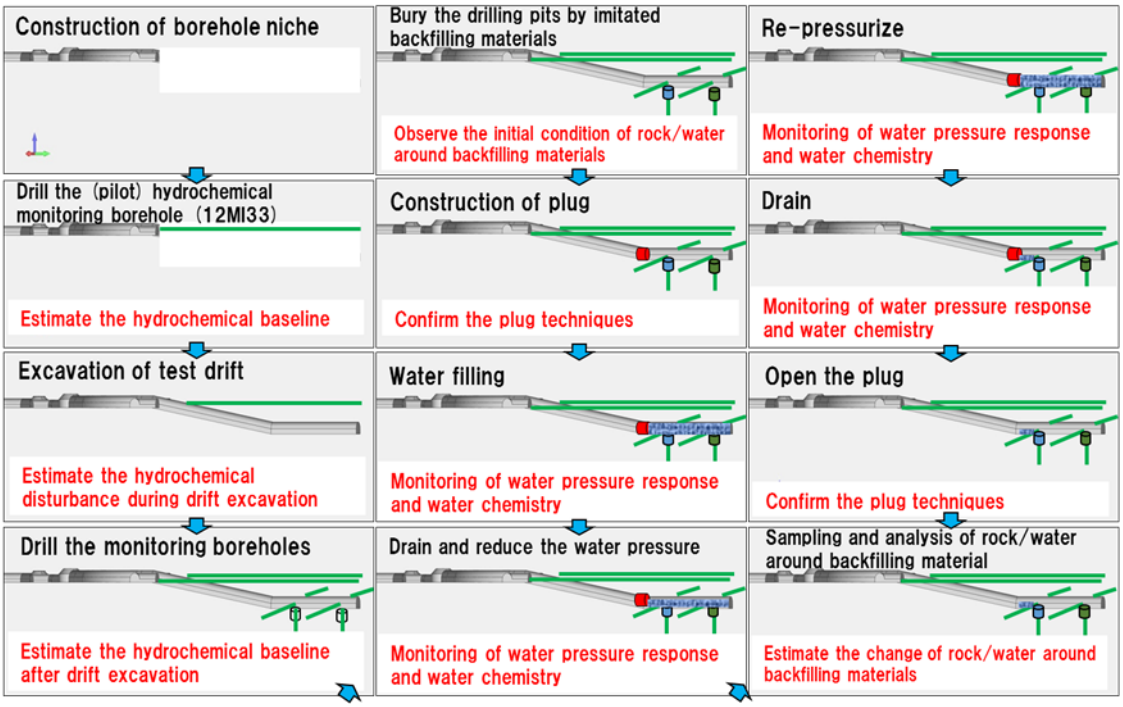

Figure 7. Outline programme for the GREET field experiments

Initial hydraulic pressures and hydrochemical distributions around the experiment gallery were determined using a multi-interval monitoring system in the 12MI33 borehole. This system also aimed to monitor hydraulic response and hydrochemical disturbance during the experiment gallery construction. After the construction of the experiment gallery, additional monitoring boreholes were drilled and a multi-interval monitoring system installed for observation of hydraulic pressure, hydrochemical and rock mechanics response during the water filling and draining events.

The main purpose of hydraulic and chemical monitoring is to observe the hydraulic response, chemical evolution and any heterogeneities influenced by fracture distribution in the rock mass. The main purpose of fibre-optical rock mechanics monitoring is to determine what may be induced by hydraulic pressure disturbance rock displacement and stress changes.

Seismic tomography and electrical resistivity surveys were carried out prior to and after the water filling and draining events in order to identify the excavation damaged zone

(EDZ) and any changes to the EDZ. Fracture distributions around gallery wall were characterized using ground penetrating radar.

The conceptual models to estimate the long-term evolution of geological environment around gallery wall were constructed based on the monitoring data. Then, the numerical simulation with those models was performed to support the conceptual models quantitatively.

1.2 Modelling and simulation in Task C

Generally, it is difficult to confirm the validity of the simulated results concerning the far future environments over several hundred years, so prediction should be performed using a simulation method that has been validated (i.e. model outcomes have been shown to give robust predictions when compared with the data, with uncertainties and errors taken into account) based on the short-term actual data as an alternative.

Therefore, it is essential to clarify the validity and accuracy of the prediction method by repeating the following tasks; advance prediction >> experiment and observation to collect the data >> confirmation of consistency between prediction results and observation results >> review of the prediction method, and improvement >> prediction by improved method >> confirmation of the validity (Figure 8).

1.2.1 Objective of simulation

The purpose of Task C through the modelling of GREET are a reproduction and quantitative evaluation of interactions between Hydro-Mechanical-Chemical (H-M-C) phenomena. In addition, the establishment of a modelling method for fractured media in H-M-C simulations is included in this task because prediction of disturbance of the geological environment through excavation through to repository closure is common issue. This is also one of the reasons that Task C was run in parallel with the progress of the GREET experiment, so that the performance of the adopted modelling approaches could be judged.

Spatial heterogeneity of hydrogeological properties has been observed in the volume of interest. Characterization of fracture distribution at drift scale using modelling tools such as Discrete Fracture Network (Long et al., 1989) modelling is included as an objective. Moreover, several cycles of water pressurizing and depressurizing by water inflow and

drainage were planned in this project. From such cycles, it is possible to verify and validate of constructed model and modelling methodology.

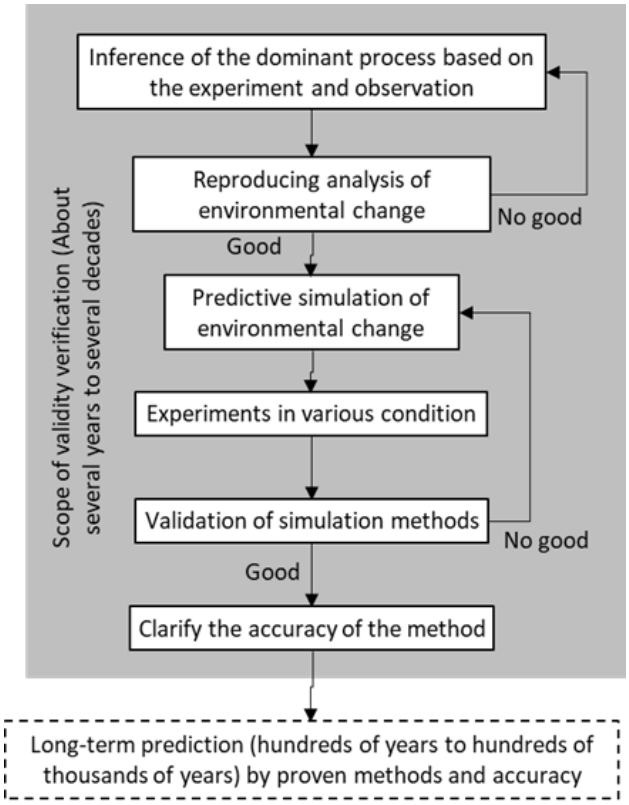

Figure 8. R & D of predictive analysis method of long-term environmental disturbance

To achieve this objective, Task C was scheduled along the actual operation of the experiment. The simulation works in Task C were divided into three steps (Figure 9 and Figure 10).

- In the Step 1, a blind simulation was conducted to verify the basic concept and methods of the prediction analysis of the environmental disturbance of the baseline condition during the excavation of Closure test drift (CTD) using baseline hydrogeological and hydraulic/hydrochemical data.
- In the Step 2, calibration of models was conducted based on the observation data during the CTD excavation. Furthermore, blind simulations were conducted to infer the recovery by the water-inflow.
- The Step 3 was calibration of previous models and simulations to predict the steady state condition of the wider geological environment.

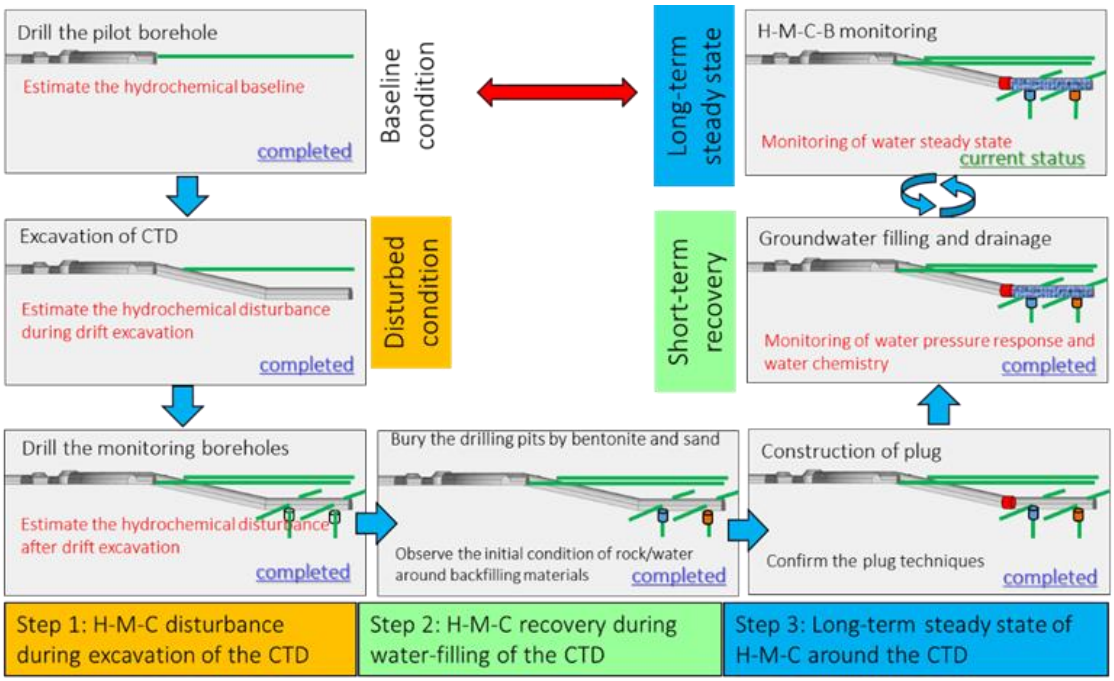

Figure 9. Simulation image of Task C

Step	Simulation ⟺	Validation data
Step 1: H-M-C disturbance during excavation of the CTD	• Water pressure drawdown • Groundwater chemistry (pH-Eh condition) • Groundwater inflow rate	• Water pressure and groundwater chemistry in monitoring boreholes during the excavation • Groundwater inflow rate
Step 2: H-M-C recovery during water filling of the CTD	• Water pressure recovery • Groundwater chemistry (pH-Eh condition) • Rock displacement	• Water pressure, groundwater chemistry and rock displacement in CTD and monitoring boreholes after the water filling
Step 3: Long-term steady state of H-M-C around the CTD	• Water pressure • Groundwater chemistry (pH-Eh condition) • Rock displacement	• Water pressure, groundwater chemistry and rock displacement in CTD and monitoring boreholes during monitoring

Figure 10. Simulation and validation data in each Step

1.2.2 General setting of numerical simulation

In Task C, the scale of modelling area, mesh size and degree of heterogeneity for numerical simulation are not standardized because this condition should depend on the method to set the boundary condition, computer resources that each group uses, etc.

On the other hand, it is important to standardize the visualization area and output points for the comparison of numerical simulation results of each group.

The mandatory visualization area in 150 m × 100 m × 100 m square domain as shown in Figure 11, was set to the surroundings of the inclined drift and the CTD. The coordinate information of the visualization area is shown in Table 1. Output points of numerical simulation for graphical comparison at specific monitoring boreholes are as shown in Figure 6. The number of output points increased with the progress of step in Task C because the number of available data for comparison increased as the step proceeds.

The data used for modelling and simulation in each Step are included in the Appendix A.

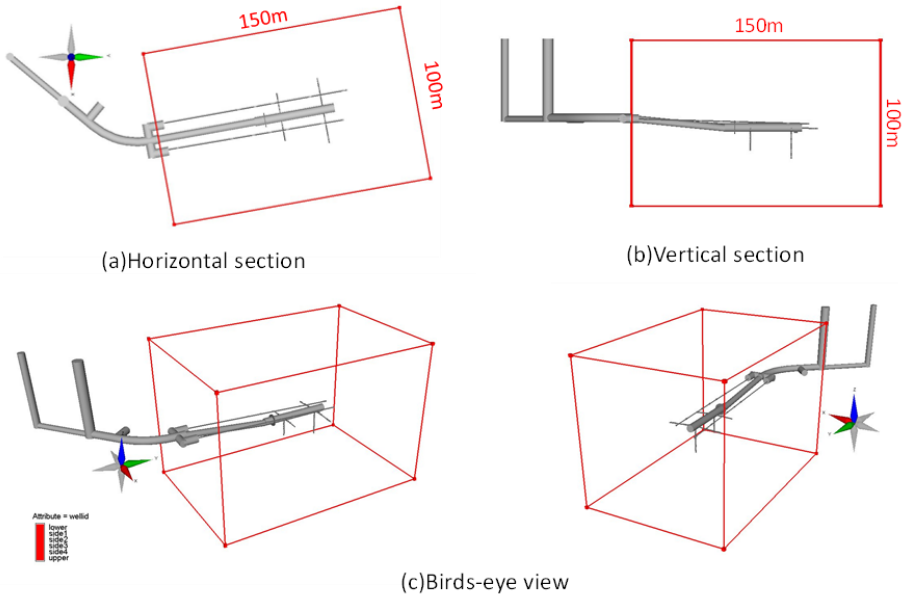

Figure 11. The visualization area of numerical results in task C

Table 1. The coordinate information of the visualization area

E-W(m)	N-S(m)	E.L.(m)	
6522.7	-68943.5	-250	Upper boundary
6496.1	-68795.9	-250	Upper boundary
6397.7	-68813.7	-250	Upper boundary
6424.3	-68961.3	-250	Upper boundary
6522.7	-68943.5	-350	Lower boundary
6496.1	-68795.9	-350	Lower boundary
6397.7	-68813.7	-350	Lower boundary
6424.3	-68961.3	-350	Lower boundary

2 Step 1: modelling of “environmental disturbance by the tunnel excavation”

In Step 1, previous hydrogeological data and newly gained data from the pilot borehole investigation (12MI33) were provided to each team and the following simulation targets were set to compare the results with each other.

- Inflow rate into the incline and closure test drift
- Time variation of water head in the monitoring borehole
- Cl concentration in the monitoring borehole

2.1 Data for the modelling and simulation

2.1.1 Tunnel excavation

The experimental area including the monitoring borehole was established from 2013 to 2015 (Figure 12). The excavation of CTD began in April 2013 and was completed in October. Borehole 12MI33 was drilled before the tunnel excavation. After the excavation, another monitoring borehole named 13MI38-44 was drilled from the CTD (Figure 6). The CTD walls, except the floor, were covered with 5-10 cm deep shotcrete for safety. Ordinary portland cement (OPC) and low heat portland cement was used for the shotcrete and concrete plug, respectively. During the tunnel excavation, fracture orientation, frequency, length, water inflow rate, etc. were mapped to illustrate the hydrogeological property around the CTD (Figure 13).

2.1.2 Preliminary information

Around the MIU site, geological investigation such as the drill core description, borehole TV observation, X-Y calliper logging, flow meter logging, and hydraulic packer test, geophysical logging (electrical, micro electrical, natural gamma, spectral gamma, neutron, density, acoustic, borehole radar, etc.) was conducted at over 60 boreholes drilled from ground surface.

The borehole 12MI33 is parallel to the CTD at a distance of 5 m from the drift. Geological surveys, hydraulic tests and water sampling were conducted in the borehole, and the baseline condition before CTD drilling was estimated. The borehole had been divided

into 6 sampling intervals using hydraulic packers. Before the CTD excavation, snapshot data on baseline water pressure and chemistry was obtained. Because the excavation was conducted by blasting, the measurement during the CTD excavation was paused. After the CTD excavation, the water pressure was monitored continuously, and groundwater was collected from each packer interval 3 times a year. As an example, the outline of the geological data set collected from borehole 12MI33 is shown in Figure 14 and Figure 15.

The CTD is located in the 'Lower Sparsely Fractured' domain of the granitic rocks. Hydraulic parameters at that depth was measured by hydraulic packer tests in the boreholes (Figure 16). Average hydraulic conductivity of this rock domain is of the order of 10^{-8} m/s. Other hydraulic and chemical parameters are shown in Table 2 and Table 3.

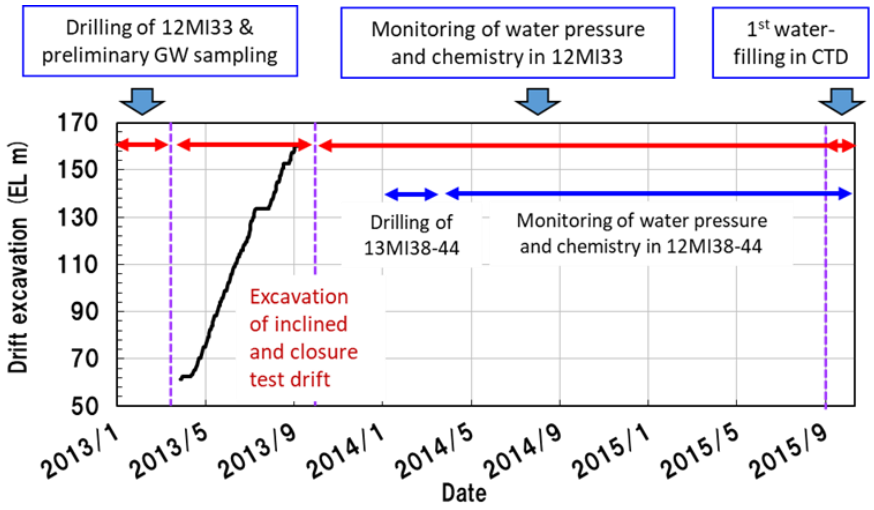

Figure 12. Log record of the excavation of the CTD

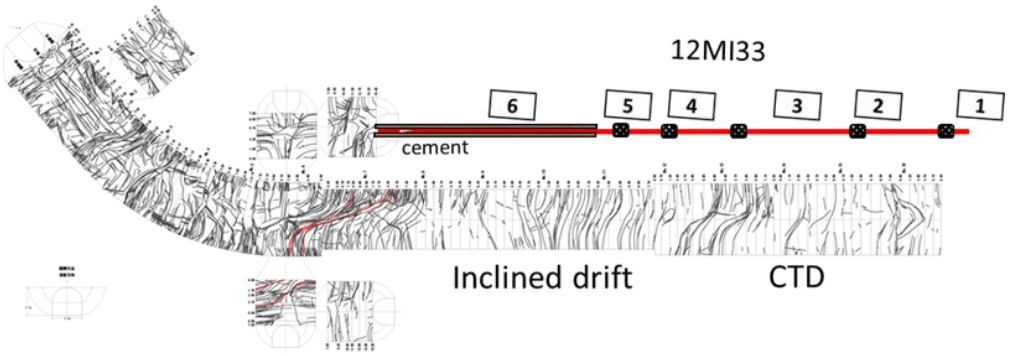

Figure 13. Fractures observed in inclined and closure test drift

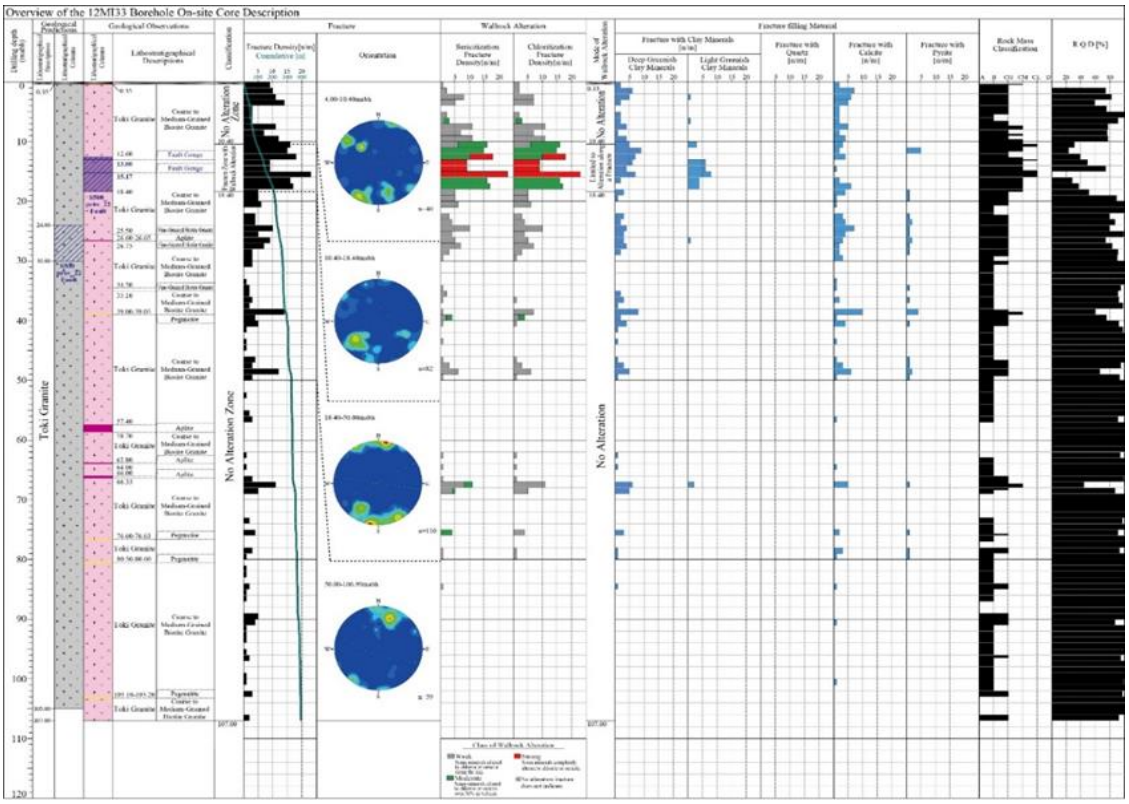

Figure 14. Fracture and mineral data obtained in 12MI33

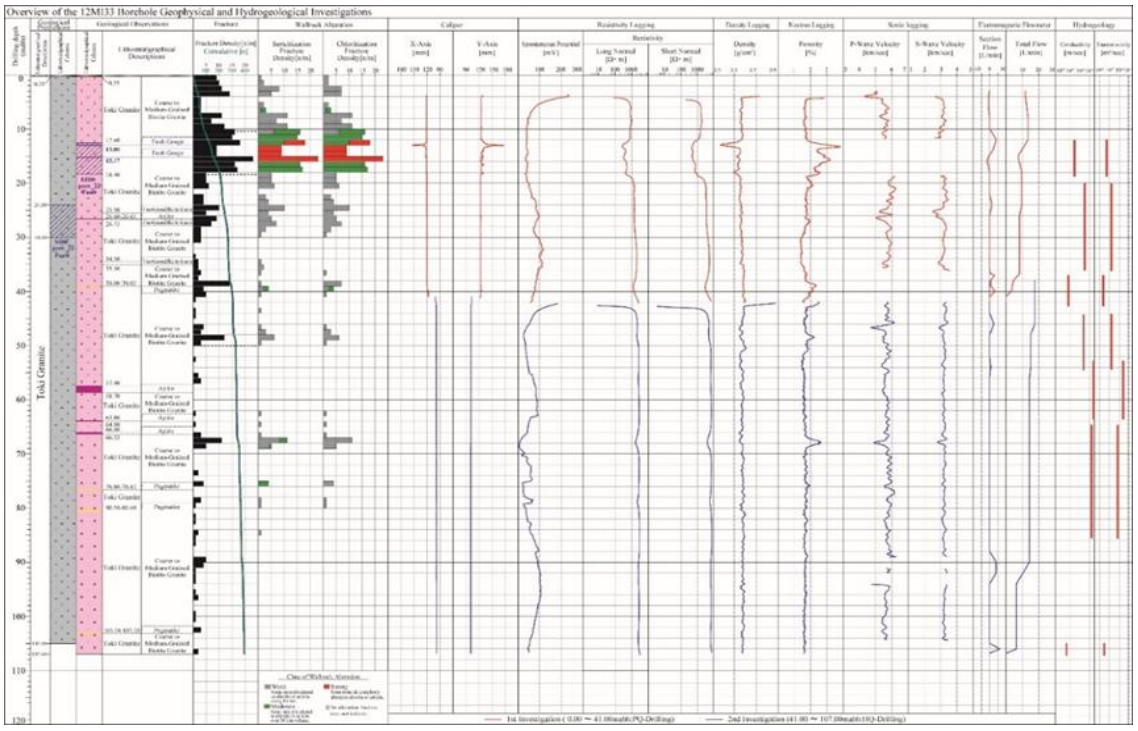

Figure 15. The result of geophysical logging in 12MI33

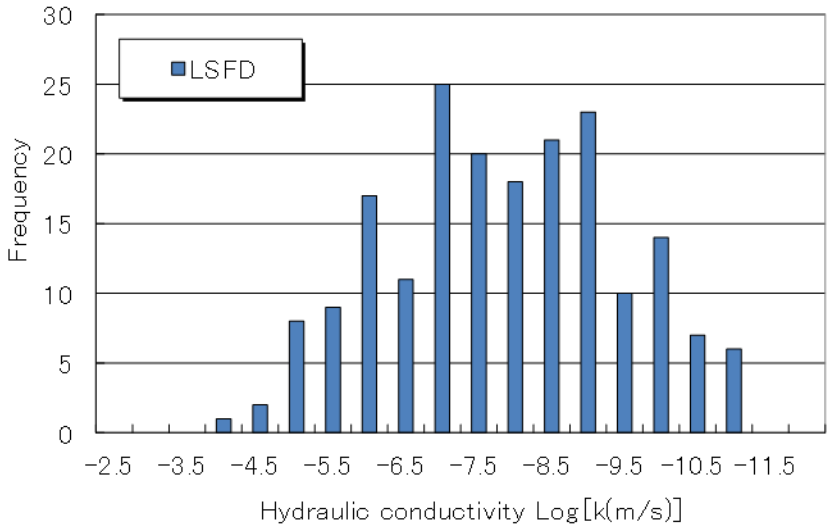

Figure 16. Hydraulic conductivity around the CTD

Table 2. Result of hydraulic tests in 12MI33

Borehole	Test No.	Top of test section (mabh)	Bottom of test section (mabh)	Test length (m)	Inflow rate (L/min)	Hydraulic pressure (MPa)	Hydraulic pressure (m)	Depth of test section (Elm)	head (Elm)	T (m^2/sec)	k (m/sec)	S	Ss (1/m)	Analysis method	Test method
12MI33	No.1	12.10	18.90	6.80	2.50	3.73	380.40	-298.55	81.85	1.78E-07	2.62E-08	7.95E-08	1.17E-08	Cooper-Jacob	RW
	No.2	37.10	42.56	5.46	7.50	4.02	410.05	-299.85	110.20	6.01E-07	1.10E-07	1.08E-15	1.97E-16	nSIGHTS	RW
	No.2'	20.10	36.10	16.00	0.10	3.84	391.49	-299.20	92.29	9.78E-08	6.11E-09	1.21E-08	7.59E-10	Cooper	PW
	No.3	44.20	54.50	10.30	1.90	3.98	406.34	-300.35	105.99	8.65E-08	8.40E-09	6.93E-09	6.73E-10	nSIGHTS	PW1
	No.4	53.20	63.50	10.30	0.42	4.00	407.59	-300.80	106.79	4.96E-09	4.82E-10	4.45E-04	4.32E-05	Cooper	PW1
	No.5	65.20	85.50	20.30	0.50	4.00	408.01	-301.70	106.31	1.93E-08	9.53E-10	1.73E-06	8.53E-08	Cooper	PW1
	No.6	105.20	107.00	1.80	5.20	4.02	409.65	-303.35	106.30	4.91E-07	2.73E-07	1.58E-12	8.75E-13	nSIGHTS	RW/RWS

Table 3. Result of groundwater sampling and analysis in 12MI33

Sample Name	pH	Na^+	K^+	Ca^{2+}	Mg^{2+}	DIC	Alkalinity	SO_4^{2-}	F^-	Cl^-	Si	Al	T-Fe	Mn
	—	mg/L	mg/L	mg/L	mg/L	mg/L	meq/L	mg/L	mg/L	mg/L	mg/L	mg/L	mg/L	mg/L
12MI33_No.1	8.5	167	0.8	60	0.1	3.8	0.35	<0.1	6.8	343	6.4	0.04	0.062	0.018
12MI33_No.2	8.4	170	0.8	70	0.1	4.2	0.35	0.2	6.9	366	6.5	0.01	0.008	0.013
12MI33_No.6	8.5	183	0.9	80	0.1	3.7	0.31	0.2	6.3	408	6.5	<0.01	0.008	0.009

3 Results of Step 1 modelling (JAEA)

3.1 Modelling strategy and approach

JAEA used the H-M-C coupled simulator “Couplys”, JAEA’s in-house software. Couplys consists of “Thames”, “Dtransu3D” and “PHREEQC” (Figure 17). “Thames” is a full coupled simulator of the hydro-mechanical problem, “Dtransu3D” solves the advective-dispersive problem by the Eulerian-Lagrangian method and “PHREEQC” addressed hydrochemical problems. These three simulators are executed sequentially. A Continuum Porous Medium (CPM) model was applied as the modelling approach in Step 1. The CPM model was a base model to evaluate an improved model by introducing heterogeneity representing fracture as step in task proceeds. In Step 1, the simulation of groundwater flow was solved as part of the H-M-C problem. The fully coupled problem of groundwater flow and mechanics was solved and interaction between hydraulic pressure and rock stress was considered.

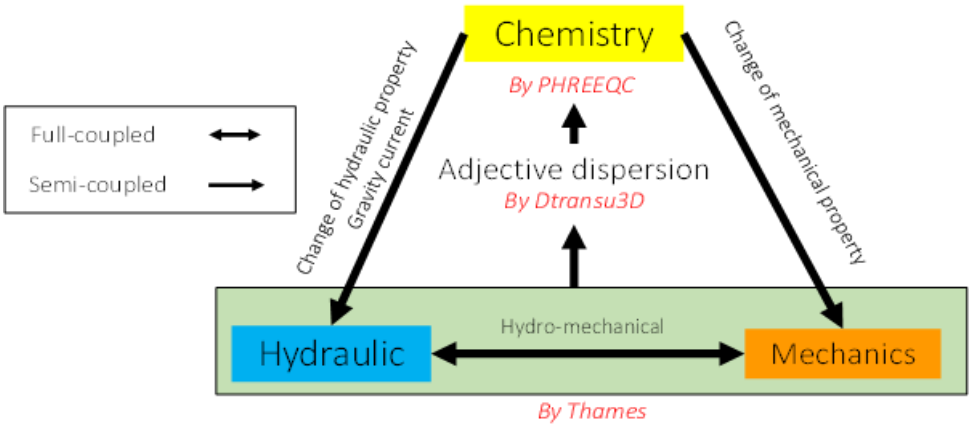

Figure 17. Modelling method of Couplys, H-M-C coupled simulator

3.2 Model setting for simulation

Thames simulates T-H-M components, and transport (advection-diffusion) component is then calculated using Dtransu3D. The Thames constitutive model is based on Biot’s theory for coupling of hydro-mechanical behaviour and Duhamel-Neuman’s theory for

the thermal effect on deformation. Then, the energy balance equation is solved for thermal transfers (Koyama et al., 2013). The detail of the theory and implementation is described in Kobayashi and Ohnishi (1986) and Ohnishi et al. (1987). Dtransu (Nishigaki et al., 2001) solves the advective-diffusive equation according to the flow calculated by Thames. Dtransu employs the Eulerian-Lagrangian method for numerical accuracy. This simulator, in addition to PHREEQC, is incorporated into the simulation of T-H-M-C process as Couplys.

The distribution of geological units in the modelling area is shown in Figure 18. The UHFD, Elements near the tunnel surface were discretized with a fine mesh for modelling the shape of the tunnel, and location of monitoring sections and the tunnel. The shortest length of the edge in the fine mesh was set to about 1 m for evaluating more detailed variation of geological environment near the tunnel considering the convergence of the simulation in Step 1. The simulation domain was discretized with hexahedral elements. Mesh size was set to larger as it was far from the tunnel. The total number of elements was planned to be less than 100,000 elements. These restrictions of model discretization come from limit of simulation code ability.

3.2.1 Parameters

(1) Hydrogeology

Hydraulic parameters for the LSFD for CPM modelling were set based on the previous result of the MIU project (Table 4. Hydraulic parameters of LSFD). Logarithmic mean value of the results of hydraulic packer tests in 12MI33 borehole (Table 5) were applied as the hydraulic conductivity of the LSFD.

(2) Rock mechanics

Elastic modulus, porosity, Poisson's ratio, etc. was measured by core sample tests performed as a part of rock stress measurements and were used to define the rock mechanics parameters (Table 6).

(3) Chemistry

The advective-dispersive analysis was focused on disturbance of Cl concentration in groundwater due to hydraulic pressure change during drift excavation. Input parameters for advective-dispersive analysis are shown in Table 4.

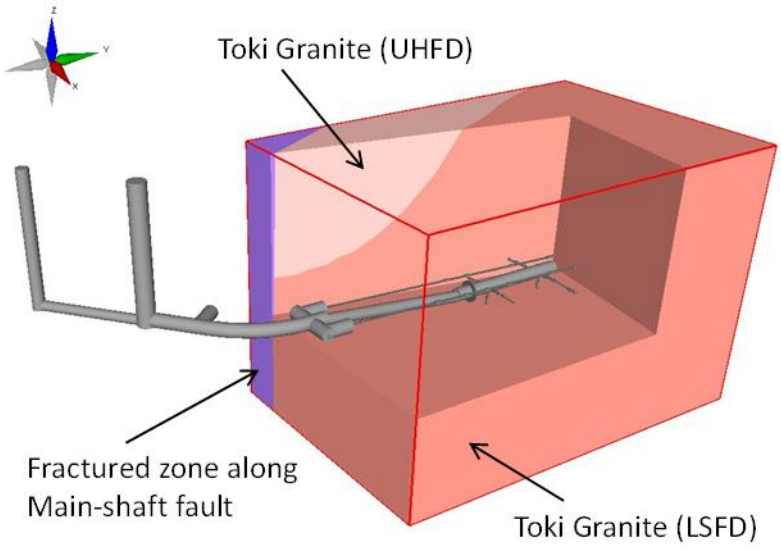

Figure 18. Distribution of geological units in the modelling area

Table 4. Hydraulic parameters of LSFD

Hydrogeological units	Hydraulic conductivity (ms^{-1})	Specific storage coefficient (m^{-1})	Porosity	Vertical dispersion length (m)	Horizontal dispersion length (m)	Effective diffusion coefficient (m^2/s)	Retardation coefficient	Damping ratio
	logK	logSs						
Toki Granite (LSFD)	-8.0	-6.0	0.001	4.3	0.43	1.0E-12	1.0	0.0

Table 5. Result of hydraulic packer test in 12MI33 borehole

Borehole	Test No.	Top of test section (mabh)	Bottom of test section (mabh)	Test length (m)	Inflow rate (L/min)	Hydraulic pressure (MPa)	head (Elm)	T (m^2/s)	k (m/s)
12MI33	No.1	12.10	18.90	6.80	2.50	3.73	81.85	1.78E-07	2.62E-08
	No.2	37.10	42.56	5.46	7.50	4.02	110.20	6.01E-07	1.10E-07
	No.2'	20.10	36.10	16.00	0.10	3.84	92.29	9.78E-08	6.11E-09
	No.3	44.20	54.50	10.30	1.90	3.98	105.99	8.65E-08	8.40E-09
	No.4	53.20	63.50	10.30	0.42	4.00	106.79	4.96E-09	4.82E-10
	No.5	65.20	85.50	20.30	0.50	4.00	106.31	1.93E-08	9.53E-10
	No.6	105.20	107.00	1.80	5.20	4.02	106.30	4.91E-07	2.73E-07

Table 6. Result of rock mechanical test in 12MI35 borehole

13MI35									
Borehole information	Direction of borehole	N174.7E 7.8							
	Depth (m)	20.5							
	Number of measurement	6							
Measurement information	Measurement method	CCBO							
	Section name	OC35-1	OC35-2	OC35-3	OC35-4	OC35-5	OC35-6	OC35-7	OC35-8
	Section depth(m)	12.66	14.16	14.16	14.26	15.05	16.03	17.03	18.03
Elastic property	Young's modulus(GPa)	53.6	52.6(OC35-1)	–	–	54.8	–	46.7	–
	Poissons ratio	0.22	0.25(OC35-1)	–	–	0.22	–	0.25	–
Stress tensor(MPa)	σx	9.01	–	–	13.7	7.94	8.06	6.87	7.7
	σy	28.85	–	–	5.29	12.26	11.28	12.07	10.59
	σz	9.82	–	–	6.65	7.6	8.23	6.9	8.15
	τxy	2.96	–	–	1.72	0.07	1.05	2.51	−4.26
	τyz	0.16	–	–	0.21	1.92	−1.17	−1.61	−1.09
	τzx	−0.84	–	–	0.33	1.66	1.42	1.58	0.5
Principle stress	σ1	29.28	–	–	14.06	13.03	11.77	13.22	13.88
	H (Horizontal direction)	8	–	–	79	8	−170	−161	145
	V (Vertical direction)	0	–	–	3	22	14	9	12
	σ2	10.25	–	–	6.64	8.98	9.56	8.41	7.92
	H (Horizontal direction)	−82	–	–	−41	112	86	99	−55
	V (Vertical direction)	63	–	–	84	31	45	50	78
	σ3	8.14	–	–	4.94	5.78	6.24	4.21	4.63
	H (Horizontal direction)	98	–	–	169	−111	−67	−63	54
	V (Vertical direction)	27	–	–	5	51	42	38	4

3.2.2 Initial condition

The initial condition for hydraulic head was set based on the monitoring data from the boreholes around the CTD. 12MI33 and MIZ-1 boreholes are located in the modelling area and 09MI21 is located at 300 m below ground level (Figure 19). The hydraulic head of these monitoring boreholes before the drift excavation was almost same value, therefore a uniform distribution of hydraulic head in the modelling area was applied as an initial condition (Table 7).

The Cl concentration in groundwater with depth was estimated from the monitoring data (Table 8). A vertical gradient of Cl concentration assuming a linear approximation was considered as an initial condition.

3.2.3 Boundary condition and drift excavation modelling

The boundary condition of the model boundary was set according to the initial condition of modelling area. Atmospheric pressure was set at the drift wall as a boundary condition of hydraulic pressure (essentially assuming 100% water relative humidity in the tunnel). The free boundary condition was used as a boundary condition of Cl concentration and rock stress. The boundary condition is shown in Figure 20.

The excavation progress of the inclined drift and the CTD was simplified for the purposes of the numerical simulation (Figure 21). Drift excavation was modelled by the

progressive removal of elements that form the drift according the to the excavation stage. The total simulation term is about 1 year; 180 days for simulation of excavation of inclined drift and the CTD, and 180 days for simulation of the post-excavation behaviour.

3.3 Sensitivity cases

Sensitivity analyses focused on the uncertainty of geological parameters and the boundary condition during Step 1 was performed in order to understand the influence of key parameters. The results of sensitivity analyses are useful information for model calibration of later steps. Sensitivity parameters are shown in Table 9.

- Distribution of hydraulic pressure, rock stress and Cl concentration on the horizontal and vertical slices along the CTD was visualized at several time steps in the numerical simulation of drift excavation.
- Disturbance of hydraulic pressure and Cl concentration due to drift excavation at the monitoring section of the borehole, 12MI33 was shown graphically. The coordinate information of monitoring section in 12MI33 is shown in Table 10.

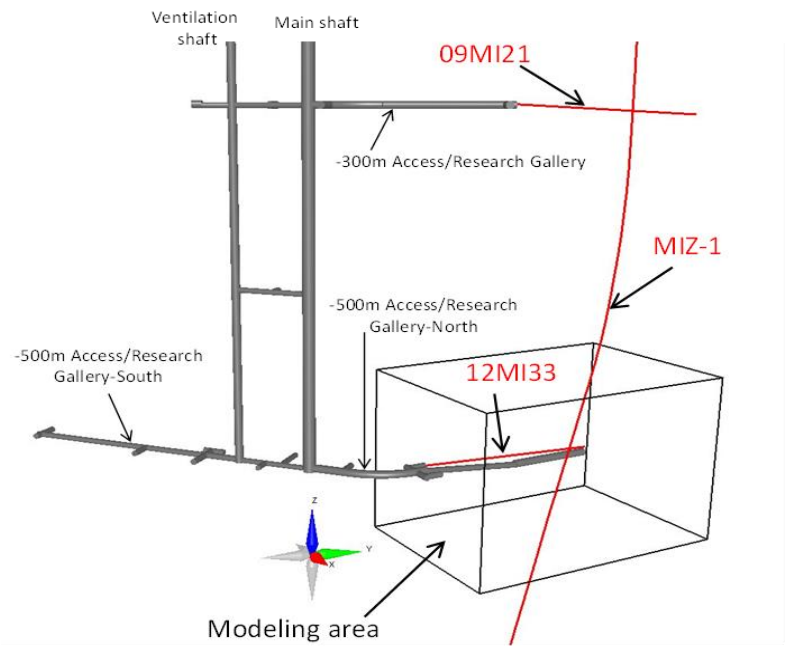

Figure 19. Location of monitoring boreholes around the CTD

Table 7. Initial condition of hydraulic pressure for numerical simulation

Borehole	Section ID	Top of section	Bottom of section	Hydraulic head (m)	Remarks
12MI33	No.1	12.1 mabh	18.9 mabh	81.8	Hydraulic packer test data
	No.2	37.1 mabh	42.6 mabh	110.2	
	No.2'	20.1 mabh	36.1 mabh	92.3	
	No.3	44.2 mabh	54.5 mabh	106.0	
	No.4	53.2 mabh	63.5 mabh	106.8	
	No.5	65.2 mabh	85.5 mabh	106.3	
	No.6	105.2 mabh	107.0 mabh	106.3	
MIZ-1	No.3	-84.1 E.L.m	-434.1 E.L.m	111.9	Long-term monitoring data (2013/3/31)
09MI21	No.1	0.0 mabh	66.1 mabh	102.8	
	No.2	67.1 mabh	77.1 mabh	111.3	
	No.3	78.1 mabh	88.1 mabh	107.8	
	No.4	89.0 mabh	103.0 mabh	111.0	
Initial condition of hydraulic pressure in the simulation area				110.0	Uniform distribution

Table 8. Initial condition of Cl concentration for numerical simulation

Borehole	Date	Monitoring point (mabh)			Cl^- (mg/L)	Average of Cl^- (mg/L)	Monitoring depth (E.L.m)
09MI21-1-21	2013/3/11	-0.6	-	66.1	198	189	-100
09MI21-2-21	2013/3/11	67.1	-	77.1	193		
09MI21-3-21	2013/3/11	78.1	-	88.1	150		
09MI21-4-21	2013/3/11	89.0	-	103.0	214		
12MI33_Pumping test _No.1(3)	2013/2/19	12.1	-	18.9	344	380	-300
12MI33_Pumping test _No.2(3)	2013/2/18	37.1	-	42.6	366		
12MI33_Pumping test _No.6(3)	2013/3/8	105.2	-	107.0	409		
12MI33_Zone 1	2013/3/18	105.4	-	107.0	431		
12MI33_Zone 1	2013/6/27	105.4	-	107.0	376		
12MI33_Zone 2	2013/6/27	85.7	-	104.5	413		
12MI33_Zone 3	2013/6/27	64.0	-	84.8	401		
12MI33_Zone 4	2013/3/19	53.8	-	63.1	327		
12MI33_Zone 4	2013/6/27	53.8	-	63.1	329		
12MI33_Zone 5	2013/6/27	44.1	-	52.9	402		
Initial condition of chloride ion concentration in the simulation area					C=-0.9553*Z+93.225 C: Chloride ion concentration (mg/L) Z: Depth (E.L.m)		

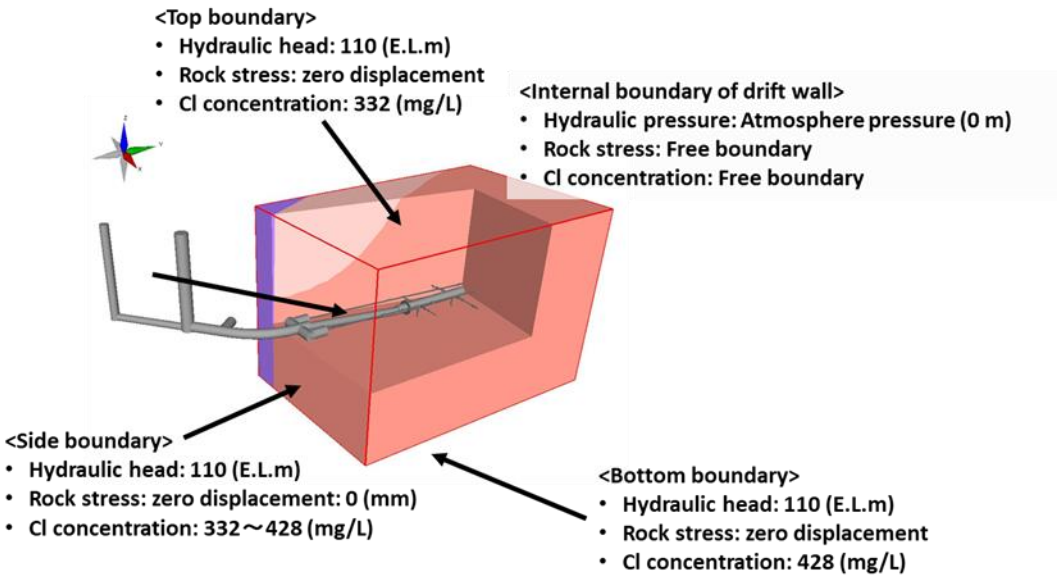

Figure 20. Boundary condition for numerical simulation

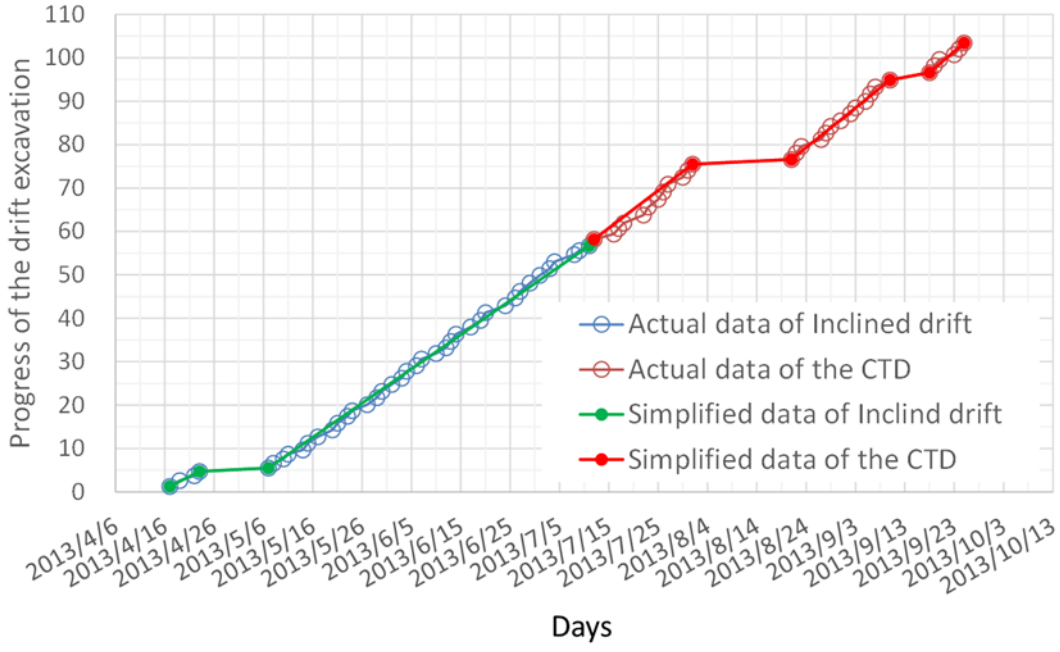

Figure 21. Input condition of drift excavation for numerical simulation

Table 9. Sensitivity parameters

Sensitivity parameter		Outline
Paramters	Hydrogeology	-To understand influence of variability of hydraulic conductivity and specific storage coefficient -Several cases
	Rock mechanics	-To understand influence of variability of poisson's ratio and Young's modulus -Several cases
	Chemistry	-To understand influence of variability of porosity -Several cases
Boundary condition	Model boundary (Modeling area)	-To understand influence of boundary condition of modeling area as size of modeling area -3 cases, reference model, twice and five times the size of model
	Internal boundary of drift wall	-To understand influence of internal boundary condition of drift wall as modeling of shotcrete -2 cases: reference model, modeling of shotcrete of drift wall

Table 10. The coordinate information of monitoring section in 12MI33 borehole

Section ID	Top			Middle			Bottom		
	E-W(m)	N-S(m)	E.L.(m)	E-W(m)	N-S(m)	E.L.(m)	E-W(m)	N-S(m)	E.L.(m)
12MI33_P1	6445.46	-68845.50	-303.27	6445.30	-68844.80	-303.30	6445.19	-68844.00	-303.36
12MI33_P2	6448.96	-68864.90	-302.24	6447.30	-68855.70	-302.70	6445.63	-68846.50	-303.22
12MI33_P3	6452.81	-68886.20	-301.11	6451.00	-68876.00	-301.60	6449.13	-68865.80	-302.19
12MI33_P4	6454.62	-68896.30	-300.57	6453.80	-68891.80	-300.80	6452.98	-68887.20	-301.06
12MI33_P5	6456.34	-68905.80	-300.07	6455.60	-68901.50	-300.30	6454.78	-68897.20	-300.52
12MI33_P6	6464.16	-68949.20	-297.76	6460.30	-68928.00	-298.90	6456.50	-68906.70	-300.02

3.4 Discretization of model domain

Figure 22 shows the mesh used for finite element modelling. The total number of nodes and hexahedral elements are 145,440 and 136,560 before the excavation of inclined and CTD tunnel and 145,680 and 137,040 at the end of excavation. We modelled the tunnel excavation by removing the elements located at tunnel step by step and the number of elements and nodes change during simulation. The number of elements is decreased for the modelling of step by step according to the exaction history for the simulation of

excavation. The size of whole calculation domain is 317.858 m × 213.25 m × 208.25 m that is larger than focused domain described in section 3 to avoid the boundary effects.

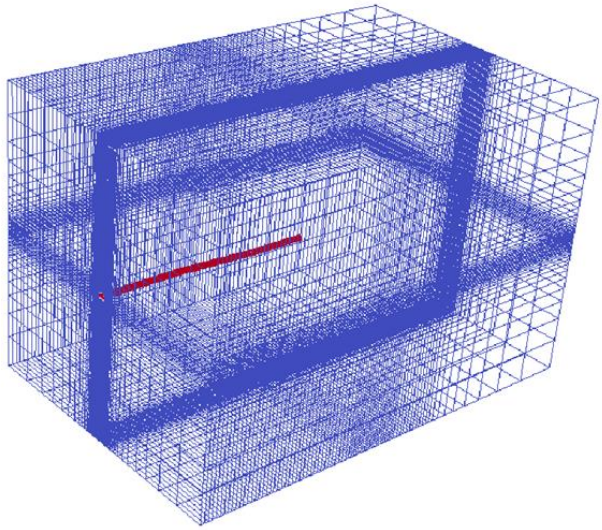

Figure 22. Mesh for JAEA Step 1 simulation

3.5 Prediction results of the disturbance during the excavation of CTD using the homogeneous continuum model

3.5.1 Spatial distribution of hydraulic pressure, displacement and Cl concentration around the CTD

Figure 23 shows the simulated spatial distribution of hydraulic head. Simulation results before excavation of research tunnel, the end of excavation of the inclined drift and at end of excavation of the CTD are shown, respectively. In each column, two horizontal sections and a vertical section including the CTD are shown. Hydraulic pressure drops around the tunnel and the area expands according to the length of tunnel excavation concentrically due to the homogeneous hydraulic properties.

Figure 24 is the spatial distribution of displacement. These results are arranged in the same manner as those of hydraulic pressure. Compressive deformation occurs by excavation of the research tunnel. We performed coupled simulation of the hydro-mechanical problem and these deformations are affected by both effects of the release

of stress according to the excavation of tunnel and change of pore pressure. The largest deformation appears at the tip of tunnel face during excavation.

Figure 25 shows the spatial distribution of Cl concentration. For this simulation, we didn't employ Couplys due to numerical accuracy issues, but use the original Dtransu code that consists of Couplys and open source simulator for the advective-diffusive problem by Eulerian Lagrangian method. The distribution of concentration around tunnel is slightly affected by excavation of the tunnel. Groundwater flow towards the research tunnel advects the Cl concentration. Both low and high concentration zones move to tunnel slightly by this flow. Around the floor of the entrance of the inclined tunnel, a high concentration zone appears. In addition, a low concentration zone also appears at the entrance of CTD. It is estimated that high and low concentrations are influenced by the setting of the time step for simulation. In other words, convergence of simulation is not sufficient. Shorter time steps would be needed to set for the removal of these overestimates and higher accuracy estimation.

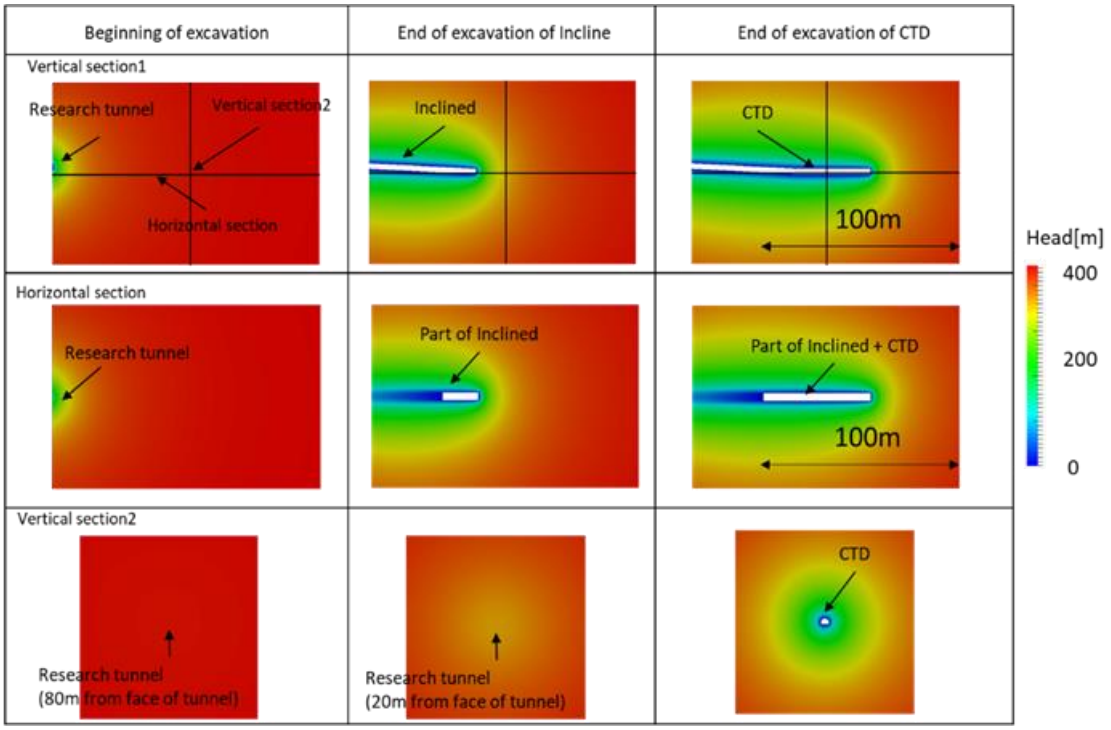

Figure 23. Spatial distribution of hydraulic head.

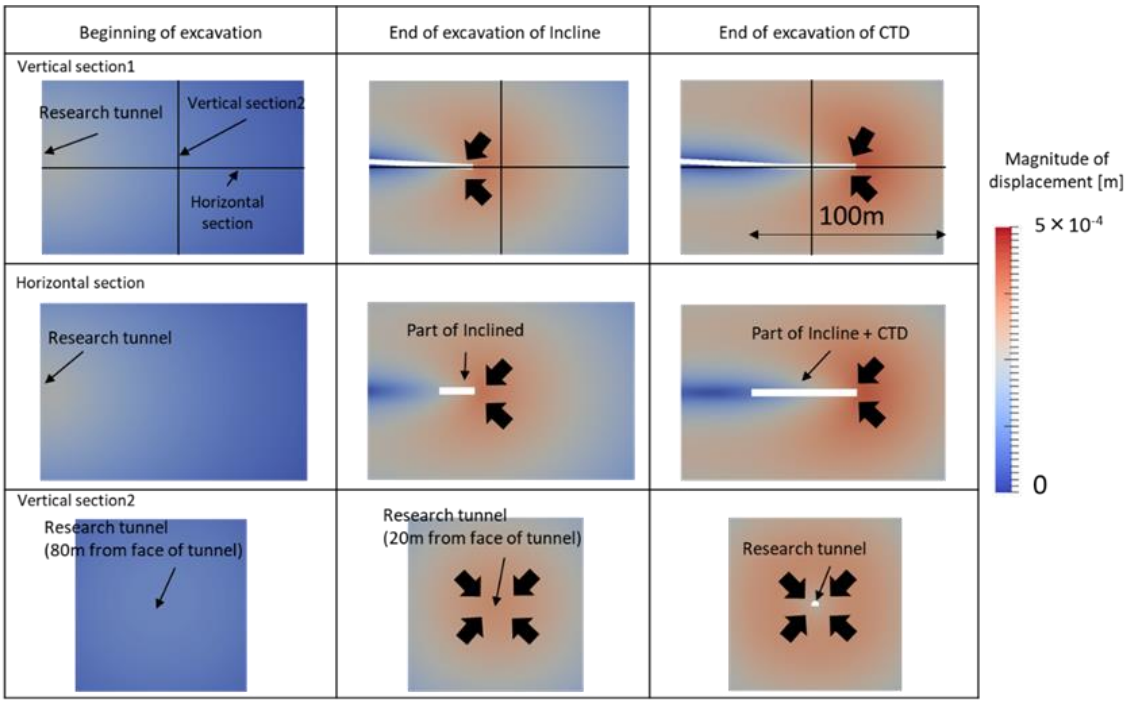

Figure 24. Distribution of displacement.

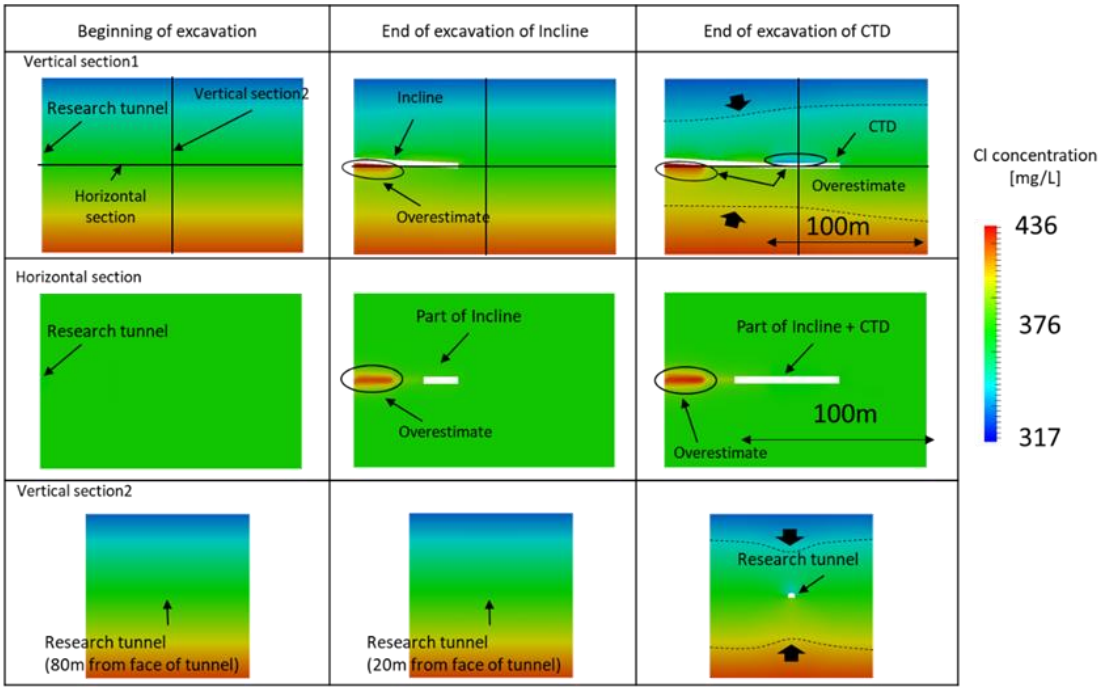

Figure 25. Distribution of Cl concentration.

3.5.2 Time variation of hydraulic pressure and Cl concentration in 12MI33 borehole and its sensitivity to hydraulic properties

Observation data on the drawdown of hydraulic pressure in borehole 12MI33 during excavation has been recorded. For the comparison of simulated drawdown and observed data, the time variation of predicted hydraulic head is shown in Figure 26. The arrows indicate the timing when the tunnel face reaches the horizontal location of each monitoring point. Predicted hydraulic pressure starts to decrease before the tunnel edge reached the horizontal location of monitoring point and continues to decrease until the hydraulic pressure declines to 1.6 MPa. The drop of hydraulic pressure at sections 1 and 2 do not down to 1.6 MPa and the final hydraulic pressure would depend on the distance from the tunnel end in this case.

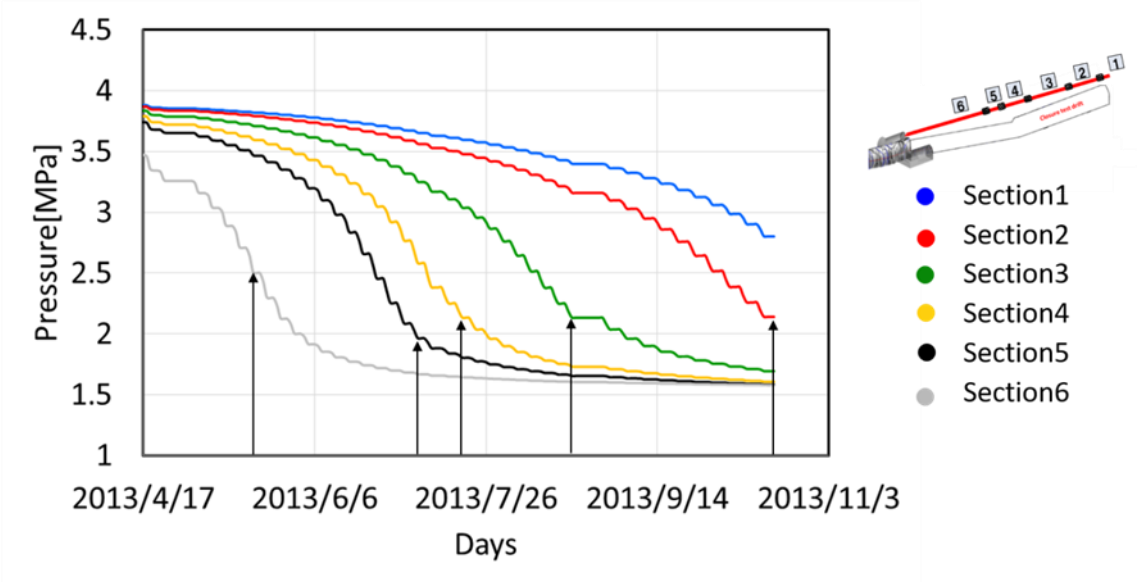

Figure 26. Time variation of predicted drawdown in 12MI33.

Figure 27 shows the results of the sensitivity of hydraulic pressure in each monitoring point to the value of physical properties. Both sensitivities of hydraulic conductivity and specific storage were evaluated. In addition to the homogeneous model case, a model that consists of rock-mass and shotcrete was evaluated. Shotcrete with the thickness of about 5 to 10 cm was implemented immediately after the drift excavation. This model has two physical properties representing the rock-mass and shotcrete. Elements of 1 layer were set to 100 times lower permeability than the rock-mass to consider the skin effect of shotcrete based on the result of previous observation. In the simulation, the

hydraulic conductivity of the elements that corresponds to the shotcrete was extended step by step at the same speed as the excavation of research tunnel. We assigned just one layer to shotcrete and the thickness is 0.625 m ~ 1.75 m. The variation of thickness comes from the discretization with different element size. We set the thickness of shotcrete to the value due to the computational limit though the actual thickness of shotcrete is several centimetres.

When the subsurface structure is homogeneous where the effect of shotcrete is ignored, all results show the same responses to both hydraulic conductivity and specific storage. Therefore, the decrease of hydraulic pressure in the borehole is almost entirely controlled by the boundary condition.

When the skin effect of shotcrete is considered, less permeable layer blocks the decrease of hydraulic pressure and the change of hydraulic pressure is reduced at most about 0.2 MPa. This is because pressure gradient in the lower permeability shotcrete is much larger than one in surrounding rock to conserve the continuity of Darcy's velocity through over a small region of 100 times lower hydraulic conductivity. The boundary condition limits the change of pressure between model boundaries and drift boundary to 4 MPa. Nearly 4 MPa divergence of hydraulic pressure occurred within the shotcrete layer in this case. As a result, the pressure at monitoring point located outside shotcrete layer remains high. This predicted result suggests that any skin effect of the shotcrete would significantly affect the hydraulic pressure change in the monitoring sections.

Figure 28 shows the predicted time variation of Cl concentration in 12MI33. The arrows in the graph indicate the timing when the tunnel edge reaches the monitoring point horizontally as with the graph of Figure 26. The Cl concentration starts to change according to the excavation of the tunnel. The fluctuation of Cl concentration is delayed compared to the drawdown of hydraulic pressure in monitoring points. Although the simulated Cl concentration shows the deviation during the tunnel excavation, the change is slight.

3.5.3 Inflow into inclined tunnel and closure test drift

The time variation of inflow rate into these drifts are shown for the comparison with predicted results. Figure 29 shows the predicted time variation of inflow during excavation at the inclined drift, CTD and both. The inflow rates increase as the excavation progressed. The inflow rate is proportional to the hydraulic conductivity as shown in the results of the homogeneous model case with a basic model and low hydraulic conductivity model. This is because that the distribution of hydraulic head is

controlled by boundary condition as shown in the results of pressure decline and the groundwater flow velocity only reflects the value of hydraulic conductivity according to Darcy's law. When the skin effect is considered, inflow rates decreases compared to the basic case because low permeable layer blocks the flow into the tunnel. Modelling of skin effect influences both drawdown and inflow prediction significantly.

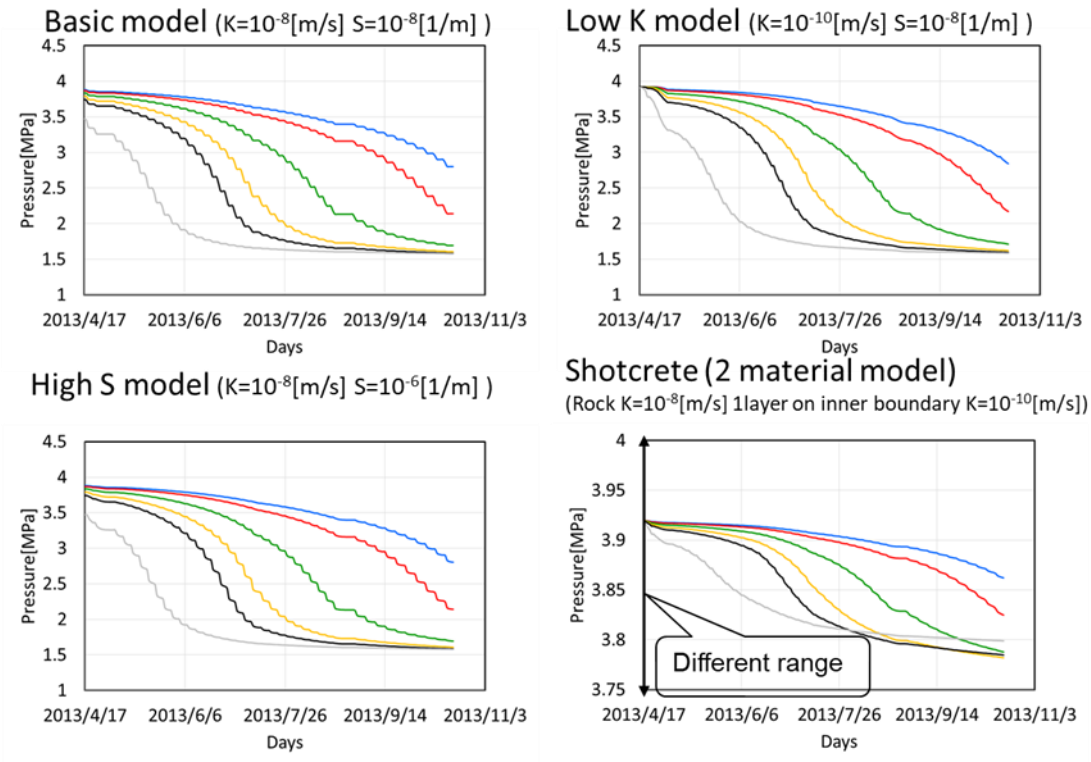

Figure 27. Sensitivity of hydraulic properties for the drawdown.

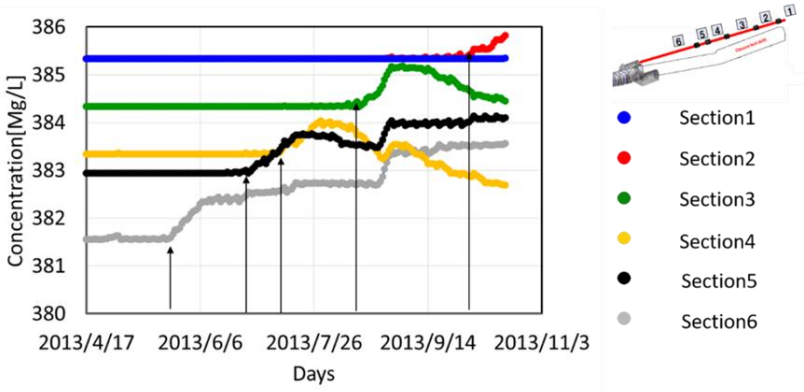

Figure 28. Time variation of Cl concentration in 12MI33

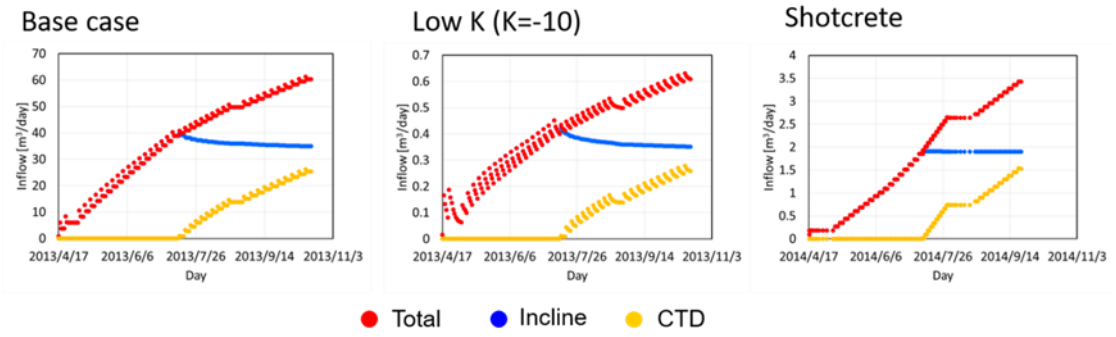

Figure 29. Prediction of results inflows into the tunnel.

3.5.4 Summary of prediction results

We performed a hydro-mechanical and advective-diffusive simulation to predict a disturbance due to the excavation of the CTD. We set the model and simulation conditions from data observed before the CTD excavation. The summary are as follows:

- The level of drawdown in 12MI33 does not significantly depend on K and is controlled by the boundary conditions when the structure is homogeneous. The boundary condition limits the range of pressure drop between outer and inner boundaries and pressure gradually change between them. Gradient of hydraulic pressure is also independent on K in this situation. Therefore, K cannot be evaluated from pressure distribution but will be estimated from the inflow rate into the CTD because inflow rate reflects the Darcy's velocity that is product of K and pressure gradient (Figure 27).
- The influence radius of disturbance of hydraulic head due to the excavation of CTD is about 50m from CTD and does not grow according to the extension of CTD. Note that the calculation domain is enough large to avoid the boundary effects (Figure 22).
- Variations of Cl concentration do not show a significant change during the excavation of CTD comparing to the range of Cl concentration given as an initial condition. Stronger advection such as channel flow would be necessary to lead the high and low concentration around the model boundary to the monitoring borehole along the tunnel.

3.6 Prediction results of the disturbance during the excavation of CTD using the heterogeneous continuum model

We made heterogeneous continuum (equivalent continuum porous media; ECPM) model based on discrete fracture network (DFN) models. This section describes methodology and result of DFN modelling, conversion of the DFN to ECPM model, and simulation predictions.

3.6.1 Construction of DFN model and ECPM model around the CTD

(1) Estimation of parameter set and DFN modelling

Table 11 shows used data for estimating the parameter set needed to make the DFN model. Our simulation aims to know how to predict (or to what extent we can predict) the subsurface phenomenon prior to an actual facility construction phase. For this purpose, we used the data obtained before excavation of the tunnel. Fracture orientation distribution, permeability distribution, and three-dimensional fracture frequency (P32) were estimated based on data from 12MI33 borehole investigations. The fracture radius distribution was estimated by outcrop and lineament data obtained from the surface investigation because this cannot be obtained by borehole investigation. For the estimation of fracture radius, we follow the strategy of the previous study (Saegusa and Matsuoka, 2011) that are different from Sandia's strategy in Section 4. Table 12 shows the result of the estimated parameter set. Each estimation methods described below.

a) Fracture orientation distribution

Figure 30 shows orientations of each fracture which observed in BTV investigation and core logging of 12MI33. We modelled only open fractures, assuming that hair cracks do not function as a groundwater flow path in the rock-mass. 78 out of 297 fractures are identified as an obvious open fracture. The fracture orientation distributions were regressed on the Bingham distribution and they were classified into two groups by using ISIS function of FracMan® version7.

b) Three dimensional fracture frequency (P32)

P32 of each set observed by the 12MI33 investigation was calculated by (3.1) and (3.2).

$$P_{32} = \frac{\sum area}{volume} = \frac{\sum \pi r_1 r_2}{l \pi r_1^2} = \frac{\sum \pi r_1 f_{Terz}}{l \pi r_1^2} = \frac{\sum f_{Terz}}{l} \qquad (3.1)$$

Where r1 is the minimum length of fracture surface intersected with the borehole, r2 is the maximum length of fracture surface intersected with borehole, f_{Trez} is the Terzaghi weighting, and l is the borehole length (Wang, 2005; Follin et al., 2007).

$$P_{32[r>r_{min}]} = P_{32[r>r_0]} \left(\frac{r_0}{r_{min}}\right)^{(k_r-2)} \qquad (3.2)$$

Where, P32[r>r_{min}] is the P32 of all fractures with r greater than the size r_{min}, P32[r>r0] is the P32 of all fractures with r greater than the size r0, r0 is the minimum fracture radius of base data (this study assumes r0 is the borehole radius of 0.125 m), r_{min} is the minimum fracture radius for DFN model (this study sets r_{min} is 1.0 m), and kr is the exponent of fracture radius distribution.

c) Fracture radius distribution

The fracture radius distribution was estimated using previously collected data (outcrops and lineaments based on surface investigations; Figure 31). We assumed fracture radius distribution shows a power-low distribution based on the previous study (Bruines et al., 2014). Scaling exponents of outcrops and lineaments show 1.75 and 1.72 respectively. The equation 3.3 shows the relationship between scaling exponent of fracture radius distribution (Dr) and fracture trace length distribution (Dt). Thus, a scaling exponent of fracture radius distribution was set to 2.75. In the relationship between trace length and CDF (Figure 32), all data fit the linear regression curve (approximated CDF) and dispersion from the line that indicates the independent component from the approximated CDF does not appear. Therefore, we used only one CDF of fracture radios for all fracture sets.

d) Transmissivity distribution of fractures

The transmissivity of fractures was estimated by a regression analysis of the cumulative distribution function (CDF) in hydraulic conductivity. The results of hydraulic packer test of 12MI33 are compiled as a CDF that consists of six points (shown by red dots in right picture of Figure 33) and then the CDF is approximated by the CDF derived from the virtual well test with DFN models.

$$D_r = D_t + 1 \qquad (3.3)$$

Table 11. Date for estimating the parameter set

Parameters	Data
Fracture orientation distribution	BTV* of 12MI33
Fracture frequency (P_{32})	BTV* and core logging of 12MI33
Fracture radius distribution	Previous data (Outcrops and lineament at surface)
Transmissivity distribution of fractures	Hydraulic packer test of 12MI33

* BTV means Borehole Television observation.

Table 12. Parameter set for simulation

Set	Orientation (Bingham distribution)				P_{32} (m^2/m^3)	Radius (Power-low distribution)	Transmissivity Distribution
	Pole-trend	Pole-plunge	k1	k2			
1	334.39	0.92	-19.50	-7.30	0.08	Dr = 2.7 r_{min} = 1.0	m = -8.4 σ = 1.0 C = 2.3
2	19.14	0.05	-12.00	-4.95	0.22		

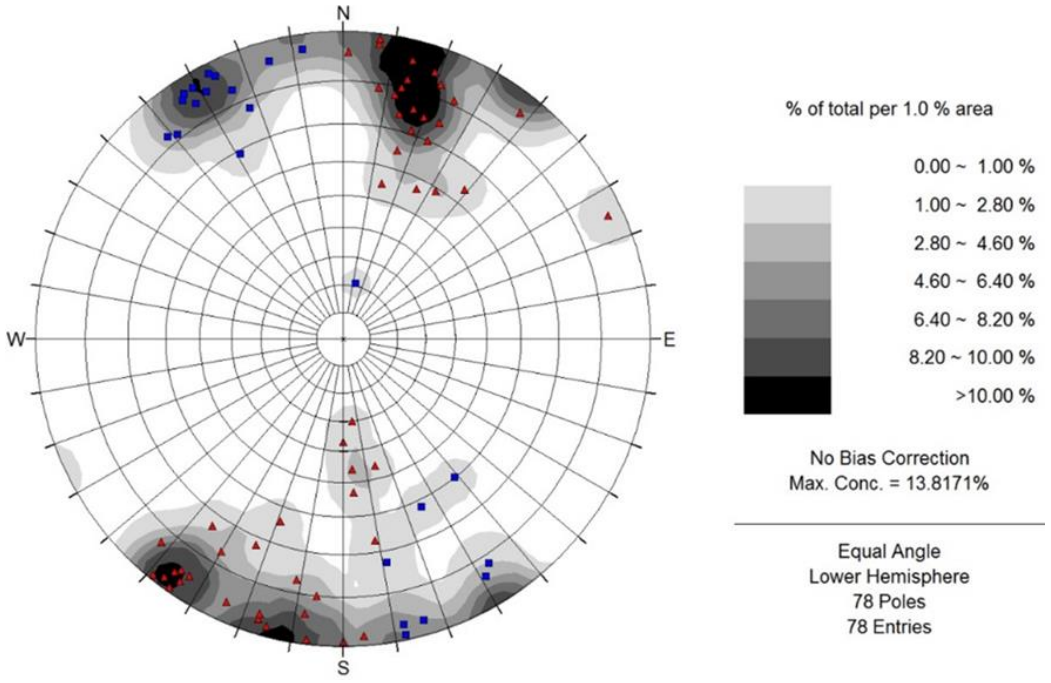

Figure 30. Equal angle lower hemisphere stereo net of the 12MI33 fracture poles and fisher concentration plot. Blue quadrangle dot shows Set1 and red triangle dot shows Set 2 for DFN model.

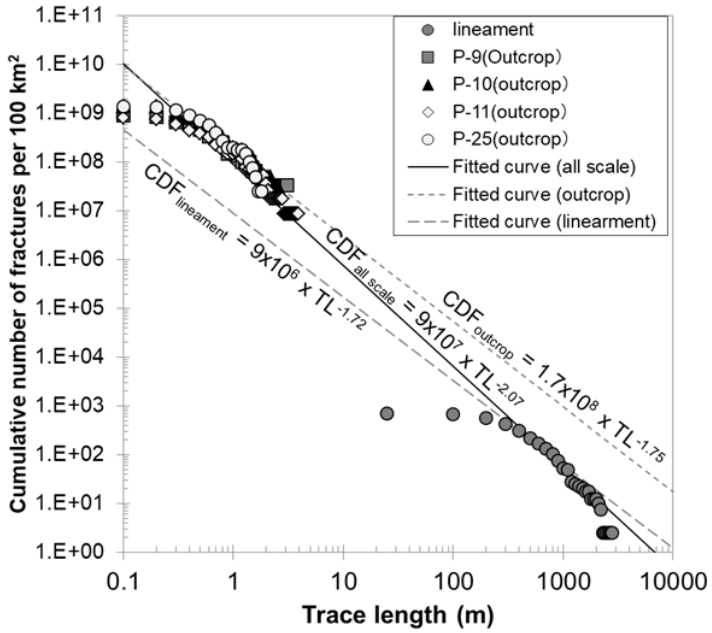

Figure 31. Cumulative number of fractures of outcrops and lineaments per 100 km^2 around MIU site (Saegusa and Matsuoka, 2011). Note the P-9, P-10, P-11 and P-25 in legend indicates the name of the dataset (Not mean characteristics of DFN such as P32).

We assume fracture radius and its hydraulic transmissivity correlate with variability (3.4), then decide the unknown parameter, μ and C, in (3.4) to relate fracture radius to transmissivity,

$$T = lognorm(\mu, \sigma) \times r^C \qquad (3.4)$$

where T is transmissivity, μ is mean in the natural logarithm distribution, σ is a standard deviation in the natural logarithm distribution (this study assumed σlog10 = 1.0), r is the fracture radius, C is exponent value. The virtual well test was conducted as steady flow simulation, outside boundary condition is the constant head (0.0 m), and test section boundary condition (virtual borehole which length (13.3m) is the average length of monitoring section in12MI33) is the constant head (1.0 m; Figure 32). We calculated the transmissivity or hydraulic conductivity in the virtual test according to the Thiem's theory (Eqs. 3.5 and 3.6) and simulated inflow,

$$T = \frac{Q\ ln\left(R/r_w\right)}{2\pi\ \Delta h} \qquad (3.5)$$

$$K = T/L \qquad (3.6)$$

where T is transmissivity, Q is flow rate, R is the radius of influence, r is the radius of the borehole, Δh is a drawdown, K is hydraulic conductivity and L is the length of simulated inflow width. At each set of μ and C, 100 realization models was simulated for the derivation of CDF and then the error between two CDFs, one is from the packer test and the other is from virtual tests, are calculated. The error map is shown in the left picture in Figure 33. The parameters that connect fractures to transmissivity distribution (μlog10 = -8.4, σlog10 = 1.0, and C = 2.3) are decided by minimization of the error.

(2) Construction of the ECPM model

Equivalent conductivity values (Oda K) in each 2 m, 5 m, 10 m, and 20 m grids are calculated based on the DFN model (1 realization which shows 50% value of K, hereinafter refer Mod50; Figure 34) for construction of the ECPM model. In our simulation, we consider the heterogeneity only in the hydraulic conductivity structure and set other parameters are to be homogeneous for simplicity.

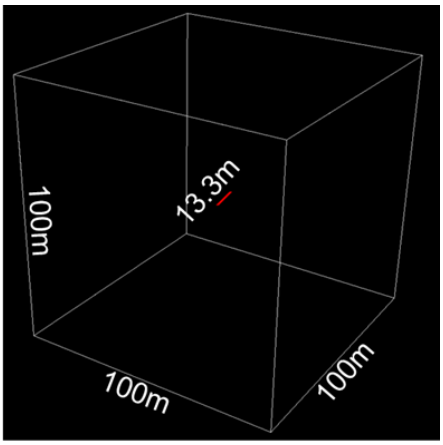

Figure 32. Analytical region of virtual well test

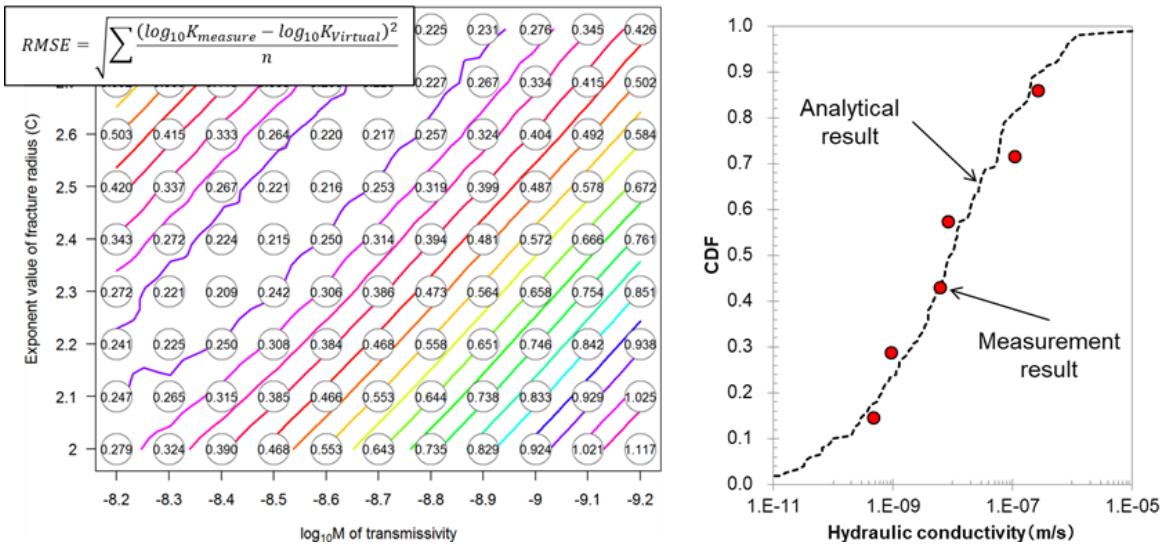

Figure 33. RMSE map and relationship between measurement values and analytical values of K

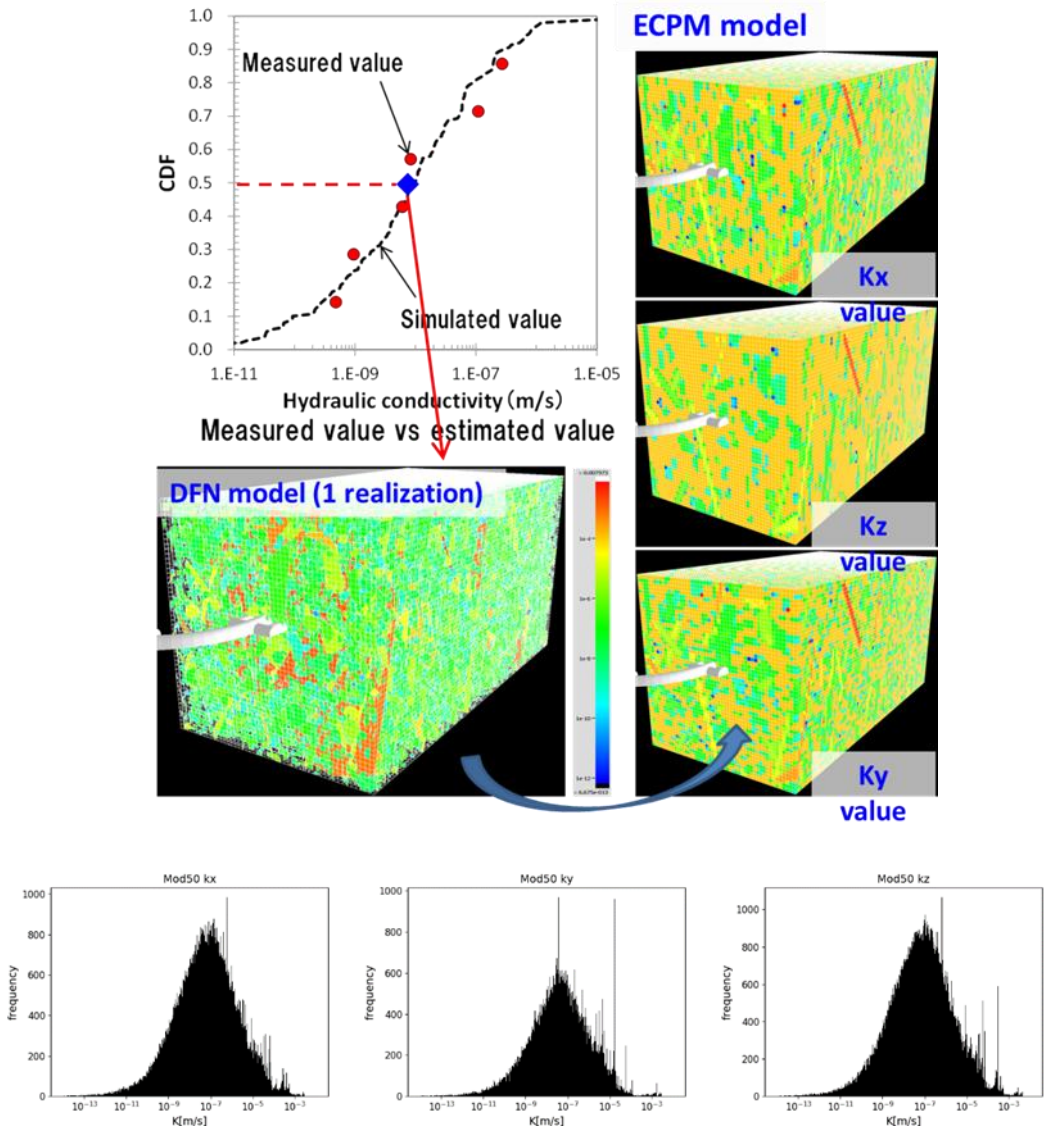

Figure 34. DFN model for ECPM modelling. Spatial distribution of anisotropic hydraulic conductivity (upper right) and its frequency (lower)

3.6.2 Simulation with ECPM model

FracMan® generates an anisotropic hydraulic conductivity structure from the realized fracture field. Because of H-M simulator limitation, we calculated geometric mean of hydraulic conductivity of each direction and input the isotropic structure into the ECPM model. Hydraulic conductivity of 0 m/s is returned from FracMan® at the elements where any fractures do not exist; a hydraulic conductivity of 1E-12 m/s is assigned there. Hydraulic conductivity higher than 1E-4 m/s was also limited to 1E-4 m/s for the stability

of numerical calculation. The skin effect of shotcrete is considered by setting the hydraulic conductivity of elements in 1 layer of the tunnel boundary to 1E-8 m/s.

Thames, a part of Couplys used for our simulation employs the Block Gauss Seidel scheme (e.g., Whiteley et al., 2011) that solves different coupled physical problems separately and iterates the calculation until the error related to the coupled effect gets convergence. When we simulate the H-M problem with the heterogeneous model, Block Gauss Seidel iteration for fully coupled simulation does not converge. Therefore, the results of Step1b are the results considering only the weakly coupled effects. The convergence rate of this scheme becomes slow or is not satisfied when the solver is applied to the problem including the matrices with a small diagonal value due to the heterogeneous model (Yeckel et al., 2009). SA-AMG (smoothed aggregated algebraic multigrid method (Vaněk et al., 1996) is employed to solve each physical problem for the convergence of the numerical calculation with the ECPM model that has a highly heterogeneous structure.

3.6.3 Spatial distribution of hydraulic head, Cl concentration and displacement calculated from a realized sample model

Figure 35 shows the distribution of hydraulic conductivity, hydraulic head, displacement and Cl concentration in two vertical and one horizontal slice after the excavation of CTD. The results from one of the realizations of the model are shown.

Due to the heterogeneous features of hydraulic conductivity structure, the calculated hydraulic head is totally different from the distribution in the case of the homogeneous model shown in Figure 23. The areas where the hydraulic head drops do not correspond to the fractures that have a continuous high conductive zone in the model. For example, hydraulic head decreased along a fracture is distributed on bottom of CTD, while the hydraulic head remains about 4 MPa around two vertical fracture zones in the inclined tunnel. The change of hydraulic head is not affected by locally distributed high conductivity zone but seems to relate to the connectivity of high hydraulic conductive zone there. In this case, the hydraulic pressure seems to remain high due to the water supply from boundary along continuous high conductive zone. This illustrates the difficulty of estimating the change in the hydraulic head during excavation by using a model derived from limited fracture data. It is also necessary to confirm the influence of boundary conditions on the simulation results.

The distribution of Cl concentration is highly affected by advection. The high and low Cl concentration water are conveyed along the continuous high conductive zones, and high

and low Cl concentration zones are formed below and above the tunnel, respectively. These Cl concentrations reflect the distribution of fractures (hydraulic conductivity structure) in the model rather than the distribution of hydraulic pressure. This indicates that the fast flow towards the drift occurs due to the continuous high conductive zone although the pressure drop along the conductive zone is slight. On the horizontal slice including the CTD, distribution of Cl concentration does not change compared to the distribution in other vertical slices and is almost the same as the initial distribution before the inclined tunnel excavation. This is because that the vertical flow conveying Cl ions stagnates on the boundary where the upper flow changes to downward flow due to the flow into the tunnel.

The compressive deformation appears according to the pressure release by excavation of the tunnel. Due to the hydro-mechanical coupling effect, the magnitude of displacement becomes large around the area where hydraulic pressure decreases. We do not use a heterogeneous property model for the mechanical simulation, but instead assume uniform properties. However, the estimated deformation in rock mass clearly appears around the location where hydraulic head decreases, illustrating the H-M coupling.

3.6.4 Time variation of hydraulic head and Cl concentration in 12MI33

Figure 36 shows the predicted time variation of drawdown in 12MI33 during excavation. The hydraulic pressure at sections 2, 3 and 4 are decreased following the excavation. On the other hand, hydraulic pressure at section 1, 5 and 6 remains higher than 3.8 MPa. The hydraulic pressure at steady state does not show the correlation with hydraulic pressure at another monitoring point. Due to several high conductive flow paths in the structure of hydraulic conductivity, the drawdown of hydraulic pressure is independent on the distance from tunnel face to monitoring point as shown Figure 26.

Figure 37 shows the time variation of Cl concentration in 12MI33 during and about 1 year after excavation. Though the concentration at other monitoring points does not change, Cl concentration estimated in section 4 and 5 does deviate. The deviation of Cl concentration is slightly less than 10% of initial concentration.

3.6.5 Inflow into inclined drift and the CTD

Figure 38 shows the time variation of inflow into the inclined tunnel and CTD during and after excavation. The order of total inflow is almost same as the homogeneous model

case. However, a fraction of inflow into inclined tunnel or research tunnel differs from the homogeneous model case. In the fractured model, almost all of flux into tunnel part occur around inclined tunnel though the fraction of inflow into inclined and CTD is proportional to the tunnel length of the homogeneous model case.

To confirm the distribution of inflow into the tunnel, a spatial distribution of magnitude of Darcy velocity in horizontal and vertical slice along tunnel are displayed in Figure 39. Fractured parts in the model are clearly highlighted as a large magnitude of Darcy velocity zone and correlate with high or low concentration zone in Figure 25. Several path lines with high Darcy velocity about 10^{-5} m/s reaches the inclined tunnel, while only a few flow paths of 10^{-6} m/s crosses the CTD. The inflow rate into each part of research tunnel reflects this distribution of Darcy velocity and the different fracture density between the inclined drift and the CTD.

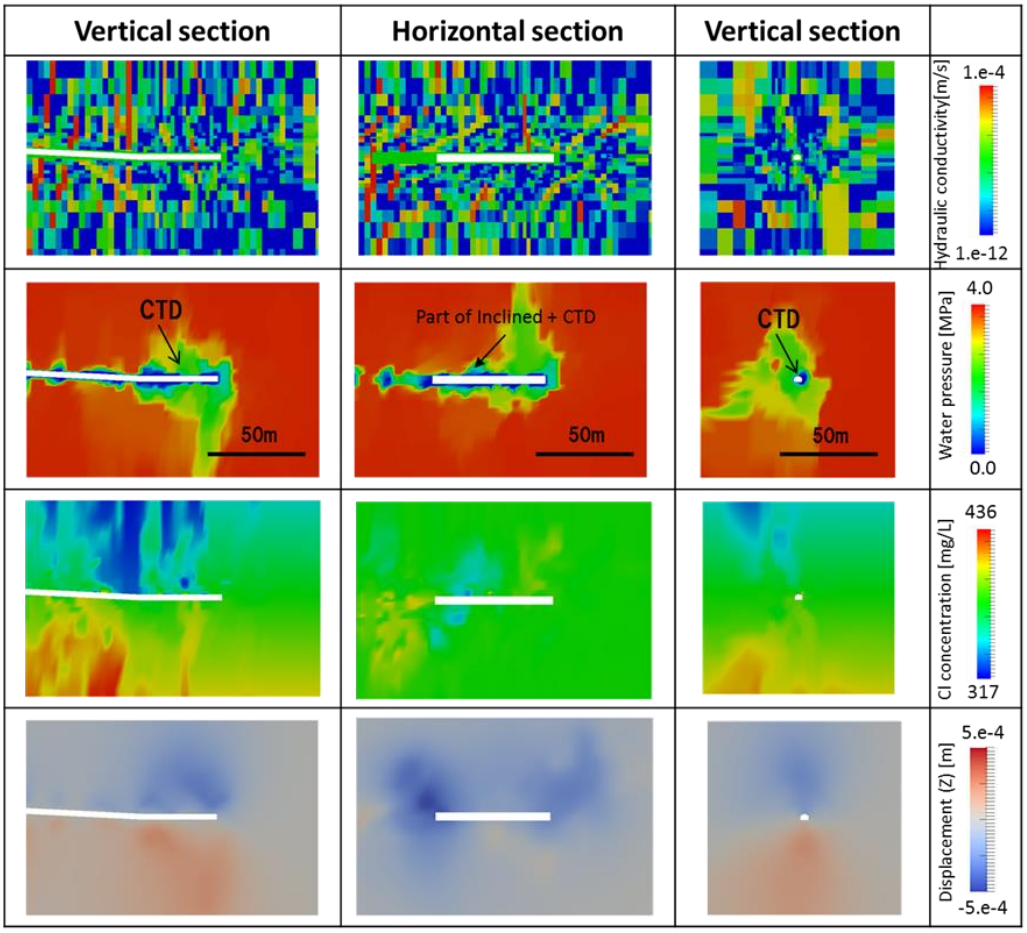

Figure 35. The simulation results from a realized model after excavation of CTD. Hydraulic conductivity, pressure, Cl concentration and displacement in Z direction are shown from top to bottom.

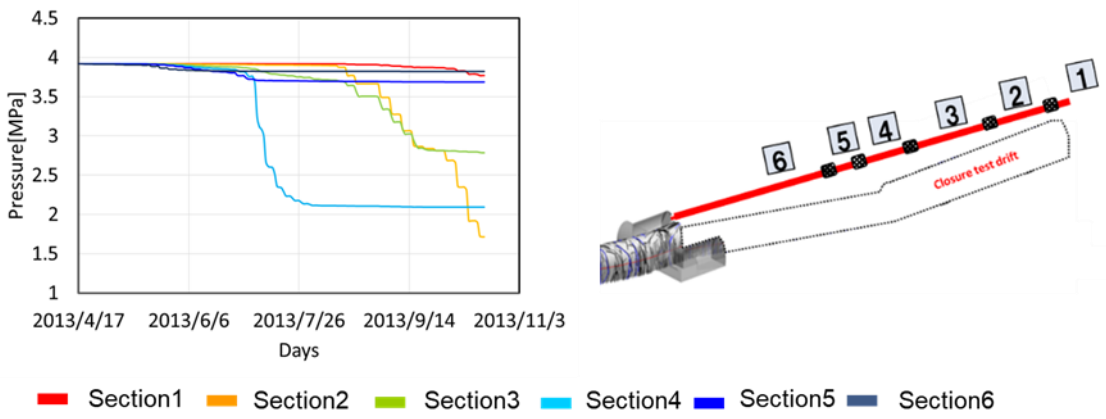

Figure 36. Time variation of hydraulic head in 12MI33 (Mod50)

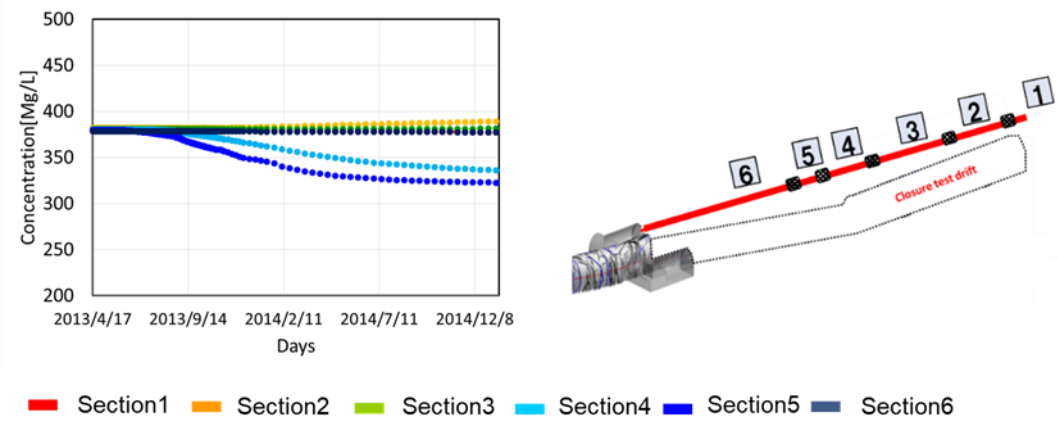

Figure 37. Time variation of Cl concentration in 12MI33 (Mod50)

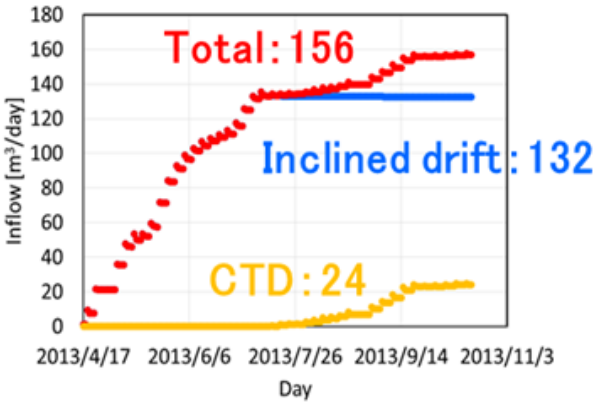

Figure 38. Time variation of inflow into research tunnel.

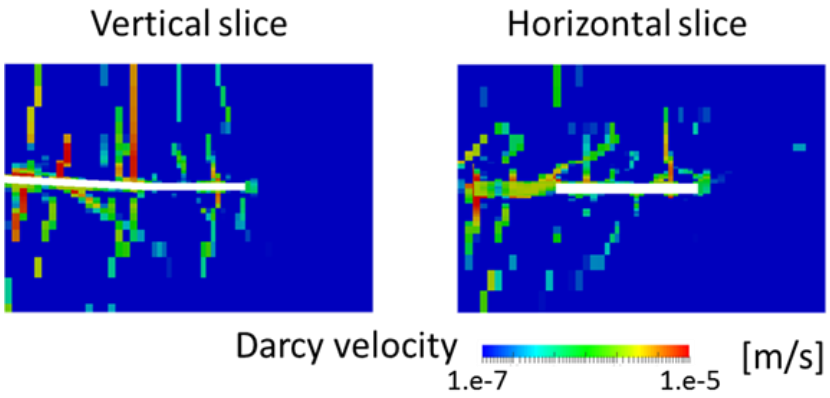

Figure 39. special distribution of Darcy velocity

3.7 Model update and calibration based on the data of Step 1

3.7.1 Theory and method of model update

Hydraulic heads after drift construction in each monitoring section were calculated using the DFN models which were constructed from the parameter set in Table 11 (Figure 40). Refer to previous study (Sawada and Sakamoto, 2016), 100 realisations of steady state simulation were calculated in order to capture the heterogeneity of rock mass roughly. The result shows that the pressure at section No.1 is almost deterministic while the pressure at other points could take a variable value between 0 and 4 MPa.

Among 100 realizations, the model that shows the 69% value of hydraulic conductivity in CDF reproduce the observed pressure the best (Figure 41). Therefore, we chose the model (hereinafter referred to as Opt69) as a calibrated model.

3.7.2 ECPM modelling based on the fracture data

The equivalent conductivity value (Oda K) in each 2 m, 5 m, 10 m, and 20 m grid size are calculated based on the DFN model (Opt69) for construction of the ECPM model (Figure 42).

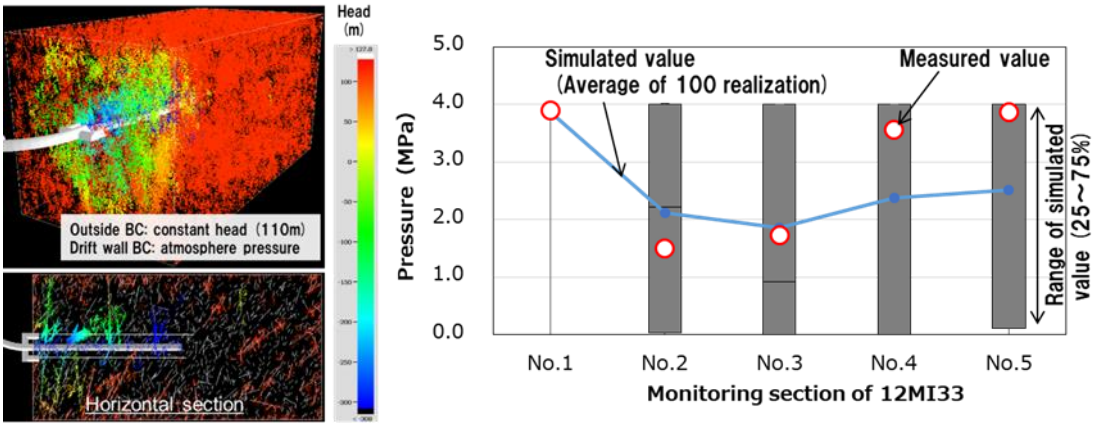

Figure 40. Example of head distribution (left) and prediction result of each section (right)

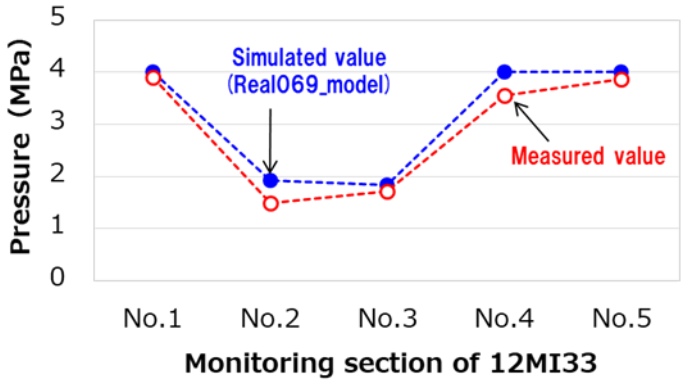

Figure 41. Hydraulic head distribution of extracted DFN model (Opt69) and measured value

3.7.3 Result of spatial distribution of hydraulic pressure, Cl concentration and deformation from Opt69

Figure 43 shows the simulation results of the spatial distribution of hydraulic conductivity, hydraulic pressure, Cl concentration and displacement in the vertical direction. These results are arranged in the same manner as Figure 35. In this simulation, we set the hydraulic conductivity of shotcrete to 2.0×10^{-8} m/s for calibration purposes.

In this model, average hydraulic conductivity is lower than that in the Mod50. The high conductivity zones representing the fracture zones are clearly seen compared with Figure 35. The relationship between pressure decrease and fracture distribution is clearer than the case with Mod50, especially on the horizontal slice. In the results of Cl

concentration, almost whole domain does not change compared to the initial state except for low concentration zone along the fracture around the entrance of CTD. Note that the high and low Cl concentration zones along the upper CTD is an artefact from the lack of numerical accuracy due to the time step size and should be ignored. This distribution of Cl concentration indicates that the almost all of inflow into drift occurs at the entrance of CTD. The rock mass deforms in a compressive way and shows the strong relation with the decrease of hydraulic pressure.

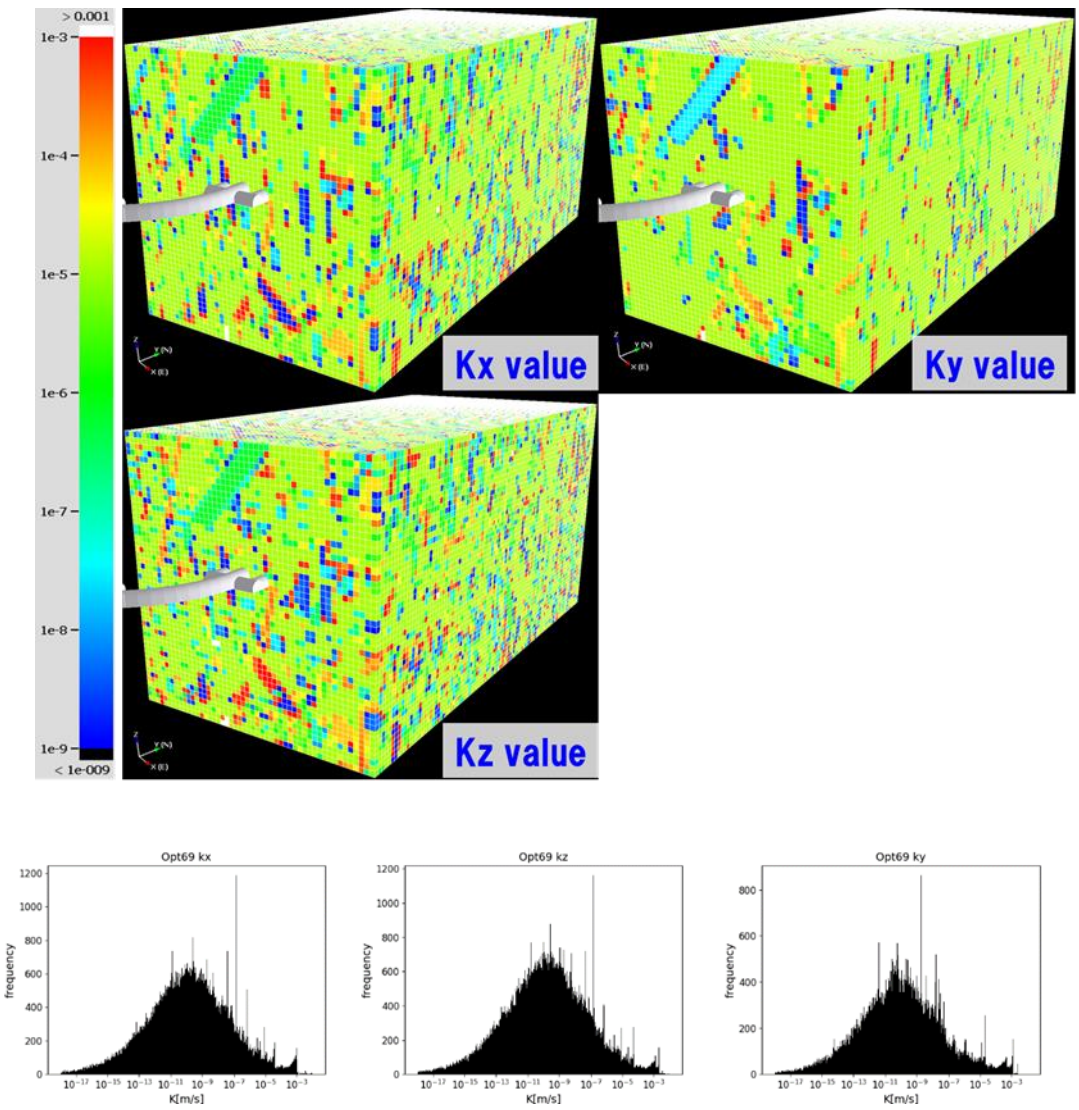

Figure 42. DFN model for ECPM modelling. Spatial distribution of anisotropic hydraulic conductivity (upper right) and its frequency (lower)

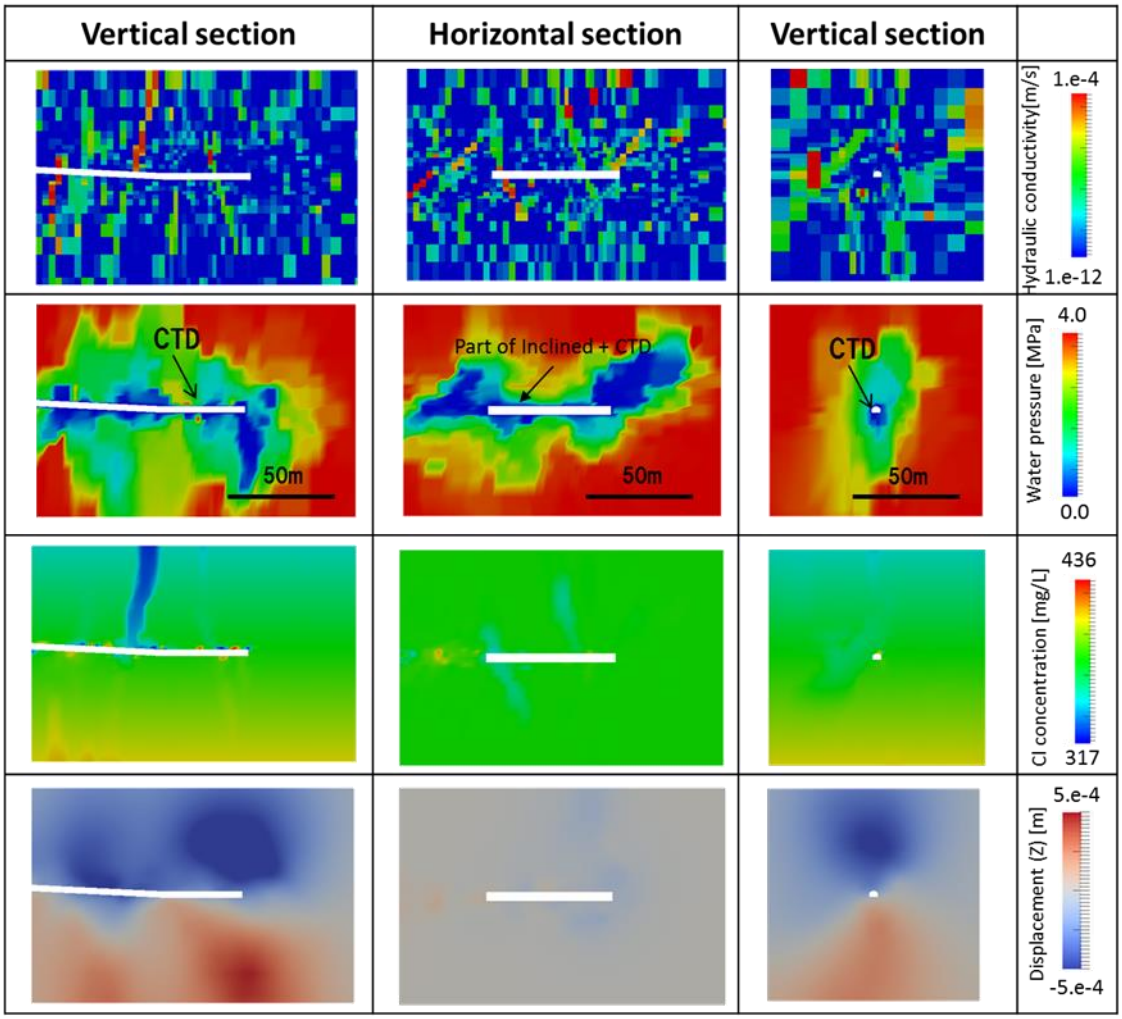

Figure 43. The simulation results from Opt69 after excavation of CTD. Hydraulic conductivity, pressure, Cl concentration and displacement in Z direction are shown from top to bottom. Distribution in two vertical and horizontal sections are shown from left to right.

3.7.4 Time variation of hydraulic head and Cl concentration in 12MI33 (Opt69)

Figure 44 shows the change in hydraulic pressure in 12MI33. In this model, the hydraulic pressure in all monitoring points decreases as the excavation proceeds. Hydraulic pressure in sections 1, 2 and 6 reaches almost 0 MPa due to a fracture across the research tunnel. The hydraulic pressure after excavation differs from that predicted by the DFN modelling as shown in Figure 41. We use the cell with the size of 2m to generate the equivalent continuous porous medium model. Modelling with this size cells make different monitoring sections in the borehole share the same cell and communicate the

hydraulic pressure response to different monitoring sections. To avoid this inconsistency between DFN and ECPM, we would need to use a finer mesh (not performed in this Step). The behaviour or hydraulic pressure at section 1 and 2 is almost same. The high conductive fracture is located at the tip of research tunnel. Elements consisting of this conductive zone are shared by each element including the monitoring point and strongly affects the simulated data at the monitoring point.

Figure 45 shows the time variation of Cl concentration in 12MI33 during excavation and one year after excavation. Cl concentration in these monitoring points does not fluctuate at all as shown in Figure 45 compared with hydraulic pressure in Figure 44. The change in Cl concentration is not necessarily related to the change in hydraulic pressure.

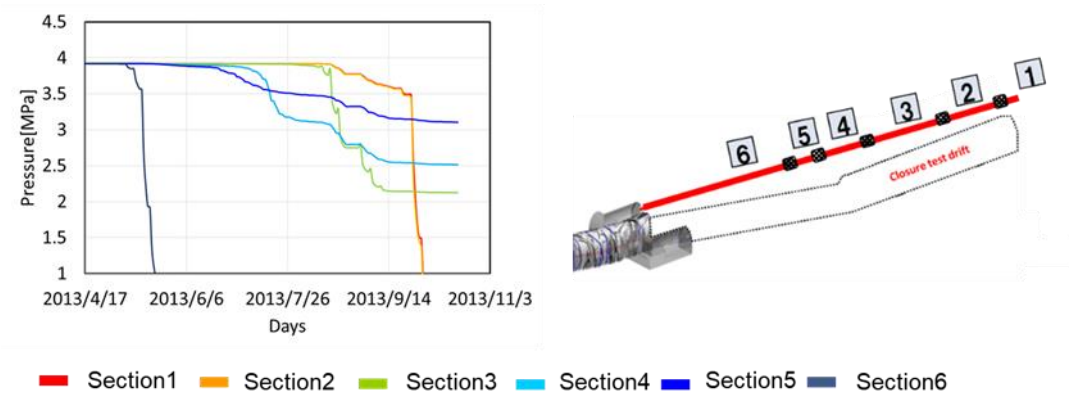

Figure 44. Time variation of hydraulic head in 12MI33 (Opt69)

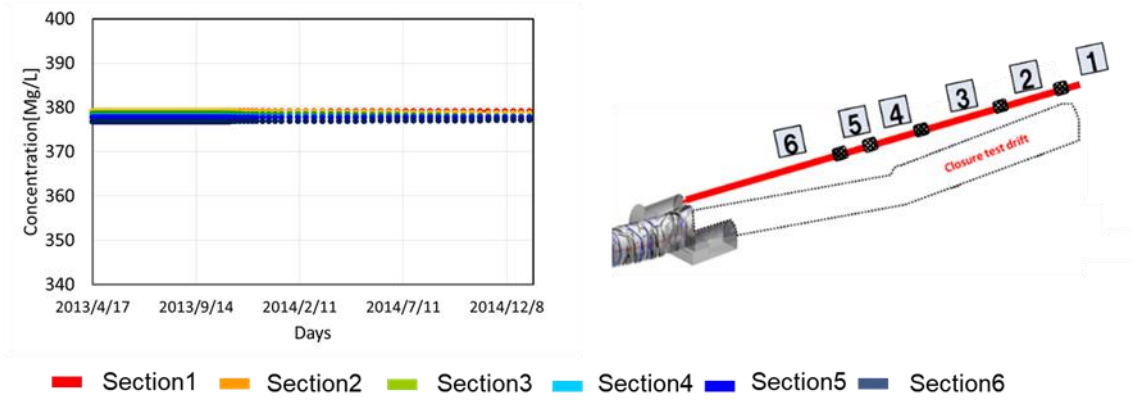

Figure 45. Time variation of Cl concentration in 12MI33 (Opt69)

3.7.5 Inflow into inclined drift and CTD (Opt69)

Figure 46 shows the time variation of inflow into the research tunnel. The inflow rate around inclined tunnel accounts for more than 95% of total inflow rate. The bias of the fraction of inflow rate between the inclined tunnel and the CTD is bigger than that in Figure 38. The high Darcy velocity area appears only along three fracture zones as shown in Figure 47, two in the inclined tunnel and one in CTD. These two fractures in the inclined tunnel connect to the outside of focused domain as shown in Figure 47 and a high proportion of water would be channelled through these fracture zones. On the other hand, the high-velocity zone across the CTD is included within the domain and the velocity is slower than that in other fractures. Less connectivity of fractures across the CTD than that across inclined tunnel would cause the smaller inflow rate.

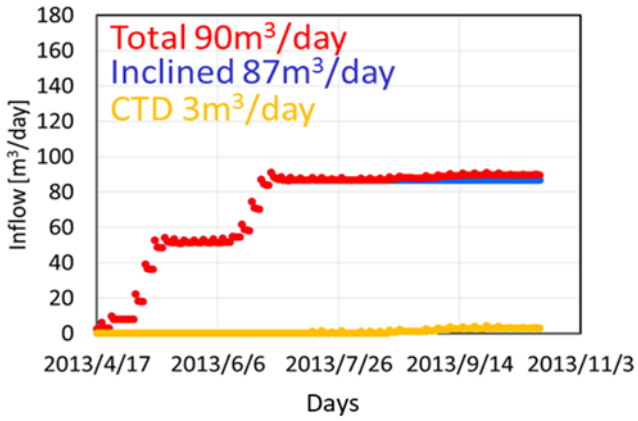

Figure 46. Inflow rate into research tunnel.

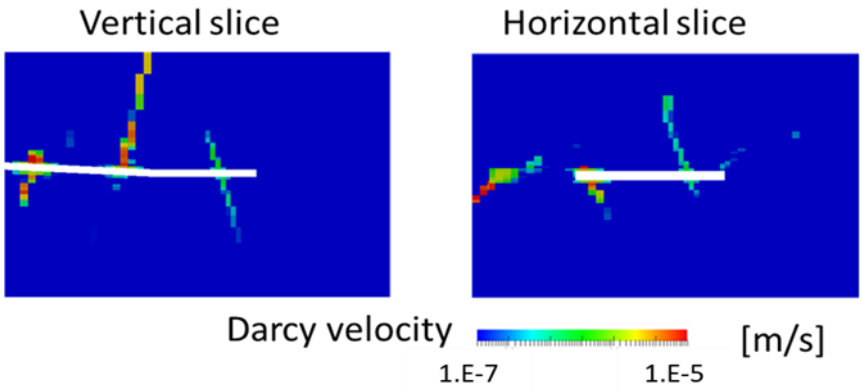

Figure 47. Darcy velocity in vertical and horizontal section along research tunnel.

3.8 Effect of length of monitoring point

In this study, we define the mid-points of each monitoring section in 12MI33 as monitoring points to compare the simulated results with observed data. However, our models include several nodes in the monitoring sections which allows the variation in hydraulic pressure along the borehole to be seen.

Figure 48 shows the hydraulic pressure at steady state along the 12MI33 borehole. The width and height of the coloured bars indicate the length of monitoring section and observed hydraulic pressure, respectively. The monitoring sections except for section 1 include more than two nodes and several of the monitoring zones show very large changes in pressure within the that zone. In such case that the monitoring sections locates within highly heterogeneous structure, the value picked up at specific points are not necessarily a representative value at a measurement point. The modelling of monitoring borehole or some averaging technique is needed to be applied for the appropriate comparison in such case.

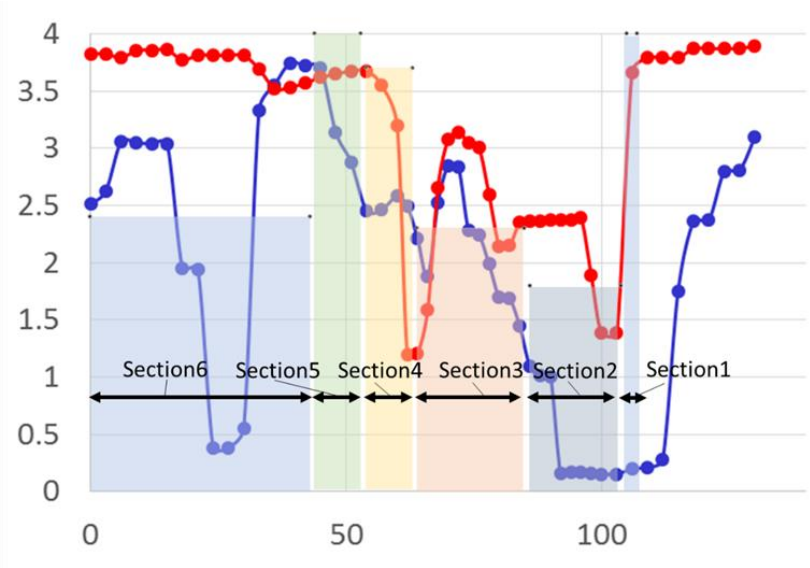

Figure 48. Length of each monitoring section and simulation results on nodes along 12MI33.

3.9 Summary of ECPM model and simulation results

In this Step, we performed a hydro-mechanical and advective-diffusive simulation to predict a disturbance due to the excavation of research tunnel within a heterogeneous model. Several fracture models are constructed using a stochastic method according to the probability function derived from geological data. Two of them are chosen for coupled simulation, one is a realization that shows the 50% value of the observed hydraulic conductivity CDF generated through a virtual hydraulic packer test (Mod50) and the other is the model that the hydraulic pressure in 12MI33 after excavation best matches the observations (Opt69). Then, they are converted to equivalent continuous porous medium for finite element modelling. We estimate the pressure field, deformation and Cl concentration by this method. The summary of simulation results are as follows:

- The hydraulic pressure in the monitoring sections in Borehole 12MI33 does not correlate with the hydraulic conductivity structure but would be affected by the connectivity of high conductive zone representing fracture zone.
- Cl concentration along the 12MI33 borehole does not show the significant change although the complex hydraulic pressure change and high Darcy velocity along fracture zones are present.
- Deformation of around the tunnel shows the good correlation with the decrease of hydraulic pressure due to the coupled effect.

3.10 Comparison of each simulation result with the observed data

In this Step, we constructed three models, a homogeneous model and two heterogeneous models. To evaluate the ability to predict a disturbance due to the excavation, we compared the simulated results to the observed data. In this step, the data of time variation of hydraulic pressure and Cl concentration in 12MI33 hydraulic pressure and inflow into research tunnel are available. We compared these results.

Figure 49 shows the comparison of time variation of hydraulic pressure in 12MI33. Observed data, simulation results from a homogeneous model and two heterogeneous models are shown respectively. In case of the homogeneous model, the drawdown of hydraulic pressure smoothly occurs compared to the observed data. All data in six monitoring points are predicted to decrease during the excavation, though the data for

sections 1, 5 do not decrease at all in observed data. Hydraulic pressure at section 2, 3 and 6 shows a reasonable fit, less than 1 MPa difference, to the observed data at steady state. When the Mod50 is used, the hydraulic pressure at section 2 shows good agreement and that of section 6 shows a reasonable fit compared to the observed data. In addition, the pressure at sections 1 and 5 also shows good agreement with the observed data. In this case, both rapid decrease and stable state of hydraulic pressure can be reproduced. When Opt69 is used, the hydraulic pressure at section 1, 2 and 6 reaches almost 0 MPa as soon as the hydraulic pressure started to decrease. In this case, the hydraulic pressure in section 3 shows good agreement with the observed data, though the hydraulic pressure in other points is too low.

Figure 50 shows the comparison of time variation of Cl concentration in 12MI33 during and 1 year after excavation. The results are arranged in the same manner as Figure 50. All of the simulated results show a slight change or almost no change when compared with the observed data.

Figure 51 shows the comparison of inflow rate into inclined tunnel and CTD. Only the inflow rate after excavation is available as shown in Figure 51. The total inflow rates of all results show good agreement with observed data. However, the fraction of inflow rate between the inclined tunnel and CTD in simulated results are largely different from the measurements. This is due to the random generation of highly conductive zones in the model. Two models, we used to include, as Figure 35 and Figure 43 show, fewer fractures in CTD than inclined zone. Conditioning the randomly generated model with the observed geological data would improve the fraction of inflow rate in each tunnel section. From these results, total inflow rate into the tunnel would be more predictive than with the variation of hydraulic pressure or Cl concentration.

3.11 Conclusions of Step 1

In this step, we try to predict a disturbance during the excavation of the research tunnel. We use the datasets observed before excavation of inclined tunnel and CTD to define the simulation for prediction purposes. We consider the fractures stochastically using a DFN model and convert the fracture model to an equivalent continuous porous media (ECPM) by Oda's model (Oda, 1985). The prediction simulation is performed using the ECPM model. The data on hydraulic pressure, Cl concentration and inflow are available for the comparison of simulated results with the observed data. In addition to these parameters, we simulated the mechanical behaviour affected by hydraulic pressure,

though there is no mechanical data for comparison. From the simulated results and their comparison with the observed data, we summarize the conclusions of Step1 as:

- The simulation with models considering the fractures could reproduce the time variation of hydraulic pressure independent of the location of monitoring points. However, the prediction of hydraulic pressure to fit all observed data is difficult by using a model that randomly generates high conductivity zones.
- The predicted Cl concentrations along the 12MI33 borehole do not show a significant change even though the flow paths corresponding to the fracture zones are considered. Comparison of simulated results with observed data suggests that the drainage by the drift gathers water from deeper or shallower parts than our model domain.
- The total predicted inflow into the research tunnel from both homogeneous and heterogeneous models, show good agreement with the observed data. The prediction of inflow at the tunnel scale would be possible.

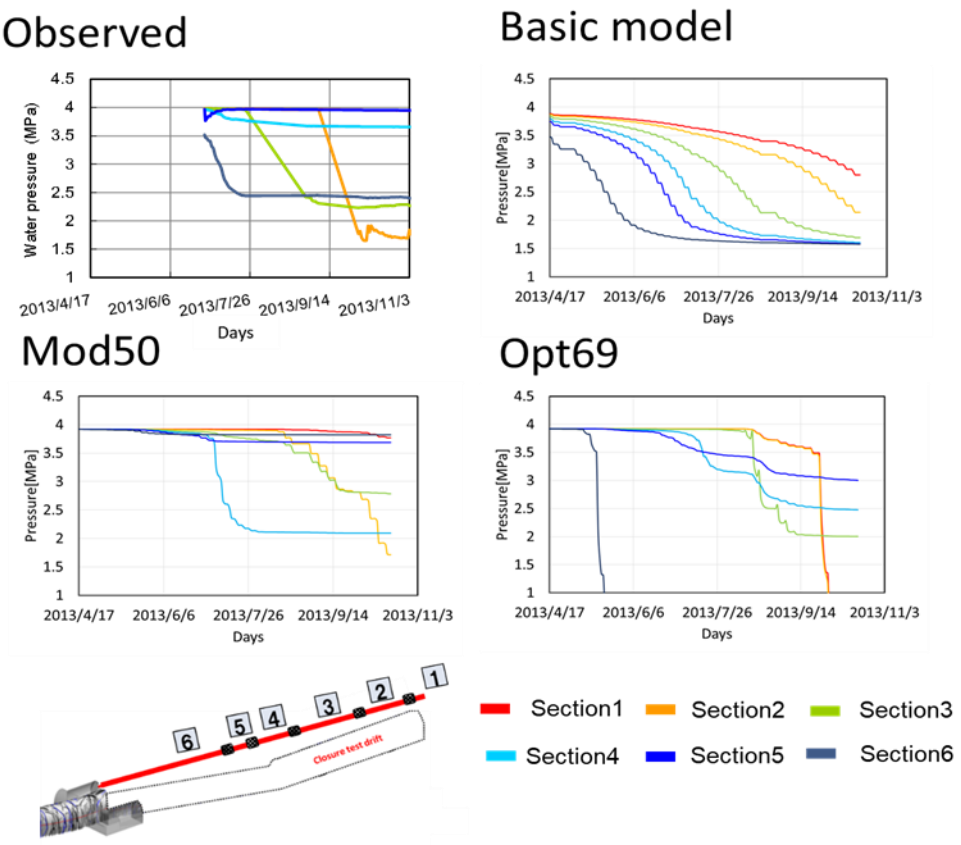

Figure 49. Comparison of time variation of hydraulic pressure in 12MI33.

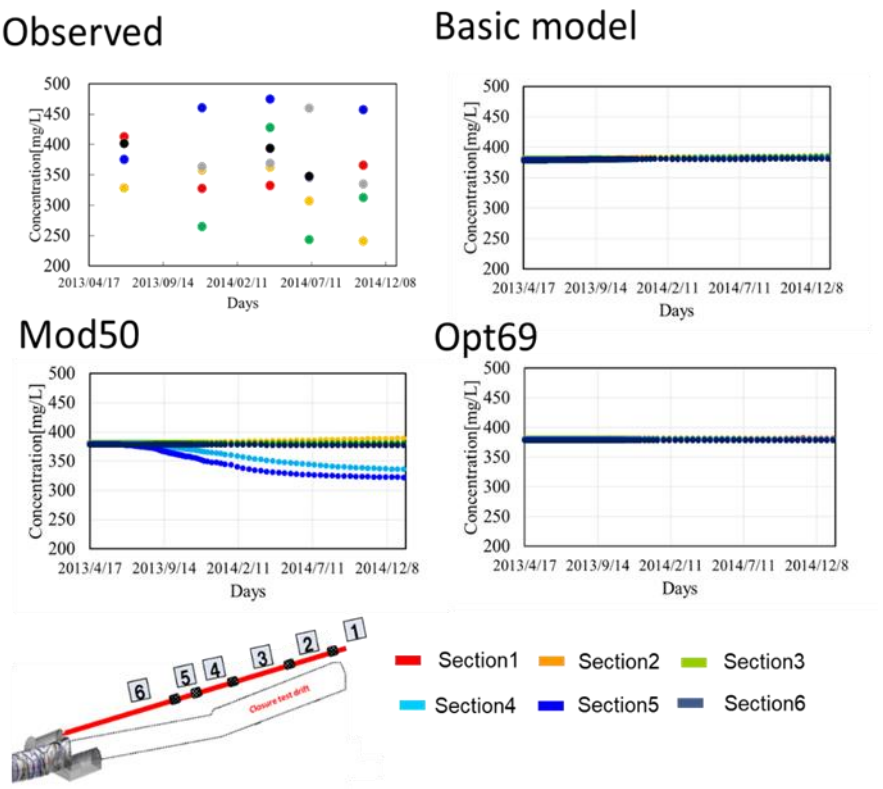

Figure 50. Comparison of time variation of Cl concentration in 12MI33.

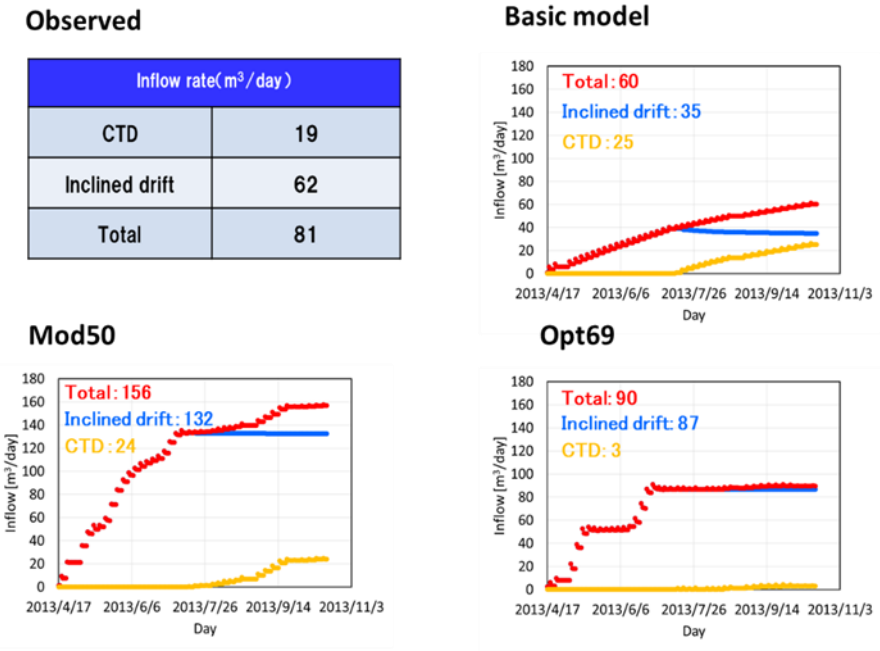

Figure 51. Comparison of time variation of Cl concentration in 12MI33.

4 Results of Step 1 modelling (SNL)

4.1 Modelling strategy and approach

The SNL team developed a general workflow or methodology to synthesize these data into a flow and transport model. Fracture data analysis and preliminary modelling analysis were conducted as part of Step 1. The fracture data analysis utilizes fracture data collected in the research tunnel and monitoring borehole 12MI33 as well as data from the literature. A discrete fracture model was developed based on fracture orientation, size and intensity derived from the fracture data analysis. The discrete fracture model was then up-scaled to an effective continuum model to be used in flow and transport simulations. Section 4.2 provides specific details of the fracture model development. The flow and non-reactive transport modelling analysis used project data and the fracture model to construct simulation models to predict inflow into the inclined drift and the Closure Test Drift (CTD) during excavation. The modelling analysis also predicts pressure and Cl concentration histories at observation points. The modelling analysis is described in Section 4.3. Geochemical modelling was also conducted using project geochemical data and the PFLOTRAN code. Reactive transport modelling using thermodynamic databases was used to predict hydro-chemical behaviour in the model area.

4.2 Fracture data analysis and model development

4.2.1 Introduction

The major goal of this study was to develop a fracture model of the granite rocks for the area surrounding the MIU Research Tunnel at 500 m depth. The fracture model is needed for simulation of hydrogeological and geochemical conditions in the various experiments being conducted as a part of the GREET project.

The modelling domain is 100 × 150 × 100 m with the main experimental part of the tunnel, Closure Test Drift (CTD), located approximately in the centre. The majority of the model is within the lower sparsely fractured domain (LSFD) of the Toki granite. Figure 52 shows the modelling domain, the research tunnel (CTD and Inclined Drift), the horizontal monitoring borehole 12MI33 (with 6 test intervals), and the vertical exploratory borehole MIZ-1 (only 2 test intervals are inside the modelling domain).

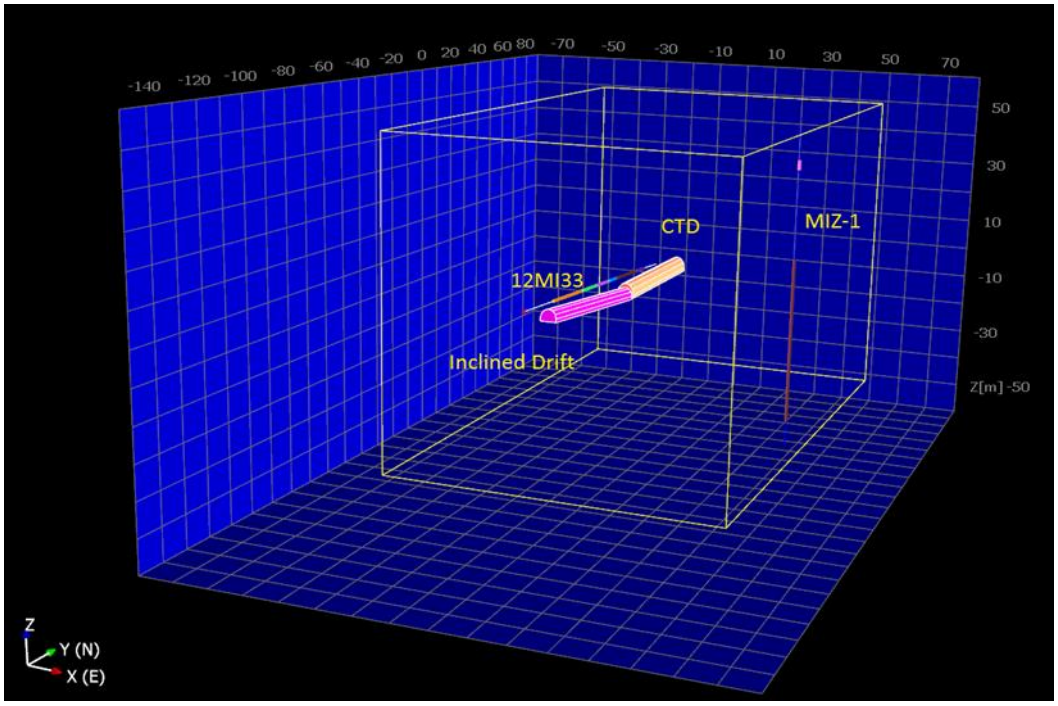

Figure 52. SNL Step 1 Modelling domain and location of research tunnel and boreholes.

The following data were used in the fracture analysis:

- Fracture traces on the walls of CTD, Inclined Drift, and Access Drift. Note that Access drift fracture data were used in the initial analysis even though this drift is outside the modelling domain. However, these fractures were not used in the developing of fracture properties because they were found to be different from the fractures in the Inclined Drift and CTD.
- Fractures observed in borehole 12MI33.
- Packer test data in 6 test intervals of 12MI33 and 2 test intervals of borehole MIZ-1.
- Measured inflow into the research drift.

The goal of the fracture analysis was to estimate fracture orientation, size, and intensity and use these estimates to develop the discrete fracture model (DFN). The DFN model is then converted to an equivalent continuum model with the grid cell size 1 × 1 × 1 m (1,500,000 grid blocks) using Oda's method (Oda, 1985). The grid cell size was designed to provide a refined mesh. Multiple realization of DFN and the corresponding equivalent continuum model was used to simulate groundwater flow and transport in the vicinity

of the research tunnel. The development of a DFN is demonstrated using one realization as an example. FracMan® 7.6 12) was used to develop the model.

4.2.2 Generating fractures using research tunnel fracture trace data

Two thousand and twenty-three fractures were considered on the wall of the research tunnel. Figure 53 shows the observed fracture traces and location of monitoring points in borehole 12MI33. The fracture trace data include trace segment coordinates, length, dip, strike, alteration (if any), and flow range (if any). If an alteration was observed, the filling was described using the following categories carbonate, chlorite and/or sericite, and unconsolidated clayey filling including smectite.

It was assumed that the fractures that did not exhibit any flow discharge are either closed fractures or small fractures not connected to the fracture network. There are 146 fractures (7.2 %) with the observed flow discharge. They are characterized in the original data set based on the flow range as “flow” (F) fractures (>1 L / min), “drop” (D) fractures (>0.1 L / min), and “wet” (W) (< 0.1 L / min) fractures. These fractures were selected for the analysis and fracture model development (Table 13). The trace data were imported into the model and are shown in Figure 54.

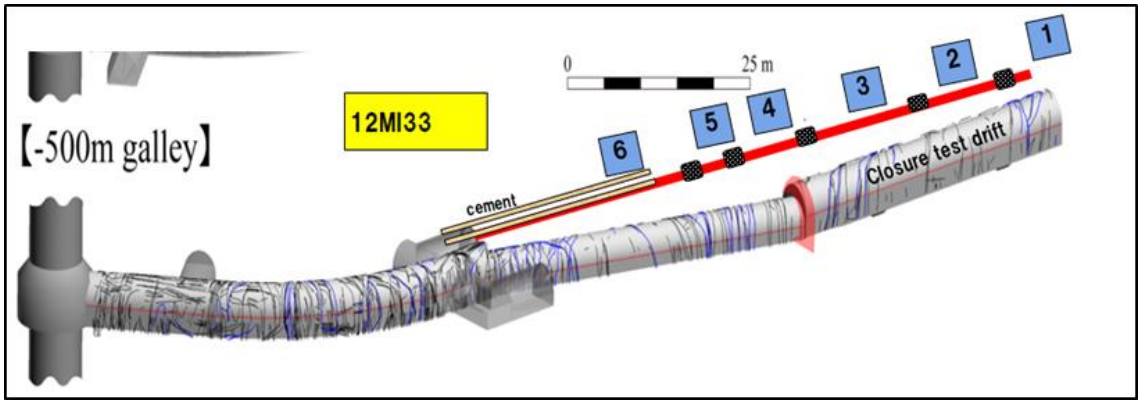

Figure 53. Observed fracture traces in the research tunnel and location of monitoring points in borehole 12MI33.

The observed fracture traces can be used to generate each individual fracture. The dip direction and dip angle of the fracture are derived from the plane containing the fracture traces. Thus, the location of the fracture plane centre and its orientation is fixed. However, the fracture size and shape are generally not known and need to be defined.

This analysis assumes that the fractures have a circular shape (aspect ratio 1:1), which is a common assumption of DFN models.

The fracture size was derived from the trace length analysis. It was assumed that the fractures with different flow discharges may have different sizes. Consequently, the analysis was conducted separately for F-, D-, and W- fractures. FracMan uses an algorithm described in Zhang (2002) and La Pointe (2002) to estimate fracture size (equivalent radius) from the trace length and offers different probability distributions for fitting the data. The power-law and lognormal distributions were considered in this analysis.

Table 13. Research Tunnel fractures included in the fracture analysis.

Research Tunnel Area	F-Fractures (flow>1.0 L/min)	D-Fractures (flow>0.1 L/min)	W-Fractures (flow<0.1 L/min)	All Fractures with Flow
CTD	4	15	3	22
Inclined Drift	14	42	N/A	56
Access Drift	N/A	65	3	68
Total	18	122	6	146

The results of the fracture size analysis are shown in Figure 55 for the power-law and in Figure 56 for the lognormal distribution. The distributions of W- and D- fractures are very similar and were combined in one. The F-fracture distribution is different from D- and W- fracture distributions. The trace length distributions of all sets are best described with the lognormal distribution. The power-law distribution that is often assumed for fracture size is not a good fit to these data.

The equivalent fracture radius distributions estimated from the trace length data are summarized in Table 14. The F- fractures with greater flow rates are also the ones with the larger size. This is consistent with the common concept that the fracture parameters affecting the flow (transmissivity and aperture) are positively correlated with the fracture radius.

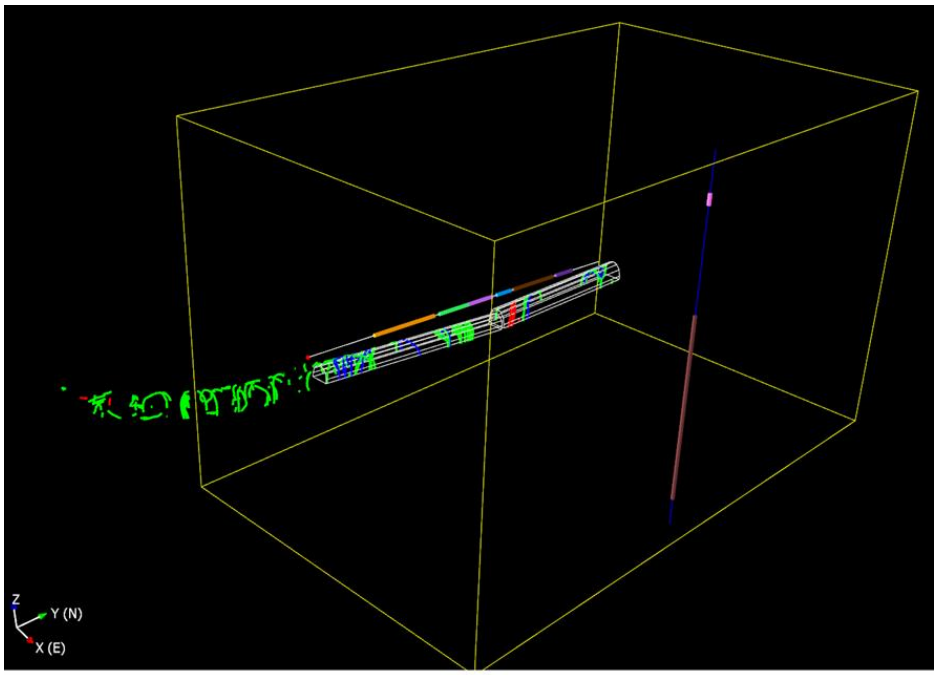

Note: F-fractures are shown in blue, D-fractures are shown in green, and W-fractures are shown in red colour.

Figure 54. Traces of the fractures on the Research Tunnel walls included in the analysis.

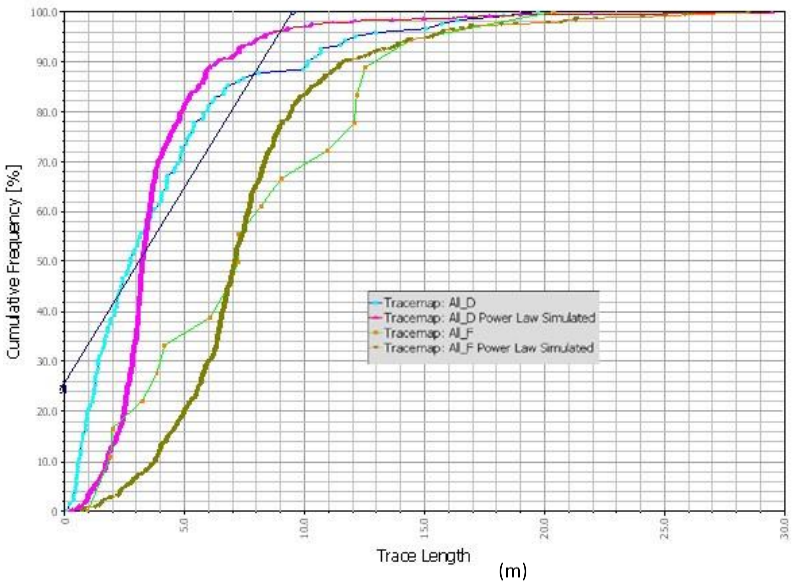

Figure 55. Power-Law Distribution Fit to the Fracture Trace Data.

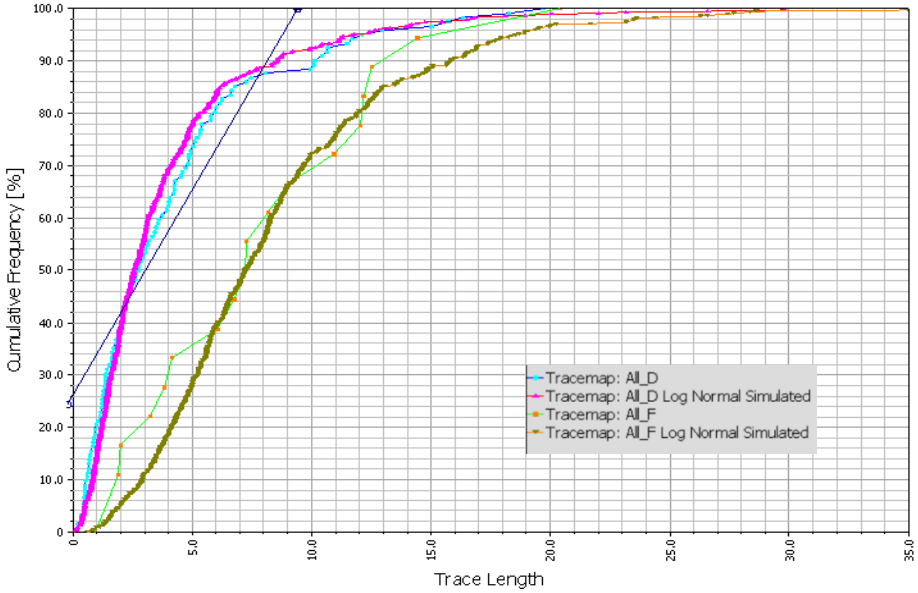

Figure 56. Lognormal distribution fit to the fracture trace data.

Table 14. Equivalent fracture radius distribution parameters.

Fracture Set	Distribution Type	Mean/Minimum Radius (m)	Standard Deviation/Exponent
D- and W-Fractures	Lognormal	1.42	1.29
F-Fractures	Lognormal	3.88	2.15
D- and W-Fractures	Power-Law	1.5	3.4
F-Fractures	Power-Law	3.3	3.9

One hundred and forty-six fractures were generated in the Research Tunnel using the lognormal distributions defined in Table 14 for the equivalent fracture radius (either F- or W- and D- depending on the fracture type). Note that the size of fractures will vary from realization to realization. Figure 57 shows the generated fractures for one realization.

The remaining fracture parameters that must be defined for DFN are fracture hydraulic conductivity (or permeability) and fracture aperture. Very few data are available on fracture aperture. Even when fracture aperture is reported, it seems to apply only to the surface of the tunnel or borehole walls. The values are too large (1 mm or greater) to be

representative of the conditions within the rock mass. The fracture aperture values typical for granite rocks are in the order of tenths to hundreds of microns, except for the large fractures in fault zones (Klint et al., 2004).

The hydraulic conductivity k_{int} was derived from the transmissivity evaluated in the packer tests T_{int} as:

$$k_{int} = \frac{T_{int}}{l_{int}} \qquad (4.2.1)$$

where lint is the length of the test interval.

Tint measured in these tests represents the transmissivity of the test interval. A test interval may intersect different types of fractures with different connections to the fracture network. These fractures may have different size, hydraulic conductivity, and aperture. Thus, the interval transmissivity and hydraulic conductivity values cannot be easily converted to fracture transmissivity and hydraulic conductivity. The same principle applies to the observed inflow into the tunnel.

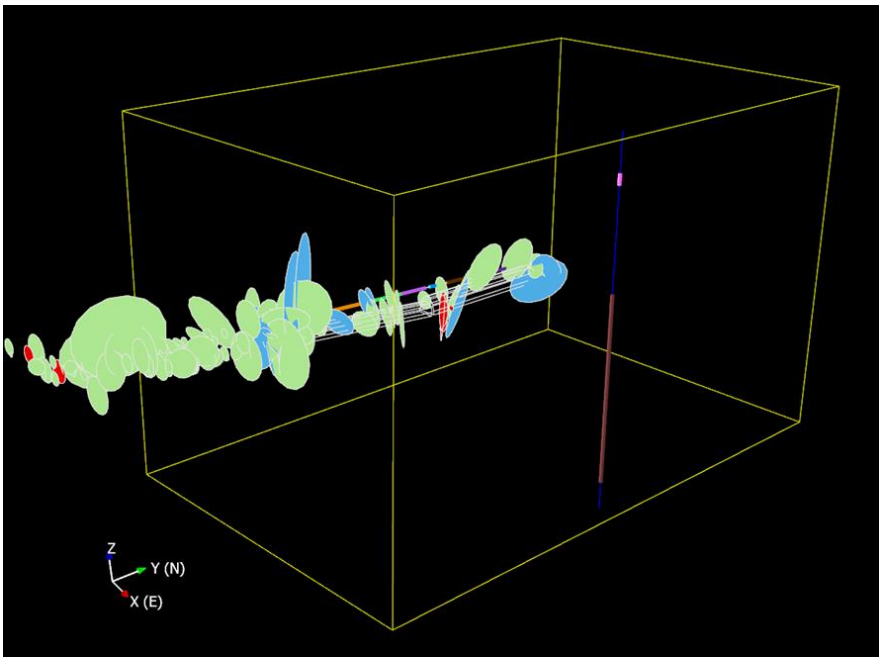

Note: F-fractures are shown in blue; D-fractures are shown in green; and -fractures are shown in red colour.

Figure 57. Fracture generated in the research tunnel.

This analysis uses all available data in combination with the discrete fractures generated in the tunnel and borehole 12MI33 to evaluate fracture transmissivity. The initial evaluation of fracture transmissivity is based on the observed range of flow through the different types of fracture. The analytical solution for the unit inflow (Q) into a circular tunnel with radius r located at depth h (Butscher, 2012) is:

$$Q = \frac{2\pi k(A+H)}{\ln\left(\frac{h}{r}+\sqrt{\frac{h^2}{r^2}-1}\right.} \qquad (4.2.2)$$

$$A = h(1-\alpha^2)/(1+\alpha^2) \text{ and } = \frac{1}{r}(h-\sqrt{h^2-r^2}$$

where k is the hydraulic conductivity.

The inflow through the fracture (Qfr) with aperture b is:

$$Q_{fr} = Q \cdot b \; = \frac{2\pi T(A+H)}{\ln\left(\frac{h}{r}+\sqrt{\frac{h^2}{r^2}-1}\right.} \qquad (4.2.3)$$

$$T = k \cdot b$$

where T is fracture transmissivity.

Fracture transmissivity T was calculated from Eq. 7.2.3 assuming r = 2.5 m, h = 500m, and H = 110 m. The transmissivity of F- fractures (Q_{fr} > 1.0 L / min) is > 2.6×10^{-8} m^2 / s, transmissivity of D- fractures (Q_{fr} > 0.1 L / min) is > 2.6×10^{-9} m^2 / s, and the transmissivity of W- fractures (Q_{fr} < 0.1 L / min) is < 2.6×10^{-9} m^2 / s.

It was assumed that the inflow into CTD (QCTD) and Inclined Drift (Q_{Incl}) can be approximated by the following equations:

$$Q_{CTD} = Q_{CTD\_F} + Q_{CTD\_D} + Q_{CTD\_W} \qquad (4.2.4)$$

$$Q_{CTD\_F} = 1.0\frac{L}{min} \cdot N_{F_{CTD}} \cdot c, \quad Q_{CTD\_D} = 0.1\frac{L}{min} \cdot N_{D_{CTD}} \cdot c, \quad Q_{CTD\_W} = 0.1\frac{L}{min} \cdot N_{W_{CTD}}$$

$$Q_{Incl} = Q_{Incl\_F} + Q_{Incl\_D} + Q_{Incl\_W} \qquad (4.2.5)$$

$$Q_{Incl\_F} = 1.0\frac{L}{min} \cdot N_{F_{Incl}} \cdot c, \quad Q_{Incl\_D} = 0.1\frac{L}{min} \cdot \mathrm{N}_{D_{Incl}} \cdot c, \quad Q_{Incl\_W} = 0.1\frac{L}{min} \cdot N_{W_{Incl}}$$

where N_{F_CTD} and N_{F_Incl} is the number of F-fractures in CTD and Inclined Drift respectively, ND_CTD and N_{D_Incl} is the number of D-fractures, NW_CTD and N_{W_Incl} is the number of W-fractures, and c is a constant. Introducing c accounts for the fact that the flow through a fracture was express in terms of a value greater or smaller than a specific limit. The value of c = 2.3 was derived by matching the observed inflow into CTD and Inclined Drift with the inflow values calculated with Eqs. 4.2.4 and 4.2.5.

The Access Drift was not considered because of two reasons: it is outside the modelling domain and it is affected by the proximity to the Main Shaft fault and UHFD.

The observed and calculated values are summarized in Table 15. The fracture transmissivity values that correspond to the calculated inflow values are: 6.0×10^{-8} m^2 / s (F-fractures), 6.0×10^{-9} m^2 / s (D- fractures), and 2.6×10^{-9} m^2 / s (W- fractures).

Table 15. Comparison of measured and calculated inflow into the Research Tunnel.

Research Tunnel Area	Measured Tunnel Inflow (L/min)	Number of Fractures			Calculated Inflow (L/min)			
		F	D	W	F	D	W	Total
CTD	13	4	15	3	9.2	3.45	0.3	12.95
Inclined Drift	43	14	42	N/A	32.2	9.66	0	41.86

The fracture aperture can be estimated from the cubic law relationship (Snow, 1969) between the transmissivity and aperture:

$$T = \frac{b^3}{12}\frac{\rho g}{\mu} \qquad (4.2.6)$$

Where ρ is the water density, g is the gravity acceleration and μ is the water viscosity. Assuming ρ=998 kg / m^3 and μ=0.001 N s / m^2 the calculated aperture values are: 42 microns (F-fractures), 20 microns (D-fractures), and 15 microns (W-fractures).

The fracture permeability (k) can be calculated as:

$$k = \frac{b^2}{12}\frac{\rho g}{\mu} \qquad (4.2.7)$$

The calculated fracture permeability values (approximation of mean) are: 1.5×10^{-10} m^2 (F-fractures), 3.2×10^{-11} m^2 (D-fractures) and 1.8×10^{-11} m^2 (W-fractures).

The following ranges were derived for the fracture parameters:

Fracture transmissivity: 2.6×10^{-9} - 6.0×10^{-8} m^2/s

Fracture permeability: 1.8×10^{-11} - 1.5×10^{-10} m^2

Fracture aperture: 15 - 42 micron

Note that these ranges apply to the average parameter values.

There is not enough data to develop probability distributions for permeability and aperture. Instead, this analysis assumes correlations between the lognormally distributed fracture equivalent radius (R) and fracture permeability (k) and aperture (b) in the following form:

$$k = \gamma_1 \cdot R^{\omega} \qquad (4.2.8)$$

$$b = \gamma_2 \cdot R \qquad (4.2.9)$$

where γ1, γ2, and ω are coefficients.

The coefficients were adjusted to match the calculated inflow into the tunnel with the observed inflow. Eq. 4.2.3 was used to calculate the inflow through each fracture shown in Figure 57. Fracture generated in the research tunnel. Each fracture has a different radius and, thus, different permeability and aperture (Eqs. 4.2.8 and 4.2.9) and different transmissivity (Eq. 4.2.6). A good match was obtained with the following coefficient values:

γ1 =1.55×10^{-12}

γ2 =1.16×10^{-5}

ω =2.3

The results of the calculations with these coefficients are summarized in Table 16. The average transmissivity of fracture is 2.5×10^{-8} m^2/s. This falls into the estimated transmissivity range 2.6×10^{-9} - 6.0×10^{-8} m^2/s.

4.2.3 Generating fractures using borehole 12MI33 fracture data

Borehole 12MI33 is a horizontal borehole that is parallel to the Research Tunnel (Figure 52). The packer tests were conducted in 6 test intervals. The test intervals also serve as the monitoring points (Figure 53) for observation of temporal variations in pressure and geochemistry in the vicinity of the Research Tunnel. Two hundred and ninety-seven fractures were recorded in the borehole. The fractures were classified as “crack”, “hair crack”, “discontinuity crack”, and “mineral vein”. The fractures described as cracks that had recorded aperture values were assumed to be permeable fractures, such as F-, D-, and W-fractures observed in the Research Tunnel. Seventeen such fractures were identified. The fracture data were imported into the model. The fractures were generated in accordance with these data (depth and orientation) using F-fracture lognormal distribution for fracture radius. F-fracture radius distribution produced closer results to the packer test results as shown below.

Table 16. Comparison of calculated inflow from generated fractures and observed inflow into Research Tunnel.

Generated Fractures		
Type	$\sum$ **Transmissivity** (m^2/s)	$\sum$ **Inflow** (L/min)
D	1.94E-06	61.03
F	1.58E-06	49.78
W	9.71E-08	3.06
Total	3.62E-06	113.87
Measured Inflow into the Research Tunnel (L/min): 104		

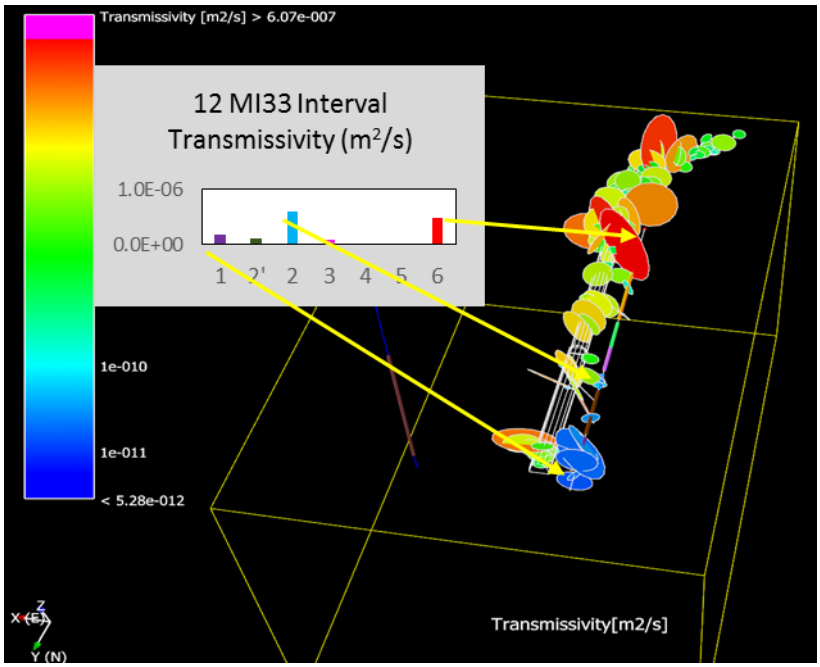

Figure 58. Transmissivity of fractures in the Research Tunnel and borehole 12MI33.

The fractures generated in the borehole are shown in Figure 58 along with the Research Tunnel fractures. Figure 58 also shows the transmissivity of the test intervals obtained in the packer tests. The high transmissivity intervals 1, 2 and 6 coincide with the zones in which fractures generated in both, Research Tunnel and borehole, are present. Intervals 2 and 3 intersect a few fractures and their transmissivity is lower. Intervals 4 and 5 do not intersect any of generated fractures and their transmissivity is significantly lower.

Table 17 and

Table 18 compare the transmissivity of the generated fractures in borehole 12MI33 and the transmissivity of the test intervals from the packer tests in this borehole. The total transmissivity of fractures generated in the borehole (7.6×10^{-7} m^2 / s) is close to the total transmissivity of the test intervals (9.9×10^{-7} m^2 / s).

The following can be concluded:

- The locations of 17 fractures generated in borehole 12MI33 are consistent with the locations of fractures in the Research Tunnel.
- Fracture properties derived from the Research Tunnel fracture trace analysis are consistent with the packer test data in borehole 12MI33.

Table 17. Transmissivity of the generated fractures in borehole 12MI33.

Fracture	Transmissivity (m^2/s)	Fracture	Transmissivity (m^2/s)
1	1.14E-08	10	8.30E-09
2	2.71E-09	11	5.36E-09
3	1.74E-08	12	2.62E-09
4	7.26E-09	13	1.60E-08
5	1.39E-08	14	2.34E-08
6	2.94E-09	15	4.27E-07
7	6.28E-08	16	6.59E-08
8	5.01E-08	17	1.82E-08
9	2.30E-08	Total	7.58E-07

Table 18. Transmissivity of the test intervals from borehole 12MI33 packer tests

Interval	Transmissivity (m^2/s)
1	1.78E-07
2'	9.78E-08
2	6.01E-07
3	8.65E-08
4	4.96E-09
5	1.93E-08
6	4.91E-07
Total	9.88E-07

4.2.4 Generating stochastic fractures in the modelling domain

The Research Tunnel fracture trace analysis considered in Section 4.2.2 provided estimates of the fracture size, permeability, and aperture. These estimates were corroborated by comparing the packer test results with the transmissivity of fractures generated in borehole 12MI33 in Section 4.2.3. The fractures with the deterministic locations and stochastic properties (radius and correlated with radius permeability and aperture) were generated in the Research Tunnel and borehole 12MI33 (Figure 58).

The size and properties of the fractures outside the Research Tunnel and borehole 12MI33 can be assumed in accordance with the above estimates. However, the locations of these fractures are not known. Thus, the stochastic approach is needed. The stochastic generation of fractures requires the following input parameters:

- Number of fracture sets
- Orientation distribution of each set
- Fracture intensity in each set

4.2.4.1 Number of fracture sets and fracture orientation

The number of fracture sets and their orientation was obtained from the analysis of the fractures generated from the tunnel traces using FracMan tool Interactive Set Identification System (ISIS). ISIS (Golder, 2017) defines fracture sets from field data using an adaptive probabilistic pattern recognition algorithm. ISIS calculates the distribution of orientations for the fractures assigned to each set and then reassigns fractures to sets according to probabilistic weights proportional to their similarity to other fractures in the set. The orientations of the sets are then recalculated and the process is repeated until the set assignment is optimized.

Figure 59 shows the ISIS set assignment results for the Research Tunnel fractures. Even though 3 sets are defined, most of the fractures are in Set 2. The significance levels of the fitted Fischer distributions are low for all sets meaning there is no clear separation into the different sets.

In the next step, the fractures in the Access Drift were removed from the analysis because they may be affected by the Main Shaft fault. For example, set 3 in Figure 59 contains only the Access Drift fractures. The ISIS analysis of fractures in the Inclined Drift and CTD identified only one fracture set. The best distribution (Kolmogorov-Smirnov probability 87%) was Fisher distribution with the flowing parameters:

- mean trend 2080
- mean plunge 80
- concentration parameter ķ equal to 7

Note that orientation is given in the local coordinate system. The actual coordinate system was rotated 10.20 clockwise in the x-y plane to align the tunnel with the y-axis. The calculated Fisher distribution is shown in Figure 60. The low ķ signifies a large dispersion or wide range of fracture orientations.

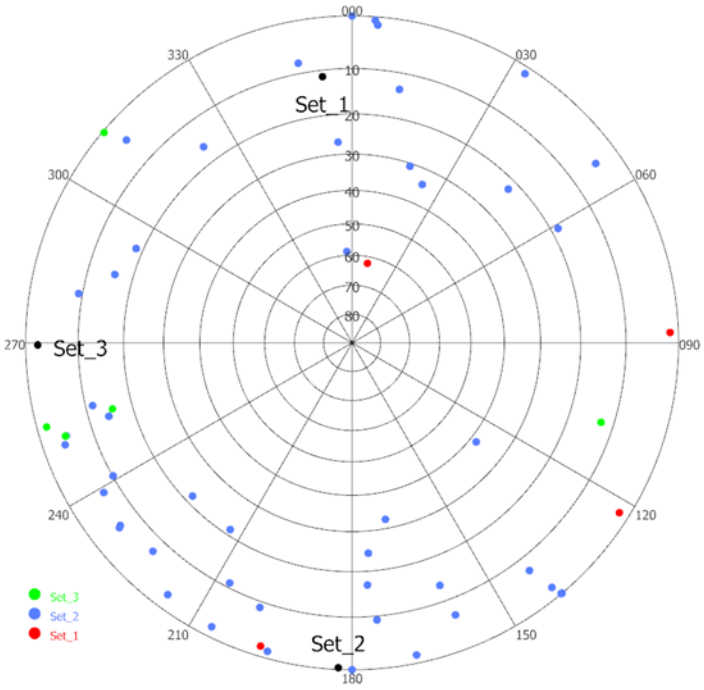

Figure 59. ISIS set assignment results for the Research Tunnel fractures.

4.2.4.2 Fracture intensity

Fracture intensity has a direct impact on how many fractures will be generated in the modelling domain. Fracture intensity can be specified either as number of fractures in the set (not recommended because it is scale dependent) or as volumetric intensity of fractures in the set, also known as P32. P32 [1/m] is scale independent (invariant with respect to the distribution of fracture size) and represents fracture area per unit volume of rock. Neither number of fractures or P32 can be directly measured.

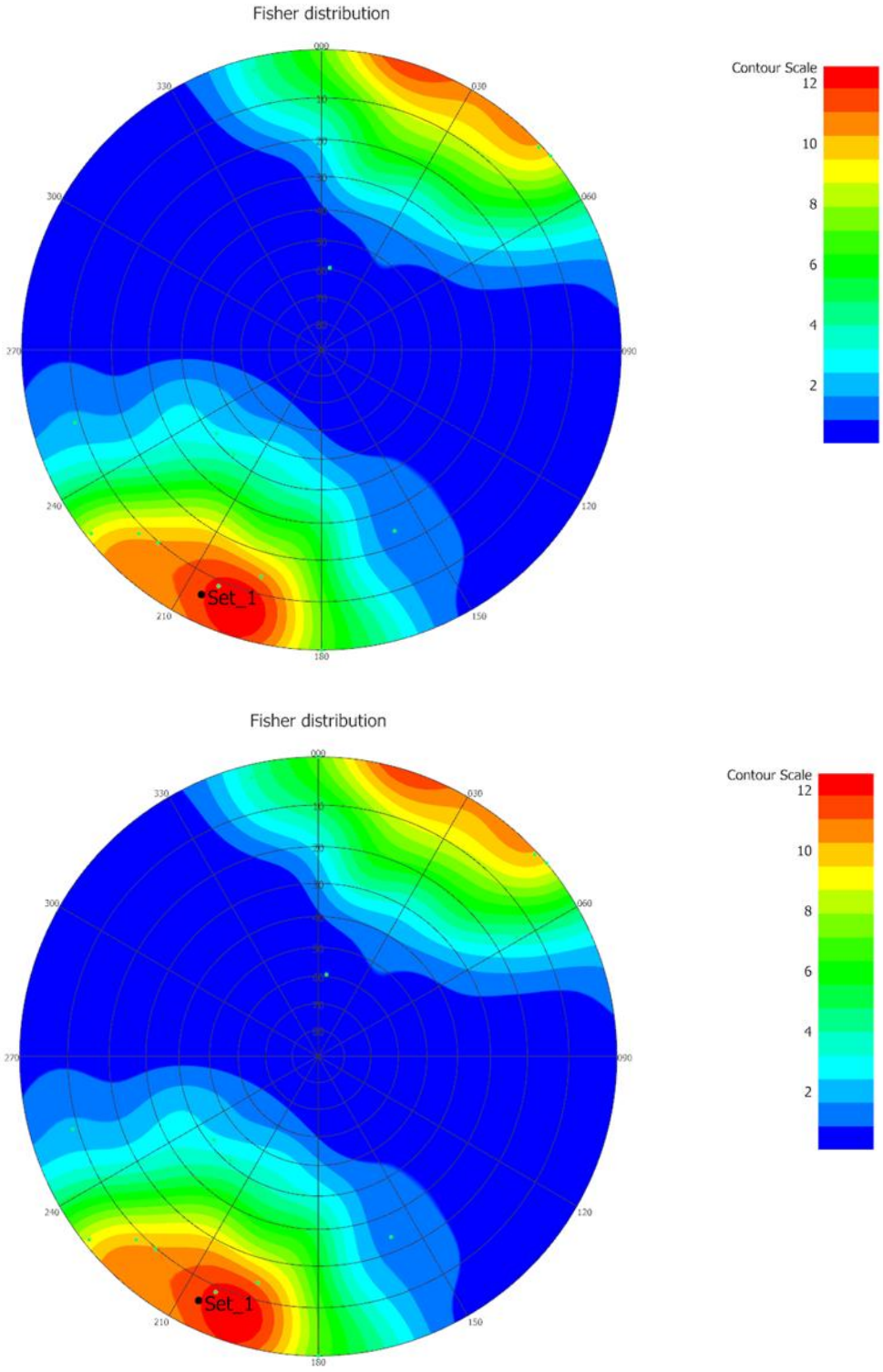

Figure 60. Calculated Fisher distribution for inclined drift and CTD fractures.

This analysis uses the observed linear intensity P10 (number of fractures per unit length) of fractures in the Research Tunnel (0.19 fractures/m) and in the borehole 12MI33 (0.17 fractures/m) to evaluate P32. The stochastic fractures were generated using Fisher

distribution (Section 4.2.4.1), fracture radius (Table 14), fracture permeability (Eq. 4.2.8), and fracture aperture (Eq. 4.2.9). The fracture P32 value is iteratively redefined until the P10 values in 2 arbitrary placed imaginary horizontal boreholes matched P10 of fractures observed in the Research Tunnel and borehole 12MI33.

Figure 61 shows the stochastic fractures intersected by the two imaginary horizontal boreholes with P32 = 0.22 1/m. P10 in both imaginary boreholes (0.19 fractures/m) matches the observed P10 in the Research Tunnel and is very close to the observed P10 in borehole 12MI33.

The significantly lower P10 values (0.04) were calculated for two arbitrarily placed vertical boreholes (Figure 62). This is because the vertical borehole has lower probability of intersecting sub-vertical fractures.

4.2.4.3 Comparison to the Packer Test results in Borehole MIZ-1

Figure 63 shows the stochastic fractures that intersect upper and lower test intervals of the vertical borehole MIZ-1. The transmissivity of the generated fractures is provided in Table 19. The packer test results are summarized in Table 20. The total transmissivity of generated stochastic fractures (2.1×10^{-7} m^2/s) is higher than the total transmissivity obtained in the packer tests (4.2×10^{-8} m^2/s). The horizontal flow to the vertical borehole in the packer tests is affected by the horizontal permeability. The horizontal permeability is lower than vertical because the fractures are sub-vertical. This can explain some of the difference. Also, only one realization was used in this comparison.

4.2.4.4 Stochastic fracture generation

The stochastic fractures were generated assuming one fracture set with the orientation defined in Section 4.2.4.1 and P32 = 0.22 calculated in Section 4.2.4.2. The Enhanced Baecher model in FracMan was used. In the original Baecher model (Baecher et al., 1977) the fracture centres are located uniformly in space, and, using a Poisson process, the fractures are generated as disks with a given radius and orientation. The Enhanced Baecher model extends the Baecher model by providing a provision for fracture terminations and more general fracture shapes.

Figure 64 shows one realization of the stochastic fractures generated in the modelling domain. The colour scale is used to show fracture transmissivity. One realization of the fractures in the Research Tunnel and borehole 12MI33 is also included.

Figure 65 shows the stereonet of the generated stochastic fractures. Figure 66 and Figure 67 show the sampled distribution of fracture permeability and aperture respectively. The median permeability is 2.3×10^{-11} m^2 and the median aperture is 27 microns.

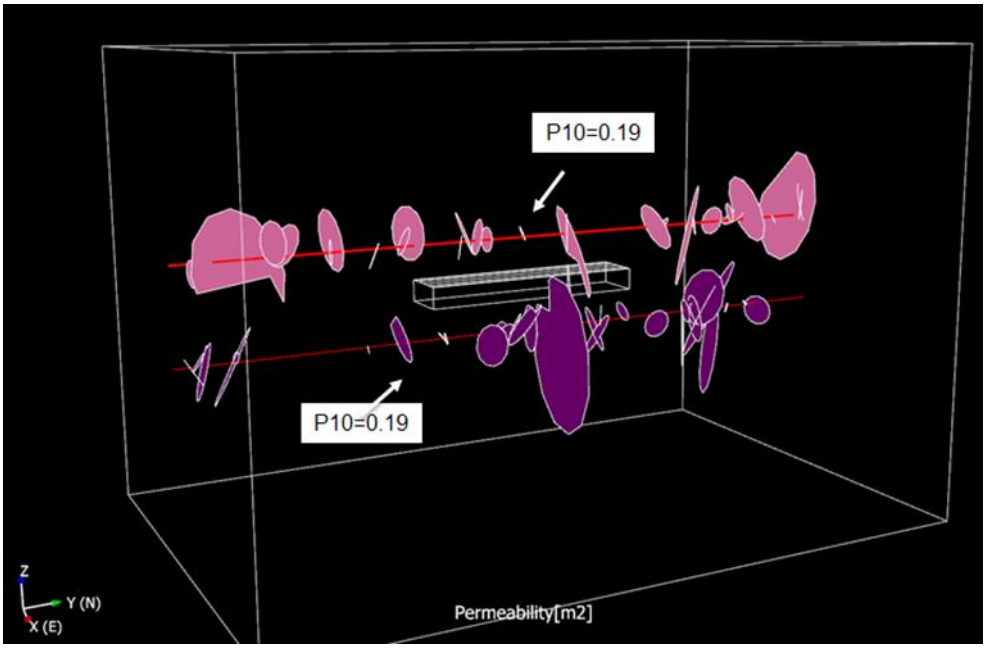

Figure 61. Stochastic fractures intersecting two imaginary horizontal boreholes.

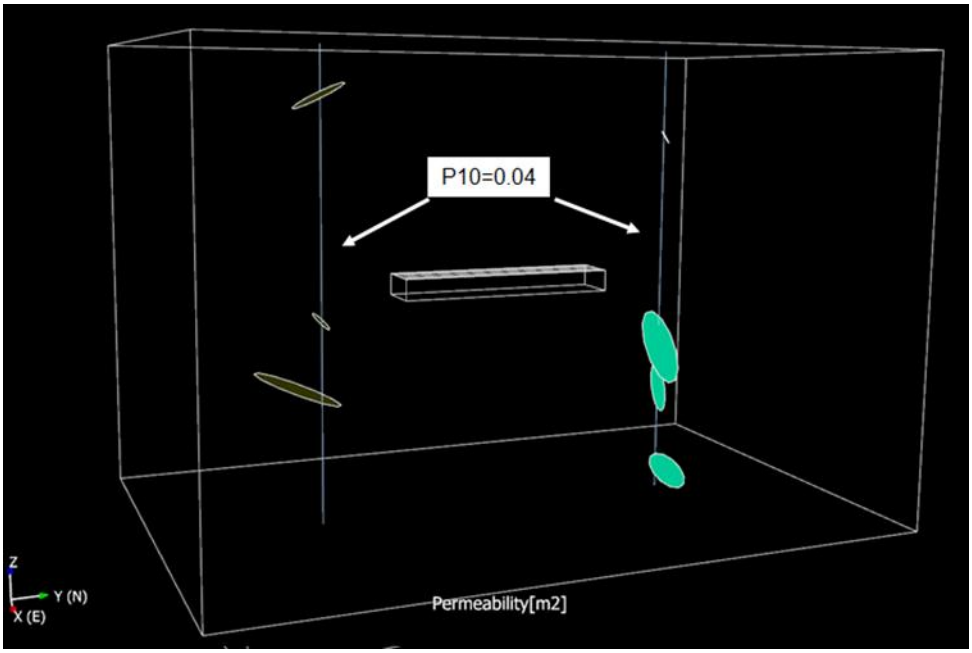

Figure 62. Stochastic fractures intersecting two imaginary vertical boreholes.

Table 19. Transmissivity of stochastic fractures intersected by Borehole MIZ-1.

Fracture	Transmissivity (m^2/s)
1	9.54E-08
2	3.54E-08
3	7.34E-09
4	2.52E-08
5	4.38E-08
Total	2.07E-07

Table 20. Packer Test results in Borehole MIZ-1.

Interval		Transmissivity (m^2/s)
Top (m)	Bottom (m)	
-260.4	-263.3	3.69E-08
-290.9	-342.4	5.16E-09
Total		4.20E-08

NOTE: Only the test intervals within the modelling domain are considered.

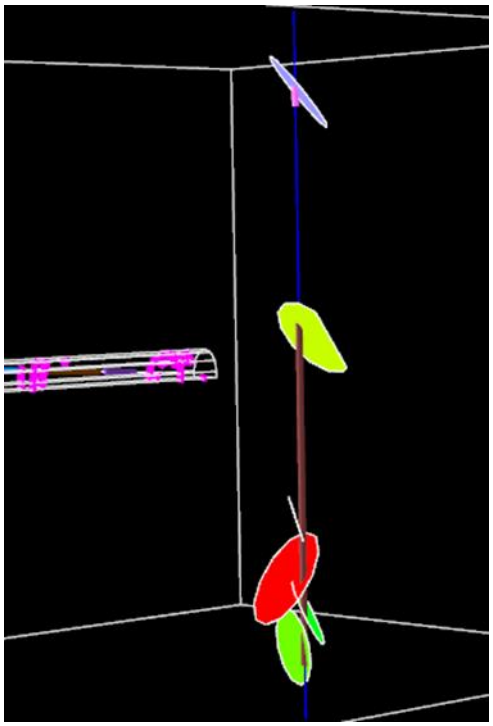

Figure 63. Stochastic fractures intersected by Borehole MIZ-1.

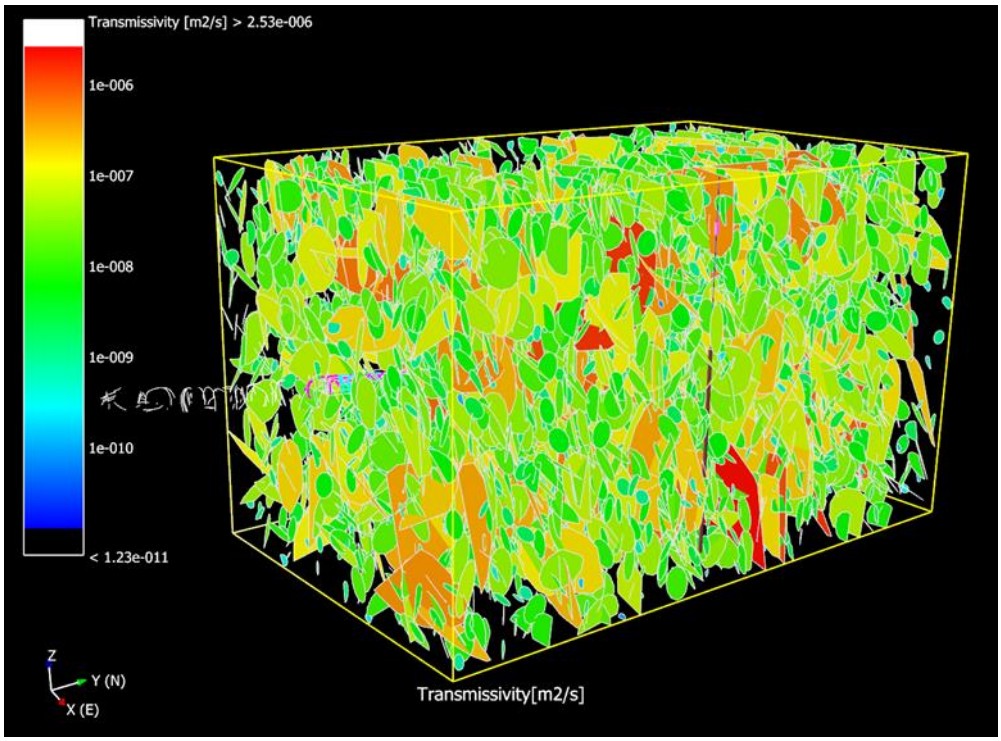

Figure 64. One realization of stochastic fractures generated in the modelling domain.

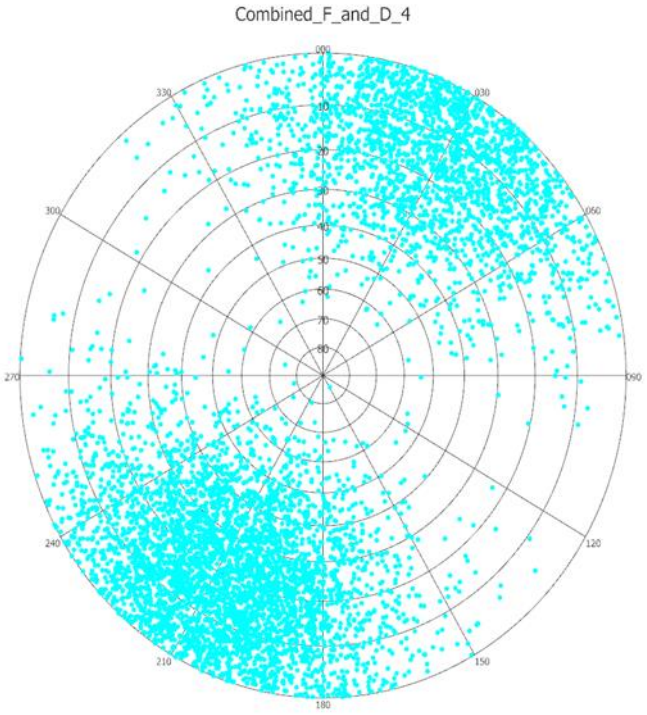

Figure 65. Sampled stochastic fracture stereonet.

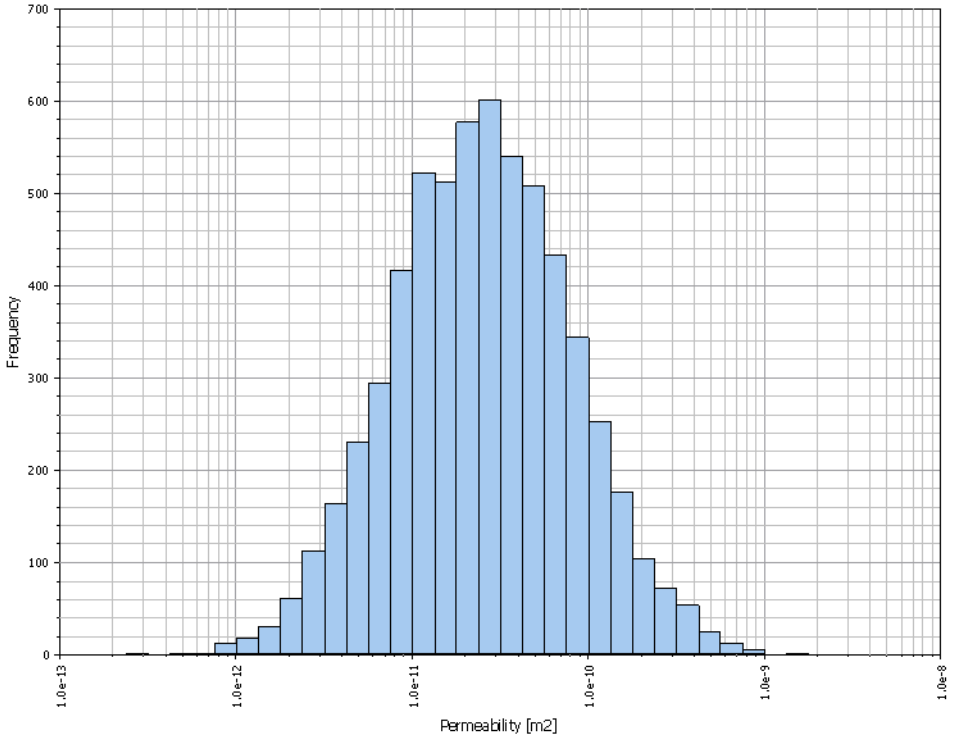

Figure 66. Sampled stochastic fracture permeability.

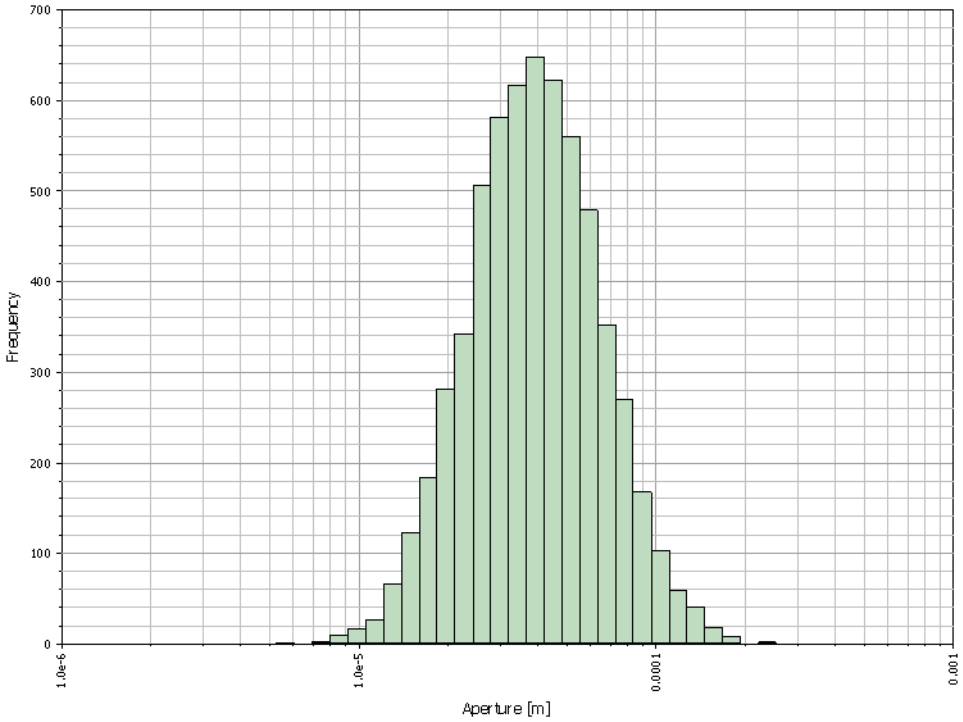

Figure 67. Sampled stochastic fracture aperture.

4.2.5 Upscaling DFN to the equivalent continuum model

After DFN is generated, it can be upscaled to an equivalent continuum model using Oda's method. Oda's method calculates permeability tensors in 3 dimensions for each cell. Oda tensor is a simplification of Darcy's Law for flow through anisotropic porous medium. The fracture permeability (k) is projected onto the plane of the fracture and scaled by the ratio between the fracture volume (porosity) and the volume of the grid cell. The method is implemented in FracMan in accordance with the following equation:

$$K_{i,j} = \frac{1}{12}(F_{k,k}\delta_{i,j} - F_{i,j}) \qquad (4.2.10)$$

$$F_{i,j} = \frac{1}{V}\sum_{k=1}^{N} A_k T_k n_{i,k} n_{j,k}$$

where Ki,j is permeability tensor; δi,j is Kronecker's delta; Fi,j is fracture tensor; V is grid cell volume; N is total number of fractures in grid cell; Ak is area of fracture k; Tk is

transmissivity of fracture k; and ni,k, nj,k are the components of a unit normal to the fracture k. Note that only principal components of the permeability tensor (Kxx, Kyy, and Kzz) are the inputs into the flow and transport model.

Fracture porosity (€) of the grid cell is calculated as:

$$\epsilon = \frac{1}{V}\sum_{k=1}^{N} A_k b_k \qquad (4.2.11)$$

where bk is the aperture of fracture k.

The permeability and porosity of the grid cells without fractures can be defined in accordance with the matrix permeability and porosity. Figure 68 shows the grid cell permeability (Kxx) of the DFN realization shown in Figure 64. Figure 69 shows the vertical slices through CTD and Inclined drift.

Table 21 summarizes the mean properties of the grid cells in the modelling domain. The calculated mean permeability values are close to suggested reference permeability (10^{-15} m^2). However, the permeability is anisotropic and changes over a few orders of magnitudes.

Note that the permeability and porosity values calculated with Eqs. 4.2.10 and 4.2.11 will be very low if the total area of the fractures ($\sum A_k$) is very small. The proposed cut-offs for permeability and porosity values are 1×10^{-19} m^2 and 1×10^{-8}. The cells with the permeability lower than 1×10^{-19} m^2 or / and porosity lower than 1×10^{-8} were matrix cells. The number of cells that were below the cut-off values is 1.1% of the total number of cells with fractures in the considered example.

4.2.6 Corroboration with the other studies of the Tono Area

A large amount of fracture data was collected in the Tono area. The fracture data analysis and development of the fracture models at the different scales is an ongoing effort. Bruines et al. (2014) describes the development of the discrete fracture network models for 2 scales – local (9 km × 9 km) and site-scale (2 km × 2 km). Both models extend from the surface to the depth of 2 km and are based on the data from MIU Project Phase I and II investigations.

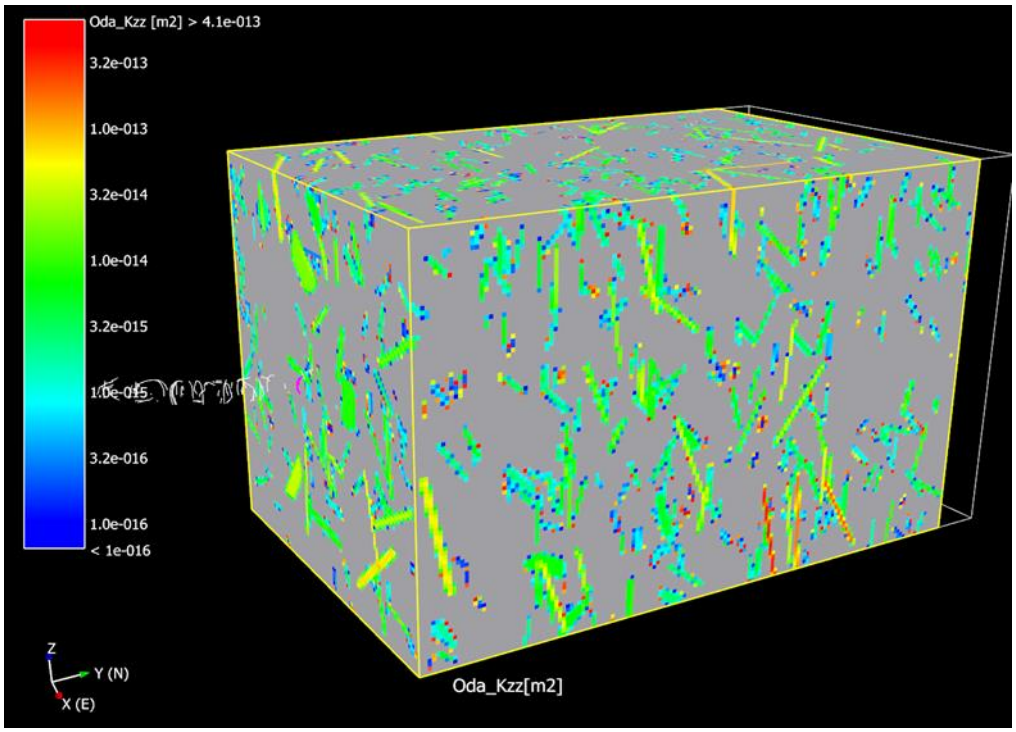

Figure 68. Vertical grid cell permeability for DFN realization shown in Figure 64.

Table 21. Effective continuum model means grid cell properties.

Parameter	Notation	Mean Value
Permeability (m^2)	K_{xx}	3.04E-15
	K_{yy}	1.31E-15
	K_{zz}	3.5E-15
Anisotropy	K_{xx}/K_{zz}	0.87
	K_{yy}/K_{zz}	0.37
	K_{yy}/K_{xx}	0.43
Fracture Porosity	€	1.64E-05
Number of cells with fractures		40%

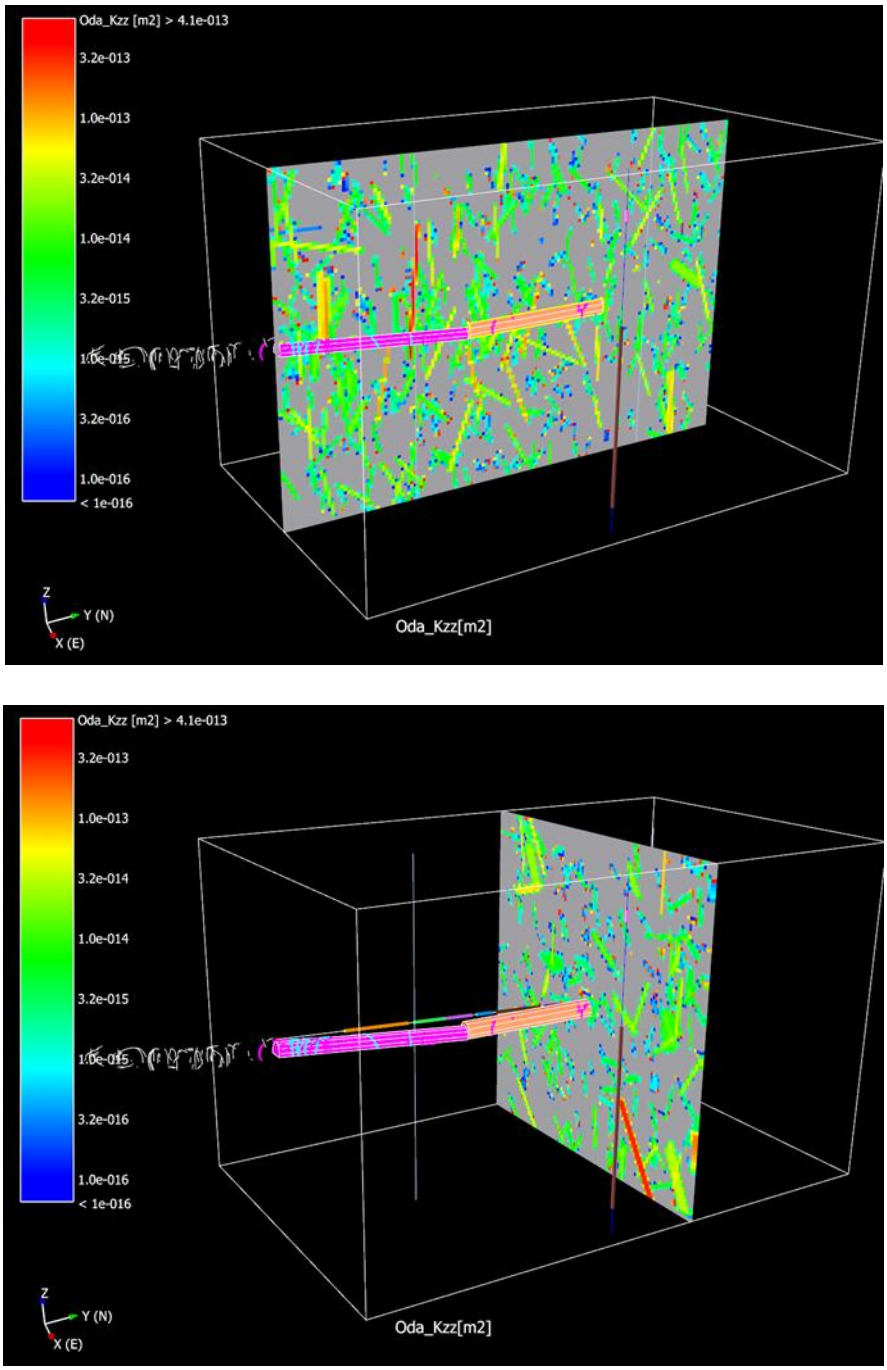

Figure 69. Vertical slices of vertical grid cell permeability for DFN realization shown in Figure 64.

The characterization of the fractured crystalline rock at the depth of the MIU is based on the data from the boreholes DH-2, DH-15, and MIZ-1 (Phase I data) and 33 boreholes drilled from galleries (Phase II data). The data includes well log data and hydraulic test data. Hydraulic tests were conducted in different sections of the boreholes on the different scales. The models consider both, UHFD and LSFD. The DFN models were

upscaled to the equivalent continuum models for transport simulations. Bruines et al. (2014) provided a discussion of the methodology used to develop DFN and equivalent continuum models. However, the results of the analysis were provided only for UHFD. The authors noted that significantly fewer data are available for the LSFD. The fracture data for LSFD data can be found in Ishibashi and Sasao (2015) for boreholes DH-2, DH-15 and MIZ-1.

The modelling domain considered in this study is within the LSFD. It occupies a very small volume of the site-scale model (Bruines et al., 2014). The data used to develop the fracture model are primarily based on the Research Tunnel fracture traces and fracture observations in borehole 12MI33. A portion of borehole MIZ-1 is within the modelling domain. The other boreholes are outside the modelling domain. The major goal of this section is to compare the parameters derived for the small-scale model to the parameters developed for the large-scale models.

The large-scale models use the following conceptual assumptions:

- The fractures are square shaped.
- The fracture size follows a power-law distribution.
- The fracture transmissivity is lognormally distributed and independent of fracture size.

The large-scale DFN was upscaled to the equivalent continuum model using three different grid block sizes: 30 m, 70 m, and 100 m.

As previously discussed, the small-scale model assumes circular shaped fractures. The fracture size follows a lognormal distribution (Section 4.2.2, Figure 55 and Figure 56). The fracture permeability and aperture are correlated with fracture radius (the larger fractures have larger transmissivity). The small-scale DFN is upscaled to the equivalent continuum model with the grid block size of 1 m.

Both, large-scale and small-scale models assume that not all the fractures conduct flow. As it was shown in Ishibashi and Sasao (2015), only a small portion of all observed fractures are open fractures. The large-scale model further assumes that only open fractures connected to the network conduct flow. These fractures are called the water-conducting features (WCFs). The fractures used in developing the small-scale model are the fractures in the Research Tunnel that showed water discharge and the fracture in 12MI33 borehole with the recorded apertures (~10% of observed fractures).

4.2.6.1 Fracture size

The fracture size defined in Ando et al. (2012) for LSFD follows a power-law distribution with minimum 2.5 m, maximum 3,000 m and slope 4.1 (Table 5.3.3-1 in Ando et al., 2012). The fracture size in the small-scale model is based on the analysis of the fracture traces in the tunnel. The power-law distributions derived from this analysis (Table 14) have minimum size of 1.5 m and 3.3 m and slopes 3.4 and 3.9. These values are close to the large-scale model size distribution. However, as it was shown in Section 4.2.2, the lognormal distributions provided better fit to the data. The comparison between the large-scale and small-scale models is shown in Figure 70. While there are some differences, the distributions are similar.

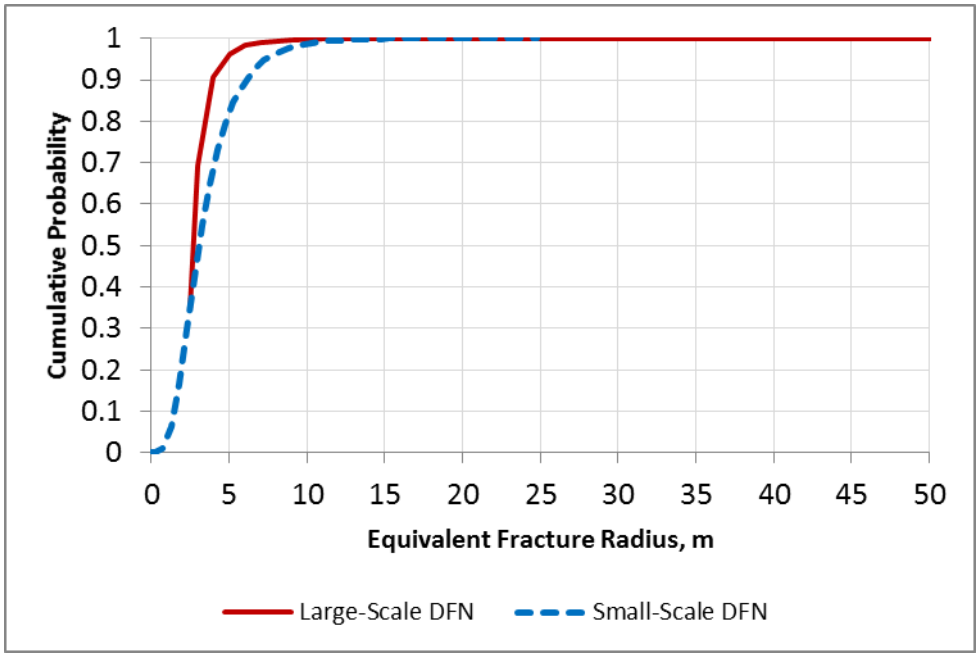

Figure 70. Equivalent fracture radius distributions in large-scale and small-scale models.

4.2.6.2 Fracture orientation and intensity

Ando et al. (2012) described 4 sets of fractures in borehole MIZ-1 (Ando et al. 2012: Table 5.3.1.6). Three of these sets consist of north-trending sub-vertical fractures (total number of fractures in these sets is 12). The small number of fractures in each set and high values of Fisher dispersion coefficient (k is 80-147) suggests that 3 sets could, in fact, be one set with lower k (higher dispersion). Note that Golder (2017) recommends using k in the range from 20 to 50 for the low orientation variability. The average plunge

in 3 sub-vertical fracture sets is 80, which is the same as the plunge defined for the stochastic fractures in the small-scale model. The fractures in the small-scale model are north-south trending as well. The additional set of sub-horizontal fractures could have been in the depth interval that is outside the small-scale model domain. The total liner intensity of the 3 sets of sub-vertical fractures in borehole MIZ-1 is 0.045 fractures/m (Table 5.3.1-6). This is consistent with P10 = 0.04 calculated for two arbitrarily placed imaginary vertical boreholes intersecting one realization of stochastic fractures (Figure 62).

The range in calculated (3 sets total) volumetric intensity (P32) is from 0.01 to 0.28 m^2 / m^3 (Figure 5.3.1-20). The calculated P32 of the stochastic fractures (0.22) is within this range.

4.2.6.3 Equivalent continuum model hydraulic conductivity

The hydraulic conductivity of the large-scale equivalent continuum model was calculated using dynamic upscaling of large-scale DFN. Figure 71 shows the cumulative probability distribution of the effective hydraulic conductivity (borehole MIZ-1) for 100-m, 70-m, and 30-m grid block resolution cases (Figure 6.2.2-1). The effective value represents the mean of the hydraulic conductivity in 3 principal directions. The effective hydraulic conductivity of the small-scale equivalent continuum model (1-m grid block) was added to this figure for comparison.

The hydraulic conductivity distribution of the small-scale equivalent continuum model is very similar to the hydraulic conductivity in the 30-m grid block large-scale model. Note that the distributions shift to the right when the grid block size decreases. Consequently, the additional shift can be expected when the grid block size change to 1 m (small-scale model).

The large-scale equivalent continuum model cumulative probabilities of the hydraulic conductivity in 3 principal directions (borehole MIZ-1) are shown in Figure 72 for 30-m grid block case (Figure 6.2.2-1 (b) in Ando et al., 2012). The up-scaled permeability tensor has evident anisotropy consistent with the fracture orientation – the vertical hydraulic conductivity (K11) is higher than horizontal (K22) and the horizontal hydraulic conductivity is higher along the predominant fracture plane (K33). The hydraulic conductivity in 3 principal directions of the small-scale equivalent continuum model was added to this figure for comparison. The anisotropy in hydraulic conductivity in the small-scale equivalent continuum model is similar to the one in the large-scale model - Kzz > Kxx > Kyy.

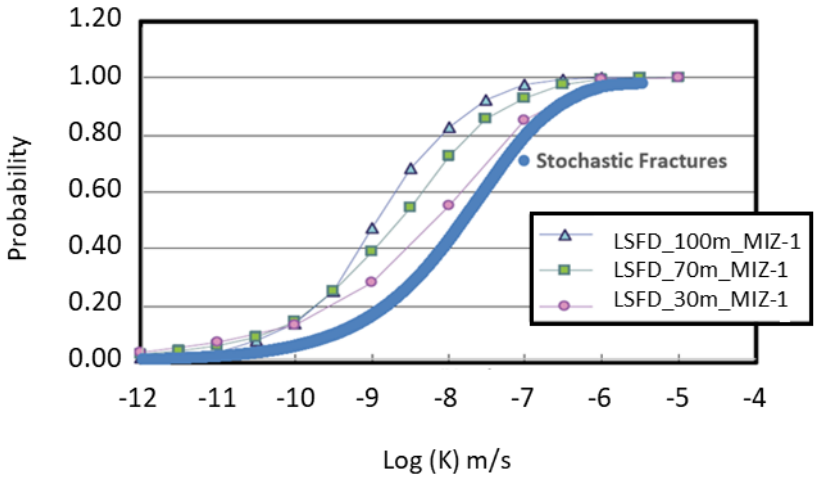

NOTE: This figure was copied from Figure 6.2.2-1 (a) in Ando, 2012). The distribution obtained from the small-scale equivalent continuum model (stochastic fractures) was added to this figure for comparison.

Figure 71. Cumulative probability distribution of effective hydraulic conductivity in LSFD.

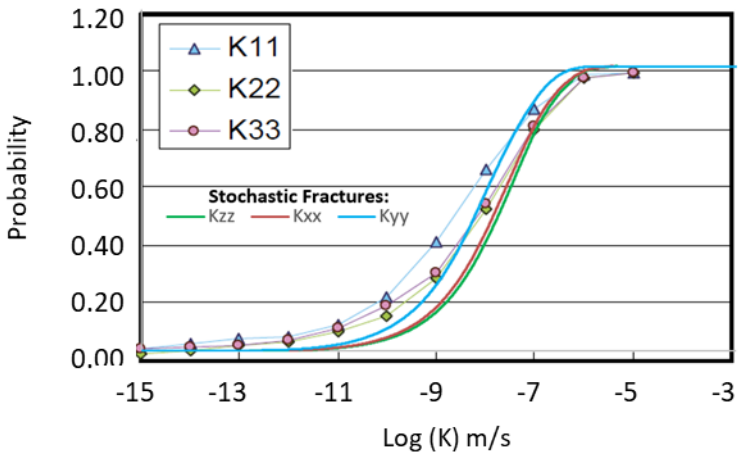

NOTE: This figure was copied from Figure 6.2.2-1 (b) in Ando, 2012). The distributions obtained from the small-scale equivalent continuum model (Kxx, Kyy, and Kzz) were added to this figure for comparison.

Figure 72. Cumulative probability distribution of hydraulic conductivity in 3 principal directions in LSFD in large-scale and small-scale models.

4.2.7 Stochastic fractures with two fracture sets

The stochastic fractures were also generated assuming two fracture sets. The first fracture set is the set described in Section 4.2.4.3. The second set is the north-west trending set in Figure 59. The Fisher distribution parameters for this set are:

- mean trend 303.500
- mean plunge 1.300
- concentration parameter ķ equal to 3.6

The set fracture intensity was calculated the same way as described in Section 4.2.4.2. The set P10 was estimated to be 0.06 fractures/m. The calculated set P32 was 0.086 1/m.

The DFN with two fracture sets was upscaled to the ECM using the method described in Section 4.2.5. Table 22 summarizes the mean properties of the grid cells in the modelling domain with two fracture sets. Note that the anisotropy in permeability is similar to the anisotropy obtained with one fracture set. The mean effective permeability is 1.2 - 1.4 times higher in the case with two fracture sets.

Table 22. Two Fracture Sets Effective Continuum Model Mean Grid Cell Properties.

Parameter	Notation	Mean Value
Permeability (m^2)	K_{xx}	3.50E-15
	K_{yy}	1.84E-15
	K_{zz}	4.15E-15
Anisotropy	K_{xx}/K_{zz}	0.84
	K_{yy}/K_{zz}	0.44
	K_{yy}/K_{xx}	0.52
Fracture porosity	€	2.1E-05

4.2.8 Summary

The goal of this analysis was to develop the DFN for the small-scale area surrounding the MIU Research Tunnel at 500 m depth. The DFN model was upscaled to an equivalent continuum model with the grid cell size 1 × 1 × 1 m using Oda's method for the flow and transport simulations (Section 4.2).

The DFN model includes:

- The fractures observed in the Research Tunnel and borehole 12MI33. These fractures have deterministic locations and stochastic (radius, permeability, and aperture) properties derived from the fracture analysis.
- Stochastic fractures (the location changes with each realization) generated based on the fracture size, orientation, intensity, and properties derived from the fracture analysis.

The major results of the fracture analysis are summarized in Table 23 and described below.

Table 23. Stochastic Fracture Properties

Fracture Set	Trend (^{0})	Plunge (^{0})	Fisher Dispersion k	Volumetric Intensity P_{32} (1/m)
Set 1	208	8	7	0.22
Set 2	303	1.3	3.6	0.086

Analysis of fractures traces on the walls of CTD, inclined drift, and access drift

The analysis of the fracture traces in the Research Tunnel considered 146 fractures that showed flow discharge. It concluded that the fracture size is best described with the lognormal distributions. The fractures with observed flow >1 L/min (F-fractures) have the mean radius of 3.9 m (standard deviation 2.2). The fractures with the observed flow >0.1 L / min (D-fractures) have the mean radius of 1.4 m (standard deviation 1.3).

The analytical solution was used to calculate fracture transmissivity from the observed range of fracture discharge and the total discharge into the Research Tunnel. The fracture aperture was calculated from the cubic law relationship between the transmissivity and aperture. The fracture permeability was calculated from

transmissivity and aperture. The following ranges were derived for the fracture parameters:

- Fracture transmissivity: 2.6×10^{-9} - 6.0×10^{-8} m^2/s.
- Fracture permeability: 1.8×10^{-11} - 1.5×10^{-10} m^2
- Fracture aperture: 15 - 42 microns

It was assumed that fracture permeability (k) and aperture (b) are correlated with the equivalent radius (R). The following relationships were proposed:

$$k = 1.55 \cdot 10^{-12} \cdot R^{2.3} \quad \text{and} \quad b = 1.16 \cdot 10^{-5} \cdot R$$

Analysis of fractures observed in Borehole 12MI33

Seventeen fractures with the recorded aperture values were assumed to be permeable fractures in borehole 12MI33. These fractures were generated using the same parameters as in the Research Tunnel. The following conclusions were made:

- The locations of 17 fractures generated in borehole 12MI33 are consistent with the locations of fractures in the Research Tunnel.
- Fracture properties derived from the Research Tunnel fracture trace analysis are consistent with the packer test data in borehole 12MI33.

Analysis of fracture orientation and intensity for stochastic fracture generation

- Analysis of fracture orientation concluded that there is one fracture set with the following Fisher distribution parameters:
- mean trend 2080
- mean plunge 80
- concentration parameter ķ equal to 7

Note that orientation is given in the local coordinate system. The actual coordinate system was rotated 10.20 clockwise in x-y plane to align the tunnel with the y-axis.

The observed linear intensity of the fractures in the Research Tunnel and borehole 12MI33 P10 was used to calculate volumetric intensity P32. The fracture P32 value was iteratively redefined until the P10 values in selected locations matched the observed P10. The calculated P32 is 0.22.

Upscaling to equivalent continuum model

The DFN was upscaled to an equivalent continuum model using Oda's method. The following mean effective parameters were obtained (one realization):

- Kxx 3.04E-15
- Kyy 1.31E-15
- Kzz 3.50E-15
- Porosity 1.64E-05

The calculated mean permeability values are close to suggested reference permeability (10^{-15} m^2). However, the permeability is anisotropic and changes over a few orders of magnitudes.

Corroboration with the other studies of the Tono Area

The parameters developed for the small-scale model were compared to the parameters incorporated in the large-scale models. The discrete fracture network models were developed for 2 scales – local (9 km × 9 km) and site-scale (2 km × 2 km). Both models extend from the surface to the depth of 2 km and are based on the data from MIU Project Phase I and II investigations.

The comparison was done for fracture size, orientation, intensity, and effective permeability. It was concluded that the parameters of the small-scale model are consistent with the parameters of the large-scale models.

4.3 Step 1 Flow and transport modelling analysis

4.3.1 Introduction

The main aim of the work described in this section is to predict inflow into the tunnel as excavation progresses and provide pressure histories at selected monitoring locations. The project provided data of tunnel excavation progress as the Inclined Drift and the CTD were excavated. The original data was in the form of excavation progress in meters along the axis of the tunnel as a function of excavation dates. Figure 73 shows a modified version of the excavation progress obtained from the project in terms of days since excavation began. Time zero in Figure 73 refers to 4/6/2013 in the project data. Time 173 days refers to the completion of excavation of the CTD on or around 9/25/2013. The excavation data in Figure 73 have been used in simulations of inflow into the tunnel.

Simulations were conducted with PFLOTRAN, an open source, state-of-the-art massively parallel subsurface flow and reactive transport code (Hammond et al., 2014) in a high-performance computing environment. For the analysis a computing system with a capacity of 1848 nodes with 29568 cores; and 64 GB RAM per compute node was used. The system has 600 teraFLOPS. The individual machines are 2.6 GHz Intel processors. For our simulations 5 nodes with 80 processors were sufficient.

The excavation progress was modelled by progressively removing material assigned as the host rock. This is equivalent to increasing the grid blocks representing the tunnel. A schematic diagram of the process is shown in Figure 74. To get a better representation of the excavation progress, a small portion of rock material was removed at a time. Thus, the material removal was in 1 m increments for a total of 103 m (i.e. 57 m of the Inclined Drift and 46 m of the CTD). This resulted in 103 PFLOTRAN runs applying the pressure and Cl concentration boundary conditions assigned for the excavated area. The modelling was carried out with output of each PFLOTRAN run used as input for the next run until the complete excavation of the tunnel parts was complete. To automate the simulation process, the Sandia National Laboratories-developed optimization code, DAKOTA, Adam, et al. (2017) was used as a driver to PFLOTRAN. A schematic diagram of the process is shown in Figure 75. DAKOTA also provides statistical analysis of the process, which will be used in future simulations.

Simulations were carried out for a homogenous representation using the Visualization Area domain, which is a CTD-scale domain recommended by the project, and a larger domain to test the boundary conditions. These simulations are detailed in Section 4.3.2. Simulations were also conducted for a fracture system developed based on the fracture analysis described in Section 4.2. The fracture modelling is described in Section 4.3.3. A summary of the simulation exercise is given in Section 4.3.4.

4.3.2 Homogenous model

4.3.2.1 Visualization Area Domain

Simulations were conducted for a homogenous model with reference hydraulic conductivity. As outlined by the Task C project, simulations were based on the Visualization Area domain specified by the project. The model has a geometry of 100 m × 150 m × 100 m in the x, y and z directions. The modelling domain is a CTD-scale model and incorporates the Inclined Drift and the CTD. The physical coordinates of the simulation domain are given in Table 24. The simulation domain also incorporates the

monitoring sections in Well 12MI33. The coordinates of the monitoring section are given Table 25. A schematic representation of the modelled part of the tunnel and the monitoring well is shown in Figure 76.

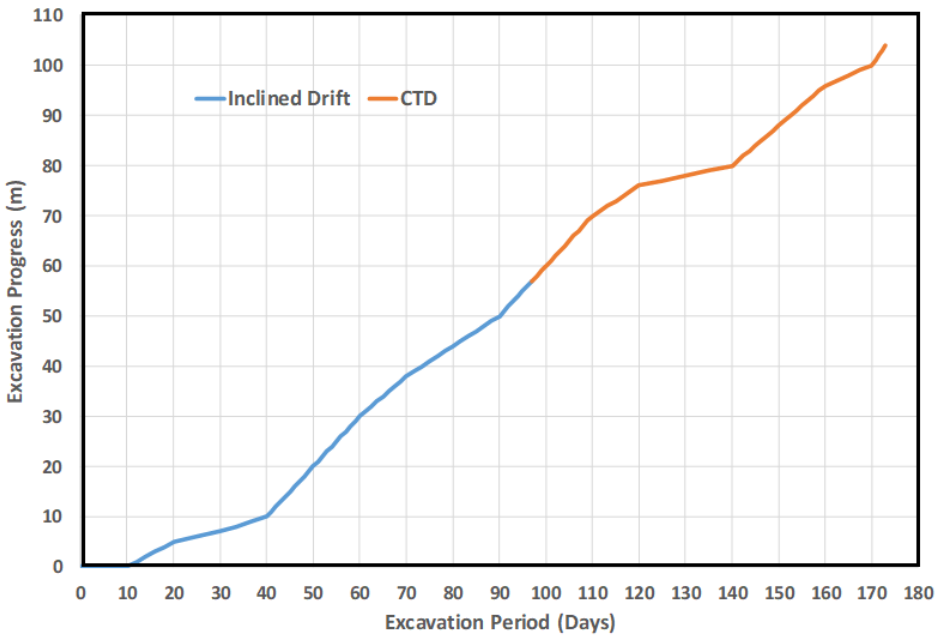

Figure 73. Data of excavation progress

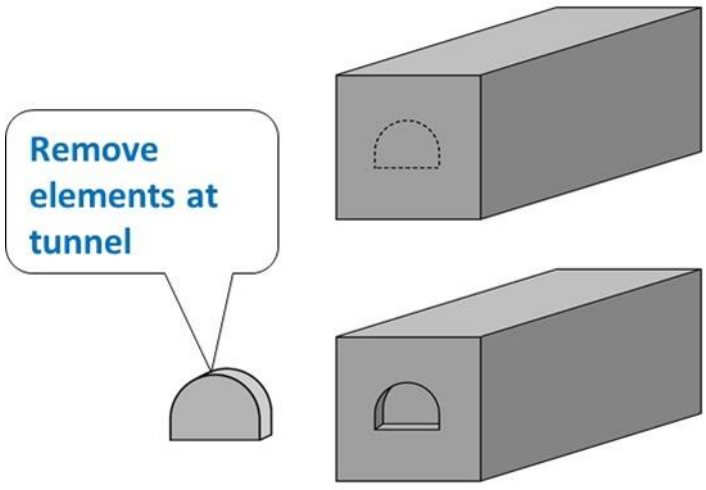

Figure 74. Schematic diagram showing simulation approach.

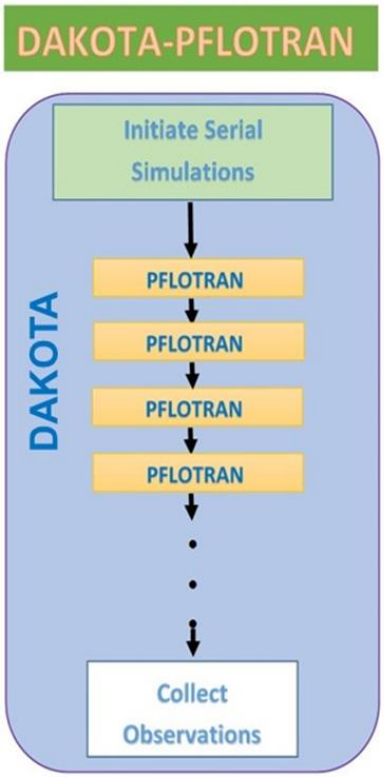

Figure 75. Schematic diagram for DAKOTA-PFLOTRAN coupling.

For the simulations, a refined uniform (structured) grid was selected, with grid block size of 1 m × 1m × 1m for a total of 1,500,000 grid blocks. The Inclined Drift is slightly inclined but was modelled as horizontal for ease of meshing. The tunnel was represented using a rectangular shape. The dimensions of these two tunnel parts are given below.

Inclined Drift	CTD
Length = 57 m	Length = 46.5 m
Width = 4.5 m	Width = 5.0 m
Height = 3.5 m	Height = 4.5 m

For the simulations, physical properties obtained from the monitoring borehole 12MI33 and other sources were used. The estimated hydraulic conductivity for Toki granite is in the range of log10 (-8 ± 1) m/s. The homogenous simulations used:

- Reference hydraulic conductivity 10^{-8} m/s (permeability 10^{-15} m^2)
- Porosity 0.001
- Effective diffusion coefficient 10^{-12} m^2/s

Initial and boundary conditions were based on those specified for Task C. Hydrostatic initial pressure conditions are represented by average head measurements of 110 EL m,

based on data from monitoring wells. Top, bottom and side boundary conditions were also assigned head of 110 EL m. The excavated area was assigned a constant pressure boundary condition of 1.0 atmosphere. Head data were converted to pressure as shown below. For the conversion, the head of 110 EL m and elevation data in Table 24 were used.

Pressure at domain top = density × g × (head + elevation) = 3.6 MPa

Pressure at domain bottom = density × g × (head + elevation) = 4.6 MPa

A hydrostatic pressure boundary was assigned on the sides. Top and bottom boundary pressure values shown above were assigned. The initial and boundary conditions also include Cl concentrations based on data from monitoring wells. For the simulations, the top and bottom boundaries were assigned 332 mg/L and 428 mg/L Cl concentrations, respectively. The side boundaries were assigned a concentration gradient varying between the top and bottom boundary values. The excavated region was modelled as a free boundary.

Pressure monitoring points were setup using the coordinates in Table 25. The points were selected to be in the middle of the monitoring section. The Cl concentration units were converted to molarity (M) for use in PFLOTRAN. The conversion is shown below, using Cl molecular weight of 35.453 g/mol:

Concentration at top = 332 mg/L / (1000 × 35.453 g/mol) = 0.0094 M

Concentration at bottom = 428 mg/L / (1000 × 35.453 g/mol) = 0.012 M

Table 24. Coordinates of CTD-scale simulation domain

E-W(m)	N-S(m)	E.L.(m)	
6522.7	-68943.5	-250.0	Upper boundary
6496.1	-68795.9	-250.0	Upper boundary
6397.7	-68813.7	-250.0	Upper boundary
6424.3	-68961.3	-250.0	Upper boundary
6522.7	-68943.5	-350.0	Lower boundary
6496.1	-68795.9	-350.0	Lower boundary
6397.7	-68813.7	-350.0	Lower boundary
6424.3	-68961.3	-350.0	Lower boundary

Table 25. Coordinates of monitoring section in borehole 12MI33

Section ID	Top			Middle			Bottom		
	E-W(m)	N-S(m)	E.L.(m)	E-W(m)	N-S(m)	E.L.(m)	E-W(m)	N-S(m)	E.L.(m)
12MI33_P1	6445.46	-68845.50	-303.27	6445.30	-68844.80	-303.30	6445.19	-68844.00	-303.36
12MI33_P2	6448.96	-68864.90	-302.24	6447.30	-68855.70	-302.70	6445.63	-68846.50	-303.22
12MI33_P3	6452.81	-68886.20	-301.11	6451.00	-68876.00	-301.60	6449.13	-68865.80	-302.19
12MI33_P4	6454.62	-68896.30	-300.57	6453.80	-68891.80	-300.80	6452.98	-68887.20	-301.06
12MI33_P5	6456.34	-68905.80	-300.07	6455.60	-68901.50	-300.30	6454.78	-68897.20	-300.52
12MI33_P6	6464.16	-68949.20	-297.76	6460.30	-68928.00	-298.90	6456.50	-68906.70	-300.02

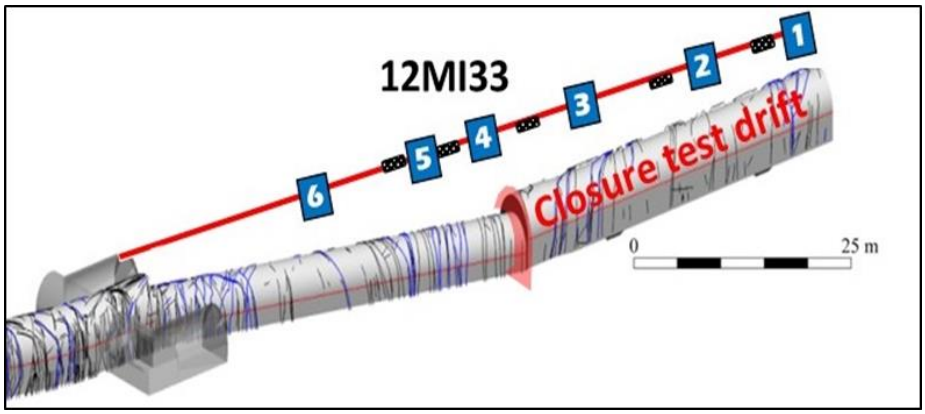

Figure 76. Schematic diagram showing the modelled part of the tunnel and the monitoring well 12MI33 with the monitoring sections

4.3.2.1.1 Homogenous model with Visualization Area domain simulation results

A steady state run was made to obtain initial pressure and Cl concentration conditions before the excavation progress was modelled. Note that the steady state represents the condition before any excavation and is designed to apply the project specified boundary and initial conditions. Representation of the Inclined Drift and the CTD in the model are shown in Figure 77. Figure 78 shows distributions of the steady state pressure and Cl concentration using the initial and boundary conditions described above. The figures show the pressure and concentration gradients as a function of depth.

Simulations of excavation progress were conducted using the steady state pressure distributions and constant pressure boundary conditions inside the tunnel. The DAKOTA-PFLOTRAN system described above was used to separately model excavation progress in the Inclined Drift and the CTD. The outputs were post-processed to evaluate inflow into the tunnel and pressure history at the observation points. Results of pressure

and Cl concentration distributions at 173 simulation time are shown in Figure 79. The figures represent fluid flow and Cl transport into the tunnel as a result of the initial and boundary conditions. The left (south) side boundary conditions were set close to the inclined tunnel entrance, and the effect of that is shown in the figures. The left side of the figure in Figure 79b shows high concentrations at the inclined tunnel entrance. Figure 80 and Figure 81 show predicted pressure vs. time and Cl concentration vs. time at the selected monitoring points. Figure 80 shows higher pressure drawdown in Observation Section 6, which is closer to the Inclined Drift entrance (see Figure 76 for the relative location of monitoring points). The figure shows the lowest pressure drawdown in Section 1, which is close to the edge of the CTD. This is in line with expectations as the inclined tunnel was open for a longer period of time and thus more inflow compared to the CTD.

The flow of water into the excavated space (Inclined Drift and CTD) was also predicted based on the excavation progress. The output of the simulation was post-processed to determine inflow rate. The resulting inflow into the tunnel (Inclined Drift and CTD) is shown in Figure 82. Task C project experimental data on inflow into the Inclined Drift and the CTD are given in Table 15. The recorded inflow into the Inclined Drift is about 43 L/min, or 62.0 m^3/day. The recorded combined inflow is about 56 L/min, or 80.6 m^3/day. These two data points are shown in Figure 82. The predicted inflow for the homogenous model with Visualization Area domain matches the data point for the Inclined Drift but over predicts the data point for the combined inflow. The inflow is a function of the boundary and initial conditions as well as material properties selected. Any of these variables could influence the prediction.

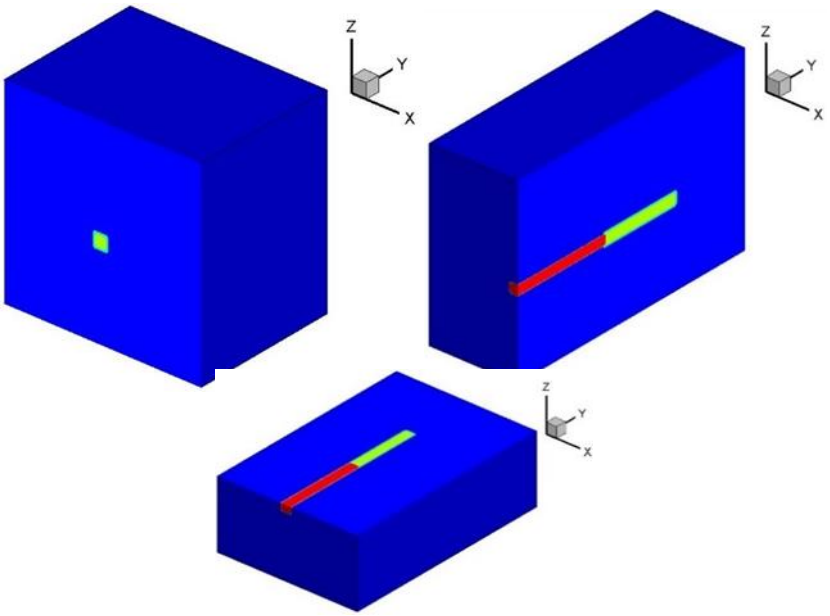

Figure 77. Placement of tunnel in simulation domain: Inclined Drift and CTD: Cross-section along a) x-axis, b) y-axis and c) z-axis.

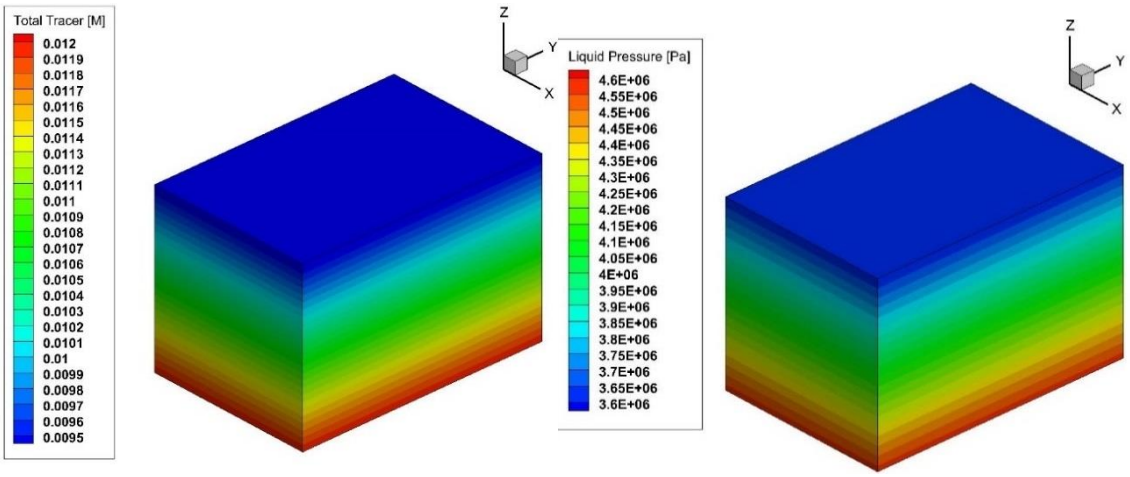

Figure 78. Steady state pressure and Cl concentration distribution (molarity units): homogenous system.

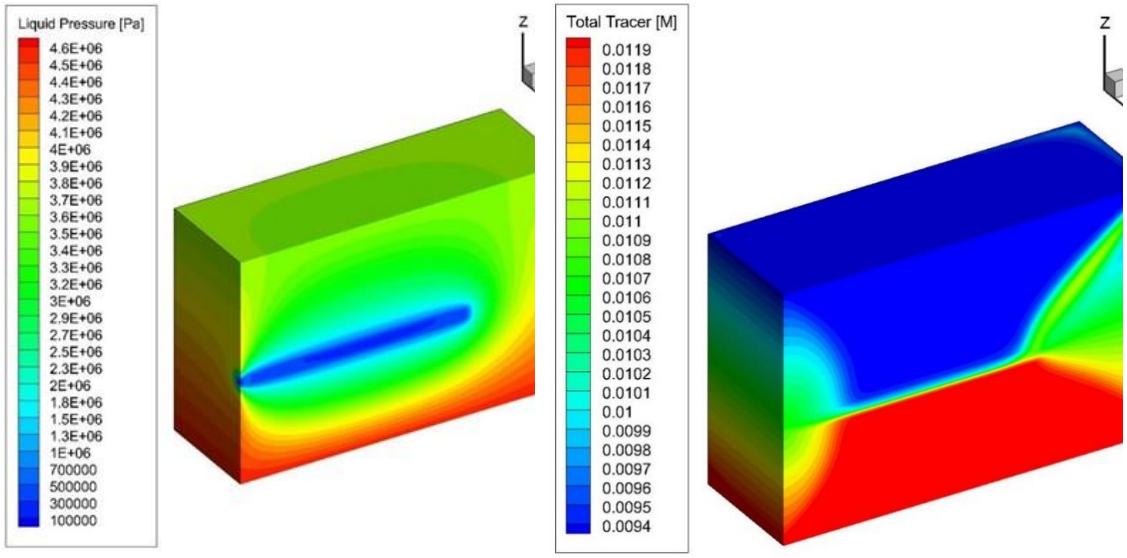

a) Pressure distribution: cross-section along the axis of the tunnel b) Cl concentration distribution: cross-section along the axis of the tunnel

Figure 79. Predicted pressure and Cl concentration distributions after 173 days simulation time: homogenous system with Visualization Area domain.

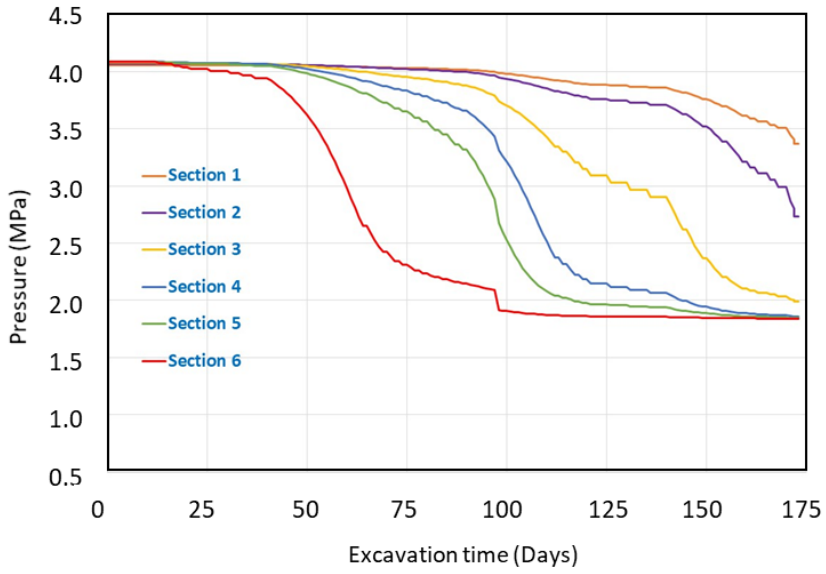

Figure 80. Predicted pressure history at observation points (in 12MI33) during excavation: homogenous system with Visualization Area domain.

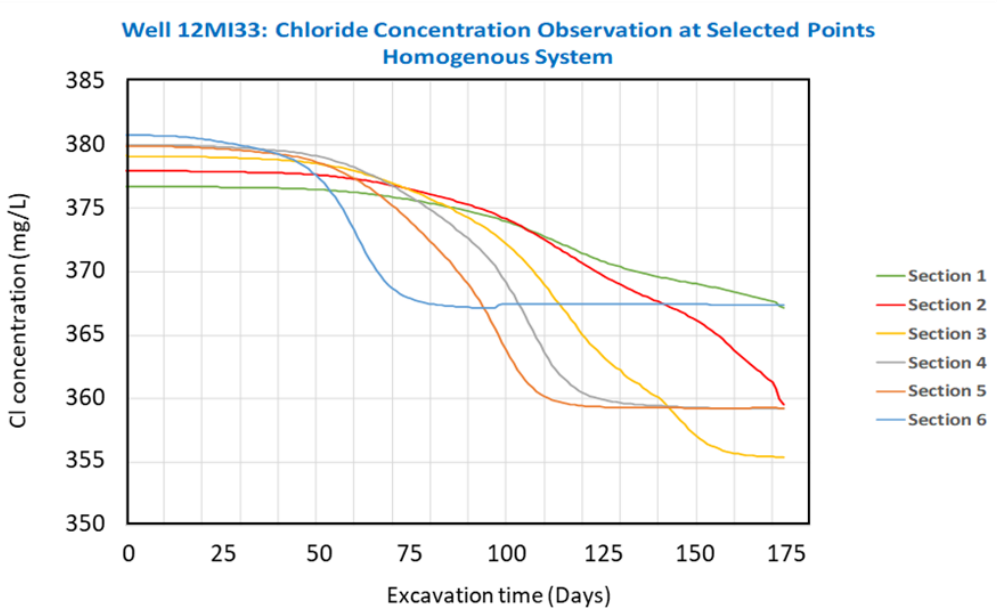

Figure 81. Predicted Cl concentration history at observation points (in 12MI33) during excavation: homogenous system with Visualization Area domain.

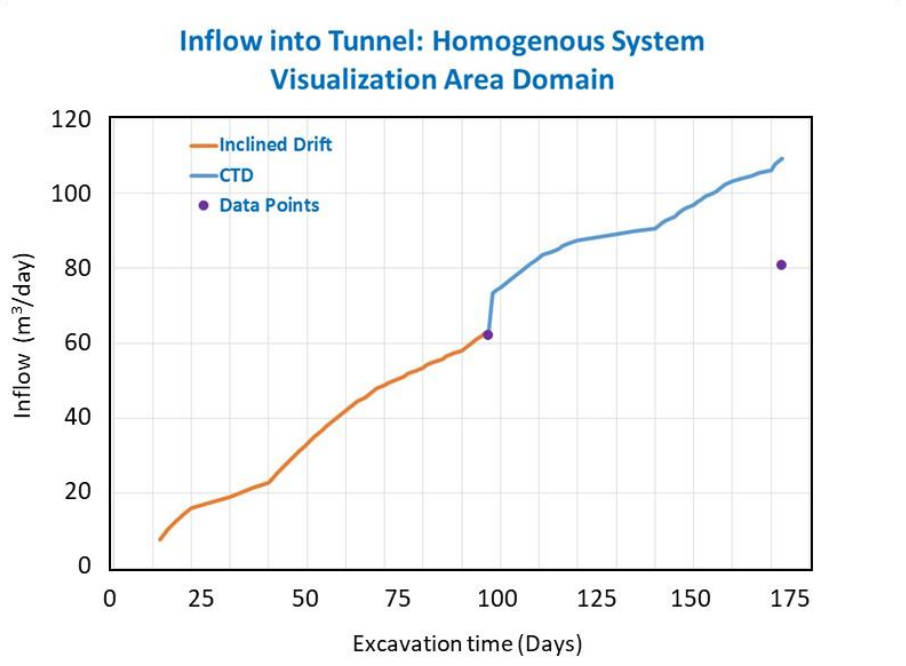

Figure 82. Predicted inflow into the Inclined Drift and CTD during excavation: homogenous system, Visualization Area domain. Note that the data points represent inflow at inclined drift-only and inclined drift + CTD.

4.3.2.2 Model with large domain

To study the effect of boundary conditions on the predicted output, a larger domain was selected. For the simulations, a grid with 2080 m × 2130 m × 700 m in the x, y, and z directions was used. The same grid block size (i.e. 1 m × 1m × 1m) as the previous model was applied to the Visualization Area. Outside of the Visualization Area, a progressive grid size was used. The new mesh size is 122 × 122 × 117 for a total 1,741,428 grid blocks. The larger domain mesh is shown in Figure 83. The same pressure and concentration gradient initial and boundary conditions as the previous model were applied. The same material properties were also used.

Simulations described in Section 4.3.2.1 for the Visualization Area domain using the coupled DAKOTA-PFLOTRAN codes were conducted. Simulation results are shown in Figure 84 to Figure 88. Figure 84 and Figure 85 show pressure and concentration distributions, respectively, at 173-days simulation time. The results do not show effects of boundary conditions as those of Figure 79 for the Visualization Area domain. The boundary conditions imposed on the left boundary of the Visualization Area domain that is more visible for Cl concentration (Figure 79b), are absent in Figure 85.

Predictions of pressure and concentration histories at observation points for the large domain case are shown in Figure 86 and Figure 87, respectively. The pressure profiles at observation points are similar to those of the Visualization Area domain (Figure 80) but with larger drawdowns. The same trend is observed when comparing Cl concentration profiles.

The flow of water into the excavated space (Inclined Drift and CTD) was also evaluated for the large domain homogenous model. The resulting inflow into the tunnel (Inclined Drift and CTD) is shown in Figure 88 together with the results for the Visualization domain and the data points. The predicted inflow for the homogenous model with large domain under-predicts the data points but is close.

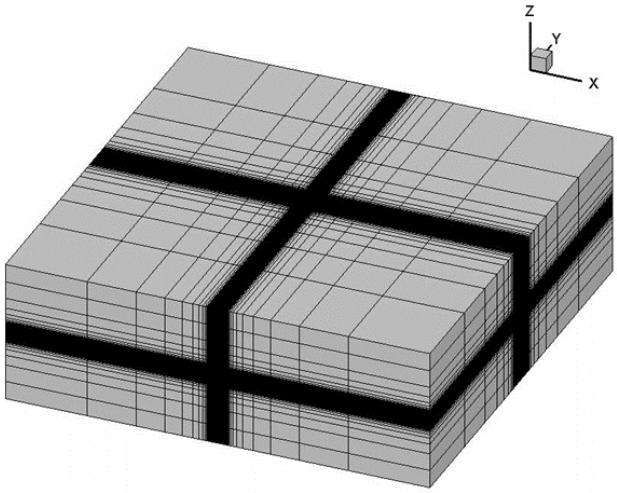

Figure 83. Grid for large domain

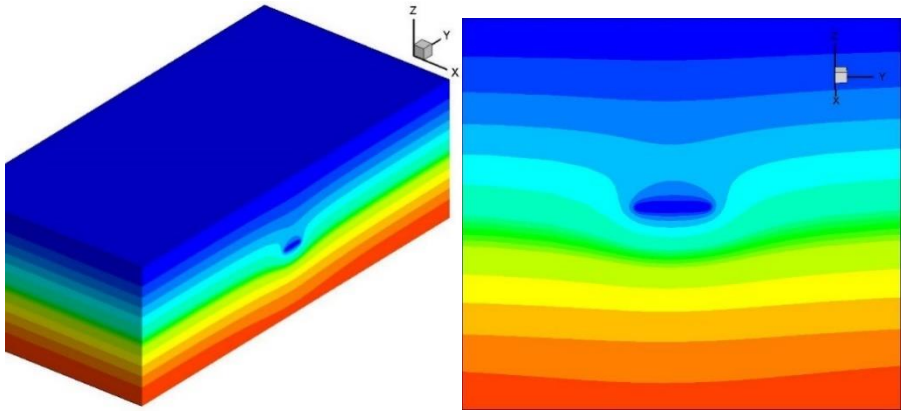

Cross-section along the axis of the tunnel

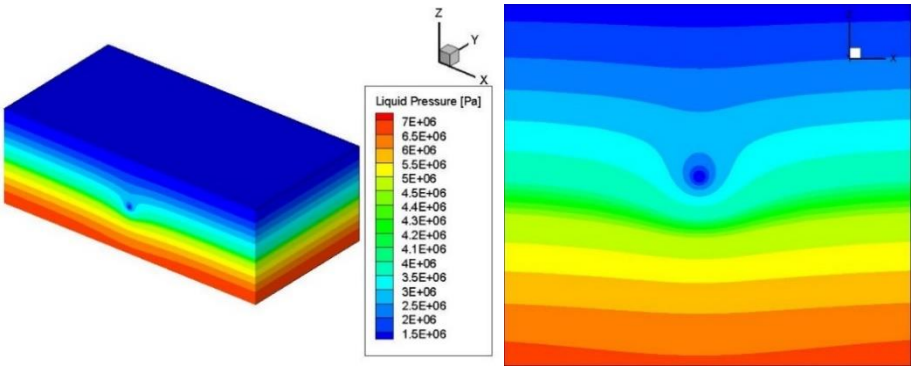

Cross-section perpendicular to tunnel axis

Figure 84. Predicted pressure distribution after 173-days simulation time: homogenous system with large domain.

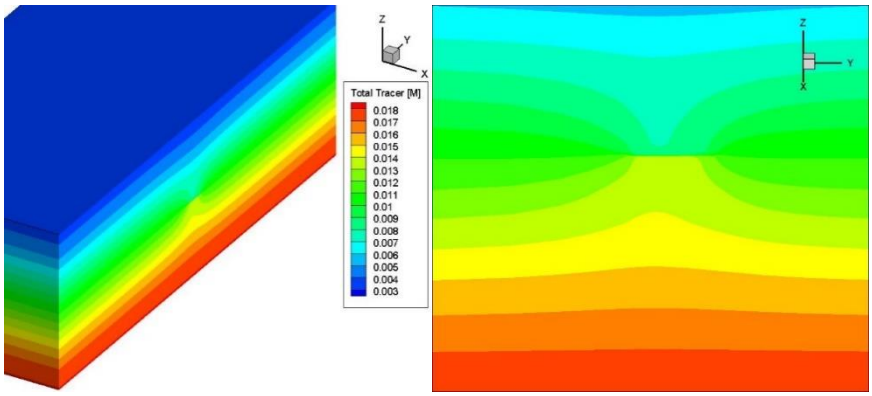

Cross-section along the axis of the tunnel

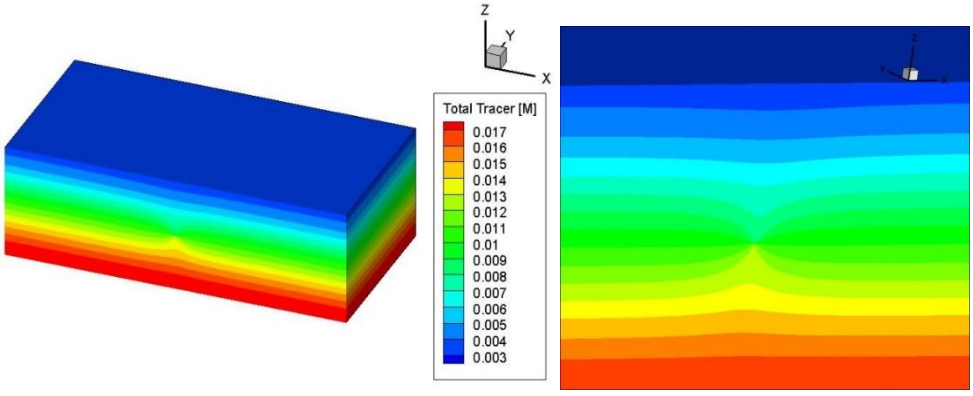

Cross-section perpendicular to tunnel axis

Figure 85. Predicted Cl concentration distributions after 173-days simulation time: homogenous system with large domain.

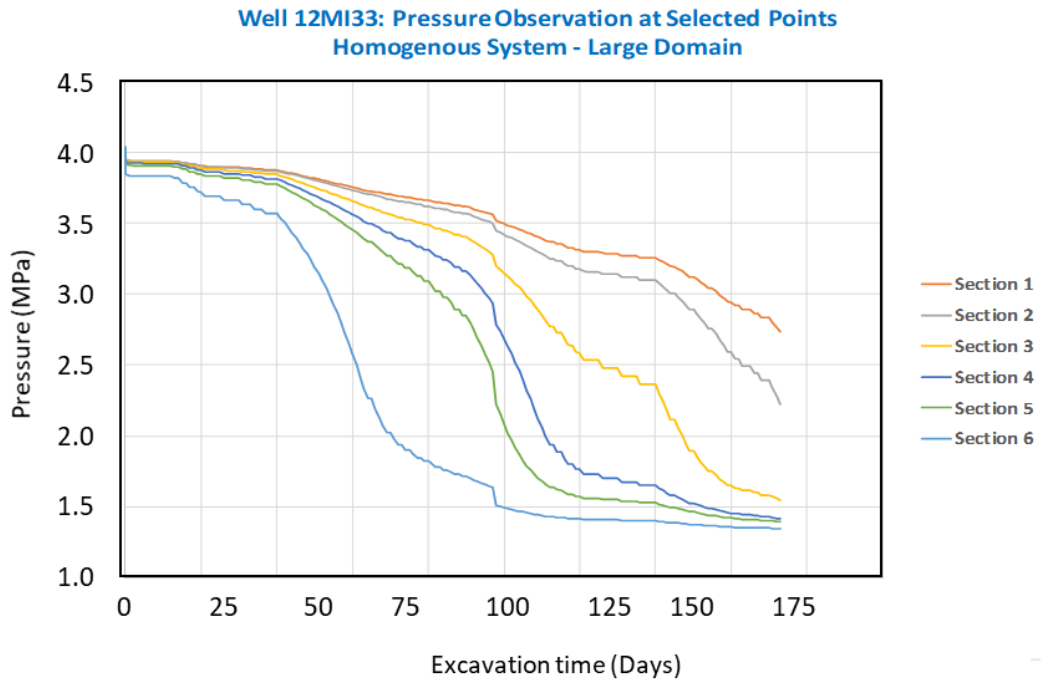

Figure 86. Predicted pressure history at observation points (in 12MI33) during excavation: homogenous system with large domain.

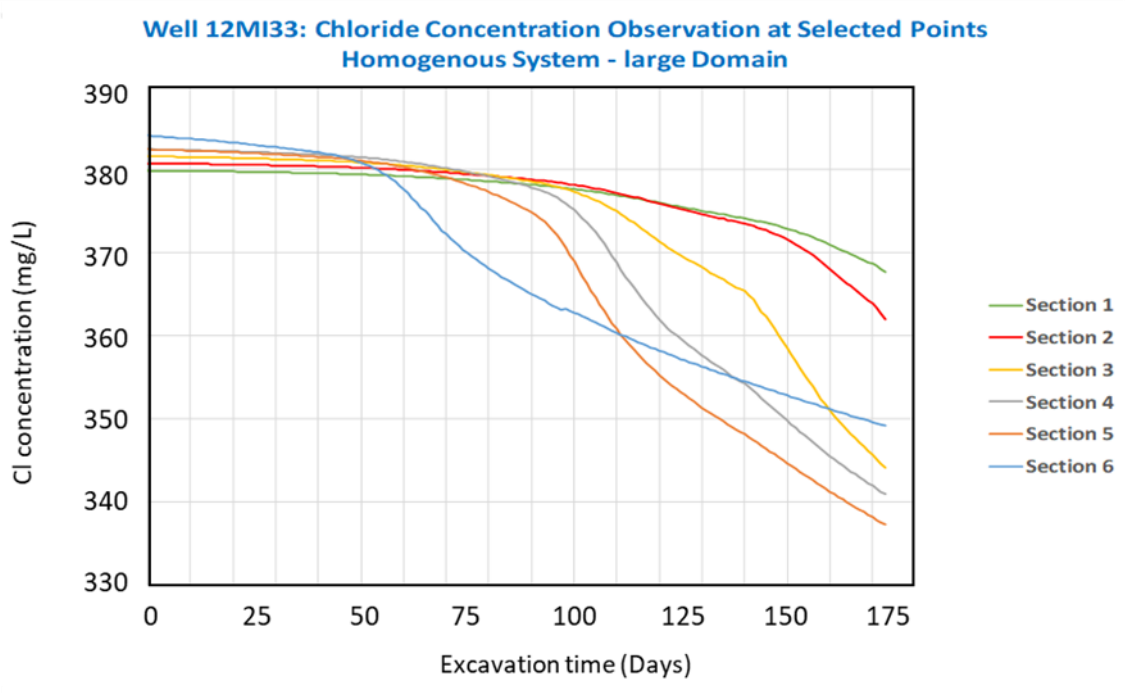

Figure 87. Predicted Cl concentration history at observation points (in 12MI33) during excavation: homogenous system with large domain.

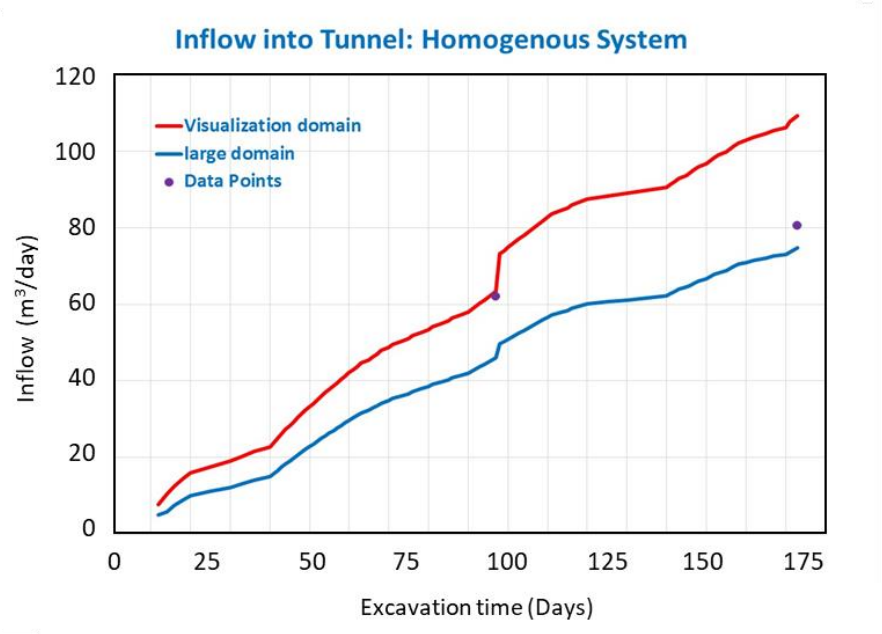

Figure 88. Predicted inflow into the Inclined Drift and CTD during excavation: homogenous system.

4.3.3 Fractured system model

Section 4.2 describes the fracture model development based on fracture data collected from the excavated areas and boreholes. The analysis produced up-scaled permeability and porosity data for flow and transport modelling of the excavation process. Permeability and porosity fields were obtained for two realizations, for the Visualization Area domain. The first realization is based on a single fracture set while the second realization includes two fracture sets. In generating the permeability and porosity fields the matrix rock was assigned a permeability of 10^{-19} m^2 and a porosity of 0.001. Figure 89 shows the resulting permeability and porosity fields for the realization with single fracture set. An analysis (Wang et al., 2015; 2016; 2017) was carried out to obtain the effective permeability for both realizations. Flow based effective permeability was calculated using Darcy's law and liquid flux at steady state:

$$q = \frac{-k_{eff}\Delta P}{\mu L} \qquad (4.3.1)$$

where

q = flux,

k_{eff} = effective permeability,

DP = pressure difference between west and east faces (1000 Pa)

m = dynamic viscosity

L = distance between west and east faces (100 m)

PFLOTRAN flow simulations were carried out using the permeability and porosity fields for the two realizations to estimate flow-based effective permeability. A pressure gradient was imposed between the west and east faces of the Visualization Domain. Equation (4.3.1) was then used to estimate the effective permeability values using flux output on the east face, distance between west and east faces (100 m) and cross-sectional area (1.5 × 104 m^2). The resulting calculated effective permeability along the x-axis (perpendicular to tunnel axis) for the realization with a single fracture set was 1.62 × 10^{-16} m^2. This value is an order of magnitude lower than the permeability used for the homogenous model. The corresponding effective permeability of the realization with two fracture sets was 3.27 × 10^{-16} m^2, which is approximately double the value for the realization with single fracture set. Flow-related effective permeability values were also calculated for flow in the other directions. The complete results are shown below. The effective permeability in the vertical direction is higher than the horizontal values indicating more flow in the vertical direction.

- Flow-related effective permeability for the realization with two fracture sets.
- Horizontal perpendicular to the tunnel axis (x-axis): 3.27 × 10^{-16} m^2
- Horizontal along the tunnel axis (y-axis): 1.95 × 10^{-16} m^2
- Ratio of effective permeability y-axis/x-axis: 0.6
- Vertical (z-axis): 5.14 × 10^{-16} m^2
- Ratio of effective permeability z-axis/x-axis: 1.6

The same simulations as described in Section 4.3.2.1 for the Visualization Area domain using the coupled DAKOTA-PFLOTRAN codes were conducted for the fractured system runs. The permeability and porosity fields for the two fracture model realizations were used. Simulation results are shown in Figure 90 to Figure 96. Figure 90 and Figure 91 show pressure and concentration distributions, respectively, at 173 days simulation time for the realization with a single fracture set. The pressure distributions in Figure 90 indicate flow into the tunnel in a fractured system. It is evident that use of the Visualization Area domain resulted in boundary effects. The concentration distributions shown in Figure 91 are not as smooth as results of the homogenous model. The concentration gradient is a function of the porosity field as well as the hydrology of the system.

Predictions of pressure and concentration histories at observation points for the single fracture realization are shown in Figure 92 and Figure 93, respectively. The pressure profiles at observation points show larger pressure drawdowns when compared to those of the Visualization Area domain (Figure 80) and the large domain (Figure 86) homogenous models. Profiles of Cl concentration are very different from those of the homogenous model. As also shown in Figure 91, concentrations are highly affected by the fracture system. Predictions of pressure and concentration histories at observation points for the realization with two fracture sets are shown in Figure 94 and Figure 95, respectively. The pressure profiles are similar to the single fracture set. The Cl concentration profiles are also similar to that of the single fracture set, except for Section 5 which shows a different profile.

The flow of water into the excavated space (Inclined Drift and CTD) was also evaluated for the two fractured system realizations. The resulting inflow into the tunnel (Inclined Drift and CTD) is shown in Figure 96 together with the results for the homogenous model. Task C project inflow data points (for Inclined Drift and CTD) are also included. The predicted inflow for the single fracture set realization is lower than the other cases and the data points. The predicted inflow for the realization with two fracture sets matches the data points. Note that the results of the fracture system are for two realizations only. Additional realizations would be needed to get better representation of the fractured system.

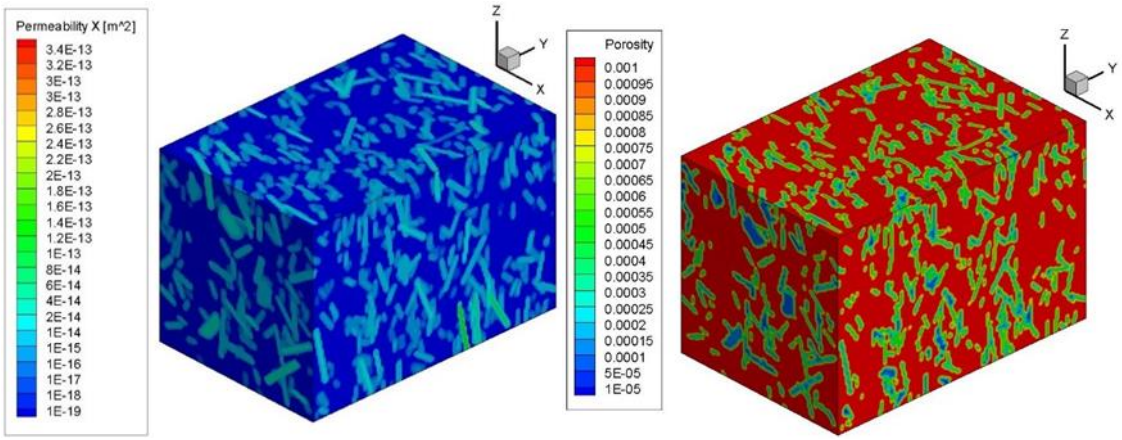

a) XX-permeability tensor b) porosity

Figure 89. Fracture permeability and porosity for Realization 1: fractured system with Visualization Area Domain.

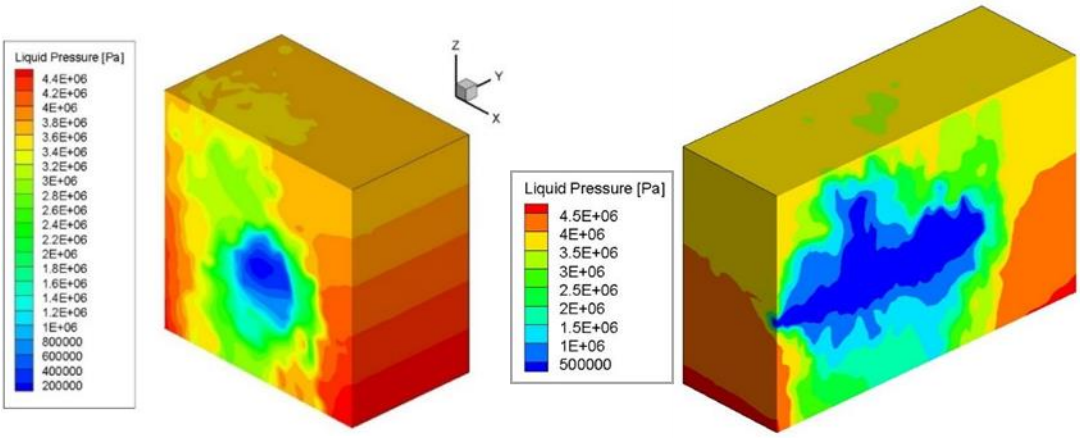

a) Cross-section along the axis of axis of tunnel

b) Cross-section perpendicular to the tunnel

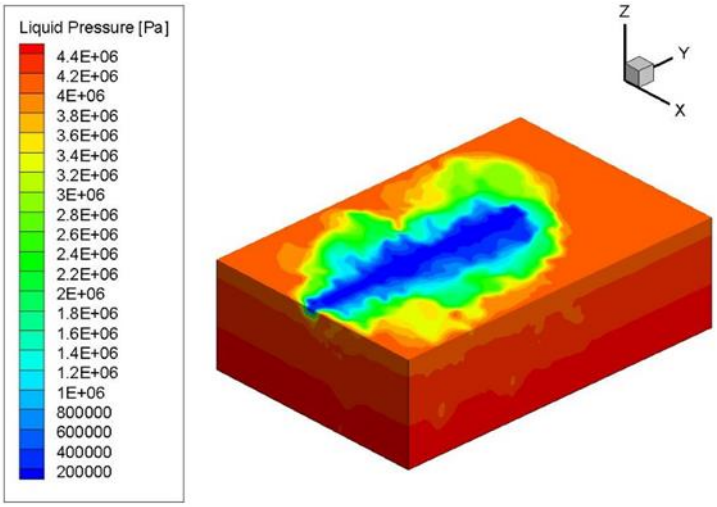

c) Vertical cross-section at location of tunnel

Figure 90. Predicted pressure distribution after 173-days simulation time: fractured system with Visualization Area domain. Realization 1.

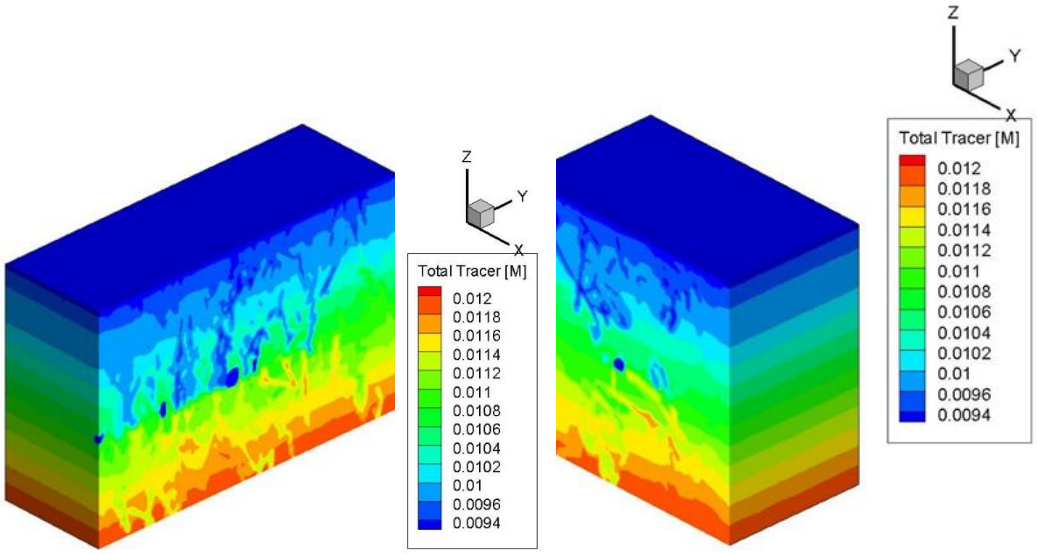

a) Cross-section along the axis of the tunnel b) Cross-section perpendicular to tunnel axis

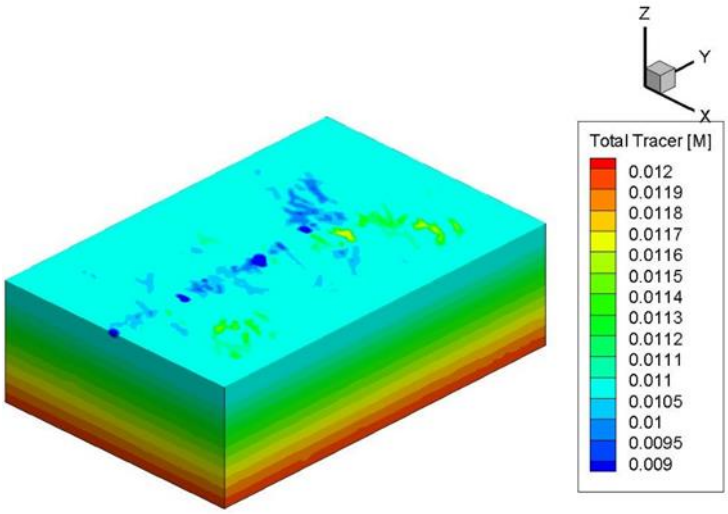

c) Vertical cross-section at location of tunnel

Figure 91. Predicted Cl concentration distribution after 173-days simulation time: fractured system with Visualization Area domain. Realization 1. Fracture system with one fracture set.

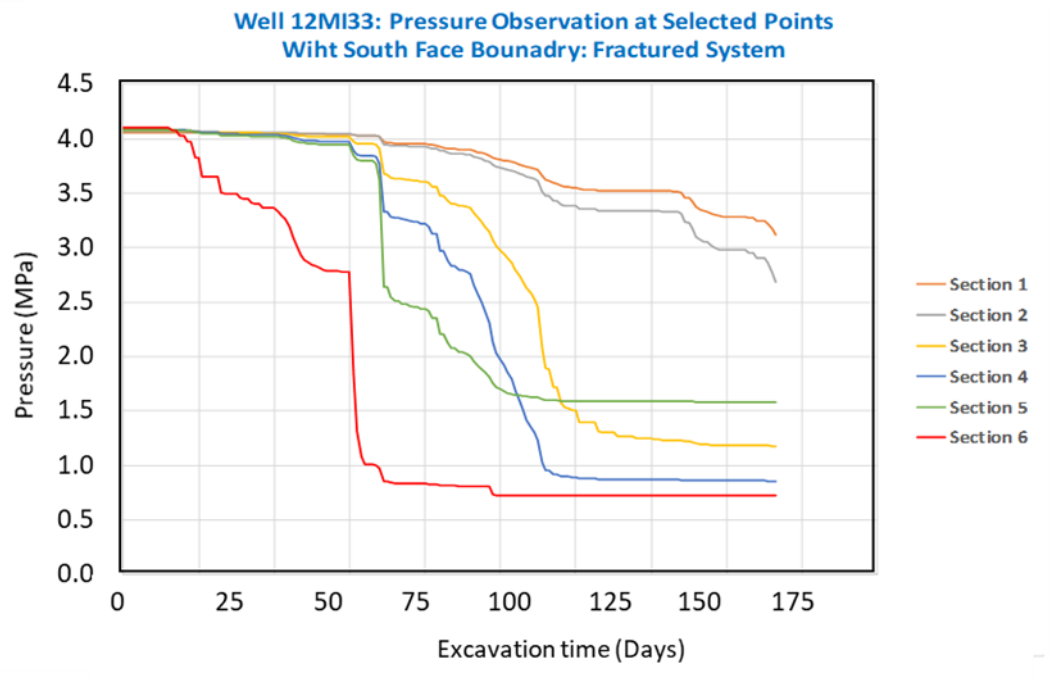

Figure 92. Predicted pressure history at observation points (in 12MI33) during excavation: fractured system with Visualization Area domain. Realization 1. Fracture system with one fracture set.

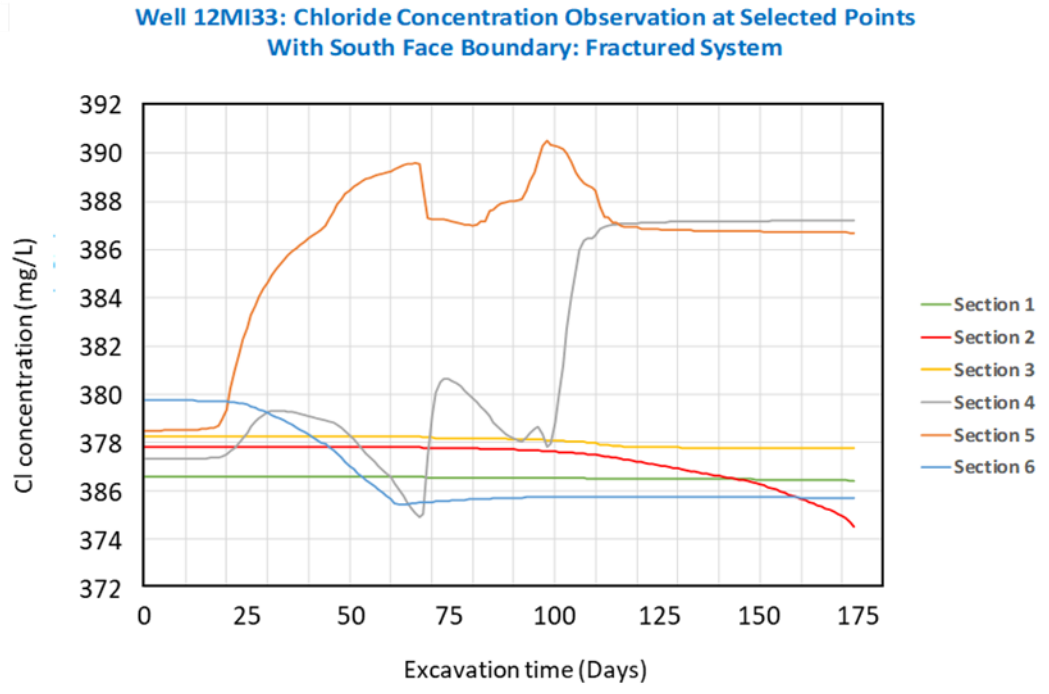

Figure 93. Predicted Cl concentration history at observation points (in 12MI33) during excavation: fractured system with Visualization Area domain. Realization 1.

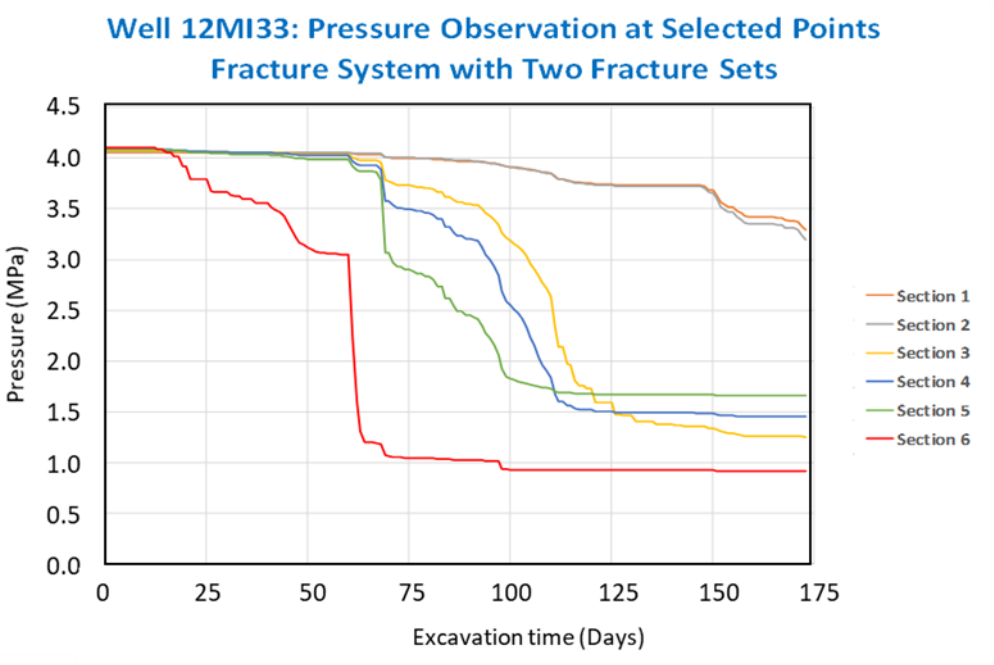

Figure 94. Predicted pressure history at observation points (in 12MI33) during excavation: fractured system with Visualization Area domain. Realization 1. Fracture system with two fracture sets.

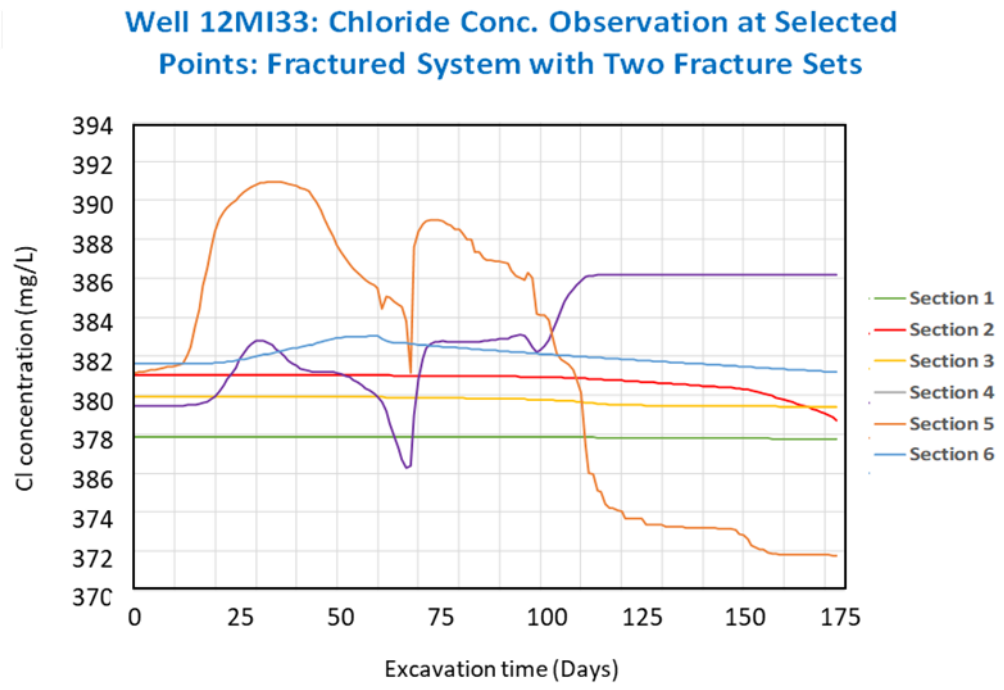

Figure 95. Predicted Cl concentration history at observation points (in 12MI33) during excavation: fractured system with Visualization Area domain. Realization 1. Fracture system with two fracture sets.

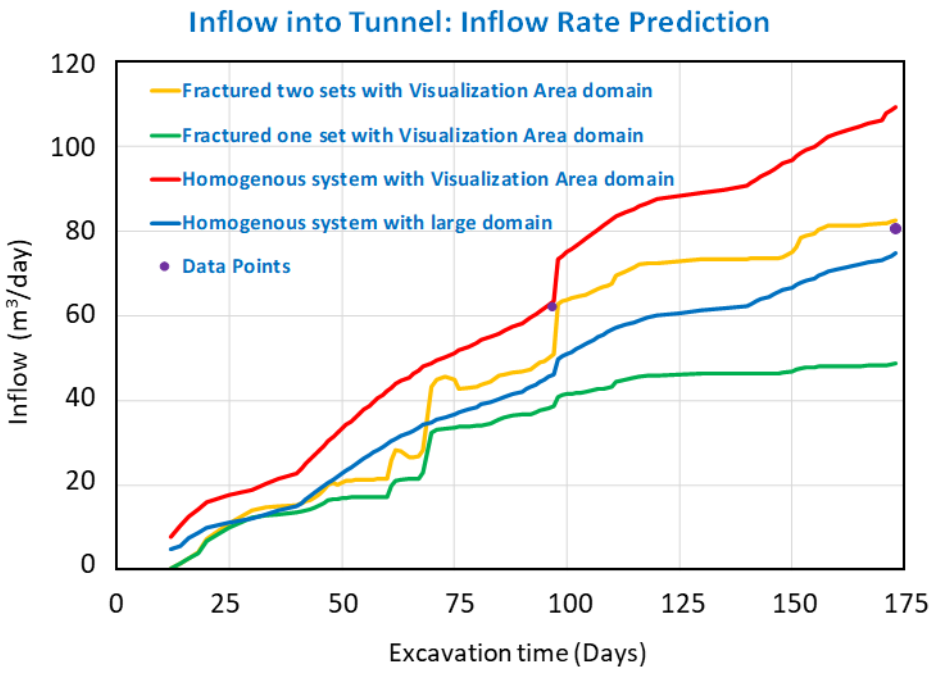

Figure 96. Predicted inflow into Inclined Drift and CTD: comparison of results of homogenous and fracture systems.

4.4 Summary of Step 1 modelling work

The analysis looked at the use of a homogenous model with reference hydraulic conductivity, and a fracture model developed in Section 4.2, above. For the base case, the CTD-scale Visualization Area domain was used (100 m × 150 m × 100 m). Boundary and initial conditions specified by the project, based on data from wells, were applied to flow and transport. The data include head and Cl concentration at different parts of the modelling domain. Parameter data also obtained from wells were used. Data of excavation progress for the Inclined Drift and the CTD were also provided. A simulation method was developed to simulate excavation progress by continuously removing material from the excavated area. The DAKOTA statistical analysis and optimization code and the PFLOTRAN numerical flow and transport code were used. Simulations of flow and transport for the homogenous model with the Visualization Area domain indicated boundary effects at the Inclined Drift entrance. The boundary effects were caused by the application of side boundary conditions close to the tunnel entrance. To study the extent of the boundary effects, a new grid was developed with a larger domain (2080 m × 2130 m × 700 m). Simulation results of the larger domain eliminated the boundary

effects, which would indicate the need to enlarge the boundaries of the CTD-scale model. The results of the larger domain also showed a predicted inflow rate close to the experimental inflow data.

The modelling analysis also included use of a fracture model developed in Section 4.2. This allowed realistic representation of the system in the excavated region. For the analysis permeability and porosity fields obtained for two realizations were used instead of the constant permeability used in the previous simulations. The same simulation approach as the homogenous model was followed for the CTD-scale Visualization domain. The simulation results provided detailed flow and transport distributions in a fractured system. The inflow predictions with the single set fracture model under-predicted the experimental data, while the predicted inflow of the realization with two fracture sets matched the experimental data. The results are preliminary output for two realizations. More realizations will be needed to obtain average representative output.

5 Results of Step 1 modelling (TUL)

5.1 Modelling strategy and approach

The H-M-C changes during the construction of inclined and closure tunnel were originally planned to be simulated as separate processes at the beginning of the project and extended to a coupled form as work progresses. The work was finally concentrated on hydraulic and chemical processes, without considering effect of mechanics. For the flow and transport modelling, in-house developed open-source simulation code Flow123d (TUL, 2017) has been used, employing its features of the discrete fracture network and continuum coupling (Brezina and Hokr, 2011) amongst other capabilities. Other open-source GMSH (Geuzaine and Remacle, 2009) and SALOME (SALOME, 2018) were used for preparing geometry and discretisation.

5.1.1 Simulation condition, Model setting

Simulation area

The reference case was made with the recommended domain in the assignment (Figure 11). Besides this, a larger-scale model was used, for a general understanding of the site and to evaluate proper boundary conditions for the reference model.

Geological unit

As given: The whole domain of the focused area is located in the lower sparsely fractured domain (LSFD). The level of structural detail was various, with options specified below (5.1.10).

5.1.2 Parameters

(1) Hydrogeology

Hydraulic conductivity and specific storage measured in a borehole were preferred for defining parameters, considering also more general ranges resulting from all the site boreholes. In case the data for deterministic discrete fractures were not provided directly, they could be derived from the borehole pressure test considering the intersections of particular borehole interval and fractures.

(2) Rock mechanics

The available data of elastic modulus, density, porosity, Poisson's ratio, etc. measured from local core samples were not finally used.

(3) Chemistry

The thermodynamic database is included in the simulation software Geochemist's Workbench. For transport, porosity was used from experimental data and expected to improve by inverse modelling, and dispersivity was set based on general formulas in literature.

5.1.3 Initial conditions

(1) Hydrogeology

The measured hydraulic pressure at the borehole in the vicinity of the experiment drift was used to specify the initial groundwater pressure condition. Uniform initial pressure or the initial pressure linearly changing according to the depth were tested, as well as projection form a hydraulic model of the whole site.

(2) Rock mechanics

The measured rock stress was considered for the initial condition. The calculation was not finally made.

(3) Chemistry

The chemical composition of groundwater as an input was defined during Step 1, based on the profiles observed in boreholes.

5.1.4 Boundary conditions

(1) Model boundary: Hydrogeology, Rock mechanics, Chemistry

The boundary conditions were based on a large-scale hydraulic model or simplified to a uniform or linearly changing field derived from the depth and the exploration borehole profile. It was mostly used to define the prescribed head and groundwater chemical composition.

(2) Drift wall: Hydrogeology, Rock mechanics, Chemistry

Zero pressure was set on the drift wall as a boundary condition of water head (essentially 100% relative humidity at approximately atmospheric pressure). Zero dispersion flux,

i.e. advective only transport, was prescribed for the chlorine transport during drainage. The prescribed concentration from measurement was used during flooding. The free boundary condition (zero traction) was planned as a boundary condition of displacement.

5.1.5 Drift excavation modelling

In most cases, the excavation was represented by a time varying boundary condition (no flow before excavation and zero pressure after excavation, this could be possibly made in a continuous sense in the software). If necessary, different geometries with coarse steps of changing void size were considered.

5.1.6 Output of simulation

The distribution of water head and rock stress on the horizontal and vertical slice along the closure tunnel was visualized at several time steps in the numerical simulation. The time variation of change in water head, rock, and chemistry at the location of monitoring borehole were plotted.

5.1.7 Hydraulic model details

In-house developed software Flow123d (TUL, 2017) was used, which is based on multidimensional conceptual model (combining 3D continuum and 1D/2D fractures) and mixed-hybrid finite element solution, with discretization either in tetrahedrons or triangles. The phenomena are unsteady flow, variably-saturated flow, multicomponent transport, simple reactions (decay, sorption). An interface to geochemical codes is in development.

The initial step is an understanding of the long-time borehole pressure evolution: Model of site scale (approx. km) was prepared, with the simplified geometry of excavation (main shaft, experiment tunnel as straight lines or cylinders), considering gradual excavation in time. In this way, we expected to detect main inhomogeneity, necessary to establish boundary communication of the local model (reference geometry around the CTD; Figure 20). Given hydraulic conductivities related to geological units were verified through the excavation inflow rates and comparison of the model results and the borehole pressure monitoring.

Next, the reference geometry model was planned to be solved based on the given assignment, i.e. prediction of the CTD excavation effect in term of pressure/head temporal evolution. We conducted modelling in gradual steps from simpler to more complex models

- From uniform (hydrostatic) boundary conditions, through 12MI33 borehole data regression (extrapolation), to general spatial distribution resulting from the large-scale model
- From homogeneous to use of structural data: First, the inhomogeneity was based on zones used for 12MI33 hydraulic testing. During calibration, discrete fractures based on tunnel wall mapping and borehole logging were added.

The hydraulic models were planned to be also validated by the tracer and geochemical data (origin of water, flow direction, residence time, mixing).

Before the modelling, there were several preparation steps of data understanding during the first months of the project: a conceptual model of pressure monitoring reaction on excavation progress, distribution of pressure along boreholes, the variability of permeability, relation to tracer and geochemical data.

5.1.8 Transport model details

The available data of natural tracers in the water sample analyses (oxygen and hydrogen stable isotopes, tritium, radiocarbon) were studied, e.g. plotted to understand the spatial distribution and time evolution. It was considered for use as a background for the hydraulic and chemical model. From initial investigations of the natural tracers ^{2}H, ^{18}O, ^{3}H and ^{13}C, it seems that the water is a combination of several thousand years old water and some amount of meteoric water, or water from only a few decades old. The hydraulic model, especially any inhomogeneous concept, could be checked to be in accordance with this observation. Also, the mixing interpretation of chemical composition analysis can be compared to the tracer data.

The transport model in the CTD scale considered chlorine as a non-reactive tracer, using its natural concentration vertical gradient. If the reactive transport needed to be used for temporal chemical composition changes resulting from excavation, it would be constructed based on the chlorine model. It was planned to provide the calibrated transport data like porosity (eventually scale-dependent) and dispersity on a simpler case, before adding the reaction effects.

The simulation was be made in Flow123d together with hydraulics (3D), or as part of detail reactive-transport models (below) in The Geochemist's Workbench (GWB; Bethke and Yeakel, 2018).

5.1.9 Chemistry evaluation

The work was composed of data analysis/understanding and of predictive simulations. Data analysis was expected to be a substantial part of the introductory phase of the project. The commercial software The Geochemist's Workbench (GWB) was used.

The particular steps were the following

- Understanding site configuration, borehole placement, type of data.

- Processing of geochemical data:

  - definition of basic groundwater types, finding key differences between groundwater types
  - evaluation of temporal and spatial distribution for physicochemical parameters and chemical components concentrations
  - finding differences between original (natural) and disturbed conditions that developed during the building of the MIU
  - finding a relationship between the rock type and the groundwater type (if any exists)
  - comparing results to geochemical conditions in Czech granite sites.

- Identification of the main processes that determine the chemical composition of individual water types.

- Modelling of water-rock equilibrium:

  - the purpose of this stage was to define reference conditions before excavation disturbance as well as a need to check a consistency of data (e.g. charge balance)
  - comparing geochemical model outputs with real conditions developed at MIU site
  - special attention was paid to the in situ measured redox potential and its relation to the redox sensitive groundwater components.

- Defining the key points (physico-chemical parameters, groundwater chemical composition) which the system of groundwater-rock will pass over the opening,

operation, closure and flooding at the MIU site, especially including the interaction with shotcrete, as input parameters for reactive-transport modelling.

More options depending on quantitative condition were considered: In case of dominant transport, 1D reactive-transport models could be used. In case of dominant reaction (dissolution/precipitation kinetics), it could be approximated as a batch experiment with changing water composition. Additionally, a suitable model of impact of oxygen in the rock could be tested (e.g. some simplification by means of sensitivity study).

5.1.10 Model Variants

Following the task definition, the modelling was oriented on prediction of the tunnel excavation effects on the hydraulic field and on chlorine transport modelling as a non-reactive tracer. Although the model geometry and boundaries were recommended by the task coordinators for this phase (referred "CTD-scale" below), we made an additional larger URL-scale model besides the one mostly used by the other teams. The purpose was to justify the pressure field on the CTD-scale model boundary. The given concept of the CTD-scale model was also made in several variants, distinguished by the boundary condition and by permeability inhomogeneity. It depends on individual understanding of the term "prediction", what level of the model details could be available: the variants below correspond to the following: (1) only URL-scale averages or variations of parameters, (2) data from the pilot borehole logging (12MI33), (3) limited data from the tunnel itself.

5.2 Large-scale model definition (URL-scale)

The domain is a block with the square base of 5000 m and the height of 1300 m. The URL is modelled as one vertical cylinder representing the two shafts (diameter 5 m) and one horizontal cylinder representing the access drift to CTD simplified to straight and horizontal shape (length 150 m, diameter 5 m).

The geometry and boundary conditions are illustrated in Figure 97. We define simplified hydraulic conditions without local topography effects, i.e. the model has a flat top boundary. The lateral sides are impermeable (meaning the symmetry between inside and outside of the model, assuming out of reach of the URL drainage effect), the top and bottom side have a prescribed pressure or head defining the reference conditions. The

URL excavation is simulated by switching the no-flow boundary to zero pressure boundary on the shaft/tunnel walls. There are two variants of the top/bottom pressures:

- Higher pressure, considering water table on the top, i.e. p=0 (head of 200 m) on the top and p=11 MPa on the bottom (head of 0 m)
- Lower pressure with higher gradient, water table 40 m below top, p=-0.4 MPa (head 160 m) on the top and p=9.6 MPa (head -140 m) on the bottom (it is 45 m head at the -300 m lab level)

The parameters were set based on the provided data for hydrogeological units (UHFD, LSFD) and individual borehole packer tests: hydraulic conductivity K=10^{-7} m/s (rounded value, little higher than the geometric mean of the packer data) and storage S=10^{-5} m^{-1}.

5.3 CTD-scale model definition

The conceptual model is common for all variants below. The outer dimensions follow the JAEA suggestion and are the same for all variants, i.e. a block 150 m long in the direction of the tunnel, 100 m transversally and 100 m vertically (Figure 98). We consider one fixed geometry, where the CTD tunnel is represented as empty space in its maximum extent and the gradual excavation is represented only by time-variable boundary condition described in a special Section 5.3.4 below. The model geometry keeps some features of the real tunnel shape: the vertical position of the inclined gallery (approx. 3 m difference) and the CTD is consistent with the documentation. Note that the tunnel is not therefore exactly in the middle of the model vertically (Figure 99). The tunnel profile has a horizontal bottom, vertical lower parts of the side walls and semi-circular top, the size is different for the inclined drift and for the CTD. The boundary conditions on the outer walls come from the assumption of no influence by the excavation (inclined + CTD). But there are various approximations of the initial (and unchanged) state around the CTD (Section 5.3.3).

The problem of transient flow and single-component non-reactive transport will be solved (chlorine ions). Considering the other inputs, we need to define:

- Hydraulic conductivity
- Specific storativity
- Porosity
- Molecular diffusion coefficient and longitudinal and transversal dispersivity

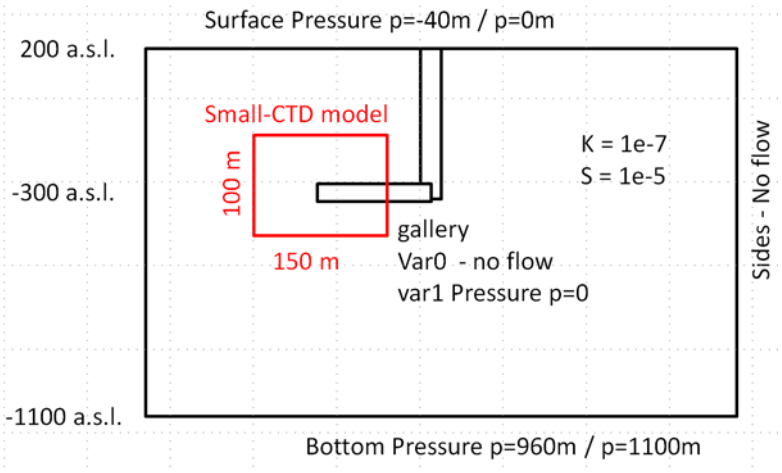

Figure 97. Geometry and boundary conditions of the large-scale model (vertical section).

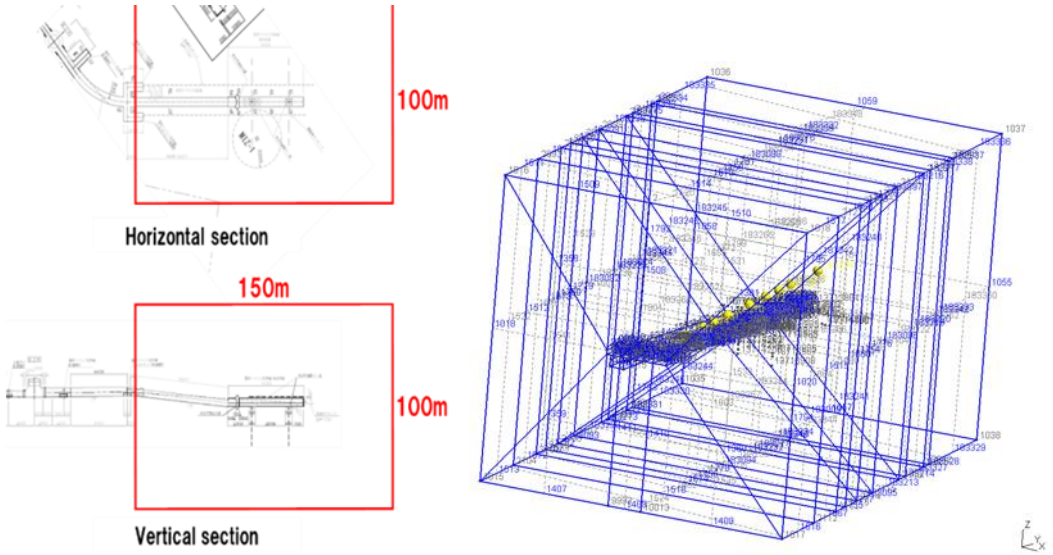

Figure 98. Geometry of CTD-scale model – vertical and horizontal view with respect to the real drawing, and the GMSH realization of the model for simulation input.

While the hydraulic data are well supported by the measurements provided in the data (pressure tests in many of the URL boreholes, including the 12MI33), the transport data were not explicitly measured or not present in the provided data. The porosity was set initially to 0.01, based on generic data of granite in literature, while the provided data in Table 4 were considered later in Step 2 solution. The remaining data are generic, 5 x 10^{-10} m^2/s pore-water diffusion coefficient and 4.3 m and 0.43 m respectively for the dispersivities (less than the typical 1/10 of the model scale for the reason that the

studied process scale is actually smaller – around the tunnel). We assume the effect of dispersion is dominant.

The inhomogeneous model variants consider only hydraulic conductivity variations while the other parameters are constant values (due to unavailability of data).

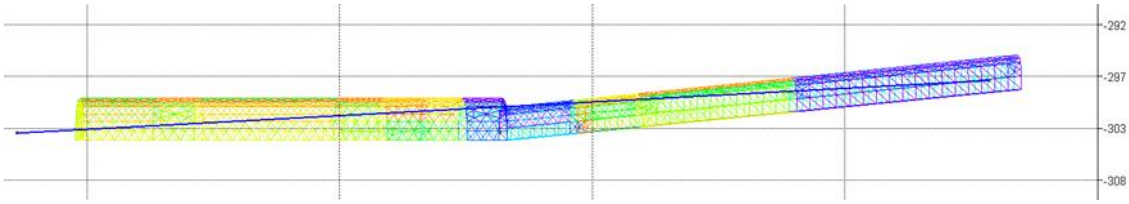

Figure 99. Tunnel boundary in the model with meshing – inclined gallery on the right and CTD on the left. The line of 12MI33 is plotted in blue.

5.3.1 Variants of permeability heterogeneity

We consider two models of equivalent continuum

- Homogeneous hydraulic conductivity and storativity as an average from the borehole pressure tests evaluation rounded to an order of magnitude K = 10^{-8} m/s, S = 10^{-8} m^{-1}.
- Heterogeneous hydraulic conductivity based on the 12MI33 packer intervals.

The latter case considers several significant simplifications but it was suggested as a straightforward use of the only explicit local permeability information before the drift excavation. The model is composed of blocks sorted in the direction of the borehole (i.e. direction of the tunnel) covering the whole perpendicular plane between the boundaries (Figure 100). We assume the spatial scale of the hydraulic tests is enough to cover the distance between the 12MI33 borehole and the CTD and could predict the permeability near the tunnel wall with possible meter-scale shift in position. The extension to boundaries is only meant as a technical simplification and was abandoned in the model variants in the following sections.

The packer test intervals do not cover the whole model length. In the places where the packer tests follow each other, there is typically a gap of 1 - 2 meters, so the interface between the two continuum blocks with different hydraulic conductivity is made in the middle of such packer test gap (Figure 100, Table 26), i.e. a half of the packer own length

is accounted to the measured interval. Then the remaining volume is covered by a background value of K = 10^{-9} m/s which is a generic estimate on the lower range of the packer tests, as we can expect the larger permeability would be observable on the borehole inflow. The inflow is a part of the logging and is given (almost) continuously, but on the other hand there are also some inconsistency in the data (disappearing water, no full correlation of the inflow and the packer test permeability). In Table 26 the model blocks are denoted based on the packer test intervals and the additionally defined blocks are either numbered sequentially, or a symbol is used, similar to the number two packer interval. The interval 86 m to 105 m is not covered by packer tests and the inflow meter data (consistently with other graphic output in the logging protocol) indicate a place at about 90 m with larger permeability. So two different sections No.5' and No.5'' are used in the model. The actual K values are order of magnitude estimates within the range of other intervals, not based on any calculation.

To simplify the multiple model variant processing, the geometry and meshing are the same for both homogeneous and heterogeneous model, differing only by the input data – hydraulic conductivities. The mesh has 13637 nodes and 81752 elements (tetrahedra) and is shown in Figure 100.

Table 26. Parameters of the heterogeneous model – positions of blocks and hydraulic conductivities. The consideration for "own" estimates is given in the text. In the last row shows the monitoring sections in the borehole (see also Figure 100).

	No.0	No.1	No.2	No.2'	No.3	No.4	No.5	No.5'	No.5''	No.6	No.6'
Data from	own	Packer test	Packer test	Packer test	Packer test	Packer test	Packer test	own	own	Packer test	own
K [m/s]	1E-9	2.6E-8	1.1E-7	6.1E-9	8.4E-9	4.8E-10	9.5E-10	1E-8	1E-9	2.73E-7	1E-9
Begin [m]	0.0	12.1	37.1	20.1	44.2	53.2	65.2	90.0	95.0	105.2	107.0
End [m]	12.1	18.9	42.6	36.1	54.5	63.5	90.0	95.0	105.0	107.0	end
Monitoring	Sec. 6				Sec.5	Sec.4	Sec.3	Sec.2		Sec.1	

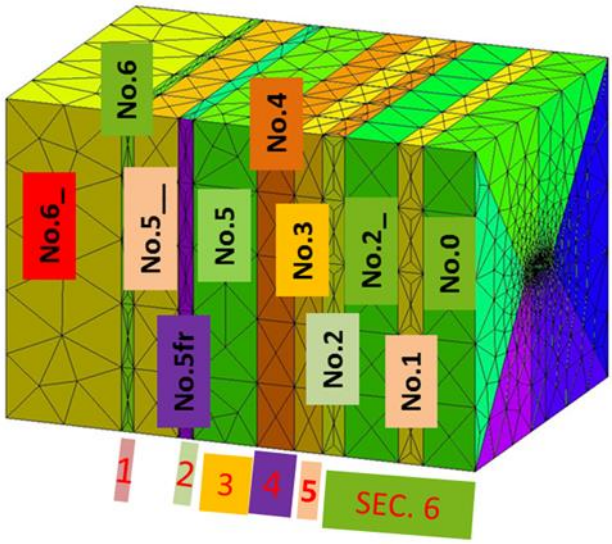

Figure 100. Heterogeneous model concept of TUL team – blocks of different permeability aligned with borehole monitoring sections (below the picture).

5.3.2 Fracture model

The fracture model variant could be also understood as a third variant of the permeability spatial distribution; but due to specific data processing, there is a need for a separate discussion. The idea behind this approach is to use the capability of Flow123d code to combine the deterministic discrete fractures and equivalent continuum of the remaining rock blocks among these fractures. The task therefore is mainly how to select the small number of the deterministic fractures which would be representative for the hydraulic properties. Similar to the block heterogeneity construction, the fractures are extended to the model boundary, although such a spatial extent should be understood as not being supported by the data (as the introductory step, it was simpler for processing then to define the outer part of the model e.g. homogeneous).

There are two main groups of the source data: (1) The tunnel wall mapping of the inclined drift and CTD, including a classification by water inflow. (2) The borehole logging and packer pressure tests. These sources are partly complementary, but also they should be ensured to be consistent between each other.

The procedure of data use is the following:

- Take into account only the fractures with some “water attribute”, i.e. either F (flow) or D (drop), assuming these could be highly connected and having impact on the pressure field. It is 78 of 2023 total. The W (wet) fractures were

neglected, because they would be too many for the model concept (geometry processing).

- Project them to the vertical direction (within a common line of intersection in the plan view) only to simplify the processing, most of them are close to vertical
- Make a plot (plan view) where the fractures' intersections with 12MI33 packer intervals are visible (Figure 101).
- Select "main" fractures so that especially the higher conductivity packer intervals are covered (intersect with at least one fracture) and F fractures have a priority. Groups of fractures of similar position and direction can be represented by one (i.e. fracture zone), typically around one or two F fractures with kept position or their average, respectively. There were 14 of such, which were afterwards digitized from the hand-drawing.
- Assign the transmissivities to the individual fractures. This is made using a packer interval transmissivity as constraints, together with one common rock block hydraulic conductivity, explained below in details.

The assignment of the fractures and 12MI33 borehole intervals is shown in Table 27, including the evaluated data and additional supporting information of the F and D attributes and aperture. The overall idea is that the set of hydraulic parameters of the model should be able to reproduce the packer test data, simply by summing the contributions of the continuum blocks and individual fractures in each packer interval. So, the overall hydraulic effect is emphasized instead of realistic fracture density (i.e. one model fracture plane can represent more "real" fractures). The conductivity of the "rock matrix" (incorporating the fractures not represented explicitly) is estimated so that its contribution for the least permeable packer sections (4 and 5) is balanced with the explicit fractures. The problem is little underdetermined, but most of the relations are unique with one fracture for one borehole interval.

While the result of the above procedure is only the individual fracture description data, i.e. fracture positions, direction and transmissivities, the simulation code input geometry needs a full hierarchy of nodes, lines, areas and volumes, including especially all the fracture intersections among each other and with the boundaries. This task was made in the SALOME software (CAD-like open-source project). The meshing was not yet optimized and resulted in a large mesh of approx. 750000 elements which corresponds to about 3 million degrees of freedom of the flow problem (Figure 102). The calculations were limited by memory consumption and time, so only one pilot simulation of the transient hydraulics was made, i.e. without the tracer transport.

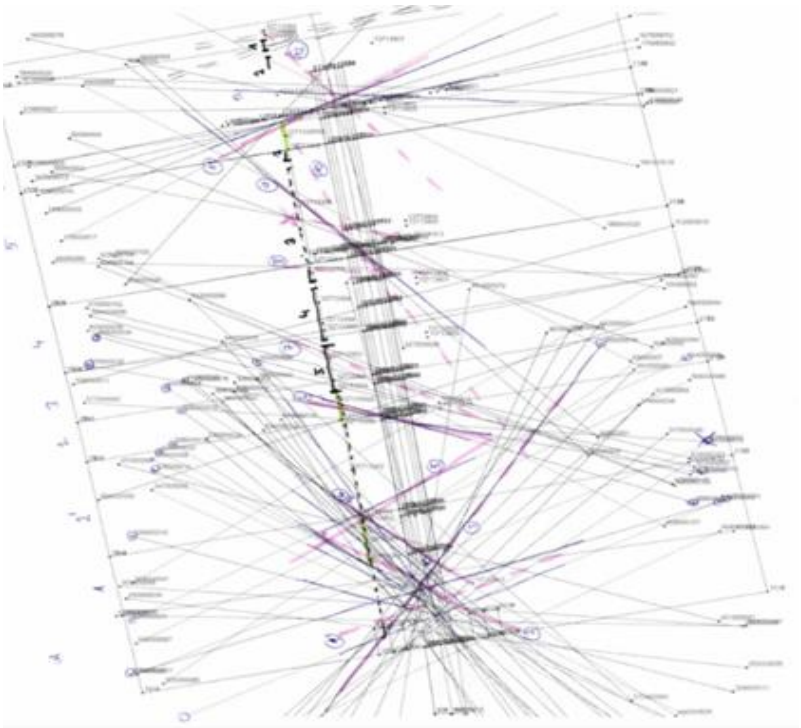

Figure 101. Processing of fracture data – traces of the fractures in a horizontal plane in the level of the tunnel and their intersections with the 12MI33 borehole intervals. Selection of 14 model fracture planes as pink hand-drawing. Orientation in the given coordinate system, tunnel entrance on the bottom and CTD end on the top.

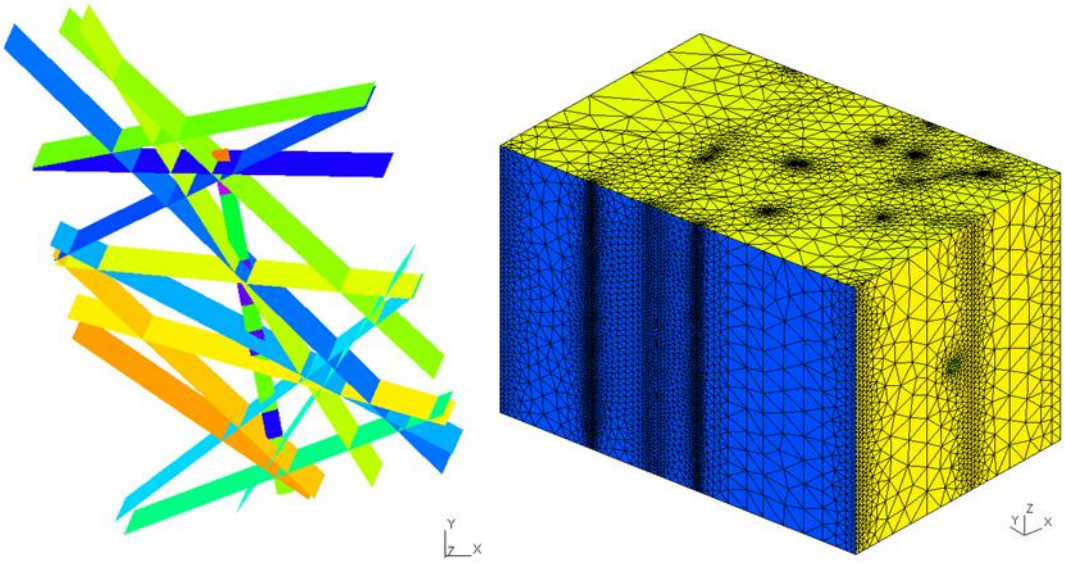

Figure 102. Positions of the fractures with respect to the tunnel in few degrees off the top view (left, see the axes), mesh of the coupled fracture-continuum model (right).

Table 27. Determination of the fracture transmissivities from the 12MI33 packer test and other reference data (own selection in red). The "x" symbol denotes the existing intersection and a contribution to the measured transmissivity. The blue numbers are manually set such that the calculated sums of intervals in the bottom table block fit their measured or prescribed counterparts.

			packer intervals intersected by model fractures (added own additional - red)											represented items from fracture list		
		No.	0	1	2a	2	3	4	5	5a	5aa	6	7	their parameters		
		length	16.6	6.8	16	5.46	10.3	10.3	20.3	5	14.5	1.8	20			
model objects		conductivity														
rock		2.00E-10														
		transmissivity												number	water	aperture
fracture	1	1.00E-08	x											303+427	F (short)	1+3
fracture	2	1.15E-07		x										356+336+426	F	0+0+5
fracture	3	5.00E-09	x											385	F (short)	1
fracture	4	9.50E-08			x									443+446 +393	F	1+0+1
fracture	5	6.00E-08		x										524	F	20
fracture	6	6.00E-07				x								588+576	F	1+0
fracture	7	8.50E-08					x							626+628+etc	D	0+0
fracture	8	3.00E-09						x						28	D	0
fracture	9	1.50E-08							x					90+94	F	5+0
fracture	10	5.00E-09								x				none		
fracture	11	4.50E-08								x				179+170+175	F+D	1+2+0
fracture	12	5.00E-09										x		none		
fracture	13	1.20E-08									x			187	F	1
fracture	14	4.50E-07										x		none (12MI33 based)		
transmissivity total			1.83E-08	1.76E-07	9.82E-08	6.01E-07	8.71E-08	5.06E-09	1.91E-08	5.10E-08	1.49E-08	4.55E-07	4.00E-09			
conductivity total			1.10E-09	2.59E-08	6.14E-09	1.10E-07	8.45E-09	4.91E-10	9.39E-10	1.02E-08	1.03E-09	2.53E-07	2.00E-10			
measured conductivity packer				**2.62E-08**	**6.11E-09**	**1.1E-07**	**8.4E-09**	**4.82E-10**	**9.53E-10**			2.73E-07				
own estimated conductivity			1.00E-09							1.00E-08	1.00E-09		1.00E-09			

5.3.3 Outer boundary conditions

The boundary conditions for both the flow and the transport are illustrated in Figure 103. Simply, the outer model boundaries have prescribed head and concentrations corresponding to the undisturbed state, based on a simple measurement averaging or regression. The tunnel hydraulic boundary is described in the next section. The transport boundary on the tunnel wall is a usual "free outflow" condition, defined as the total mass flux is equal to the advective flux corresponding to the hydraulic model flux value. There are two kinds of additional variants:

Choice of "hydraulic undisturbed state"

- Hydrostatic case with uniform head suggested by JAEA
- Non-uniform head field resulting from the large-scale model, i.e. including drainage effect of the remaining URL constructions, especially the shaft (other horizontal drifts than CTD are not included). The values from the large-scale mesh are interpolated to different positions of element faces in the CTD-scale mesh.

Choice of "front" vertical boundary (intersected by the tunnel)

- In the default case, it is the same as other boundaries, which leads to a discontinuity of pressure/head on the edge of the tunnel/boundary intersection
- No-flow boundary corresponding to an assumption of the symmetry, i.e. assuming long open tunnel on both sides of the boundary, which is true in the later period of the excavation (except the deviation of the tunnel from the direct line), as well as should be a result of the large-scale model pressure field. The tunnel drainage should dominate the pressure gradient over possible inhomogeneity.

Table 28. Variants of the TUL model based on various choices of heterogeneity and boundary conditions. Only the filled fields correspond to the evaluated combinations.

Name:	BC from Reference	BC from Large scale
CTD model Homogeneous/Base model/Reference	**REF** BC+IC: Head = 110 m K = 1×10^{-8} m/s Storativity = 1×10^{-8}	X
Heterogeneous/TUL model	**TUL1** BC+IC: Head = 110 m K directly from 12MI33 test	**TUL2** IC from steady state BC from large model + front side is no flow
Fracture	**TUL3 Fracture** BC+IC: Head = 110 m K inversely from 12MI33 (Table 27) Storativity = 1×10^{-8}	X

The described variants actually make four total combinations, but only three of them were evaluated (especially there was no more motivation for the non-realistic velocities at the discontinuous edge for the second head value choice). The combinations of model structure concepts and boundary condition choices used for the evaluation below are listed in Table 28.

The values of the concentrations both in the initial and the boundary condition are defined as linear increase with depth with the stated top and bottom side values.

The variant with a large-scale model head projection was expected to capture a possible different weighting between the CTD inflow from upwards and downwards. In particular, the resulting head field from the large-scale model contains a significant vertical gradient component (although the horizontal is larger), so that possibly more of the deeper water is drained to the tunnel compared to the shallower water. We note that this consideration was obtained based on the previously measured data presentation, so it is not a true prediction (contrary to the intent), but the assumptions and ideas could be in principle obtained without such knowledge.

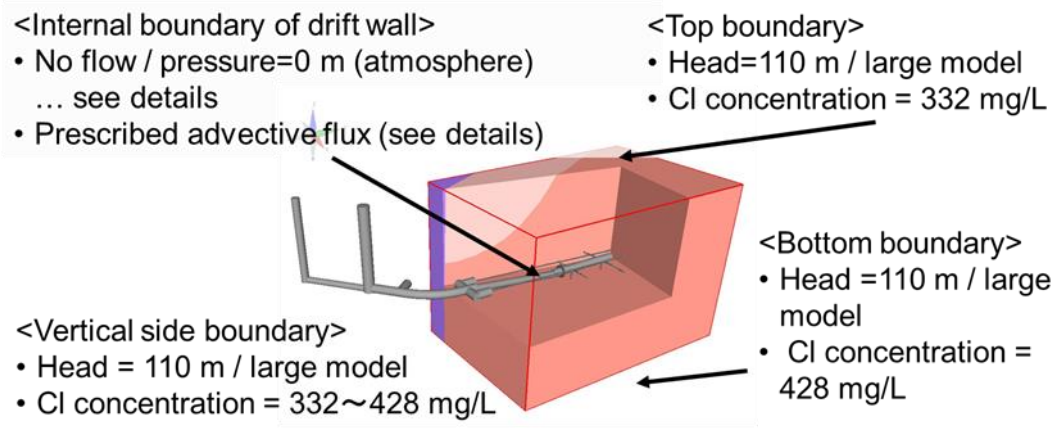

Figure 103. Boundary conditions for the flow and the transport problems.

5.3.4 Excavation progress modelling

In principle, the excavation of the drifts means a changing model geometry. To avoid such difficulty, it can be almost equivalently solved by a switch of the boundary condition: if the no-flow condition is prescribed on the tunnel wall, it is equivalent to rock filled tunnel in terms of its hydraulic effect around (assuming no significant gradient

across the tunnel is present). Technically, we prescribe zero pressure on the excavated part and no-flow on the remaining part, with the interface between them moving in time. This neglects the flow in the unexcavated rock, but within a relatively short time period. Although the progress of the excavation has a detailed definition in the documentation, including distinguishing the upper and lower parts, we suggested a constant speed of the front movement is sufficient for the current level of modelling. The difference is illustrated in Figure 105.

The movement of the two boundaries interface is conveniently achieved by two features of the Flow123d code: the first, quite standard, is the 3rd type (Robin) boundary condition for general flux, which can represent both the 1st type (Dirichlet) and the 2nd type (Neumann) depending on a coefficient

$$-q_d \cdot n = \delta_d\left(q_d^N + \sigma_d^R(h_d^R - h_d)\right)$$

where q^N is the prescribed flux (we use zero), h^R is the prescribed head (we use a z-dependent value appropriate to the zero pressure) and sigma is the Robin coefficient – it leads to dominant flux if close to zero, while to the dominant head difference if close to infinity. We chose 10^{-12} and 10^{12} respectively (units can be disregarded). The second feature, more unique one, is a use of formula parser in the input file, so that any input value can be given as a function of space and time coordinates (predefined symbols x, y, z, t) and includes a "if" construct with the syntax similar to MS Excel. The respective line of the input file is in Figure 104, where the numbers mean the space (meters) and time (seconds) values of the excavation front (even if the tunnel is not parallel to y-axis, the position is correct and the little deviation of the front orientation is unimportant).

5.4 Prediction results of the disturbance during the excavation of CTD

The results of prediction are structured to the flow and the transport parts and based on the post-processed values. For the temporal evolution, the evaluated period corresponds to the excavation period, from Apr 2013 until Oct 2013.

5.4.1 Pressure

For compatibility with other teams, the hydraulic conditions are evaluated in the form of pressure (in units of MPa). It is more illustrative than the head (m) values, especially concerning the zero level and relating to the tunnel boundary (zero pressure and -300 m head). The initial (undisturbed) values are 110 m head and 4.1 MPa pressure.

```
bc_type: total_flux
bc_pressure: 0
bc_robin_sigma: !FieldFormula
value: if((y+68949)<(t-518400)*(106/14342400),1e12,1e-12)
```

Figure 104. Input file lines of Flow123d defining the boundary condition on the tunnel wall for temporal progress of the excavation by means of relation between y position and t time in the formula.

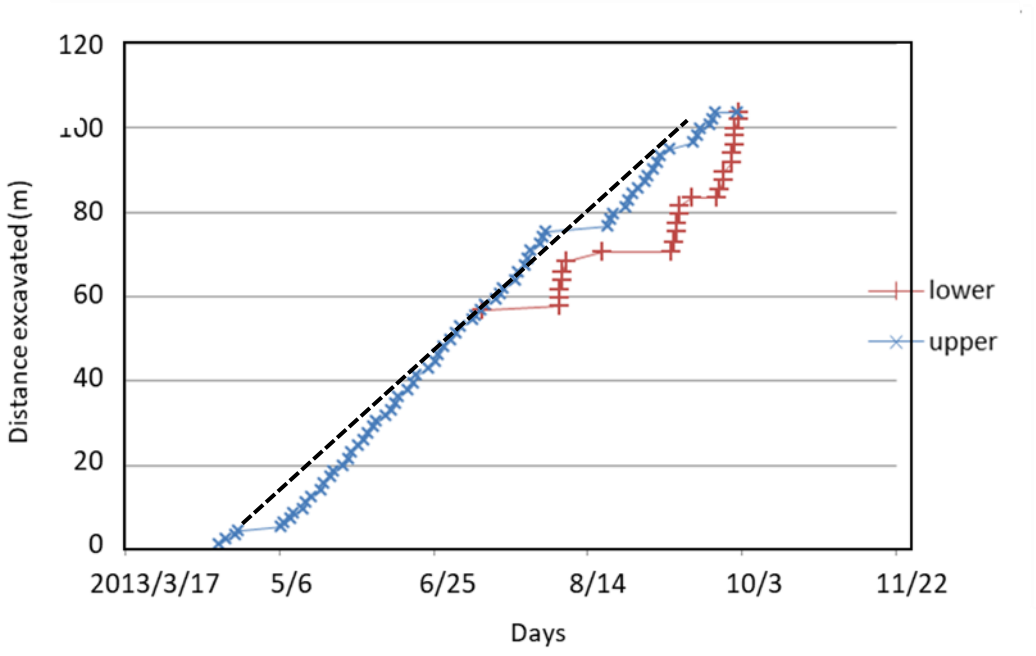

Figure 105. Progress of drifts excavation – the documentation data and the linear regression used for the modelling

The results for four model variants (or variant combinations) are compared in Figure 106. The variants correspond to Table 28 concerning the heterogeneity and outer boundary condition source. The REF variant uses the prescribed head on the whole boundary while the other three use the no-flow (symmetry) on the “front” side (intersected by the tunnel).

In all cases, we can clearly observe the drawdown resulting from the excavation drainage. The temporal sequence corresponds to the alignment of the excavation progress position with the monitoring point position. All the heterogeneous models show more steep pressure drops, which correspond to crossing of the interfaces between different permeability or crossing of fractures.

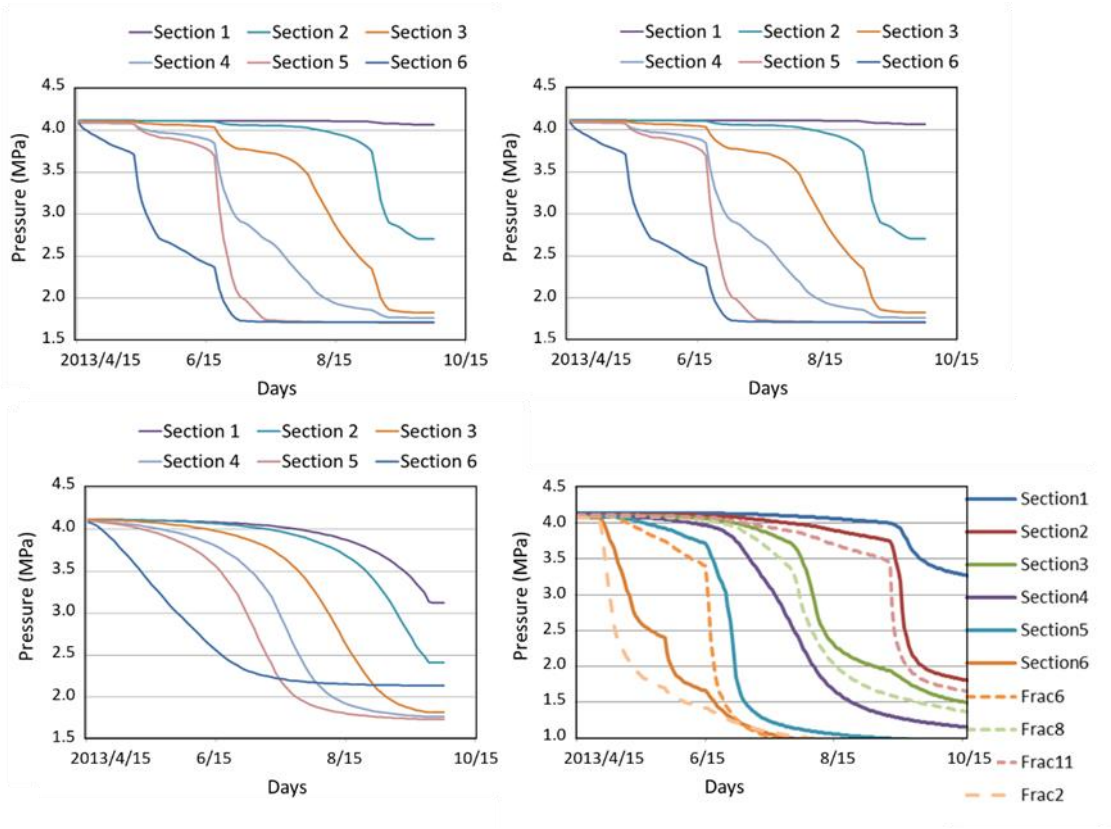

Figure 106. Pressure evolution model results in the points corresponding to the monitoring sections – upper left: heterogeneous model (original b.c. – TUL1); upper right: heterogeneous model (large-scale b.c. – TUL2); lower left: homogeneous model (with head b.c. on the front – REF); lower right: fracture model (TUL3 Fractures).

Next, the variants differ by the asymptotic values of the pressures after the excavation. Sections 3-5 always reach the lowest final value between 1.5 and 2 MPa, section 2 stays in the middle of the range and section 1 decreases significantly for homogeneous model but negligibly for the model with blocks (TUL1 and TUL2). As expected, the use of boundary values from the large-scale model (TUL2) has no effect on temporal trends, but determines the overall pressure levels with about 0.1-0.2 MPa difference (10-20 m of head). The different asymptotic value of section 6 for REF model is a result of the front side boundary with a prescribed head. Therefore, we find the boundary condition option of TUL1 and TUL2 more suitable, leading to the tunnel drainage controlled pressure similar in section 6 to the sections 3-5 which should be more realistic.

Concerning the future comparison of the model prediction and the data, we note that use of the central point of a packer monitoring interval for a respective model output is not necessarily realistic. In principle, the measured packer pressure is dominated by pressure in the most permeable structure intersected by the borehole. On the other hand, it would not be worth evaluating this kind of weighting from the model values along the borehole interval line, given the current coarse prediction level. To demonstrate the possible impact, we have additionally plotted the pressure evolution in the points of the borehole/fracture intersections for the fracture model, as part of the Figure 106 graph set. The colours correspond to those of the packed interval intersected and we can see visible effect mainly concerning the time of reaction.

In the remaining figures, the spatial hydraulic field is illustrated. The differences between the two boundary conditions, hydrostatic and large-scale projection, are shown in Figure 107. A horizontal gradient directed towards the shafts is visible in the upper part of the model. Figure 108 shows the spatial reach of the excavation-induced pressure decrease. The front side (on the right in the picture) has a no-flow boundary in this case. We can also observe a gradient normal to the boundary (top, bottom, lateral) which suggests that the boundary condition can have some effect on the model or, vice-versa, would not be constant with time in reality. Figure 109 demonstrates the features of the fracture model.

5.4.2 Gallery inflow

It was straightforward to evaluate the inflow as a time evolution from the transient hydraulic model, although it was not evaluated with temporal changes. We understand the final model values are those to be compared with the measurement (one value of the gallery inflow and one value of the CTD inflow).

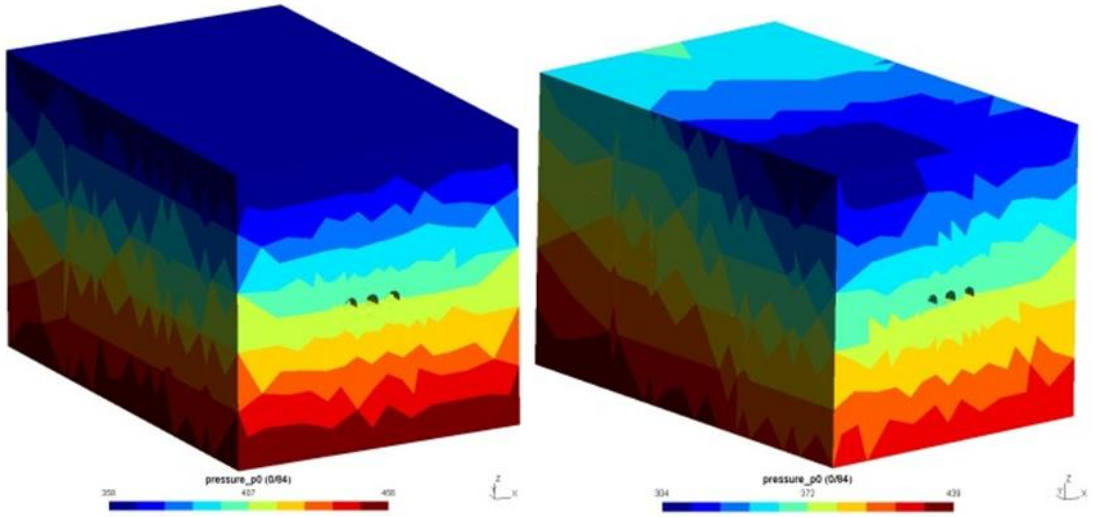

Figure 107. Result of field of hydraulic head. Left is the homogeneous model with the hydrostatic boundary and right is the heterogeneous model with the large-scale projection boundary.

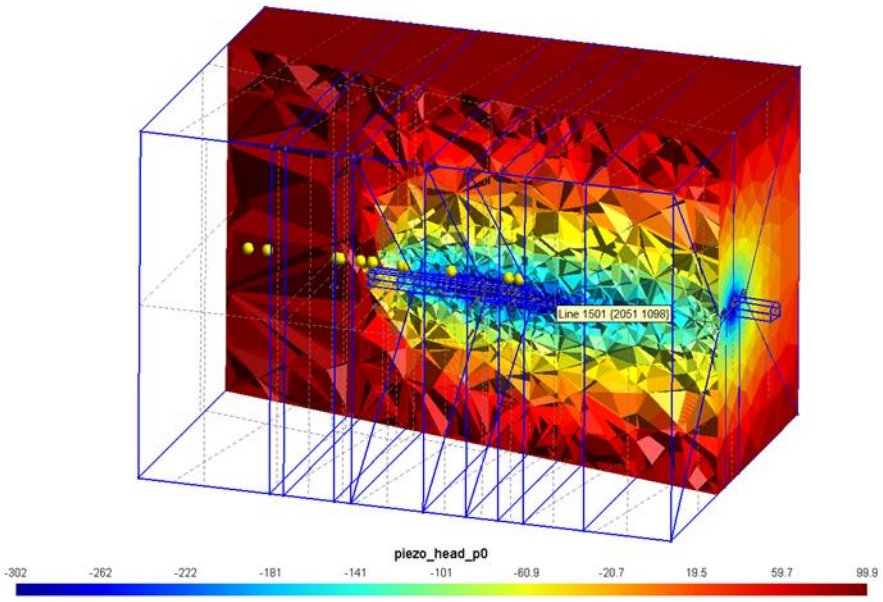

Figure 108. Result of field of hydraulic head [m] in the vertical section along the tunnel – effect of the excavation drawdown in the final time.

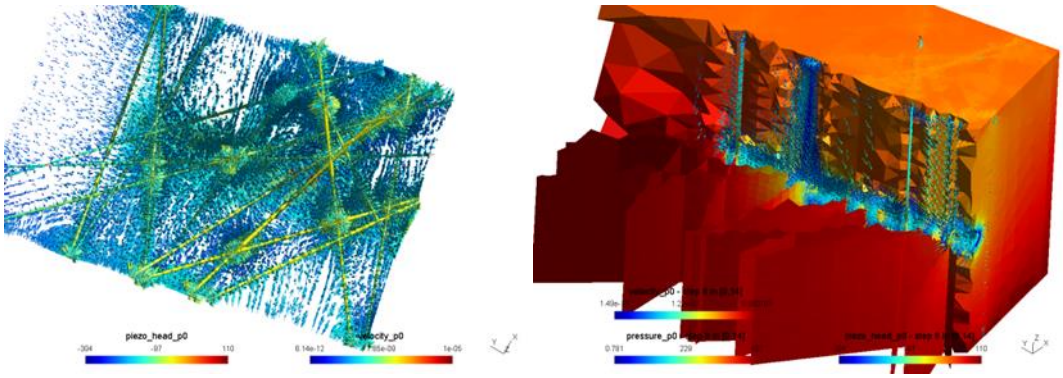

Figure 109. Illustrations of the fracture model results – velocity field concentrated to the fracture planes and the hydraulic head field in the middle of the excavation progress (partial section keeping the fracture planes in the front).

In Figure 110, three of the model variants are presented, so that the effects of the heterogeneity can be observed while the boundary condition variants effects are not significant. It is clear that the inflow to the homogeneous model is quite uniform, the same contribution of both inclined gallery and CTD, while for others, the inclined and CTD differ by several factors. It is a direct consequence of the lower permeability in the CTD part than the average permeability. On the other hand, we could not explain the total inflow difference of about factor of 2 between TUL2 and TUL3 cases, which were defined with the equivalent transmissivity assumption. Also the time trends are more uniform for the homogeneous while with some steps for the heterogeneous cases. Especially for the fracture case, we assume the peaks are results of a sudden intersection with a fracture followed by a flow rate decrease after the pressure gradient decreases.

5.4.3 Results of transport modelling

The advection-diffusion transport was evaluated only for the continuum models (homogeneous and heterogeneous) but not for the fracture model. Again, the post-processing is adapted to the expected monitoring data, i.e. the chemical sampling from the 12MI33 borehole sections. Additionally we evaluated the concentration in the tunnel drainage water, which also can be a value available for measurement and can be considered as some validation of the representativeness of both values for the spatial distribution.

The borehole section values are calculated inside the simulation code as a direct result, only interpolated to the required observation point from the nearest mesh degrees of freedom. The temporal evolutions are plotted in Figure 111, for the two representative

model variants. The little differences and temporal changes could seem to be numerical error effects (commented below), but there are physical arguments related to model configuration, for some of them:

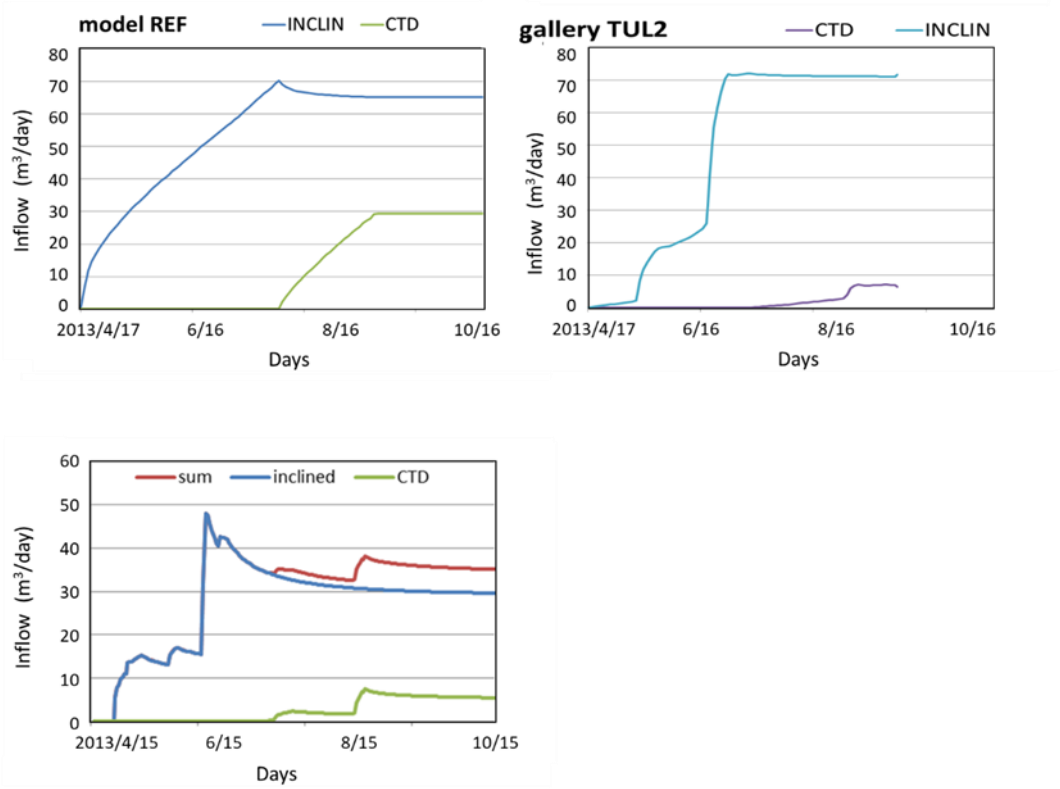

Figure 110. Temporal evolution of the inclined gallery and CTD groundwater inflow – upper left: result of the homogeneous model (REF); upper right: result of the heterogeneous model (TUL2); lower left: result of the fracture model (TUL3 Fractures).

First, the borehole is not horizontal (Figure 99), so that it crosses the concentration field controlled by the z value in a non-constant profile. Therefore, the initial values (visually same for both models) are sorted from the lowest concentration for the highest placed section 6, except the unexplained changed order of section 1 and section 3.

Second, the trend of temporal change should be then controlled by the relative borehole and tunnel position. Assuming the tunnel is draining the water symmetrically around, the water from the lower space is transported to any point below the tunnel axis and vice versa. This is, on the other hand, made more complicated by the non-circular tunnel profile. This consideration is only significant theoretically to understand the model, while the measured data have much less accuracy (the chemical analyses are typically

reported with percent to tens of percent uncertainty) than the discussed model variations which are less than one percent.

In principle, the effect of lower concentration flow downwards and higher concentration flow upwards should lead to a sharpened interface between low and high concentration on the level of the tunnel axis (middle height). This is hardly visible on the concentration field plot of a vertical section perpendicular to the tunnel, especially through a block of larger permeability (Figure 112).

The concentrations in the water seeping into the tunnel are evaluated indirectly from the available software outputs – fluxes through the boundary parts, in particular the volumetric flux from the hydraulic model ("volume per time") and the mass flux from the transport model ("mass per time"). The ratio of these fluxes equals to the concentration in the mix of discharged water, in "mass per volume" units. It is simpler than evaluating a weighted average of concentrations along the boundary elements or nodes. The results are plotted in Figure 113. The values are consistent with those of the 12MI33 borehole, with the difference appropriate to the vertical position. There are significant fluctuations which we believe result of the numerical errors in the calculation procedure: first, the volumetric and mass fluxes are calculated from the model discrete unknowns inside the software and second, the concentrations are calculated as the mass flux to volume flux ratio (above) outside the simulation software.

5.5 Model calibration

Although the Step 1 was intended for predictive models rather than the calibration, this section was included as natural extension, implementing mainly particular model corrections after comparison of the predictive version with measured data. The full-extent calibration is subject of Chapter 10.

The idea of the model calibration for the period of excavation is in using all data available until the end of drainage period, which include the pressure and concentration monitoring in the six sections of the 12MI33 borehole, all the CTD wall structural mapping, and the tunnel inflow rate. Unfortunately, a significant part of the time evolution is not available, due to the reported power switch-off during the excavation.

For the current simulation, the above mentioned data were used; but based on the task definition, other data should be available for this period, such as other borehole pressure tests and monitoring in the boreholes from CTD or parallel to the CTD. These will be used in the continuing work.

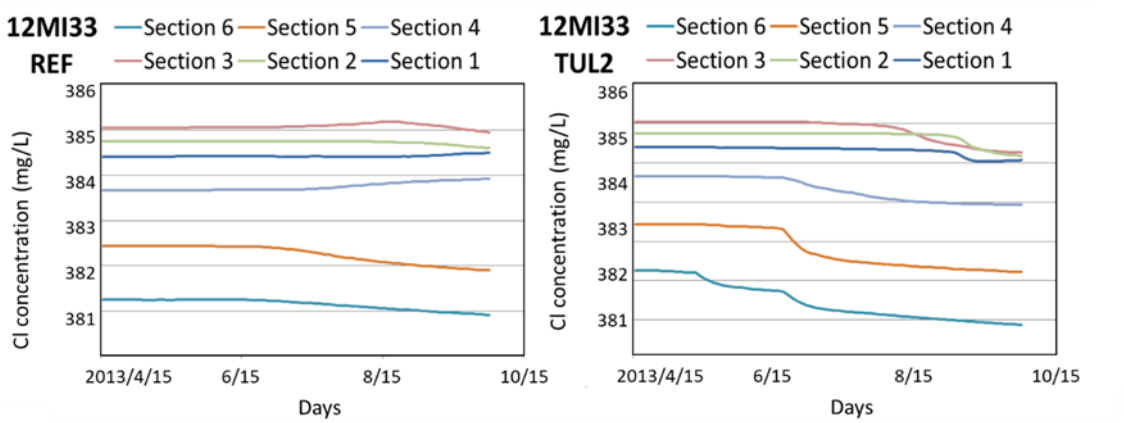

Figure 111. Concentration of chlorine during excavation in 12MI33 borehole for two model variants – homogeneous with hydrostatic b.c. and heterogeneous with large-scale pressure field b.c.

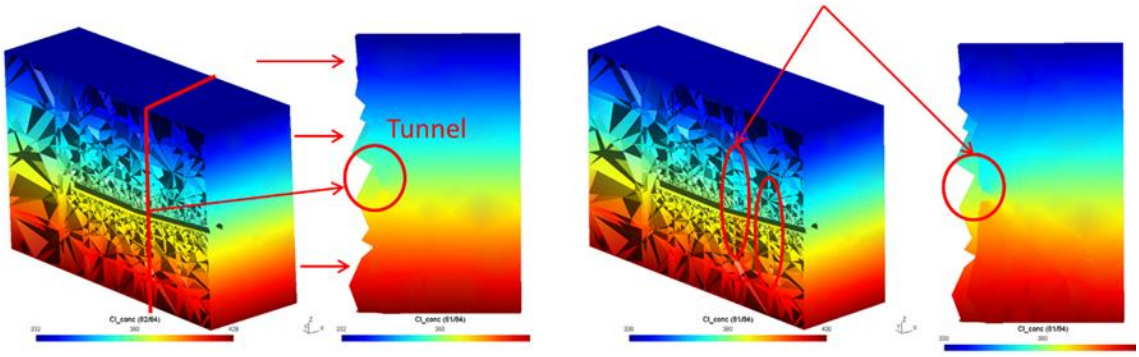

Figure 112. Concentration of chlorine in water flux through the tunnel wall, during the time of excavation, for the two model variants (defined in Table 28).

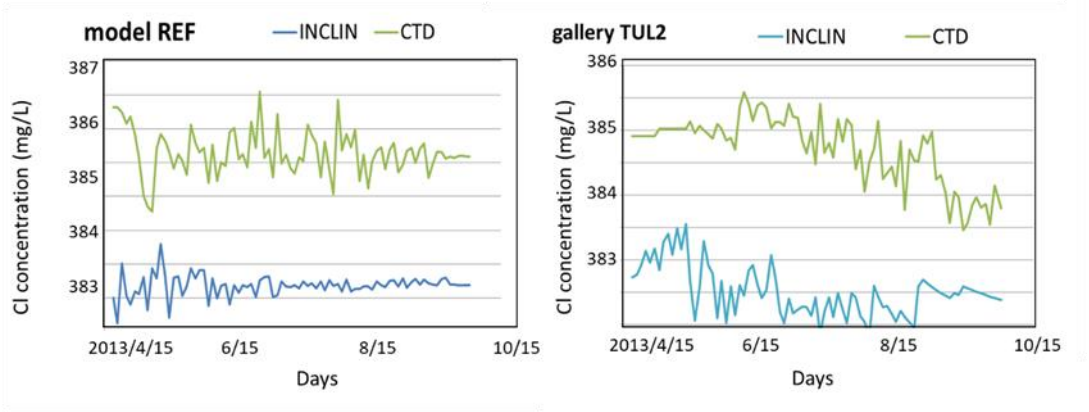

Figure 113. Concentration of Chlorine with pointed place, where the concentration makes a little change during excavation.

5.5.1 Fitted data observations

The main opportunity to calibrate the model was in the choice of inhomogeneity structure. As mentioned above, the configuration options used in the predictions, i.e. blocks of different conductivity changing along the CTD or pilot borehole (while constant in the perpendicular direction from the CTD out to the boundary) cannot itself explain the behaviour observed in the 12MI33 monitoring sections. From the general complex temporal evolution and mutual relationships of the sections, we can select the following features that we will concentrate on in the calibration:

- The sequence of the pressure drops corresponding to the excavation advance: In the sections with some reaction (i.e. No.2,3,4,6), the order of the reaction corresponds to their position, although some of the relations are not unique, as they can happen with a quite long interval of missing data. In general, any of the model variants are not in contradiction with the data in this behaviour.
- The final value of pressure after the excavation monitoring period, which is different for each section – some fall to the value similar to that predicted while others keep almost unchanged. This is controlled by outer effect and internal model geometry. To capture this behaviour in the model with simple boundary condition, we need to include some inhomogeneity along the path between the tunnel and the boundary – the smaller pressure is the effect of larger conductivity between the tunnel and monitoring section and the larger pressure is the effect of larger conductivity between the boundary and the monitoring section (and smaller conductivity between the tunnel and the section).
- The slope of the pressure decrease period: This is influenced by the model inhomogeneity, there is a sharp drop in such model (including the fracture model) compared to the gradual decrease in the homogeneous model. On the other hand, the measured data have gaps which do not allow to distinguish fast or gradual decrease for sections No.3 and 2, but the limits suggest rather faster decrease.

Although the chlorine concentration evolution appears to be a good observation of the flow field inhomogeneity, we did not consider the new transport data for the calibration in this stage. The chlorine concentration is evaluated by the models but only for illustration.

5.5.2 Model configuration

The model configuration is based on the previous CTD-scale model geometry and boundary conditions. The difference is in the inhomogeneity concept. The motivation is as follows: (1) we need to introduce a varying permeability in the direction perpendicular to the tunnel (Figure 114) and (2) the data used as a basis for permeability changes along the tunnel are related to the tunnel and the borehole sections scale, so it should be relevant for such scale in the model (i.e. not for the whole volume as used in prediction). Thus, the model geometry is composed of two "nested" parts: the inner one 30 m × 30 m × 100 m using the permeability inhomogeneity and the outer part of homogeneous equivalent continuum with site-scale average permeability. The choice should normally be based on expected spatial scale covered by observation on the tunnel wall and in the borehole, but it is also motivated by more illustrative visualization at this stage.

This conceptual idea is applied to the particular model variant with the set of deterministic fractures coupled to "matrix" blocks in between (TUL3 in Section 5.3.2); the fracture set and geometry is exactly the same (data of the tunnel wall mapping) except the clipping by the inner model block. The views are shown in Figure 115.

The parameters to be found by the calibration procedure are the following:

- The permeability and the storativity of each fracture individually
- The permeability and the storativity of the rock blocks between the fractures (homogeneous inner 3D subdomain, as a "matrix")
- The permeability and the storativity of the rock continuum in the outer model subdomain (3D "equivalent continuum")

Practically, we first tested a simpler variant with one common parameter of 3D domains (Rock1) and then the two independent settings as listed above (Rock2). Also, the calibration was done manually, so we did not use all the possible degrees of freedom and tried to get an "optimal" result by changing a few of the fracture parameters with the most necessary impact to the resulting pressure evolution (e.g. making some fractures impermeable, using one common storativity for all).

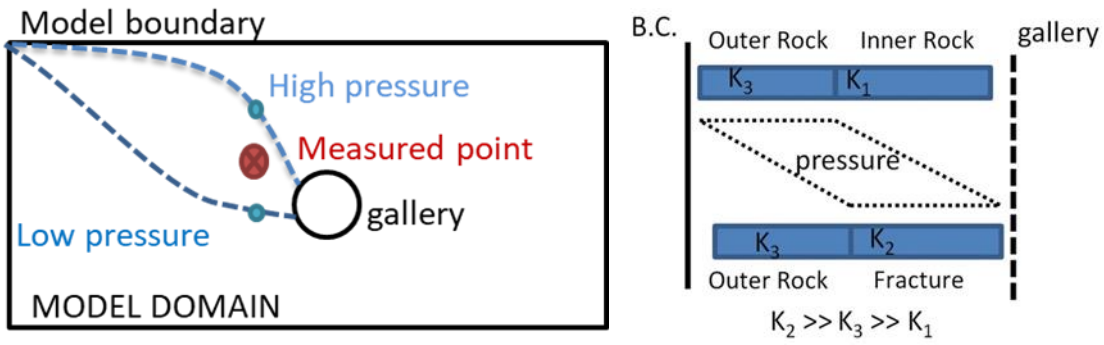

Figure 114. Concept explaining different reaction of pressure in a borehole near a tunnel, depending on near/far permeability ratio and a quantitative illustration with data of the Rock3 model variant.

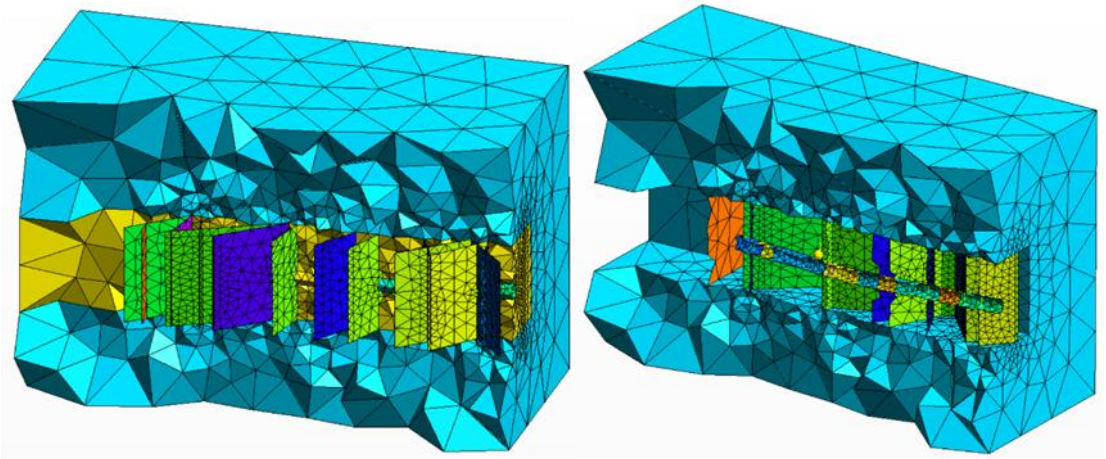

Figure 115. Model geometry with domain visibility – left are the whole fractures and half of inner rock; right are half of fractures and no inner rock.

5.5.3 Model Rock3 - coupling fractures and continuum

Due to the principles of the mixed-hybrid FEM in the Flow123d code, the pressure unknowns and fluxes in the fracture subdomain cannot be directly coupled to the discrete unknowns of the 3D domain if the fracture edge touches the surface of the 3D volume. Therefore, the hydraulic communication between the inner domain fractures and the outer domain is only possible through the inner domain rock block. It is illustrated in Figure 116 left (the 2D-3D communication is “perpendicular” to the 2D plane).

Supposed the inner rock (matrix) is much less permeable, some of the model inhomogeneity choices can result into artificial (non-physical) large hydraulic resistance between the inner and the outer domain. The model Rock3 was created so that the fractures will penetrate a little into the outer 3D continuum domain and the fracture triangular element become a side of at least one 3D domain tetrahedral element to provide the proper communication (Figure 116 right). Without this correction, the Rock1 and Rock2 results could only be treated qualitatively with respect to the inner/outer inhomogeneity effects, without relevant relationships between the input permeability and the resulting fluxes and pressure gradients.

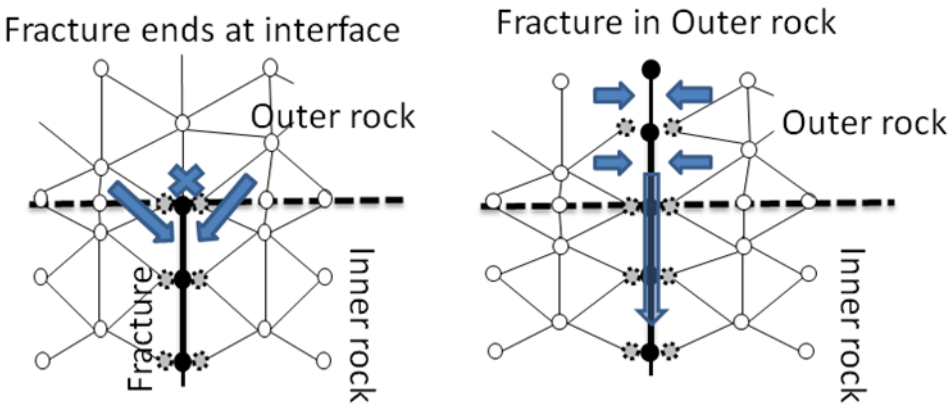

Figure 116. 2D-3D coupling in the discretisation: Comparison of the Rock 1 and Rock 2 model configuration (left – fractures end at the interface) and the Rock3 model configuration (right – fractures penetrate into the outer rock domain).

5.5.4 Model input data

As mentioned before, this stage was intended to demonstrate the capability to fit the data with various model inputs, but not to perform the full optimization procedure. The settings are demonstrated on two models' options Rock1 and Rock2 described above, with either common or independent values of the inner and outer 3D subdomains. The Rock2 variant was later updated to Rock3.

The set of parameters found to fit the measured data with at least some of the quantitative and qualitative features (not all together at the moment) is presented in Table 29. The fracture permeability is only changed for one case, where there is clearly

very limited communication between the gallery and the respective borehole section, with almost no pressure disturbance during excavation (fracture No.108 in the section No.4). The storativities had very limited effect in some range, but can provide effects on the slope within about two orders of magnitude range. On the other hand, the steady pressure in Section 2 and 5 cannot be seen as “very slow reaction” from very large storativity, which would not have any physical meaning.

So, the main values to set are the rock continuum permeabilities. To provide the desired effect, the inner permeability must be significantly smaller than the fractures (in the sense of the total volume transmissivity).

The parameters of Rock3 model and Rock2 model are similar (Table 29). The differences between parameters are only in hydraulic conductivity of the outer rock $K = 5 \times 10^{-9}$ m/s and in fracture 108 (where $K = 3 \times 10^{-9}$ m/s). The hydraulic conductivity of the inner rock for model Rock3 is the lowest compared to the outer and the fracture hydraulic conductivity. Then the undisturbed pressure can be transferred through the outer rock to the borehole isolated from the tunnel (upper line in Figure 114 right) or the drainage effect can be transferred by a fracture against the pressure in the outer rock (lower line in Figure 114 right).

Table 29. Set of input parameters for the two variants of partially calibrated hydraulic models.

	Model Rock1		Model Rock2	Model Rock3	Model Rock2 and Rock3
	Conductivity m/s	Storativity 1/m	Conductivity m/s		Storativity 1/m
Inner rock	1E-12	1E-5	1E-10	1E-10	1E-10
Outer rock			1E-7	5E-9	1E-6
Fracture 108	3E-11	7E-8	3E-12	3E-9	5E-8
All fractures	Original various	5E-10	Original various	Original various	5E-8

5.5.5 Introductory results – hydraulic

The resulting pressure evolutions are shown in Figure 117 for the Rock1 model and Figure 118 for the Rock2 model. In the former case, the model is successful in fitting the final pressure values: the lowest for No.2 and No.3 with a continuing decreasing trend, No.6 with slightly higher pressure but the trend not captured (even if we disregard the later pressure rise which cannot be modelled as natural hydraulic-only process), No.4 with very small decrease, and No.1 and No.5 with almost no decrease (still the model has some decreasing trend contrary to the steady measured value). The gradual pressure decrease could be related to relatively large specific storativity value of the rock continuum or wider drainage from the remainder of the facility, the very little pressure decreases of No.1 and 5 to the combination of large storativity and small permeability, which could be seen as unrealistic in the large-scale outer continuum domain.

In the second case (Rock2), the fit was oriented on capturing the pressure decrease trends, in particular on their sharp fall in the relatively narrow times of the data gap. A fragment of No.6 measured pressure evolution shows the slope. We expected a similar slope for No.3 and No.2, where the measurement is not available. The temporal position of the pressure reaction for No.2, 3, 4 was well-captured, including the slope, but we lost many other representative features of the results. In particular, the No.6 pressure drop is too early and too large, and although the No.1, 4, 5 pressure drops are smaller in the group, it is again too large compared to the measurement. The final pressure is well fitted only in the sections 2 and 3, but with a steady value instead of a slight decrease trend.

Next, we can evaluate the tunnel inflow evolution, presented in Figure 119 for both Rock1 and Rock2. We did not attempt to calibrate to this data, which would be two single values of the inflow at the time of finished excavation. The reason is that we detected the problem of the limited numerical hydraulic communication between the inner domain fractures and outer domain continuum (described above) – hence the calibrated data would not be representative. The flow is smaller than it should be with a correct coupling of the outer block conductivity and fracture transmissivity. In general, we see the rather small inflow, especially for Rock1 (which is clearly related to small rock continuum permeability) but can be significantly decreased by the “numerical resistance” between the inner and the outer domains (the case of Rock2).

The effect of model inhomogeneity is well seen on the pressure contours in the model sections (Figure 120). We can see the intended effect of the fractures with larger

drainage side by side with the block of conserved hydraulic pressure. On the other hand, there is the significant effect of the artificial numerical resistance on the inner/outer subdomain interface (large pressure difference through the interface).

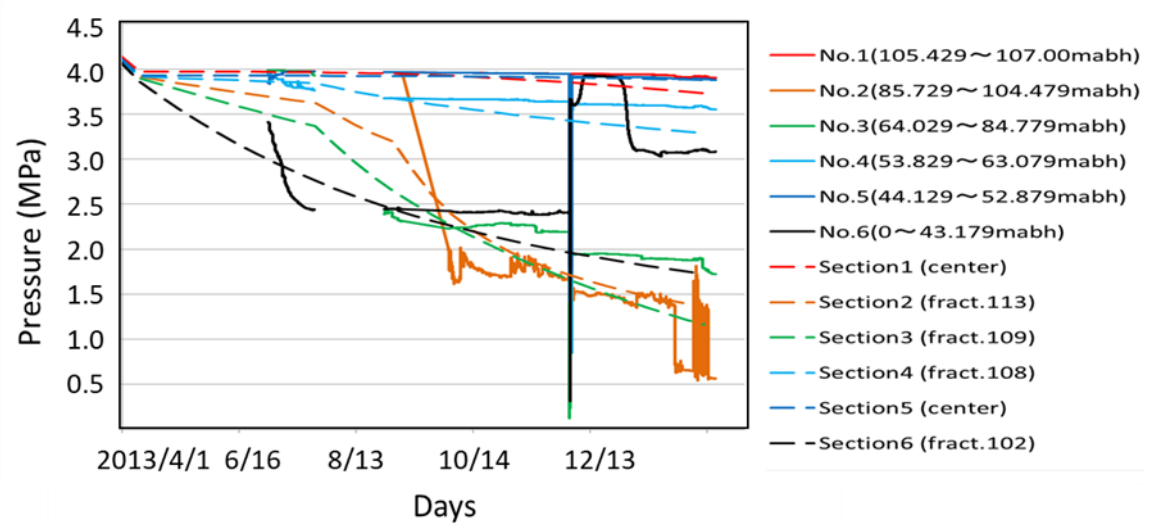

Figure 117. Evolution of pressure in Rock1 model, comparison between the measurement (upper legend) and the calculation (lower legend, defining the model observation point).

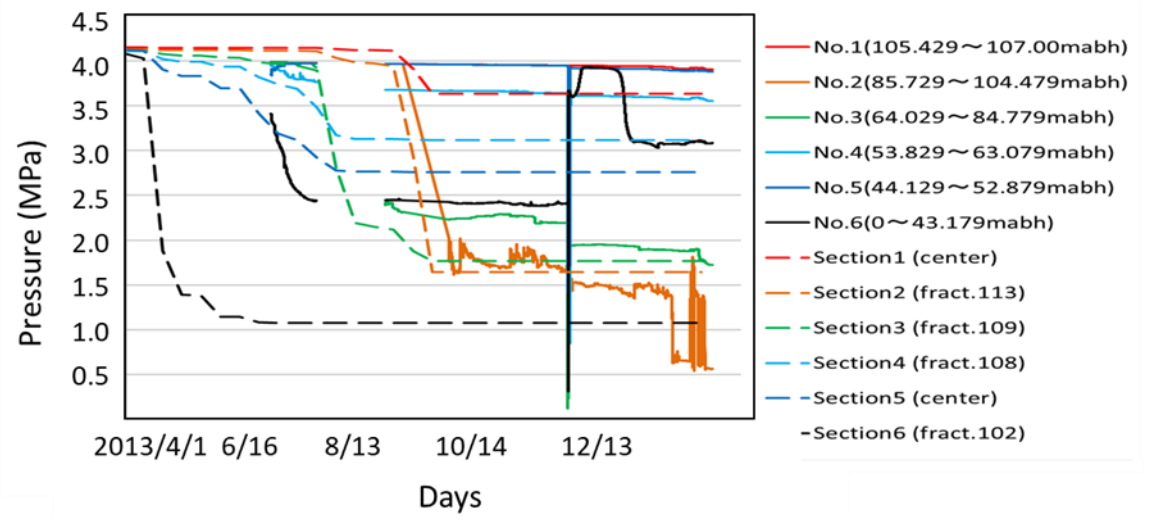

Figure 118. Evolution of pressure in Rock2 model, comparison between the measurement (upper legend) and the calculation (lower legend, defining the model observation point).

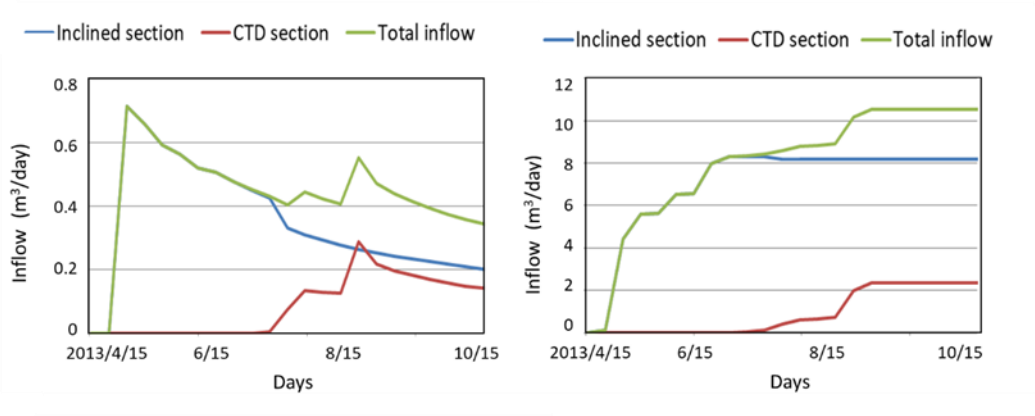

Figure 119. Evolution of the tunnel inflow into its two parts, Rock1 variant in the left, Rock2 variant in the right.

Rock1 vertical section

Rock1 horizontal section

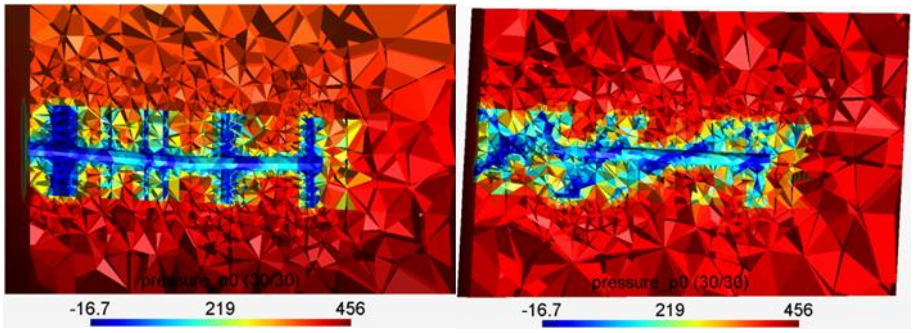

Rock2 vertical section

Rock2 horizontal section

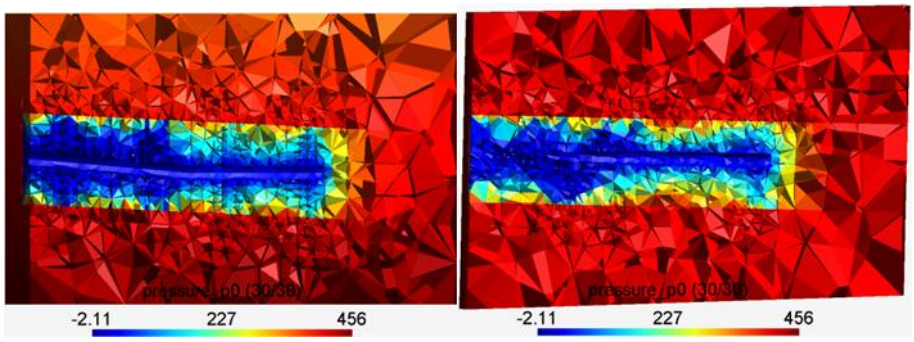

Figure 120. Spatial distribution of pressure head [m] in the two calibrated variants and in two sections along the tunnel.

5.5.6 Introductory results – transport

In this case, the transport data were not used for calibration. The purpose of the presenting them here is to help understanding the effects of the updated model structure and of the partly fitted hydraulic parameters, on the chlorine transport behaviour. The input parameters were the same as those in Section 5.3.1 as well as the initial and boundary concentration distribution (linear increase with depth). The results are shown in Figure 121 for the Rock2 variant. We can see the sharpening of the concentration gradient near the tunnel, which is most intensive at the gallery beginning and gradually decreasing further inside, where the time between the local excavation and the model output is smaller. Also, the locations of larger flow along the fractures enlarges the effect.

5.5.7 Results of Rock3 model

The results of pressure evolution are shown in Figure 122 for the Rock3 model. Contrary to previous results, the model mostly exhibits a better fit of the measured data trends, and the pressure is not so low overall. For No.6, the model is closer to measurements. For No.2, the model captured the decreasing time precisely but did not capture the final value exactly. Other results of models No.1 and No.3 captured the trend of measurements but the final value of No.3 is worse. No.5 and No.4 models are off the measurements and the final values are farther from measurements than in the previous results of Rock2. We note that the comparison describes the effect of the more physical numerical configuration (a correction of the Rock2 insufficiencies), with the same conceptual consideration and input data.

The spatial distribution of pressure in Figure 123 (left) confirms a realistic hydraulic connection between the fractures and the inner and outer rock. Evidently, the penetrated fractures into the outer rock are very helpful for gradient evolution on the connection between the outer and inner domains. The pressure gradient on fractures is depicted on Figure 124. The differences between more conductive fractures and low conductive fractures are shown.

The results of chlorine concentration of Rock3 model are similar to previous results of Rock2 model. The spatial contrast of concentration in and around fractures is more obvious (Figure 123 right). Consequently, the effect of establishing high concentration gradient at the tunnel level is more visible than in the other results.

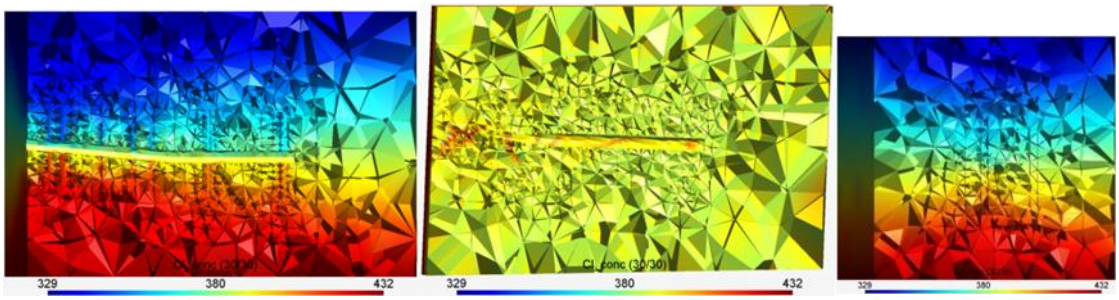

Figure 121. Figure 8-25 Spatial distribution of the chlorine concentration for Rock2, the order of the sections is the vertical along the tunnel, the horizontal and the vertical across the tunnel.

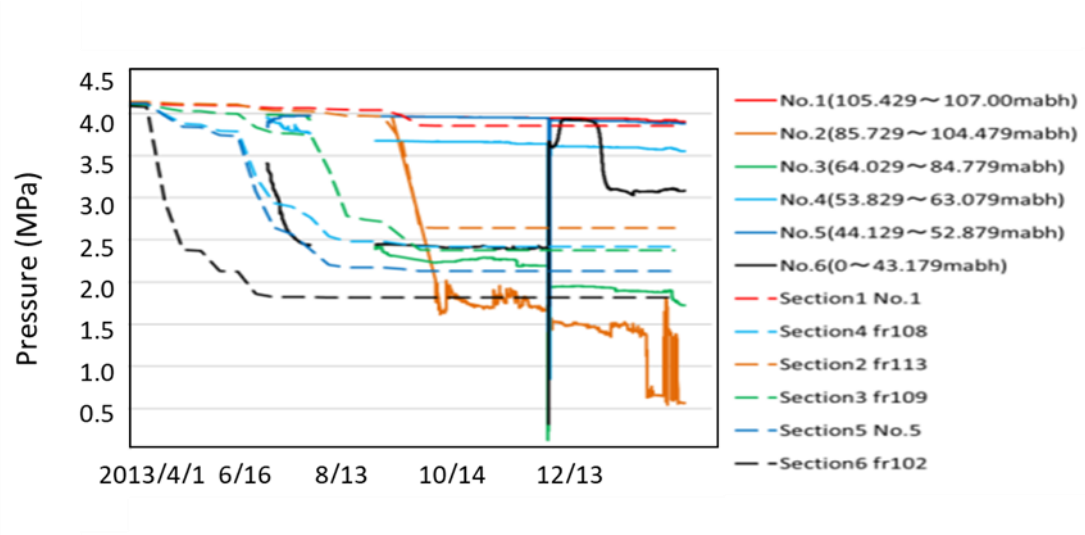

Figure 122. Pressure evolutions in Rock3 model, comparison between the measurement (upper legend) and the calculation (lower legend, defining the model observation point).

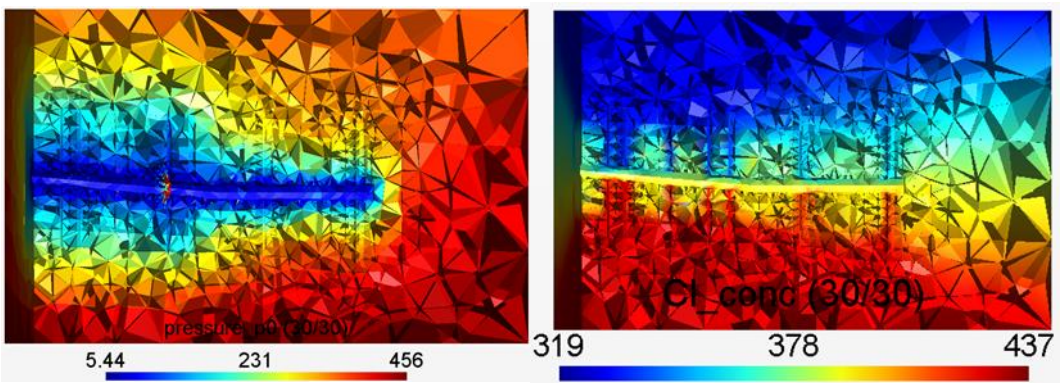

Figure 123. Spatial distribution of pressure head [m] (left) and the chlorine concentration [g/L] (right) for Rock3.

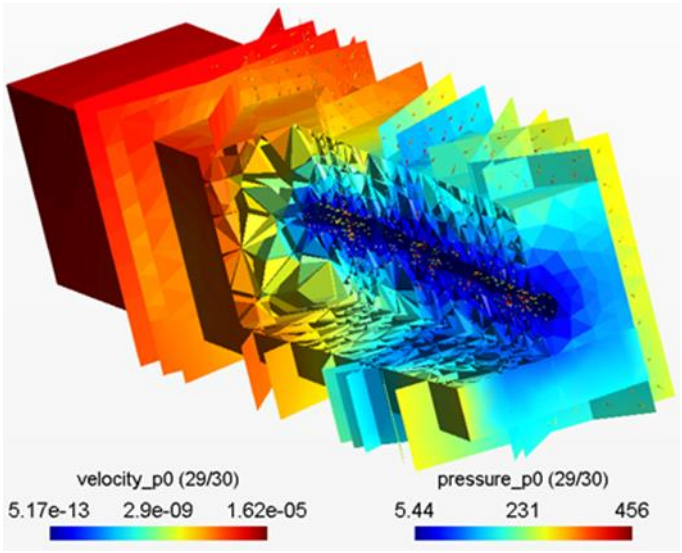

Figure 124. Spatial distribution of pressure head and velocity for Rock3 (the outer rock is excluded, the fractures are visible including the penetrating parts, and the inner block is partly cut).

5.6 Evaluation of Step 1

The prediction has been made with several model variants, based on different details selection from the available data. Through this, we get some idea of the impact of conceptual and parameter uncertainty.

The heterogeneity affects the main features of model results partially – the final pressure values are similar, but the rate of change is increased and the inflow rate is strongly controlled by the permeability. For model calibration, a more sophisticated spatial distribution must be considered, e.g. to distinguish the affected and non-affected monitoring sections by the tunnel drainage. This was demonstrated on some examples with different permeability in the near field and the far field of the tunnel. The Rock3 variant appears to be an appropriate start for the Step 2 modelling.

The transport model was expected to show how the concentration changes are affected by the movement of the water of different original depths. Because the heterogeneity models used were symmetric (concerning upper/lower parts), its effect was very small. Possibly, longer a time could be also needed for the arrival of water with more difference in concentration to the monitoring points. Also, we could consider alternative porosity values (i.e. the transport porosity different from the total porosity), an inhomogeneity in the vertical direction as well as an impact of channelization.

5.7 Geochemical data processing

This aspect has been addressed separately from the main task definition. The specific features of the geochemical study do not readily allow it to be split into the three Steps of subsequent prediction and calibration. One of the reasons is that the necessary introductory step is understanding the processes, i.e. select the components and reactions which control the phenomena observed during the phases of excavation (drainage), re-saturation, and long-term processes. This makes a blind prediction much more difficult that for e.g. the hydraulics and is unlikely to be informative. Therefore, the time period of the work on Step 1 is intended to the initial study of geochemical processes in the site scale to get the proper background for studying the CTD scale processes related to the rock and groundwater disturbance. For this reason, the measured chlorine concentrations were not used for improvement of the boundary conditions in the hydraulic and transport model in this chapter, but they help to define the boundary conditions in Step 2. The processed data exceed the GREET experiment itself, but are part of the provided data set defined in Appendix B.

Basic hydrochemical characterization of MIU groundwater was already published by Iwatsuki et al. (2015). The aim of this work was to prepare geochemical models of individual groundwater types that could serve for transport and reactive transport modelling. At the same time, models were expected to predict how each type of groundwater responds to changing conditions (oxidative, anoxic and reductive) and how it affects the construction materials tested at the MIU Research Laboratory.

5.7.1 Overview of work in Step 1

Finished work:

- Prepared internally consistent database in Geochemist's Workbench format including data about redox potential and with unique identification of each sample
    - ✓ 3875 samples in 109 zones from 18 boreholes
    - ✓ time interval: years 2003 - 2016

Partial results from Step 1 are the following (in examples in the next section):

- There are several types of groundwater.
- Concentrations of some major components do not change during sampling period, others are increasing or decreasing.

- Concentrations of physicochemical parameters and some major components change depending on depth or sampling zone for horizontal boreholes.
- Concentration relationships of the major and minor groundwater components differ for different groundwater types.
- The rock environment has a significant effect on the composition of groundwater but it also happens that groundwaters in the same rock type have different composition and vice versa.
- MIU deep groundwater differs from ocean water not only by salinity but also by the relative proportion of major cations.

5.7.2 Time and depth geochemical groundwater development

The overall picture of groundwater composition for the main shaft is shown in Figure 125. The Piper and Durov diagrams allow to distinguish individual water types and their development in time and space using colour coding – they represent the depth levels of sampling, called “water rings” (WR).

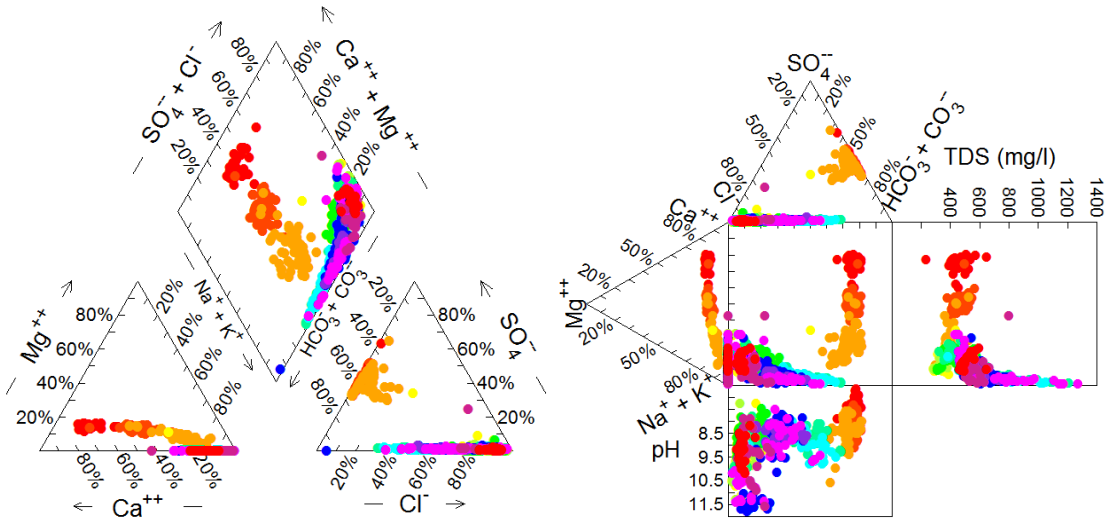

Figure 125. Piper and Durov diagrams of water-ring (WR) samples from Main shaft (A-WR). The depth of WR in each colour is shown in Figure 127.

Diagrams in Figure 126 allow to track the development of concentrations of individual components and physico-chemical parameters over time. Concentrations of some components do not change from the beginning and are stable, others are increasing or decreasing.

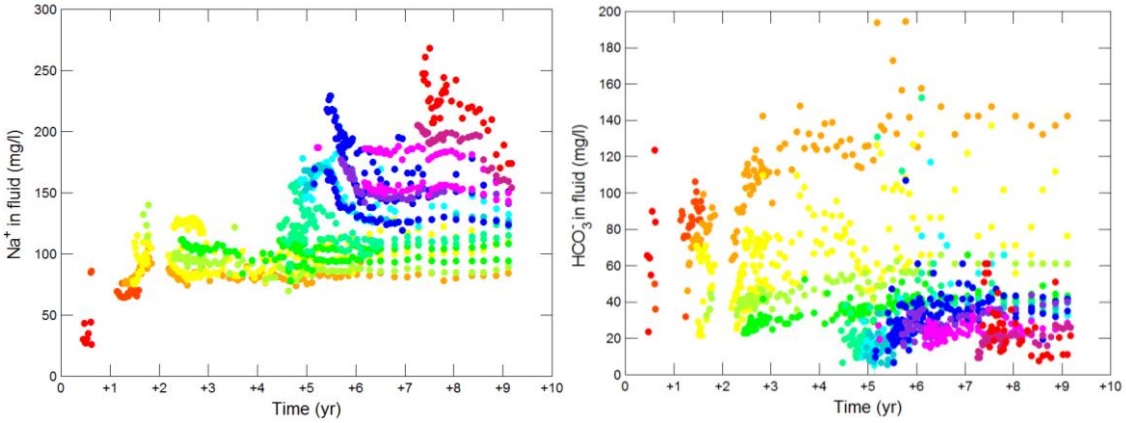

Figure 126. Development of Na and HCO3 components in water-ring in Ventilation shaft (B-WR) beginning 1/1/2004. Colour coding corresponds to individual sampling zones (depths). The depth of WR in each colour is shown in Figure 127.

Diagrams in Figure 127 allow to track the development of component concentrations depending on depth and defines the depth-related colour coding for the remaining diagrams.

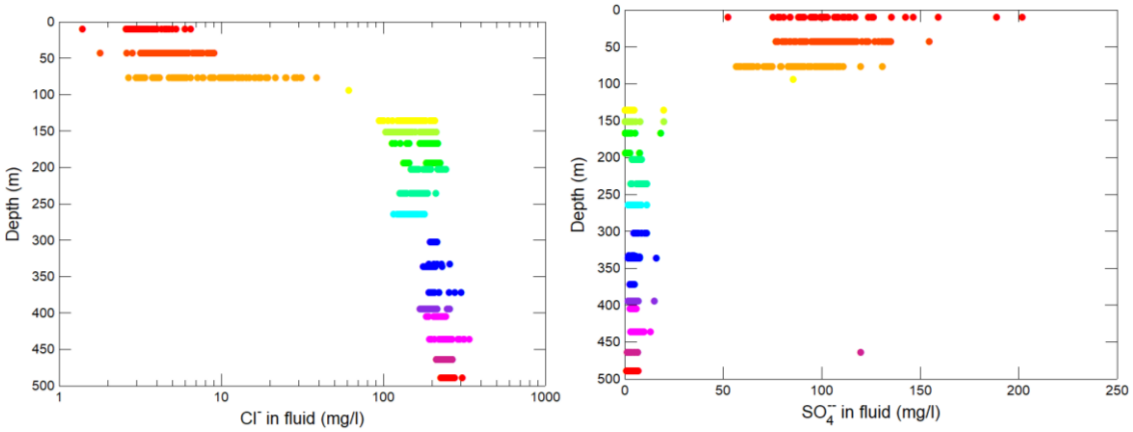

Figure 127. Profiles of Cl and SO_4 components concentrations in depth in the main shaft (A-WR samples), defining also the depth-colour link for other figures.

Concentration relationships of the major and minor groundwater components provide important information for identifying processes that determine their composition.

These relationships are different for water types identified so far; an example in shown in Figure 128.

Using the Piper and Durov diagrams, it is possible to determine whether there is a relationship between the groundwater composition (type of groundwater) and the rock type and, if so, what the relationship is. Otherwise, other processes beyond water-rock interaction will be required to interpret the data.

The rock environment has a significant effect on the composition of groundwater, but it also happens that in the same rock the groundwater differs in composition and vice versa, that in different rock types, the groundwater has similar or the same composition (primarily caused by the impact of fractured zones and the direction and rate of water flow). This is shown in a set of diagrams in .

MIU deep groundwater differs from ocean water not only by salinity but also by the relative proportion of main cations. Data from depth more than 500 m are available only in the MIZ-1 borehole, shown in Figure 129.

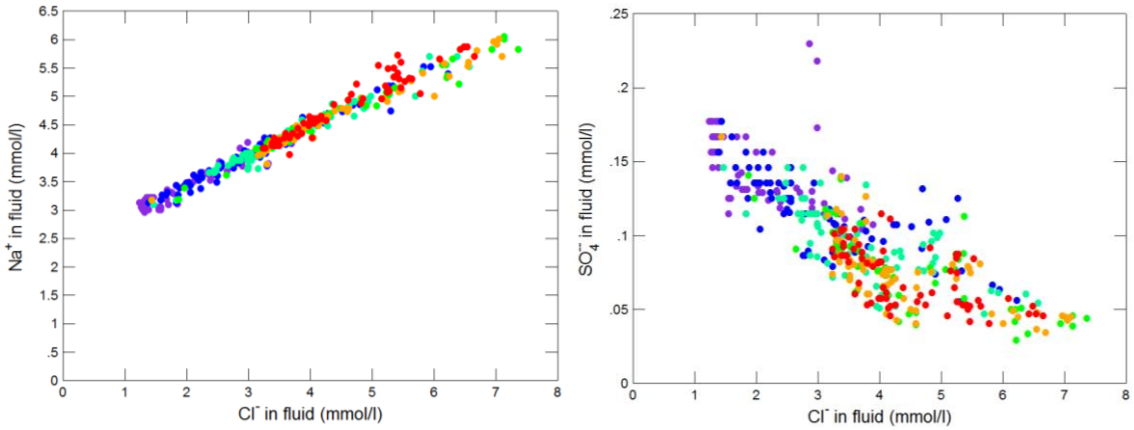

Figure 128. Relationships of selected components in 07MI07 borehole samples.

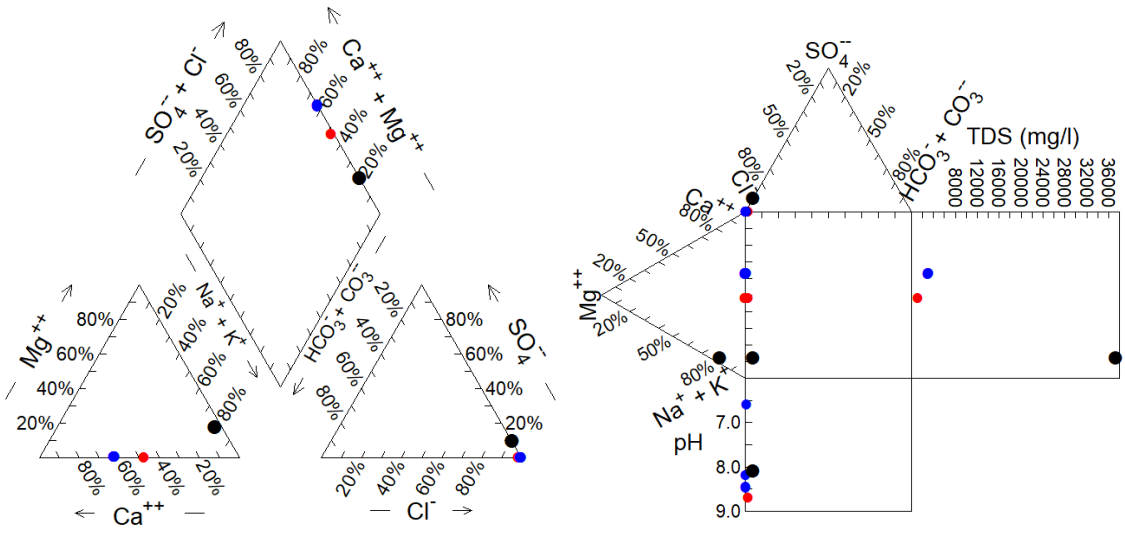

Figure 129. Piper and Durov diagrams for deep groundwater from borehole MIZ-1 and their comparison with sea water composition. Red 648.3 m: Na-(Ca)-Cl type, blue 1148.8 - 1169.8 m: Ca-(Na)-Cl type, black Sea water: Na-(Mg)-Cl.

6 Summary of Step 1

In Step 1, the three research teams tested their respective simulation method to estimate the environmental change caused by tunnel excavation based only on preliminary information of granite and pilot borehole investigation. Such a simulation technique would be indispensable for the project administrator of geological disposal to plan the facility layout and perform a risk assessment (e.g. financial management for water drainage treatment etc.) in the facility construction phase.

One of the aims of this Step is to know how to predict, or to what extent we can predict, the subsurface phenomenon prior to an actual facility construction phase. As an index to know the technical ability to predict environmental disturbance, we estimated water inflow rate into the tunnel, the drawdown of hydraulic pressure and change of Cl concentration during/after the excavation of the tunnel.

The approach, results and key points from the modelling work by each research team are summarized as follows;

JAEA team

- Steady state flow simulation using DFN model (100 realizations) by FracMan®
- Extracted the DFN model which reproduces the pressure distribution well
- Convert the DFN model to an ECPM model. Estimate transient disturbance of water pressure, chemistry, and rock displacement using the Couplys code.

The results obtained show that the ECPM model can reproduce the difference of hydraulic pressure changes in each monitoring section by tunnel excavation, but the timing of the drawdown is not well-matched with the observed data. The total inflow rate roughly matches with the observations, but inflow rate in CTD is estimated at a much lower value. The ECPM model for the Step 1 cannot reproduce the large changes in Cl concentration seen in the observation data.

The nature of the fracture distribution and hydraulic connectivity between the CTD and monitoring sections could be a key matter for the poor prediction accuracy of Cl concentration.

SNL team

- Deterministically set the fractures on CTD wall and in borehole (focused on water-conducting features with aperture)

- Set the permeability of deterministic fractures estimated by inflow rate.
- Constructed DFN model around the CTD (parameter set are estimated by boreholes [intensity] and CTD [intensity & radius & orientation]) using FracMan. Upscaled from DFN model to ECPM model (Grid size: 1m x 1m x 1m) using Oda's method.
- Conducted steady state flow and transport simulations using homogenous and fracture (ECPM) models with DAKOTA-PFLOTRAN coupled codes.

This ECPM model was able to reproduce the difference of hydraulic pressure values in each section and inflow rates at drifts. However, estimations of the Cl concentration profiles using the ECPM model differed from the experimental data.

The results in Step 1 are preliminary output for only two realizations of the fractured system. More realizations will be needed to obtain representative output for more detailed comparison with the observed data. Future simulations will also be based on a larger modelling domain to minimize boundary effects.

TUL team

- Deterministically set the fractures only around drift
- Set the permeability (K) and storativity (S) of rock matrix two variations; Rock1 (K & S of all rock matrix are same), Rock2 (K & S are different value for around drift and for the remaining part), Rock3 (fractures are penetrated to rock continuum in the far area)
- Manually calibrated the K and S of rock matrix and fracture using Flow123d

"Rock1" could reproduce the difference of pressure value of each section, while "Rock2" reproduces trend of the drawdown of only section 2 and 3. Both models could not reproduce the inflow values (much lower value calculated). Both models could not reproduce the large variation in the observation data. The optimization of K and S in the near area and the far area from the drift is still necessary.

Achievements for the Step1 task by each team are shown in Table 30.

To sum up, the simulation techniques in the pre-excavation stage of the facility construction, groundwater inflow rates into the tunnel can be approximately predicted by current modelling procedure. The highest and lowest drawdown of water pressure can be estimated while the rate of the drawdown can't be predicted easily. Moreover, it's difficult to predict the variation of groundwater chemistry. When performing transport modelling to estimate Cl concentration, it is necessary to reflect the continuity

of the fracture network in the model with reference to the spatial distribution of Cl concentration.

The main tasks in Step 2 are to develop the modelling and prediction method to estimate environmental recovery during/after the drift closure based on the data of drift and borehole investigations. Such technique would be available for the project administrator to perform a more reliable safety assessment of the potential for radionuclide transport before the facility closure phase.

Table 30. Simulation results of environmental disturbance during tunnel excavation at the end of Step1

Modelling/simulation target	JAEA	SNL	TUL
Code	FracMan, Couplys	FracMan, DAKOTA, PFLOTRAN	Flow123d
GW inflow rate	Total: Good CTD: No good	Total: Good CTD: Good	Total: No good CTD: No good
Hydraulic pressure	yet	Good	Good
Cl concentration	No good	No good	No good

7 Step 2: modelling of “environmental recovery during a water-filling experiment in the CTD”

The objective of Step 2 is to develop the simulation methods to estimate environmental recovery after the drift closure, based on the data of drift and borehole investigations. Such a technique is indispensable for the project administrator to assess the potential impacts of the radionuclide transport on safety when considering the environmental condition of the facility after disposal and closure.

Towards this aim, we calibrated the Step 1 model, which was constructed based on the data of environmental disturbance during drift excavation at the pilot borehole, then further improved it to Step 2 model by including additional data.

The following additional data from boreholes (13MI38 - 13MI48) were allocated to each team;

- Geology and mineralogy of fracture fillings (core logging, BTV observation)
- Hydraulic properties (transmissivity, hydraulic conductivity, specific storage, hydraulic pressure, flow-meter logging)
- Hydraulic response during hydraulic packer test
- Chemical composition of groundwater, redox condition
- Initial rock stress, elastic properties
- Composition of the shotcrete, mineralogical data
- Rock displacement around the CTD

The water-filling experiment was conducted from Jan. 2016 to Sep. 2017 (Figure 130). Water pressure recovery and chemical evolution of isolated groundwater in the CTD were observed during this period. In parallel, pressure responses and chemical variation according to the water-filling experiment were monitored in the surrounding boreholes. Moreover, repeated water drainage/refill tests were carried out in order to examine the reproducibility of the recovery phenomena of geological environments.

Simulation targets for the Step 2 models are the water pressure variation at monitoring boreholes, the chemical evolution of groundwater at monitoring boreholes and the CTD. Especially, we focused on hydraulic environmental variation at the borehole 12MI33, because we could observe not only the variation during the water-filling, but also the initial condition before the drift excavation.

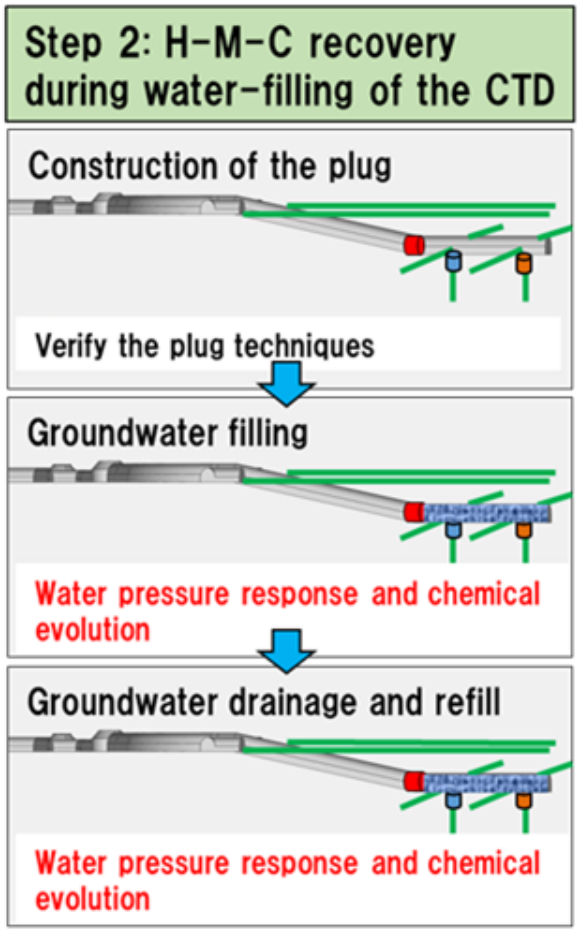

Figure 130. Experimental process regarding Step 2

7.1 Observed environmental recovery at 12MI33 borehole and the CTD for the validation of simulation

Figure 131 shows the hydraulic and chemical variation of groundwater at the monitoring points in borehole 12MI33 through a series of events from the tunnel excavation to closure and re-opening. Water pressure recovered to near the background level after the tunnel closure at No. 2 and 3 monitoring points whose water pressure dropped immediately after the tunnel excavation. Cl concentrations widely changed after the tunnel excavation regardless of the water pressure change. During the tunnel closure, Cl concentrations slightly increased at sections No. 2, 3, and 4 while decreased at section No. 1. The pH, with the exception of section No. 6, showed no obvious variation during the experiment. It is thought the groundwater in section No. 6 became alkaline due to the cementing support in the borehole. Interestingly, the redox condition around the tunnel gradually increased during the opening of the tunnel and decreased by the time of closure.

Figure 132 shows the hydraulic and chemical variation of the groundwater in the CTD. Immediately after the tunnel was flooded, the water pressure rose sharply. It was close to baseline water pressure, but due to a slight leak at the watertight plug, it did not reach the initial water pressure. The pH increased with time, while sodium, Ca and Cl concentration decreased. Such changes were probably caused by groundwater mixing and water-cement interactions.

7.2 Observed hydraulic and chemical variation in the other boreholes

The monitoring of water pressure response and change of groundwater chemistry was also carried out at other boreholes (13MI38 - 41; shown in Figure 6) during the water-filling of the CTD. The observed results are shown in Figure 133 - Figure 136.

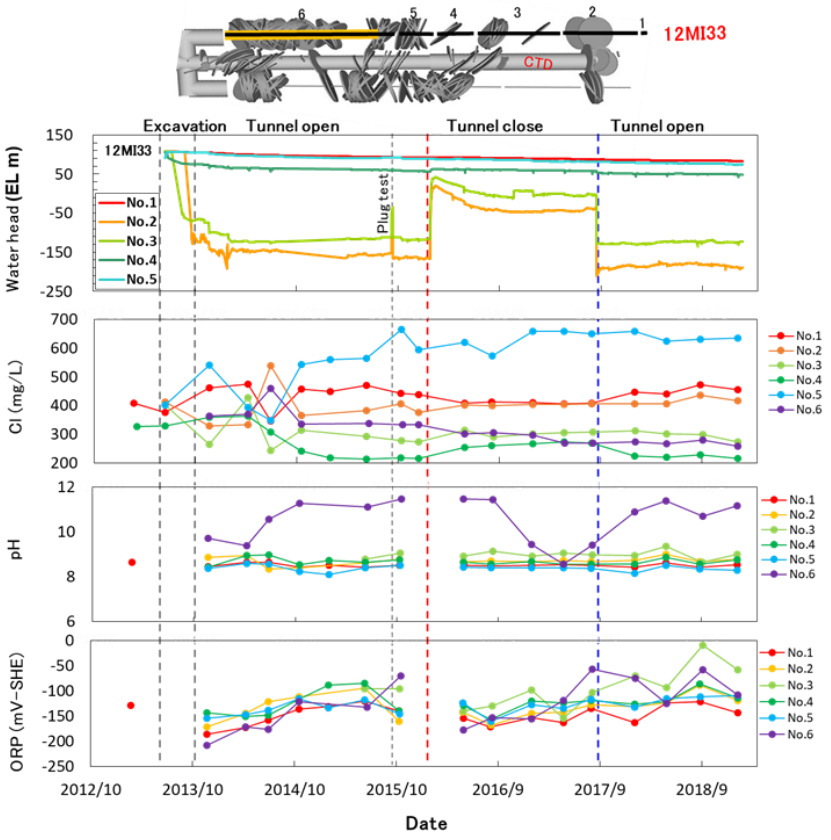

Figure 131. Hydrochemical variation of groundwater around the tunnel in a series of experiment

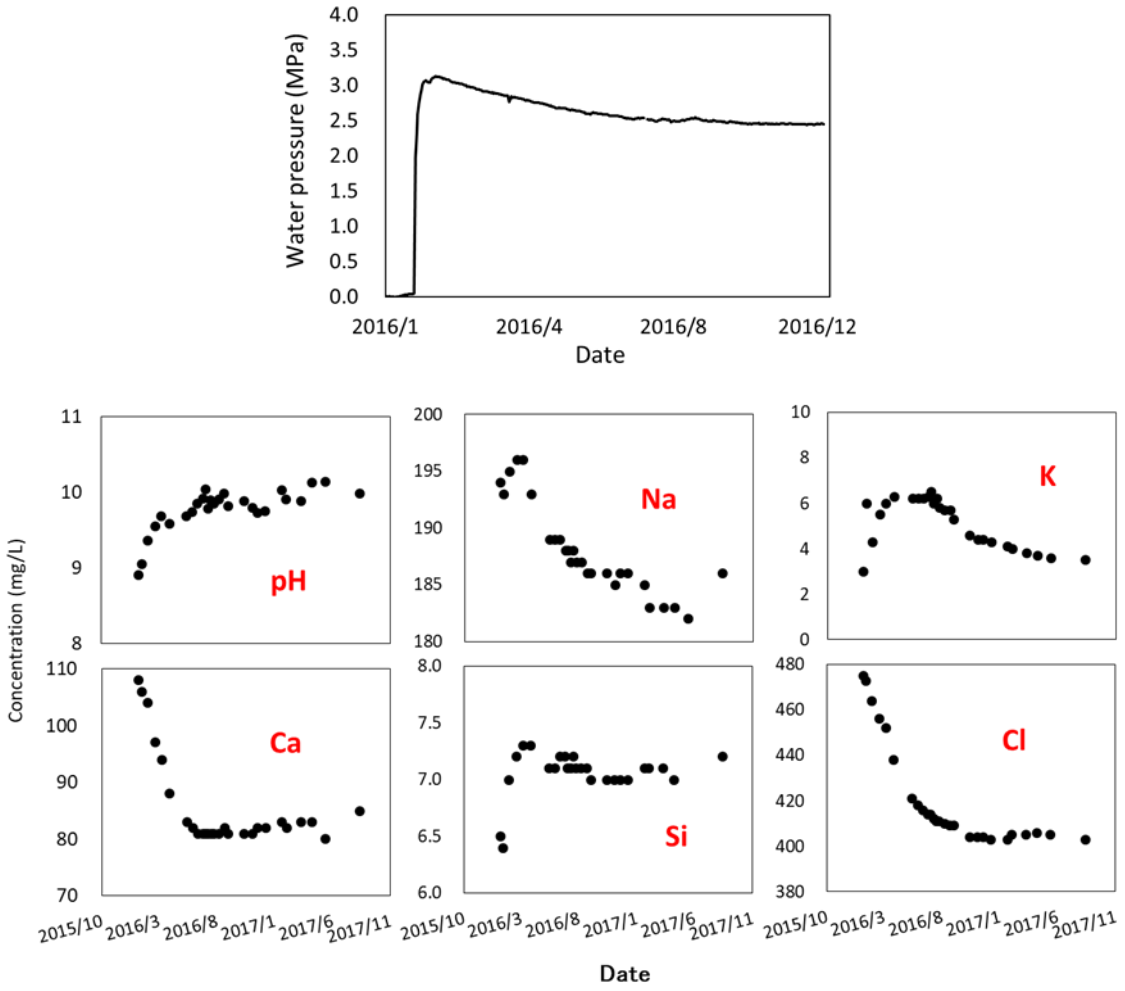

Figure 132. Hydrochemical variation of isolated groundwater in the CTD

The water pressures declined due to the excavation were then recovered in several sections depending on the distance from the CTD. Based on the data from 13MI39 to 13MI41 drilled perpendicular to the tunnel wall, we can roughly estimate the effect of tunnel excavation on water pressure. The water pressure in the borehole located about 15 m away from the tunnel was not reduced by the tunnel excavation. By the water-filling into the CTD, water pressure within 5 m from the tunnel did not recover to baseline water pressure because of the water leak around the water-tight plug.

Figure 137 and Figure 138 show the chemical variation in these boreholes. Cl concentration decreased at about 15 m away from the tunnel (13MI39-No.1, 13MI41-No.1), though the water pressure didn't change. This seems to be due to the low salinity groundwater distributed at shallower depth being drawn by the opening of the tunnel. While Cl showed a large increase at 13MI38-No.5. Hydrochemical disturbance and recovery probably depend on the connectivity and continuity of water conducting

fracture around the tunnel. If the water pressure does not change even if the Cl concentration changes in the same section, it probably means that there is sufficient groundwater supply capacity in the fracture network to compensate against groundwater drainage to the tunnel.

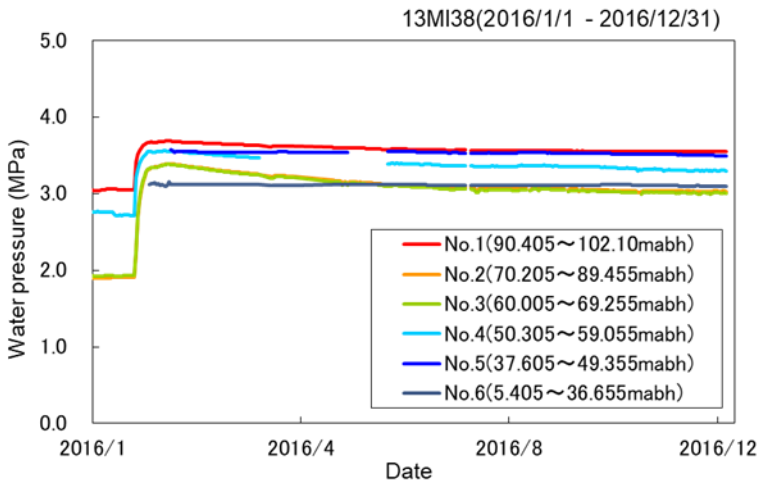

Figure 133. Hydraulic response in 13MI38

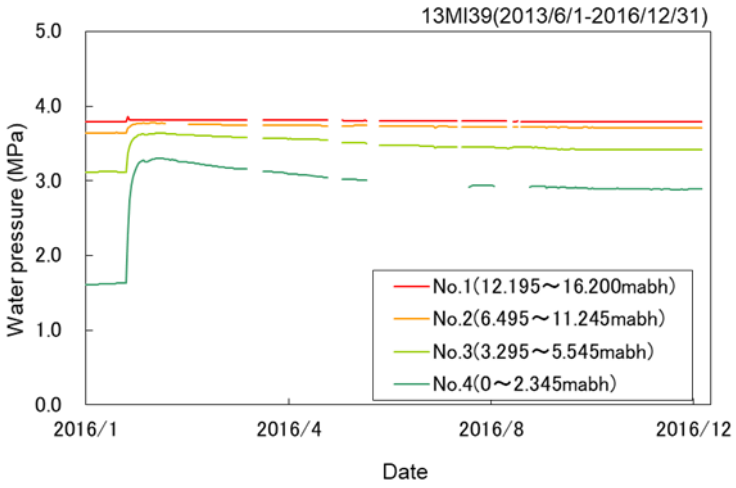

Figure 134. Hydraulic response in 13MI39

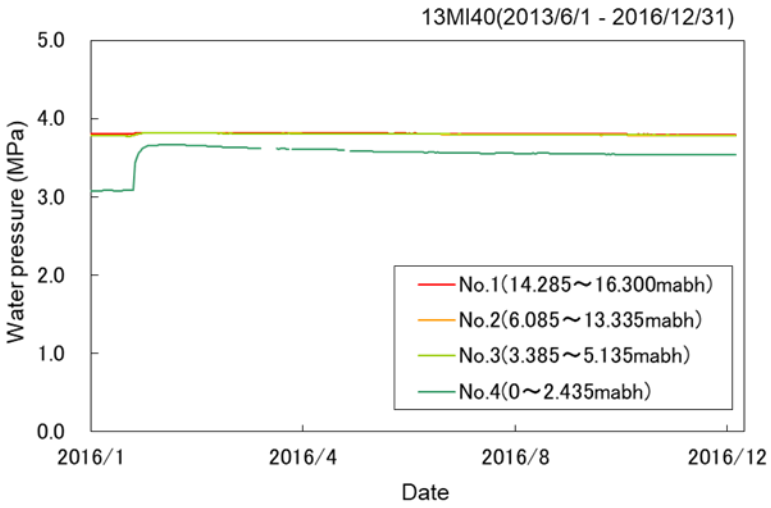

Figure 135. Hydraulic response in 13MI40

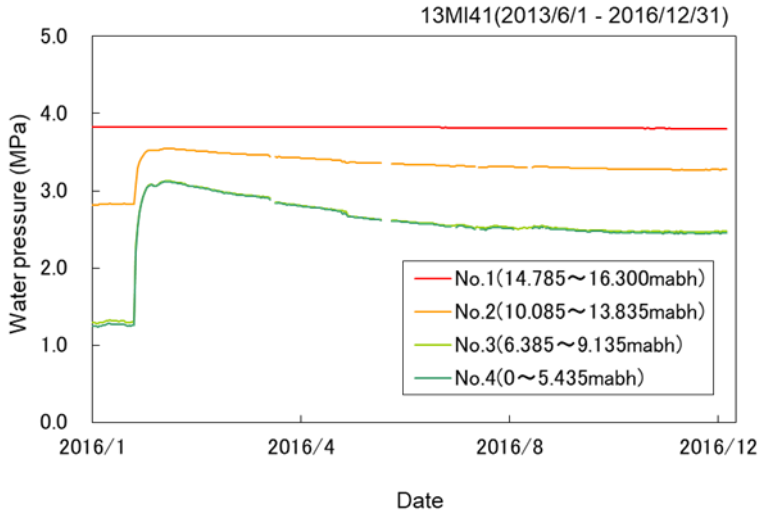

Figure 136. Hydraulic response in 13MI41

*Because of the slow flow rate during groundwater sampling, ORP was not measured at section 13MI38-No.3, 13MI39- No.1, 2, 3. The red box shows the tunnel closure period.

Figure 137. Hydrochemical variation in 13MI38 and 13MI39.

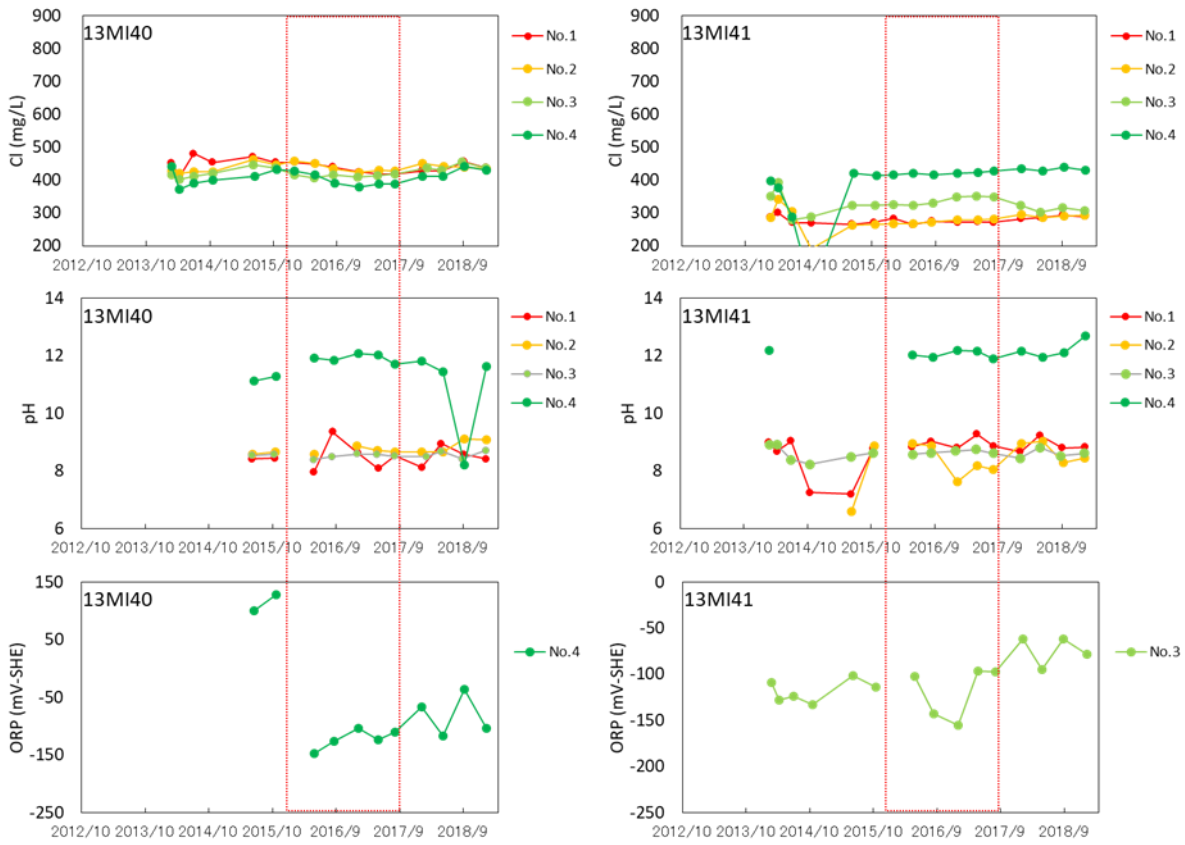

* Because of the slow flow rate during groundwater sampling, ORP was not measured at section 13MI40-No.1, 2, 3, 13MI41- No.1, 2, 4. The red box shows the tunnel closure period.

Figure 138. Hydrochemical variation in 13MI40 and 13MI41.

8 Results of Step 2 modelling (JAEA)

8.1 Model update with additional fracture data

In Step 1, we used the geological data acquired before the excavation of our target area for DFN modelling. The data included fracture data from outcrop observation at the shallower stage of MIU and lineament observed on the ground surface. Among them, the fracture data observed in 12MI33 by BTV is only data acquired near the experimental site. In Step 1 we did not use the fracture data observed at 500m stage except for the data in 12MI33 to test the ability to predict the hydrochemical disturbance by using the data acquired before the excavation. In Step2, we used the fracture data observed around CTD as Figure 139 shows to improve the simulation results.

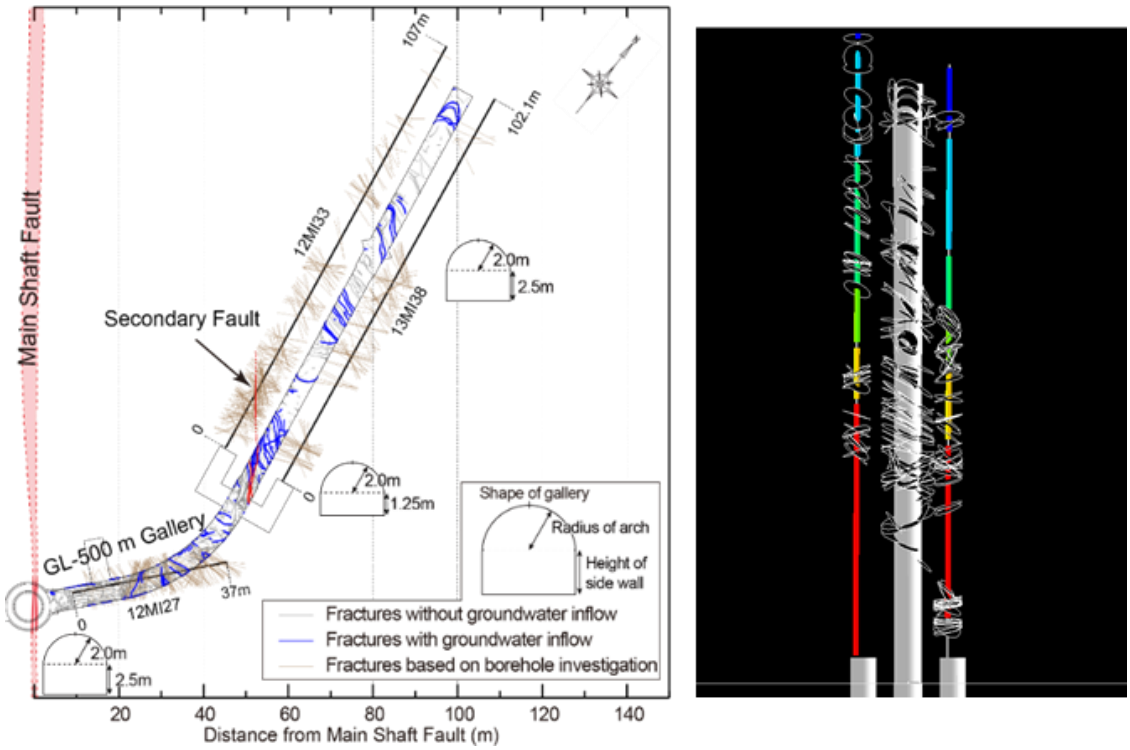

Figure 139. Additional fracture data from BTV observation and outcrop of the drift wall around inclined drift and CTD.

The fracture data observed around the inclined drift and CTD can be divided into two parts (Ishibashi et al., 2016). One is the area that is affected by Main Shaft Fault. This part includes the secondary fault of Main Shaft Fault. The other part is the area farther

than 60m from Main Shaft Fault. The fracture density is clearly different between these two parts and the fracture density decreases as it is far from Main Shaft Fault. This suggests that the stochastic field of fracture distributions is not a stationary process in this site. Our target domain is mostly located in the part that is not affected by the Main Shaft Fault. The data observed farther than 60m from Main Shaft Faults is used to update our model. The right picture in Figure 139 shows the extracted fractures for the analysis. Both the direction and position of observed fractures are displayed with the sections of monitoring borehole around the experimental site.

The approach of fracture analysis we applied to update the model in Step 2 is the same as in Step 1. The first step of the analysis is the clustering of fracture with respect to its direction. In the Step 2, we defined the fractures with inflow as water conducting fractures (hereinafter refer WCFs) based on drift wall observation. Figure 140 shows the clustering results of fracture direction observed around the target area. We classified all fractures into 4 groups according to the direction using FracMan®.

The number of all fractures observed in the target domain is 382. Among them, about 10% of fractures are recorded as being wet. In Figure 140, the clustering results are shown separately according to whether the fracture is WCFs or not. In the clustering results, there is not a clear difference between wet and dry fractures. The wet fractures, that are expected to be highly permeable or well-connected, are mainly distributed in Set 1, 2 and 3. We describe the direction of each fracture group with a Fisher distribution.

The left figure in Figure 141 shows the observed cumulative number of fractures versus the trace length. The acquired data of WCFs and other fractures are shown separately. This data is used to determine the stochastic parameters of fracture length and fracture intensity in the DFN model. The relationship is expected to be linear in the log-log plot due to the fractal feature of fractures. However, the relationship can be divided into three parts where the gradients of slopes are different. This would be due to the characteristics scale of the observed fracture data and only the data of several meters scale is meaningful. For DFN modelling, we fit this with the power law equation by using the data around the range of about several meters.

In our approach, the hydraulic conductivity is assigned to each fracture based on its length. Around inclined drift and CTD, 12 hydraulic tests were performed in 12MI33 and 13MI38. We consider the results of the hydraulic test as a sampling from the stochastic distribution of hydraulic conductivity in a random field and the resultant cumulative distribution function (CDF) of hydraulic conductivity is plotted on the graph (right in Figure 141). This data is used to calibrate the equation connecting the fracture length to

the hydraulic conductivity. We generate several DFN models and perform a hydraulic test numerically in each realized model. Then the parameters are calibrated by fitting the simulated CDF with this observed CDF from in-situ measurements.

All parameters for the DFN modelling are derived from observed data at the 500m stage are summarized in Table 31. In the drift wall mapping, the fractures with a trace length of 1m or more are object of observation. Therefore, considering the consistency with the observation data, we modelled the fractures with a radius of 1m or more.

The DFN model is generated stochastically according to the stochastic distribution of direction and fracture size calibrated by the observed fracture data. These generated DFN models have the same stochastic character with observed data. However, the location of the simulated fracture in DFN model is different from the observed location of fractures.

We conducted conditioning of fracture distribution to consistent with fractures intersected to drift and boreholes. Firstly, the location of model fractures is adjusted to reproduce the observed fracture distribution by FracMan®. Secondly, we adjusted transmissivity of fractures intersected to drift and boreholes to match with flow discharge of WCFs on drift wall and hydraulic conductivity of rock mass. Figure 142 shows the realized DFN model before conditioning and Figure 143 shows the conditioned DFN model according to the observed fracture location. Several model fractures are moved to match the positions of the real fractures.

We simulate the hydraulic pressure by using the conditioned DFN model as shown in Figure 143 to confirm model reliability before the conversion to ECPM. We compare them with the observed data to check the validity of conditioned DFN model. Figure 144 shows the comparison of the hydraulic pressure and inflow rate into inclined and CTD after excavation. The trend of observed data in 12MI33 can be captured. However, we could not reproduce the hydraulic pressure at section3 in 13MI38. Around section 3 in 13MI38, the fractures that intersects the CTD are not distributed in the observed data as shown in Figure 143, although the hydraulic pressure decreased after the excavation. From this result, it can be seen that conditioned DFN model cannot reproduce the heterogeneity and channelling of the rock mass around the 13MI38 sufficiently. One of the caused is considered to be lack of information on fractures of rock mass around the 13MI38. Concerning the inflow rate into the drift, the simulated inflow rate agrees with the observed data.

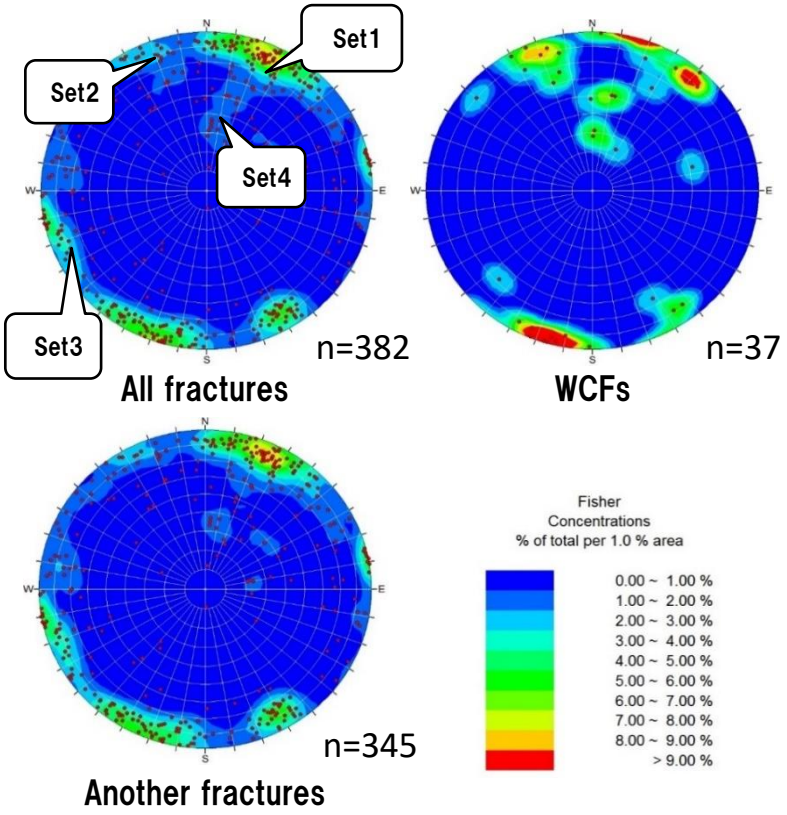

Figure 140. Fracture orientation on the drift wall (Lower hemisphere projection).

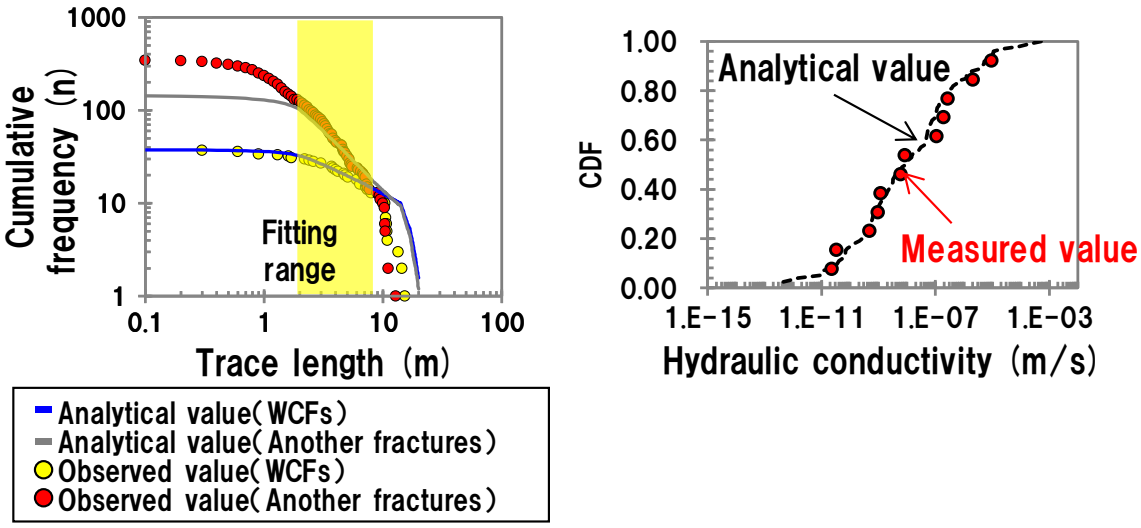

Figure 141. Results of stochastic analysis of trace length (left) and hydraulic conductivity.

Table 31. Summary of the derived stochastic parameter for DFN.

Fracture set	Fracture orientation			Fracture size (Power-law distribution)		Volumetric intensity (P_{32}; m^2/m^3)	Transmissivity distribution
	Pole-trend (degree)	Pole-Plunge (degree)	Fisher K	Power-law factor (b)	r_{min} (m)		
Set1	22.9	2.2	18.5	3.1	1.00	0.429	μ : -11.0 σ : 2.5 C : 2.0
Set2	330.6	0.4	17.8	3.4	1.00	0.129	
Set3	260.7	3.8	15.3	4.7	1.00	0.045	
Set4	30.7	59.7	12.1	3.3	1.00	0.082	

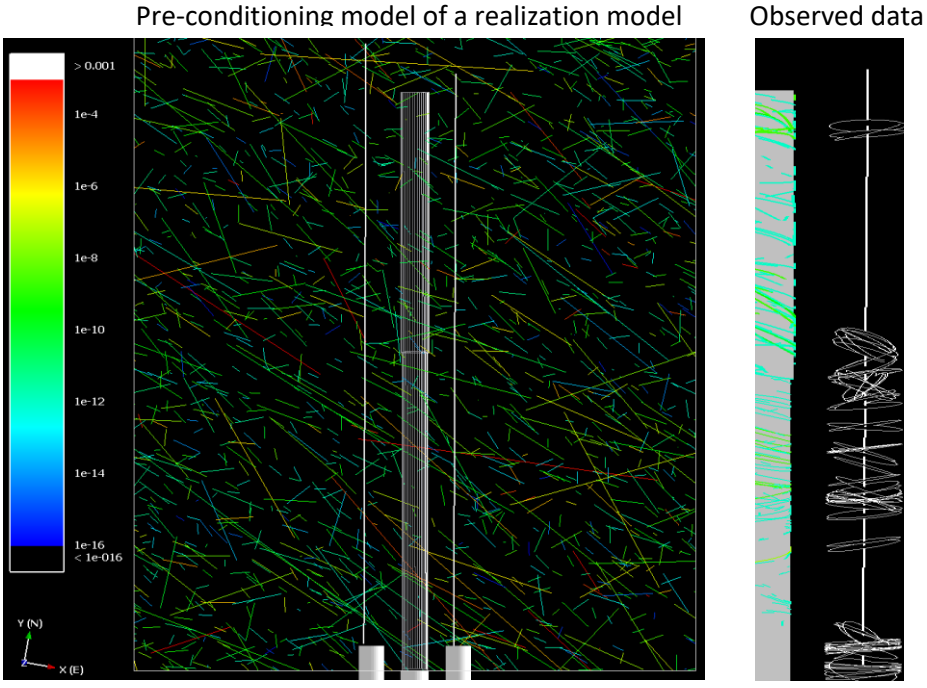

Figure 142. A realization example of DFN model from additional data sets before conditioning. The colour scale represents transmissivity of fracture.

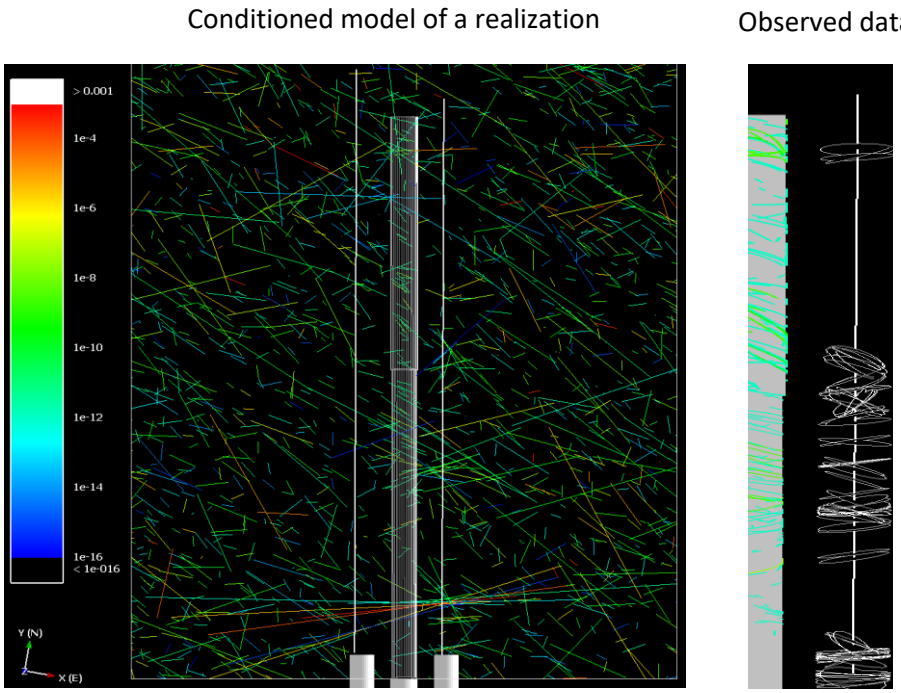

Figure 143. A conditioned DFN model by observed fracture data. The colour scale represents transmissivity of fracture.

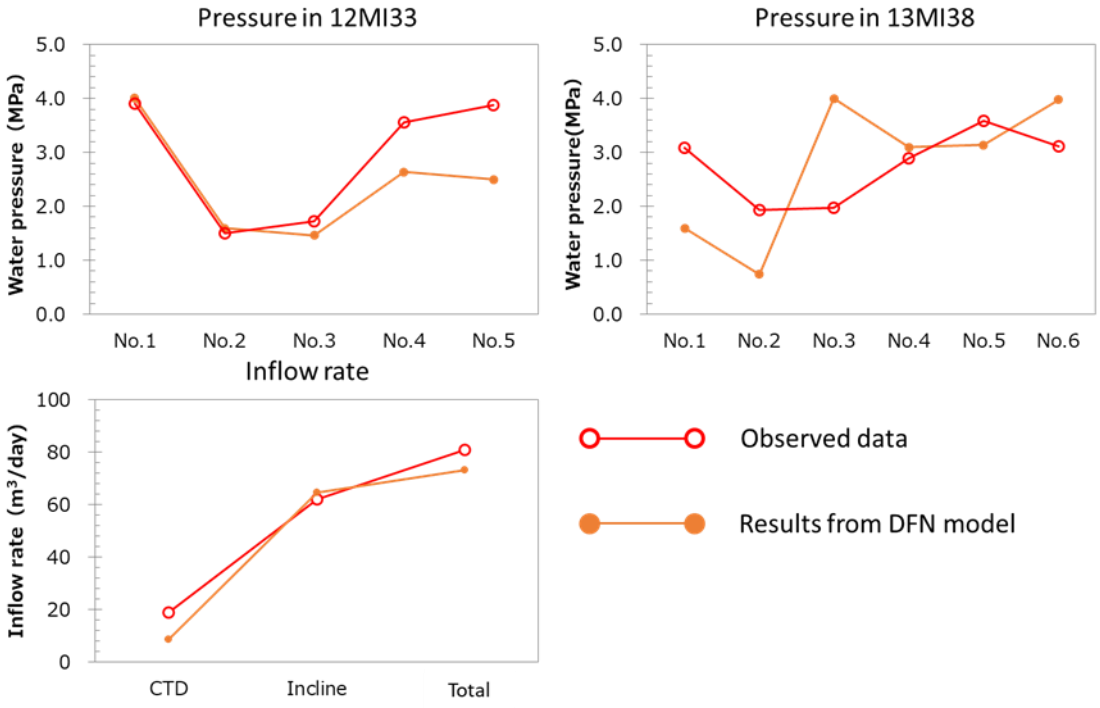

Figure 144. Results of water pressure in 12MI33 and 13MI38 and inflow rate after excavation by the DFN model.

For the coupled simulation, we converted the conditioned DFN model to the equivalent continuous porous model (ECPM) as we described in Step1. Figure 145 shows the converted ECPM model from the DFN model. Both the horizontal and vertical slices of hydraulic conductivity structure are shown. In these slices, the sequential high permeable zones that correspond to the fractures are clearly seen. The original ECPM approach generates the anisotropic hydraulic conductivity where the hydraulic field is described by hydraulic conductivity tensor according to the theory of Oda's homogenization method. The generated hydraulic conductivity tensor is sometimes highly anisotropic model and the use of the derived parameters for numerical simulation leads to the instability of calculation. To avoid this, we converted the tensor to scalar value by taking the geometric average of diagonal components of the tensor. The hydraulic conductivity of the intact part of the rock in ECPM model is set to 10^{-12} m/s based on the result of hydraulic packer test around the CTD. We also limit the highest value of hydraulic conductivity to 10^{-4} m/s for the stability of the simulation.

Figure 146 shows the vertical slices of simulated results of hydraulic head and Cl concentration. In the results of hydraulic head, the decrease of the hydraulic head along the permeable fractures is simulated. In the result of Cl concentration, both high and low salinity water around deeper and shallower part of the model domain is conveyed toward the drift along permeable fractures. However, the Cl concentration around the drift does not change so much compared to the initial condition. This may be due to the mixing of high and low salinity groundwater around the drift as we pointed out in Step 1. On its own, the update of hydraulic conductivity model does not seem sufficient for the calibration of Cl concentration.

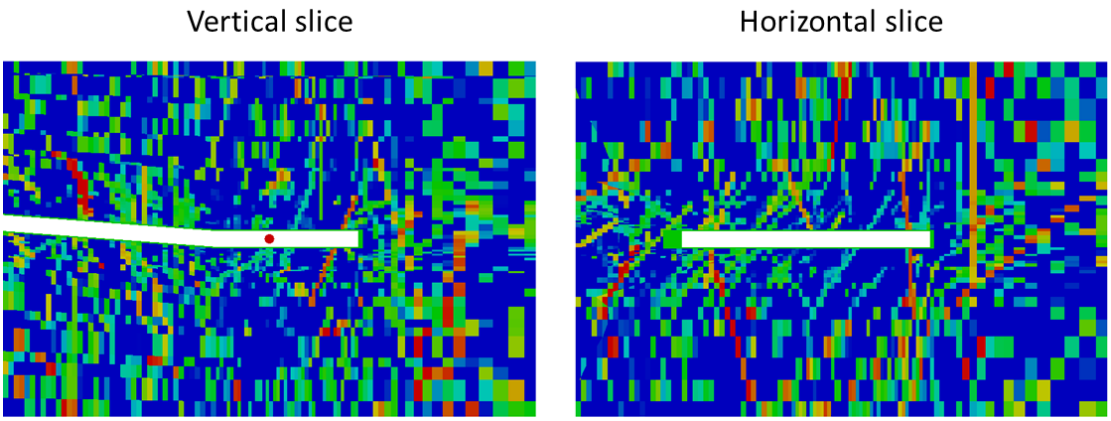

Figure 145. ECPM model from the updated DFN model

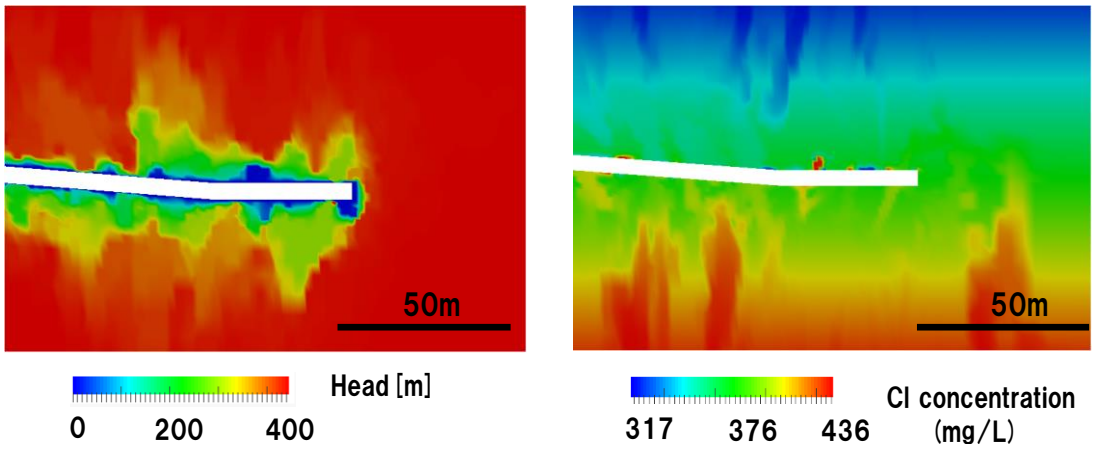

Figure 146. Simulation results of hydraulic head and Cl concentration at immediately after drift excavation from ECPM model derived by updated DFN model.

Figure 147 shows the comparison of simulated results from the updated model with observed data. The time series of hydraulic pressure in 12MI33 during the excavation of drift and inflow rate after the excavation is displayed. The inflow rates into the drift are well reproduced as the case in Step1. We apply the progressive removal element approach for drift excavation modelling, so the simulated result of the inflow rate fluctuates at each excavation step. The hydraulic pressure is reproduced except for section 5. At section 1 and 2, the observed hydraulic pressure changes abruptly along the borehole and both high and low pressure are adjacent. We could simulate such a spatial change in pressure after the conversion from the DFN model to ECPM model. It is desirable to confirm the appropriate mesh size that we can safely convert the DFN model to ECPM model by considering the fracture density, to advance our modelling approach.

Figure 148 shows the simulation results of the time variation of Cl concentration in 12MI33. The observed Cl concentration continued changing after the termination of drift excavation although the observed hydraulic pressure was at steady state. The simulation results that the period is about 1 year longer than the simulation results of hydraulic pressure are displayed here. Our simulated results also continued changing after the excavation. However, the variation of all simulated results is much smaller than the observed data. We could improve the results of hydraulic pressure and inflow rate by additional fracture data and conditioning of fracture distribution of the realized model. However, the simulated results of Cl concentration are still poor. For the calibration of Cl concentration, we need to improve not only heterogeneous fracture distribution and channelization in the rock mass but also initial and boundary conditions.

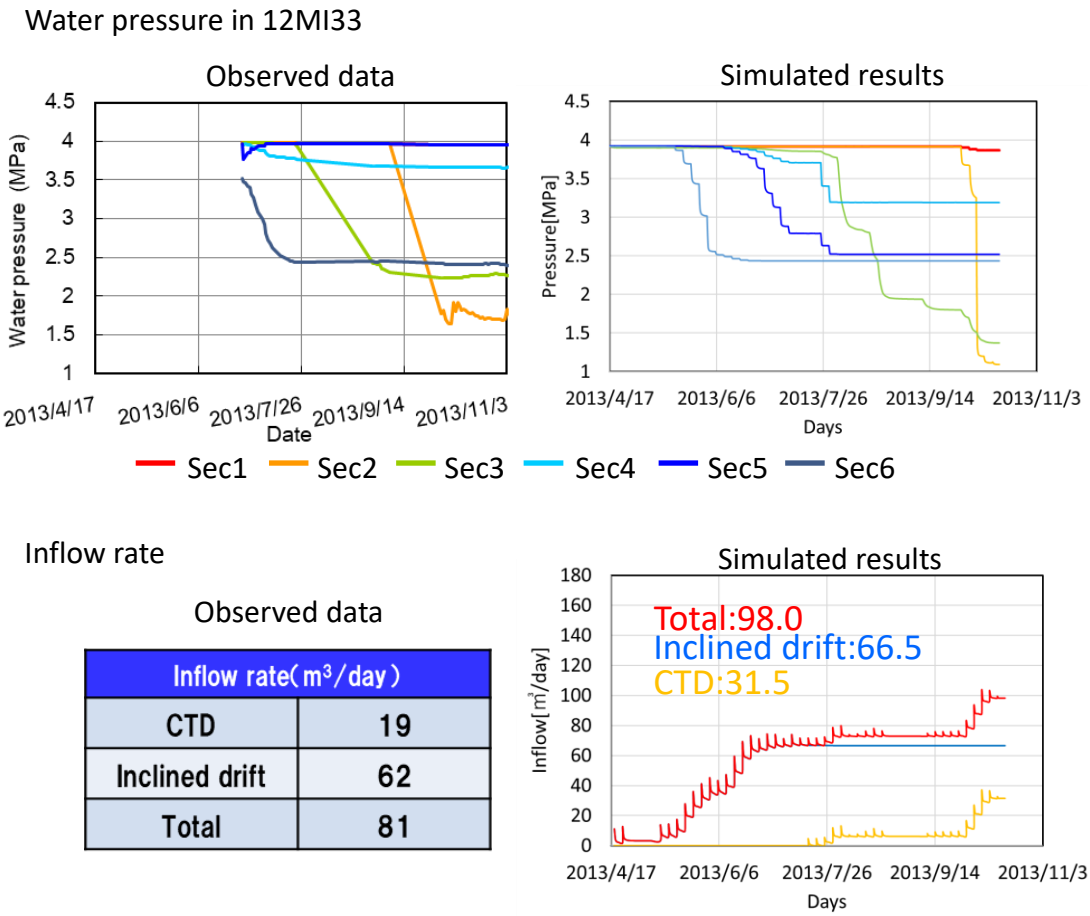

Figure 147. Comparison of the simulation hydraulic pressure in 12MI33 and inflow rate into the drift with observed data.

8.2 Simulation of closure test

8.2.1 Simulation results during closure test

In the real case of GREET, the CTD is closed by in-situ water. However, the modelling of the behaviour of free fluid by computed fluid dynamics (CFD) is time-consuming and the module to solve the Naiver-Stokes equation is not implemented in our simulator. Instead of modelling of free water in CTD, we approximate the movement of free water in CTD with high permeable porous medium. We set the hydraulic conductivity in CTD as 10^{-4}m/s during closure test. We confirmed that this parameter setting does not adversely affect the simulation result and reproduce the real condition of free water in the drift. The hydraulic conductivity of the water-tight plug to 10^{-8} m/s.

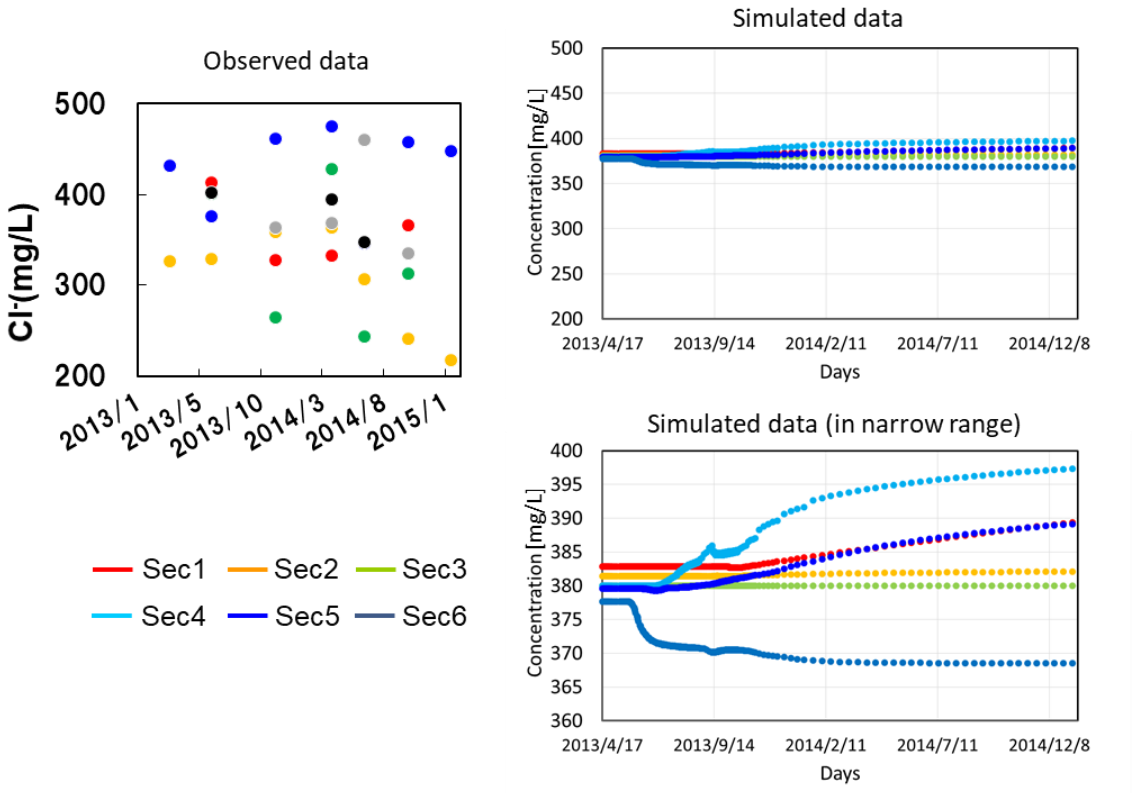

Figure 148. Comparison of simulated results of Cl concentration in 12MI33 with observed data.

Figure 149 is the vertical slice of the simulated hydraulic head during closure test. The results for 1day, 10day, and 1year after the closure are shown. The water head in CTD starts to increase just after the closure of drift and reached about 300m after 10 days of closure. In the result 10 days after closure, there are some points in the intact rock where the water head is lower than CTD. These low-pressure spots would be due to the difference of pressure propagation speed between free water (high permeability area in our model) and rock. The water head in CTD is abruptly increased after the closure of drift because the CTD is filled with free water. On the other hand, the change in water pressure in the rock is slower than CTD because the permeability in rock is low. Then, the recovery of water pressure in CTD is faster than in the surrounding rock. As a result, these low-pressure spots remain in vicinity of drift wall after 10 days. These low-pressure spots are dissipated and hydraulic pressure around the CTD become uniform after 1 year of closure. This simulated evolution of water head indicates that the groundwater flows from CTD to the intact rock for several days after the closure of drift. Then the drainage condition to the closed drift is formed after the relatively slower recovery of water pressure in rock than in the closed drift. The final water pressure in

the CTD is lower than surrounding rock even 1 year after the closure. This would be due to the leakage of water from CTD to the drift.

Figure 150 shows the simulation results of displacement in Z (vertical) direction by hydro-mechanical coupled simulation. The mechanical model setting and parameters are same as Step 1. The expansion of CTD is simulated according to the increase of water pressure in CTD after the closure of drift. In the observed data, the mode of deformation of CTD is also expansion. Concerning the rock mechanical part, the observed strain by optical fibre is very small (order of micro strain). Then, we think that the hydro-mechanical effect is enough to be negligible in GREET. Then, we decoupled the hydro-mechanical effect and do not consider the rock deformation after this section.

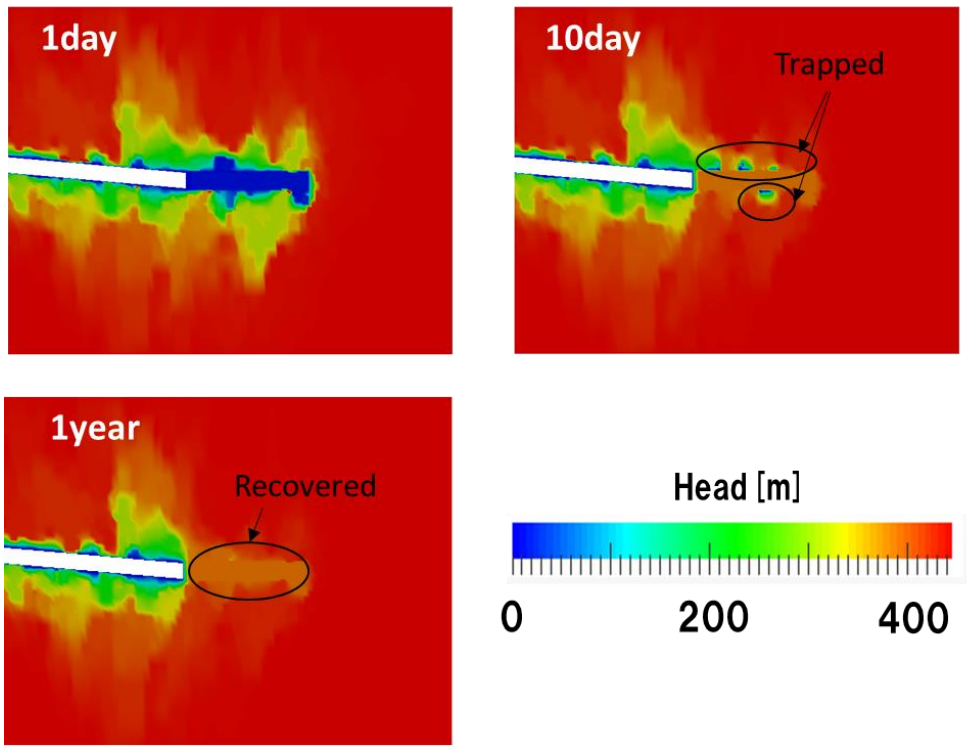

Figure 149. Vertical slice of simulated results of the hydraulic head after the closure

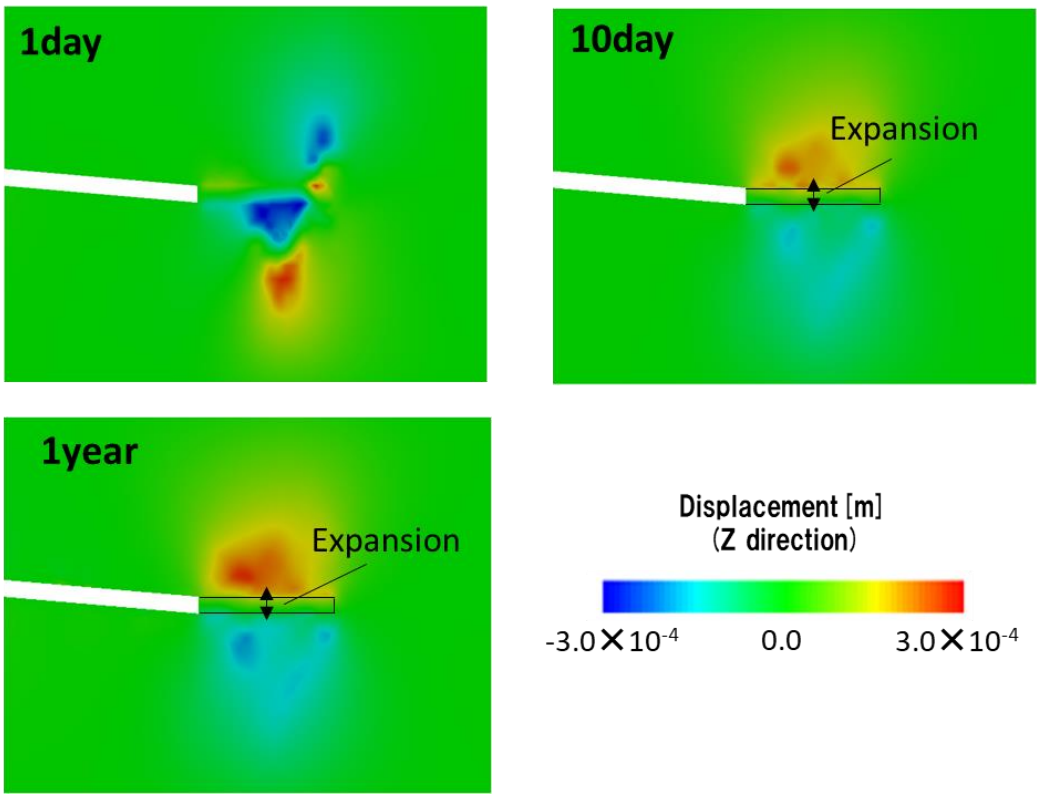

Figure 150. Vertical slice of simulated results of displacement in the vertical direction

Figure 151 shows the Cl concentration during closure test. In this simulation, we set the initial Cl concentration of the water in the CTD as low as the concentration of the shallower domain boundary. However, the Cl concentration in the CTD in our simulation increased soon after the closure, and the simulated Cl concentration after 1 year becomes higher than the surroundings. This suggests that the groundwater water flowing through the CTD is supplied more from the deeper part of the model domain than the shallower part. The distribution of Cl concentration, except for the CTD, does not seem to change much during closure test compared to the water pressure. This suggests that the recovery process of chemical disturbance after closure depends on either diffusion or regional groundwater flow that are both slow and it takes a long time to recover the chemical disturbance after the closure.

Figure 152 shows the time series of water pressure in CTD. Both simulated and observed pressure increased abruptly just after the closure of drift then reach 3MPa. In the observed data, the water pressure in CTD gradually decreased though the simulated water pressure keeps high. We expect that this would be due to the increase of leakage water from CTD. We did not consider the increase in leakage here. So, the gradual

decrease in water pressure is not simulated in our results. We will investigate the effect on the water pressure in CTD in next section.

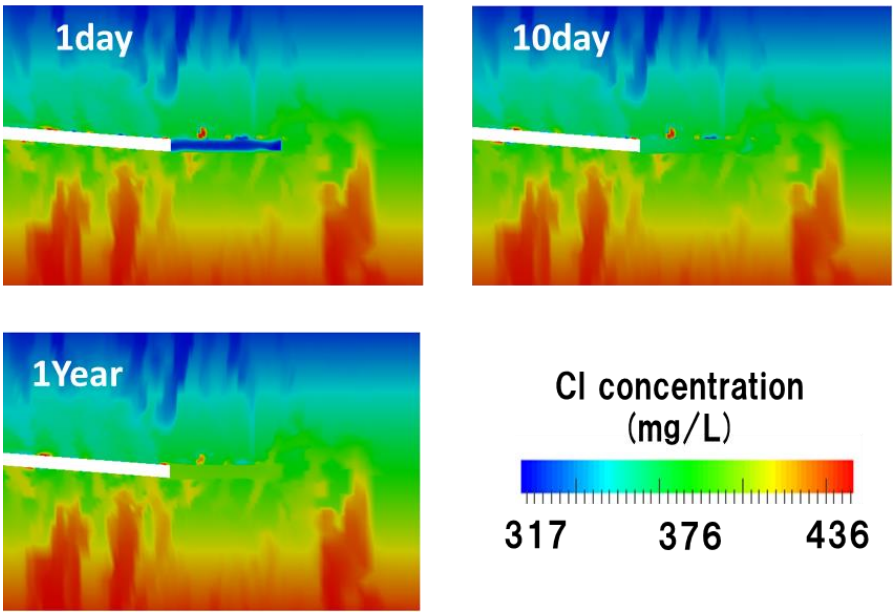

Figure 151. The vertical slice of simulation results of Cl concentration during closure test

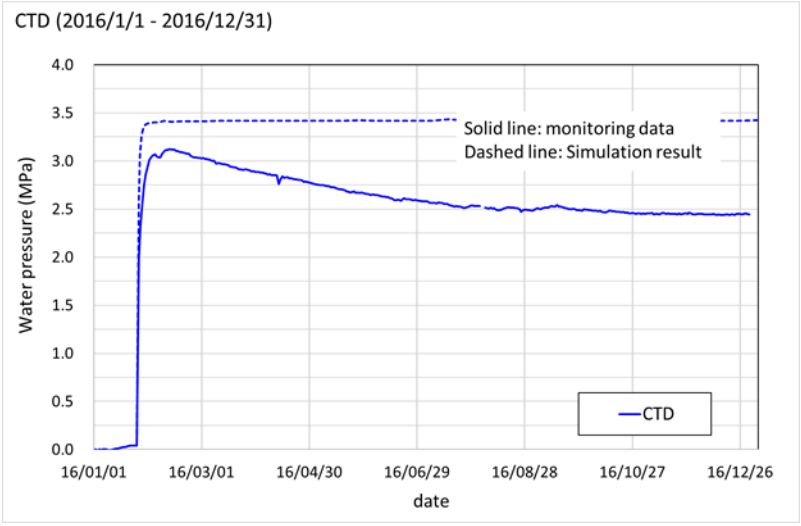

Figure 152. Comparison of time variation of water pressure in the CTD during the closure test

Figure 153 and Figure 154 show the comparison of observed and simulated water pressure during closure test in 12MI33 and 13MI38, respectively. In these boreholes, both the observed and simulated water pressure increased abruptly just after the closure. The water pressure recovered soon after the closure even in the intact rock. In these boreholes, the observed water pressure also gradually decreased according to the decrease of water pressure in CTD. This drawdown is conspicuous at monitoring section 2 horizontal to the CTD. In our simulated result, the simulation results of water pressure in section 3 in both boreholes show the gradual increase after closure. The reason for the slow recovery of water pressure in section 3 compared to other sections is thought to be due to the poor hydraulic connectivity with the CTD. We think that the local hydrogeological structure generated by the connection of fractures causes this gradual increase of water pressure after the closure. In observed data, such a gradual increase in water pressure did not appear and recovery was instantaneous.

Figure 155 shows the time series of Cl concentration in 12MI33. This data is an extension of the data in Figure 148 and the data for about four years (twice in Figure 148) from excavation to closure test is shown. In the observed data, Cl concentration continued increasing during closure test in section 5. Cl concentration in section 3, 4 and 6 decreased after the termination of excavation and kept low during closure test. The variation of the observed Cl concentration between each monitoring section became large although the initial concentration in all monitoring section was about 400mg/L. A response of the Cl concentration due to the closure of CTD was not clearly in observed in the data.

Compared to the observed data, our simulated results of concentration do not vary so much and keep almost the same concentration as the initial state. The bottom figure in Figure 155 is the simulated Cl concentration and the range of graph is adjusted to see the change of simulated results. In the results, a gradual increase of Cl concentration in section 1, 4 and 5 and drop of concentration after excavation in section 6 appeared in this range. However, the change is too small compared to the observed data and even the trend of change at each monitoring section was not reproduced. The simulated trend of the variation seems to reach a steady state. Even if we extended the simulation period, the variation of Cl concentration did not reach the level of observed data. During the closure test, the concentration of simulated results slightly changed. However, the deviation was small and the effect of the closure of drift on the distribution of Cl concentration would be very small from both the observed data and simulation results.

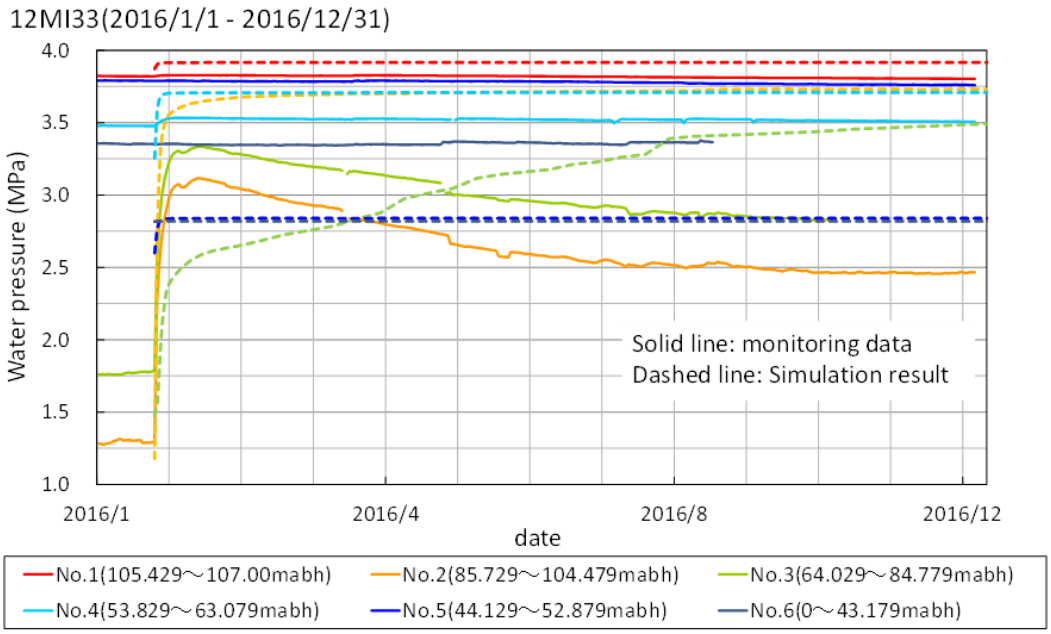

Figure 153. Comparison of water pressure in 12MI33 during the closure test.

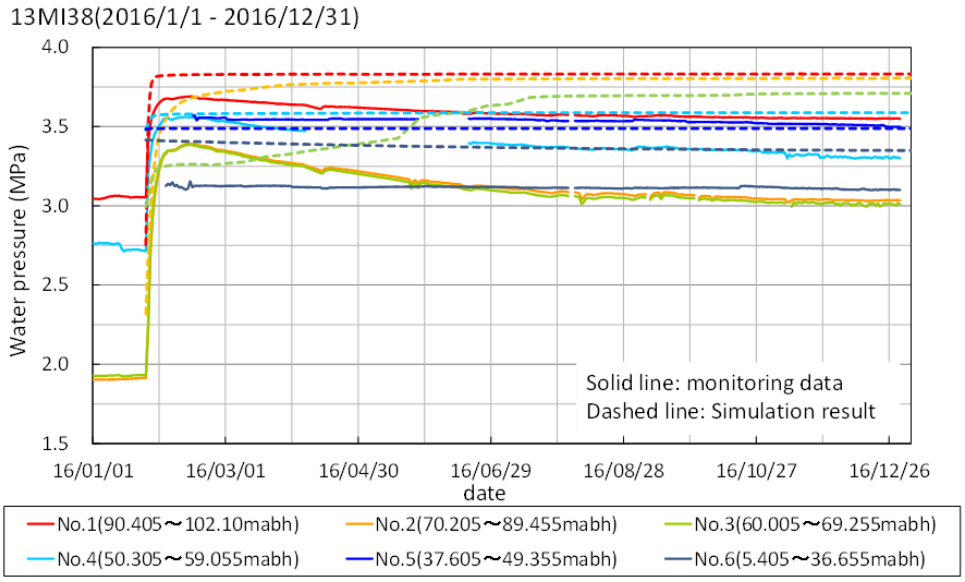

Figure 154. Comparison of water pressure in 13MI38 during the closure test.

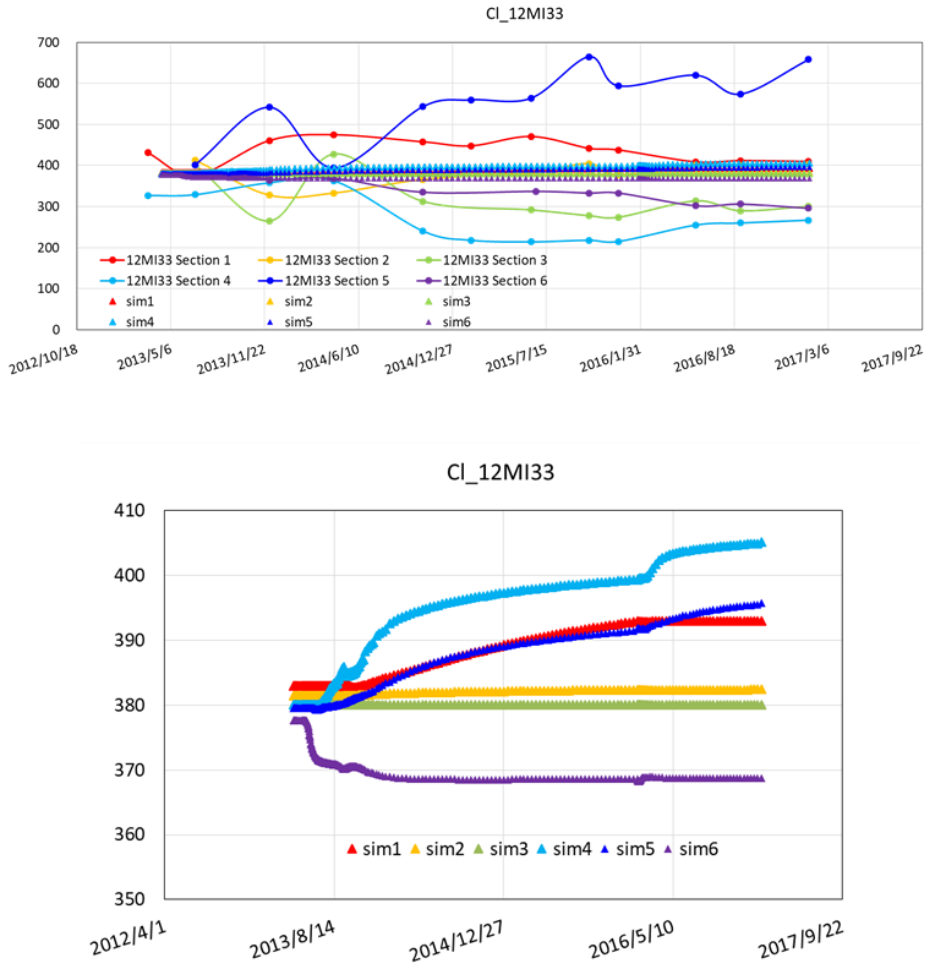

Figure 155. Cl concentration during the excavation of drift and the closure test in 12MI33 borehole.

8.2.2 Additional calibration for water pressure

The water pressure in the CTD decreased during the closure test as Figure 156 shows although we could not simulate this trend, as noted in the previous section. We expect that this decrease in water pressure in CTD is be due to the water leakage around plug. We suspect the dissolution of cement in plug and growth of water pass in the plug as a reason for the degradation of the plug. The high-pressure water in the CTD would permeate while dissolving the cement plug. The other factor we suspect was the increase of water saturation in the plug due to the closure test. In two-phase flow in a porous material, the permeability of water increases as the water saturation of the porous material becomes high. In GREET, the water saturation of the plug before the

closure test would be low and saturation would increase after the closure due to the high-water pressure in CTD. This also would increase the effective permeability around the plug. Although we did not identify the reason for the decrease in water pressure in CTD, we have listed some suspected reasons. To clear this problem and more realistic simulation, it is better to model such a process. However, the modelling of these factors is beyond our scope in this task and we simplify the modelling of this phenomena by making the hydraulic conductivity of plug time dependent.

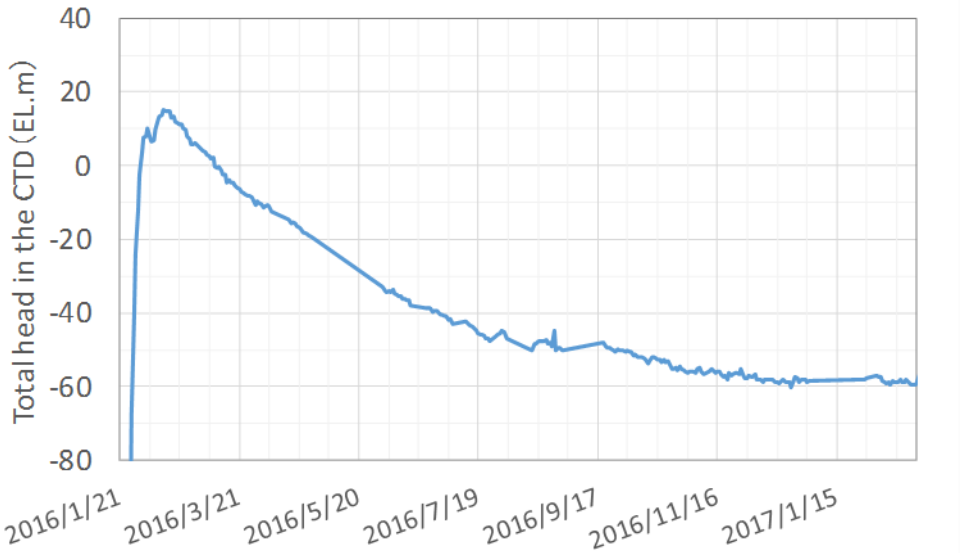

Figure 156. Decrease of water pressure in CTD during the closure test.

For the simulation of the decrease of water pressure in the CTD, the hydraulic conductivity in the plug was set to increase as a function of time after the closure of drift.

During the closure test, the inflow rate around the plug was measured. In addition, we added the uranine in the CTD water to trace the groundwater flow. The water collected around the plug contained the almost same concentration of uranine as water in the CTD. The volume of replacement of water in the CTD was calculated from the dilution of the uranine concentration in the CTD is almost the same as the inflow rate around the CTD we measured. Therefore, we judged that the leakage of water from CTD was totally discharged around the plug and the inflow rate measured around the plug is the almost the same volume as leakage water from the CTD.

Figure 157 shows the simulated and observed data of leakage from CTD. We used this data to set the change of hydraulic conductivity in and around the plug. The initial hydraulic conductivity in the plug was set to 10^{-8} m/s, same as rock mass. We test the

three cases where the final hydraulic conductivity in the plug becomes 3, 5 and 10 times higher than initial hydraulic conductivity. Our simulated results show that the leakage from the plug increased as the hydraulic conductivity of the plug becomes higher. When we set the hydraulic conductivity that the final value becomes five times higher than the initial value, our simulated result matches well with the observed data.

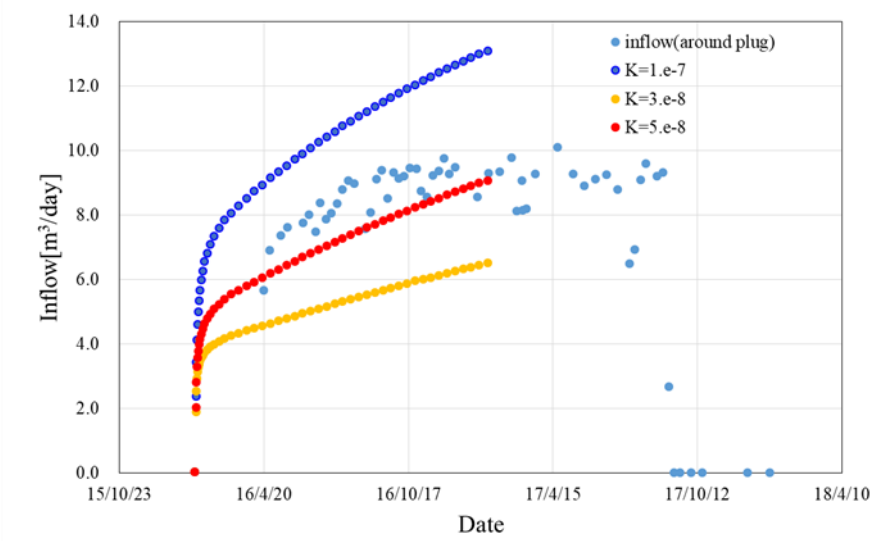

Figure 157. Time variation of simulated and observed leakage of water from CTD.

Figure 158 shows the time series of water pressure in the CTD when the hydraulic conductivity of plug changes. Both the observed data and simulated results with and without plug degradation are shown. The decrease of water pressure in the CTD is well simulated by the change of hydraulic conductivity in the plug. When we use the hydraulic conductivity that the final value becomes five times higher than the initial value, the simulated results match with the observed data.

Both the increase of leakage volume and decrease of water pressure can be explained by the five times increase of hydraulic conductivity of plug. This consistency of our simulation results, that both decrease of water pressure in CTD and increase of leakage rate can be simulated simultaneously by changing the hydraulic conductivity in the plug, would support that the observed decrease of water pressure in CTD was due to the plug degradation and increase of its hydraulic conductivity.

Figure 159 shows the water pressure in 12MI33. Simulated results with plug degradation and observed data are plotted. By considering the leakage from the plug, the peak of water pressure was reduced, especially in section 2 and 3 that is located horizontally to

the CTD. At section 4 and section 3, the pressure value at steady state becomes close to the observed data and the results are better than in Figure 153. The water pressure in 12MI33 during closure test also is affected by the leakage from CTD.

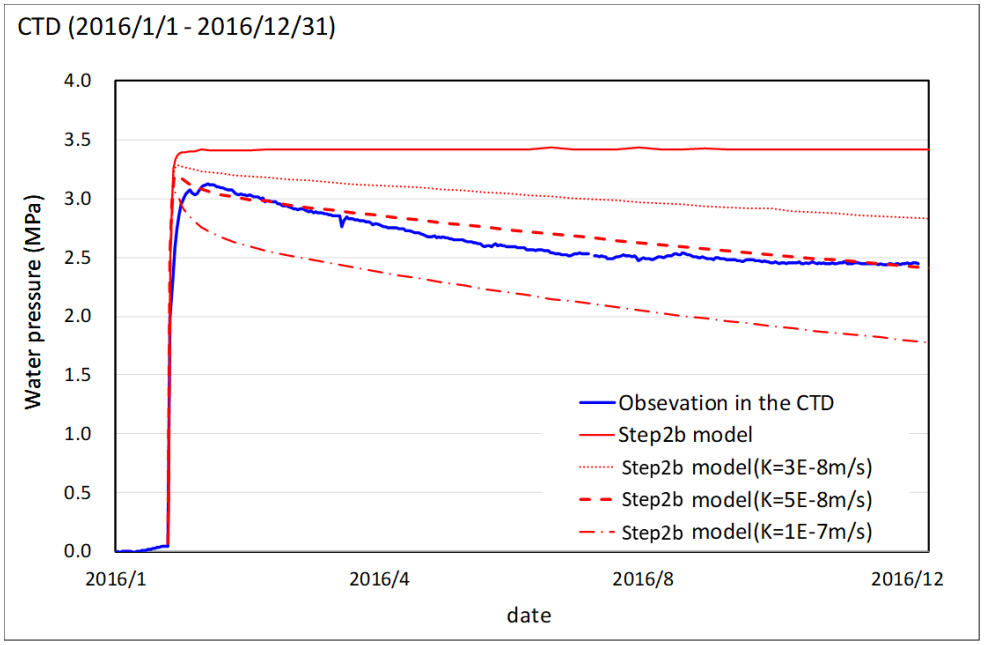

Figure 158. Water pressure in the CTD during closure test when the hydraulic conductivity in plug changes.

8.2.3 Additional calibration for Cl concentration

Concerning the hydraulic modelling, we could derive better results by including additional fracture data and conditioning. We could simulate the hydraulic pressure in 12MI33 and inflow rate that matches the observed data by our approach. Even in the case that water in the CTD would leak during closure test, we could reproduce the observed data of hydraulic pressure and inflow rate. Then, our modelling approach based on the fracture distribution would be appropriate for the simulation of the hydraulic part.

However, the simulation results of Cl concentration are still poor. We expected that this is not only due to the modelling of hydraulic fields but also the basic understanding of the chemical condition. In this chapter, we focus on the improvement of the Cl concentration simulation results.

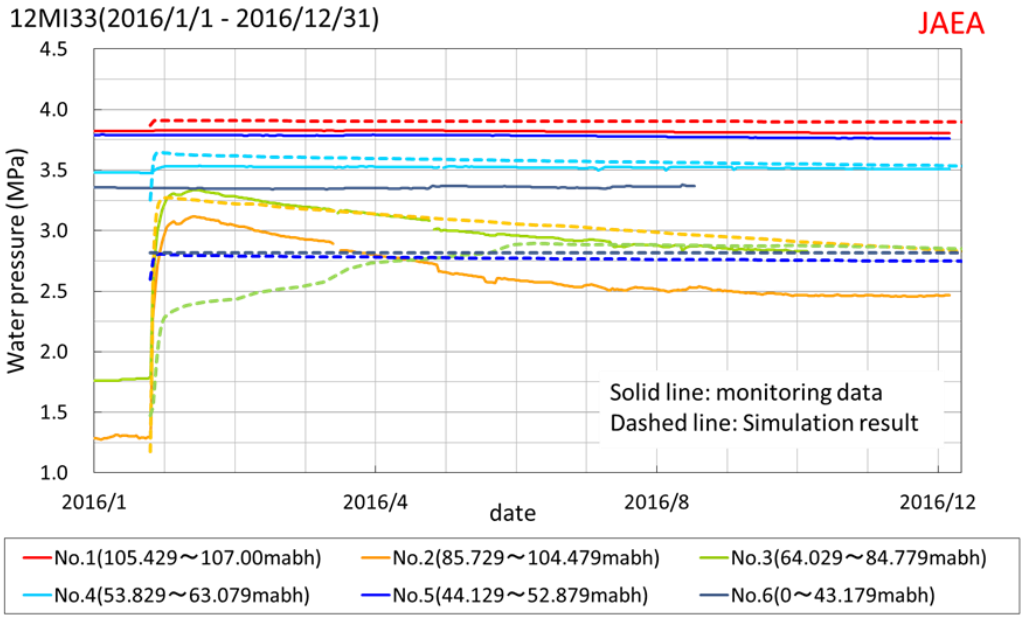

Figure 159. Water pressure in 12MI33 during the closure test when the hydraulic conductivity in the plug changes.

(1) Resetting of initial and boundary condition

In our initial modelling plan, we used the observed data of Cl concentration to set initial and boundary values. The data at 09MI21 at the 300m stage, 12MI33 at 500m and vertical borehole of MIZ1 were used as Figure 160 shows. The Cl concentration data for these boreholes show the proportional dependency on the depth. So, for the initial and boundary conditions, we inter/extrapolate the data. The range of Cl concentration in our model domain by this approach was from 317mg/L to 477mg/L. The biggest problem by this approach is that the observed data exceeds both high and low limit of our simulation range as Figure 160 shows. The simulation range by our initial approach is very narrow comparing to the observed data and resultant deviation of simulated Cl concentration would become small. To solve this problem, we reset this initial and boundary condition of Cl concentration.

To improve the initial and boundary condition of Cl concentration, we reviewed the observed distribution of Cl concentration. We reviewed the data acquired not only around our target domain but also from ground surface to deeper part than the facility. Figure 161 shows the distribution of Cl concentration. The inter/extrapolated distribution of observed data before and after the excavation of two shafts (left) and the simulated result after the excavation of two shafts are displayed. Before the excavation

of the Main shaft, the clear dependency of concentration on the depth was seen. In this situation, the Cl concentration about 500 m is about 350 mg/L and the high salinity plume does not exist.

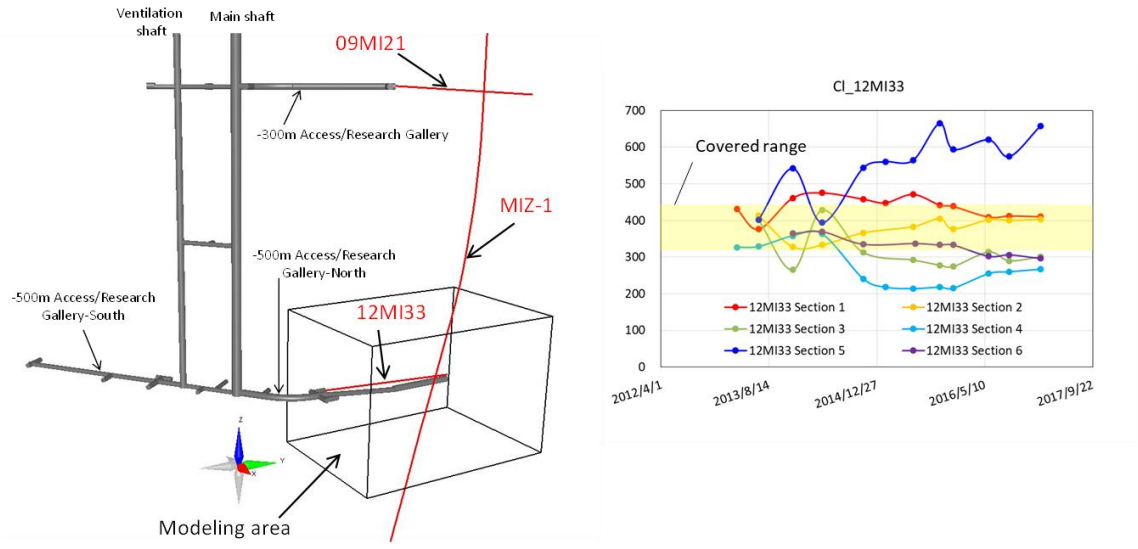

Figure 160. The locations of boreholes used for the initial and boundary conditions for the Cl simulation and the covered range by this approach (right).

However, after excavation, this layered distribution of Cl concentration was disturbed due to the long-term continuous drainage of groundwater to the two shafts. This drainage leads to the low salinity water around the ground surface moving to the deeper part and brings the high salinity water from deeper to the level of the excavated shafts as Figure 161 shows. This movement of Cl concentration is called 'up-coning' and this effect makes the concentration gradient around the bottom of the shaft steep. The simulated results with geological heterogeneity indicate that the groundwater with higher salinity than 500 mg/L would appear about the 300 m stage. This suggests that high salinity water that we could not see at the borehole far from shafts that were used for the initial and boundary conditions would come close to the GREET drift. In this step, we update the initial and boundary condition by considering the influence due to shafts excavation.

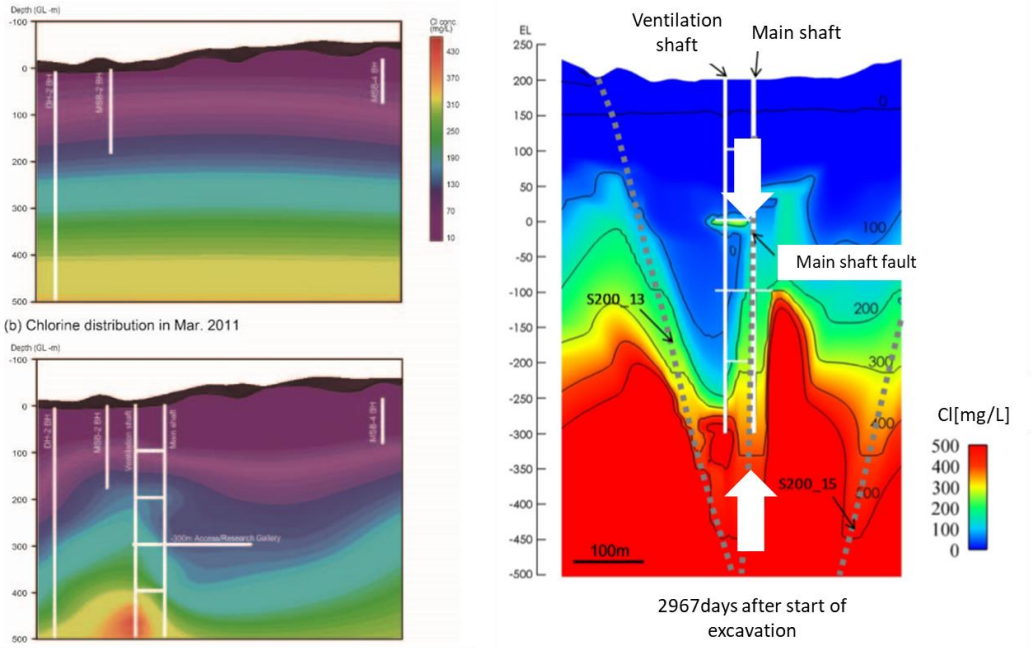

Figure 161. Cl concentration at facility scale in MIU. Observed data (left, Mizuno et al., 2013) and simulated (right, Onoe et al., 2014)

To update the model, we take a two-step strategy. At first, we perform the simulation of Cl concentration in the scale in which the subsurface facility is fully included. Then, we extracted the data around our focused domain and we use the data as initial and boundary condition. We perform the long-term drainage simulation to form the upconing of Cl concentration for the initial and boundary condition with a simple uniform model for the first step. Only the size of the simulation domain is considered for the first step of the modelling. In MIU, it is known that the hydraulic field under subsurface is separated by the low permeable faults. Figure 162 shows the distribution of faults around MIU. We can define the simulation domain for the first step according to these faults' disposition. In this study, we test three simulation domains based on this fault map for the first step. The considered simulation domain is summarized in Table 32 with the lateral boundary condition of specific hydraulic head. We set these three cases considering the case that the main shaft is impermeable; the domain where S200_13 fault is impermeable while the main shaft fault is permeable; and all faults are ignored. The boundary conditions for Cl concentration are summarized in Table 33. We do not simulate the excavation process of two shafts. The movement of water and Cl is only according to the drainage from the excavated shafts for 10 years.

The initial and boundary condition of Cl is also important even in the simulation for the facility scale simulation. We set the initial and boundary condition based on the depth

distribution of Cl concentration of boreholes from the ground surface. Figure 163 shows the Cl concentration observed in 5 boreholes. All data acquired there is compiled as a graph with depth. This data can be fitted by an exponential function very well. The fitting by exponential function is reasonable from the point of view of diffusive behaviour of mass transportation although we inter/extrapolated observed data by linear function for the initial and boundary conditions in Step 1, which was appropriate over a small domain. We set the initial and boundary condition for concentration according to the calibrated exponential function. Then the drainage and uplift of high salinity water are simulated. Figure 164 shows the example of a hydraulic head of drainage simulation from two shafts.

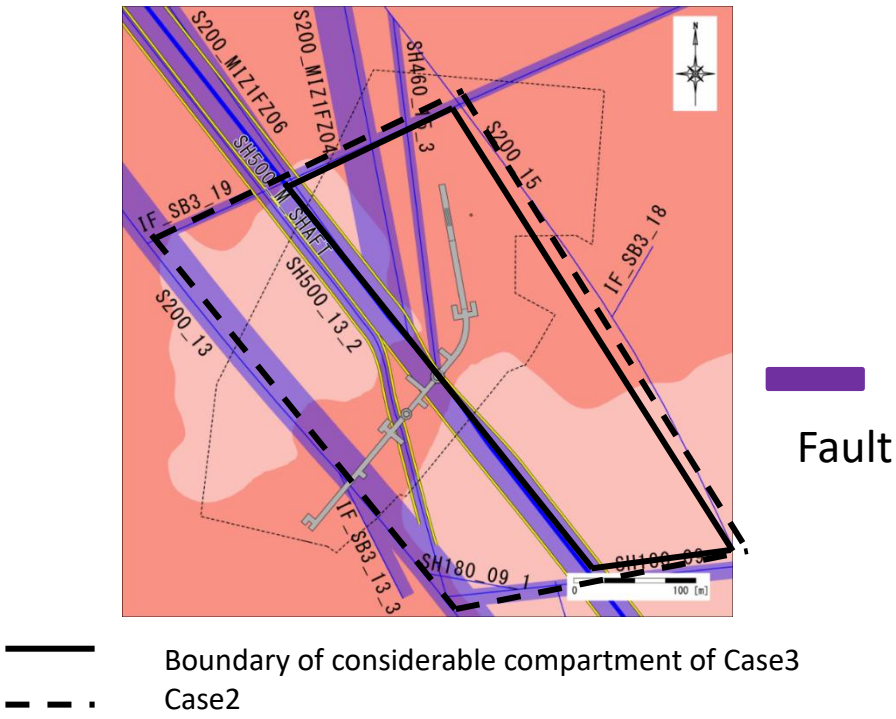

Figure 162. Fault around MIU and simulation domain for the first step.

Table 32. Simulation domain of facility scale simulation

Case	Situation	Simulation domain
Case1	Without compartment	x=1000; y=1000; z=1200
Case2	Large compartment	x=1000; y=500; z=1200
Case3	Small compartment	x=1000; y=250; z=1200

Table 33. Boundary condition of facility scale simulation

Top boundary	**Head**	**Fixed (Hydrostatic)**
	Cl	**Fixed**
Side boundary	Head	Case 1: Fixed (Hydrostatic) Case 2: Fixed (Hydrostatic) Case 3: No flow
	Cl	No flow
Bottom boundary	Head	Fixed (Hydrostatic)
	Cl	Fixed
Inner boundary	Head	Fixed (0 MPa)
	Cl	Free

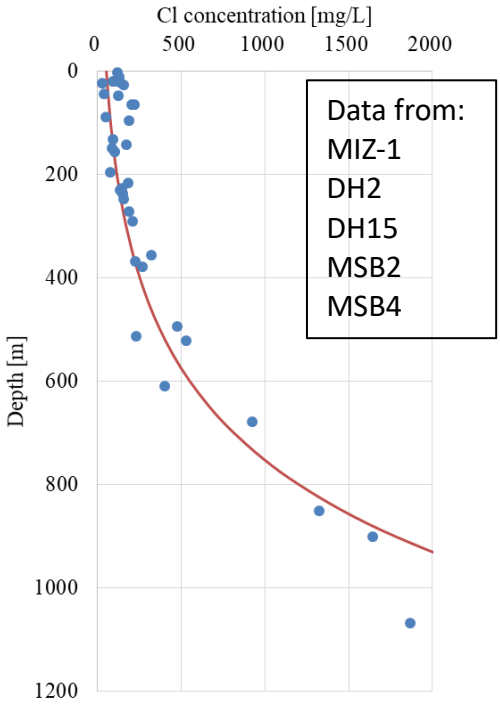

Figure 163. Observed Cl concentration data from five boreholes for the first step simulation

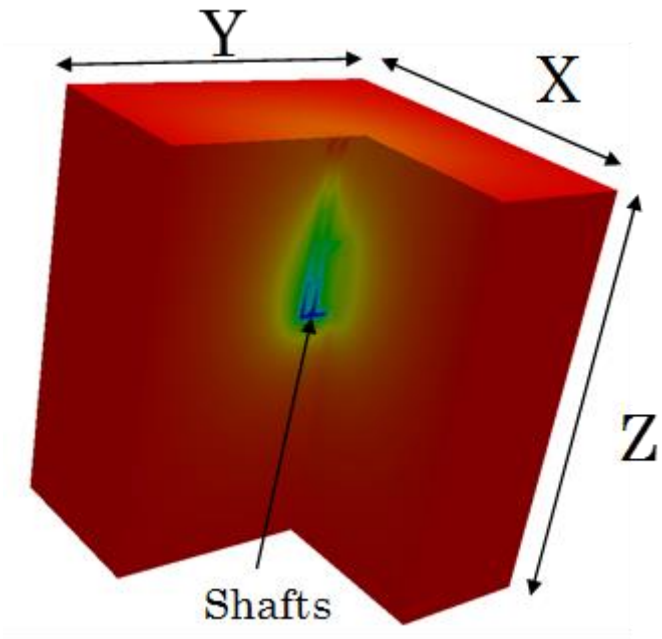

Figure 164. Example of a simulation result showing hydraulic head by a drainage from two shafts in the first step (case2).

Figure 165 compares the initial and boundary condition defined in step 1 and updated initial and boundary condition derived from the facility scale simulation. From the 3 cases we tested in the first step, the range of concentration is the widest in case 3 where the area of the compartment is the smallest. Then, the simulation range derived from case 3 was shown. In the updated condition, high salinity zone due to the drainage from shaft appeared beneath the inclined drift although the previous condition is horizontally layered. In updated condition, both low and high limit of simulation range are extended and gradient in concentration becomes steeper in the model domain.

Figure 166 compares the updated simulation range and the observed Cl concentration. The updated simulation range covers the concentration from 248 mg/L to 881mg/L. The updated range is wide enough to capture the high concentration, although the lower limit is a little bit higher than the observed data in section 4 in 12MI33. We simplify the facility scale simulation by using the uniform structure. Because of this simplification, the updated model cannot reproduce the movement of high/low salinity water via some channels in the fracture network.

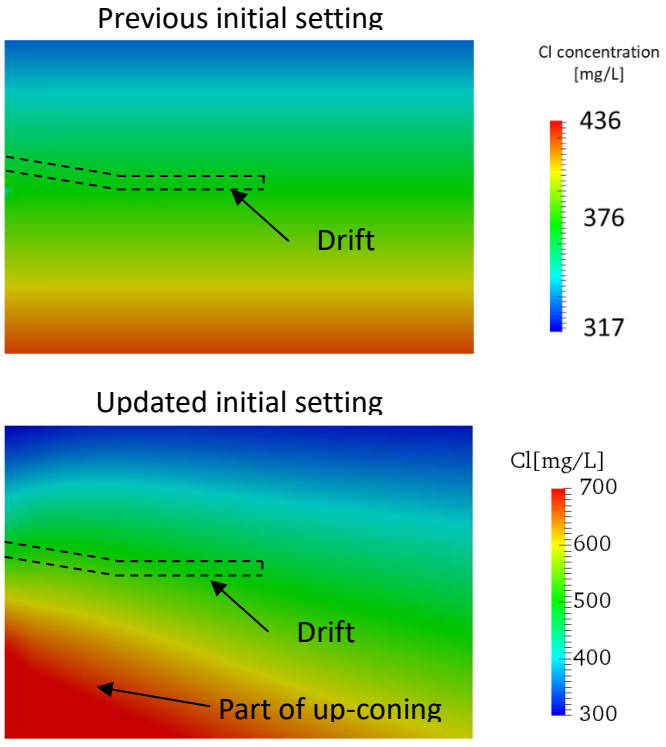

Figure 165. Comparison of updated and previous initial and boundary condition of Cl concentration for focused domain

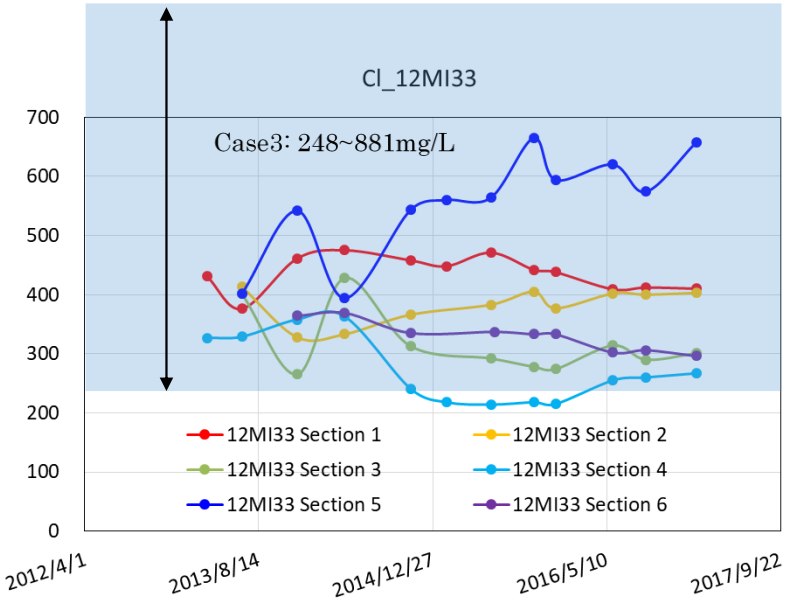

Figure 166. Comparison of simulation range (blue area) from the new model configuration and the observed data.

Using this approach, we could get a better initial and boundary conditions that covers the observed data. So, we then simulate the Cl concentration by using the updated initial and boundary condition with the model of hydraulic conductivity in Figure 145. Figure 167 shows the vertical slice of simulated results along drift and the cross-section across the monitoring section 5 in 12MI33 and 13MI38 where the Cl concentration increased prominently after excavation. For the comparison, previously simulated results and updated results are shown. In both cases, the lower and higher salinity water is brought toward the inclined drift and the CTD due to the drainage from drift along with the fractures. The concentration around drift is diluted by the mixing of high/low salinity water coming from a shallower and deeper part of the model domain. The concentration level around drift is not high/low compared to the concentration around the boundary. The pattern of movement of Cl concentration does not change so much whether we use the previous initial and boundary condition or not. However, the higher and lower salinity water comes closer to the drift in updated model and Cl concentration higher than 600mg/L that is similar value to the observed data comes close to the monitoring point 5 in the updated model. By updated model, the simulated value enables to take the higher and lower value that is comparative to the observed data. However, the deviation of simulated concentration at the monitoring point is still smaller than the observed data and further improvement is required.

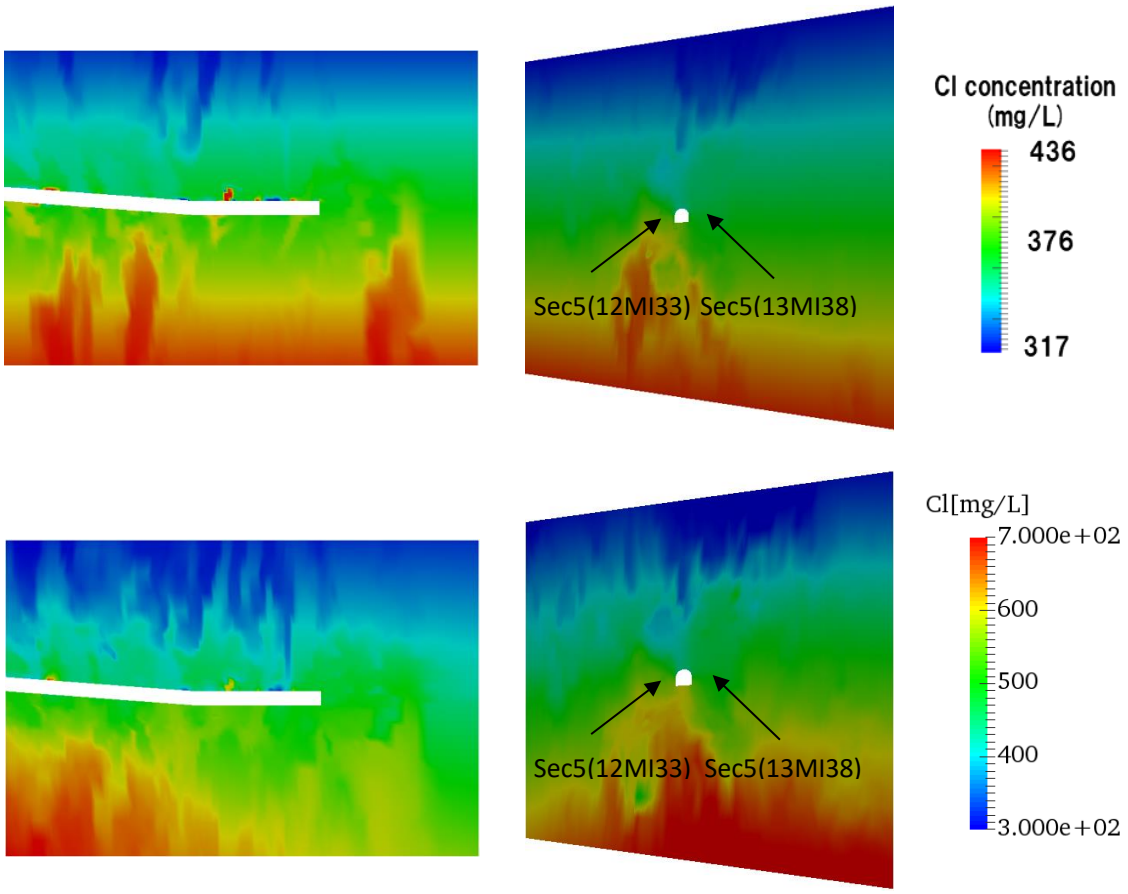

Figure 167. Simulation results of Cl concentration with previous and updated initial and boundary condition.

(2) Single fracture calibration

By considering the up-coning effect arising from the long-term drainage to the two shafts, both a large enough salinity range to cover the range of observed data could be set in our model. However, even by using this updated boundary and initial condition, the simulated Cl concentration at the monitoring section does not cover the range in the observed data as shown in Figure 167. This could be due to the mixing of high and low salinity water that comes from a shallower and deeper part of modelling domain, respectively. To overcome this mixing effect that makes the simulated concentration at monitoring dilute, we think that preferential flow conveying the high or low salinity to the monitoring sections directly is necessary as Figure 168. Figure 168 shows, potentially reflecting channelization within the fracture network.

Our modelling approach depends on using a stochastic method. Although we perform the conditioning of fracture to fit the location of simulated fracture to the observed location of fractures, the models having a preferential path connecting only the shallower or deeper part would be rarely generated and the mixing effects would be difficult to avoid. So, in this section, we calibrate our model deterministically to remove the mixing effect to get the high/low salinity at the monitoring points. We introduce the additional fracture connecting to only shallower or deeper part directly into our model according to the observed Cl concentration.

In this section, we focus on the calibration of Cl concentration observed in section 5, where the observed data show the increasing trend prominently. A single fracture connecting to the deeper part of the model was added around section 5 for the calibration.

We expected that there is a trade-off between Cl concentration observed at the monitoring point and the property of fractures such as size and hydraulic conductivity. The preferential path as Figure 168 is necessary to transmit the high/low salinity water to the monitoring point. However, if the width of fracture is too large or the additional fracture is connected with many fractures, the water pressure that is driven force of groundwater flow would be lost and the high/low salinity water would not be conveyed to the monitoring points. To investigate this effect, we perform the calibration by changing the length of the additional fracture. Figure 168 shows the results of the calibration. Three cases where the length of the additional fracture is different are shown.

Our results show that the high salinity area around drift and monitoring section extends according to the size of the additional fracture. However, the concentration there is diluted as the size of the fracture becomes wide as we expected. This suggests that the fracture size is one of the key factors that decides the trend of observed Cl concentration.

Figure 168 and Figure 169 compare the observed data and simulated results of Cl concentration at each monitoring point in 12MI33 and 13MI38. In this section, we only calibrate the data in section 5 and the variation of concentration at other monitoring point is still small. At section 5 in 12MI33 where we tried to calibrate, the simulated results show an increase of concentration higher than 100 mg/L at section 5 in 12MI33 and 13MI38. In addition, the concentration in section 6 decreased by more than 100 mg/l. These change in concentration after calibration appears abruptly just after the termination of excavation. On the other hand, the gradual change in concentration in the observed data did not appear in calibrated results. We expect that the gradual trend would be caused by the continuous forming of up-coning in facility scale. Although it is

difficult to model the gradual trend by the deterministic calibration, we could reproduce the abrupt change just after the excavation.

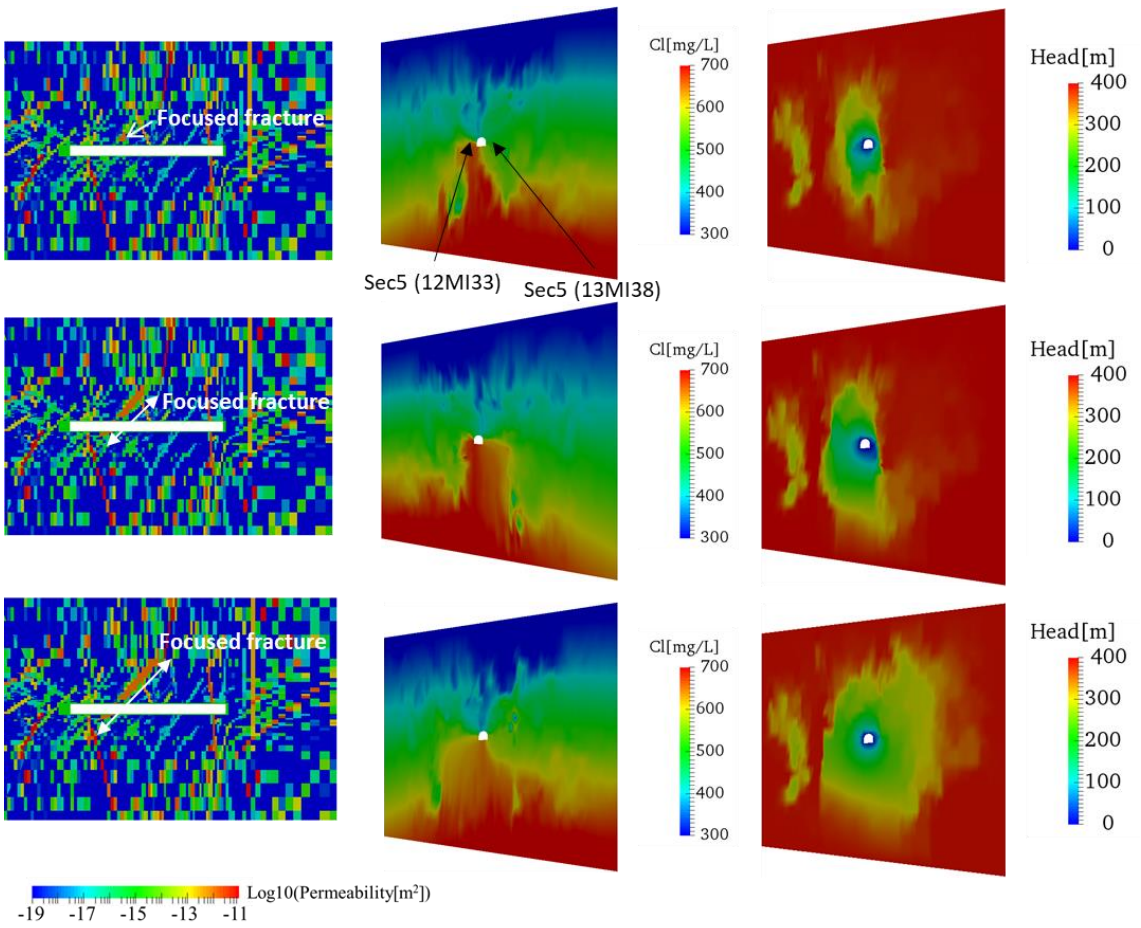

Figure 168. Sensitivity analysis of the length of the additional fracture for calibration.

(3) Multi fracture calibration

We focused on the calibration at section 5 as a first deterministic calibration step and a single fracture was introduced. In this section, we extend this approach and try to calibrate the Cl concentration at other monitoring boreholes by introducing multiple fractures. In this calibration, we not only add the fractures but also remove some fractures to fit the data. The removal and additional fractures that intersect monitoring section are selected by technical judgement to reproduce the Cl concentration.

Figure 171 shows the calibrated model by the addition and removal of multiple fractures. In this approach, we did not introduce the fractures that do not cross the drift

and the fractures that cross the monitoring point were added according to the data of Cl concentration. Figure 171 shows that this calibration approach does not change our original ECPM model so much.

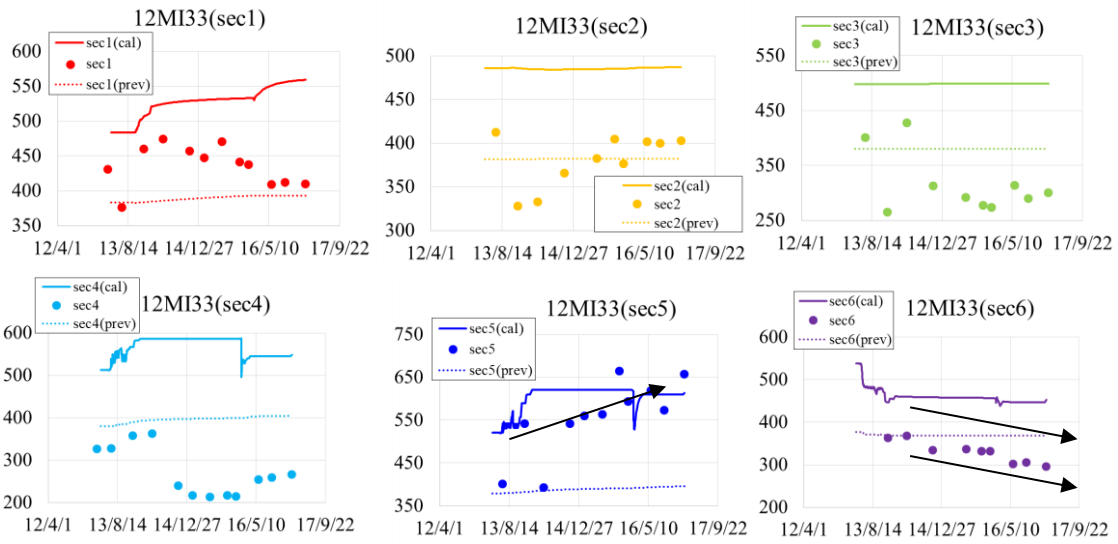

Figure 169. Comparison of simulated results (lines) and observed data (symbols) of Cl concentration in 12MI33 after single fracture calibration.

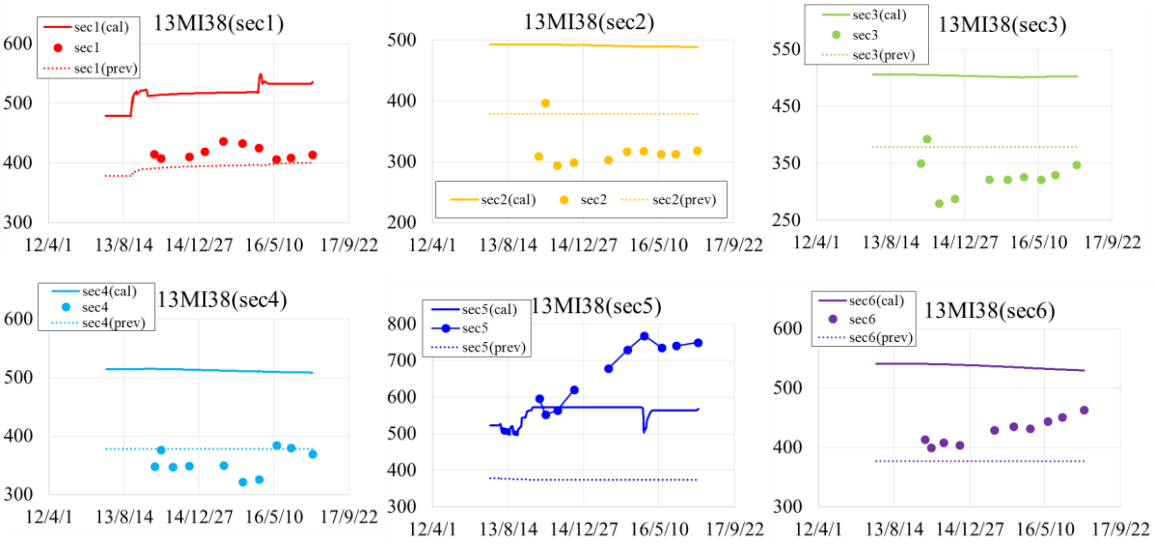

Figure 170. Comparison of simulated results and observed data of Cl concentration in 13MI38 after single fracture calibration.

As with the previous calibration with a single fracture, we directly adjusted the width and hydraulic conductivity of the fractures by calibrating the observed Cl concentration. However, this approach is time-consuming for multiple fracture calibration. In this chapter, we calibrate the width and hydraulic conductivity of fracture by fitting both hydraulic pressure and inflow rate at steady state after excavation. We then apply the model to simulate the Cl concentration during the excavation and closure test.

Figure 172 shows the calibrated hydraulic pressure at steady state after excavation. By using the multi-fracture calibration, we could capture the trend of hydraulic pressure not only in 12MI33 but also 13MI38 when comparing with the results from the model without deterministic calibration as shown in Figure 144. Figure 173 shows the resultant inflow rate after multi-fracture calibration. This result is still broadly consistent with the observed data although the simulated inflow rate into drift is decreased compared to the observed data. The slight gap between observed data and simulated result in both hydraulic pressure and inflow rate could be decreased by more careful calibration by using numerical inversion scheme.

Then, we perform the simulation of hydraulic pressure and Cl concentration during the excavation of drift and closure test by using the calibrated model. Figure 174 shows the time series of simulated hydraulic pressure in 12MI33. In this simulation, we did not consider the change in hydraulic conductivity of the water-tight plug and the increase of leakage from CTD. Hence the hydraulic pressure after during closure test become stable. We have already evaluated this effect and confirmed that a gradual decrease of hydraulic pressure can be explained quantitatively by changing the hydraulic conductivity of plug (Section 8.2.2). Therefore, we skipped the consideration of the effect of this chapter.

The simulated time series of hydraulic pressure in 12MI33 matches the observed data except for section 2 well. At section 5, the high hydraulic pressure during closure test is reproduced by the simulation. At section 3, the level of pressure becomes close to observed data.

Figure 175 shows the simulated Cl concentration during excavation and closure test by using the model calibrated by deterministic multi fractures. The high concentration in section 5 is captured. At sections 3 and 4, the decrease in concentration after the excavation is simulated. However, the levels of the concentration in these sections are still higher than the observed data. The baseline of simulated results is higher than the observed data. This is due to our two-step approach. For the calibration of baseline, we need to calibrate not only drift scale model but also facility scale model.

Figure 176 shows the Cl concentration in 13MI38. In this side, the low concentration in section 2 and 3 are reproduced well. The Cl concentration in section 5 is the same level as the simulated result in 12MI33 while the observed Cl concentration is higher in this borehole.

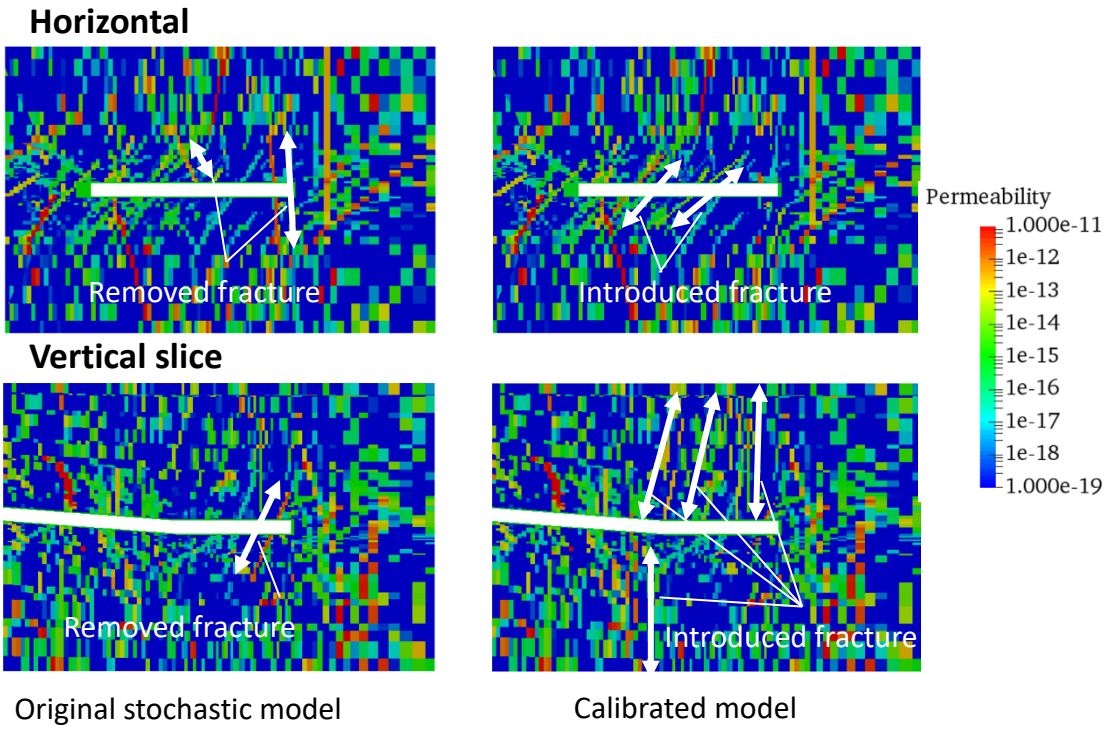

Figure 171. Calibrated model by the addition and removal of multiple fractures

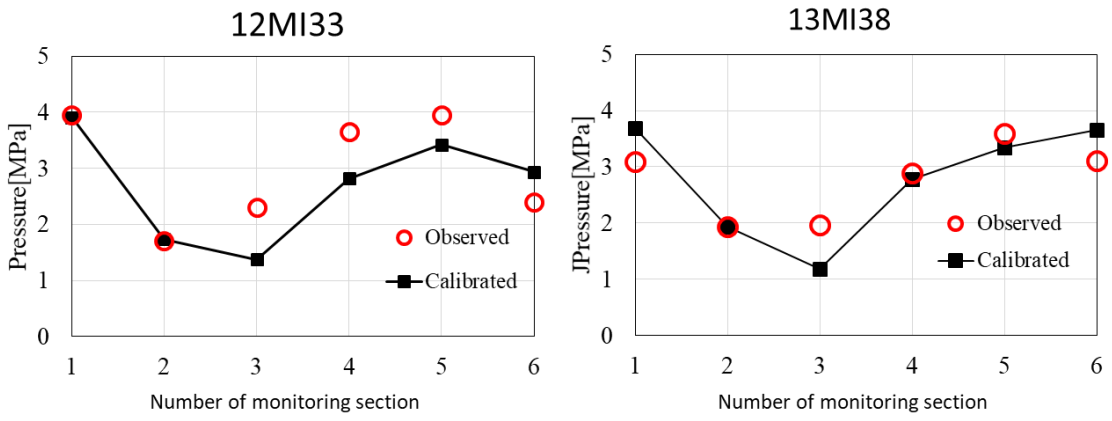

Figure 172. Calibrated hydraulic pressure at steady state after excavation for the multi-fracture calibrated case.

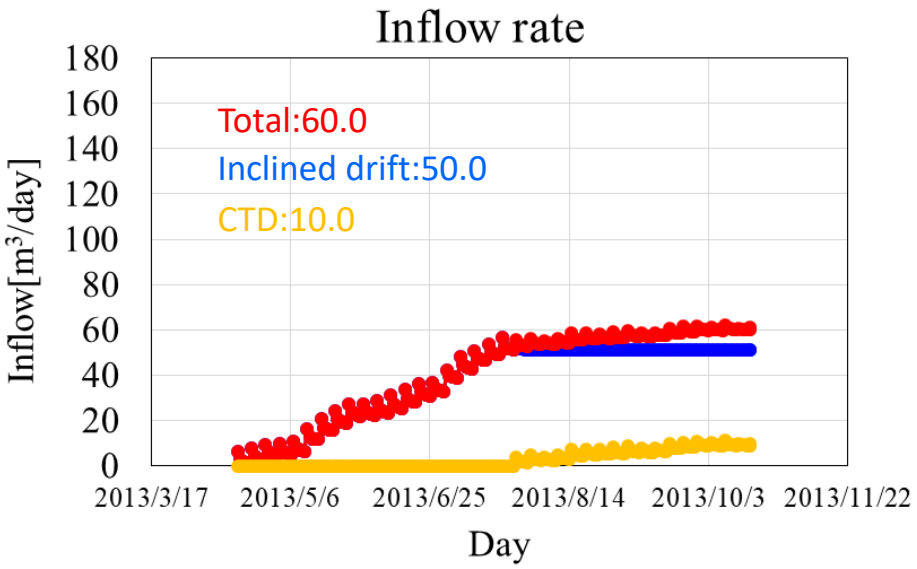

Figure 173. Inflow rate from the calibrated model

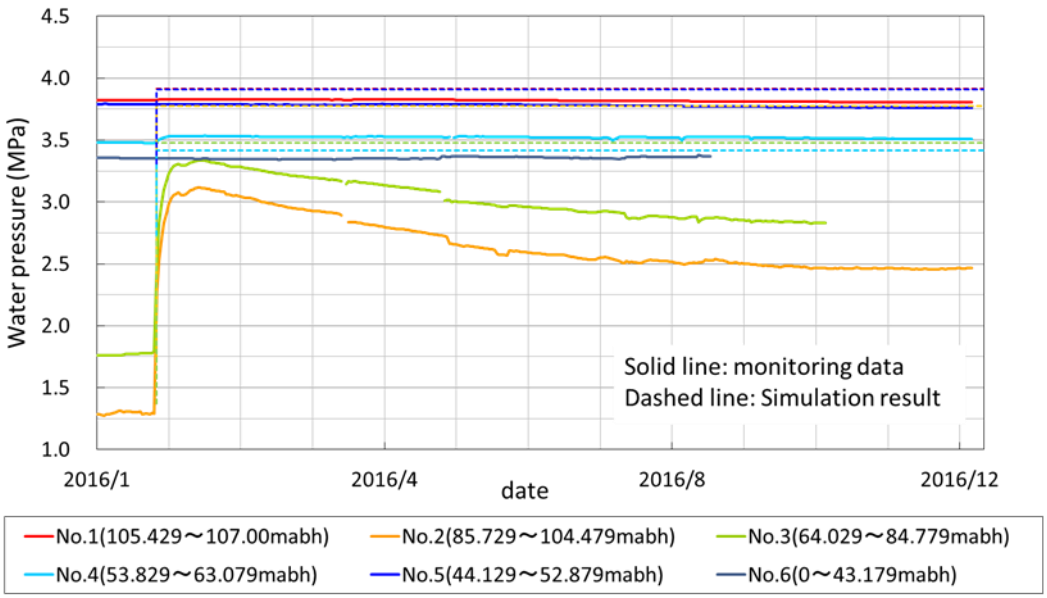

Figure 174. Calibrated hydraulic pressure during closure test by deterministic multi fractue approach in 12MI33.

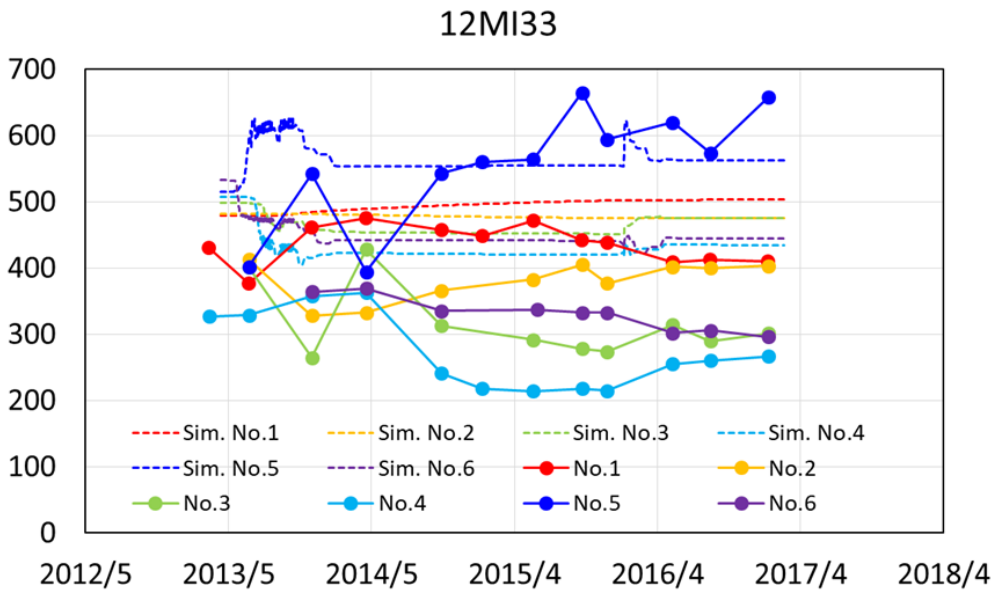

Figure 175. Simulated Cl concentration during excavation and closure phases in 12MI33 by using the model calibrated by deterministic multiple fractures

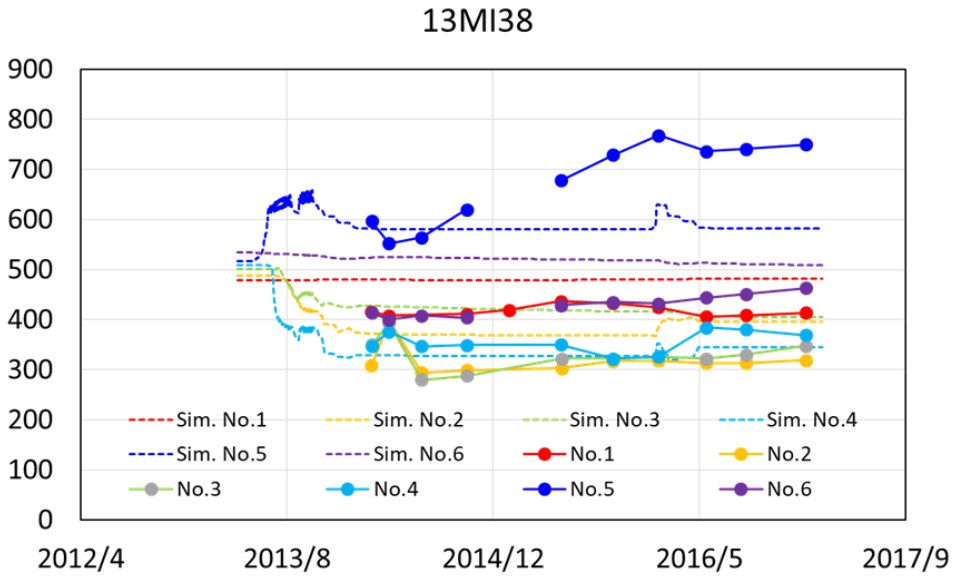

Figure 176. Simulated Cl concentration during excavation and closure phases in 13MI38

(4) Conceptual model calibration

Up until the previous section, we used a model based on the DFN and ECPM approach. The merit of using the DFN and ECPM approach is that we can integrate the geological information into the model. However, the problem in using this approach is that the calibration of the model is difficult because the generation of modelling by DFN is based on the stochastic approach and a calibration method for DFN is not well established. In addition, the geological information sometimes does not show the relationship between hydrological or chemical response. For the calibration of Cl concentration, we have performed a manual calibration and introduced deterministic fractures into the original stochastic ECPM model. These approaches show that manual calibration drastically improves the simulated results of Cl concentration. This suggests that such several deterministic fractures have a great impact on the hydro-chemical fields.

From the above considerations, we tried to reproduce the Cl concentration using a deterministic approach. We constructed the conceptual model of channelization in the rock mass based on the responses of water pressure and hydrochemistry around the CTD, and several fractures were modelled deterministically to match with the conceptual model.

The conceptual model was developed by considering the baseline of hydraulic pressure after excavation, the response of the recovery process and Cl concentration observed around CTD. Figure 177 shows the classification of the model domain according to the hydraulic pressure after excavation. We divided the area around CTD into three domains.

One is the domain (red colour domain) where the hydraulic pressure is high and we consider this as a domain where the connectivity to the drift is low. The other part is the domain (blue colour domain) where the hydraulic pressure is low by having a strong connection to the drift. Then, to relate the other area that is not classified into these two domains to the domains, we use the hydraulic pressure data during the recovery process. To analyse the hydraulic pressure change data of all monitoring section in boreholes during the recovery process, we make the derivative plots as in Figure 178. We classified the pattern of these graphs and compiled the results in Figure 177 and Figure 178 in Figure 179.

In addition to the hydraulic pressure data, we referred to the data of Cl concentration change. We use the data to add the information of connectivity to the vertical direction. Figure 180 shows the Cl concentration data for the conceptual model. We classify this data and the resulting classification of the domain around CTD is shown in Figure 181.

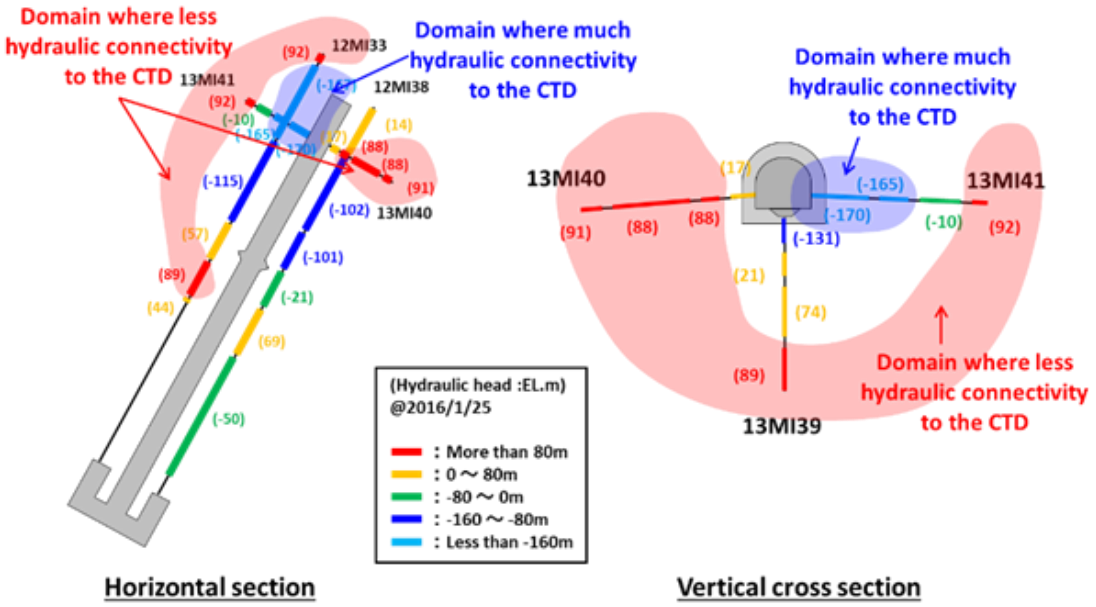

Figure 177. Classification of the model domain according to the hydraulic pressure before closure test

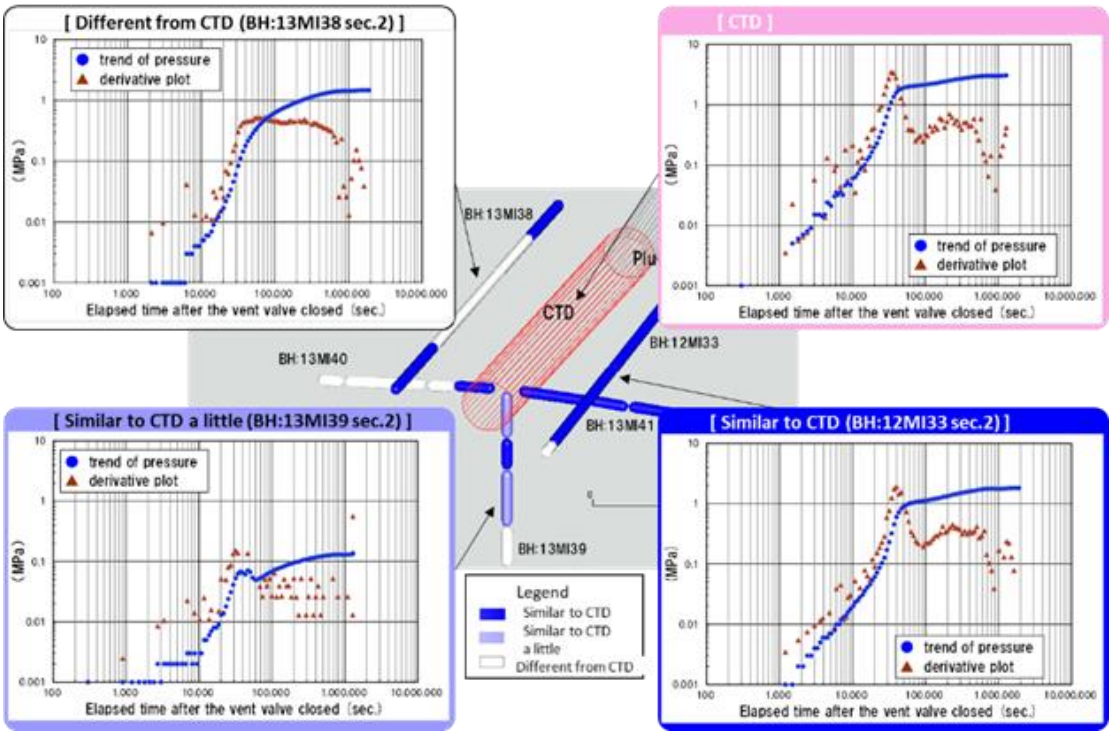

Figure 178. Example of the derivative plot during the recovery process for the concept model

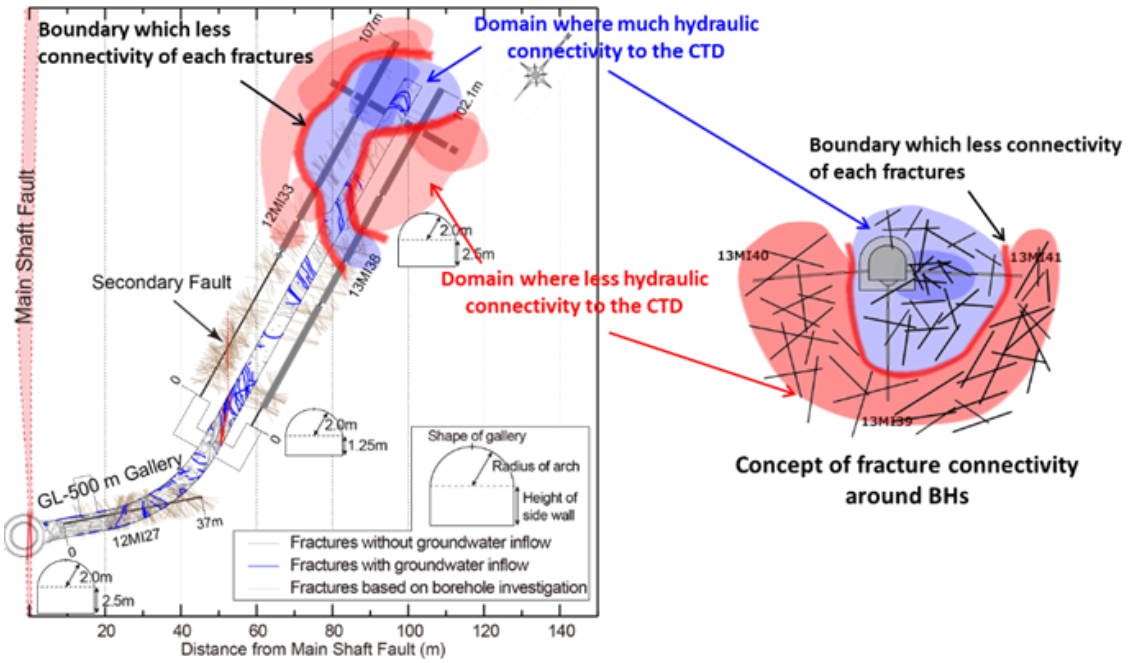

Figure 179. The results of classification into two domains according to the observed hydraulic pressure

Then, we combine the results in Figure 178 and Figure 180 and we get the conceptual model describing the connectivity as shown in

Figure 182.

Based on the classification in

Figure 182, we introduced several fractures connecting to the deeper or shallower part of the model. We introduce the fractures without considering the location of observed fracture data and we only depend on the concept model to make this simulation model. The width of each fracture and hydraulic conductivity are decided by the same way as the multiple fracture calibration, using the hydraulic pressure and inflow rate after excavation data. Figure 183 shows the model based on the conceptual model. We introduced seven fractures into the model and the model is simplified compared to the previous models.

Figure 184 and Figure 185 show the simulated results of Cl concentration in 12MI33 and 13MI38. The simulated results in 12MI33 are similar to the results in the case of multi-fracture calibration even using such a simple model. This result indicates that only several fractures, or pathways within the wider fracture network, would play an important role in form in the Cl concentration distribution around the drift. In 13MI38, both high and low concentration is simulated very well comparing to the results in Figure

176. We could capture the range of observed data by using the simple model in this monitoring borehole.

We checked the response of Cl concentration during closure test. Figure 186 shows the observed Cl concentration at section 4 in 13MI38. We display these results because the response during the closure test is clearly seen among all data. In this time series data, the temporal increase of concentration about 50 mg/L appeared during closure test. We expect that this temporal change is due to the change of the ratio of water supply from a deeper or shallower part according to the pressure change in CTD and monitoring borehole during the closure of drift.

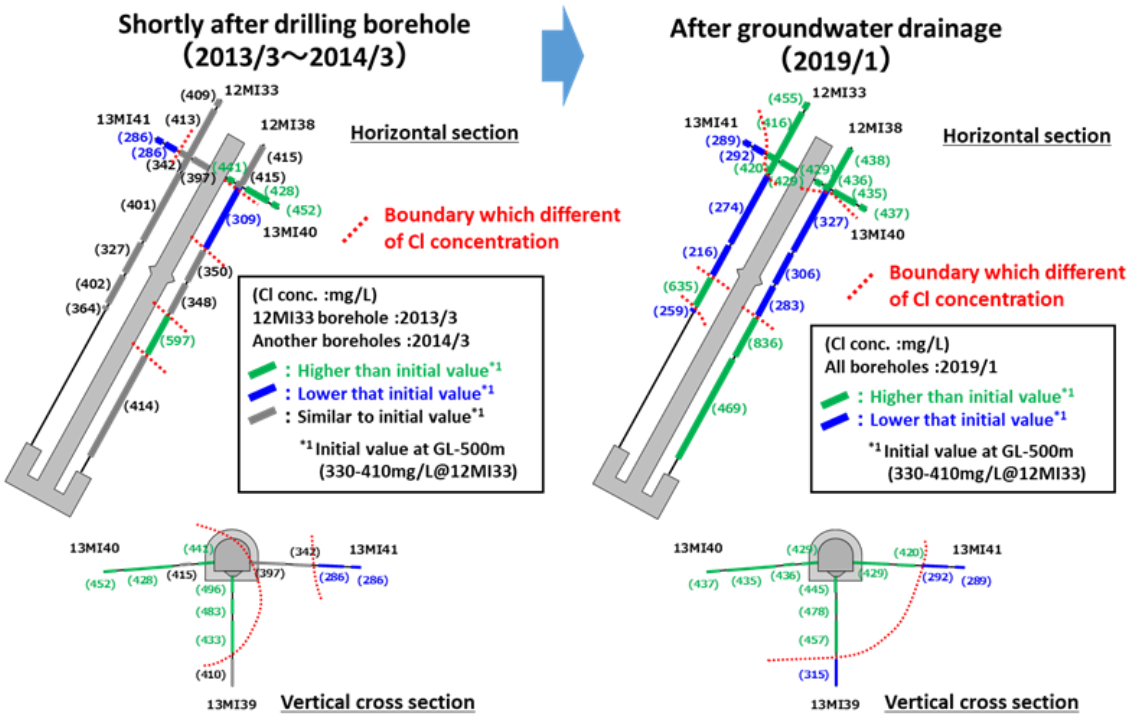

Figure 180. Transition data of Cl concentration for concept model

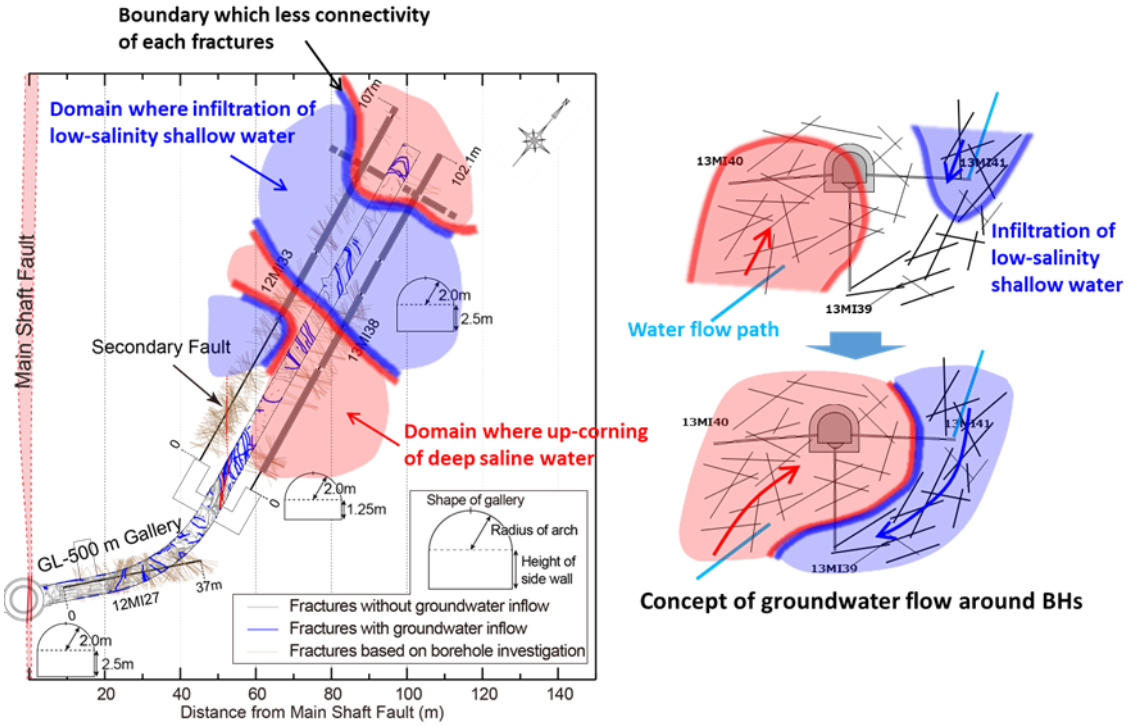

Figure 181. Classification of the model domain according to the transition data of Cl concentration

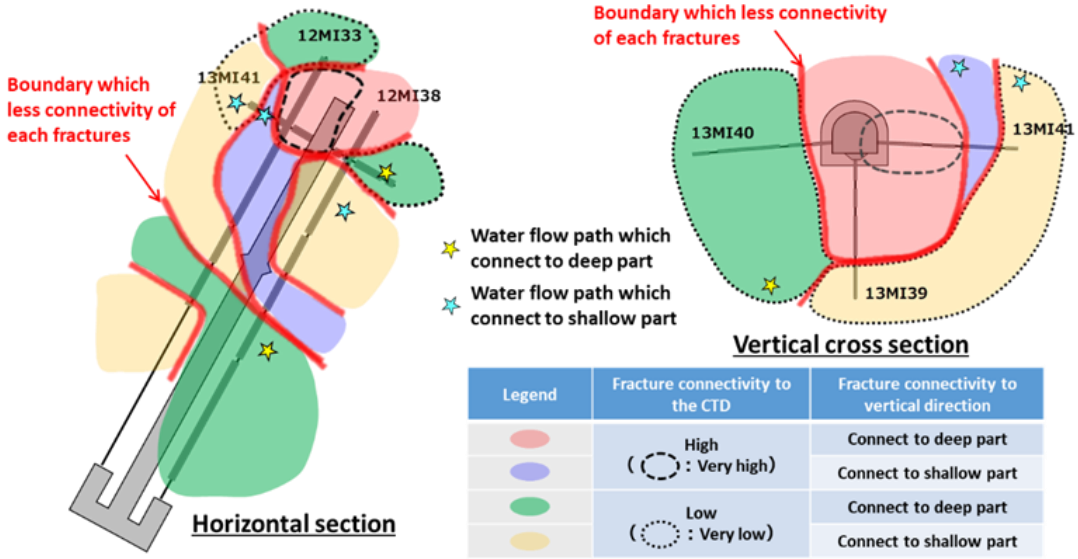

Figure 182. Concept model of connectivity around CTD

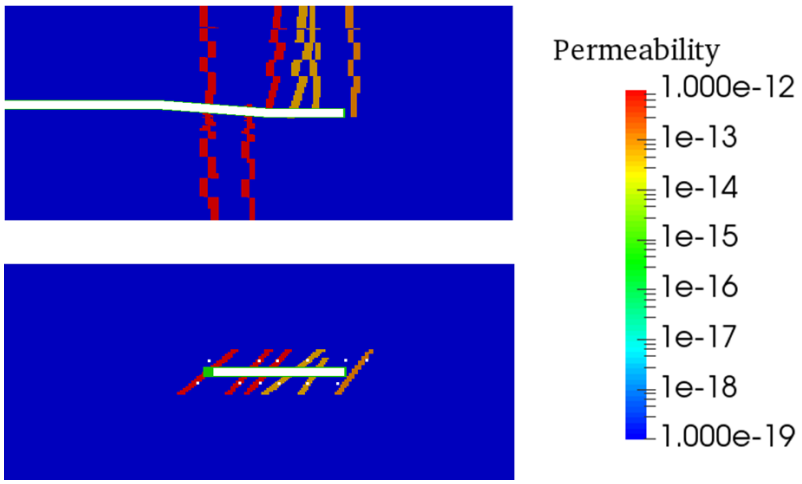

Figure 183. Simplified model based on the conceptual model

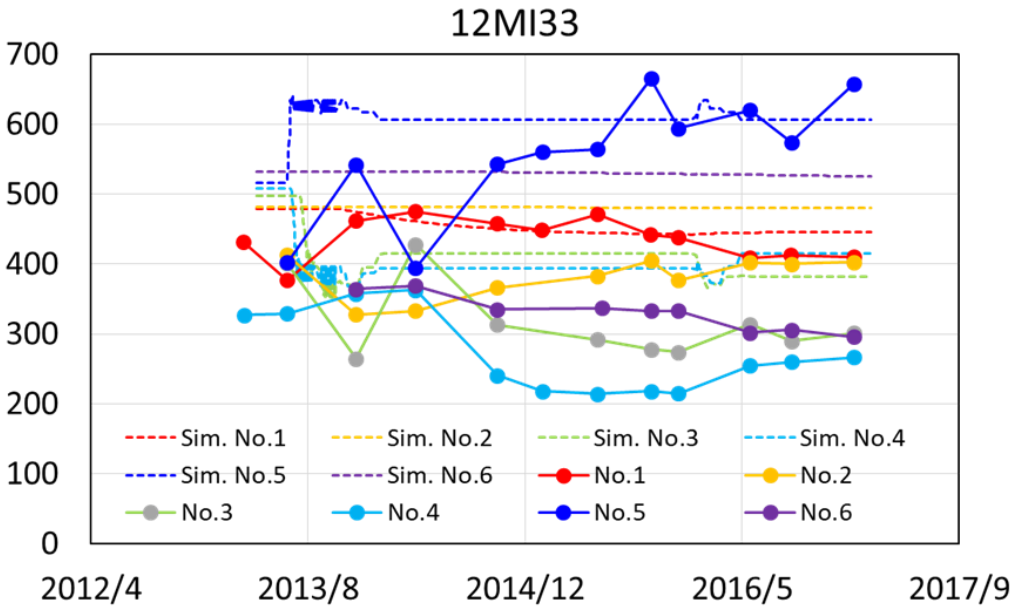

Figure 184. Simulated Cl concentration from the simple model in 12MI33

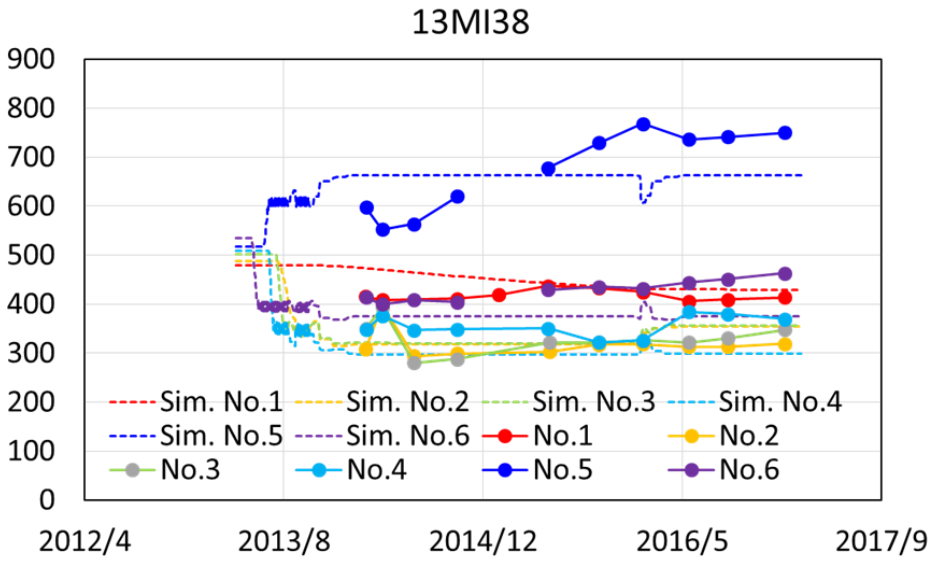

Figure 185. Simulated Cl concentration from the simple model in 13MI38

In our simulated results, this kind of response clearly appeared at section 3 in 13MI38. Figure 187 shows both simulated and observed results at section 3 in 13MI38. In our simulated results, a temporal increase of Cl concentration appeared while the response is not clear in the observed data at this monitoring section. In the model, we introduced the fracture connecting to the shallower part that is the preferential path of low salinity water. The increase of hydraulic pressure due to the closure test makes the gradient of water pressure around the CTD is decreased. Then, the Darcy velocity and supply of low salinity water from the shallower depth decreased according to the pressure recovery. Hence the Cl concentration at the monitoring section would be decreased. From these results, the disturbance of the chemical condition by excavation and operation of the underground facility would be partly affected by the change of the advective condition after the closure. However, the effect is slight and it would take a long time to recover the chemical condition after closure.

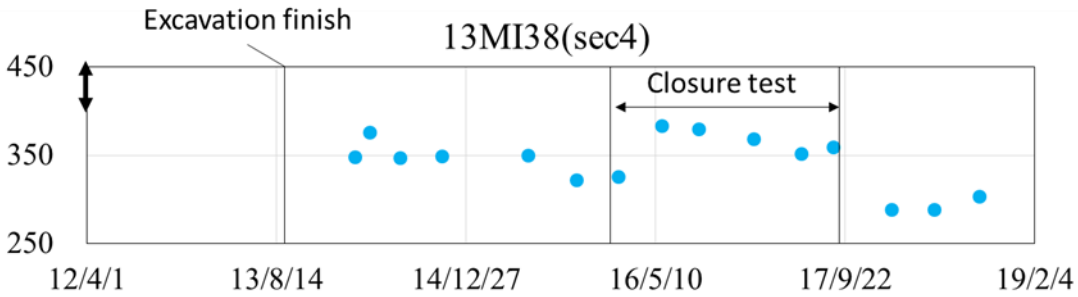

Figure 186. Reponse of Cl concentration during clorue test

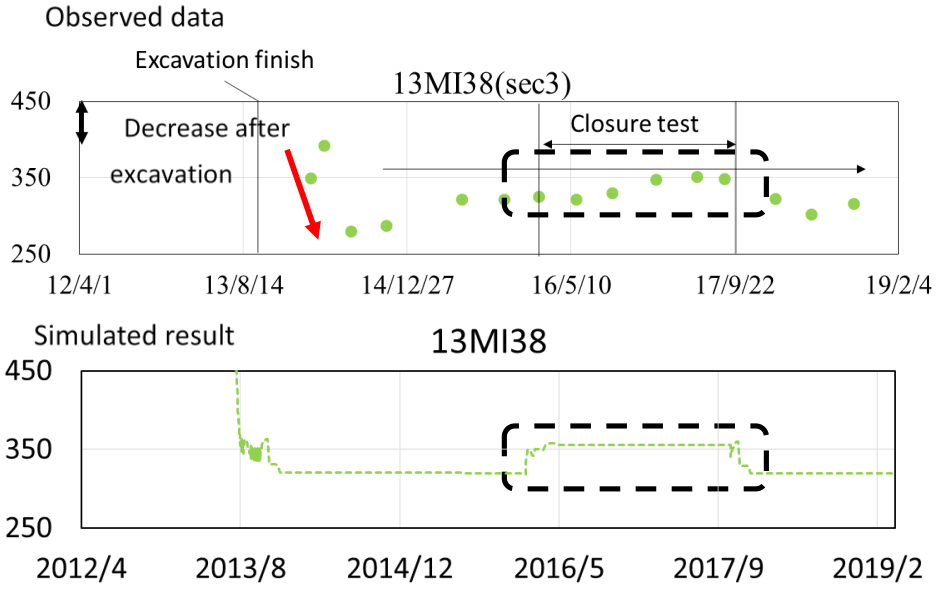

Figure 187. Simulated Cl concentration during closure test at section3 in 13MI38

9 Results of Step 2 modelling (SNL)

The work for Step 1 performed at Sandia National Laboratories reported in Section 4 has been updated to incorporate new data and to conduct new simulations using a new larger base case domain. The new simulations also include statistical analysis for different fracture realizations. A sensitivity analysis was also conducted to the study of the effect of domain size. A much larger mesh was selected to minimize boundary effects. The DFN model was upscaled (converted) to equivalent continuum for the new base case domain and the much larger domain to generate relevant permeability and porosity fields for each case. The updated calculations for Step 2 are described in Section 9.1. New calculations have also been conducted to model the flooding of the CTD and the resulting pressure recovery. The modelling includes matching of pressure and Cl experimental data at the six observation locations in 12MI33. Note that because the fracture model was not updated to include data from other wells, this chapter only deals with 12MI33. Thus, other monitoring locations were not considered. The modelling was done for the 10 fracture realizations. The Step 2 recovery simulations are described in Section 9.2. The Step 2 work is summarized in Section 9.3.

9.1 Update of inflow modelling

In Step 1 analyses (Section 4.3) simulations were carried out for a fracture model using a Visualization Area domain, which is a CTD-scale domain. In that set-up one side of the CTD-scale domain coincided with the inlet of the inclined drift. Subsequently the base domain was enlarged to reduce boundary effects. The new base case domain size is 200 m x 300 m x 200 m, with a constant cell size of 2 m x 2m x 2m, resulting in a mesh size of 1,500,000 grid blocks. The cell size was increased to keep the same number of grid blocks as in Section 4. In this set-up the inlet to the inclined drift is away from the domain side boundaries, and the tunnel is situated near the middle of the domain.

9.1.1 Statistical analysis using updated fracture model

Fracture characterization for the new domain and mesh was conducted using the method detailed in Section 4.3. Figure 188 represents the DFN method with the tunnel and location of fracture trace data. The figure shows the CTD-scale domain and the new enlarged domain. For this study 10 DFN realizations were generated to provide a

measure of uncertainty. Figure 189 and Figure 190 show DFN permeability and aperture for one of the realizations, respectively. The DFN permeability and porosity results for the 10 realizations were upscaled (converted) to a continuum mesh for use in flow and transport simulations. Figure 191 and Figure 192 show the upscaled equivalent continuum model permeability and porosity fields for the same realization.

PFLOTRAN simulations were conducted using the method described above. An initial condition run was made with the new mesh to set hydrostatic pressure and Cl concentration gradient. As was done in Step 1 specified pressure and Cl boundary conditions were applied to the top, bottom and side domain boundaries. Figure 193 shows the new mesh and location of the inclined drift and CTD tunnel components. Figure 194 shows the steady state hydrostatic pressure representing the initial condition used for Realization 2. Flow and transport simulations were then conducted as the excavation progressed, applying constant atmospheric pressure boundary conditions at the tunnel walls to the excavated portion of the tunnel. The simulations ran for the duration of the excavation. The output of the 10 realizations provided inflow rate and pressure and Cl predictions at observation points. Figure 195 shows distributions of pressure and Cl concentration along the tunnel axis at the end of the simulation time for Realization 2. Note that Cl concentrations are in molar values, the unit used in PFLOTRAN. Conversions between the original units (mg/L) and molar are described in Section 4.3.2.1. Figure 196 shows predictions of inflow for the 10 realizations together with experimental data points. The figure shows a better prediction of inflow for the inclined drift than the total inflow (inclined drift + CTD). As shown in Figure 195 the pressure drawdown reaches the boundary of the domain indicating boundary effects. Section 9.1.2 describes simulations for a larger domain. Future simulations could improve the predictions when additional fracture data are incorporated in the fracture characterization method. Note that Realization 2 was selected for illustration purposes. The inflow prediction for this realization closely matched the inflow data (Figure 196).

9.1.2 Effect of domain size on inflow modelling

In this section the effect of the boundary conditions set for the site-scale domain is studied by changing the domain size of the base case. For this study a larger domain size was used. A 1386 m x 1486 m x 806 m (vertical) domain was selected to conduct inflow simulations. The new mesh contains 2,352,987 grid blocks. The mesh includes the base case mesh together with progressively increasing grid block sizes. Discretization of the base case mesh and the new enlarged mesh are shown in Figure 197 and Figure 198,

respectively. For the larger domain the same DFN realization as in Section 4.3 was used to produce an upscaled (converted) equivalent continuum fracture model.

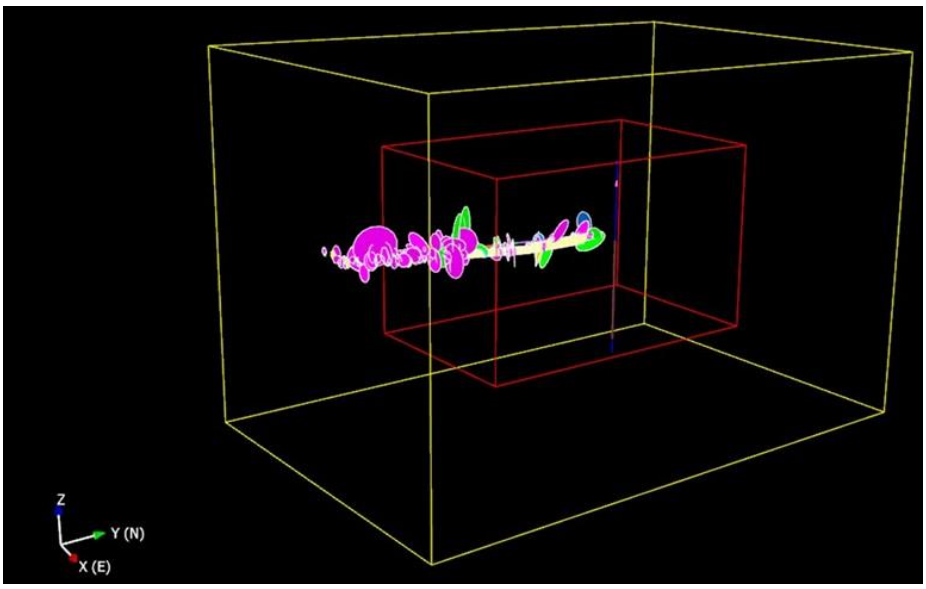

Figure 188. Representation of enlarged domain with mapping of fracture traces

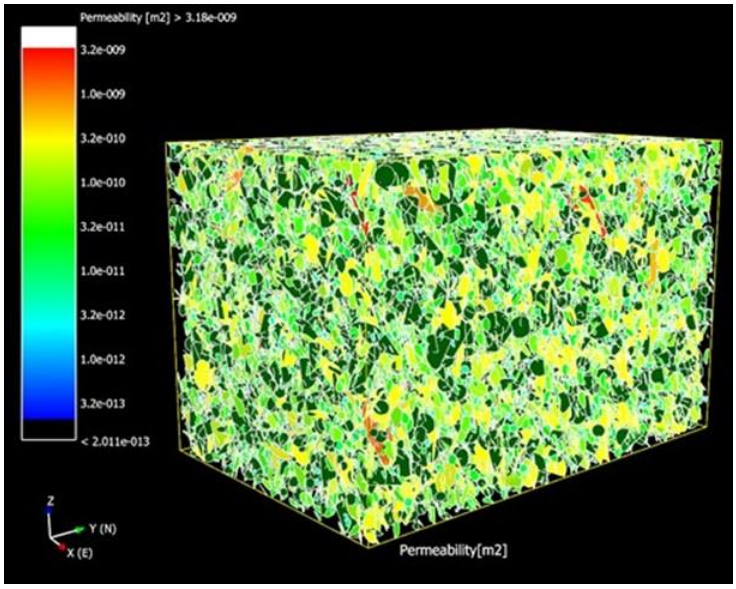

Figure 189. DFN permeability field for Realization 2

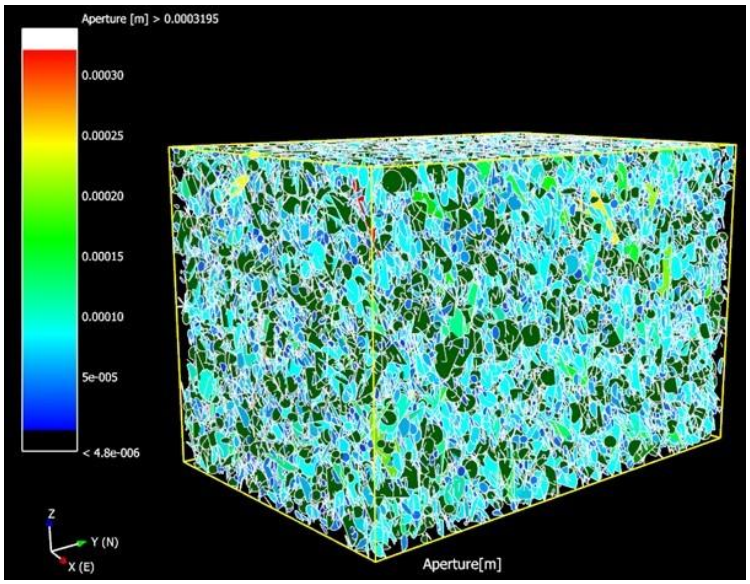

Figure 190. DFN distribution of aperture for Realization 2

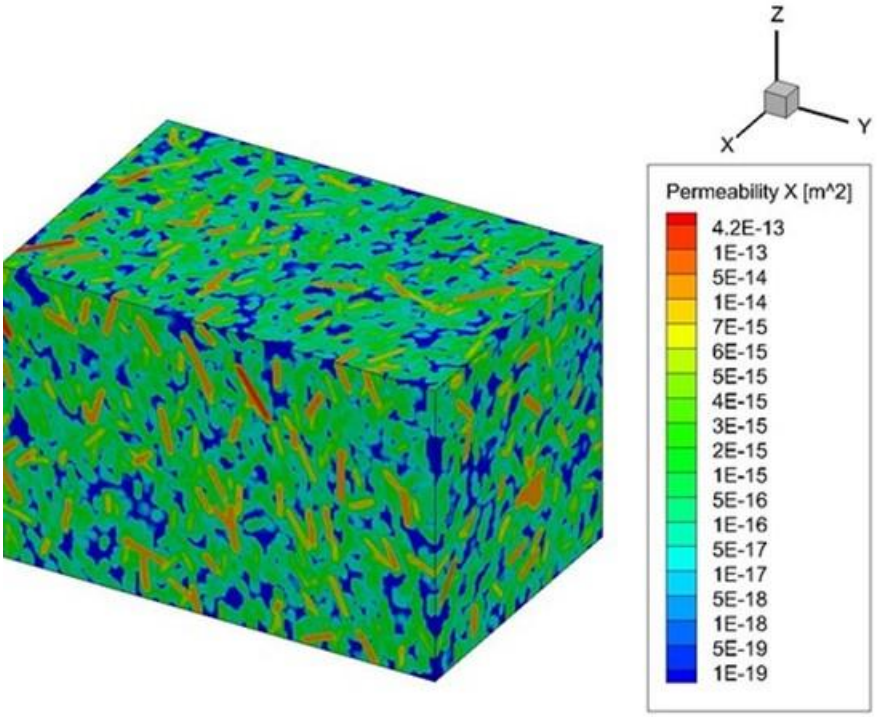

Figure 191. Upscaled permeability field for Realization 2

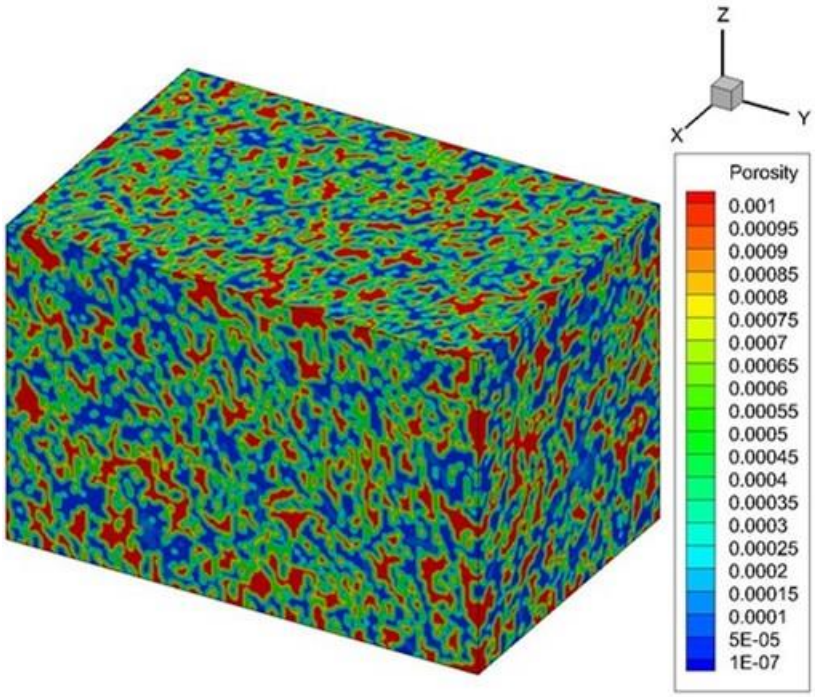

Figure 192. Upscaled porosity field for Realization 2

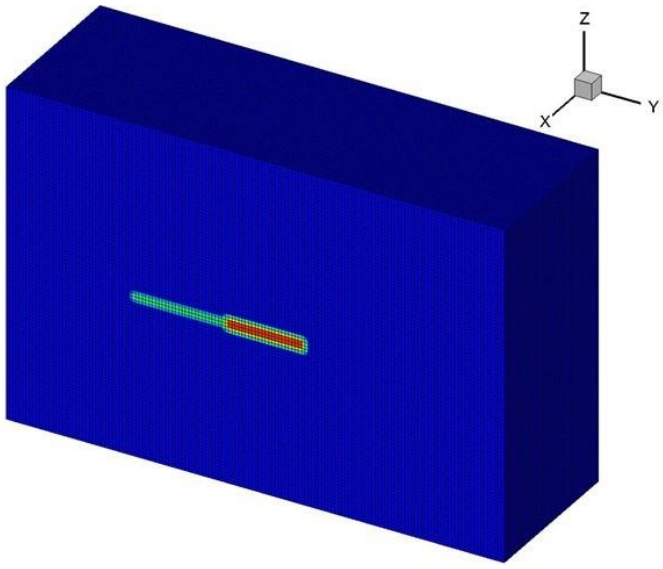

Figure 193. New base case mesh and new location of Inclined Drift and CTD near the middle of the domain. The different colours represent different materials.

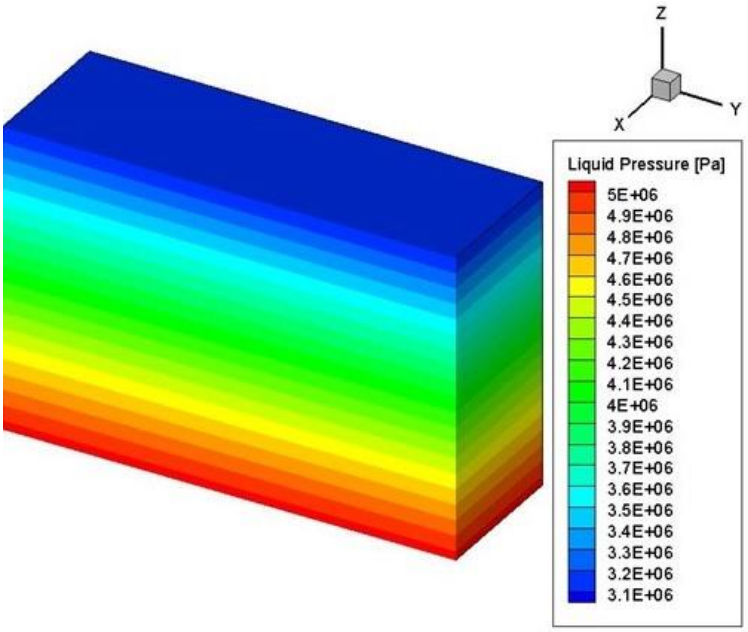

Figure 194. Step2a: Steady State Pressure Distribution for Realization 2

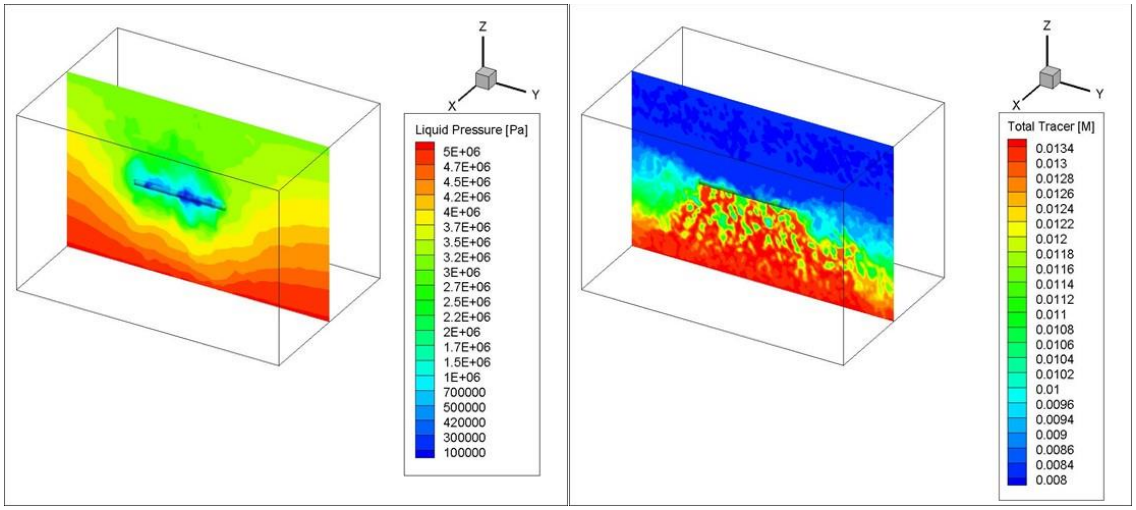

Figure 195. Pressure and Cl distribution along tunnel axis for Realization 2, after 173 days simulation time. Note that Cl concentrations are in molar values, the unit used in PFLOTRAN.

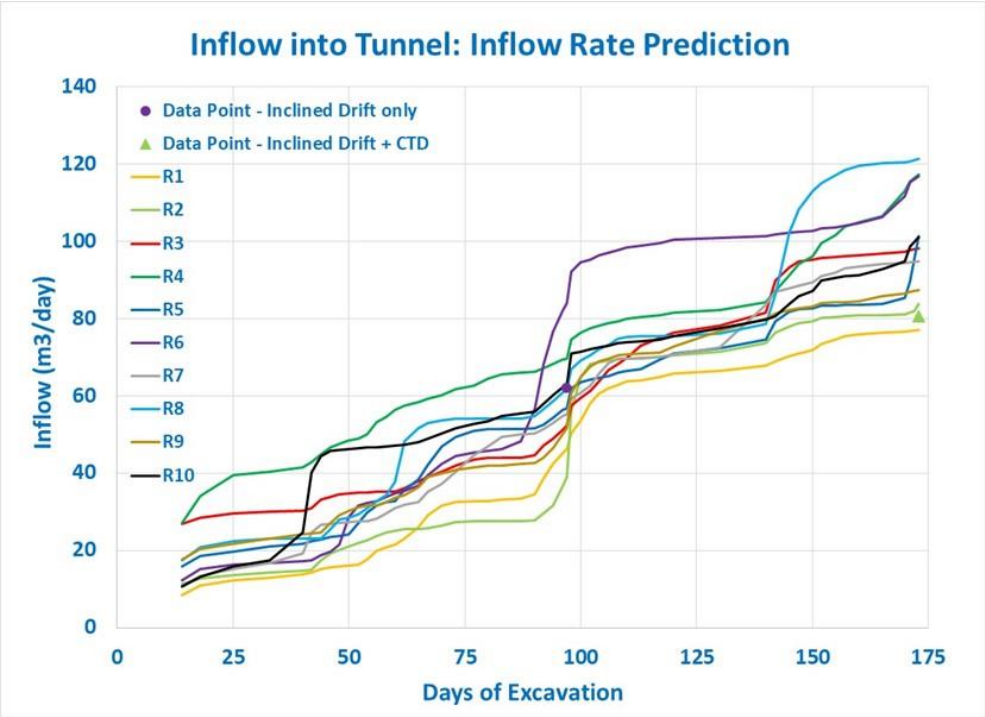

Figure 196. Inflow prediction for 10 realizations using new domain

The same procedure as in Section 4.3 was followed to estimate the inflow for the larger domain. Figure 199 shows pressure distributions along different axes for the larger domain at the end of the simulation time (173 days). The figure shows pressure drawdown around the excavated tunnel parts due to the inflow of water as the tunnel was excavated. In this case the pressure drawdown is confined to the middle of the domain, close to the excavation, as opposed to that of the base case domain where the pressure drawdown covers a large part of the domain (Figure 195). Figure 200 shows predictions of inflow for the specified 10 DFN realizations. The plot shows predictions for the base case domain (smaller domain) and the larger domain, together with experimental data. Significantly reduced inflow was predicted for the larger domain. It indicates that assigning boundary conditions close to the tunnel significantly influences inflow predictions.

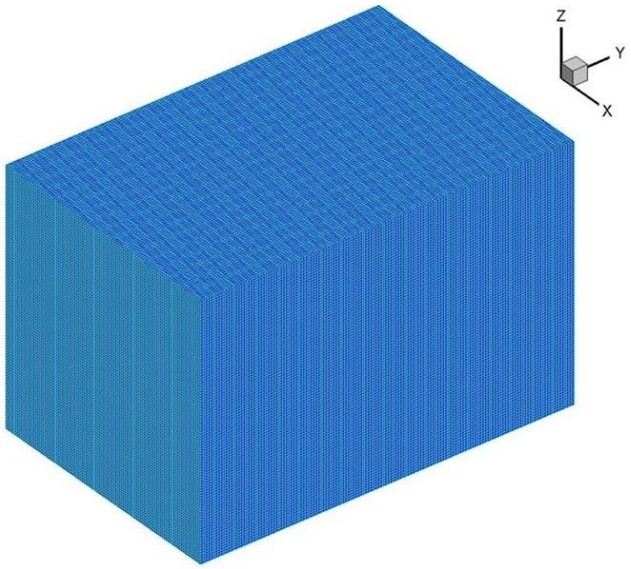

Figure 197. Base case site scale domain discretization

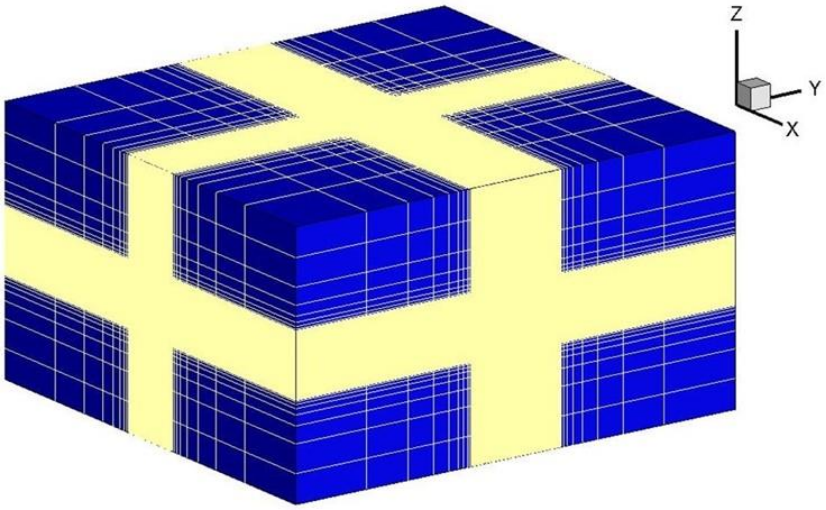

Figure 198. Discretization for the enlarged domain

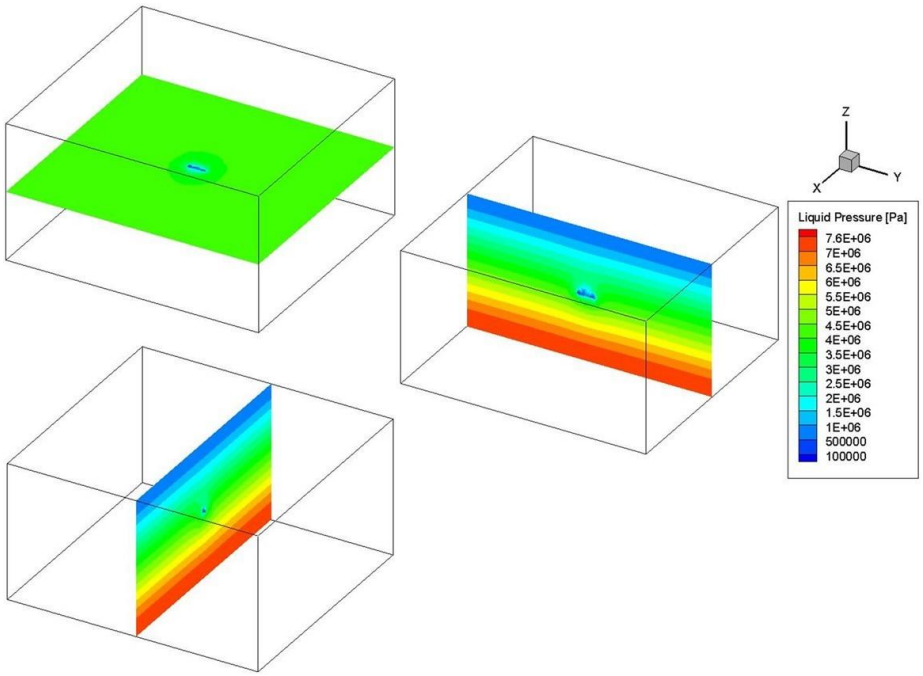

Figure 199. Predicted pressure distributions for Realization 2 after 173 days simulation time for the large domain

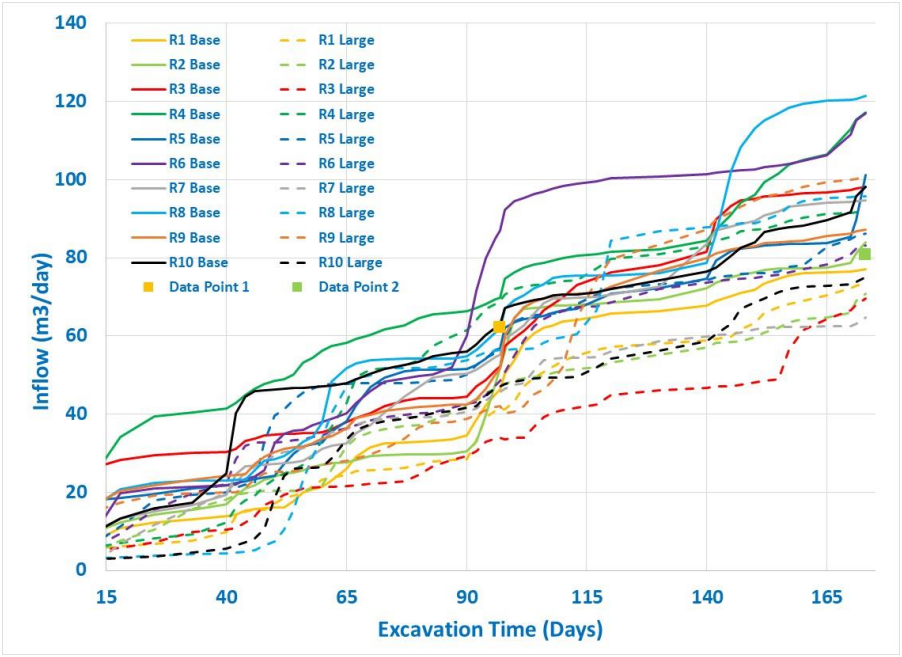

Figure 200. Predicted inflow into Inclined Drift and CTD: Comparison of predictions for the base case and larger domains, together with experimental data. Data Point 1 is for inflow into Inclined Drift only and Data Point 2 is for combined inflow into the Inclined Drift and CTD.

9.2 Modelling of recovery during water filling experiment in CTD

The GREET project conducted further flow, transport and chemical tests after the excavation of the inclined drift and the CTD. The experiments include installing a concrete plug to isolate the CTD, filling the CTD with water and observing hydraulic and chemical recovery following the excavation of the tunnel. The timeline shown below indicates durations of major tests starting from the excavation of the tunnel.

- Incline drift and CTD excavation: 4/20/2013 to 10/14/2013
- Construction of impervious plug: 11/3/2014 to 6/2/2015
- First water-filling test (plug performance test): 8/24/2015 to 10/5/2015
- Injection of water to CTD at 500 m: 1/8/2016 to 1/25/2016
- CTD full of water: 1/25/2016 to 9/5/2017

In this section filling of the CTD with water and associated hydraulic and chemical recovery only are modelled. This covers the fourth and fifth bullets shown above. Results of flow and non-reactive transport simulations are presented.

9.2.1 Modelling of flow during the recovery experiment

For recovery simulations experimental data from the CTD and borehole 12MI33 were used. The initial conditions in the CTD and at the observation points is shown below.

- Initial pressure at CTD: 1 atm.
- Initial pressure data at observation points in Borehole 12MI33:
    - P1 = 3.822 MPa
    - P2 = 1.286 MPa
    - P3 = 1.76 MPa
    - P4 = 3.48 MPa
    - P5 = 3.79 MPa
    - P6 = 3.357 MPa

Note that the experimental data also include data from borehole 13MI38. These data were not used in this study because the borehole has not been included in the fracture, flow and non-reactive transport models.

Figure 201 shows experimental pressure recovery data provided by the GREET project. The data includes pressure history at the CTD and the observation points in the monitoring borehole 12MI33. As would be expected the data show more visible

pressure changes for observation points close to the CTD. JAEA project data shows that the concrete plug isolating the CTD did not function properly and that there was some leakage. The experimental leakage data are shown in Figure 202.

For the flow simulations the base case domain and mesh described in Section 9.1 were used. It was assumed that the impermeable concrete plug totally isolates the CTD from the inclined drift. The inclined drift was initially represented with 1 atmosphere pressure boundary condition at the tunnel walls. This resulted in pressure drawdown in observation points P5 and P6. A look at the experimental data in Figure 201 shows that pressures at P5 and P6 remained constant during the recovery experiments. To match the pressure history at these two points one option would be introducing deterministic lower permeable zones between the inclined drift and 12MI33. Such modification was not applied to the inflow prediction modelling and thus was not considered. A decision was made to remove the inclined drift from modelling so that pressures at the observation points are not affected by the imposition of 1 atmosphere boundary condition. Permeability and porosity fields of Realization 2 were applied and the PFLOTRAN numerical code was used. Initial conditions were obtained by running the model using experimental initial condition data described above.

The initial condition was obtained by setting the experimental initial pressure values (given above) for the observation points and running to steady state. The flow model was then run to one year (starting Jan. 7/2016) using the steady state as initial condition. Various approaches were utilized to match the measured data. Better results were obtained by applying the experimental CTD pressure history as a boundary condition at all CTD walls. The results of the simulation are shown in Figure 203 to Figure 212. Figure 203 and Figure 204 show pressure distributions at the beginning and end of the simulation time (360 days) for fracture Realization 2. Comparing the two figures it is evident that pressures in the CTD and the rock have recovered due to the filling if the CTD.

Figure 205 shows the predicted and experimental pressure history at the CTD centre during the recovery period. The simulation results are for the 10 realizations and show that the imposed boundary condition at the CTD walls are also represented at the centre of the CTD. Figure 206 shows predictions of flow at the CTD due to the imposed time varying pressure boundary condition at CTD walls for the 10 fracture Realizations. The predicted rate of flows is all negative, indicating an outflow from the CTD during the entire simulation period. The predicted negative flowrates could be a combination of any leakage through the concrete plug as well as outflow into the fractured rock. The magnitudes of the flowrates are larger than the measured leakage rate (Figure 202)

which may indicate additional flow into the rock. This may be checked through other methods such as geochemical analysis of the rock surrounding the CTD.

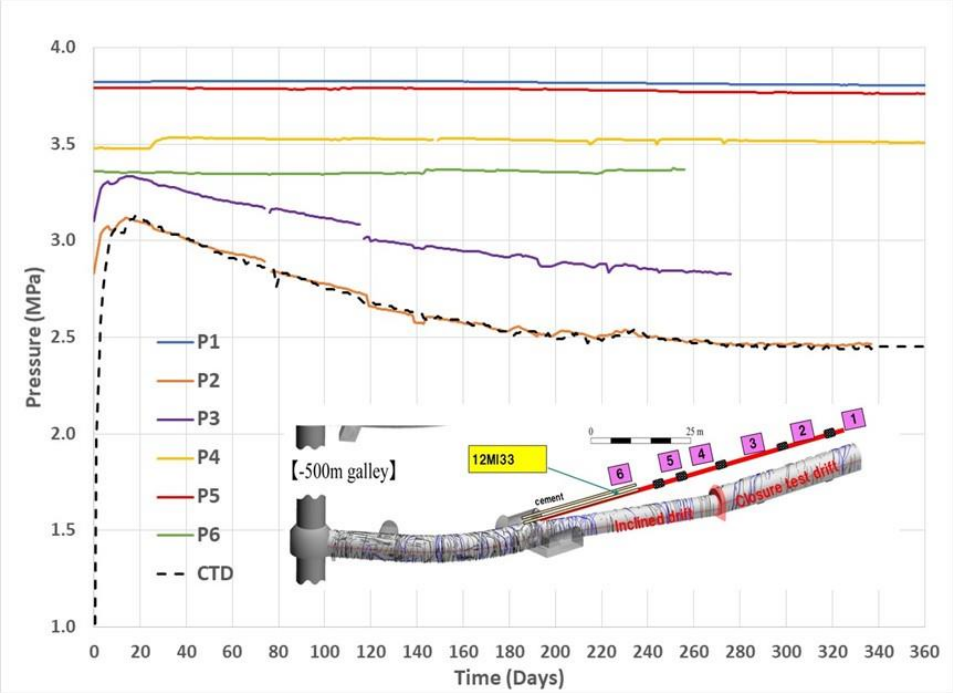

Figure 201. Experimental pressure recovery data in the CTD and at observation points in Well 12MI33

Figure 207 to Figure 212 show predictions of pressure history at the specified observation points in 12MI33 due to CTD water filling and post-filling pressure recovery. The figures show results for 10 fracture realizations together with the corresponding experimental data (dotted line). Figure 207 shows predictions for observation point P1. The experimental pressure data for P1 shows a constant pressure throughout the recovery period. This may indicate that the recovery experiment did not significantly affect pressure at P1. This may be because the location of P1 is at the edge of the CTD. The predicted pressure in P1 spans a range, with some of the realizations approaching the experimental data. A few of the realizations seem to have permeable connections to the CTD, resulting in lower pressures.

Figure 208 shows results for observation point P2. As shown in the figure, P2 is close to the CTD and is thus directly affected. The experimental data shows pressure decreases over time. Some of the predicted data closely match the trend. Figure 209 shows results for P3. As with P2, the observation point is close to the CTD. As with P2 the experimental

data show pressure decreases over time. Predicted pressure of some of the realizations match the experimental data.

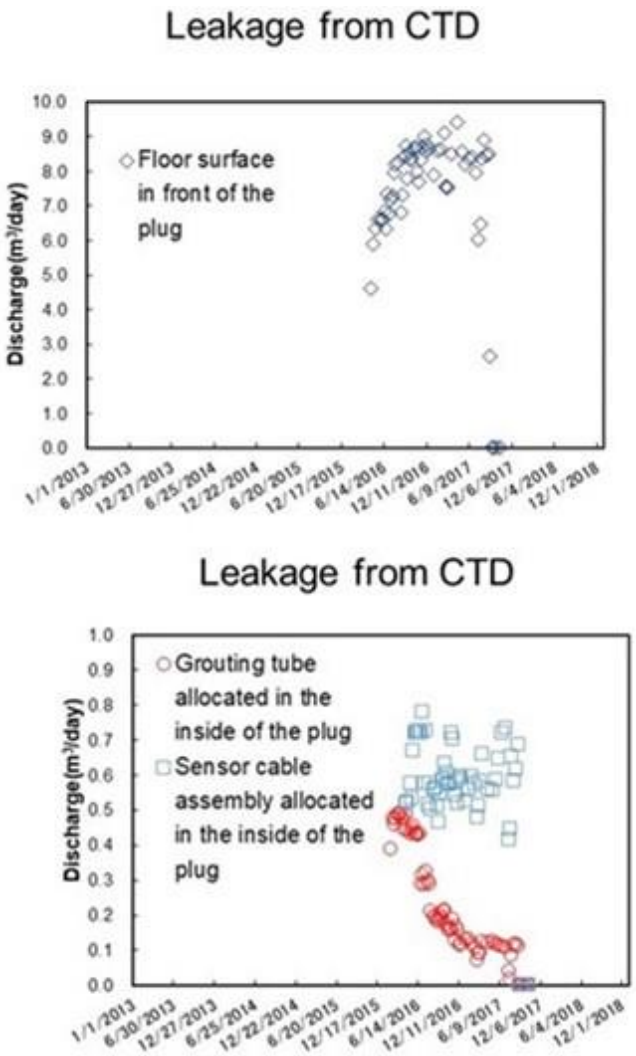

Figure 202. Experimental data of leakage from CTD during recovery experiment. Note that the upper figure includes leakage described in the lower figure.

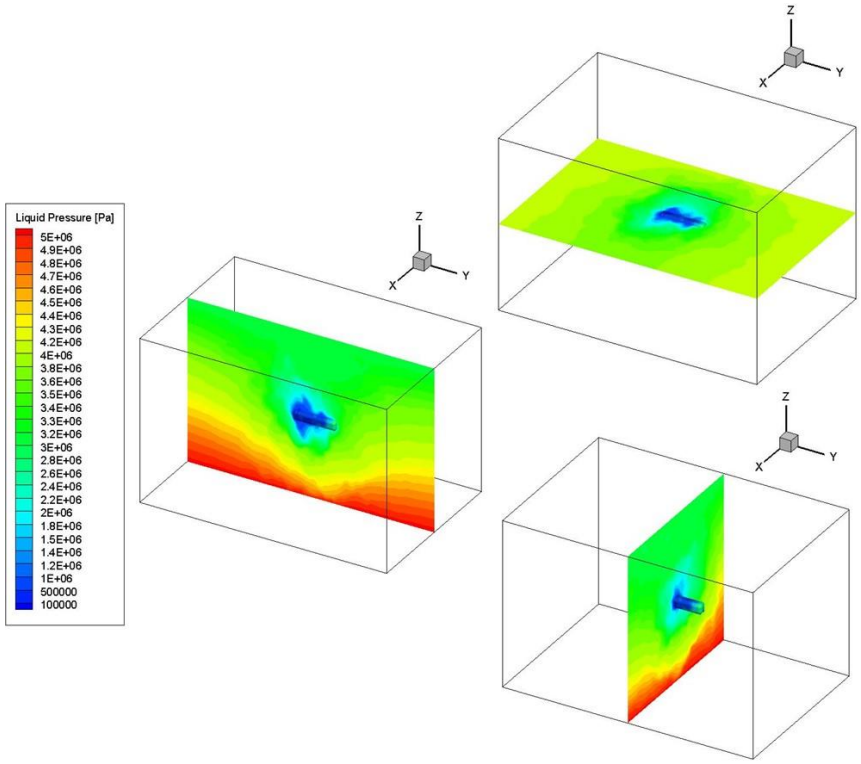

Figure 203. Predicted pressure distribution along tunnel axis at the beginning of the recovery simulation for the site-scale domain. Results are for Realization 2.

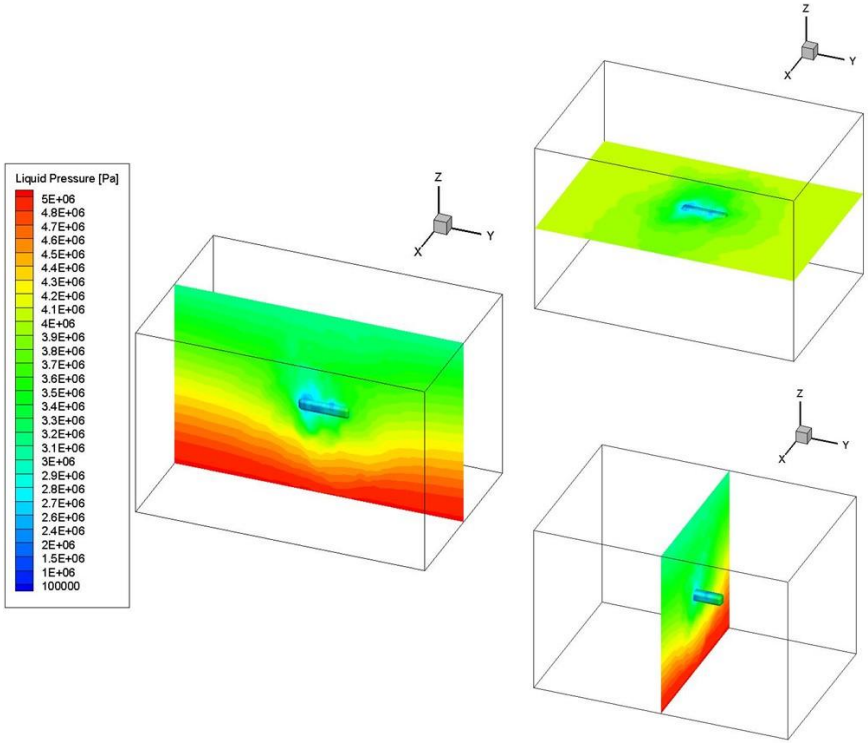

Figure 204. Predicted pressure distribution along tunnel axis after 360 days simulation time for the site-scale domain. Results are for Realization 2.

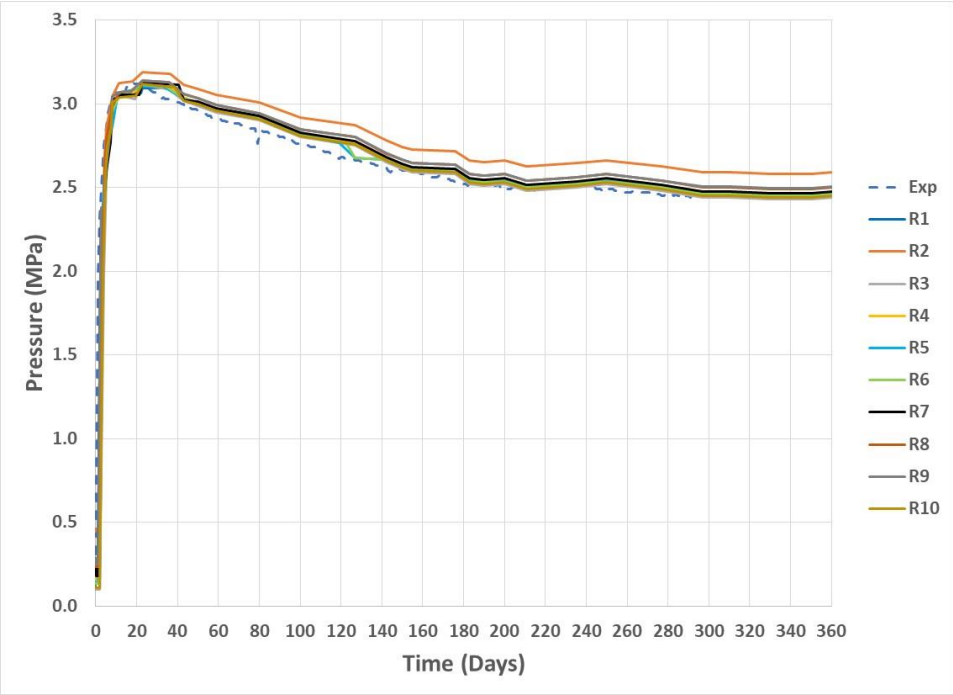

Figure 205. Predicted and experimental pressure recovery at CTD

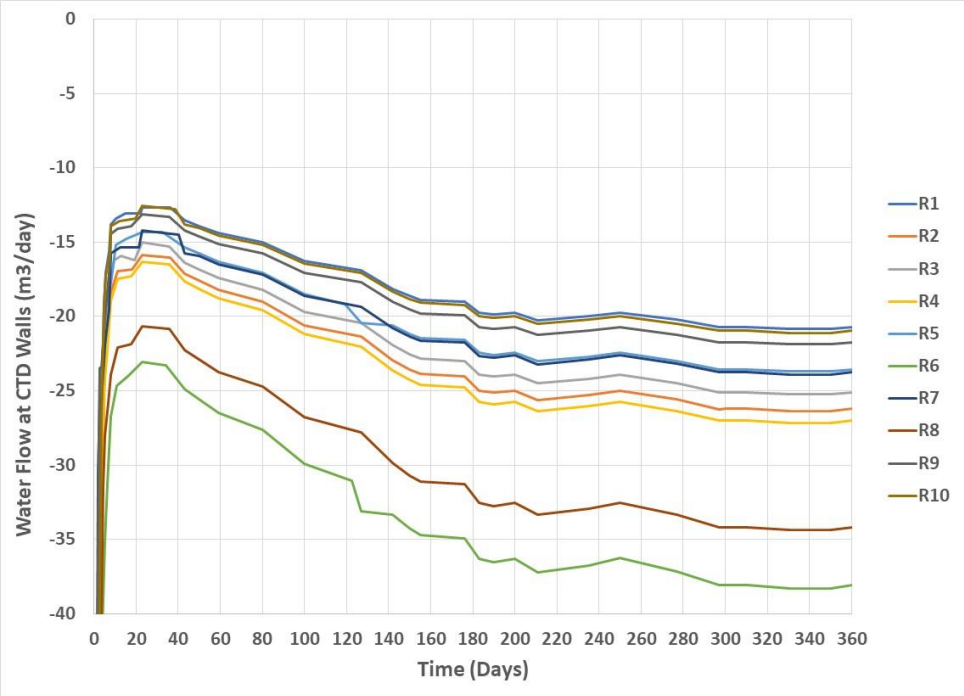

Figure 206. Predicted water flow rate at CTD during recovery for Realization 2. Positive water flow rate indicates inflow into CTD and negative flow rate shows outflow (or leakage).

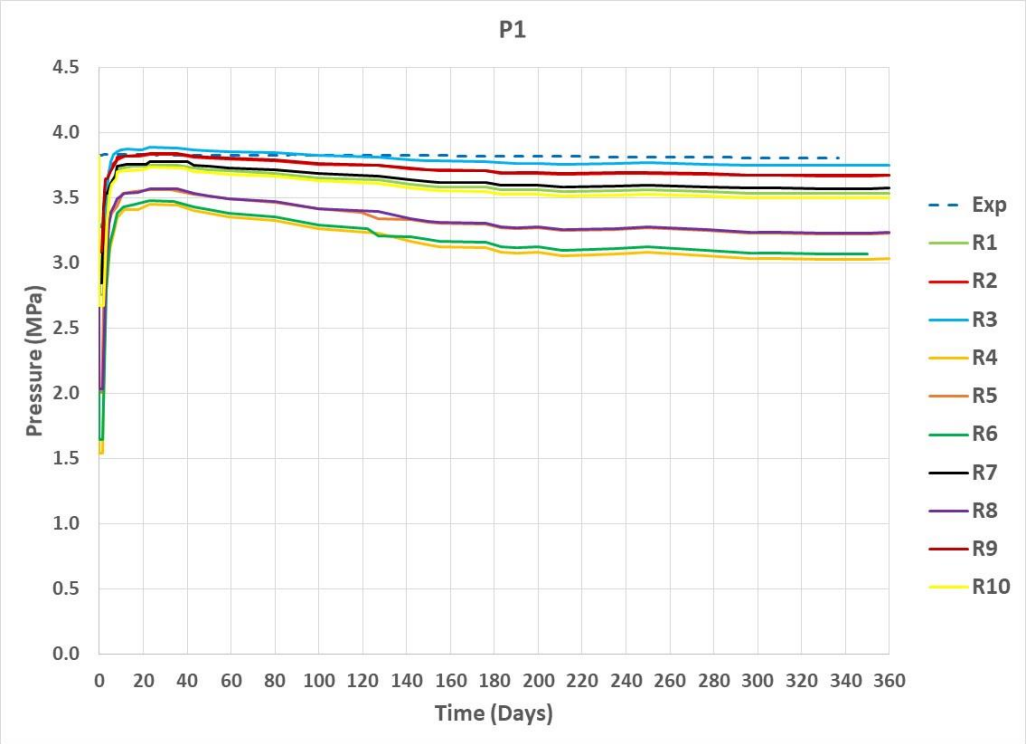

Figure 207. Predicted pressure recovery at Observation Point 1 (P1) in 12MI33 for 10 fracture realizations. The figure also includes experimental data for P1.

Figure 210 shows pressure history results for P4. The observation point is close to the inclined drift. The experimental data show a slight pressure decrease over time. As shown in the figure predicted pressure of some of the realizations match the experimental data. A few of the realizations may have permeable connections and thus resulted in decreased pressures. Figure 211 shows pressure history results for P5. The observation point is close to the inclined drift and thus may not be as influenced by the CTD filling as P3 and P2. The experimental data shows almost constant pressure over time. Predicted pressure of almost all of the realizations match the experimental data. Figure 212 shows pressure history results for P6. As with P6 the observation point is further to the left of the CTD and thus may not be as influenced by the CTD filling as the points to the right of it. The experimental data show almost constant pressure over time but lower than that of P5. In this case the predicted pressure for all realizations overpredict the experimental data. Further study would be needed to understand the discrepancy.

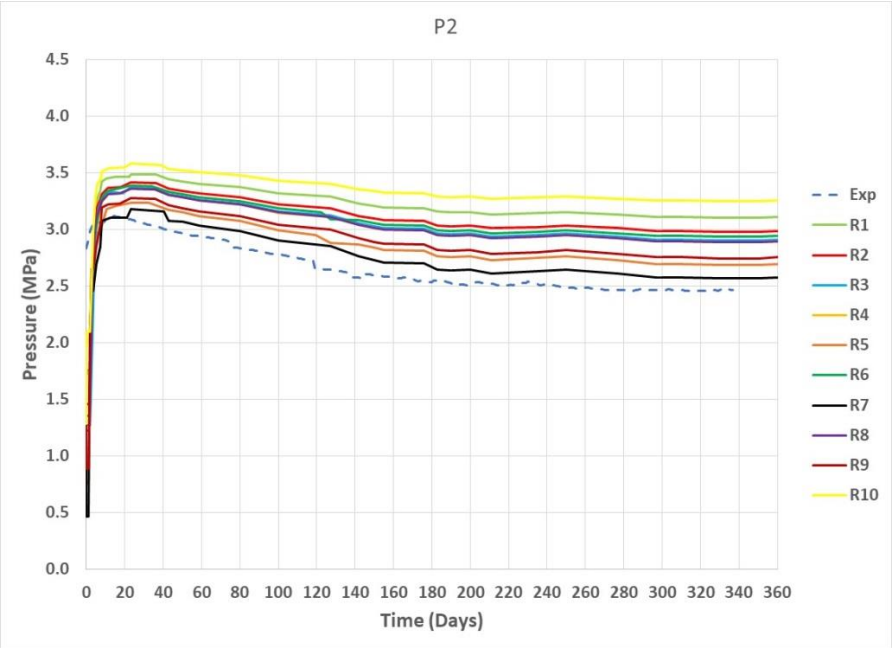

Figure 208. Predicted pressure recovery at Observation Point 2 (P2) in 12MI33 for 10 fracture realizations. The figure also includes experimental data for P2.

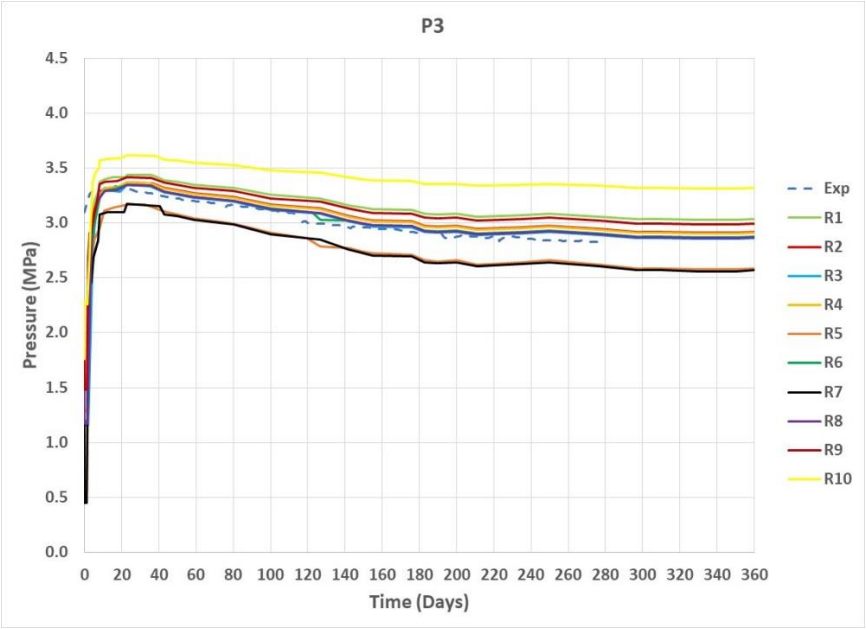

Figure 209. Predicted pressure recovery at Observation Point 3 (P3) in 12MI33 for 10 fracture realizations. The figure also includes experimental data for P3.

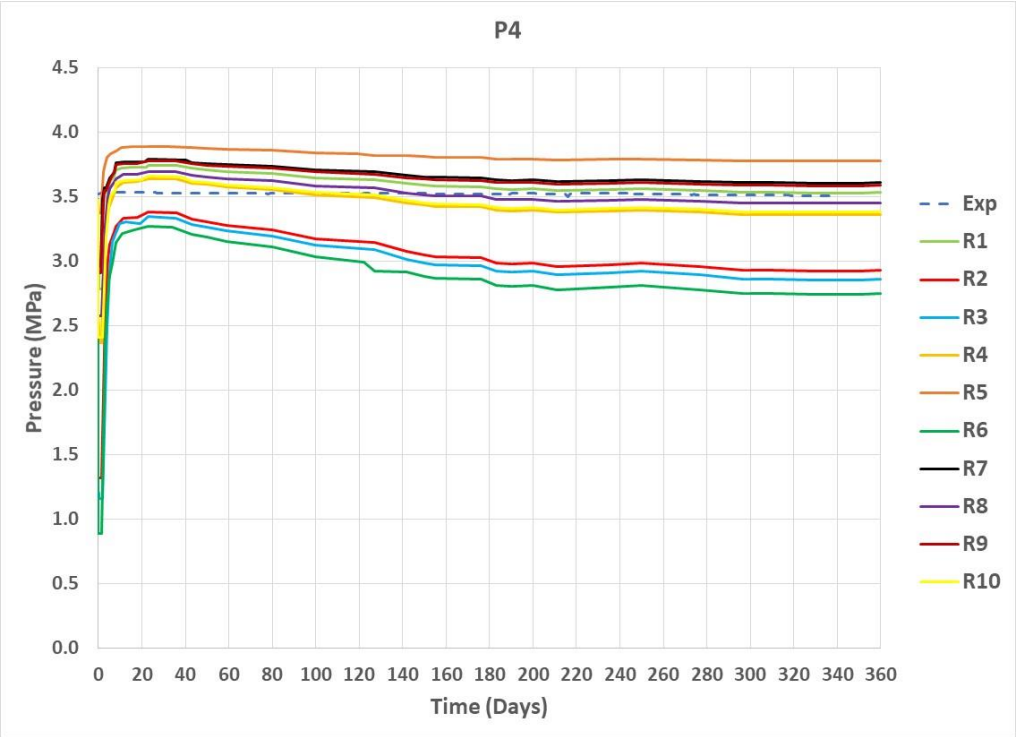

Figure 210. Predicted pressure recovery at Observation Point 4 (P4) in 12MI33 for 10 fracture realizations. The figure also includes experimental data for P4.

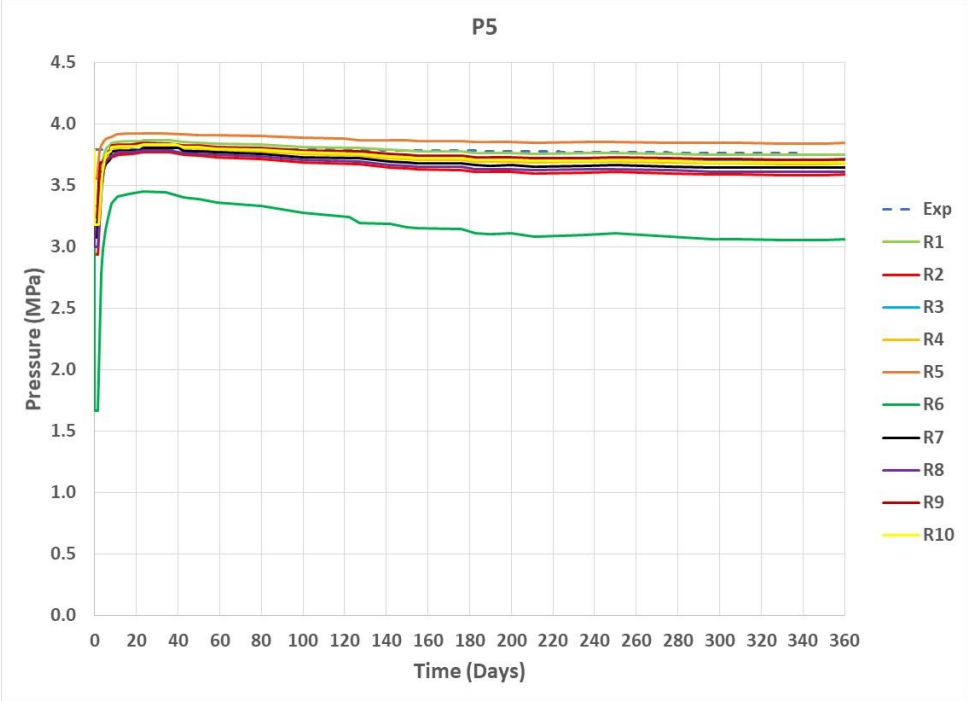

Figure 211. Predicted pressure recovery at Observation Point 5 (P5) in 12MI33 for 10 fracture realizations. The figure also includes experimental data for P5.

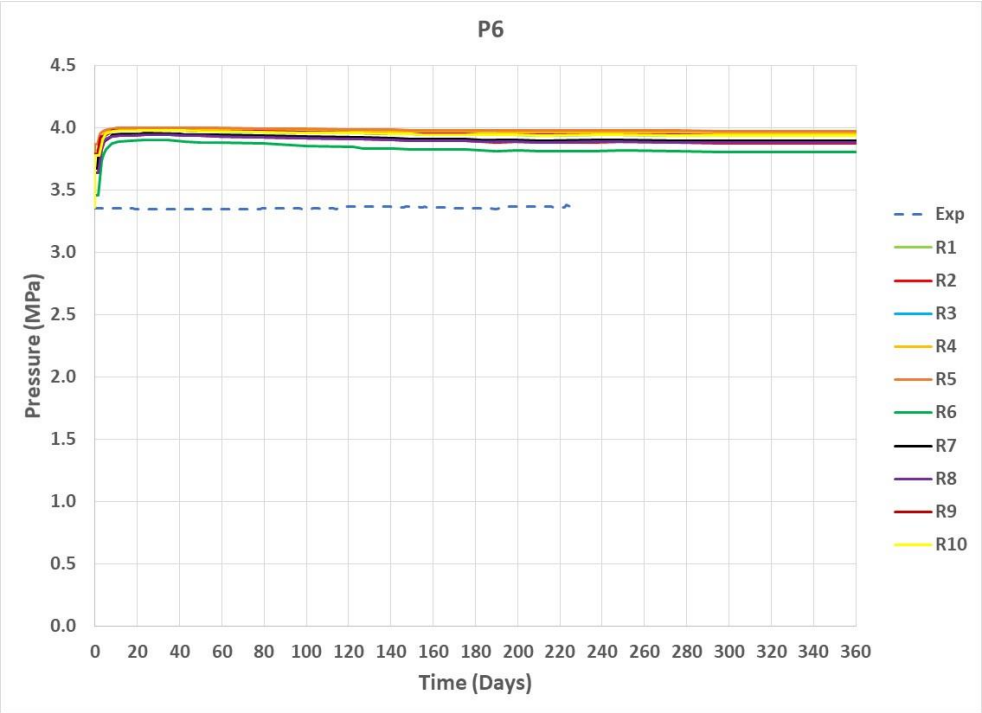

Figure 212. Predicted pressure recovery at Observation Point 6 (P6) in 12MI33 for 10 fracture realizations. The figure also includes experimental data for P6.

9.2.2 Non-reactive transport modelling during recovery experiment

For the transport simulations the same procedure as that of the flow simulations was followed. Initial conditions were obtained by running the model using experimental initial condition data described below.

- Initial Cl concentration at CTD: 475 mg/L (0.013398 M)
- Initial Cl concentration data at observation points in Borehole 12MI33:
    - P1 = 438 mg/L (0.012354 M)
    - P2 = 377 mg/L (0.010634 M)
    - P3 = 274 mg/L (0.007729 M)
    - P4 = 215 mg/L (0.006064 M)
    - P5 = 594 mg/L (0.016755 M)
    - P6 = 333 mg/L (0.009393 M)

The above concentration data were converted to molarity for use in PFLOTRAN (given in parenthesis). The conversion equation used was:

$$Conc.\,in\,M = \frac{Conc.\,in\,mg/L}{1000\ x\ 35.453}$$

with the molecular weight of Cl was 35.453 g/mol.

The initial concentrations at the CTD and the observation points in 12MI33 were used to generate the steady state conditions for the 10 fracture realizations. The non-reactive transport simulations then used the steady state conditions to model the recovery process. As with the flow simulations, the transport simulations used the experimental CTD Cl concentration history as boundary conditions on all the walls of the CTD. For all the transport simulations longitudinal dispersivity of 20.0 m and diffusion coefficient of 10^{-12} m^2/s were applied. The results were sensitive to longitudinal dispersivity but a selected value was not universally applicable to model concentrations at every observation point. Thus, a value of 20.0 m was selected for this study.

Simulation results are shown in Figure 213 to Figure 220. Figure 213 and Figure 214 show Cl concentration distributions at the beginning and end of the simulation for Realization 2.

Figure 215 to Figure 220 show predictions of Cl concentration history at the specified observation points in 12MI33 due to CTD water filling and post-filling pressure recovery. The figures show results for 10 fracture realizations together with the corresponding experimental data (dotted line). In general, matching Cl concentration data was not as smooth as that of pressure matching. Cl concentrations are highly sensitive to the hydrologic changes.

Figure 215 shows predictions for observation point P1. All the predicted concentration results for the 10 realizations underpredict the experimental data. Some of the realizations only slightly overpredict the measure data.

Figure 216 shows results for observation point P2. The predicted concentrations for the 10 realizations span a wide range. However, some of the predicted data are close to the experimental data at later times. Figure 217 shows results for P3. As with P2, the observation point is close to the CTD. The predictions are similar to that of P2.

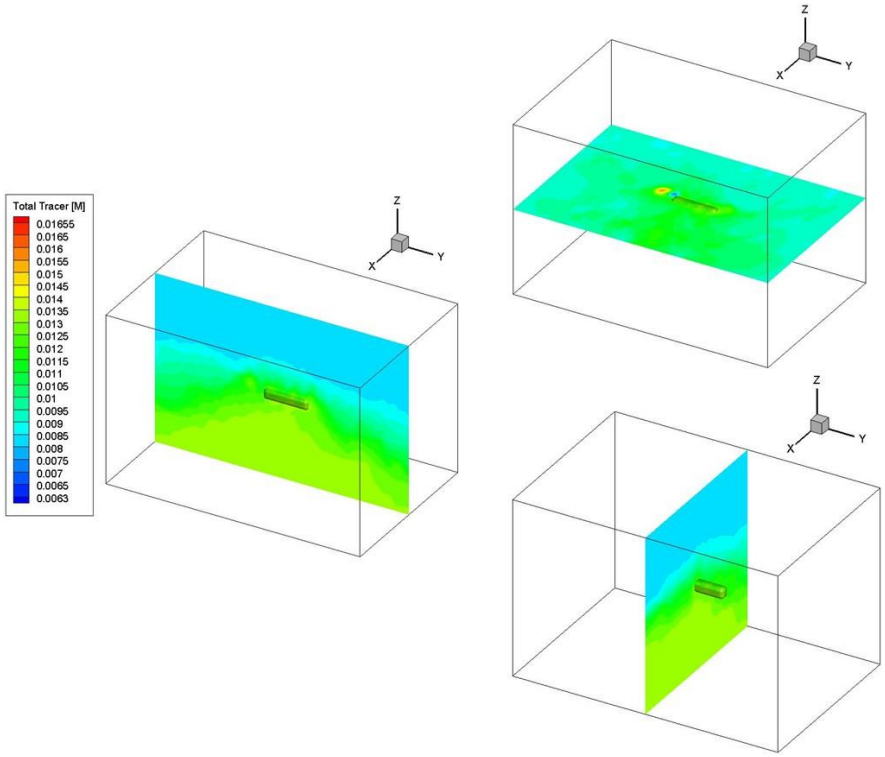

Figure 213. Predicted Cl distribution along tunnel axis at the beginning of the simulation for the base case domain. Results are for Realization 2.

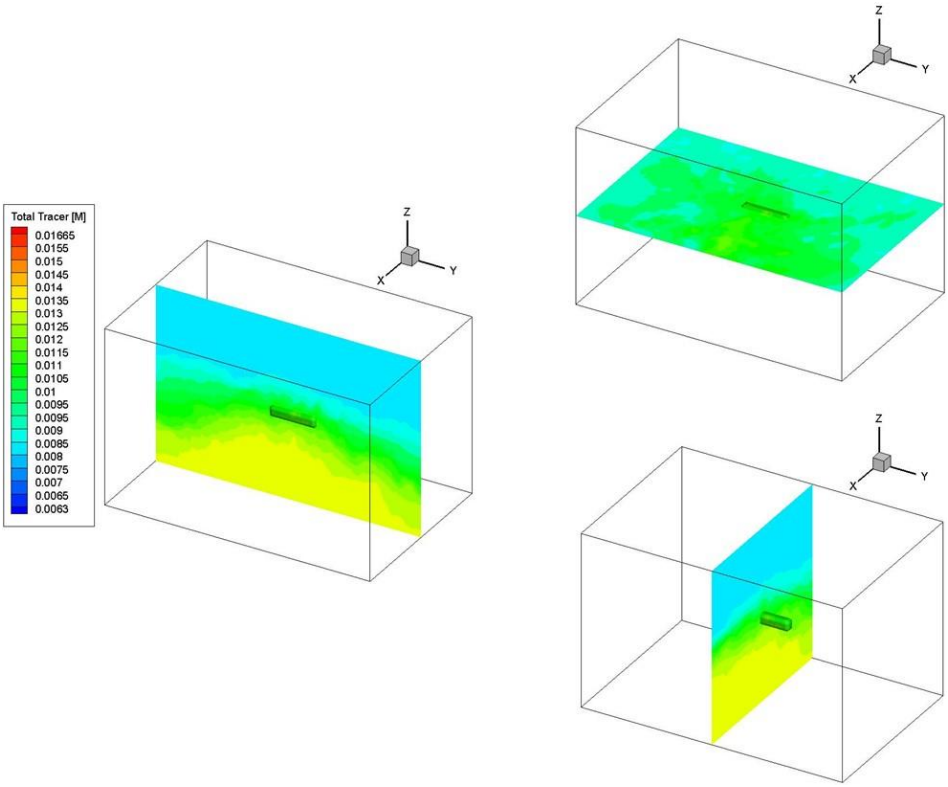

Figure 214. Predicted Cl distribution along tunnel axis after 360 days simulation time for the site-scale domain. Results are for Realization 2.

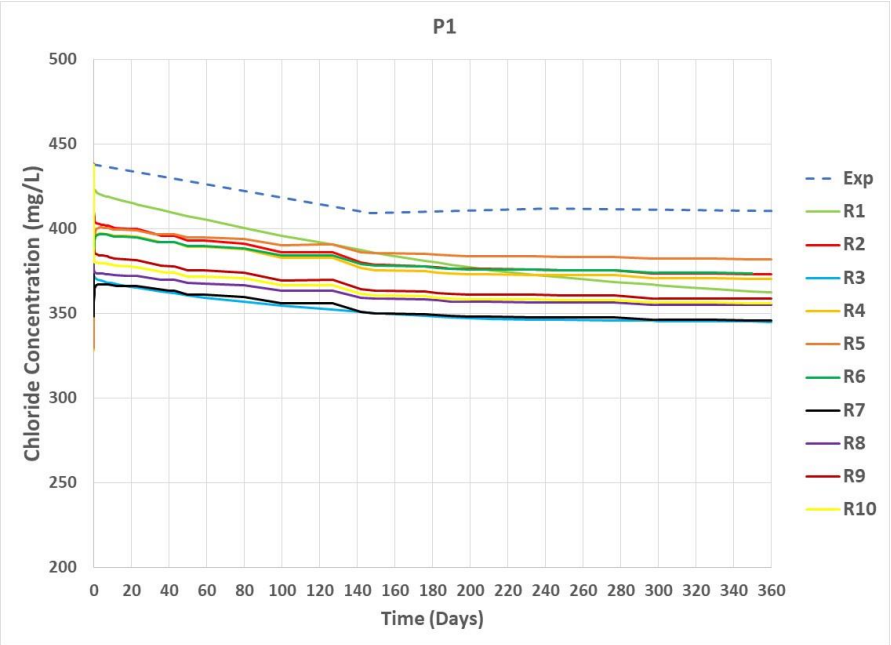

Figure 215. Predicted Cl concentration during recovery at Observation Point 1 (P1) in 12MI33 for 10 fracture realizations. The figure also includes experimental data for P1.

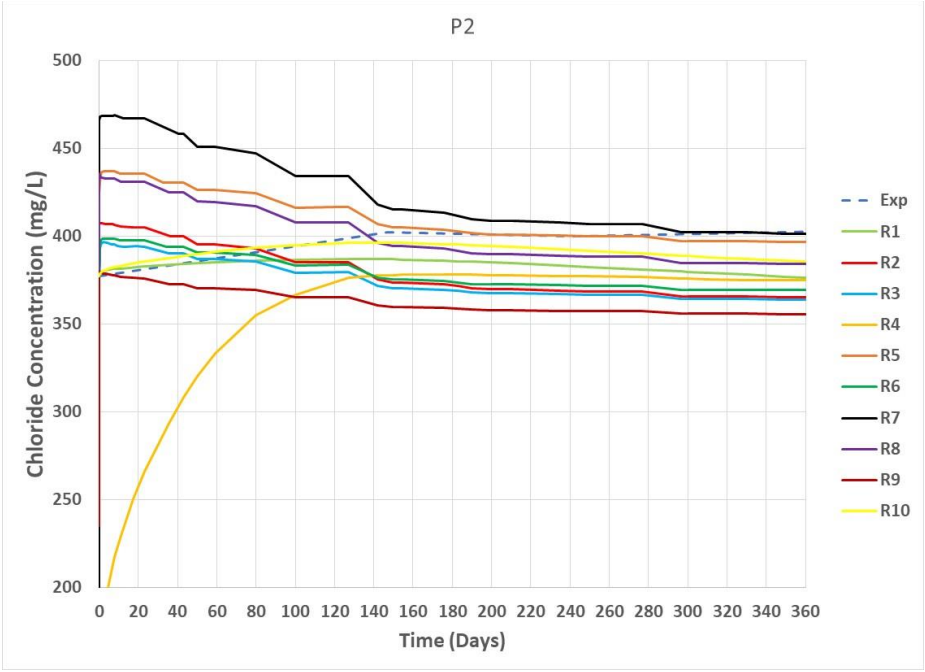

Figure 216. Predicted Cl concentration during recovery at Observation Point 2 (P2) in 12MI33 for 10 fracture realizations. The figure also includes experimental data for P2.

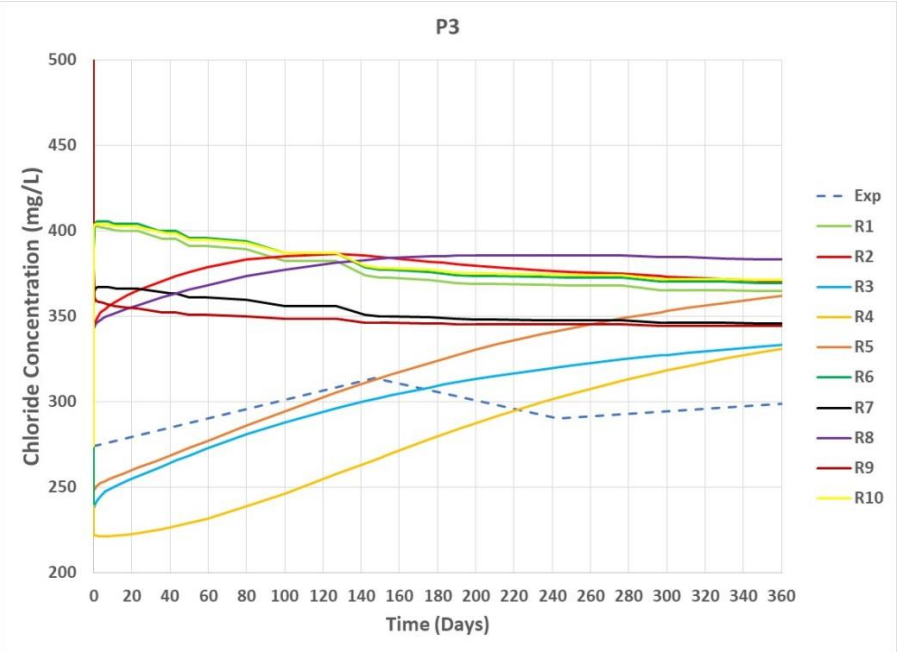

Figure 217. Predicted Cl concentration during recovery at Observation Point 3 (P3) in 12MI33 for 10 fracture realizations. The figure also includes experimental data for P3.

Figure 218 shows Cl concentration history results for P4. The observation point is close to the left side of the CTD. The results show that the predictions for all the realizations overpredict the experimental data.

Figure 219 shows Cl concentration history results for P5. The observation point is to the left of the CTD. The experimental data show much higher concentrations compared to the other observation points. It is not clear why the Cl concentrations are out of step while the pressure data are consistent with the other observation points. As would be expected, the predicted concentration values consistently underpredicted the experimental data. Additional analysis of the experimental data would be needed to address such an anomaly.

Figure 220 shows Cl concentration history results for P6. The observation point is further to the left side of the CTD. The results show that the predictions for all the realizations slightly overpredict the experimental data. The predictions are much better than that of P5.

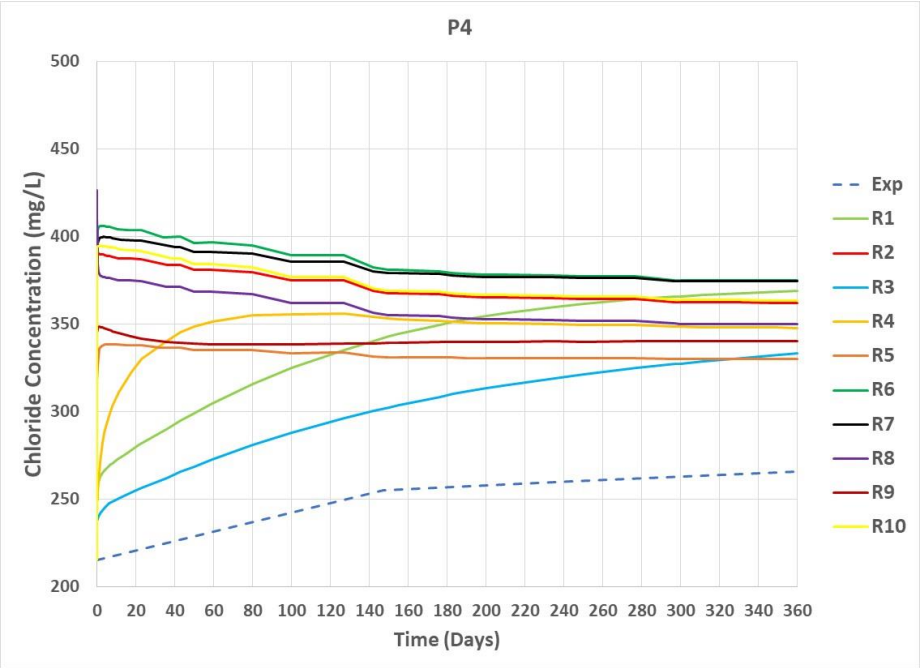

Figure 218. Predicted Cl concentration during recovery at Observation Point 4 (P4) in 12MI33 for 10 fracture realizations. The figure also includes experimental data for P4.

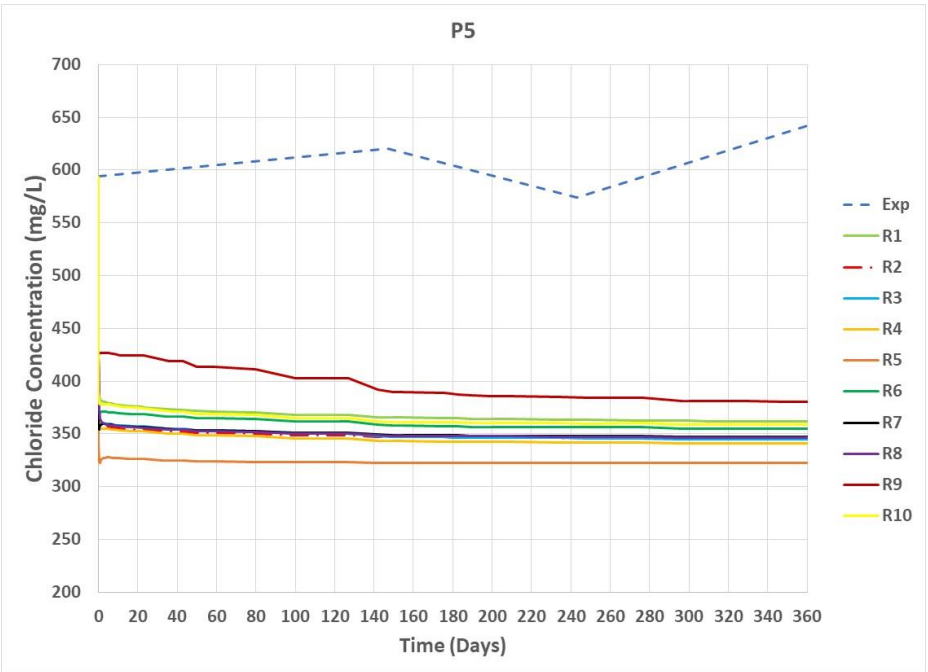

Figure 219. Predicted Cl concentration during recovery at Observation Point 5 (P5) in 12MI33 for 10 fracture realizations. The figure also includes experimental data for P5.

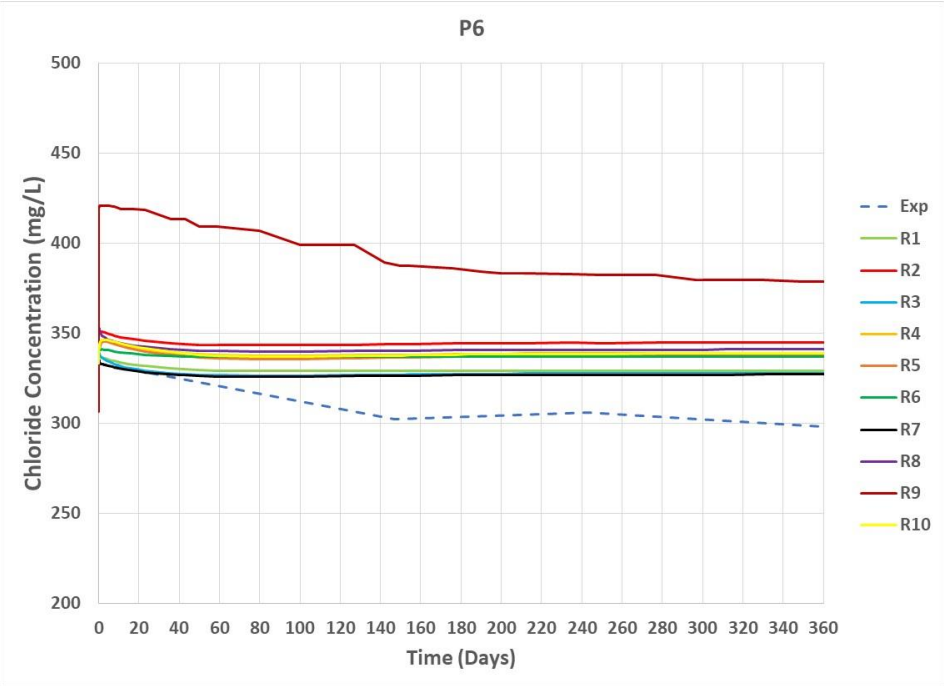

Figure 220. Predicted Cl concentration during recovery at Observation Point 6 (P6) in 12MI33 for 10 fracture realizations. The figure also includes experimental data for P6.

9.3 Summary of Step 2: flow and non-reactive transport modelling

Modelling analyses were conducted for Step 2. The analysis was based on a base case domain (200 m x 300 m x 200 m) that is larger than the original CTD-scale domain (100 m x 150 m x 200 m). The analysis also included fracture characterization using the base case domain. The fracture model produced 10 DFN realizations which were upscaled (or converted) to a continuum mesh for use in flow and transport. Boundary and initial conditions specified by the project were applied to flow and transport simulations. Project experimental data of excavation progress were also used. The simulation method previously developed and reported in Step 1 to simulate excavation progress by continuously removing material from the excavated area was utilized. The DAKOTA statistical analysis and optimization code and the PFLOTRAN numerical flow and transport code were used. Predictions of inflow into the inclined drift for the 10 realizations are reasonable when compared with the experimental data. The multiple simulations provided with a qualitative uncertainty range. For the base case domain

predicted inflow into the inclined drift was within the range of the experimental data. However, inflow of the combined inclined drift and CTD was largely overpredicted. This seems to be mainly due to boundary effects. Applying boundary conditions close to the tunnels would artificially maintain high pressures, resulting in higher inflows.

The analyses also included a study of domain size by comparing inflow results for the base case domain (200 m x 300 m x 200 m) with that of a much larger domain (1386 m x 1486 m x 806 m). The comparisons were done for all ten fracture realizations. Pressure distribution simulation results for one of the realizations show that the site-scale domain exhibited boundary effects while the larger domain had no such effects. As a result, the inflow results for the 10 realizations using the larger domain show significantly reduced values compared to the base case domain. Thus, the inflow is better predicted with the larger domain.

Simulations were also conducted to model water-filling of the plugged CTD and pressure recovery. For the analysis the base case domain with domain size of 200 m x 300 m x 200 m was used. The 10 upscaled fracture realizations were also used to provide permeability and porosity distributions. Top, bottom, and side boundary conditions and initial conditions specified by the project for the CTD-scale domain were modified to obtain values for the new domain. In addition, boundary conditions were added at the CTD walls to reflect CTD experimental data. Simulation results were compared with project experimental data. The results show that pressure predictions of many of the 10 realizations closely match the experimental data at the observation points in 12MI33. The predictions of Cl concentrations were not as close as the pressure predictions. Further study would be needed to understand all the discrepancies.

Future simulations could improve the predictions when additional fracture data (Borehole 13MI38) are incorporated in the fracture characterization method. It is also important to incorporate any damage around the tunnel as such data could influence local variations in pressure and Cl concentration. The transport results were also sensitive to longitudinal dispersivity but a selected value was not universally applicable to model concentrations at every observation point. Further examination of this would help identify the local flow and transport characteristics.

10 Results of Step 2 modelling (TUL)

The assignment for Step 2 was to calibrate the drainage phase model (excavation and after-excavation period) and to predict and calibrate the model for plug installation and CTD flooding phase of the GREET experiment. The section is structured so that the calibrations (inverse models) for both phases are discussed together, which is then split to more model variants, including separate calibration of drainage and flooding. Before this, there is a section defining the modelling procedure and configuration for the plug and the flooding. It includes the predictive model of flooding. Finally, two sections of supporting studies for understanding the chlorine transport are included. The last section contains the geochemical analysis, which has been made separately by the TUL's external expert J. Zeman. There are also consequences in this final section for modelling of transport presented before.

All the model configurations follow the "TUL3" model of Step 1 in Chapter 8 (near field / far field combination – deterministic fractures, inner continuum domain of matrix and outer equivalent continuum domain) and its latest "Rock3" variant (fractures partly penetrating from the inner domain into the outer domain).

Common notation

To simplify the work, these adaptations of the coordinates have been made:

- Besides the calendar dates, we also use time is expressed in numeric value of days in some notation, defining 17 Apr 2013 as time zero
- The spatial coordinates x, y are moved so that the origin is located in the main shaft, i.e. at x = 6451.6 m and y = -69007.4 m of the official coordinate system. Then the experimental tunnel is located in the interval of about 10 m < x < 20 m and 50 m < y < 150 m.

10.1 Plug closure modelling

The plug installation means hydraulically that the internal CTD volume is filled with water and divided from the remaining excavation by low permeability plug. In the model it is represented in two variants (simpler versus more realistic):

- By changing the boundary conditions (Figure 221 left) – specifying the zero flow on the tunnel wall at the location of the CTD. In this case, the volume of water in the filled tunnel is not considered as part of the model.

- By changing the function of the surface elements (Figure 221 right) – 2D elements on the tunnel wall (where the boundary condition was originally applied) were used to represent the volume of water in the closed part of the tunnel. The volume is represented by the thickness of the 2D elements and corresponds to the volume of the CTD tunnel. This approximation also made it possible to capture the effect of the seepage into the tunnels. The tunnel wall is therefore not the model boundary. Some of the 2D elements simulated the area with the semi-pervious plug, in contact with the free space on the opposite side, i.e. with a line boundary with zero pressure. The parameters for the 2D domain of CTD were set to values corresponding to free water: $K = 1 \times 10^{2}$ m/s as the extreme value beyond the most permeable rock, storativity 10^{-9} 1/m (water compressibility), porosity equal to 1 and an initial chlorine concentration of 475 mg/L (prescribed, known by the measurement).

Due to the difficulty in changing the boundary conditions in the area of the CTD in the first variant and the inability to change the function of the elements in the mesh during the calculation of the second variant, the flooding was approximated being as immediate. The process of rising water level is neglected and the state of the draining CTD wall is followed by the state of the fully filled CTD. The time period of the flooded state is from 10 January 2016 (day 998) to 10 May 2016 (day 1119) (the end date was chosen for variants without the transport, because the model already equilibrated). The model in the period of flooding is called the “flooding model” and the model in the period of drainage is called the “drainage model”. Shortening the period of the calculation to the flooding model only leads to its faster development. The flooding model uses the initial conditions of the previous drainage model after its stabilization.

The model does not consider the effect of the gradual flooding of the CTD and the mixing in the CTD volume in radial direction. For a comparison with the work of the other teams, the pressure in the CTD was determined roughly in the centre of the CTD on the upper and lower walls at the point of a discretization node, and the resulting value was calculated as the mean of the two values.

In this section we present the prediction results based on the calibrated set of parameters for the drainage phase (presented in the next section).

Flow123d representation

In the first variant (zero flux), the change from drainage phase to the flooding phase is made by changing boundary condition in time, similar as for excavation through a

coefficient in the 3rd type boundary – in fact inverting the model back to the pre-excavation state (which was simplified as impervious fill of the tunnel instead of the rock).

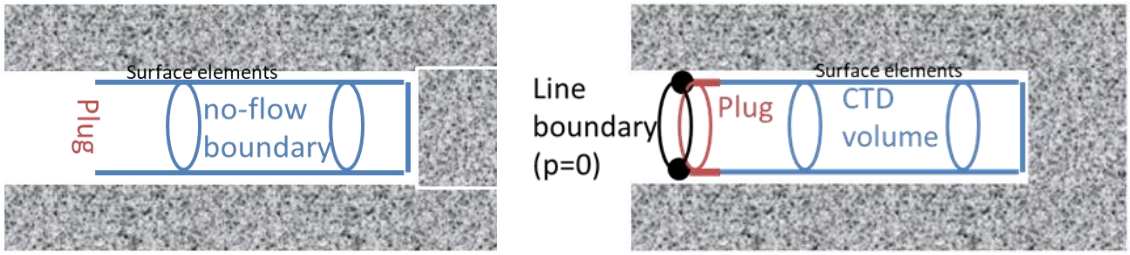

Figure 221. Illustration of the two plug installation and CTD flooding concepts – no flow on the tunnel wall (left) and tunnel wall surface elements representing the free water volume and the semi-pervious plug in contact with atmospheric pressure.

In the second variant (2D elements), both phases need a separate model run. Outputs of the drainage are exported, new initial condition extracted, and the model with new geometry/mesh runs with the initial condition partly loaded from the file into the elements existing in previous phase and partly set to given initial constant value in the added 2D elements of the water body (atmospheric pressure and measured chlorine concentration).

10.1.1 Results of prediction

The results below are presented, as a prediction, without comparison to the measured data. The comparison is part of the inverse model section, where few of the prediction results are also included.

Pressure in 12MI33

The pressure values in borehole 12MI33 stabilized very rapidly after flooding the CTD and remained at a steady value throughout the calculation of the flooding period, as well as in the drainage model before (Figure 222). Compared to the steady state of the drainage, the pressures are higher but do not return to the original values observed before the excavation (the difference is due to the inclined access gallery that remains open). The smallest change was observed in the pressure in Section 6, located

immediately next to the unflooded inclined gallery. The pressure values were again ordered from the most distant section from the CTD entrance to the nearest (No.1 – No.6). After the excavation, there was an exception in the order due to the permeable fractures near No.3, which showed the highest increase in pressure values from all the flooding model alternatives. By comparing all of model alternatives, it is clear that the greatest increase in pressure is in the homogeneous model (Figure 222c). In the fracture model, the pressure increase is likely to be prevented by the communication of the fractures to the matrix blocks. The difference between the two alternatives of the fracture model is minimal, both in the trend and in the steady pressure values, which are almost identical. This is not surprising, the effect is only due to the compressibility of the water in the transition phase and the hydraulic communication between the monitoring section is limited by the fractures, so the additional connection several meters far through the CTD water volume makes a little contribution.

Chlorine in 12MI33

Figure 223 shows the development of the chlorine concentrations for boreholes 12MI33 and 13MI38, respectively, with a specified range of initial concentrations on the walls of the tunnel of 214–565 mg/L for the flooding model. The graphs show the entire calculation period of two consecutive concentration models – the drainage model and the flooding model. The flooding model had the initial conditions of the drainage model. In the first steps, technical issues with the implementation of this condition were observed (they will be subject to further analyses by the Flow123d development team), so the initial values in the flooding model do not follow the previous drainage model in some cases. After flooding, the concentrations stabilize very rapidly to the final values for the model with zero flow in the CTD. For the model with 2D surface elements, there is a slight increase and then a decrease in the concentrations in Sections 2 and 3. The rapid stabilization corresponds to the fact that the concentrations are determined by the boundary condition and the change of the velocity field only changes the source position, i.e. the new concentration is already present in the model volume and not transported from far away. Fluctuations in the case of the surface elements correspond to the effect of mixing with water in the flooded gallery.

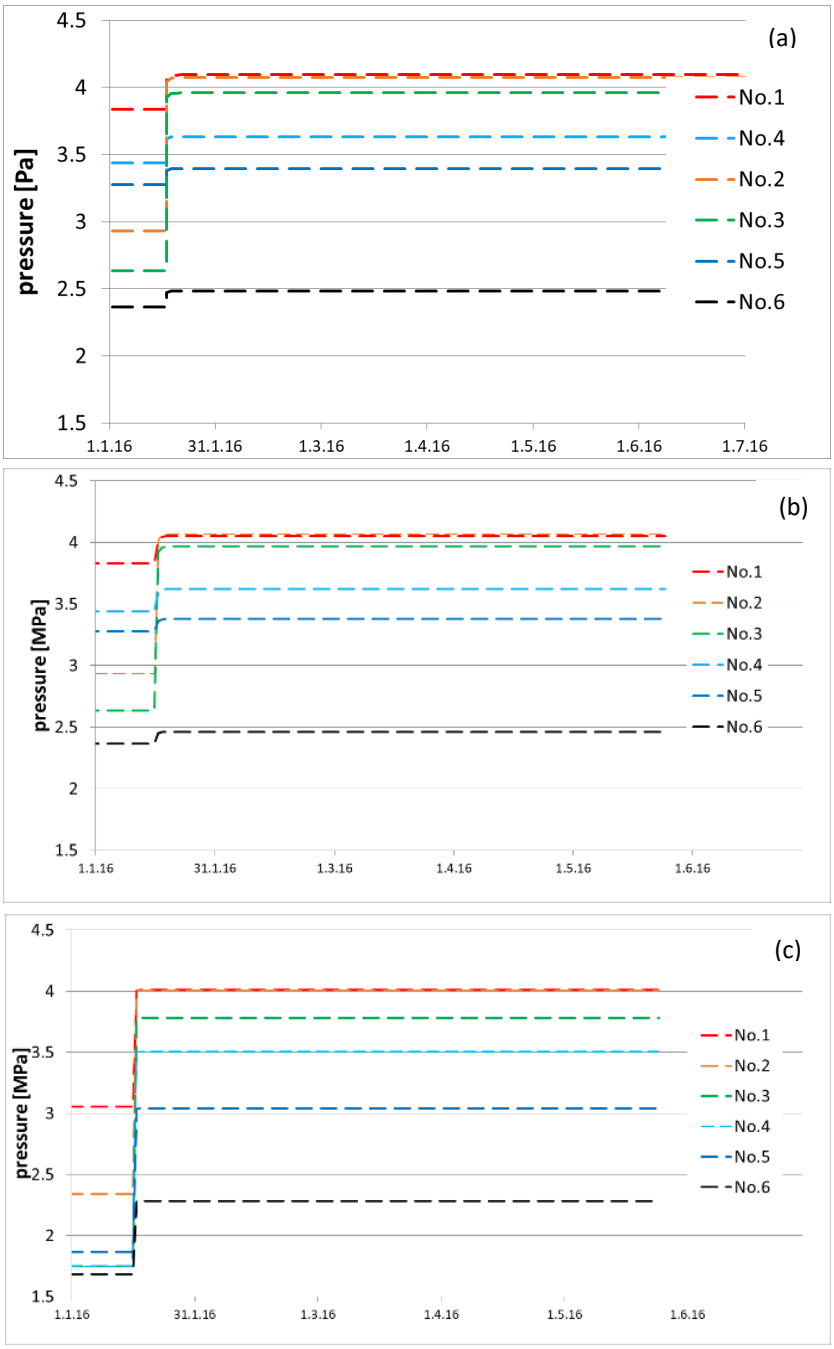

Figure 222. Pressure evolution for the model alternatives on the wall of the CTD gallery (date in the day.month.year format): a) fracture model and applied zero flow; b) fracture model and 2D surface elements; c) homogeneous model and applied zero flow

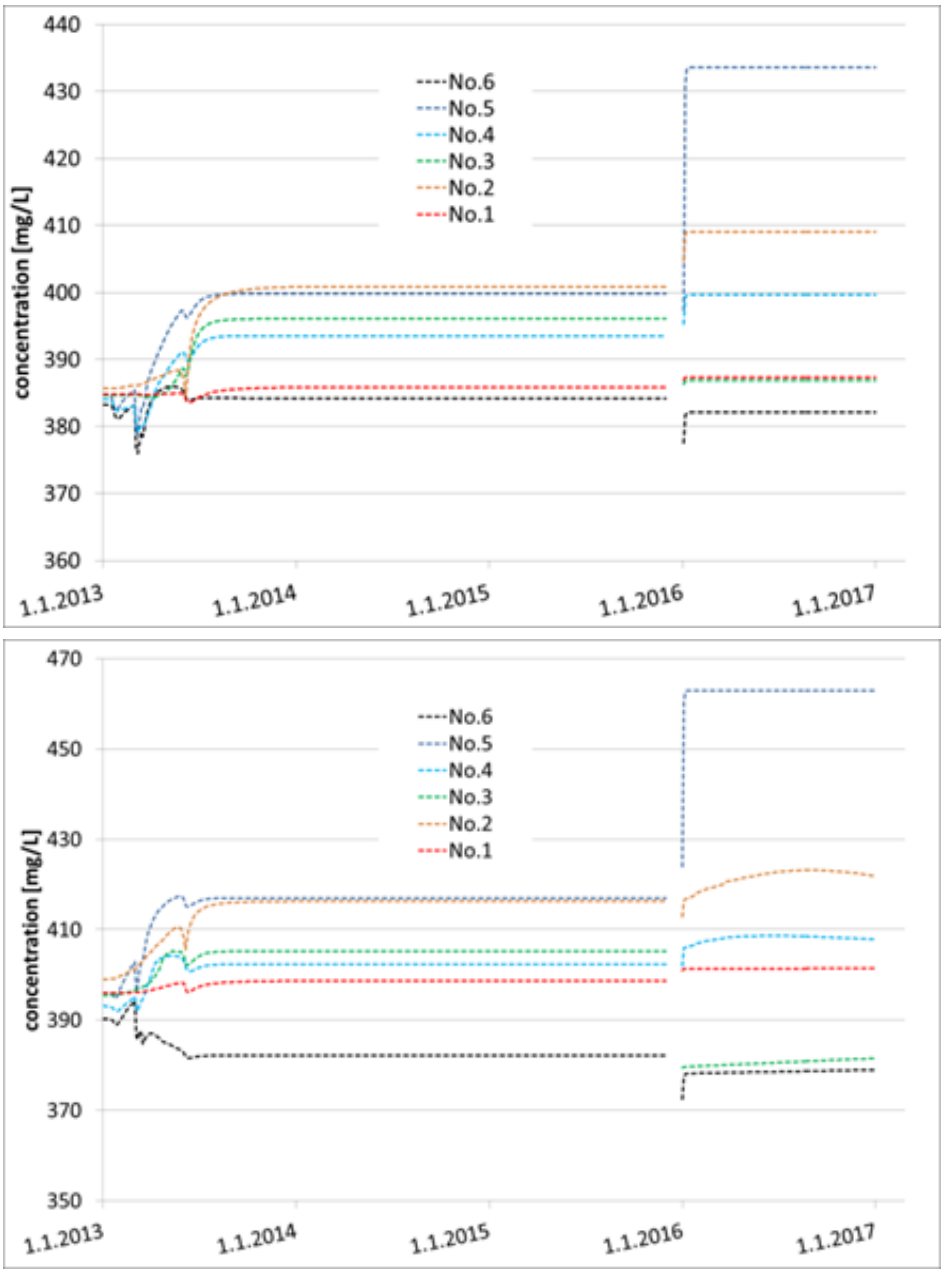

Figure 223. Concentrations in borehole 12MI33 for the zero-flow model (upper figure) and the 2D elements model (lower figure) with an initial concentration of 214–565 mg/L. The drainage period followed by the flooding period, date in day.month.year format.

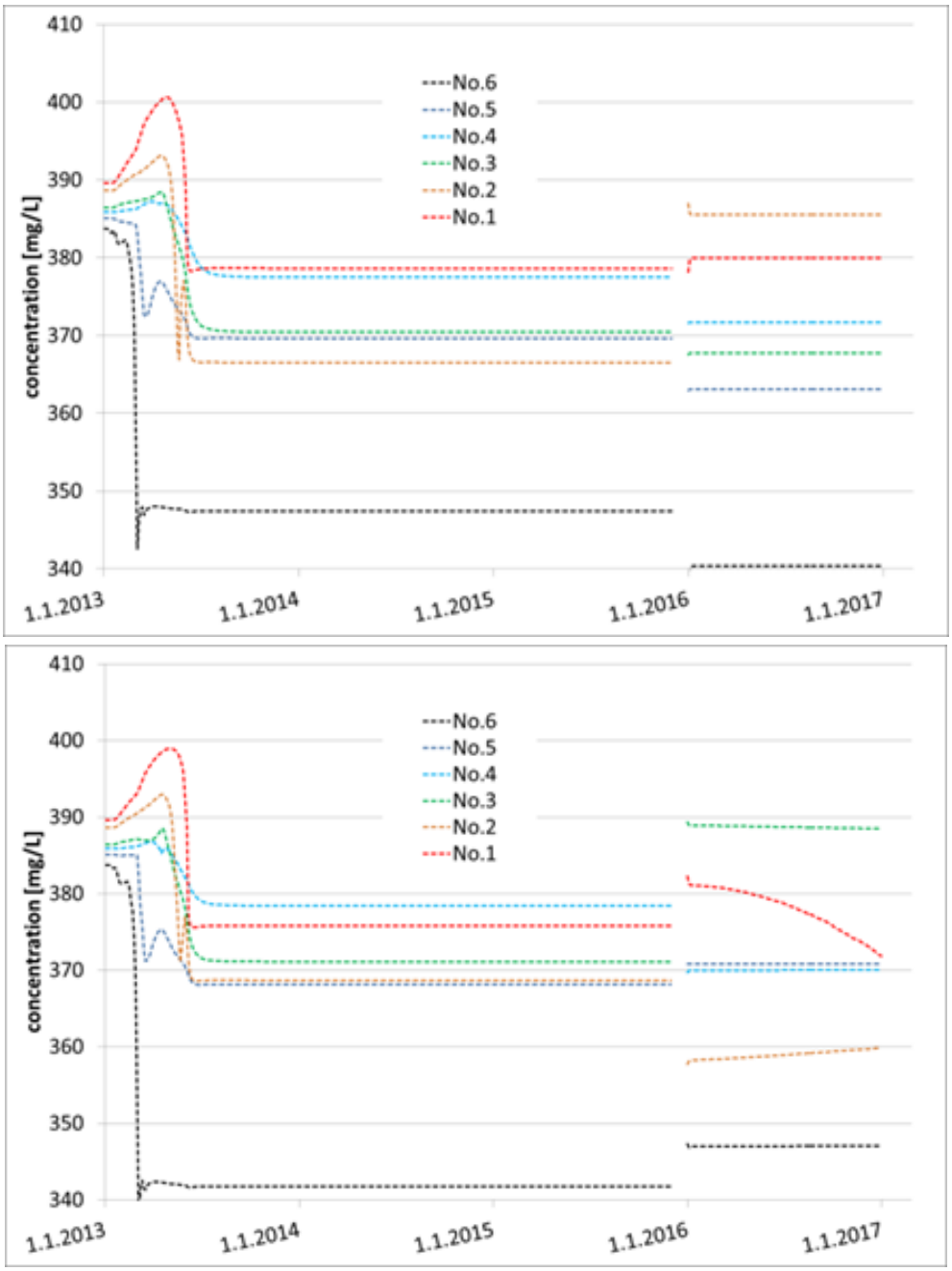

Figure 224. Concentrations in borehole 13MI38 for the zero-flow model (upper figure) and the 2D elements model (lower figure) with an initial concentration of 214–565 mg/L. The drainage period followed by the flooding period, date in day.month.year format.

10.1.2 Plug temporal evolution

To fit the observed pressure evolution, it was necessary to incorporate temporal change of material properties into the model. After the initial steep rise, the gradual decrease of pressure in the monitoring borehole can be naturally explained by a gradual increase of plug permeability e.g. due to material degradation. The idea also resulted from the visually observed leakage on the plug outer wall (although irregularly distributed).

The evolution of permeability was represented empirically, by a function with two parameters,

$$K_{plug}(t) = K_{ref} + \log(t-1) * f_K \qquad (10.1)$$

which represent the gradual increase from initial permeability with decreasing slope. The two parameters represent the hydraulic conductivity in the intact state of the material K_{ref} and the factor f_K of the permeability increase rate.

The free parameters can be calibrated. This is evaluated in the next section.

10.2 Inverse model variants

The model calibration, which was the subject of the task assignment for (1) drainage period (Step 1b/2a) and (2) flooding period (Step 2b/3a) is performed by inverse modelling, i.e. solving an optimization problem, minimizing the residuals (criterion of the model to the measurement fit) by setting the model parameters.

The individual inverse problems below differ typically by:

- Selection of measured data included in the fit criterion (“observations”).
- Weights how individual couples of measured and model output value contribute to the criterion.
- Selection of free model parameters.
- Initial estimations of the free parameter values for the iterative optimization algorithm.
- Modelled processes (temporal period, flow/transport process).

The overview list of evaluated problems is given in Table 34 – this represent the main groups, while each line represents a sequence of many inverse model runs with the

given set of data (parameter and observation selection, initial values, weights, etc.). Such lists are presented in separate tables in the corresponding subsections.

The inverse modelling follows the introductory calibration by a trial-and-error method with a reduced set of data during the Step 1 solution. We use the open source code UCODE developed by US Geological Survey (Poeter and Hill, 1998). This is a command line program with a general interface to any "forward" simulation model (process model) with text file numeric inputs and outputs, which is the case of Flow123d. The optimization algorithm uses a gradient-type method and the derivatives (parameter sensitivities) are approximated by differences obtained through running the model with perturbed individual parameter values. The computational cost is therefore mainly controlled by the number of free parameters, while independent of the number of the observations used for the residuum calculation.

The objective function represents the overall fit of the model to the measurement and it is defined as the sum of squared weighted residuals (SSWR), i.e. differences between the individual model output and observation values u_i.

$$SSWR = \sum_{i=1}^{N} w_i^2 \, (u_{i,mod} - u_{i,meas})^2 \qquad (10.2)$$

The weights w_i are subject to selection. They should balance the different scale of values or they distinguish more important (precise, certain) and less important measurements. In section 10.2.2, in case of temporal sequences with negligible trend, the weight is used so that the whole group of data contribute to the sum approximately as one value.

In total, the available data were the following (their use or exclusion is mentioned individually in Table 34, including their number):

- Parameters: Hydraulic conductivity (transmissivity) and specific storativity of each individual fracture, individual zones of the matrix domain and the whole far-field domain, parameters of the plug permeability evolution function, porosity (aperture) of fractures, matrix zone, and the far-field domain.
- Observations (given data): evolution of pressure and chlorine concentration in all borehole sections 12MI33, 13MI38-41, evolution of CTD pressure and CTD chlorine concentration, total tunnel drainage inflow after excavation, packer pressure tests in 12MI33 before the excavation.

10.2.1 Procedure for pressure test data

The results of pressure tests in packer-divided zones of a borehole are expressed as transmissivities of the "layers" of rock perpendicular to the borehole with the thickness equal to the packer interval length. From the point of view of the inverse model, these data are therefore both "input" and "output", i.e. they are a-priori given (measured, i.e. the constraint for the inverse model) but represent input parameters of the model equation which are normally the unknowns for the inverse model. The packer tests do not represent the fracture transmissivities and matrix permeability directly – the packer test transmissivity is a combination of possibly more model input data. Besides that, some uncertainty in the values related to the model configuration can be considered.

Such situation is solved by an extended inverse model, where two sets of "observations" and two "process models" are used in parallel: One is a standard simulation with input permeabilities and output pressures and the second is a simple calculation of the model component (fracture and matrix) permeabilities to the packer section transmissivities (sum of the fractures and the matrix contributions) with the packer test data in the role of observations. It is illustrated in Figure 225.

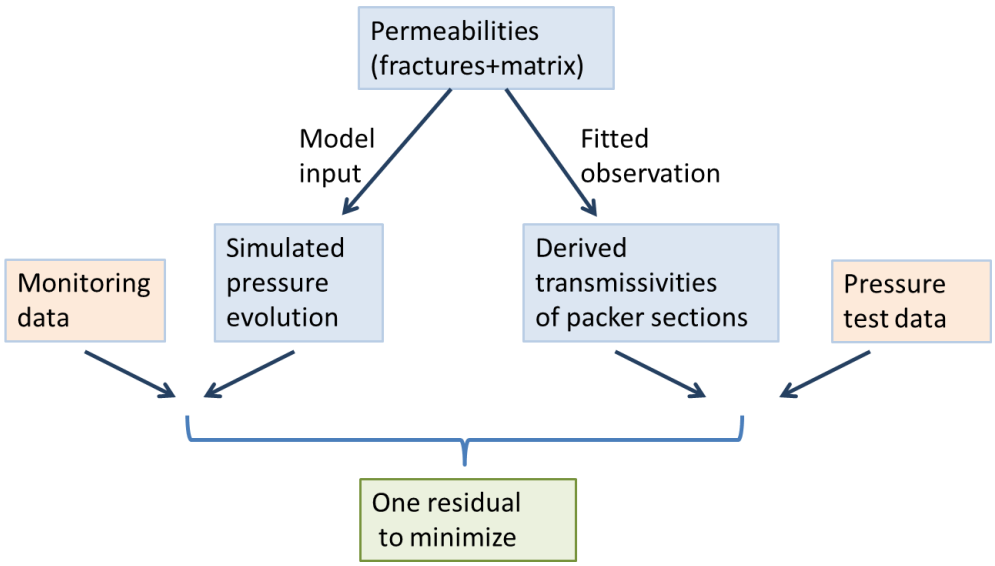

Figure 225. Diagram of data usage in the automatic calibration process in the UCODE software.

Table 34. Stages of inverse modelling compared in terms of used data: sets of parameters (P=estimated, F=fixed), sets of observations (O), selection of temporal interval and simulated processes.

Variant	fractures K	rock K	plug K(t)	Pressure 12MI33	Pressure 13MI38-41	Inflow	Packer test	Porosity	BC+init conc.	conc. monit. 5 boreholes	conc. CTD	Num. param.	Num. obs.
#1	P	P homog inner	-	O (drainage evol. 154 points)	-	O	O	-	-	-	-	14	163
#2	P	P zones	-	O (4 points)	O (3p.)	O	-	-	-	-	-	20	78
#2a	F	F zones	P	O (flood)	O	-	-	-	-	-	-	3	10
#3	F	F zones	F	-	-	O	-	P	P	O (2 p.)	O (2 p.)	36	99
#3a	P	P zones	F	O 4 points changed position	O 4 points changed position	O	O	F	P	O (4 p.)	O (4 p.)	35	186

The solution requires careful selection of weights in the sum of residuals. The transmissivities are each of different order of magnitude and all together differ from other observations. If the reciprocal of the measured value of each transmissivity is used as the weight, then the difference by a factor of two makes the contribution 1 or 0.5 to the sum of residual, i.e. corresponding to a difference of 1 MPa or 0.5 MPa of an individual pressure monitoring value (weights of 1). Such balancing of relative changes is appropriate for the considered accuracy of the measurements and for observed pressure variations in time.

10.2.2 Model #1 – drainage calibration

In the beginning, calibration based on the drainage phase data was made. Due to expected complicated capturing of chlorine concentrations, the hydraulic-only model was solved. The Cl transport was left to be compared for the final case. The set of inverse problem data is defined in row 1 of the Table 34 and the respective problem as #1.

The main purpose of the inverse model was to capture these features of the data: timing of the pressure drawdown, value of the pressure drawdown and therefore to distinguish the zones of boreholes communicating with the tunnel and isolated from the tunnel.

The included observation data are:

- Pressure monitoring in borehole 12MI33
- Pressure tests and the resulting hydraulic conductivities are used as part of calibration and not as input values (Figure 225)
- Inflow to the tunnel

The included parameters:

- Hydraulic conductivity of the outer zone (far field)
- Hydraulic conductivity of the inner zone (matrix)
- Transmissivities of the individual fractures (14 values)

The automatic calibration was performed in several successive steps with respect to the size of the task and the number of parameters and hence the computing cost of the calibration. The procedure was as follows:

1. Firstly, the hydraulic conductivity of the fractures was calibrated for sections where the model values most closely matched the measurements. The hydraulic conductivity of the fractures crossing the sections where the model pressures roughly corresponded to the monitoring was omitted and the effect of the calibration of the other fractures' permeability on this section was monitored.
2. Subsequently, the results were evaluated with respect to the measurements and a different combination of parameters was selected, for which the highest possibility to improve the model agreement was intuitively expected.
3. In the next step, each parameter that was still outside the measured data was calibrated, or sections that fit but were not yet included in the calibration were tested in terms of whether they can affect the results in other sections.
4. In the last step, the pressures from the monitoring of borehole 13MI38-40 were added as additional observations.

The new monitoring of borehole 13MI38-41 that was put into operation after the excavation of the tunnel was used to confirm the accuracy of the previous calibration.

The results of the pressure development are shown in Figure 226 and the resulting hydraulic conductivity values are summarized in Table 35, in the context of parameters from Step 1. In general, the pressures are not as low as in previous models and shows better agreement with the monitoring data (Figure 226). No.1 captures the unchanging trend relatively well and the final value is slightly lower. For No.2, the curve drop time is captured very well, but the exact final value is not consistent. No.3 also shows a relative

improvement over the previous results, both in terms of the measurement trend and the final value, which is slightly higher. Section 4 is significantly below the measurement, and Section 5, which does not cross any of the fractures, shows a more modest decrease than the previous results, yet it is significantly below the measurement. No.6 is almost consistent with the measurement, although the model responds slightly faster. Compared to the previous results, this is a significant improvement.

From the table of calibrated hydraulic parameters Table 35, we see that most fractures have a change in transmissivity value within a single order of magnitude, and some fractures are almost closed. These include fractures 109, 111 and 114, which converge to a value of 1×10^{-12} m^2/s, which is the lower limit value entered into the calibration software. The fractures transfer pressure through intersections from the surrounding fractures and their closure will help achieve the desired pressure values in the surrounding sections.

Comparison with remaining measurement

After excavating the CTD, boreholes 13MI38-41 were drilled and equipped with pressure monitoring equipment. Data from these new boreholes were provided after calibrating the model (time interval during the excavation). A comparison of the model results with the pressure monitoring is shown in Figure 228. Overall, the model captures the range of pressures well. The ranges in boreholes drilled from the CTD are captured the best, in particular borehole 13MI39, even with the final pressure values. Section 4 of borehole 13MI40 (closest to the tunnel) has a final value below the measurement. Borehole 13MI41 has nearly identical pressure values for Sections 2 to 4. Borehole 13MI38, drilled along the tunnel on the opposite side from borehole 12MI33, captured the range very well, but the order of the sections is reversed.

The new boreholes used during the automatic calibration were also successful and had a minimal effect on the resulting permeability. However, it seems necessary to make improvements to the structure of the model in order to achieve a better agreement between the model and the measurements including these new boreholes.

The fracture model with calibrated hydraulic parameters was used for the transport simulation of the Cl ions (as a non-reactive tracer). The results of the transport are compared with the monitoring (Figure 229). The modelled concentrations exhibit an almost steady state, which is due to the position of the borehole at the same vertical level with respect to the tunnel, and hence a “symmetrical” mixing for a flow controlled by the drainage.

Table 35. Comparison of the calibration results of the inverse solver with the previous estimates in Step 1 and with the prediction model.

Parameter	From a-priori data (prediction)	Manual calibration (Step 1)	Current optimal value (#1 calib.)
Hydraulic conductivity outer zone [m/s]	1×10^{-8}	5×10^{-9}	1.83×10^{-8}
Hydraulic conductivity inner zone [m/s]	2×10^{-10}	1×10^{-10}	6.91×10^{-10}
Transmis. Frac. 101 [m^2/s]	1×10^{-8}	1×10^{-8}	1×10^{-9}
Transmis. Frac. 102 [m^2/s]	1×10^{-7}	1×10^{-7}	1×10^{-8}
Transmis. Frac. 103 [m^2/s]	5×10^{-9}	5×10^{-9}	1.15×10^{-7}
Transmis. Frac. 104 [m^2/s]	9.5×10^{-8}	9.5×10^{-8}	1.18×10^{-7}
Transmis. Frac. 105 [m^2/s]	6×10^{-8}	6×10^{-8}	3.7×10^{-9}
Transmis. Frac. 106 [m^2/s]	6×10^{-7}	6×10^{-7}	5.41×10^{-7}
Transmis. Frac. 107 [m^2/s]	8×10^{-8}	8×10^{-8}	7.03×10^{-8}
Transmis. Frac. 108 [m^2/s]	3×10^{-9}	3×10^{-9}	1.47×10^{-10}
Transmis. Frac. 109 [m^2/s]	1.5×10^{-8}	1.5×10^{-8}	1.93×10^{-12}
Transmis. Frac. 110 [m^2/s]	5×10^{-9}	5×10^{-9}	5.87×10^{-10}
Transmis. Frac. 111 [m^2/s]	4.5×10^{-8}	4.5×10^{-8}	1×10^{-12}
Transmis. Frac. 112 [m^2/s]	5×10^{-9}	5×10^{-9}	4.74×10^{-8}
Transmis. Frac. 113 [m^2/s]	1.2×10^{-8}	1.2×10^{-8}	5.39×10^{-8}
Transmis. Frac. 114 [m^2/s]	4.5×10^{-7}	4.5×10^{-7}	1×10^{-12}

We also attempted to calibrate the transport to the measurements, but without a great deal of success. This is due to the use of the boundary conditions (in the range of 332 to 428 mg/L), set by the task description, which do not let the results have a concentration corresponding to the monitoring beyond this range. Therefore, the task was performed with a change in the range of the boundary condition of the concentrations. The limits were set to 214 mg/L of chlorides on the upper wall of the model and 566 mg/L on lower wall of the model. Even after this modification, the results of the model did not significantly approach the monitoring. Therefore, the results are not presented in this report. Effects of other possible changes in the concept of the model are discussed below in section10.4.

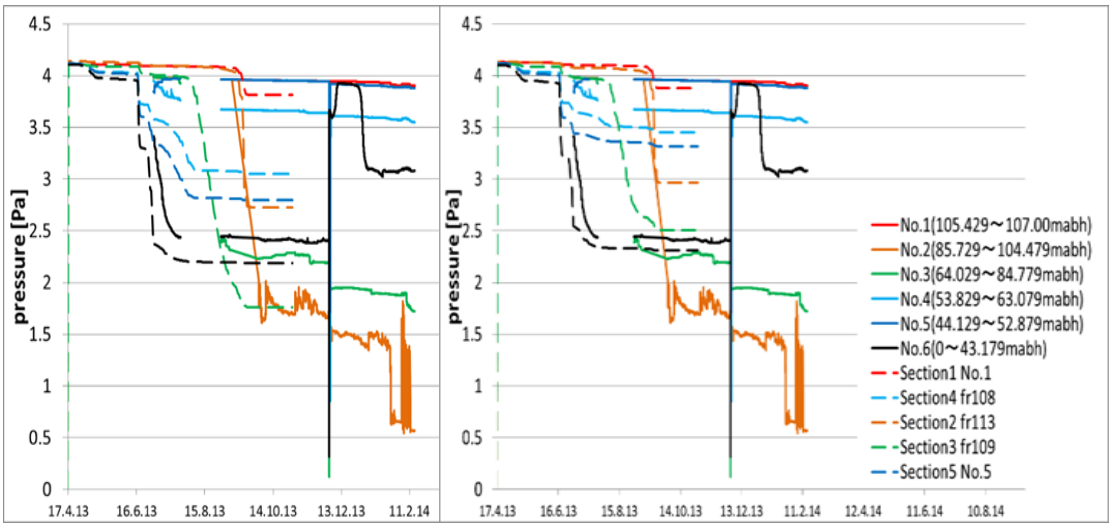

Figure 226. Pressure evolution in the calibrated models – comparison of the measured (solid) and calculated (dashed) data and comparison of larger inner zone (left) and smaller inner zone and finer mesh (right).

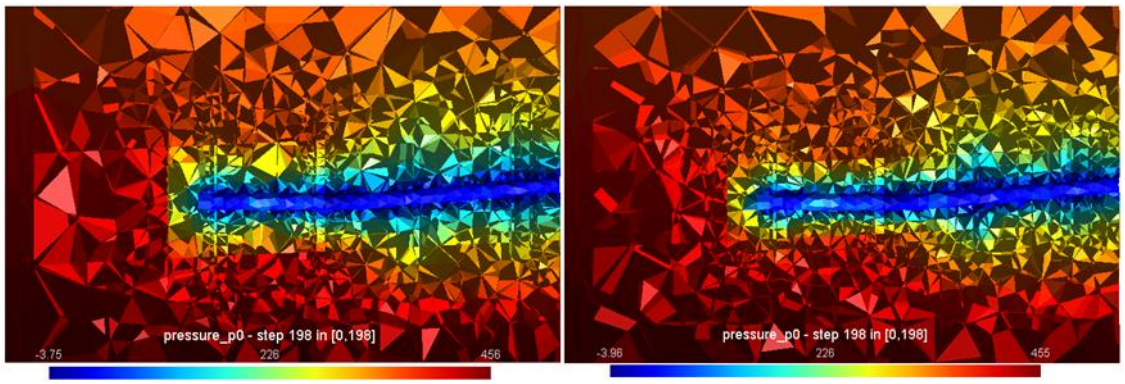

Figure 227. Modelled pressure distribution (with differing discretizations) after excavation – comparison of the variants with larger inner zone (left) and with smaller inner zone and finer mesh (right).

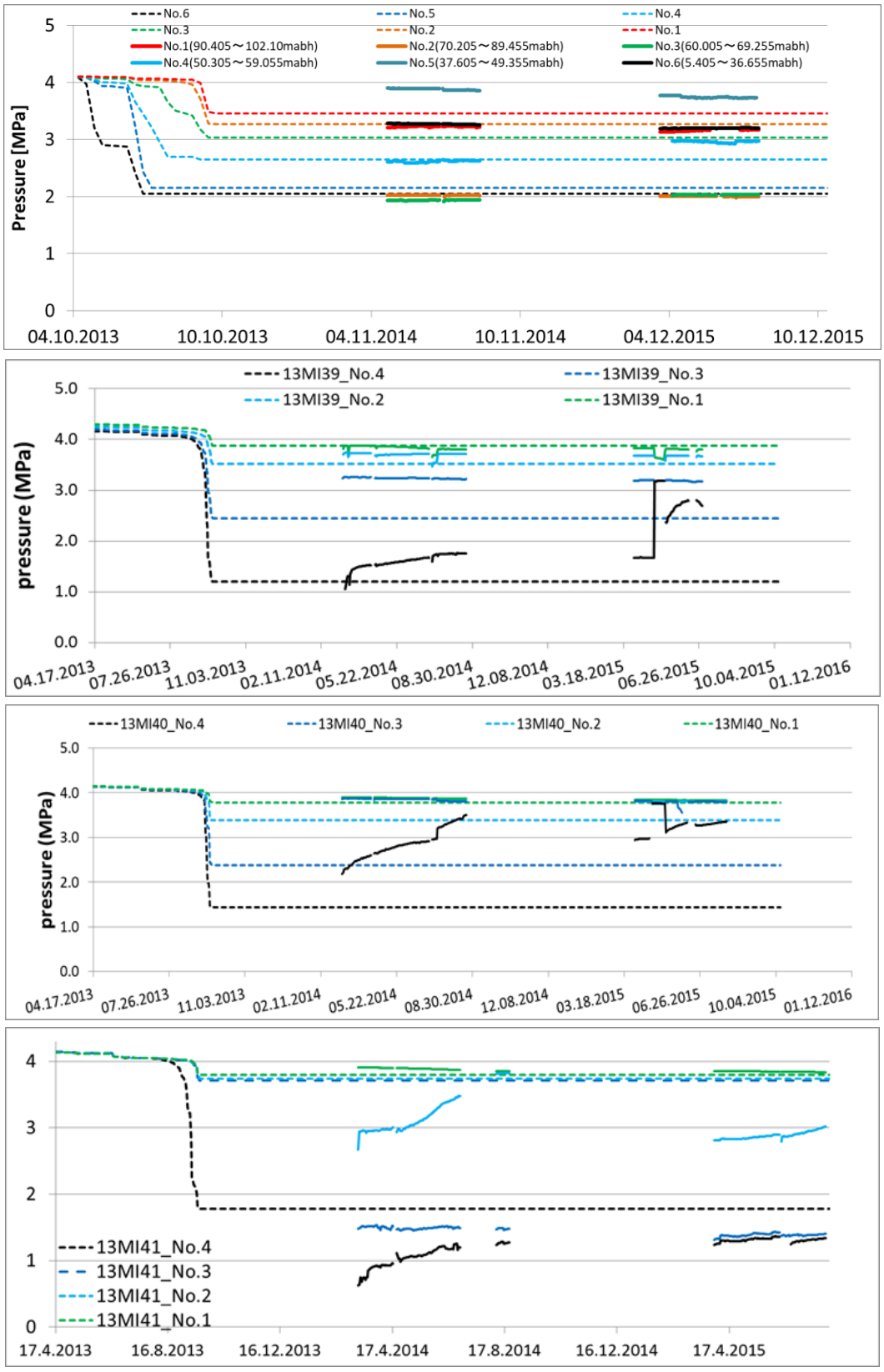

Figure 228. Pressure development in the newly added boreholes 13MI38-41 with the results of the model calibration using the UCODE automatic calibration tool.

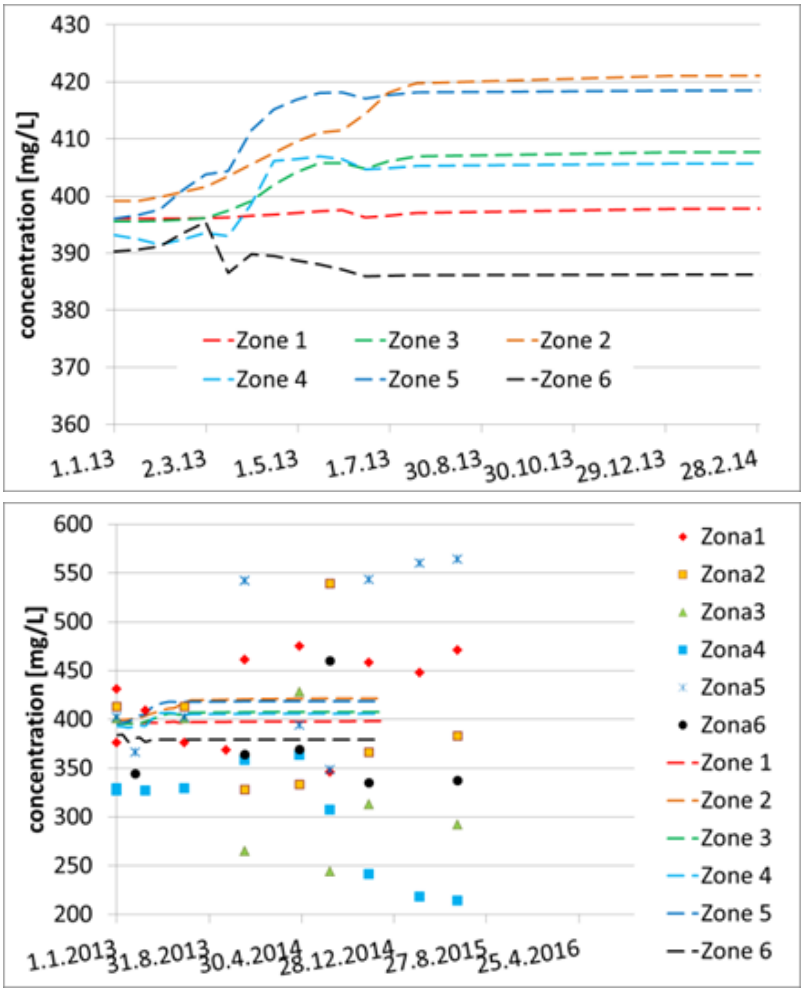

Figure 229. Development of the concentrations in the individual sections in borehole 12MI33 (upper figure); Development and values of concentrations from the monitoring (lower figure).

Mesh effects

The effect of the mesh spacing on the results was checked due to the complexity of the model, i.e. the intersection of the fractures and the tunnel plus the interfaces of the outer and the inner conductive blocks. The calibration was performed on the coarsest model (a 30 m size of the inner zone and a 5 m fracture overlap from the inner into the outer zone, see also the configuration definition in Section 8.4.3) –the results of the pressure field on the vertical section along the tunnel are shown in Figure 227. When comparing the pressure field in the model with a smaller range of the inner conductive block (20 m size perpendicular to the tunnel and a 3 m fracture overlap), there is a difference in the pressures in the surroundings of the tunnel, which do not reach such a

distance. The final result of the pressure calculation is on a fine mesh with an internal block range of 10 m from the tunnel axis. The figure shows a faster pressure change in the pressure field of the inner conductive block and a slightly longer range in the outer conductive block.

Figure 226 shows the development of the pressure monitoring and the results of the models with two alternatives meshes a) the interface inner/outer at 15 m on each side of the tunnel axis; and b) of the interface 10 m on each side of the tunnel axis. The changes are relatively small compared to the final mesh used.

10.2.3 Model #2 – drainage and flooding calibration

This set of inverse model runs includes additional available data and makes some generalization to the input data. It corresponds to Row 2 in Table 34.

One update with respect to the model #1 (previous section) is in the use of data from the pressure monitoring sequences of all the five boreholes. It is reasonable to concentrate on the main phenomenon, which is the pressure drawdown from the state before the excavation to the quasi-steady state during drainage and then the pressure recovery after the flooding. Therefore the pressure evolution can be characterised by few values in representative time points, see Figure 230: (1) initial state (only 12MI33 data available), 70 days, (2) drainage state, 260 days, (3) peak of the curve just after plug closure, 1030 days, (4) later state of the leaking plug, 1090 days. This selection is intended to capture the rock permeability distribution (communicating and non-communicating zones), while it simplifies the temporal pattern resulting from the plug properties evolution. In particular it excludes the irregular part of the measured evolution which cannot be captured in principle. The positions on the measured evolution curves are shown in Figure 230. The fitting of the plug permeability evolution function (empirical formula in section 10.1.2) is made by a separate inverse model with added temporal points.

The second update is splitting the inner rock block (matrix zone) into several intervals of different permeability (Figure 231). It seems there is no physical argument for such difference, but the motivation was to allow the local isolation between tunnel and the borehole observation points with negligible pressure changes. For the same purpose, the data of the borehole packer testing are excluded from the calibration. This means an assumption that higher permeability around a borehole section can be the result of the permeable rock contribution from other direction than towards the tunnel. Therefore, the model block permeability value can be different if extrapolated from the

relevant rock volume just between the tunnel and the borehole onto the whole section of the inner rock model domain.

Additionally, the piezometric head prescribed on the model boundary (corresponding to the approximate value in the place before the excavation) is considered as a calibrated parameter, meaning the uncertainty of the drainage to a larger distance is considered.

The observation set is balanced by the weights of individual residuals of different quantities, so that the total contribution of pressures and inflows is about the same: $w^2 = 1$ for pressures (reference value of 3MPa, total 78 values), $w^2 = 0.1$ for CTD inflow (one value of 19 m^3/d), and $w^2 = 0.01$ for inclined drift inflow (one value of 62 m^3/d). Individual contributions of one pressure value is about a half of the inflow, but there is higher number of pressure observations, they represent separate phenomena, but still are regarded as not fully independent (slightly correlated).

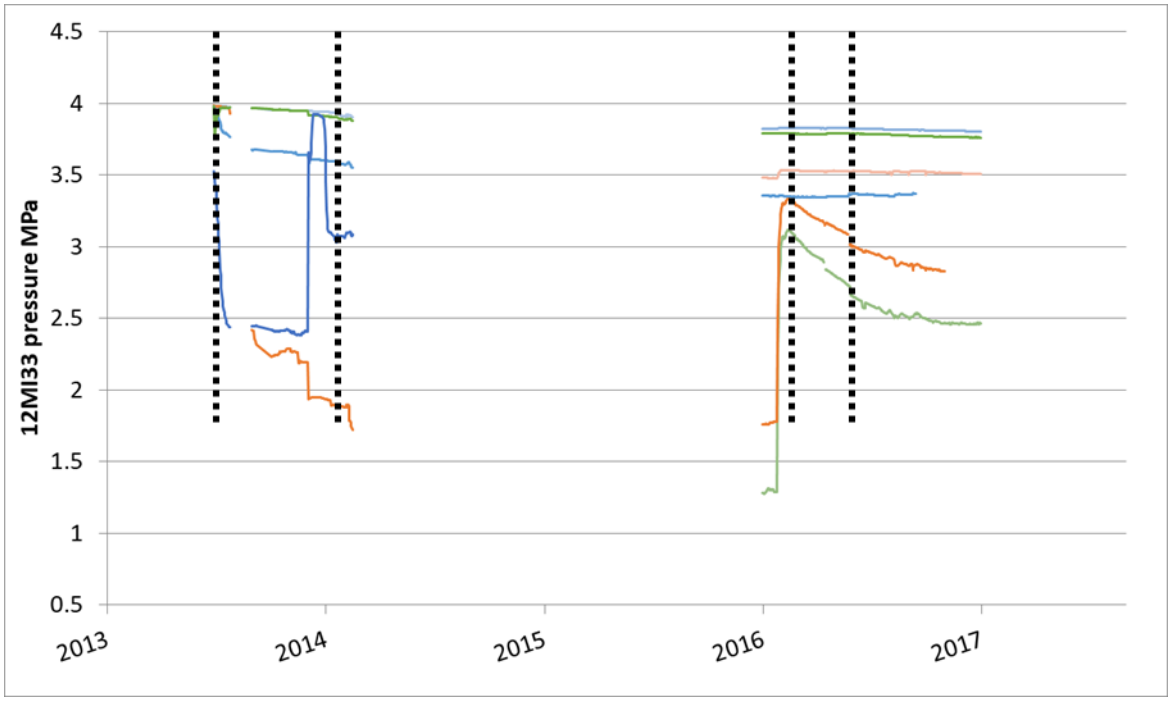

Figure 230. Choice of the temporal positions for compared values of pressure between the model and the measurement (on background of the 12MI33 measured data).

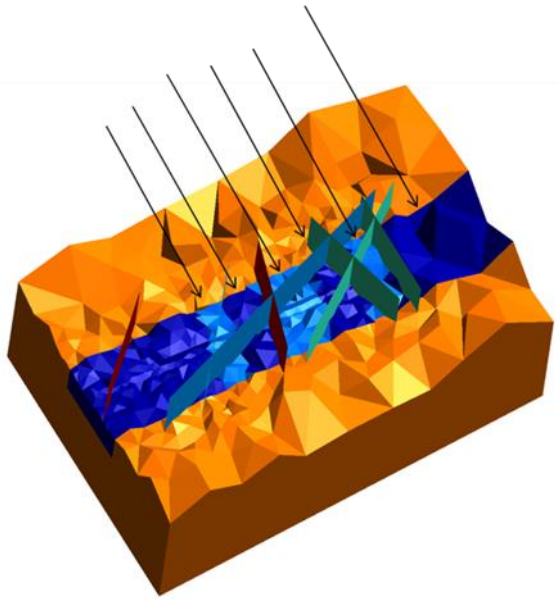

Figure 231. Generalisation of the model: zones of different permeability in the inner rock domain (matrix).

The inverse modelling is composed of many experimental runs with a partially optimized model. The reasons were computational cost for the large number of parameters and poor numerical properties of the optimization problem. In many cases, the algorithm diverged through suggestion of values out of the floating-point number range, even with properly set damping or limits, or just iterated with very little objective function improvement. The difficulty is that some of the parameters influence the output in conjunction with others (e.g. effect of change of in a low permeability zone is controlled by a presence of a higher permeability zone in contact).

Runs were made with partial sets of 4-8 “free” parameters (and others fixed) based on their physical meaning, applying some of the intuitive insight into the problem, e.g. matrix domain and fracture domains considered separately, lower and higher permeable domains considered separately, spatial positions with previously seen worse fit, reset or intuitively set parameters. Only the main solutions are presented in this report. Also, the conceptual model was improved in intermediate steps: drainage phase only, then the flooding represented as no-flow tunnel wall boundary, and finally the intended model of CTD water body and semi-pervious plug.

Table 36. Comparison of the calibration results of the inverse solver with different sets of parameters and observations (references to Table 34).

Parameter	Relevant monitoring section	#1 optimal value	#2 drain only	#2 drain+plug
Hydraulic conductivity outer zone [m/s]		1.83×10^{-8}	1.42E-08	2.25E-08
H. c. inner zone [m/s] y > 165 m		6.91×10^{-10}	1.16E-12	1.16E-12
H. c. inner zone [m/s] 165 m > y > 155 m		6.91×10^{-10}	1.16E-12	1.16E-12
H. c. inner zone [m/s] 155 m > y > 141 m		6.91×10^{-10}	1.16E-12	1.16E-12
H. c. inner zone [m/s] 141 m > y > 120 m		6.91×10^{-10}	1.16E-12	1.16E-12
H. c. inner zone [m/s] 120 m > y > 110 m		6.91×10^{-10}	1.60E-10	1.60E-10
H. c. inner zone [m/s] 110 m > y > 100 m		6.91×10^{-10}	1.16E-12	1.16E-12
H. c. inner zone [m/s] 100 m > y		6.91×10^{-10}	1.16E-12	1.16E-12
Transmis. Frac. 101 [m^2/s]	-	1×10^{-9}	7.34E-07	7.34E-07
Transmis. Frac. 102 [m^2/s]	No.6	1×10^{-8}	1.08E-08	1.08E-08
Transmis. Frac. 103 [m^2/s]	-	1.15×10^{-7}	1.15E-07	1.15E-07
Transmis. Frac. 104 [m^2/s]	No.6	1.18×10^{-7}	1.78E-07	1.78E-07
Transmis. Frac. 105 [m^2/s]	No.6	3.7×10^{-9}	3.68E-08	3.68E-08
Transmis. Frac. 106 [m^2/s]	No.6	5.41×10^{-7}	4.38E-08	1.17E-16
Transmis. Frac. 107 [m^2/s]	No.6	7.03×10^{-8}	1.17E-14	3.57E-17
Transmis. Frac. 108 [m^2/s]	No.6	1.47×10^{-10}	2.08E-09	2.08E-09
Transmis. Frac. 109 [m^2/s]	No.4	1.93×10^{-12}	2.05E-07	2.11E-07
Transmis. Frac. 110 [m^2/s]	-	5.87×10^{-10}	1.27E-19	1.27E-19
Transmis. Frac. 111 [m^2/s]	-	1×10^{-12}	2.53E-13	2.52E-14
Transmis. Frac. 112 [m^2/s]	No.3	4.74×10^{-8}	7.29E-14	7.29E-14
Transmis. Frac. 113 [m^2/s]	No.2	5.39×10^{-8}	4.27E-10	4.27E-10
Transmis. Frac. 114 [m^2/s]	No.1	4.5×10^{-7}	2.89E-12	1.64E-11
Boundary head [m]			103.0	103.6
Plug reference hydr.cond. K_{ref} [m/s]				1.16E-11
Plug h.c. function factor f_K [m/s]		…	…	5.79E-09

Results are presented in Table 36 and Figure 232 – Figure 235. The inverse algorithm tended to decrease the inner zone permeability (and some of the fracture transmissivities) significantly, which is natural but it is difficult to assess if the values below the measurable limit (e.g. 10^{-14} m/s) are physically reasonable. There is a significant change with respect to the #1 calibration (previous section) but very similar results between the optimization on the no-flow boundary variant and 2D water body element variant of the plug and flooding representation.

The qualitative representation of the different behaviour of the borehole section is improved. Sections 2 and 3 decrease to almost the desired value and sections 1 and 5 decrease slightly, being closer to the measured stable evolution. The evolution in section 4 is not captured well. The result in section 6 is sensitive on the model post-processing, due to very long borehole monitoring section (selection of the space point). Also, this is a place away from the zone of interest at the CTD, so the effort to calibrate is not justified given the relatively low importance.

The profiles for the time of 260 days (drainage phase) in Figure 233 also include the results of the predictive model and of the #1 calibration. The qualitative pattern of 12MI33, 13MI38, and 13MI41 is the best for #2, while 13MI39 and 13MI40 are almost the same for all the model variants.

10.2.4 Model #3 – drainage and flooding calibration with chlorine transport

The next step in inverse modelling was adding in the transport problem, with the new observations of concentrations and new parameters. It was made in two sub-steps: First, the transport process only was optimized, with two time points (capturing the diverging range of concentrations) – Variant #3 in Table 34. Second, both the hydraulics and transport are optimized together – Variant #3a in Table 35. The set of selected times for model–measurement comparison (residual evaluation) is shown in Table 37, they differ for the concentrations and the pressures, depending on the real sampling times for chlorine analyses. There are 24 observation values per each time, the weight $w^2 = 10^{-4}$ corresponds to about 100 factors between pressures in MPa and concentrations in mg/L.

Figure 232. Comparison of models and measurement (the model in this chapter against the previous), by means of borehole profiles (section 1 to section 4 or 6) and tunnel inflow), resulting optimized parameters, the legend common for all graphs.

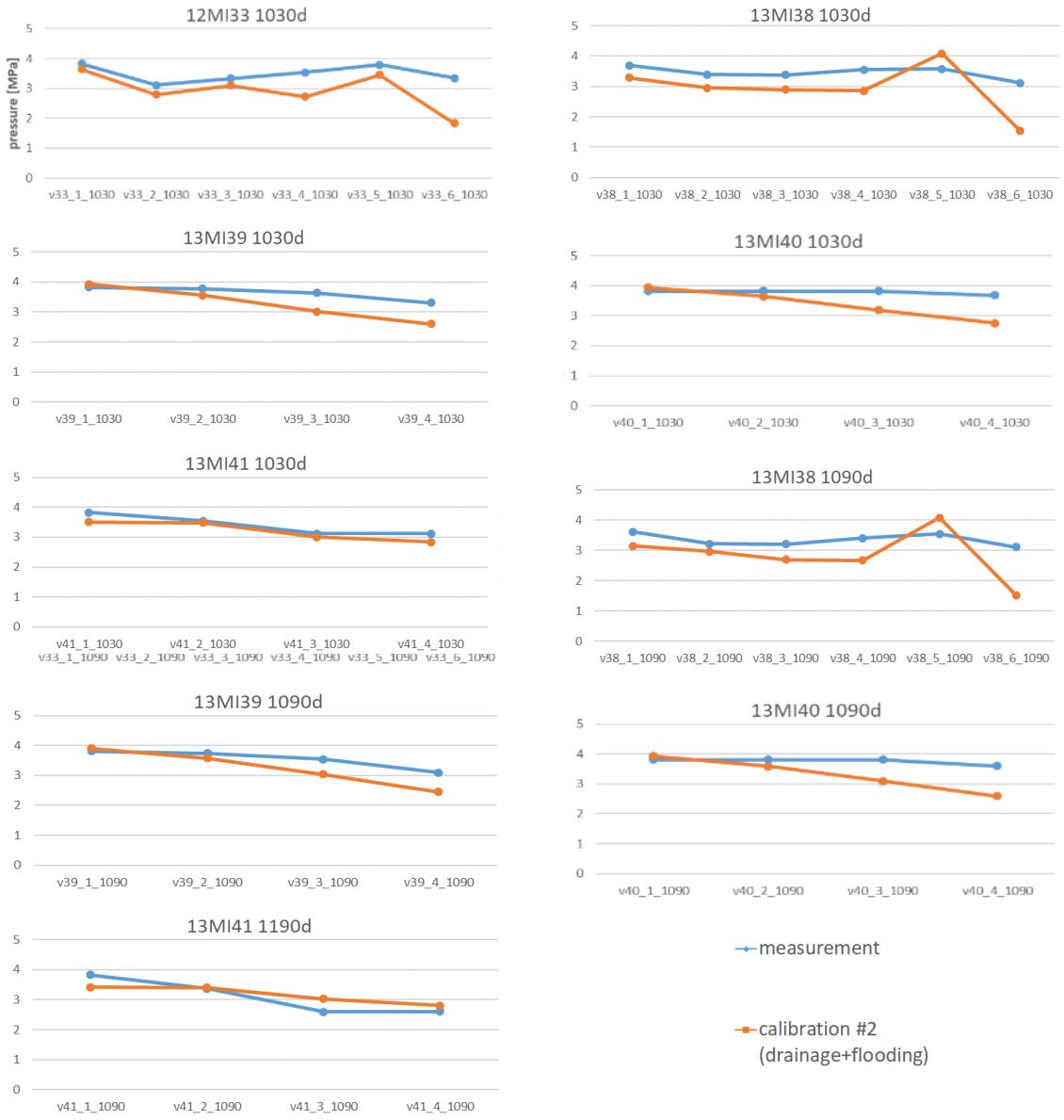

Figure 233. Comparison of model #2 and measurement by means of borehole profiles (section 1 to section 4/6) in the time of flooding, the legend common for all graphs.

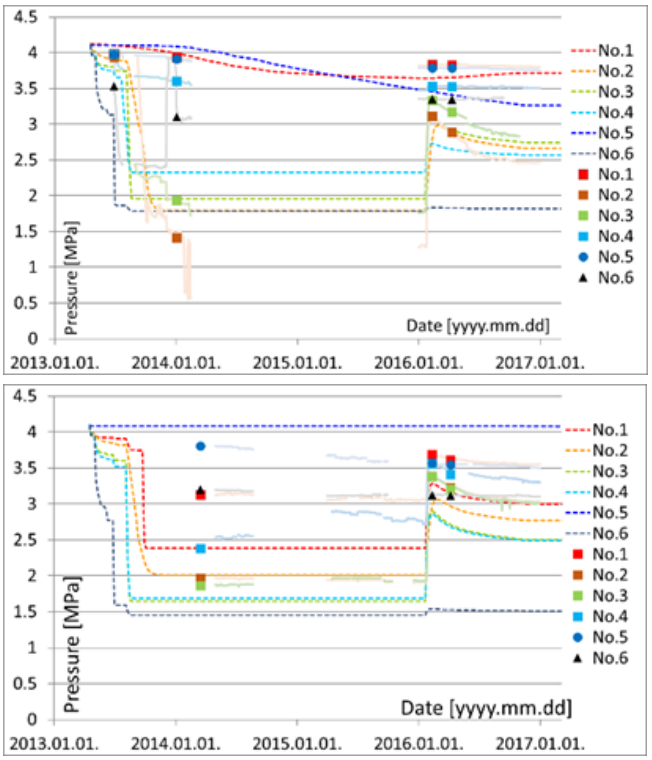

Figure 234. Comparison of calibrated model #2 with measurement (4 points used for the optimization): 12MI33 borehole left and 13MI38 right.

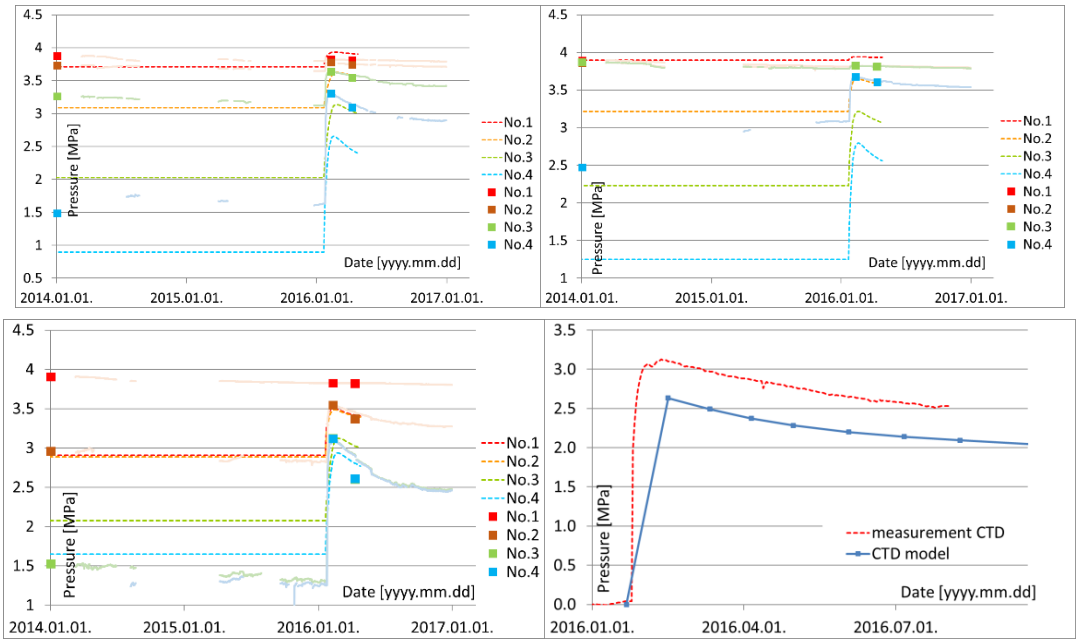

Figure 235. Comparison of calibrated model #2 with measurement (4 points used for the optimization): 13MI39 borehole upper left, 13MI40 upper right, 13MI41 lower left, and CTD free water volume lower right.

To capture the “diverging” evolution of concentration (rising range of values), some way of giving an a-priori prescription of the measured spatial distribution seemed to be necessary, besides the regular vertical gradient used in the previous models. Such pattern was suggested by the task leader (Figure 236 left, an alternative visualisation of Figure 182 concept) and similarly resulted from geochemical analysis in Section 10.5. The real irregular distribution is conceptually converted into discretely divided zones of constant concentration. Such a distribution can be applied as the boundary condition or as the initial condition. The latter can be applied either in the outer zone only or in the whole volume (Figure 236 right). While the spatial distribution in Figure 236 represents the pattern developed in later stage of the experiment (“final” pattern), it can be assumed the initial state in the near field would be different. So a similar concept is applied based on the pre-excavation data of the 12MI33 borehole.

The following variants were evaluated:

- The full-volume initial condition from the 12MI33 initial data and the boundary condition from the “final” pattern (var. A)
- Inner rock initial from the 12MI33 initial and the outer rock initial and the boundary conditions from the “final” pattern (var. B)

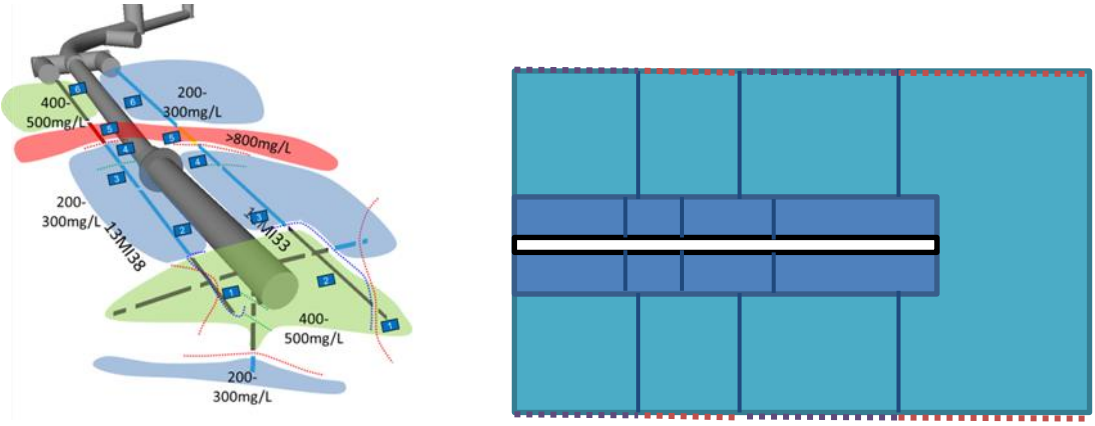

Figure 236. Implementation of the chlorine spatial distribution pattern: task leader’s interpretation (left) transformed into boundary conditions and initial conditions in the inner zone and outer zone (right). Actual positions are specified in text.

Table 37. Set of observations for the inverse model – sampling times from the measured pressure evolution and selections from the chlorine analyses.

Observation times of pressure for #3 problem [day]	Observation times of concentration for #3 problem [day]	Observation times of pressure for #3a problem [day]	Observation times of concentration for #3a problem [day]
70 (12MI33)	370	70 (12MI33)	370
260		260	970
1030	1130	1030	1130
1090		1090	2100

This model configuration cannot explain why the spatial pattern develops (likely as a result of inhomogeneity in the larger scale) but it can fit the water flow velocities related to the time of solute travel between certain distance from the tunnel and the observation borehole section.

The parameters of the inverse problem were the following:

- Porosities of the individual model subdomains (outer zone, sections of the inner zone, fractures – the "porosity of a fracture" has a meaning of aperture in metres, as a ratio of the 1 m thickness). The inner zone sections are identical with the 7 sections for permeability.
- Initial concentration of 5 (or 7) zones with divisions at y = 100, 110, and 142 m, extended later with y = 120 m and y = 160 m, through both the inner domain and the outer domain. Additionally, the zone y < 100 is divided to "left" from the tunnel (approx. x < 20m) and "right" (approx. x > 20 m)
- Boundary conditions in 5 (or 7) parts of the boundary (corresponding to the zones of the outer domain)

Full list of parameters is seen from the calibration results (Table 38). The example of concentration distribution is shown in Figure 237.

The results are presented in the form of optimal parameter table (Table 38), borehole profiles (pressures, concentration), Figure 238 and Figure 239, and concentration temporal evolution (Figure 240 and Figure 241). Since the #3 is the first inverse model with transport, with no change of the hydraulic model in its "background" (identical to #2), it makes sense to compare the final transport variant #3a against its precursor #3 (Figure 239), and to compare the final hydraulics in #3a against #2 (Figure 239).

The concentration profiles at 370 days are still without the main observed concentration changes. The #3 model fits the values in 12MI33 and 13MI38 quite well, while the

boreholes perpendicular to the tunnel are not captured. This is appropriate for the defined conceptual model of initial and boundary concentration distribution. Some of the changes at 1130 days are captured in 12MI33 and 13MI38, especially qualitatively, but the higher values in both section 5 of the boreholes is not approached. The #3a variant, combining hydraulic and transport parameters in one optimization case, was not successful. The fit is worse which is a consequence of a more constrained model (flow and transport) together with resetting the initial estimate of the parameters to their basic values, to ensure they are physically realistic.

There were many computational difficulties with the inverse algorithm, producing errors with either code crash or diverging parameter values. Therefore, many options for the initial and optimized parameter sets were not possible to evaluate and we were not able to get reasonable conclusion for the transport model parameter set.

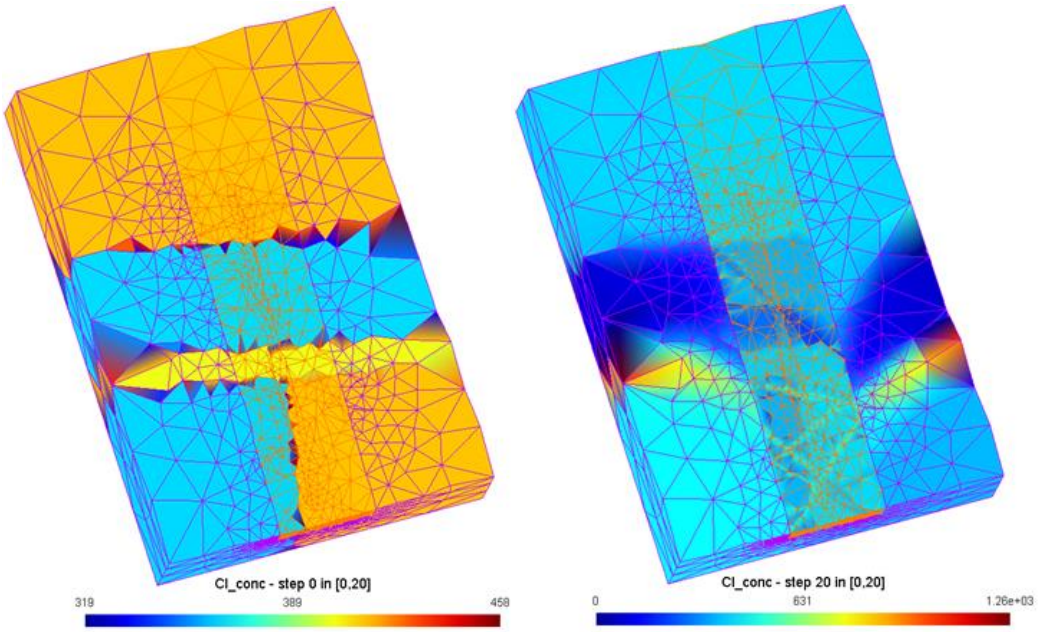

Figure 237. Spatial concentration distributions of the initial condition (left) and the final state (right). The extended range of the latter figure is a result of artificial oscillation in the numerical scheme (invisible).

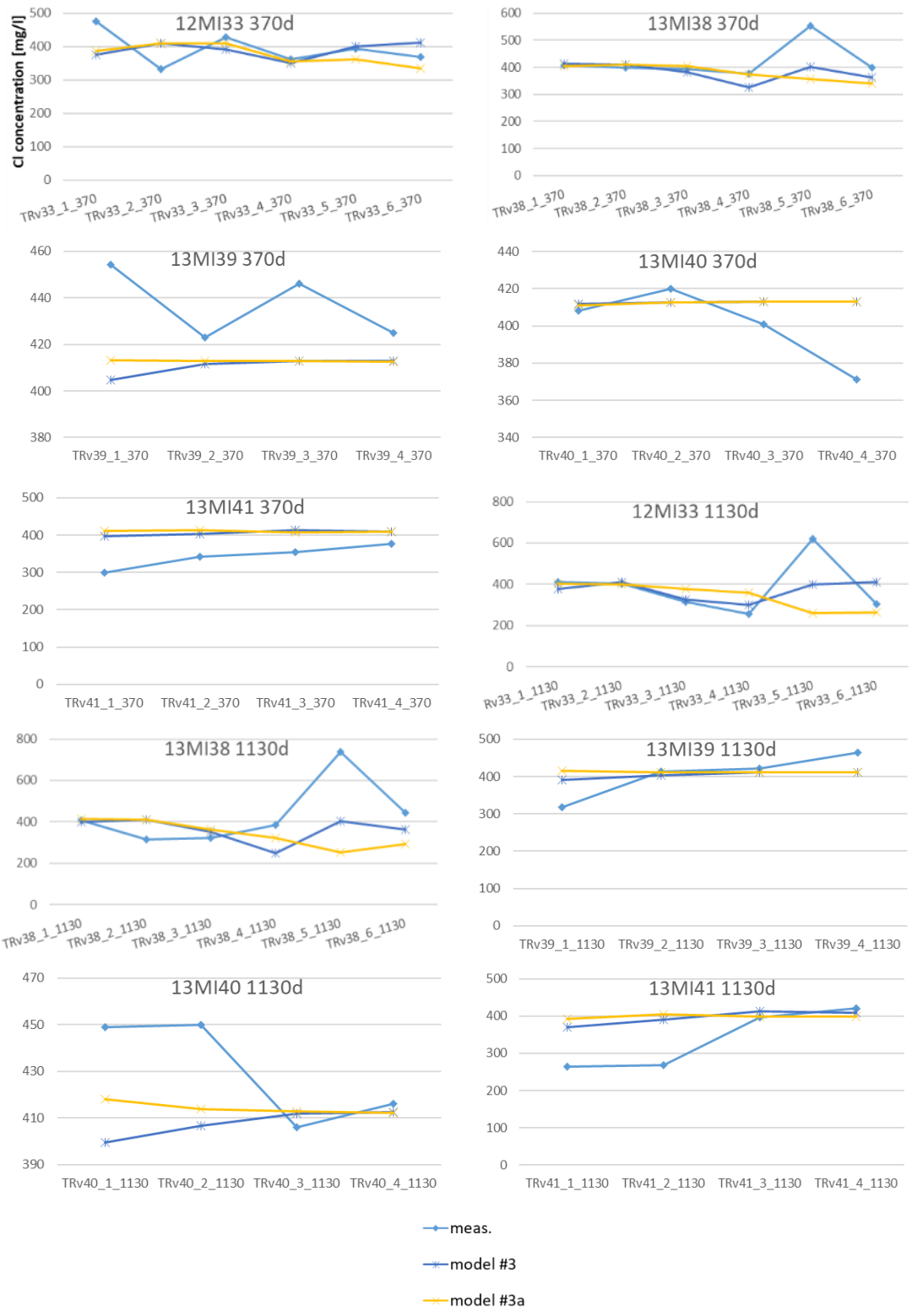

Figure 238. Profiles of concentrations in boreholes in the observation times – comparison of measurement, transport-only calibration (#3) and joint flow and transport calibration (#3a) (the legend is common for all graphs).

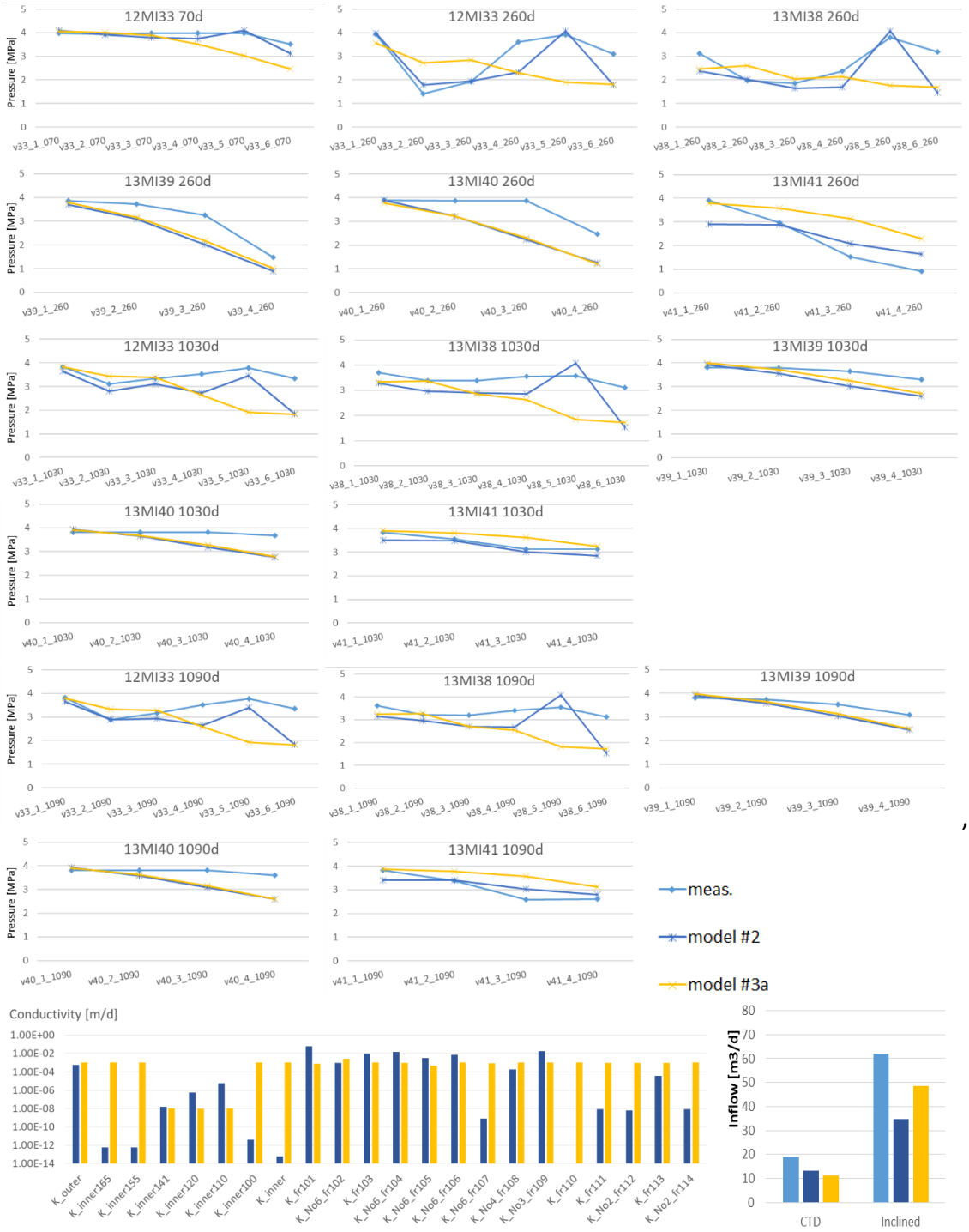

Figure 239. Profiles of pressures in boreholes in the observation times and tunnel inflow values – comparison of measurement, previous (#2) and current (#3a) calibrated model (the legend is common for all graphs).

Table 38. Results of transport problem calibration – set of optimized input parameters of the inverse model type #3. 'SSWR' is the sum of squared weighted residuals. Empty field means no change of parameter during optimization.

Parameter	Meaning	#3 initial estimate	#3 optimal	#3a initial estimate	#3a optimal
K_outer	Hydraulic conductivity [m/s]	2.26E-08	2.26E-08	1.16E-08	1.16E-08
K_inner165		1.16E-12	1.16E-12	1.16E-08	1.18E-08
K_inner155		1.16E-12	1.16E-12	1.16E-08	1.16E-08
K_inner141		1.16E-12	1.16E-12	1.16E-08	1.18E-13
K_inner120		1.16E-12	1.16E-12	1.16E-08	1.12E-13
K_inner110		1.60E-10	1.60E-10	1.16E-08	1.16E-13
K_inner100		1.16E-12	1.16E-12	1.16E-08	1.18E-08
K_inner		1.16E-12	1.16E-12	1.16E-08	1.16E-08
K_fr101	Transmissivity [m^2/s]	7.34E-07	7.34E-07	1.16E-08	9.09E-09
K_No6_fr102		1.08E-08	1.08E-08	1.16E-08	2.89E-08
K_fr103		1.15E-07	1.15E-07	1.16E-08	1.16E-08
K_No6_fr104		1.78E-07	1.78E-07	1.16E-08	1.13E-08
K_No6_fr105		3.68E-08	3.68E-08	1.16E-08	5.44E-09
K_No6_fr106		1.17E-16	1.17E-16	1.16E-08	1.17E-08
K_No6_fr107		3.56E-17	3.56E-17	1.16E-08	9.78E-09
K_No4_fr108		2.08E-09	2.08E-09	1.16E-08	1.19E-08
K_No3_fr109		2.12E-07	2.12E-07	1.16E-08	1.24E-08
K_fr110		1.27E-19	1.27E-19	1.16E-08	1.23E-08
K_fr111		2.52E-14	2.52E-14	1.16E-08	1.11E-08
K_No2_fr112		7.29E-14	7.29E-14	1.16E-08	1.08E-08
K_fr113		4.27E-10	4.27E-10	1.16E-08	1.10E-08
K_No2_fr114		1.64E-11	1.64E-11	1.16E-08	1.23E-08
headBC	Outer boundary head [m]	104	104	104	104
KplugIni	Plug evolution function	1.00E-06	1.00E-06	1.00E-06	1.00E-06
KplugFac		5.00E-04	5.00E-04	5.00E-04	5.00E-04
n_outer	Porosity (the code number refers to intervals of y coordinate in the inner domain)	0.001	3.03E-02	3.03E-02	3.03E-02
n_inner165		0.001	1.00E-03	1.00E-03	1.00E-03
n_inner155		0.001	1.00E-03	1.00E-03	1.00E-03
n_inner141		0.001	1.00E-03	1.00E-03	1.00E-03
n_inner120		0.001	1.00E-03	1.00E-03	1.00E-03
n_inner110		0.001	0.42E-02	0.42E-02	4.20E-03
n_inner100		0.001	1.00E-03	1.00E-03	1.00E-03
n_inner		0.001	1.00E-03	1.00E-03	1.00E-03

Table 38. Results of transport problem calibration – set of optimized input parameters of the inverse model type #3. 'SSWR' is the sum of squared weighted residuals. Empty field means no change of parameter during optimization (continued table)

Parameter	Meaning	#3 initial estimate	#3 optimal	#3a initial estimate	#3a optimal
n_fr101	Transport aperture of discrete fractures [m]	0.001	1.00E-03	1.00E-03	1.00E-03
n_fr102		0.001	1.00E-03	1.00E-03	1.00E-03
n_fr103		0.001	1.00E-03	1.00E-03	1.00E-03
n_fr104		0.001	1.00E-03	1.00E-03	1.00E-03
n_fr105		0.001	1.00E-03	1.00E-03	1.00E-03
n_fr106		0.001	3.06E-04	3.06E-04	3.06E-04
n_fr107		0.001	2.50E-03	2.50E-03	2.50E-03
n_fr108		0.001	1.00E-03	1.00E-03	1.00E-03
n_fr109		0.001	1.00E-03	1.00E-03	1.00E-03
n_fr110		0.001	1.00E-03	1.00E-03	1.00E-03
n_fr111		0.001	6.24E-04	6.24E-04	6.24E-04
n_fr112		0.001	1.00E-03	1.00E-03	1.00E-03
n_fr113		0.001	1.00E-03	1.00E-03	1.00E-03
n_fr114		0.001	1.00E-03	1.00E-03	1.00E-03
c_0l	Initial condition of chlorine concentration in y-coordinate interval	364	364	364	364
c_0p		413	413	413	413
c_100		402	402	402	402
c_110		329	329	329	329
c_120		410.56	410.56	410.5665	410.56
c_142		413	413	413	413
c_160		376	376	376	376
c_0l_OKP	Boundary condition of chlorine concentration in y-coordinate interval	469	469	469	469
c_0p_OKP		259	259	259	259
c_100_OKP		269	269	269	269
c_110_OKP		216	216	216	216
c_120_OKP		148.95	148.95	148.95	148.95
c_142_OKP		416	416	416	416
c_160_OKP		455	455	455	455
SSWR drain	Partial sum for selected observation	18.80	18.8	129.4957	53.75
SSWR hydro		28.17	28.17	67.94416	62.11
SSWR transp.		110.59	91.65	197.5926	174.66
SSWR		131.65	119.82	342	244.89

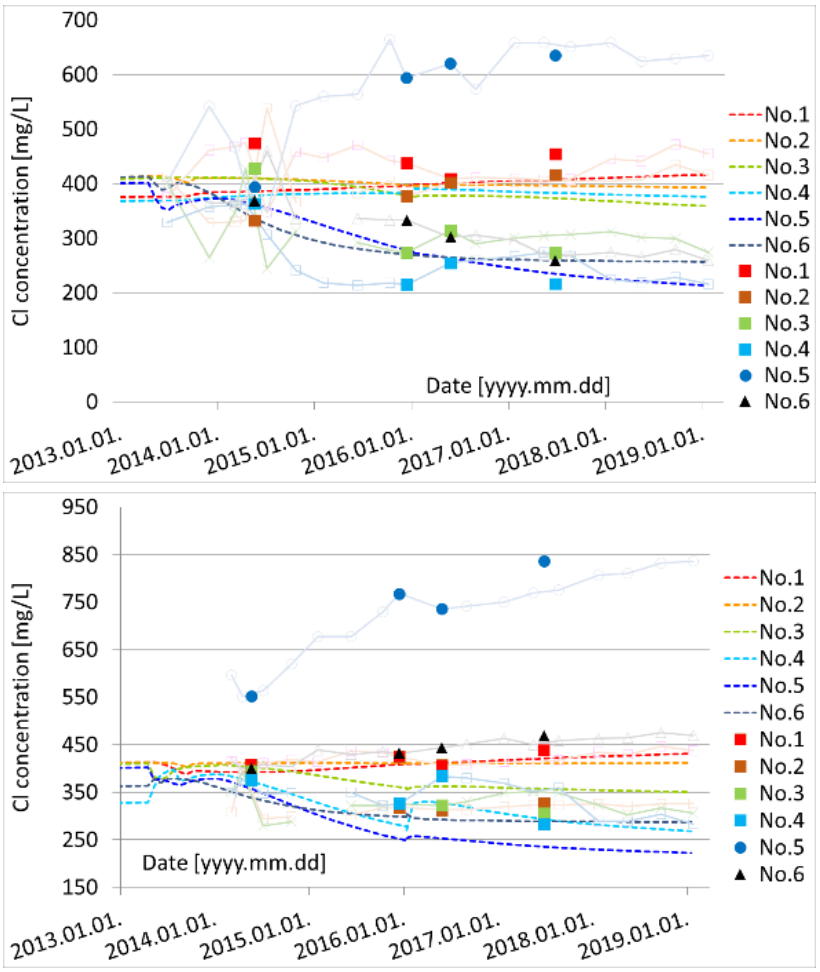

Figure 240. Comparison of calibrated model #3 (dashed lines) with measurement (2 points used for the optimization and shaded lines): 12MI33 borehole (upper) and 13MI38 (lower).

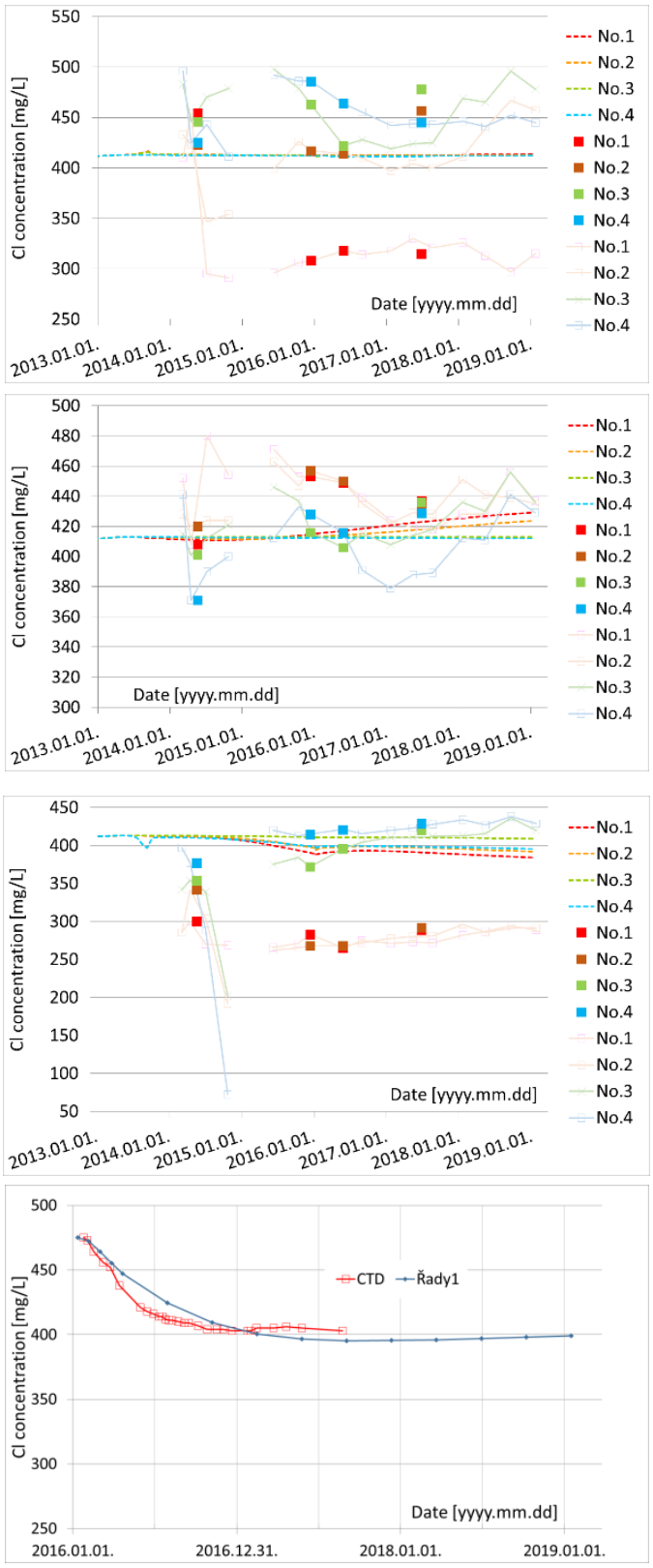

Figure 241. Comparison of calibrated model #3 (dashed lines) with measurement (2 points used for the optimization and shaded lines): 13MI39 borehole (upper), 13MI40 (middle), 13MI41 (lower middle), and CTD free water volume (lower).

10.3 Chlorine spatial distribution

This section describes an additional study trying to derive a 3D spatial distribution of chlorine concentration from the point values of borehole sample analyses, connected to external field with uniform vertical gradient. Such functionality is provided by Voxler software (Golden Software, 2018), generating a function in regular grid of points from values in an irregular cloud of points – both in the form of 'x, y, z, value' sets. It uses various interpolation/extrapolation algorithms. The motivation was also to use this 3D field of concentration as a transport model input, although it would explain only part of the process, in particular the evolution from an intermediate time onwards, while not the process of how the initial distribution has been developed. It requires additional processing to get Flow123d inputs from the Voxler data files.

There were 24 spatial points with analysed samples, but not all were available in the initial phase of the experiment before all the boreholes were drilled. Two sets are from 12MI33 only, which was not considered a meaningful input into the interpolation algorithm. The first complete set was Apr. 2014. In order to try to capture as much of the evolution at the beginning as possible, the data of Mar. 2014 were used, whereas the missing data of 12MI33 were projected from Dec. 2013 and Apr. 2014. Except for one incomplete sampling period, the remaining data are almost uniformly obtained in 4-month intervals. Then the field in Jun. 2015 was selected as a second case for processing, characterising the state after the main transition phase, before the concentrations get almost stabilised.

The volume for interpolation was a block of 120 m x 150 m x 200 m. The xy coordinates correspond to the official coordinate system, i.e. the CTD is oriented at small angle to the y axis. Besides the points of observation, 28 additional points were defined on the boundaries of the block prescribing the vertical gradient approximated from data of other analyses of MIU. The values are evaluated by formula c(z) [mg/l] = 400 – 1.33*(z+300), i.e. starting from the reference value of 400 mg/l at the CTD level. The points are placed on the corners and in middles of edges, on the top and bottom (z = -400 m and -200 m) and intermediate positions of z = -350 m and -250 m.

The concentration field calculated by the inverse distance method with power of two is visualised using various ways (transparent colour volume, shaded isosurface, and coloured isolines) in Figure 242. The evolution at four times is shown. The main pattern is of the higher concentration at the front of 13MI38 and low concentration at the middle and back of 12MI33. As the system evolves, the difference against the uniform

vertical gradient is increasing. In the two later pictures, the local reversal of the vertical distribution can be seen at the 13MI40 borehole.

The transfer of data into the transport simulation required additional processing. We did not find a functionality in Voxler to project the interpolated field to an arbitrary set of points, therefore getting the values in the given discretisation mesh (either in nodes or elements). It allows to export the 3D regular grid of (x, y, z, value). These data were processed in MATLAB, using the "griddata" function. Actually, the MATLAB functions could be used directly from the point data, without need of Voxler, which was used only in the first step of visualisation referred above.

The data projected to the discretisation mesh of Flow123d (TUL, 2017), visualised by GMSH (Geuzaine and Remacle, 2009), are shown in Figure 244, for sample campaigns of Mar. 2014 and Jun. 2015. The distribution patterns are very similar, the main observation is in the higher contrast, i.e. the range between lower and higher concentrations. Use of these fields for transport simulations is rather problematic. The typical behaviour of interpolation for irregularly spaced measurement data is that there is a fine pattern near the measuring points while a coarse pattern elsewhere. For the CTD borehole data it generates bounded volumes of minima and maxima of the concentrations, cannot be principally obtained as a numerical solution of the governing differential equation (fulfilment of the maximum principle). Therefore, we finally decided not to use these results for the simulation and only the regular "strips" of different concentrations over the model domain to the boundary, representing the idea of Cl distribution, are used for the inverse modelling in Section 10.2.4.

The distribution of the interpolated Cl values is also characterized by graph in Figure 243. The main vertical gradient is dominant and the direct effect of the measured data is localized to about 20 m thick zone around the CTD position. The variations from the gradient line in larger vertical distance appear to be artefacts.

10.4 Analysis of vertical chlorine transport

Although the use of Cl concentration data should have provided a convenient means of monitoring the flow in the surroundings of the CTD, the comparison between the model and the measurement proved to be much more complicated for all of the investigators. Therefore, the analysis in this chapter is in addition to the input steps (1 and 2). The main limitation of the model is the above-mentioned concentration range in the initial and boundary conditions, in the CTD model with a range of 100 m vertically (50 m above and 50 m below). It can be expected that a specific flow configuration has to be

established in order for the water to flow dominantly either upwards or downwards towards one of the horizontal observation boreholes. The TUL models are symmetrical in terms of the permeability distribution and a deviation from this symmetry is only seen in the slightly inclined orientation of the corridors or boreholes and the shape of the corridor profile. Although the DFN-based models may create unsymmetrical conditions, but with no deterministic input, the distribution of the communicating fractures in the given volume scale is statistically equal (resulting to similar hydraulic effects), which is likely lead to similar small range of calculated concentrations in the Step 1 results of other teams.

In order to explain the measured development and range of concentrations corresponding to the combination of flows from different directions in the individual parts of the experiment, synthetic permeability configurations were analysed, with an emphasis on asymmetry above and below the level of the CTD and a larger vertical geometric range.

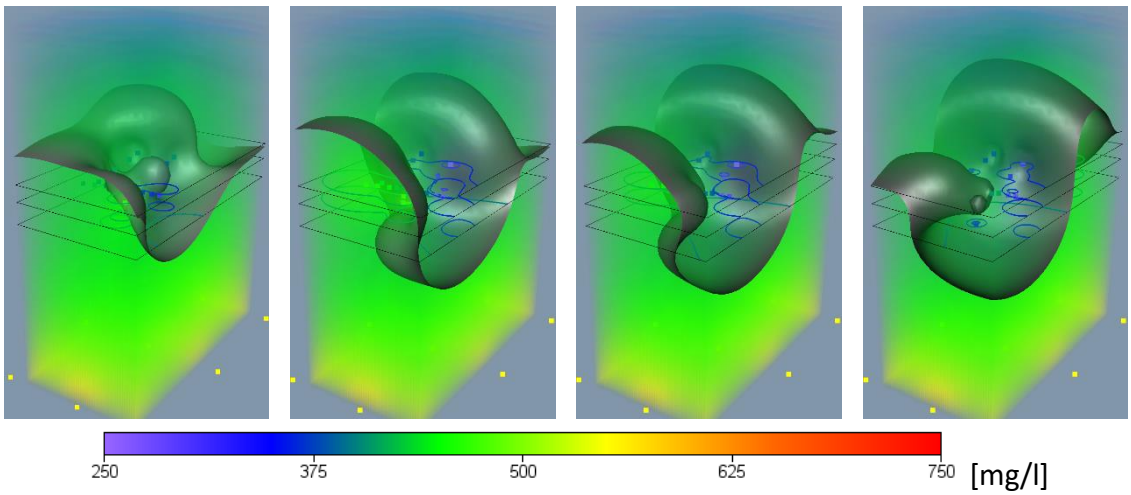

Figure 242. Visualisation of the chlorine spatial distribution by Voxler (at times Apr.2014, Jun.2015, Dec.2015, May.2017). The CTD direction is from the front left to the back right, the position in the level of the middle black rectangle. The field is shown by: colour field (full volume), shaded isosurface of 400 mg/l, and coloured isolines in three horizontal planes defined by the rectangles. The small coloured squares show the prescribed data (boreholes and outer field).

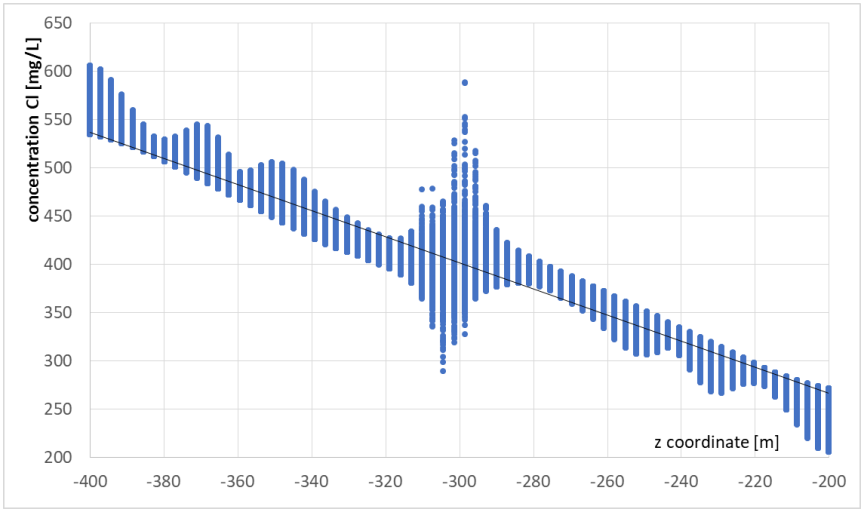

Figure 243. Distribution of interpolated Cl concentration values depending on the vertical coordinate (with respect to the sea level).

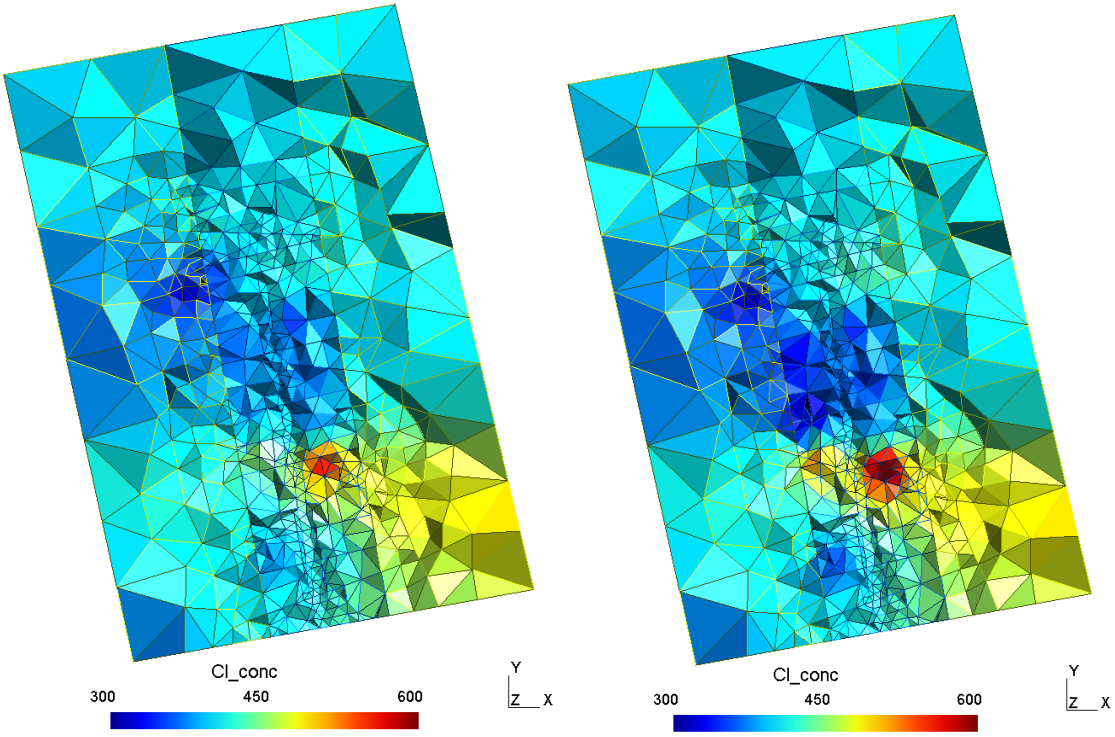

Figure 244. Distribution of chlorine concentration evaluated by interpolation of the borehole measured data and the large-scale gradient, projected to the numerical discretisation mesh. Horizontal section through the domain in -300 m level, data from Mar 2014 and Jun 2015.

The general configuration of the task is shown in Figure 245 on the left and the resulting concentration field is included in Figure 245 on the right. The model is based on the CTD model, the tunnel is circular with a diameter of 5 m, the domain size is doubled, i.e. the edge of the square is 200 m, with a corresponding double concentration range on the boundary (278 to 482 mg/l). There is an interface between lower and higher permeability zones, defined as a horizontal line a certain vertical distance from the tunnel axis. The distance and the ratio of the permeabilities are the controlling parameters of the model.

The difference in permeability (e.g. factor 10) is significantly reflected in the groundwater velocity, but changes in the shape of the trajectories are relatively small, just slightly above the vertical level of the tunnel, so the concentrations in the borehole located horizontally from the tunnel are still a mixture of water from the top and bottom. The effect is more significant above and below the tunnel in the speed of tracer front movement from the edge of the model to the tunnel (a fully saturated “cone” of boundary concentrations). The difference in the borehole area is only partially increased by moving the interface, which distorts the trajectory more. The effect of the interface position can be seen in Figure 246, which shows the time development of the concentrations in the monitored borehole (in the model, a point at a distance of 7.5 m from the tunnel axis).

These models led to changes in concentrations in the monitoring well of up to 50 mg/l, i.e. still less than the measured values. This motivated all the teams, (a) to look for the effect of permeable “channels” from a number of communicating fractures; and (b) to consider the effect of the hydraulic field due to other exposed areas of the underground laboratory.

10.4.1 Channel model

A further test was made to demonstrate how a permeable channel-like structure can influence the concentration distribution and its detection in a borehole. In the model problem setting and discretization of previous section, a set of elements was chosen going from the top down to a level little below the tunnel (to force the trajectories to lead to a borehole before they are deviated towards the tunnel). It is visualized in Figure 247 left. The ratio of the hydraulic conductivities is 10 (channel larger than the surrounding rock).

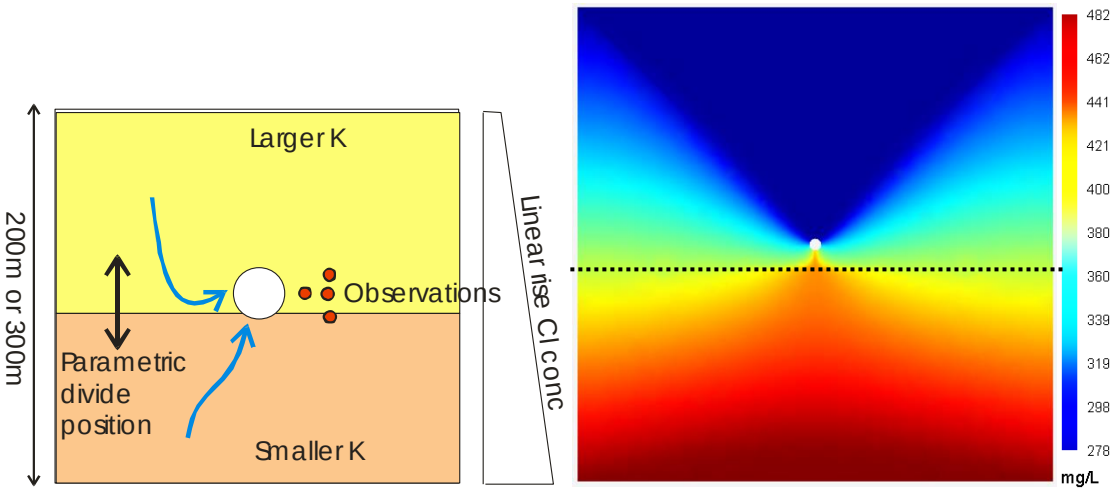

Figure 245. Left: Configuration of the model task demonstrating the effect of vertical inhomogeneity on the transport of chlorides. Right: The resulting concentration distribution over 100 days for an upper and lower zone permeability ratio of 10: 1 and an interface position 10 m below the tunnel axis.

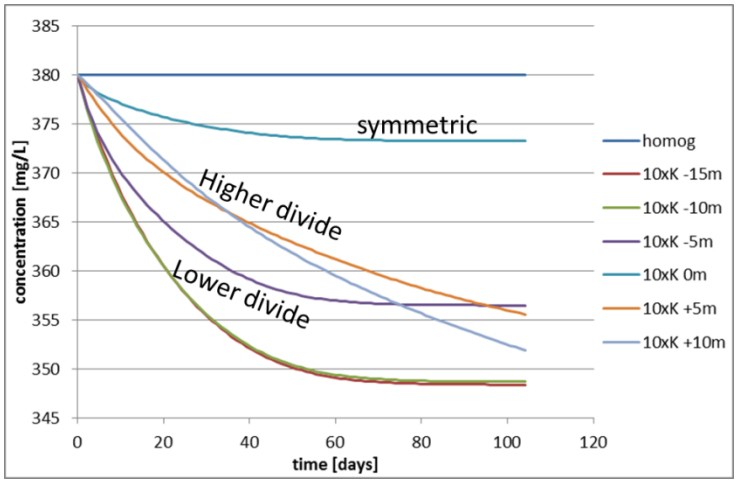

Figure 246. Evolution of concentrations for various alternatives of the synthetic 2D Cl transport tasks due to tunnel drainage with a homogeneous permeability distribution. The legend defines the ratio of the permeability of the upper and lower parts (10: 1) and the position of the interface to the tunnel axis (-15 m to + 10 m ... lower/higher divide). The comparison is also against the homogeneous model with symmetrical mixing of water from above and below.

Contrary with the conceptual idea, the tracer trajectory (Figure 247 right) visualized by a strip of lowest concentration originating at the top boundary makes a “shortcut” already above the tunnel level, so that only a little part of the concentration change reaches the area left of the tunnel at the same vertical position (where the observation

borehole is located). Although the tested configuration is not such leading to the expected concentration evolution at the observation point, it can be expected that a more appropriate channel or fracture position or their network, can reproduce the range of concentrations observed in the monitoring boreholes of GREET, by means of transport from lower or upper rock volume in the appropriate time scale. While this example is not a realistic simulation, it illustrates that fast pathways can connect low or high concentration zones to the tunnel and boreholes so that large changes in Cl concentration could be created

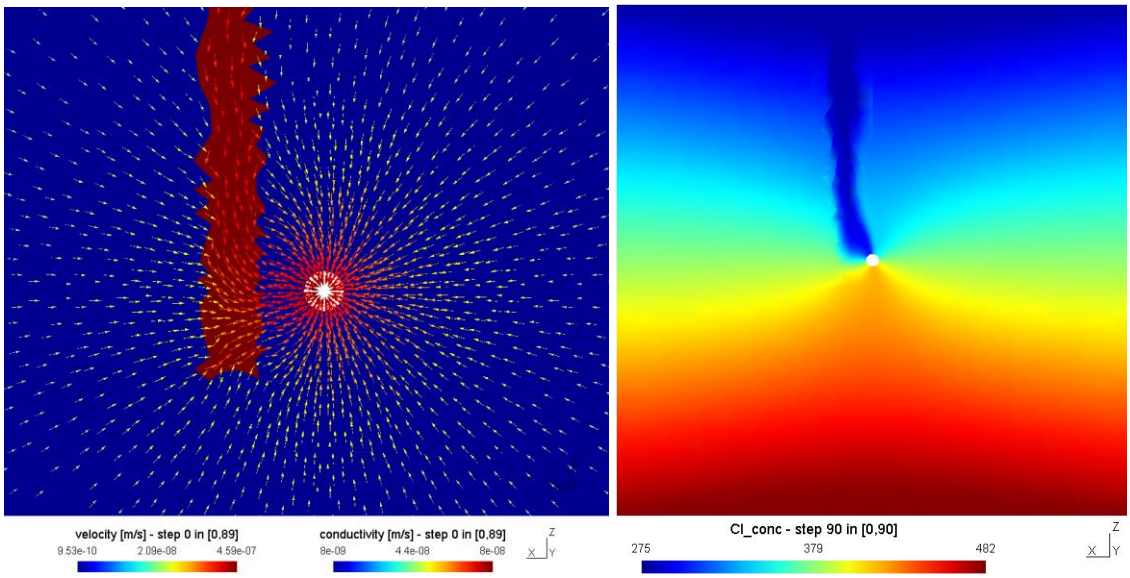

Figure 247. Channel model: In the left, a detail of the prescribed conductivity field and the resulting velocities. In the right, the concentration field in the time of 90 days (stabilized pattern).

10.5 Geochemical analysis

All the geochemical data were categorized, and a unified database was created for each monitored object. The following discussion then consists of an evaluation of the geochemistry development on the individual monitored objects followed by a summary evaluation for the group of related monitored objects in the CTD zone. For the purposes of presentation, the following relevant time intervals were distinguished:

- until June 27, 2013 period before the start of building a CTD
- June 22, 2015 the construction of the CTD has been completed

- August 29, 2015 CTD closed and filled with groundwater
- October 4, 2017 opening the CTD plug

A detailed description, evaluation and interpretation of the groundwater geochemical development in the individual boreholes and their zones is given in .

From the position of individual samples and trends of changes in chemical composition analyzed in is obvious that in the observed range of physico-chemical parameters and groundwater chemical composition, any groundwater of these parameters can be obtained by mixing the two endmembers.

The following groundwater samples were chosen as the endmembers for the groundwater mixing model (details in Figure 248):

- Borehole: 12MI33 Zone: 4 (53.83 m) Date: 5/15/2017 TDS: 517.7 mg/L
- Borehole: 13MI38 Zone: 5 (37.61 m) Date: 1/22/2018 TDS: 1 357 mg/L

The resulting development of the model mixing of water endmembers and its comparison with the sampled water is shown in Figure 249. Basically, two groups of groundwaters can be distinguished. The first is the main group which lies on the main continuous trend, a second group (smaller) is formed by groundwaters that are somehow different from the main trend.

Basically, the second group consists of groundwaters, which were sampled in zones 6 of boreholes 12MI33 and 13MI38 and from zone 4 of boreholes 13MI39–13MI41. These are groundwaters that come from zones that are adjacent to CTD walls (at 12MI33 borehole to main shaft) and are influenced by interaction with shotcrete. Their comparison with the mixing model is shown in Figure 250a for the main trend groundwaters and for the deviated samples in Figure 250b. A very good agreement between the model and the actual development was achieved, so the model borehole expresses the actual behavior of the groundwater. The waters that deviate from the mixing model show the same trend of development, differing only in the shift towards a higher relative proportion of Ca ions.

There is a clear relationship between the total dissolved species concentration, the physico-chemical parameters and the chemical composition of groundwater in the CTD rock environment. The only exceptions are zones that are adjacent to CTD and whose physico-chemical parameters and composition are affected by interaction with the shotcrete. An overall comparison of major geochemical developments and variations for CTD and individual boreholes is shown in Figure 251, and Figure 252.

The total dissolved species concentration in the groundwater of the CTD section indicates their all other parameters. Figure 253 – Figure 257 shows a comparison of

model dependencies of groundwater endmembers mixing and groundwater monitoring data around CTD. In the left column, the physico-chemical parameters and concentrations of the individual components for the main trend are plotted, in the right-hand groundwaters from zones 4 and 6, which are adjacent to the CTD walls and are influenced by the interaction with the shotcrete.

Very good agreement between the model and the actual values was achieved in all monitored parameters and concentrations of main and secondary groundwater components in the vicinity of CTD.

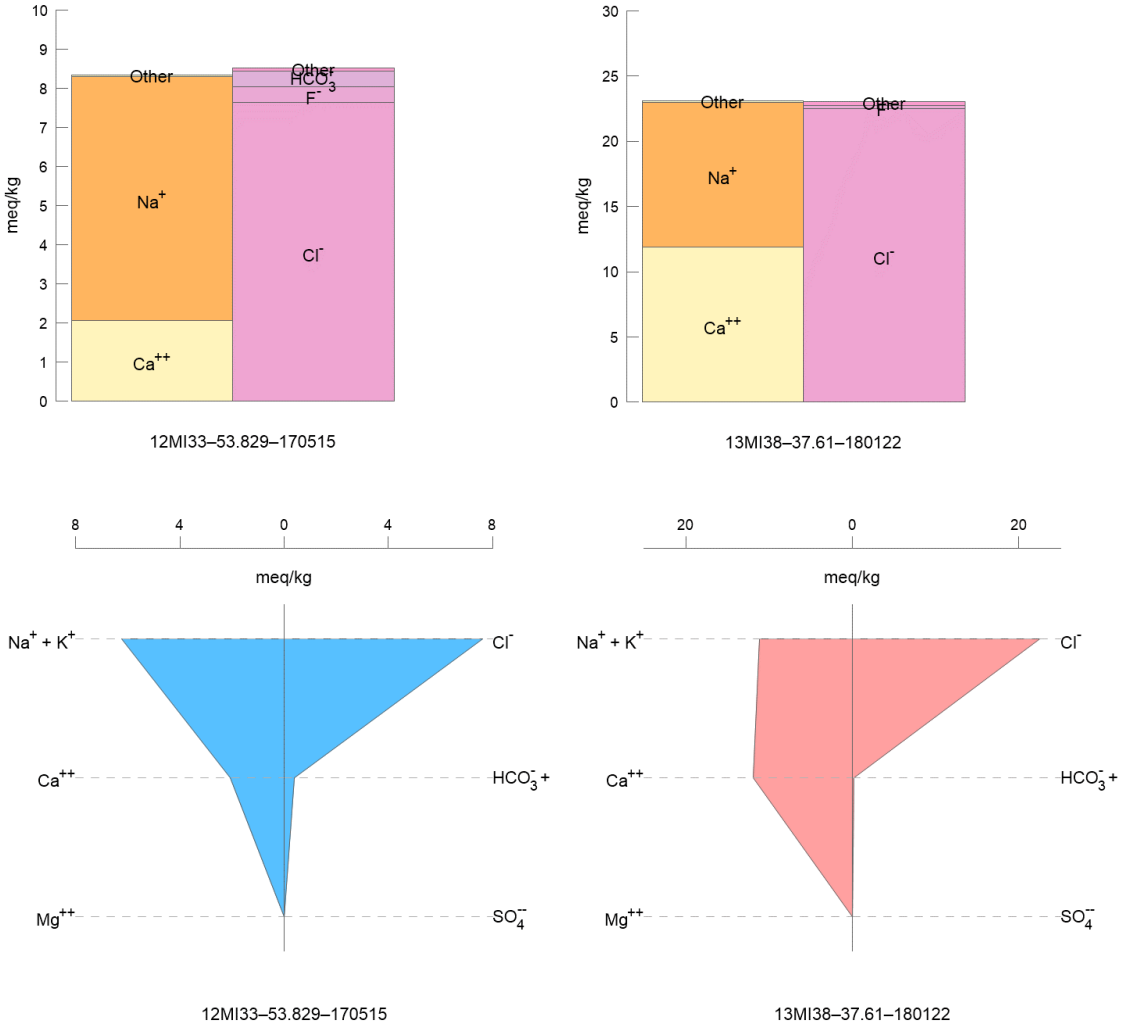

Figure 248. Bar chart and Stiff diagrams for the endmembers of the mixed water model: left for the waters with the lowest mineralization, right for the waters with the highest mineralization (note that the diagrams do not have the same scale).

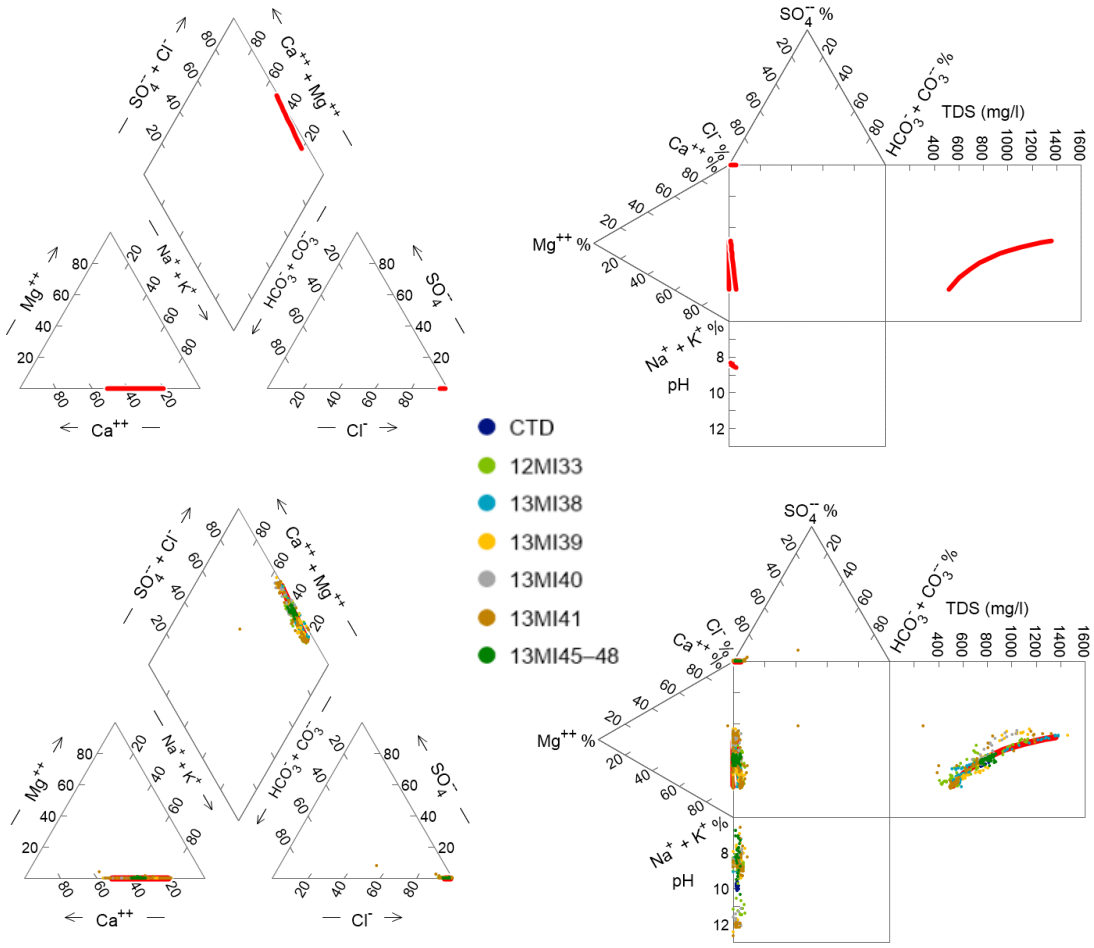

Figure 249. Piper (left) and Durov (right) diagrams for the development of groundwater composition mixed from extreme members. The bottom row shows the diagrams showing the position of the groundwaters from the CTD and boreholes.

a) without zones 4 and 6

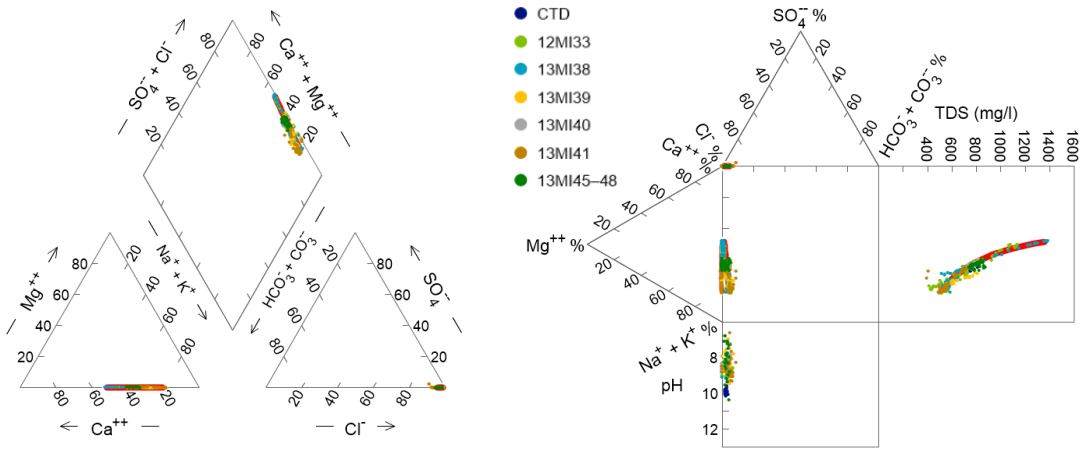

b) zones 4 and 6

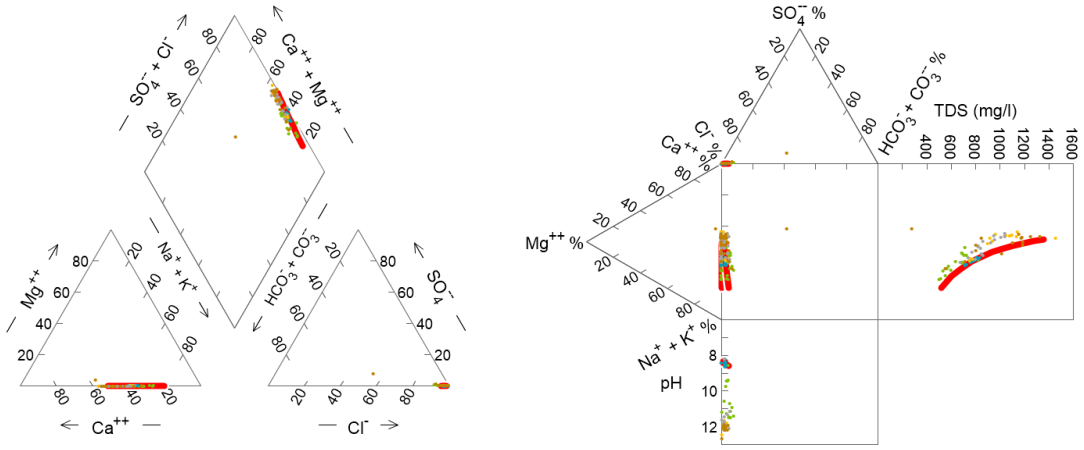

Figure 250. The same diagrams as in Figure 249 with a distinction of waters according to whether they lie on the main trend of development (upper row) and the waters that differ from the main trend (lower row).

12MI33

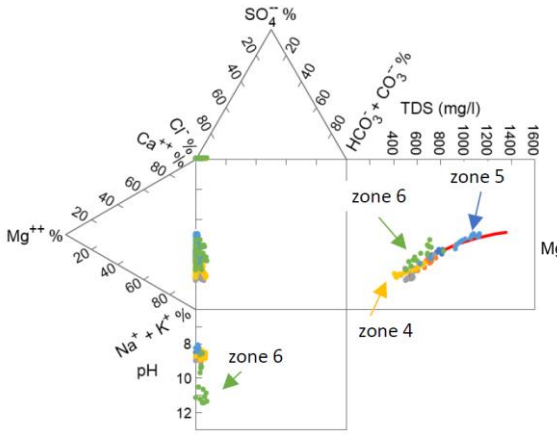

13MI38

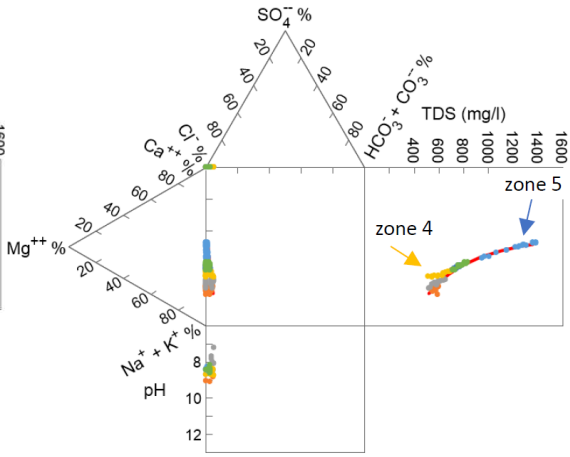

13MI39

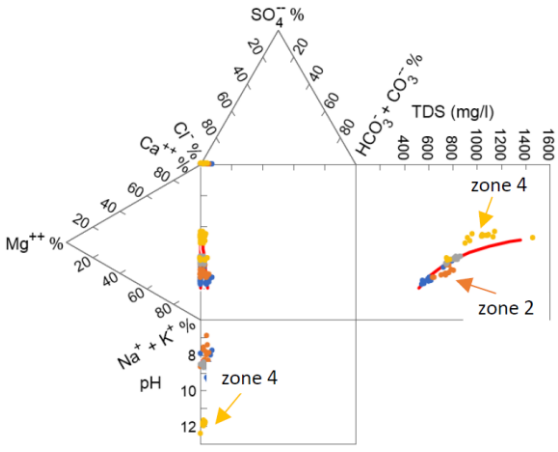

13MI40

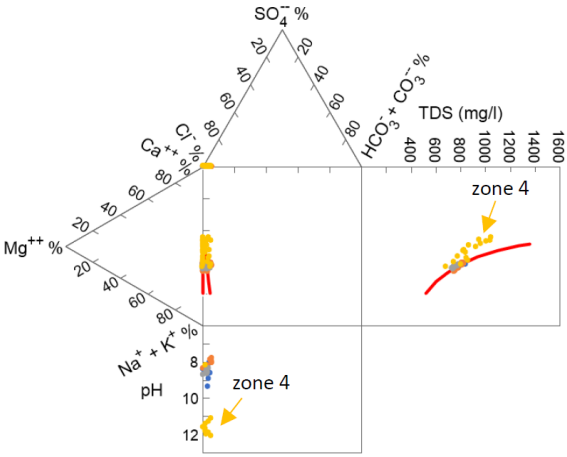

Figure 251. Comparison of the model parameters development of the mixing of extreme groundwater members (red line) and real groundwater CTD and from the zones of individual boreholes in the Durov diagrams. The color coding of the borehole zones is the same as the color coding of the zones used to evaluate the geochemistry in the previous chapters.

13MI41

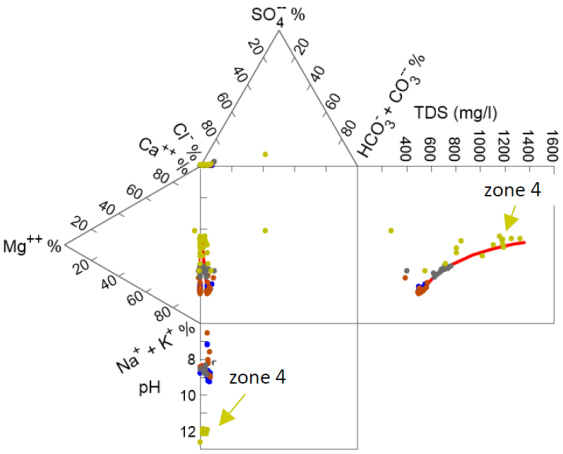

13MI45-13MI48

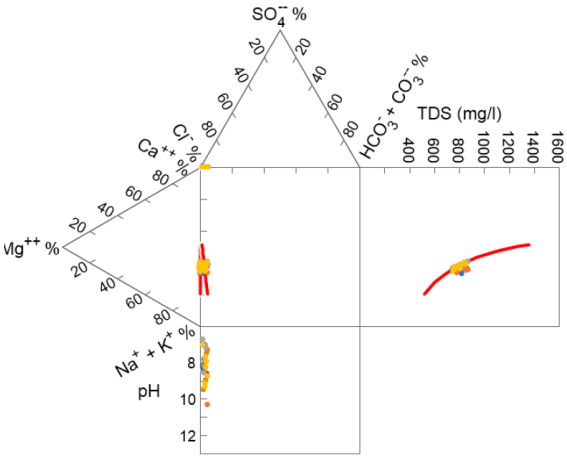

CTD

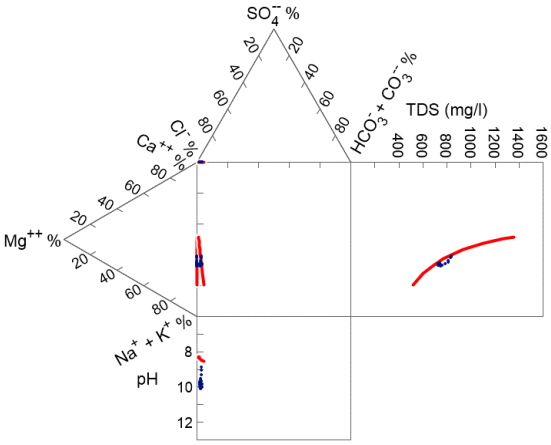

Figure 252. Comparison of the model parameters development of the mixing of extreme groundwater members (red line) and real groundwater CTD and from the zones of individual boreholes in the Durov diagrams. The color coding of the borehole zones is the same as the color coding of the zones used to evaluate the geochemistry in the previous chapters.

without zones 4 and 6

zones 4 and 6

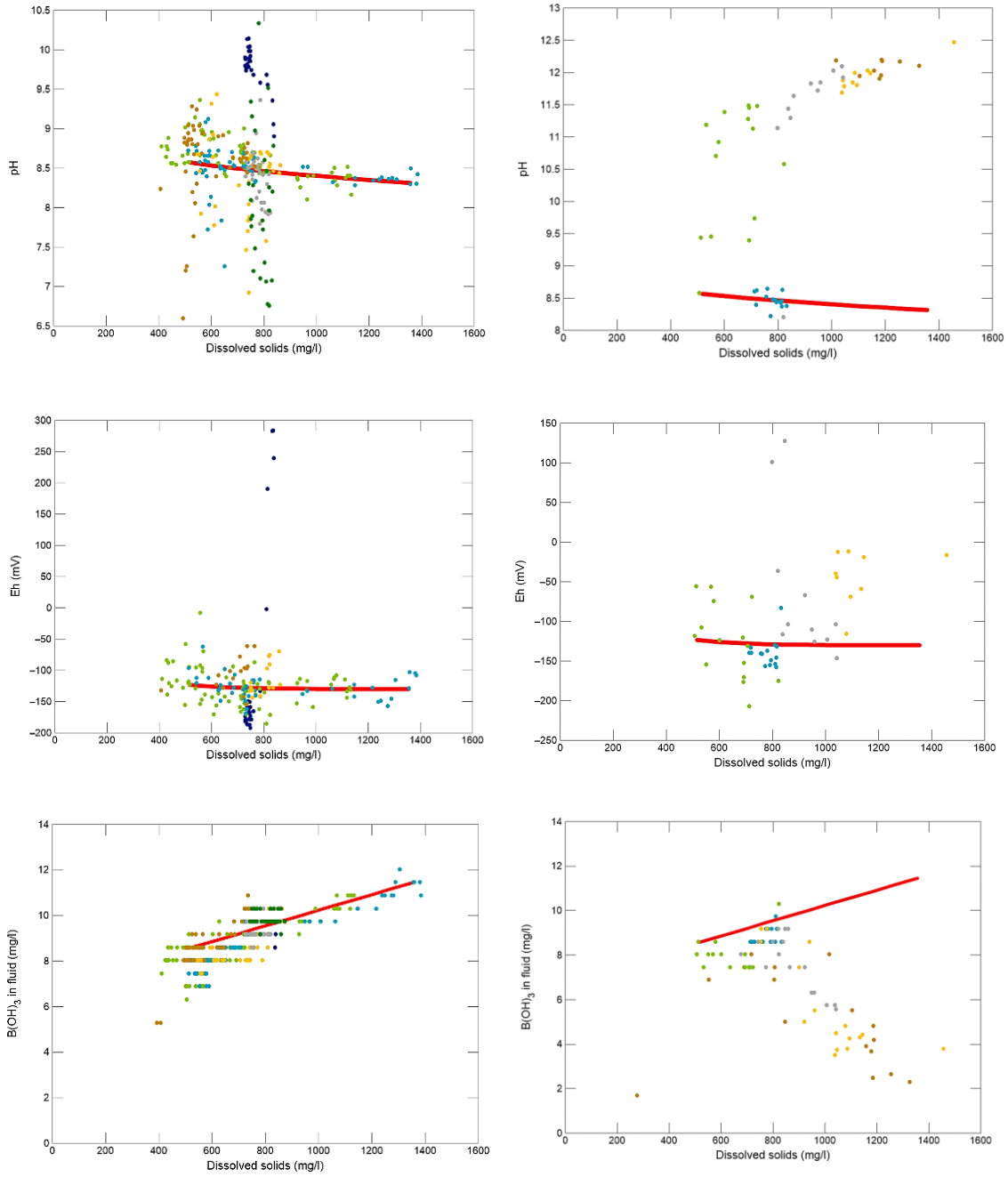

Figure 253. Relationship between total dissolved species concentration and pH, oxidation-reduction potential and $B(OH)_3$ concentration. In the left column the values for groundwaters from zones without contact with the shotcrete (zones 1-5, and zones 1-3, respectively), in the right column values for zones in contact with shotcrete (zones 4 and 6) are plotted. The color coding corresponds to individual boreholes according to the legend in Figure 249. The red line indicates the model development.

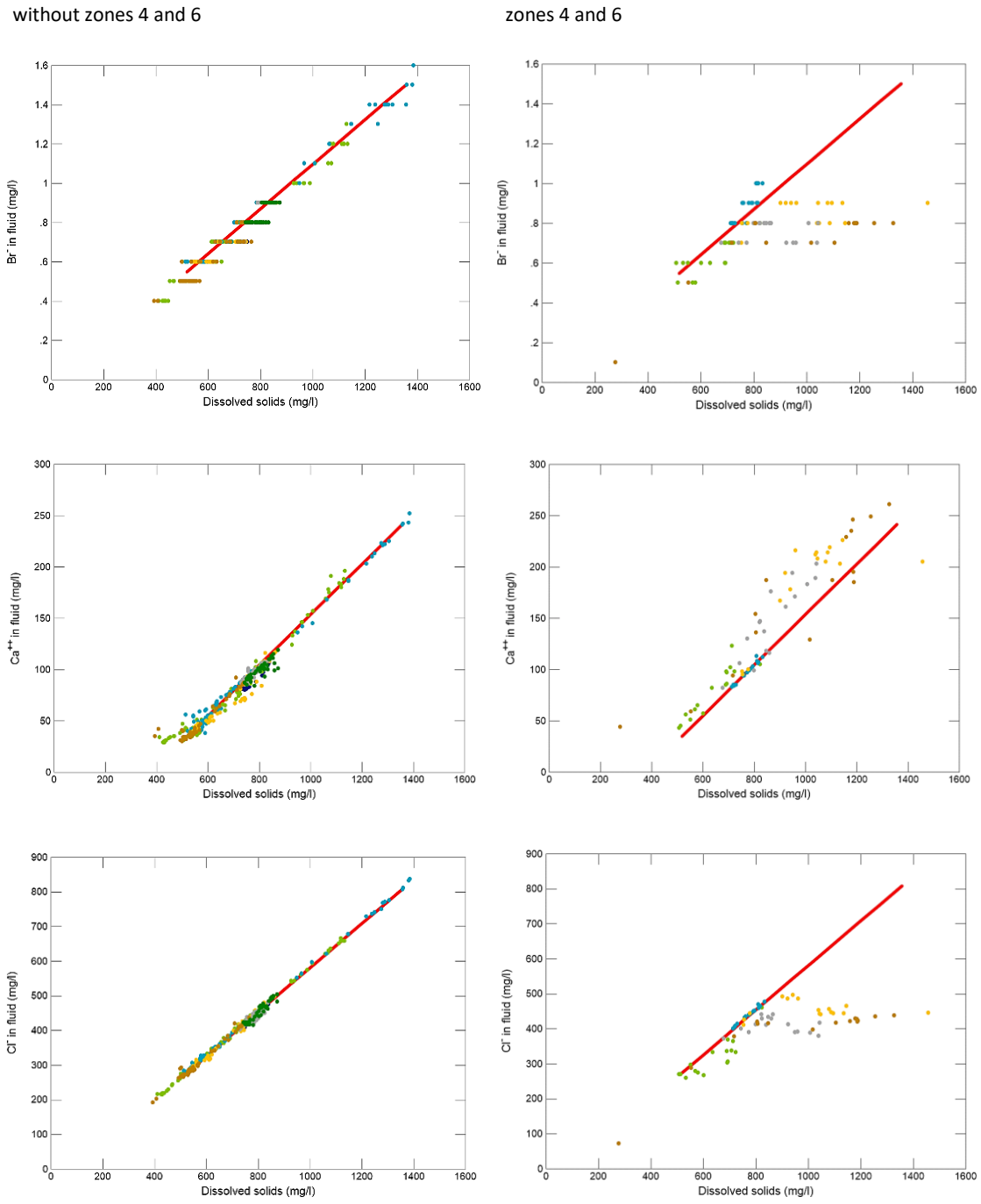

Figure 254. The relationship between the total dissolved species concentration and Br^{-}, Ca^{2+}, and Cl^{-} concentrations. In the left column the values for groundwaters from zones without contact with the shotcrete (zones 1-5, and zones 1-3, respectively), in the right column values for zones in contact with shotcrete (zones 4 and 6) are plotted. The color coding corresponds to individual boreholes according to the legend in Figure 249. The red line indicates the model development.

without zones 4 and 6

zones 4 and 6

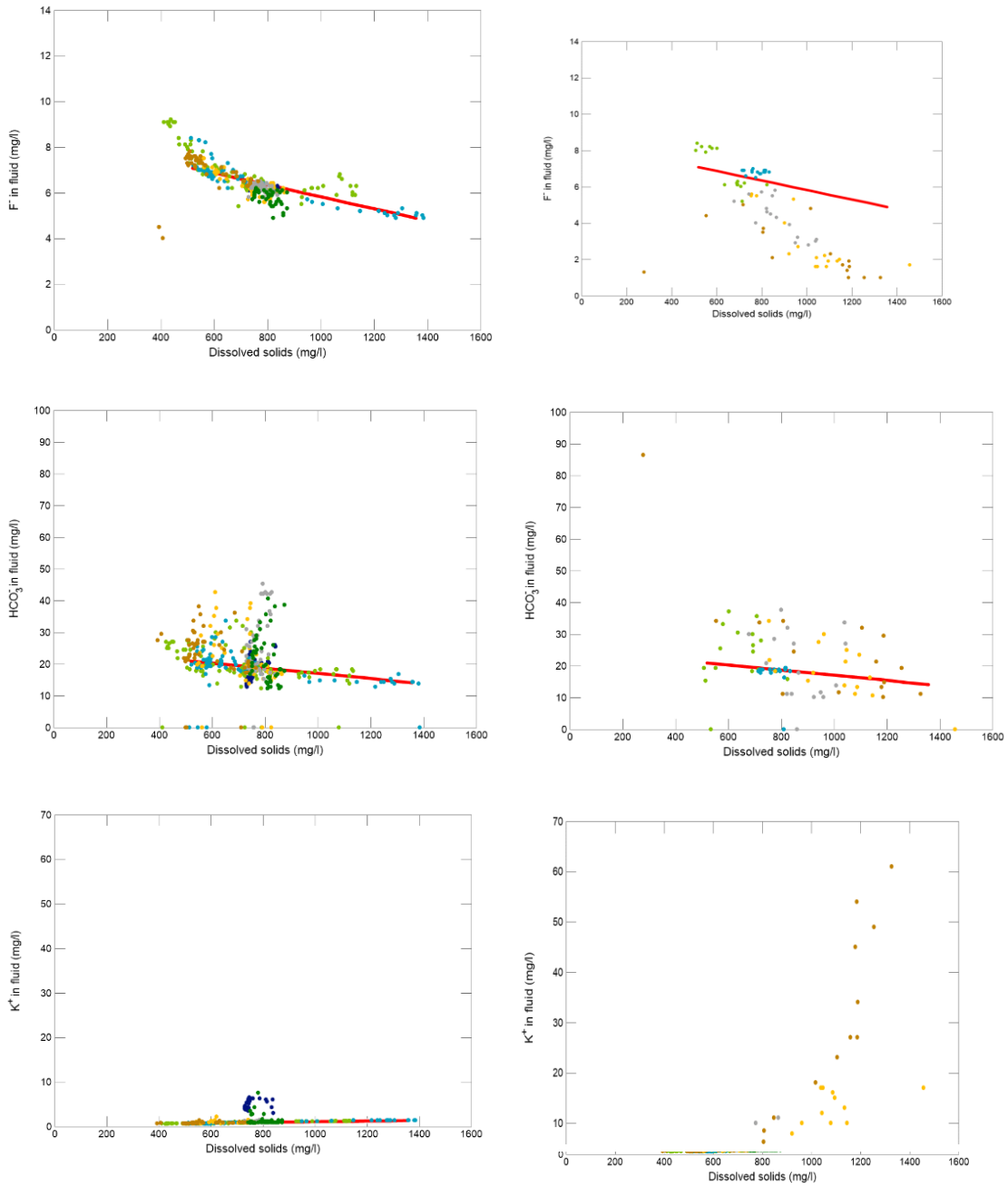

Figure 255. Relationship between total dissolved species concentration and F^-, HCO_3^-, and K^+ concentrations. In the left column the values for groundwaters from zones without contact with the shotcrete (zones 1-5, and zones 1-3, respectively), in the right column values for zones in contact with shotcrete (zones 4 and 6) are plotted. The color coding corresponds to individual boreholes according to the legend in Figure 249. The red line indicates the model development.

without zones 4 and 6

zones 4 and 6

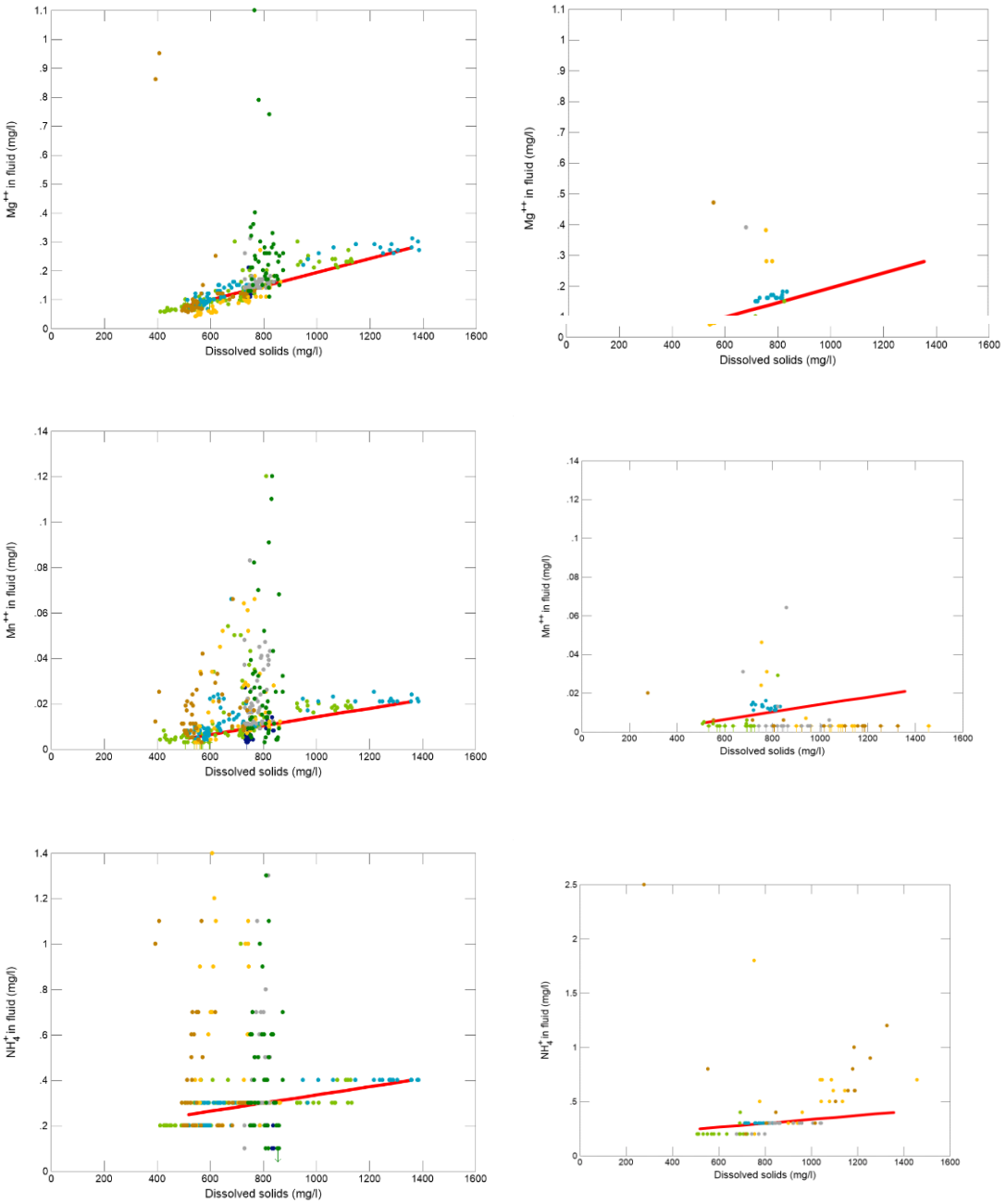

Figure 256. Relationship between total dissolved species concentration and Mg^{2+}, Mn^{2+}, and NH_4^+ concentrations. In the left column the values for groundwaters from zones without contact with the shotcrete (zones 1-5, and zones 1-3, respectively), in the right column values for zones in contact with shotcrete (zones 4 and 6) are plotted. The color coding corresponds to individual boreholes according to the legend in Figure 249. The red line indicates the model development.

without zones 4 and 6

zones 4 and 6

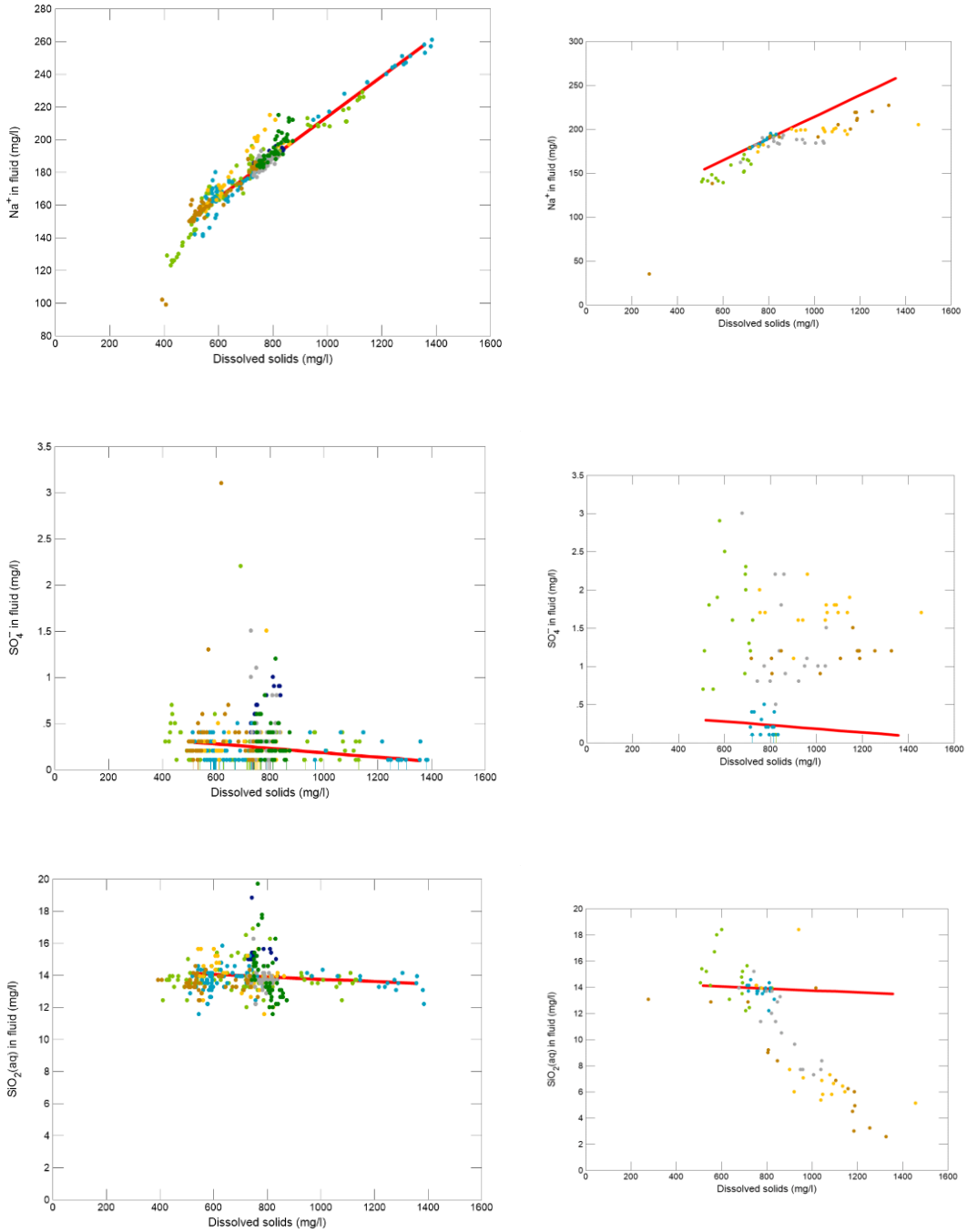

Figure 257. Relationship between total dissolved substances and Na^+, SO_4^{2-}, and $SiO_2(aq)$ concentrations. In the left column the values for groundwaters from zones without contact with the shotcrete (zones 1-5, and zones 1-3, respectively), in the right column values for zones in contact with shotcrete (zones 4 and 6) are plotted. The color coding corresponds to individual boreholes according to the legend in Figure 249. The red line indicates the model development.

Relationship between TDS, physico-chemical parameters and composition of groundwater

The groundwater mixing model allows to express the relationship between total mineralization, physico-chemical parameters and concentrations of individual constituents in groundwater for CTD section. A comparison of the physico-chemical parameters and the chemical composition of the real groundwaters and model endmember groundwaters is given in Table 39. The factors in the formulas below express linear or polynomial regression of the inter-parameter dependencies calculated by the geochemical model (displayed also in Figure 252 to Figure 256).

Table 39. Physico-chemical parameters and composition of real groundwater from boreholes 12MI33 and 13MI38 and their corresponding model waters used for groundwater mixing model.

parameter	unit	12MI33	M-517	13MI38	M-1354
pH		8.57	8.57	8.29	8.29
Eh	mV	-123.6	-123.6	-129.9	-129.9
TDS	mg/L	518.2	517.4	1357	1354
$B(OH)_3$	mg/L	8.58	8.579	11.44	11.44
Br^-	mg/L	0.5	0.55	1.4	1.5
Ca^{2+}	mg/L	42	35	241	241
Cl^-	mg/L	274	274	807	807
F^-	mg/L	7.8	7.1	5.0	4.9
HCO_3^-	mg/L	24.38	21	14.22	14.22
K^+	mg/L	0.6	0.75	1.4	1.4
Mg^{2+}	mg/L	0.08	0.08	0.28	0.28
Mn^{2+}	mg/L	0.005	0.005	0.021	0.021
NH_4^+	mg/L	0.2	0.25	0.4	0.4
Na^+	mg/L	145.0	154.7	258.0	257.7
SO_4^{2-}	mg/L	0.3	0.3	0.1	0.1
$SiO_2(aq)$	mg/L	13.48	14.12	13.48	13.48
Charge imbalance error		-0.96%	0.01%	0.14%	0.00%

Linear equations can be used to derive the chemical composition of groundwater from two groundwaters endmembers (M-517 and M-1354) that represent groundwater in the CTD section

$$C_M \text{ (mg/L)} = a_M \text{ TDS (mg/L)} + b_M$$

where C_M is the concentration of the respective groundwater component M, TDS is the total dissolved species concentration and a_M and b_M are the equation parameters for the respective groundwater component. The parameters for each component are shown in Table 40.

Table 40. Parameters of the equation for calculating the concentration of the respective component in groundwater from the total dissolved species concentration.

Component	a_M	b_M
$B(OH)_3$	3.430E-03	6.805E+00
Br^-	1.135E-03	-3.732E-02
Ca^{2+}	2.461E-01	-9.229E+01
Cl^-	6.369E-01	-5.549E+01
F^-	-2.616E-03	8.453E+00
HCO_3^-	-8.064E-03	2.517E+01
K^+	7.774E-04	3.478E-01
Mg^{2+}	2.390E-04	-4.362E-02
Mn^{2+}	1.911E-05	-4.888E-03
NH_4^+	1.795E-04	1.571E-01
Na^+	1.233E-01	9.090E+01
SO_4^{2-}	-2.384E-04	4.233E-01
$SiO_2(aq)$	-7.422E-04	1.450E+01

The pH values are not simply the result of mixing, that is, merely mixing the H^+ mixed water. During mixing, their concentrations are affected by autoprotolysis of the water

$$H_2O \leftrightarrow H^+ + OH^-$$

by altering the carbonate species concentrations, e.g.

$$HCO_3^- \leftrightarrow H^+ + CO_3^{2-}$$

and other interactions (e.g. hydroxocomplex formation). Speciation changes have a buffering effect on pH changes and cannot be estimated directly without geochemical modeling. However, based on the pH evolution in the geochemical mixing model, the dependence of the second-degree polynomial can be superimposed for a given mixing interval

$$pH = a_{pH} [TDS\ (mg/L)]^2 + b_{pH} [TDS\ (mg/L)] + c_{pH}$$

where TDS is the total dissolved species concentration and a_{pH}, b_{pH}, and c_{pH} are the equation parameters for the pH of the mixed water. The parameters are given in Table 41.

Table 41. Equation parameters for calculating the pH of groundwater from the total dissolved species concentration.

	a_{pH}	b_{pH}	c_{pH}
pH	-7.249E-08	4.483E-04	7.770E+00

The same applies to the development of the oxidation-reduction potential. During mixing, the redox speciation changes the components that depend, among other things, on pH. It is a complex of interconnected non-linear interactions. For a given mixing interval, the dependency may be fitted with a third-degree polynomial. Depending on the TDS, estimated Eh values can be calculated according to equation

$$Eh\ (mV) = a_{Eh} [TDS\ (mg/L)]^3 + b_{Eh} [TDS\ (mg/L)]^2 + c_{Eh} [TDS\ (mg/L)] + d_{Eh}$$

where TDS is the total dissolved species concentration and a_{Eh}, b_{Eh}, c_{Eh}, and d_{Eh} are parameters of the equation for calculating the Eh of the mixed water. The parameters are given in Table 42.

Table 42. Equation parameters for calculating the Eh of groundwater from the total dissolved species concentration.

	a_{Eh}	b_{Eh}	c_{Eh}	d_{Eh}
Eh	-2.217E-08	7.808E-05	-9.147E-02	-9.426E+01

Relationship between Cl concentration, physico-chemical parameters and composition of groundwater

For dependence of physico-chemical parameters and concentrations of individual groundwater components on the concentration of Cl ions, the following dependencies can be similarly derived

$$c_M \text{ (mg/L)} = a_M \text{ Cl (mg/L)} + b_M$$

$$\text{pH} = a_{pH} [\text{Cl (mg/L)}]^2 + b_{pH} [\text{Cl (mg/L)}] + c_{pH}$$

$$\text{Eh (mV)} = a_{Eh} [\text{Cl (mg/L)}]^3 + b_{Eh} [\text{Cl (mg/L)}]^2 + c_{Eh} [\text{Cl (mg/L)}] + d_{Eh}$$

with the parameters given in Table 43,

Table 44, and Table 45.

Table 43. Parameters of the equation for calculating the concentration of the respective component in groundwater from the Cl ion concentrations.

component	a_M	b_M
$B(OH)_3$	5.385E-03	7.103E+00
Br^-	1.783E-03	6.159E-02
Ca^{2+}	3.863E-01	-7.085E+01
F^-	-4.107E-03	8.225E+00
HCO_3^-	-1.266E-02	2.447E+01
K^+	1.221E-03	4.156E-01
Mg^{2+}	3.752E-04	-2.280E-02
Mn^{2+}	3.001E-05	-3.223E-03
NH_4^+	2.819E-04	1.728E-01
Na^+	1.935E-01	1.016E+02
SO_4^{2-}	-3.742E-04	4.025E-01
SiO_2(aq)	-1.165E-03	1.444E+01

Table 44. Equation parameters for calculating the pH of groundwater from the Cl ion concentration.

	a_{pH}	b_{pH}	c_{pH}
pH	2.903E-07	-7.849E-04	8.761E+00

Table 45. Equation parameters for calculating the Eh of groundwater from the total dissolved species concentration.

	a_{Eh}	b_{Eh}	c_{Eh}	d_{Eh}
Eh	-8.577E-08	1.781E-04	-1.230E-01	-1.017E+02

Relationship between the mixing ratio of the endmembers, physico-chemical parameters and composition of groundwater

For dependence of component concentrations and physicochemical parameters on the mixed groundwater ratio of mix_r, where mix_r = 0 corresponds to the lower mineralized water (M-517) and mix_r = 1 corresponds to the higher mineralized water (M-1354), then

$$c_M \text{ (mg/L)} = a_M \text{ mix\_r} + b_M$$

$$\text{pH} = a_{pH} \text{ mix\_r}^2 + b_{pH} \text{ mix\_r} + c_{pH}$$

$$\text{Eh (mV)} = a_{Eh} \text{ mix\_r}^3 + b_{Eh} \text{ mix\_r}^2 + c_{Eh} \text{ mix\_r} + d_{Eh}$$

with the parameters given in Table 46, Table 47, and Table 48.

It should be noted here that all the above dependencies apply to groundwaters that are not affected by the interaction with the shotcrete.

Table 46. Equation parameters for calculating the concentration of the respective components in groundwater from the ratio of the mixed end members.

Component	a_M	b_M
$B(OH)_3$	2.876E+00	8.579E+00
Br^-	9.520E-01	5.501E-01
Ca^{2+}	2.063E+02	3.501E+01
Cl^-	5.341E+02	2.740E+02
F^-	-6.761E+00	2.100E+01
HCO_3^-	-6.761E+00	2.100E+01
K^+	6.518E-01	7.500E-01
Mg^{2+}	2.004E-01	8.001E-02
Mn^{2+}	1.603E-02	5.001E-03
NH_4^+	1.505E-01	2.500E-01
Na^+	1.034E+02	1.547E+02
SO_4^{2-}	-1.999E-01	3.000E-01
$SiO_2(aq)$	-6.223E-01	1.412E+01

Table 47. Equation parameters for calculating the pH of groundwater from the ratio of the mixed end members.

	a_{pH}	b_{pH}	c_{pH}
pH	8.291E-02	-3.343E-01	8.567E+00

Table 48. Equation parameters for calculating the ground water Eh value from the ratio of the mixed end members.

	a_{Eh}	b_{Eh}	c_{Eh}	d_{Eh}
Eh	-1.307E+01	3.071E+01	-2.388E+01	-1.238E+02

10.6 Summary

The modelling in Step 2 was mainly aimed to explain the full set of measured data, i.e. to inform and calibrate the model, so that the conceptual configuration and parameters represent the observed physical processes. This was achieved by inverse modelling,

applying optimization algorithm to calibrate the unknown or uncertain parameters. Additionally, some supporting models and analyses has been made, to explain and capture the Cl concentration evolution and spatial distribution.

The importance of the TUL solution was also in application of the mixed-dimensional model, i.e. a configuration of selected deterministic fractures and continuum subdomains which is, in this context, original and there is hitherto little experience with it in modelling at spatial scale of meters to tens of meters. It has potential advantages in terms of portability and scalability, i.e. combining solutions at different spatial scales. Additional experience was as follows:

- The use of the inverse solver (UCODE software) had a partial success, it helped to increase the model/experiment fit but often the iterations diverged or came to results not physically meaningful. For this kind of problem, it is necessary to make some estimates manually from conceptual understanding of the problem.
- Projection of the model conditions at a larger scale onto the model of the experiment did not have a significant effect on the pressure pattern, but proved to be important for the transport.
- The calculations are largely limited by the pre-processor options, i.e. by efficiently entering the underground geometry and the fractures and discretization without unnecessary refinement outside the area of interest.

The geochemical analysis brought a new perspective on the spatial and temporal distribution of the groundwater composition in the surroundings of the laboratory, as a mixture of water from selected analyses in various proportions. This highlighted the dominant role of transport (advection and dispersion) over the reactions between the components and between the water and the rock, and defined the initial conditions for more relevant modelling of transport in 3D connected to the inhomogeneous flow field from the hydraulic model. Explicit formulas how to estimate other components and chemical parameters from the Cl concentration are derived.

Since the modelling of the phenomena in the crystalline rock is hampered by discontinuities and irregular inhomogeneity, the disagreement between the model and the measurements does not necessarily mean a wrong or inappropriate solution, but it can be accepted as uncertainty in the processes.

11 Summary of improvements in Step 2

One of the difficulties in Step 2 is to calibrate and model inhomogeneous hydrological structures such as fractures in order to capture hydraulic and chemical changes in each hydrogeological area. Each team has tried both stochastic and deterministic approaches.

Figure 258 shows the JAEA's concept to model the discrete fractures in the granite. Many DFN models were initially constructed by a stochastic approach using all observed fracture data. Then, in order to reproduce the observed changes in water pressure, JAEA chosen the most realistic realization out of 100 possible cases. As for the stochastic fractures encountered in the tunnel, the location and hydraulic parameters were corrected based on the observation data in tunnel and boreholes. The modified best-fit DFN model was converted to an ECPM model. The ECPM model was further manually calibrated to capture changes in Cl concentration and water pressure.

SNL's approach was similar to that of JAEA (Figure 259). However, they at first, classified the fracture appearance in the tunnel to set hydraulic parameters of the high permeable fracture. In parallel, SNL constructed several DFN models considering only high permeable fracture. And, integrated the stochastic DFN model and observed fracture data. Then, the DFN models were converted to the ECPM models. The reliability of such ECPM models was checked by comparing the predicted groundwater inflow rate into tunnel and observed data.

Figure 260 shows TUL's approach. TUL didn't use a stochastic methodology, instead highly permeable fractures were modelled using a deterministic approach. Hydraulic properties of the fractures were directly applied to the embedded in homogeneous rock. Furthermore, modification of detailed rock domain settings and mesh size around the tunnel was conducted to capture Cl concentration and water pressure variations.

Irrespective of whether the stochastic and deterministic approach was used, some manual deterministic settings were needed in the calibration process of fracture distribution, connectivity and continuity, in order to reproduce the inhomogeneous Cl concentration around the tunnel.

The model improvement in Step 2 was done from the 4th workshop to the 7th workshop. Advances in modelling and simulation techniques can be confirmed by comparing the results of water pressure change from each workshop.

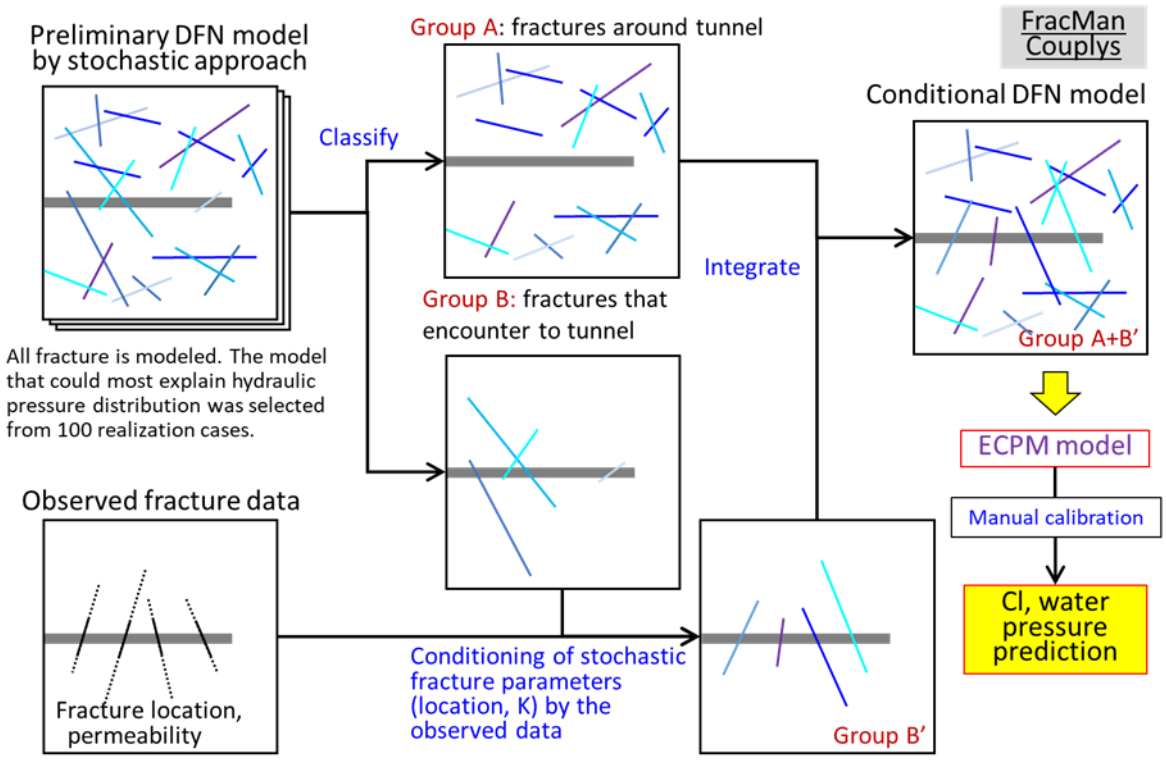

Figure 258. The concept for modelling the fractures in granite (JAEA)

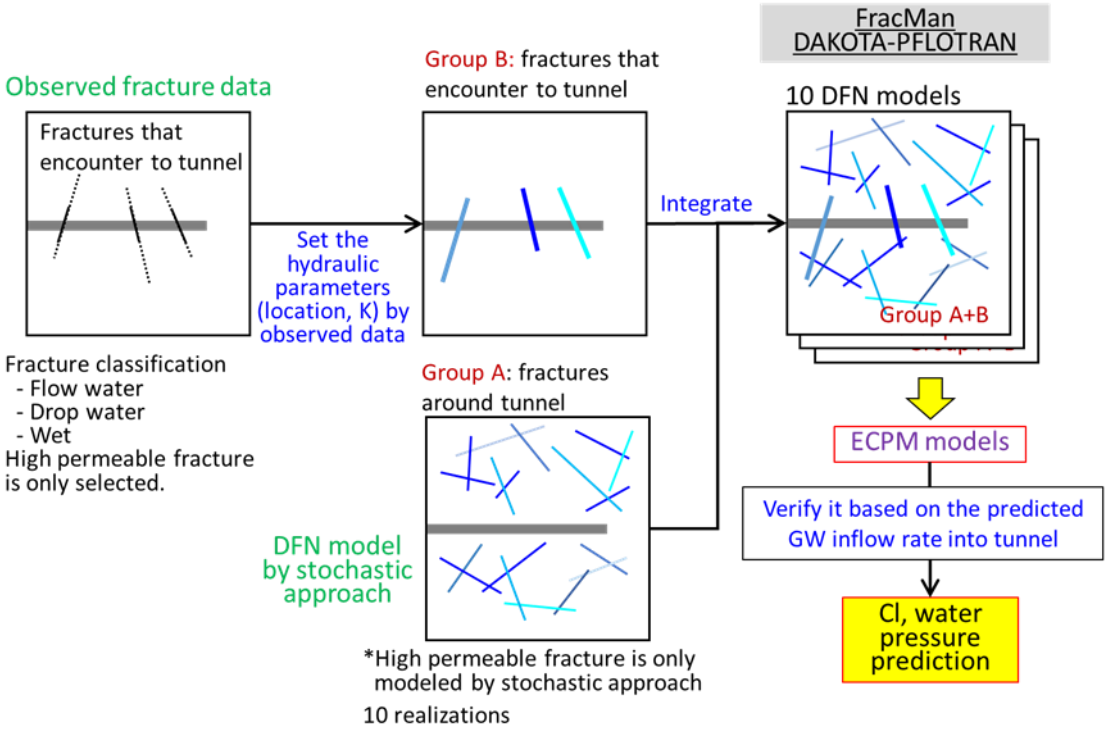

Figure 259. The concept for modelling the fractures in granite (SNL)

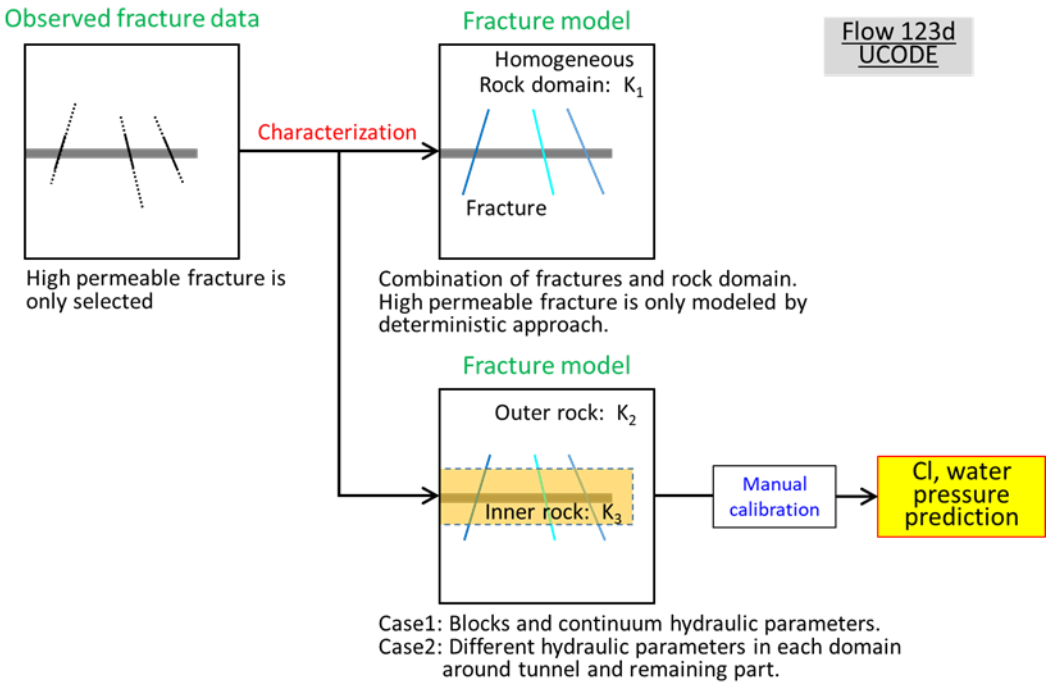

Figure 260. The concept for modelling the fractures in granite (TUL)

Figure 261 and Figure 262 show the observation water pressure in CTD and simulation results in 5th and 7th workshop, respectively. The water pressure of the CTD decreased with time due to water leakage around the watertight plug. The initial estimation by each team at the 5th workshop showed a water pressure value around 3.5 - 4.0 MPa, which is near the baseline value before the CTD excavation. Then, based on additional data provided after the 5th workshop, each team specified a more precise hydraulic conductivity around the plug. In the 7th workshop, the simulation of water pressure by each team reproduced the observed changes well, including the pressure decline. In other words, the hydraulic plug performance could be estimated by a sensitivity analysis using various hydraulic parameters to reproduce the observed water pressure changes. The K of the water-tight plug including the surrounding rock was estimated to be about 5e-8 (m/s).

The water pressure change simulation around the CTD has also been improved when examining the calibration for water pressure in the CTD. The hydraulic response after tunnel closure in each monitoring section distinctly reflected the fracture connectivity between each monitoring section and the CTD. Figure 263 shows the predicted water pressure change in each monitoring section by each team at the 6th workshop.

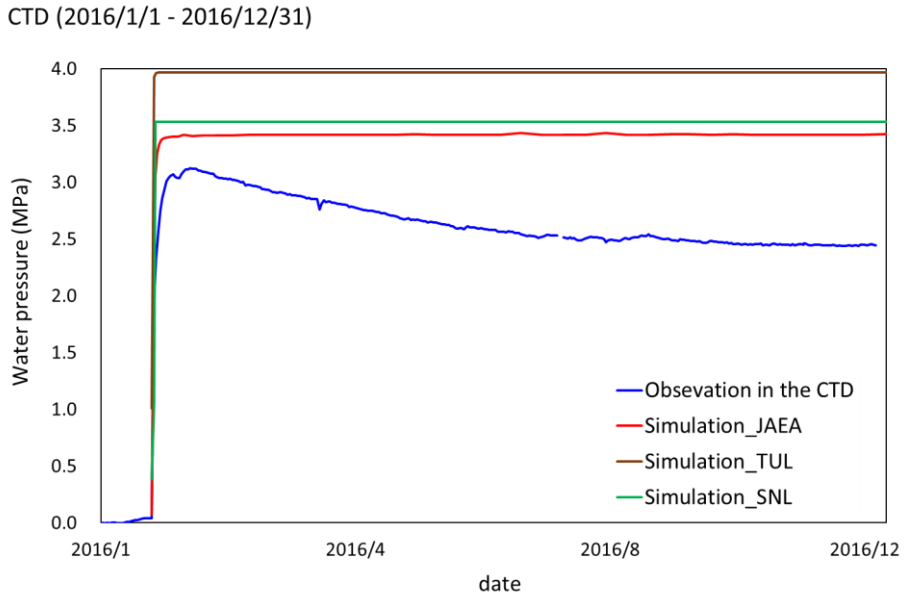

Figure 261. Simulated water pressure changes in CTD (5th workshop)

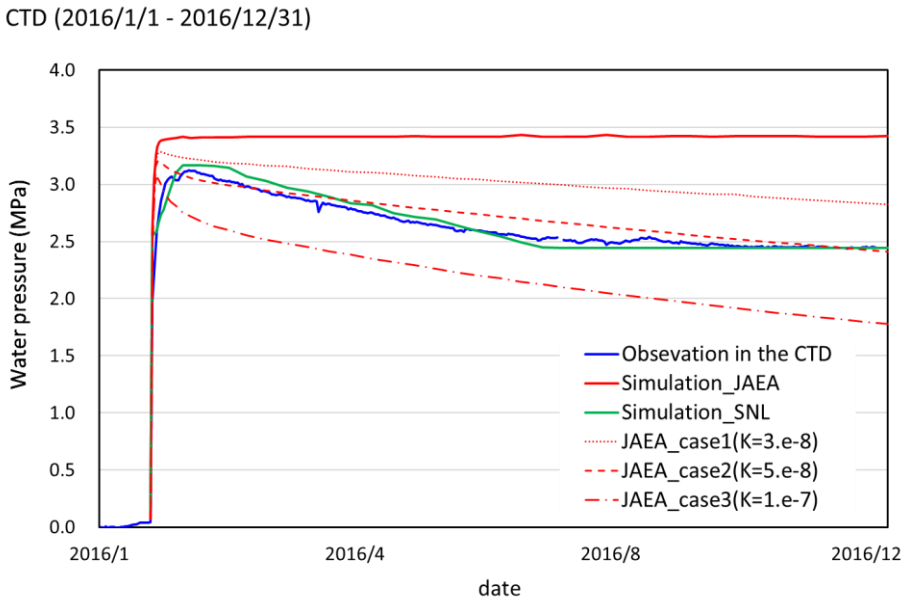

Figure 262. Simulated water pressure changes in CTD (7th workshop)

The observed water pressure shows a similar trend to the pressure variation in the CTD at monitoring points 2 and 3 where connecting to the tunnel via a fracture. In these sections, simulated values by each team were deferent from the observation. The improved JAEA and SNL's DFN models and TUL's model at the 7th workshop, which calibrated the fracture location and permeability taking into account the pressure

decrease in CTD, could capture the observed water pressure variations approximately (Figure 264).

Regarding the estimation of Cl concentration, the three teams are still struggling to reproduce a wide range of concentration in each monitoring section. Figure 265 shows the change of the simulated Cl concentration in 12MI33 demonstrated by JAEA team from the 5th to 7th workshop. The estimated Cl concentration range became wider through calibration efforts, but it still doesn't cover the lower concentration range. Additionally, the Cl concentration in each monitoring point could not be simultaneously reproduced.

On the other hand, by considering the distribution of hydrogeological compartments, the range of Cl variation can be roughly estimated. Further research is required to clarify the applicability of such simulation approach taking the hydrogeological compartment into consideration in future.

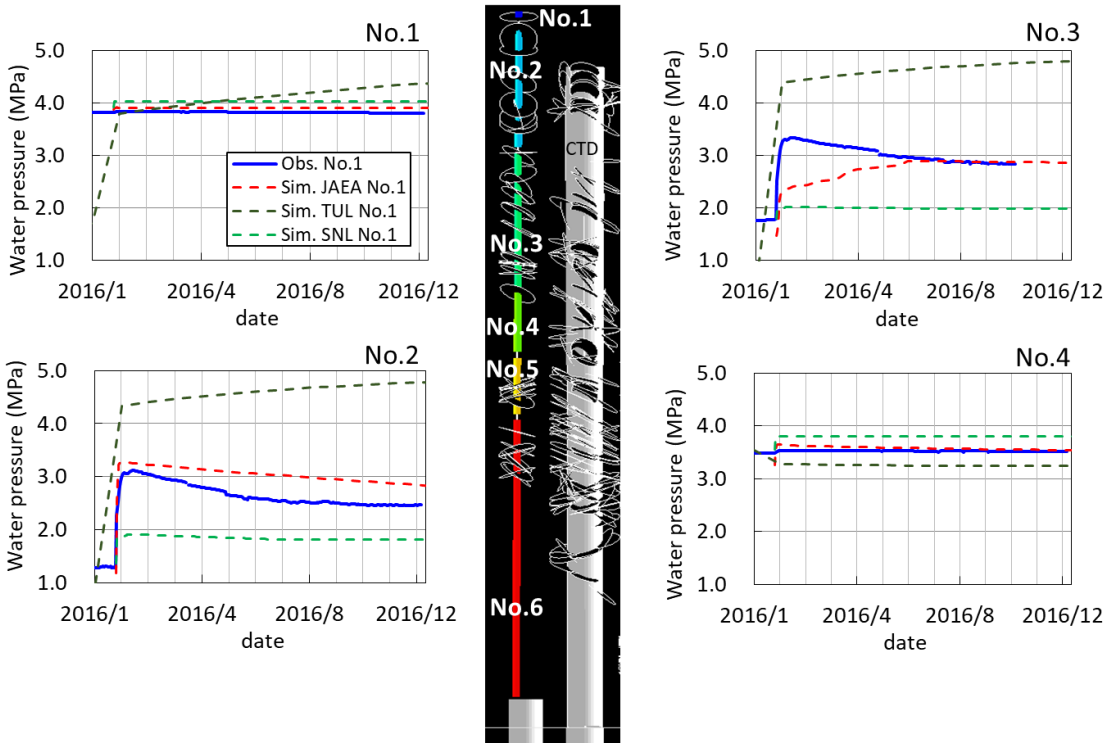

Figure 263. Simulated water pressure changes around CTD (6th workshop)

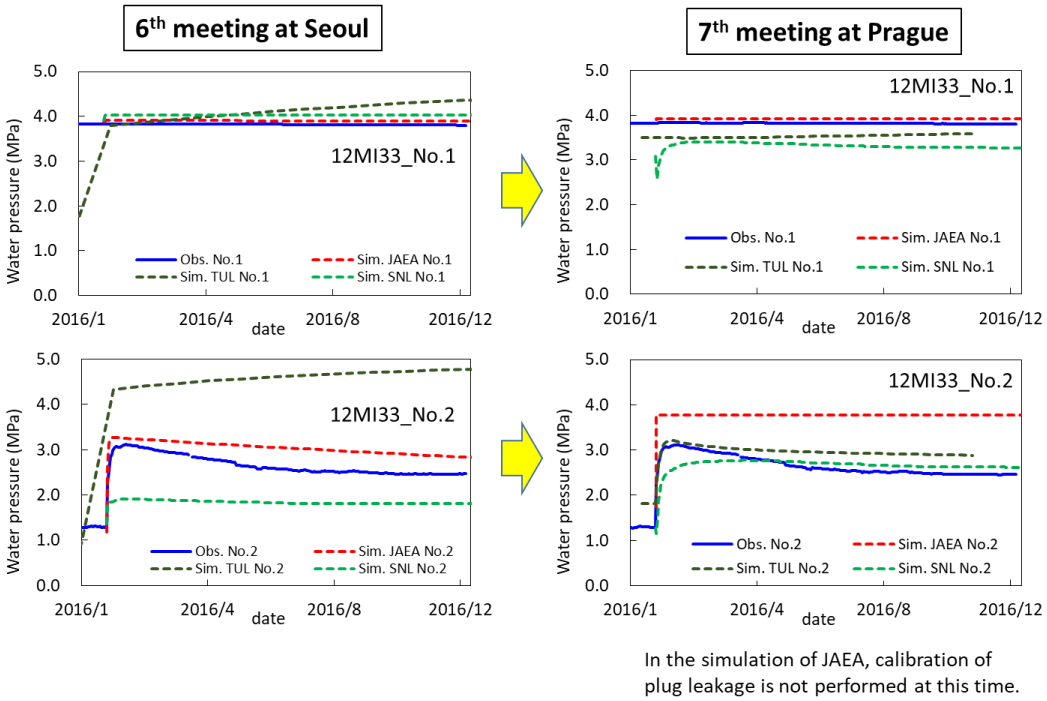

Figure 264. Improvement of simulated water pressure change around CTD (7th workshop)

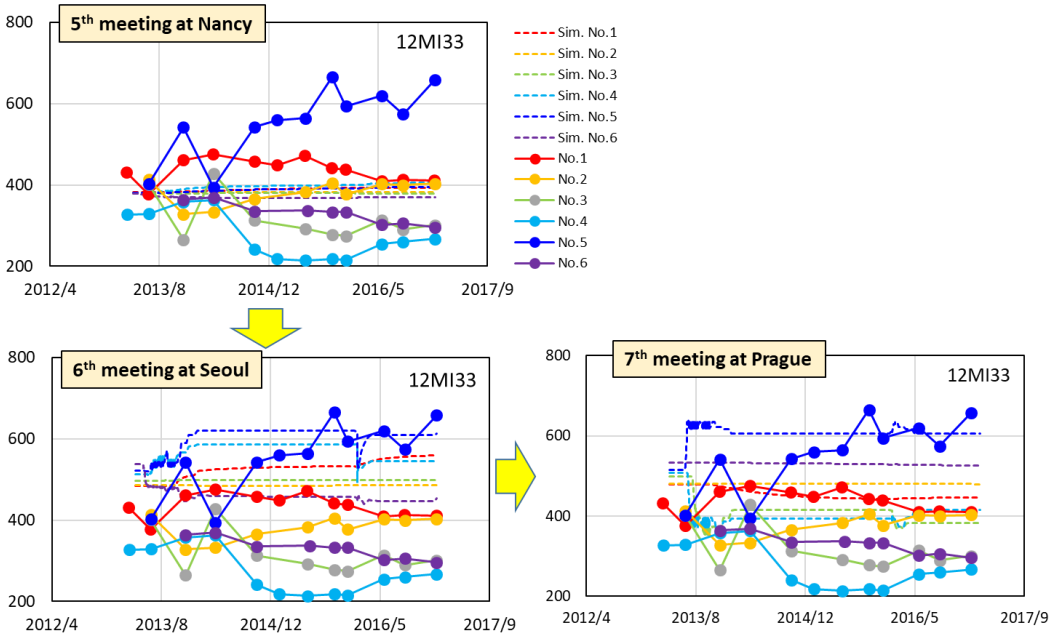

Figure 265. Chronicle of the simulated Cl concentration in 12MI33 borehole shown by JAEA team

12 Step 3: 3-D Reactive Transport Modeling of the Closure Test Drift (CTD) Experiment

Descriptions of the URL experiments for various disposal design concepts according to the host country repository program and relevance to the US program is given in Birkholzer et al., 2017, Jové Colón et al., 2012; 2014; 2016, etc. In the construction and operation of geological disposal facilities, cementitious materials and associated solids are used as backfill, seals, plugs, and linings in tunnels and disposal galleries. Groundwater interactions with cementitious barriers are important to in-drift chemistry and EBS performance during the repository post-closure period since the generated alkaline solutions can aggressively react with silica-bearing phases and other EBS materials.

During the operation period of the facility, alkaline pore water generated by the dissolution of cement material is diluted and drained by groundwater inflow from the rock to the tunnel, but after the facility is closed and inflow has stopped, the dissolution of the alkali component in cement materials forms alkaline groundwater around the tunnel. As the transport process of radioactive elements is affected by the chemical condition of groundwater, it is necessary to establish a long-term prediction method for the chemical condition formed by cement materials.

Inside and outside the CTD, changes in groundwater chemistry and shotcrete mineralogy were observed to obtain basic knowledge, and simulation analysis of changes in water chemistry over time was conducted.

Previous studies demonstrate the pore water chemistry and chemical interaction processes between water - cementing material as follows (Rochelle et al., 1992; Savage et al., 1992; Adler et al., 1999);

- Buffering by sodium, potassium hydrates (pH 13 ~ 13.5): Since those minerals are a minor constituent and have higher solubility, they are expected to dissolve in a relatively short time period.
- Buffering by portlandite [Ca(OH)2] (pH ~12.5): It continues until when the CaO/ SiO2 ratio declines to 1.8 and all portlandite dissolves and the calcium-silicate-hydrate [C-S-H: xCaO・ySiO2・nH2O] becomes the main component.
- Buffering with C-S-H (pH 12.5 ~ 10.5: until the cement component disappears)

Each buffering period depends on the groundwater flux passing through the geological disposal site (tunnel clusters) (Atkins et al., 1992). Based on previous studies (Savage et

al., 1998a, b; Hodgkinson et al., 1999), when a shotcrete concrete support was constructed on the tunnel wall and then the tunnel was closed, highly alkaline groundwater with a pH of around 13 is formed at first, and it is assumed that the pH decreases by the evolution of the dominant chemical buffering process with time.

On the other hand, in fully-closed tunnels, there is no supply of carbon dioxide from the atmosphere, there are various minerals with different degrees of alteration, the type and composition of cement used for supporting vary widely according to the geological conditions, etc. Hence a real facility is under more complex conditions than laboratory tests and previous analysis conditions.

Under such practical circumstances, there are few cases that observed and analysed the influence of cement materials on surrounding groundwater chemistry, and the main mineral types and reaction rates involved in groundwater evolution in a closed tunnel environment where cement materials are used. The reaction volume (how much the amount of groundwater changes and how much the water chemistry is changed) is the point to be confirmed in the in-situ test at the CTD whose wall is covered by shotcrete (Table 49).

12.1 Observed chemical evolution of isolated groundwater in CTD

Figure 266 and Figure 267 shows the variation of a tracer (uranine) concentration and chemical composition with time. The tracer concentration decreases with time, and it can be seen that groundwater without tracer is flowing into the tunnel. Based on the change of the tracer concentration, the inflow rate is estimated to be about 8 m^3 / day (Iwatsuki et al., 2017). Under such conditions of groundwater replacement, the pH of the groundwater in the tunnel approached steady state at a value around 10 from the initial approximate value of 8.9.

12.2 Observed mineral alteration in shotcrete

Figure 268 and Figure 269 show the results of EPMA mapping analysis of shotcrete collected inside and outside the CTD. In the following, the shotcrete collected outside the flooded tunnel will be referred to as the “non-submerged sample” and the shotcrete collected inside the CTD will be referred to as the “submerged sample”. In the mapping, in order to clarify the change of the cement paste composition, aggregate removal data

is shown, which is deleted from the data, judging that the pixels with Al_2O_3 concentration more than 10 % and SiO_2 concentration more than 40 %. In addition, Figure 270 and Figure 271 show the depth profile of the concentration of the chemical component created using the data from which the aggregate was removed.

Table 49. Shotcrete specification in the CTD

Specification of the Closure test drift		
Capacity of Closure test drift	900	m^3
Surface area of shotcrete	553	m^2
Minimum volume of shotcrete (Estimated as 5 cm thick)	28	m^3
Blending ratio of shotcrete		
Ordinary Portland cement	450	kg/m^3
Water	203	kg/m^3
Fine aggregate (sand)	1047	kg/m^3
Coarse aggregate (crushed stone)	647	kg/m^3

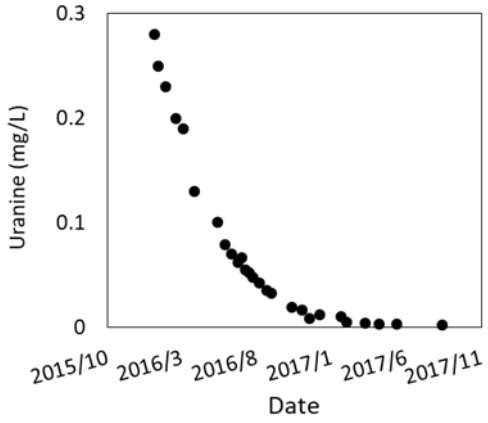

Figure 266. Variation of tracer concentration with time

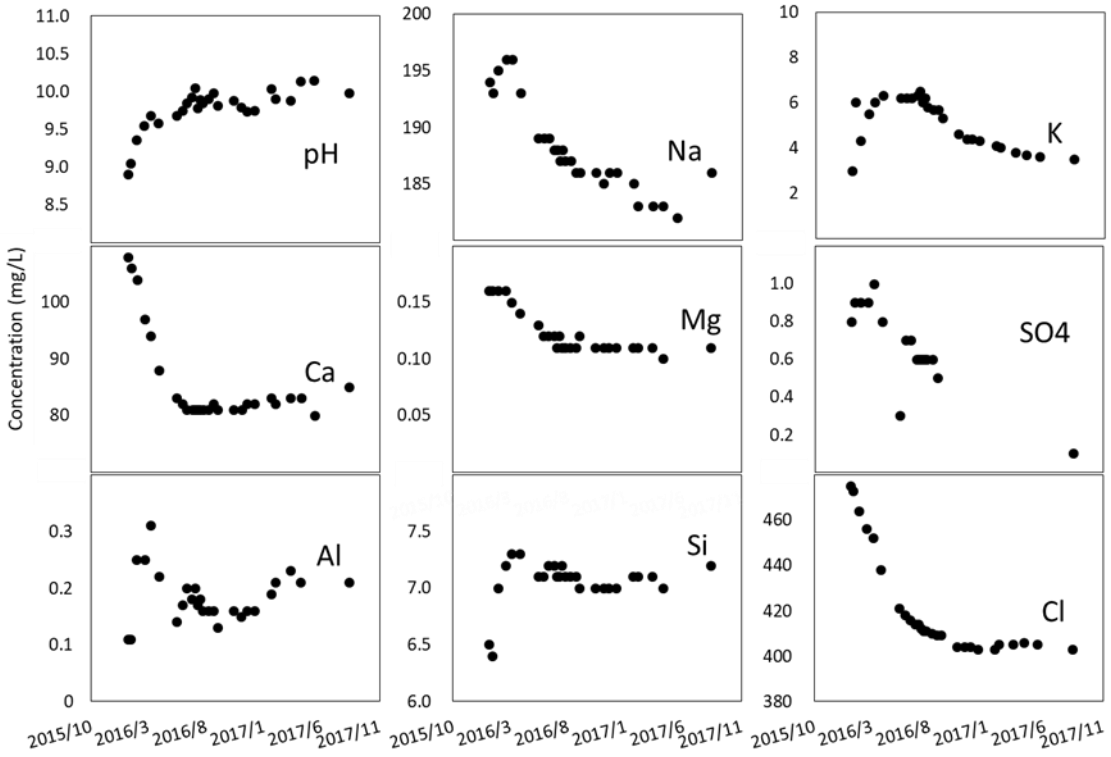

Figure 267. Variation of chemical composition with time

The non-submerged samples tend to have higher Na and K contents and lower Si, Al and S contents in the range of about 20 mm from the surface compared to the inside. In addition, the S content is high at a position of 20 to 25 mm. The Ca / Si mol ratio at depths of more than 20 mm is about 1.5, and the closer to the surface, the higher (Ca content is higher than Si content). Based on the mapping and analysis results, the sample was divided into 20 mm from the surface and 20 to 50 mm, and the results of mineral identification by XRD analysis are shown in Table 50.

The cement related minerals identified are C-S-H, portlandite, calcite, monocarbonate [$3CaO:Al_2O_3:CaCO_3:11H_2O$], ettringite [$3CaO:Al_2O_3:3CaSO_4:32H_2O$]. In the vicinity of the surface, the major minerals of cement such as portlandite, monocarbonate and ettringite have largely disappeared while the calcite ratio increased. About 10 years have passed after the spraying construction at outside of CTD, and it seems that the spread of alteration layer (neutralization front) by the air for 10 years is about 20 mm.

The disappearance of portlandite in the surface and the formation of calcite suggest the carbonation process of calcium hydrate by the atmosphere. The increase in Na and K content at the surface layer was caused by the reaction of NaOH and KOH contained in the shotcrete with carbon dioxide in the atmosphere to convert it into carbonates (Na_2CO_3, K_2CO_3, etc.), or since Na and K are easily adsorbed to CSH with a low Ca/Si ratio

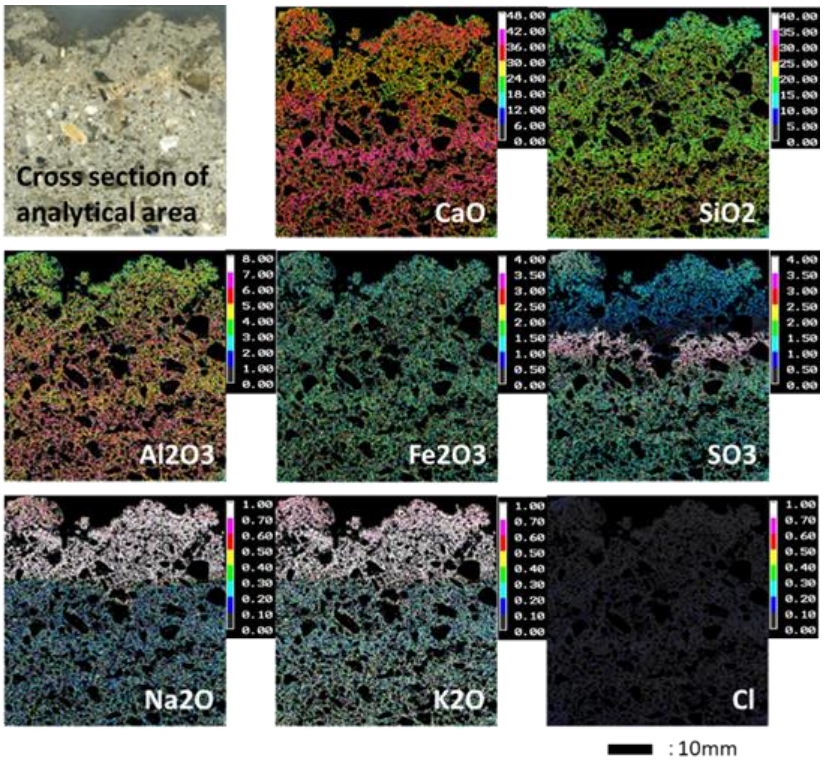

Figure 268. Elemental concentration (mass%) in shotcrete collected from outside the CTD.

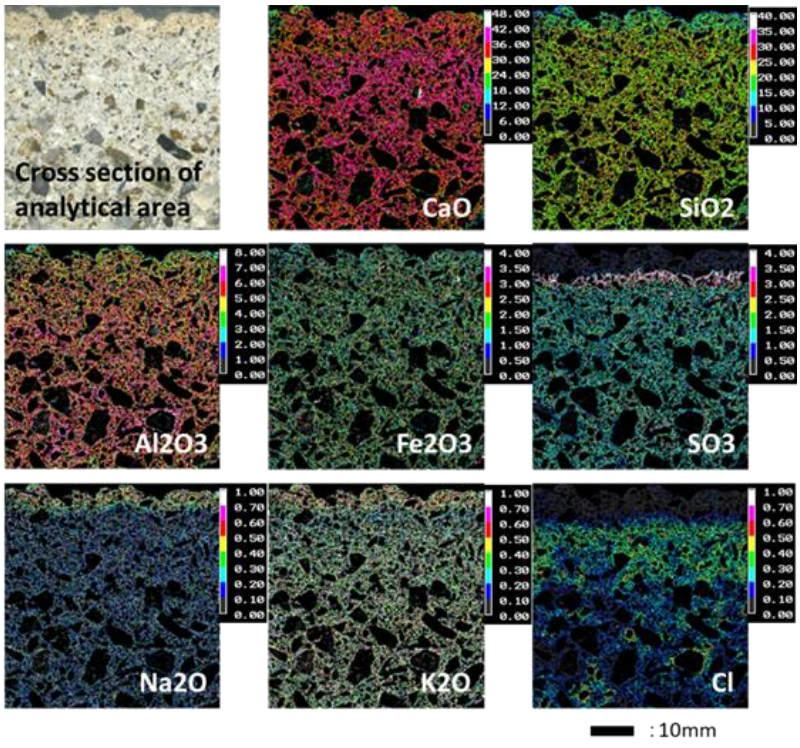

Figure 269. Elemental concentration (mass%) in shotcrete collected from inside the CTD.

(Hong et al., 1999), there is a possibility that Na and K are adsorbed to low-Ca/Si CSH and silica gel produced by carbonation of CSH. Sulphur decreases up to 20 mm from the surface and concentrates to 20-25 mm. The pH decline of pore water in the neutralization zone would cause the decomposition of the ettringite and moves the sulphur toward the interior, as a result, the content of ettringite would have been higher near the carbonation front.

In the submerged sample, a chemical distribution similar to that of the non-submerged sample was observed qualitatively, but the increase of Na and K content was observed around 5 mm from the surface, and the peak of S content was recognized around 5 ~ 10 mm. The decrease of Si and Al content was also remarkable in the range of about 5 mm from the surface. The shotcrete in the CTD was in contact with the atmosphere for about three years and four months from the construction to the start of the closure test. The distribution of chemical components found in the sample is considered to be the atmospheric alteration layer generated during that time. The carbonation front is about 5 mm from the surface, and the depth of the carbonization front is approximately proportional to the length of the period exposed to the atmosphere, as compared to the non-submerged sample. In addition, Cl immersion, which was thought to have penetrated from groundwater during flooding, was confirmed around 5 to 20 mm.

Based on these results, the sample was divided into 5 mm, 5 to 20 mm, and 20 to 50 mm from the surface, and XRD analysis, portlandite/calcite content analysis (TG-DTA analysis) and density analysis (pore measurement) were carried out. As a result, the loss of portlandite in the surface layer and the increase of calcite were confirmed as in the non-submerged sample (Table 51). In addition, the Ca content on the surface is significantly reduced (Figure 270), and it is presumed that portlandite, CSH, monocarbonate, etc. dissolved more than the increase in calcite.

Since the other components have lower molar content by one order of magnitude than the Ca and Si contents, and the decrease in Al was not remarkable, it was presumed that the decrease in Ca was mainly caused by the dissolution of portlandite or CSH, not monocarbonate. Furthermore, in the submerged sample, a peak of Friedel's salt ($3CaO \cdot Al_2O_3 \cdot CaCl_2 \cdot 10H_2O$) not identified in the non-submerged sample was identified, and a part of the aluminate minerals in the monocarbonate and ettringite was likely to be altered to the Friedel's salt by containing Cl from the groundwater.

In order to distinguish the alteration by the atmosphere, Figure 271 was adjusted so that the S-peak depths of the non-submerged sample and the submerged sample overlap by using the peak depth of S content as an index of neutralization front, and the contents of each chemical component were compared. As a result, after flooding, the contents of

Si, S, Na, and K have decreased near the surface compared to the non-submerged samples. In addition, portlandite decreased in internal and calcite increased. This is considered to be the result of the portlandite inside the shotcrete being altered by flooding.

The porosity of the cement paste excluding the aggregate of the non-submerged sample was 18.4 % in the surface layer and 16.9 % in the inside. On the other hand, the porosity of the sample after flooding was 18.6 % at 5 mm, 17.9 % at 5 to 20 mm, and 15.0 % at 20 to 50 mm from the surface, and no significant change in porosity due to flooding was observed during the test period.

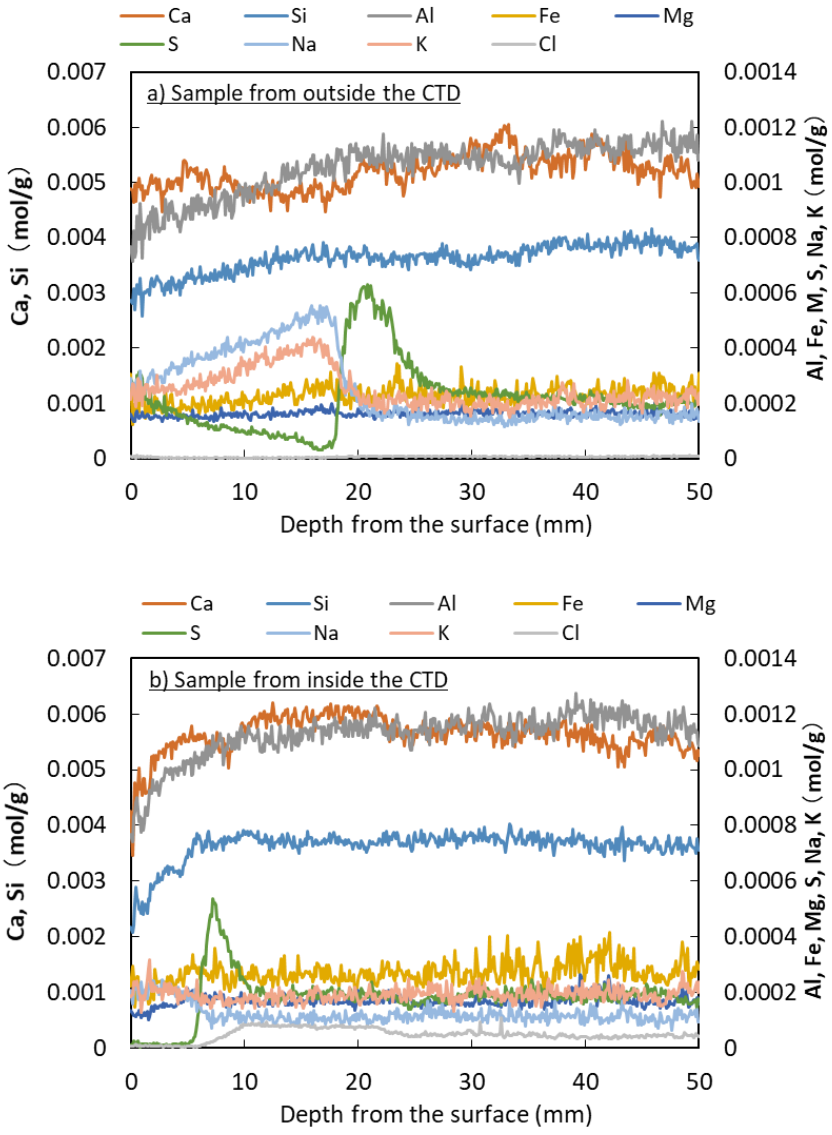

Figure 270. Elemental profile in shotcrete collected from inside and outside the CTD

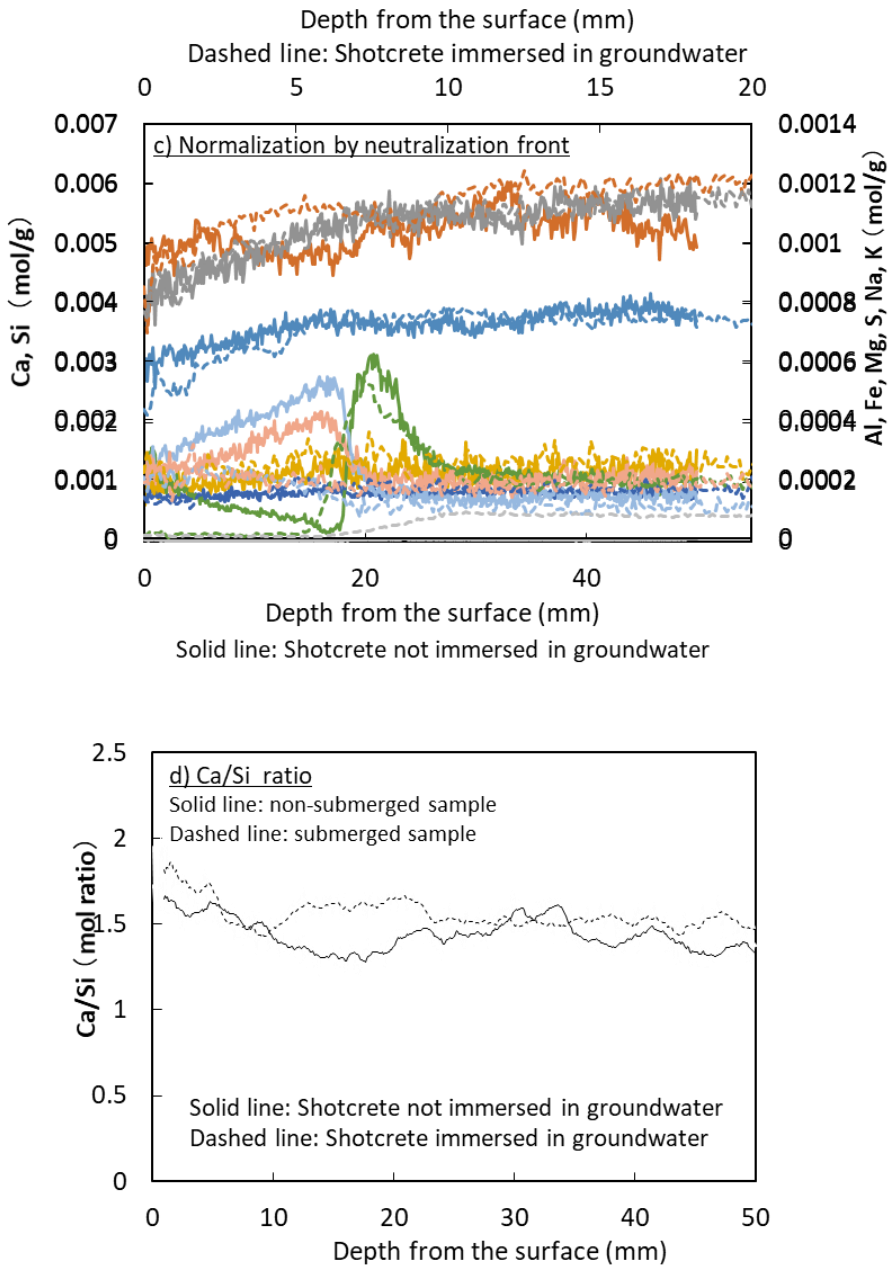

Figure 271. Comparison of the elemental profile in shotcretes

Table 50. XRD analysis of shotcrete samples

Sample	Depth from surface (mm)	Cement hydrates						Aggregates			
		C-S-H	Portlandite	Calcite	Mono Carbonate	Ettringite	Fridel's Salt	Quartz	Albite	Orthoclase	Muscovite
Shotcrete not immersed in	0-20	△		◎				◎	○	○	
	20-50	△	○	△	△	△		◎	○	○	△
Shotcrete immersed in groundwater	0-5	△		◎		△		◎	○	○	△
	5-20	△	△	△	△	△	△	◎	○	○	△
	20-50	△	△	△	○	△	△	◎	○	○	△

Peak strength: Intense ◎, Weak ○, Very weak △

Table 51. EPMA, TG-DTA analysis of shotcrete samples

Sample	Depth from surface (mm)	Average content of the EPMA analysis (m mol/g)									TG-DTA analysis			Bulk density (g/cm^3)	True density (g/cm^3)	Porosity (%)
		CaO	SiO2	Al2O3	Fe2O3	MgO	SO3	Na2O	K2O	Cl	1000℃ loss (wt%)	Ca(OH)2 wt% (m mol/g)	CaCO3 wt% (m mol/g)			
Shotcrete not immersed in	0-20	4.91	3.42	0.48	0.11	0.16	0.15	0.20	0.16	0.00	33.0	0 (0.00)	59.0 (5.90)	2.04	2.50	18.4
	20-50	5.38	3.75	0.56	0.12	0.16	0.27	0.08	0.10	0.01	27.1	6.9 (0.93)	0 (0.00)	2.00	2.40	16.9
Shotcrete immersed in groundwater	0-5	5.09	2.92	0.46	0.11	0.14	0.01	0.10	0.10	0.01	35.9	0 (0.00)	52.1 (5.21)	2.04	2.50	18.6
	5-20	5.80	3.72	0.55	0.13	0.17	0.23	0.06	0.09	0.06	27.6	4.9 (0.66)	1.2 (0.12)	1.98	2.41	17.9
	20-50	5.64	3.71	0.58	0.14	0.17	0.19	0.06	0.10	0.05	26.4	5.1 (0.70)	1.6 (0.16)	2.09	2.46	15.0

13 Results of Step 3 modelling (JAEA)

13.1 Thermodynamic analysis of groundwater evolution in CTD

The previous JAEA work shows that the groundwater mainly evolves by mixing between chemically different groundwater and water-rock interaction (Iwatsuki et al., 2017).

In this study, a theoretical analysis was conducted based on observation data collected for the purpose of quantitatively estimating the dominant water-rock interaction in a closed tunnel environment, and the reaction amount of the cement material constructed. In the analysis, the solution mixing calculation function is performed using the geochemical calculation code PHREEQC (ver. 3, database: wateq 4f. dat) which is developed by the US Geological Survey and widely used as an analysis software in the geochemical systems. By analysing the temporal change of water chemistry observed in the flooded tunnel by the function of calculating mineral-water reaction, we identified the main mineral-water reaction and estimated the amount of reaction of related minerals. As regards mineral-water reactions not included in the database: wateq 4f. dat, thermodynamic data from the Atkinson model for C-S-H and thermodynamic data of LLNL. dat for ettringite, natron and K_2CO_3 were used.

13.1.1 Procedure of the theoretical analysis

The basic procedure of thermodynamic analysis by PHREEQC is shown in Figure 272.

- The uranine and Cl concentration are generally not changed by the mineral-water reaction. In order to quantitatively analyse the chemical change of groundwater by mixing, the chemical composition of the endmember groundwater related to mixing is identified based on the uranine and Cl concentration. Since the analysis of dissolved gas in groundwater was not conducted in this research, carbon dioxide partial pressure Pco_2 of the endmember groundwater was estimated by PHREEQC based on the measured pH and inorganic carbon dioxide concentration.

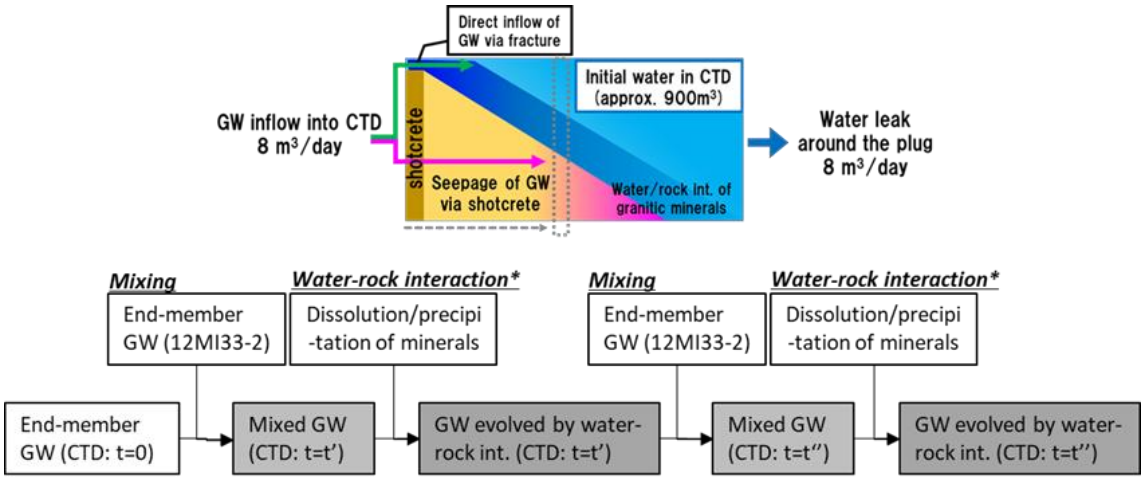

Figure 272. Analysis of groundwater evolution by mixing and water-rock interaction

- Based on the mixing ratio of endmember groundwaters estimated from uranine concentration at each time point, calculate the chemical composition of groundwater formed by mixing using the solution mixing calculation function of PHREEQC.
- Compare the measured water chemistry at each time point with the calculated water chemistry. Clarify the chemical components that cannot be explained by the mixing process, which may have been affected by the mineral-water reaction.
- Using the mineral-water reaction calculation function of PHREEQC, calculate the groundwater chemistry evolved by the interaction between the groundwater formed by mixing and the minerals at each time point. For the calculation, mineral species are selected from the following viewpoints.
  - ✓ Minerals that may be included in shotcrete
  - ✓ Minerals containing chemical components corresponding to increased solutes in groundwater
  - ✓ Minerals judged to be in unsaturated to groundwater at each time point based on the saturation index estimated by PHREEQC

  Reproduce the water chemistry evolved by the interaction of "groundwater formed by the mixing process" and various minerals selected above by inputting each mineral and its saturation index in [EQUILIBRIUM_PHASES].

  The inputted saturation index of minerals is the value derived based on the actual water chemistry at each time point. The type and combination of minerals that assume the reaction and the amount of reaction are variables.

- Compare the calculated water chemistry at each time point and the actual chemical evolution of water, and extract the combination of mineral species that they match.
- Based on the mineral combination where the calculated water quality trend agrees with the measured trend, the main reaction minerals involved in the temporal change of water chemistry are identified, and the amount of reaction is determined.

The correlation between each dissolved component concentration and tracer concentration is shown in Figure 273. A positive correlation (r = 0.99) was found between the Cl concentration, whose concentration is unlikely to change due to the mineral-water reaction, and the uranine concentration. The groundwater in the CTD is considered to reflect the mixed ratio of two different waters (endmember groundwaters).

The Cl concentration in the CTD finally became the same Cl concentration in the surrounding observation points (12MI33-1, 12MI33-2, 13MI38-1; Figure 274). Among these observation points, the hydraulic response linked to the hydraulic pressure change at the time of excavation and water-filling in the CTD was observed in 12MI33-2 and -3, and it is presumed that the CTD and the 12MI33-2 are connected via fracture (Onoe et al., 2014). Therefore, it is likely that the initial groundwater in the CTD and the groundwater in 12MI33-2 can be regarded as the endmember groundwaters of the mixing process.

The carbon dioxide partial pressures (Pco_2) of these waters was calculated to be $10^{-4.57}$ atm and $10^{-4.49}$ atm, respectively (Figure 274). Previous research (Iwatsuki et al., 2005) indicates that the carbon dioxide partial pressure of groundwater in the vicinity of a depth of 500 m in this area is around $10^{-4.5}$ atm. The calculated Pco_2 of the end-member groundwater is roughly consistent with the actual measurement data.

Concerning the variation of the dissolved component concentration with time (Figure 273; Na, K, SO_4, etc.) which deviates from the mixing line of end-member groundwaters, the influence of mineral-water reaction and microbial reaction can be also considered in addition to the mixing process. For example, formation and precipitation of carbonate particles were observed in the groundwater in the CTD (Iwatsuki et al., 2017), and thin layer deposit of calcium carbonate was observed in the entire surface of the CTD wall after drainage of groundwater. This calcium carbonate is considered to be derived from shotcrete, and it is speculated that the leaching of Ca ions from the shotcrete affects the chemistry of the groundwater.

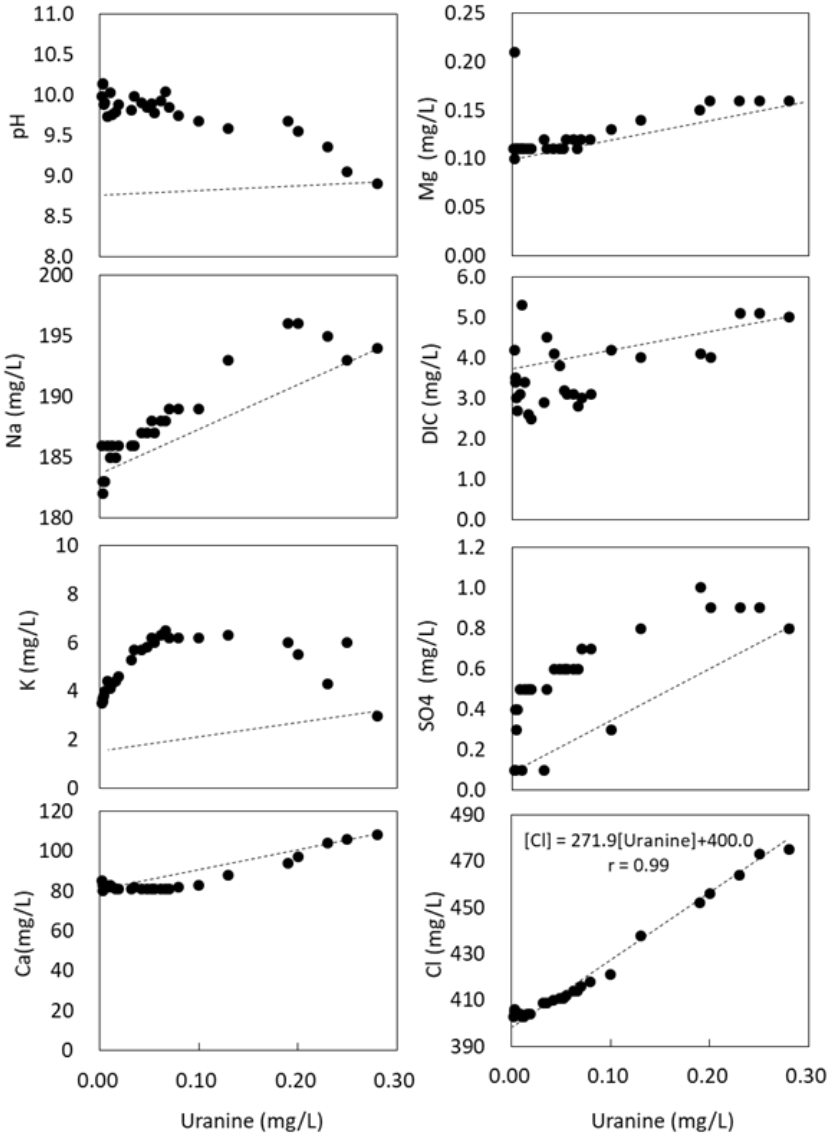

Figure 273. Relationships between tracer concentration and chemical composition

13.1.2 Identification of the dominant process in isolated groundwater evolution

Based on the analysis results of groundwater and shotcrete, we calculated the groundwater evolution by mixing of endmember groundwaters and mineral-water reaction in the CTD using PHREEQC. In addition, the validity of the endmember groundwaters used in the calculation was verified inductively, and the mineral facies involved in the chemical change of water at each time point were identified.

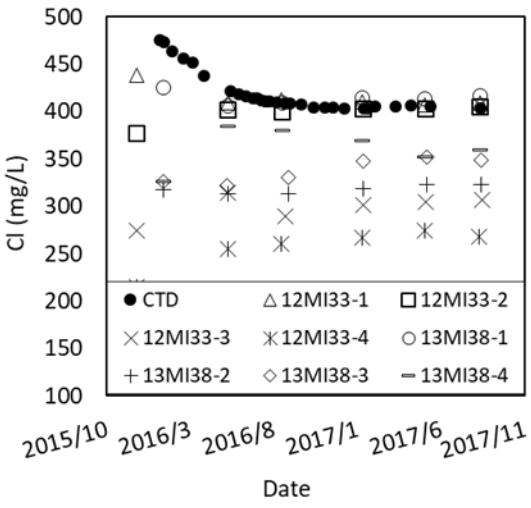

Component	Initial water in CTD	12MI33-2
Date	2016/1/25	2017/5/15
Uranine	0.28	0
Temp. C°	28	28
pH	8.90	8.7
pe (mV)	4.05	-2.15
P_{CO2} atm.*	$10^{-4.57}$	$10^{-4.49}$
Na	194	185
K	3.0	0.8
Ca	108	77
Mg	0.16	0.11
DIC	5	3.5
SO_4	0.8	0.1
F	6.2	6.3
Cl	475	403
Si	6.5	6.2
Al	0.11	0.01

* Calculated value (mg/l)

Figure 274. Chemical composition of the end-member groundwater (right) and Cl concentration evolution (left)

The mixing ratio of end component groundwater was calculated based on the tracer concentration at each time point. In the calculation, water temperature and water chemistry of endmember groundwaters as shown in Figure 274 were applied. In the analysis of mineral-water reactions, primary minerals in granite, secondary minerals formed during its alteration and minerals whose thermodynamic data is in the database of PHREEQC (e.g. Albite, anorthite, annite, calcite, chlorite, fluorite, gibbsite, kaolinite, montmorillonite, quartz), and the minerals which can generally be included in shotcrete (eg. Brucite, C_3AH_6, ettringite, portlandite, C-S-H (0.1-1.8), amorphous silica, Na_2CO_3, K_2CO_3, $CaCO_3$, $MgCO_3$, natron [Na_2CO_3. $10H_2O$], nesquehonite [$MgCO_3$. $3H_2O$]) were considered.

Carbonate (Na_2CO_3, K_2CO_3, $MgCO_3$, natron, nesquehonite) has not been identified by XRD analysis, but the EPMA analysis results show that the alkali component contained in the shotcrete reacts with carbon dioxide contained in the atmosphere. The water chemistry that could be formed by these mineral-water reactions was also calculated, and it was compared with the actual groundwater chemistry.

Water chemistries evolved by the mixing and water-mineral (various combination of mineral sets) interaction were estimated, and the most reproducible minerals that match with the observed water chemistry were identified.

The result of the PHREEQC analysis is shown in Figure 275: water chemistry formed assuming only mixing of end-member groundwaters and water chemistry formed assuming the mixing of end-member groundwater and the mineral-water reaction.

The water chemistry formed by the mixing of end-member groundwater is not consistent with the actual observed results. On the other hand, as a result of reproducing the analysis including the mineral-water reaction, as mineral combinations capable of reproducing temporal change of chemical property of water, amorphous silica, calcite, gibbsite, portlandite, ettringite, K_2CO_3, natron, brucite or nesquehonite were considered appropriate.

With regard to ettringite and natron, the concentrations of Ca and Na became much higher than the observed values, considering the reaction over the entire period, so it was assumed to contribute to the water chemistry only during the first three months of the test period. Regarding the reactions of brucite or nesquehonite that affect the Mg concentration, the observed change in the Mg concentration of groundwater was small, and the water chemistry change could be almost reproduced by either mineral (Figure 275). Since these minerals cannot be identified by XRD analysis, it is not possible to identify which mineral is related to the actual water chemistry.

It has been suggested that SO_4 concentration is affected by microbial activity but it has been shown that the change over time can also be explained by assuming the dissolution of ettringite at the initial stage after tunnel closure. In addition, since precipitation of calcium carbonate is observed in flooded tunnels, it is possible that the following buffer reactions may sequentially contribute to neutral to alkaline pH.

$$Ca^{2+} + HCO_3^- = CaCO_3 + H^+$$

$$Ca^{2+} + CO_3^{2-} = CaCO_3$$

However, the concentration of inorganic carbon involved in the reaction was also affected by the decomposition of organic substances by microorganisms, so the DIC variation was large and no clear temporal change was observed, and the trend of water chemistry could not be reproduced by the calculation.

Moreover, since the water chemistry formed assuming the dissolution and precipitation reactions of minerals other than the above is not consistent with the observed values, it is assumed that the influence on the chemical evolution of groundwater of the minerals other than the above is small. It is thought that such water chemistry reproduction analysis can clarify the minerals that can affect the groundwater under the actual geological environment conditions where cement materials and natural minerals are mixed.

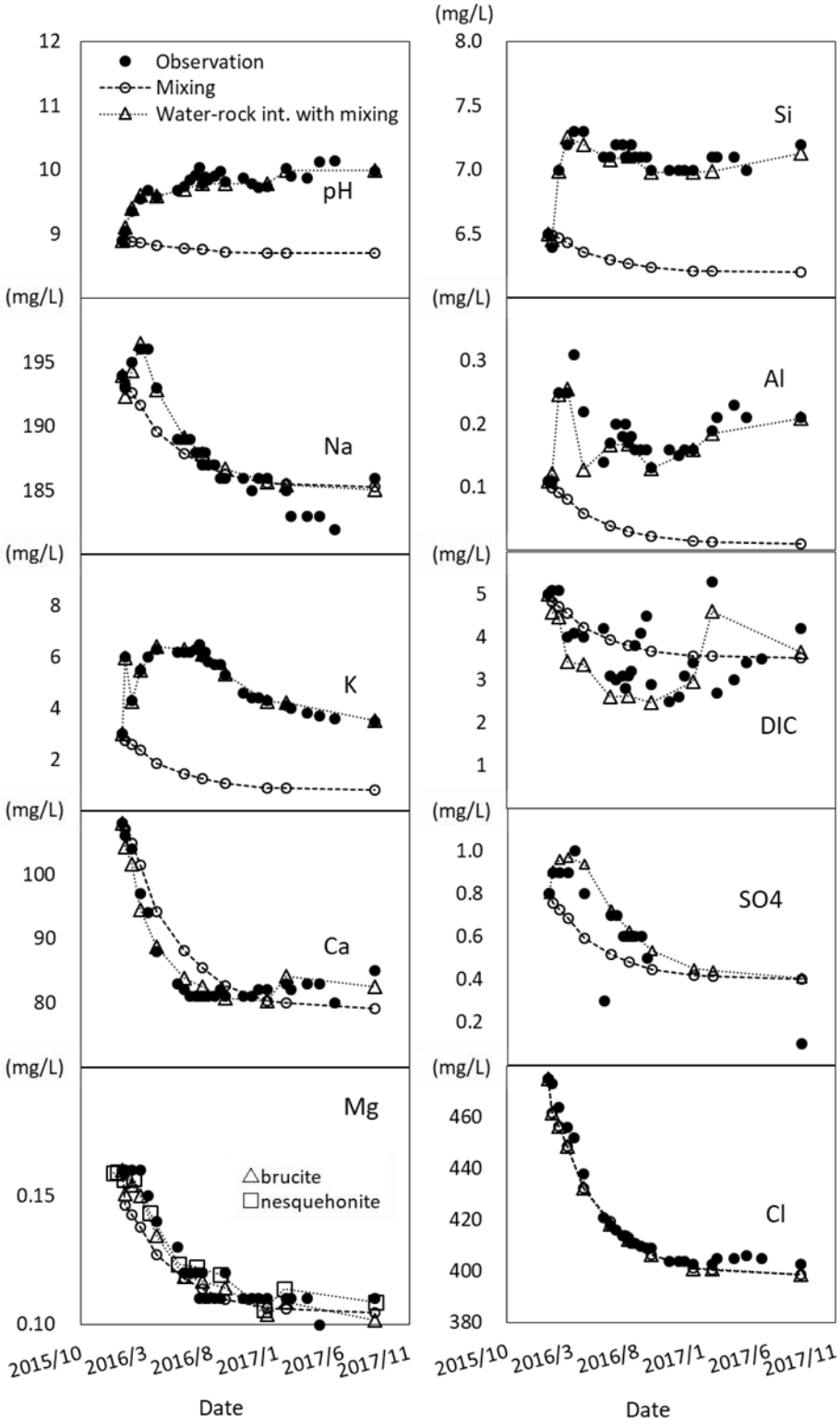

Figure 275. Reproduction of groundwater evolution based on mixing and water-rock interaction

13.2 Reactive transport modelling

We perform reactive transport simulation around drift considering the dissolution of shotcrete to evaluate long-term hydrochemical evolution after the closure of drift. As an initial step, we perform the simulation during the closure test with a homogeneous model. We model around the drift with shotcrete and intact rock. The chemical properties of preliminary input data of solid phase and liquid phase are shown in Table 52. Figure 276 shows the setting of chemical properties. The properties of shotcrete are assigned to the drift wall and plug. Figure 277 shows the structure of hydraulic conductivity. The hydraulic conductivity in CTD is set arbitrarily high.

Figure 278 shows the simulation results of evolution of pH during the closure test. The high-pH water due to the dissolution of shotcrete does not permeate into the rock except for around plug. It mainly distributed in the CTD after the drift closure. The alkaline water gradually spreads from the tunnel wall to interior of the drift. Then, the pH become high uniformly after 1 month of closure. Around water-tight plug, a part of groundwater detours around the water-tight plug to flow out from the CTD. This plume of high-pH water makes the pH in rock around the water-tight plug high. However, the area where the intact rock is alkalized is only around the water-tight plug. High-pH water in the CTD is flushed out from CTD 1 year after the closure.

Figure 279 shows the pH distribution on the line across the CTD. The high-pH water permeates into the CTD and become uniform 6 months after closure. The high-pH water is not distributed in the rock part around the CTD. Figure 280 shows the pH distribution on the line across the plug. Around the plug, high-pH water distributes in the rock due to the plume bypassing the plug. This high-pH zone in the rock is formed 10 days after the closure and reaches 2m from the drift wall. Figure 281 shows the comparison of observed pH with simulated pH in CTD. The average value in CTD is plotted for the simulated results. The simulation results overestimate the pH until 200 days after the closure, then simulated value goes below the observed data. One of the reasons for these differences would come from a critical assumption in the calculation; we assume with the chemical reaction is at equilibrium with limited reaction substances. As other reason of difference between simulated results and observed data, the hydraulic conductivity of plug would play an important role. The hydraulic conductivity of plug controls the replacement of water in CTD and hence the dilution rate of water in the CTD. For better simulation results, we need to calibrate not only end member of chemical reaction but also condition of groundwater flow to consider the hydro-chemical coupled process.

Table 52 Properties of solid and liquid phase for simulation of reaction

	pH	pe	Al	C	Ca	Cl	F	Fe	K	Mg	Na	S	Si	O(0)
Rock part	8.469	-0.713	2.30E-04	3.54E-01	1.32E+00	1.15E+01	3.83E-01	3.62E-04	2.31E-02	7.18E-01	7.96E+00	6.24E-03	6.00E-02	0.00E+00
Cement water	12.843	8.204	9.68E-04	1.47E-02	4.19E+00	1.00E+00	0.00E+00	1.00E-07	3.60E+01	1.25E-05	2.30E+01	2.12E+00	6.60E-02	1.07E+00

Solid property of intact rock

Type	Annite	Ca-Mont	Calcite	Chlorite	FEOH3	Fluorite	Kaolinit	SiO2(am)
Initial	1.15E-01	1.67E-01	1.14E-01	1.10E-01	1.15E-01	1.15E-01	7.64E-02	0.00E+00

Solid property of cement material

Type	Ca(OH)2	SiO2	Hydro Garnet	Brucite	Ettringite	Calcite
Initial	2817	1078	134	147	25	0

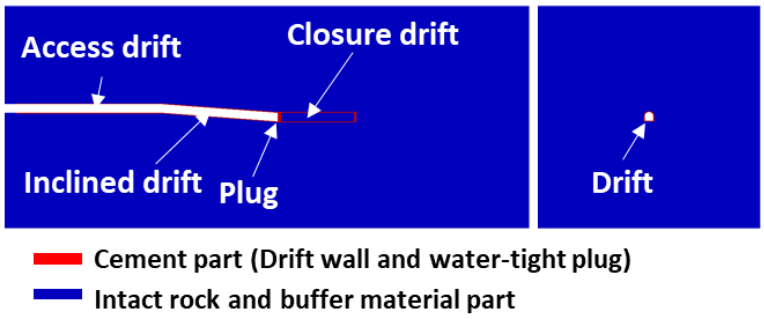

Figure 276. Setting of chemical properties.

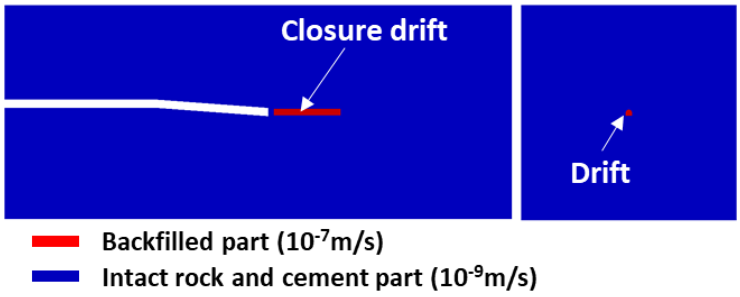

Figure 277. Setting of hydraulic conductivity

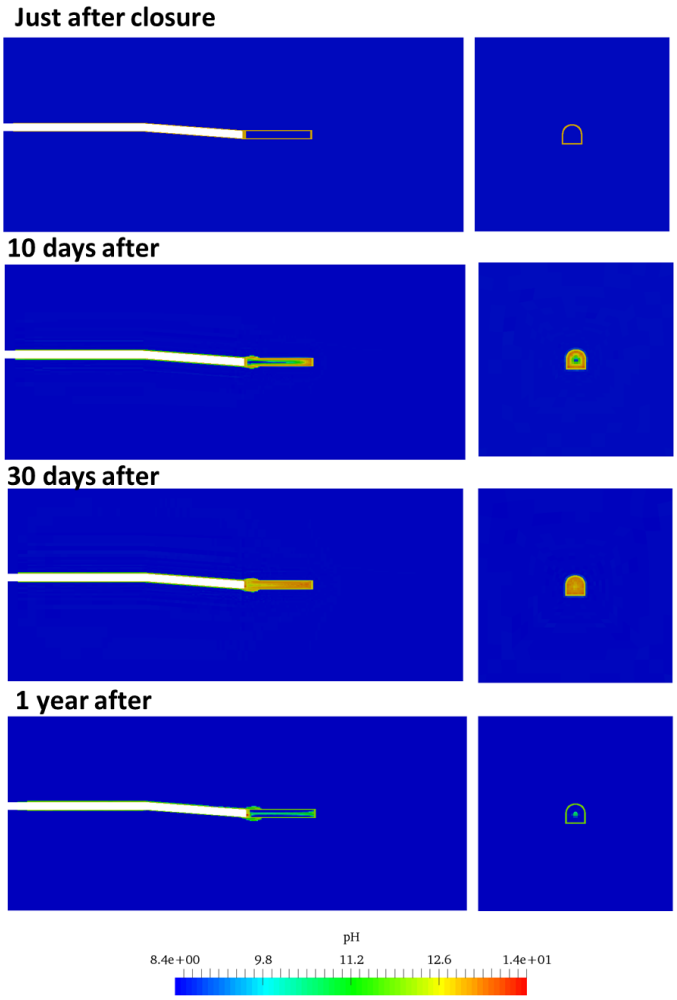

Figure 278. Evolution of pH in and around the drift

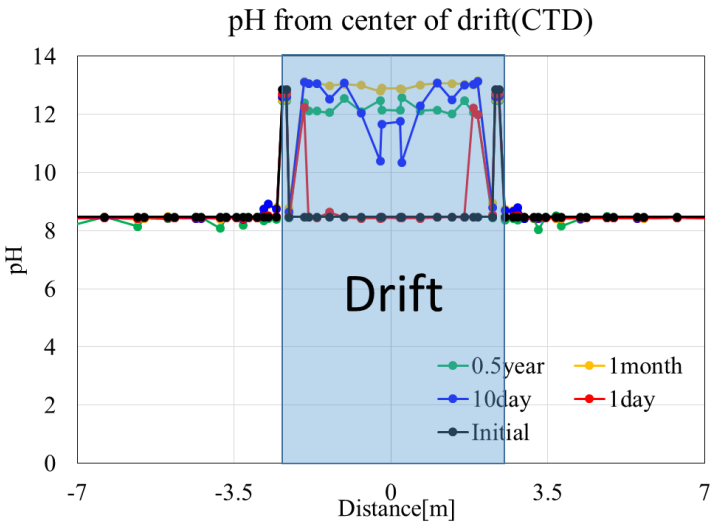

Figure 279. The pH distriburion from the drift wall around CTD

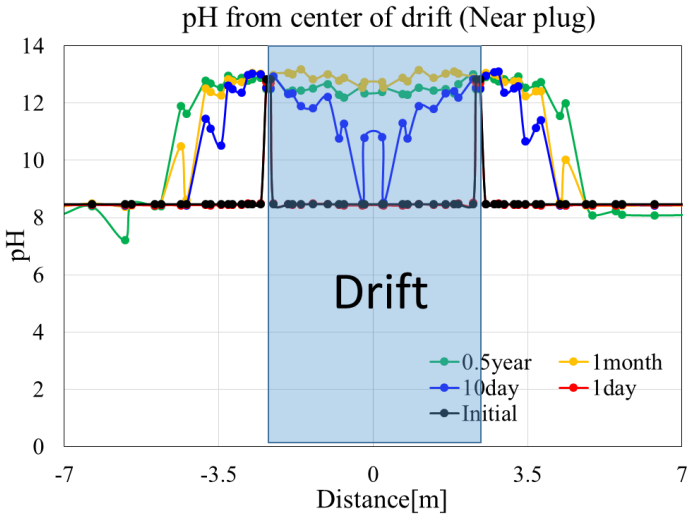

Figure 280. The pH distriburion from the drift wall around plug

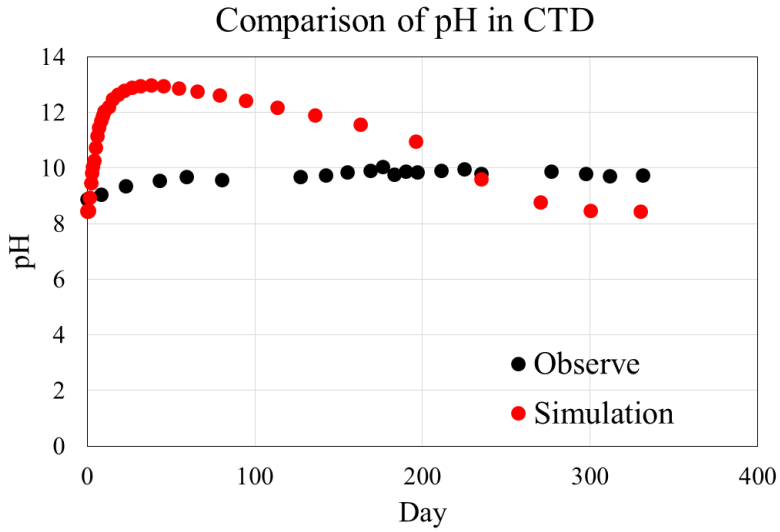

Figure 281. Comparison of pH in the CTD by observation and simulation

In addition, we carried out the long-term reactive transport simulation for the predictive study of pH evolution under a fully-closed condition. We perform two simulation cases for this study; one is simulation where the hydraulic gradient does not exist and the other case is under the condition that hydraulic gradient of horizontal direction is 1%. Note that these simulations include the recovery process of hydraulic pressure though the recovery is very fast compared with the simulation duration. In these studies, we set the simulation period to 100 years.

Figure 282 shows the evolution of pH under a diffusion dominant condition where the hydraulic gradient does not exist after the recovery of water pressure. Under the diffusion dominant condition, the growth of a high pH zone is very slow. In the CTD, a high pH zone is partially distributed even 100 years after the closure whereas it takes only two months to become uniform pH distribution under the condition of GREET. Advection flow accelerates the evolution of pH in CTD in GREET. In addition, the high pH water does not permeate into the rock in the whole domain. The distribution of pH from the drift wall is displayed in Figure 283. The increase of pH is limited in the CTD in this case. Figure 284 shows the evolution of pH under the advection dominant condition. In this case, pH in the drift becomes high 1 year after the closure. Comparing to the diffusive dominant case, the evolution of pH in CTD is fast. In addition to the increase of pH in the CTD, high pH water distributed downstream due to the groundwater flow. The permeation of high pH water into rock appears 1 year after the closure.

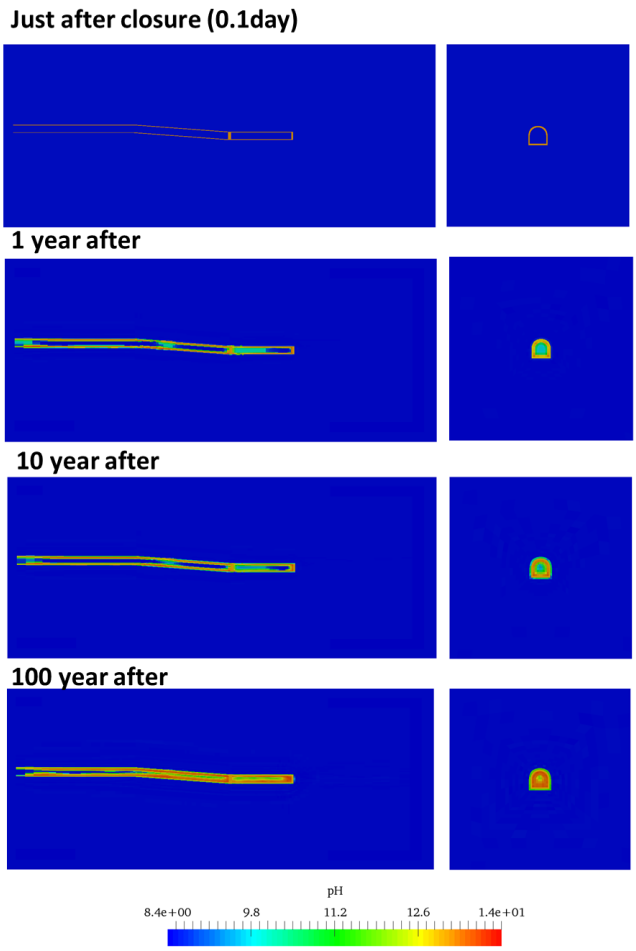

Figure 282. Evolution of pH in and around drift under diffusion dominant condition

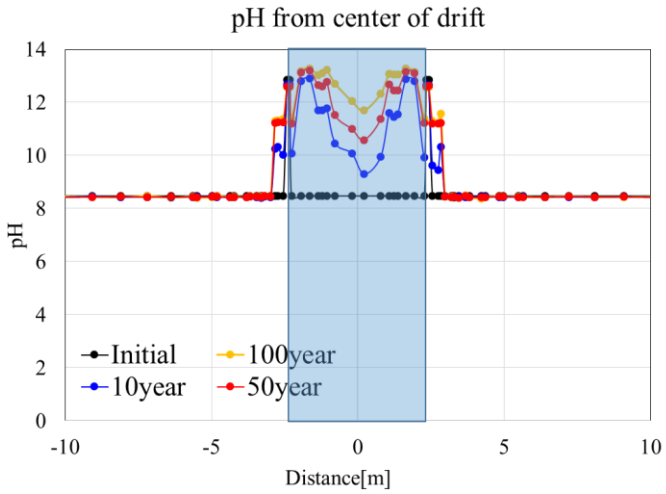

Figure 283. The pH distriburion from drift wall around CTD under diffusive condition

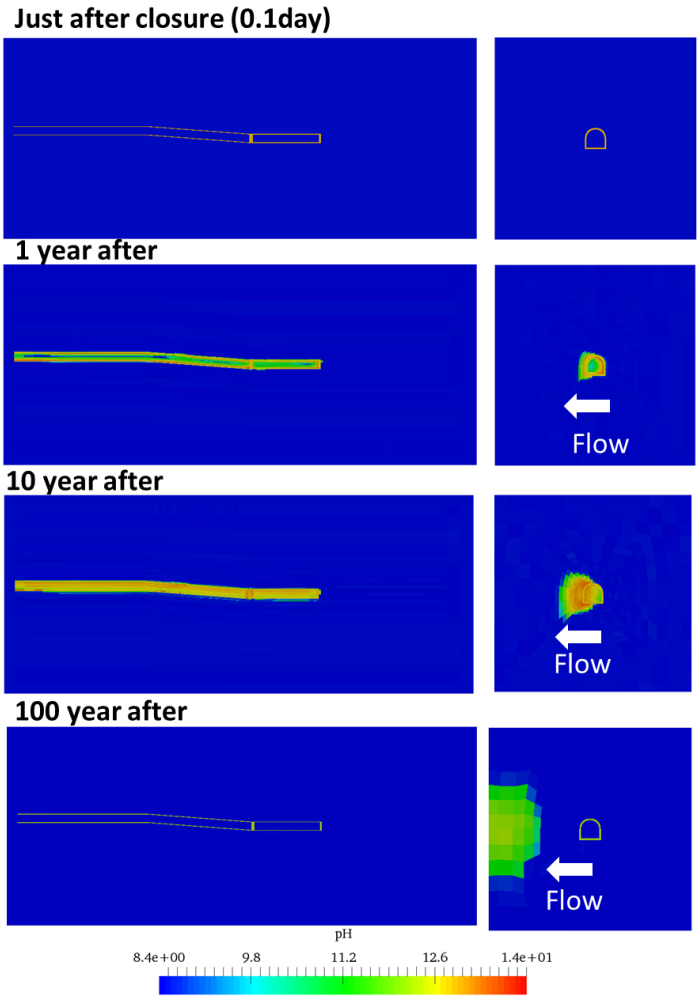

Figure 284. Evolution of pH in and around drift under advection dominant condition

The groundwater flow conveys the high-pH water and the distribution of high pH water continues to extend downstream. Figure 285 shows the distribution of pH from the drift wall. The movement of high-pH zone simulated. The movement of high pH zone is about 10m, 100 years after the closure. Figure 286 compares the evolution of pH in the CTD. The advection makes the pH in CTD high until 20 years after closure and then the high pH zone is flushed out from CTD. This trend is similar to the simulated result of GREET. These estimations critically depend on advection around CTD, so we need further simulations based on practical groundwater flow rate after the facility closure.

These simulation results indicate that the advection changes not only the distribution of high-pH zone long time after the closure but also the evolution of pH in and around the closure drift. However, even if the advection exists, the high pH zone is located near the drift 100 years after the closure and the growth of high pH zone is slow.

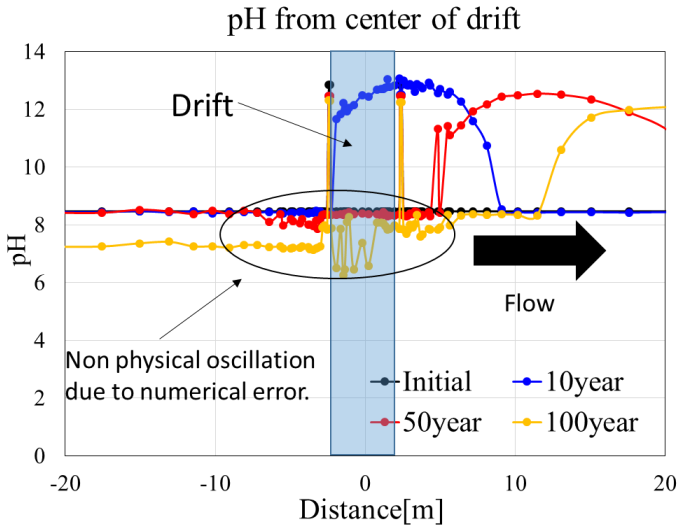

Figure 285. The pH distriburion from drift wall around CTD under advection condition

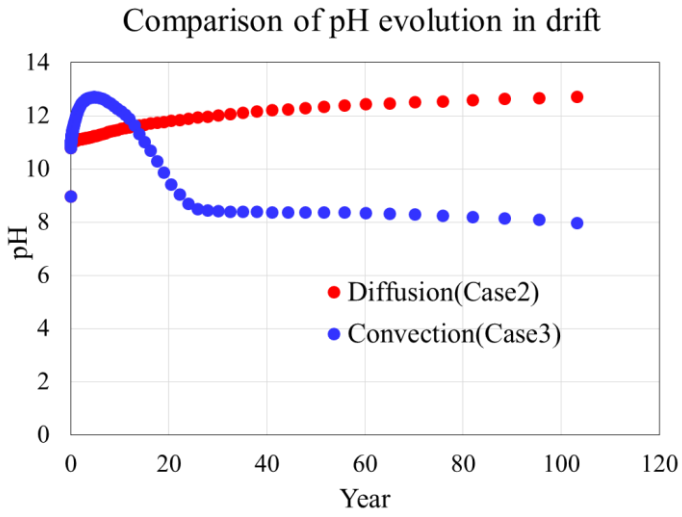

Figure 286. Comparison of pH evolution in CTD between observation and simulation

14 Results of Step 3 modelling (SNL): 3-D Reactive Transport Modeling of the Closure Test Drift (CTD) Experiment

SNL consolidated various aspects of the hydro-chemical (HC) work as part of the Task C activity:

- PFLOTRAN (Lichtner, 2013) 3D isothermal reactive transport modelling predictions of water chemistry in the 12MI33 monitoring borehole.
- PFLOTRAN 3D isothermal reactive transport modelling of the closure test drift (CTD) focusing on shotcrete – ground water interactions of the cementitious liner in the water-filled tunnel.

Geochemical modelling was applied to the analysis of dilution trends observed in monitoring borehole data through simulation of groundwater mixing. Interactions with cementitious barrier materials in the CTD were evaluated through 1D reactive-transport modelling for a water-filled tunnel scenario. The study extends the work conducted on cement interactions in the flooded CTD to evaluate shotcrete liner interactions using a 3D model representation of this domain implemented in the reactive transport simulation code PFLOTRAN.

14.1 Simulation of pH in 12MI33 borehole

Initial PFLOTRAN 3D isothermal reactive transport simulations were conducted using homogeneous permeabilities for the granite without the effects of fractures. Simulations incorporating heterogeneous permeability distributions obtained from the hydrological study were also considered in this study. The initial groundwater chemistry was constrained as that reported by Iwatsuki et al. (2015) for the Toki granite at depths of 100 and 300 meters. Volume fractions for the Toki granite used in the simulations are based on the mineral normative abundances after Yamasaki and Umeda (2012).

Figure 287a describes measured and predicted pH at the six monitoring zones in borehole 12MI33. The groundwater in this region interacts with the granitic host rock, however, zone 6 is closer to the cement liner. Possible interaction with cementitious material is illustrated in Figure 287a,b where sampled groundwaters in zone 6 reaches pH~11where sampled groundwaters in zone 6 reaches pH~11. The predicted PFLOTRAN pH trends using both homogeneous and heterogeneous permeability distributions were

essentially the same for all six zones within the respective bounds of initial groundwater pH data producing relatively flat trends. This trend is generally consistent with the scatter of the measured pH's from zones 1-5. Predictions for some of the solutes (not shown) show similar flat trends even for zone 6. However, the pH prediction for zone 6 doesn't capture the observed increase most likely because of limited interaction with the cement liner in the tunnel due to the distance between mesh cells or the need to include cementitious material adjacent to the borehole or close to the zone 6 location. To test this, PFLOTRAN simulations were conducted by assigning shotcrete material in mesh cells above and below of zone 6. The predicted pH profile shows an initial rapid increase eventually reaching a plateau at pH~11.5. In general, this trend is somewhat similar to the measured data except for the sudden pH drop at later times. Predictions for solute concentrations for Na, Ca, K, and Cl in zone 6 (not shown) indicate an initial decrease with subsequent constant concentrations. An initial spike in dissolved Si concentration in predicted in response to this initial pH increase with a subsequent decrease reaching nearly constant concentrations. This increase at early times is not observed in the measured data. This test simulation shows the likely effect of having cementitious material interactions close to the zone 6 generating high pH affecting concentration of major solutes. Despite this, the overall behaviour predicted for major solute concentrations with time agrees with the measured trends.

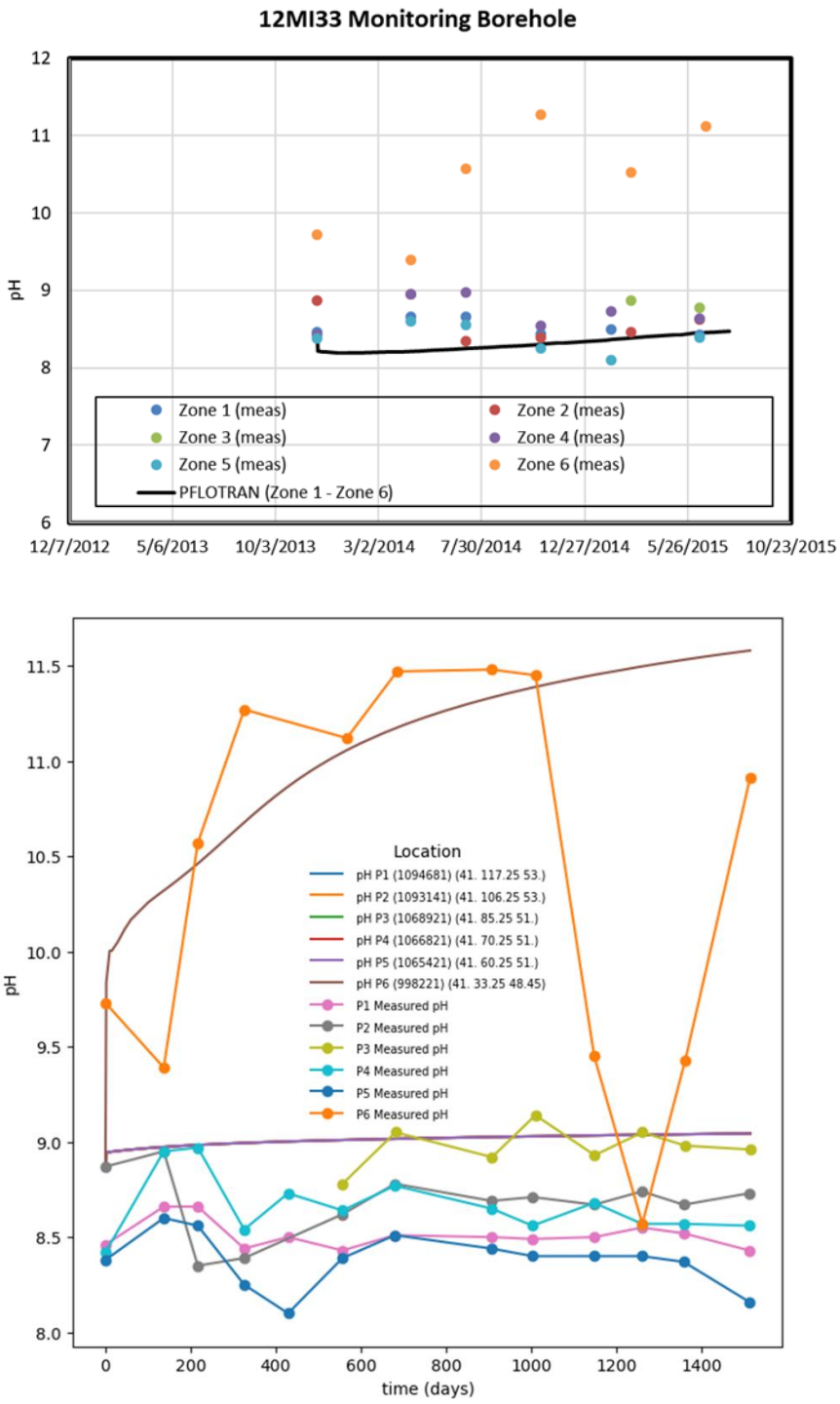

Figure 287a,b. Measured and predicted (PFLOTRAN) pH profiles at monitoring zones 1 through 6. Upper panel show results of PFLOTRAN 3D simulations using homogeneous permeability distributions. Lower panel show results using heterogeneous permeability distributions with shotcrete material at cells above and below of zone 6 (see text).

14.2 PFLOTRAN 3D H-C model of shotcrete liner interactions in the CTD

The CTD is lined with Mg-bearing ordinary Portland cement (OPC) shotcrete and is sealed by using a low-heat Portland cement plug (Iwatsuki et al., 2017). After closure, the tunnel was filled with water to study environmental changes including effects on hydrochemistry due to interactions with barrier materials such as shotcrete. Like FEBEX-DP and other international repository science activities, interactions with cementitious barrier materials (e.g., shotcrete) is important given its potential for alkaline reactions with other silicates (e.g., clay barriers, host rock) and the generation of high-pH pore solutions. These processes could lead to dissolution/precipitation processes at barrier interfaces that could affect solute (radionuclide) transport and clay barrier sorption properties. A 3D reactive transport representation (Figure 292; YZ cross section) has been implemented on a hydrological model of the site near the CTD. The goal is to extend the hydrological model to capture the extent of high pH effects within the flooded tunnel and with distance from the cement-water interface.

A 3D reactive transport representation (**Error! Reference source not found.**; YZ cross section) has been implemented using the computer code PFLOTRAN on a hydrological model of the site near the CTD. The goal is to extend the hydrological model to capture the extent of high pH effects within the flooded tunnel and with distance from the cement-water interface. Such interactions in the water-filled zone may influence pore solution chemistry in the nearby monitoring boreholes where fractures in the excavated disturbed zone (EDZ) are present throughout the length of the CTD. Initial simulations involved the use of homogeneous permeability distributions to evaluate shotcrete liner interactions. The presented results make use of a hydrological model that includes heterogeneous permeability distributions to represent the effect of fractures along with the reactive transport model. The permeability distributions from the hydrological model only apply to the surrounding granite host-rock and not to the shotcrete liner in the tunnels. A homogeneous permeability of 1×10^{-14} m^2 and porosity of 0.196 was assigned to the shotcrete liner.

The Visualization Area domain, which is a CTD-scale domain recommended by the project has been adopted. The domain size is 100 m x 150 m x 100 m. Mesh refinements were added around the CTD to capture the cement plug and the shotcrete on the walls of the CTD. The mesh size is now 70 x 302 x 75, resulting in 1,585,500 grid blocks. Figure 288 and Figure 289 show a slice along the axis of the tunnel and mesh refinements at the CTD, respectively, to allow modelling of the shotcrete and cement plug.

Fracture characterization was conducted using the method detailed in Section 4 and 9. Measured fracture data from tunnel walls and from packer tests in monitoring wells were used to develop the fracture model. A discrete fracture network (DFN) model was developed for the modelling domain for a selected number of realizations. For this study, the DFN "Realization 2" was used. The DFN permeability and porosity results for the selected realization were upscaled to the refined continuum mesh for use in flow and transport simulations. Figure 290 and Figure 291**Error! Reference source not found.** show the upscaled permeability and porosity fields, respectively. The reactive transport simulations with the heterogeneous permeability and porosity fields need to be updated in the future.

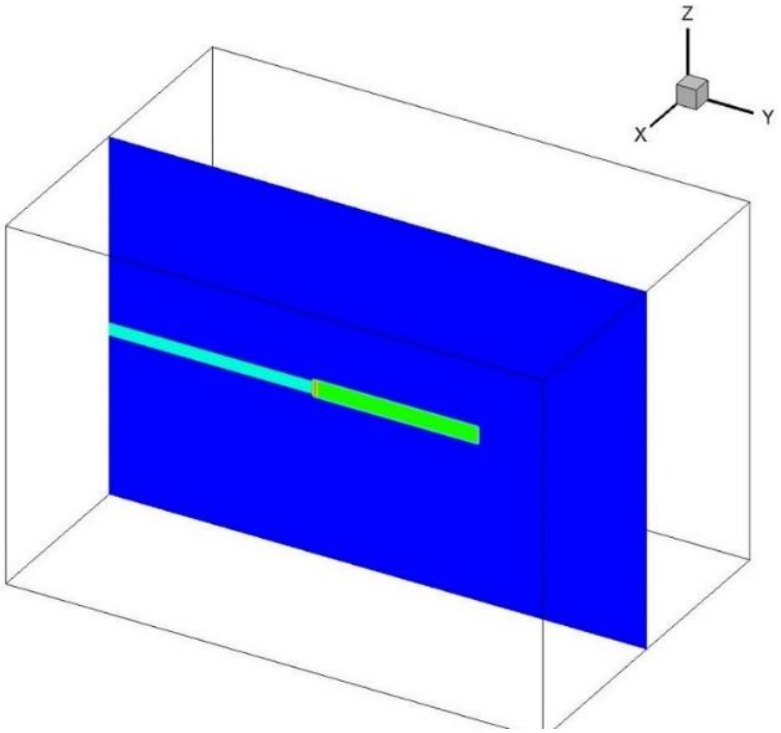

Figure 288. Vertical slice along the axis of the tunnel showing the CTD region (light green) and inclined drift (light blue).

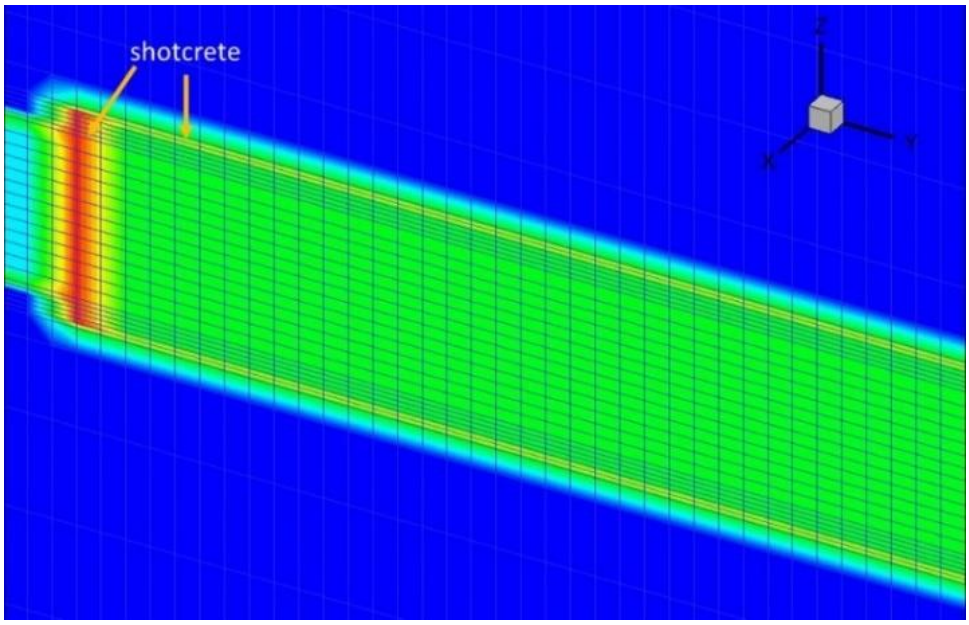

Figure 289. Mesh refinement showing shotcrete plug and lining around the CTD.

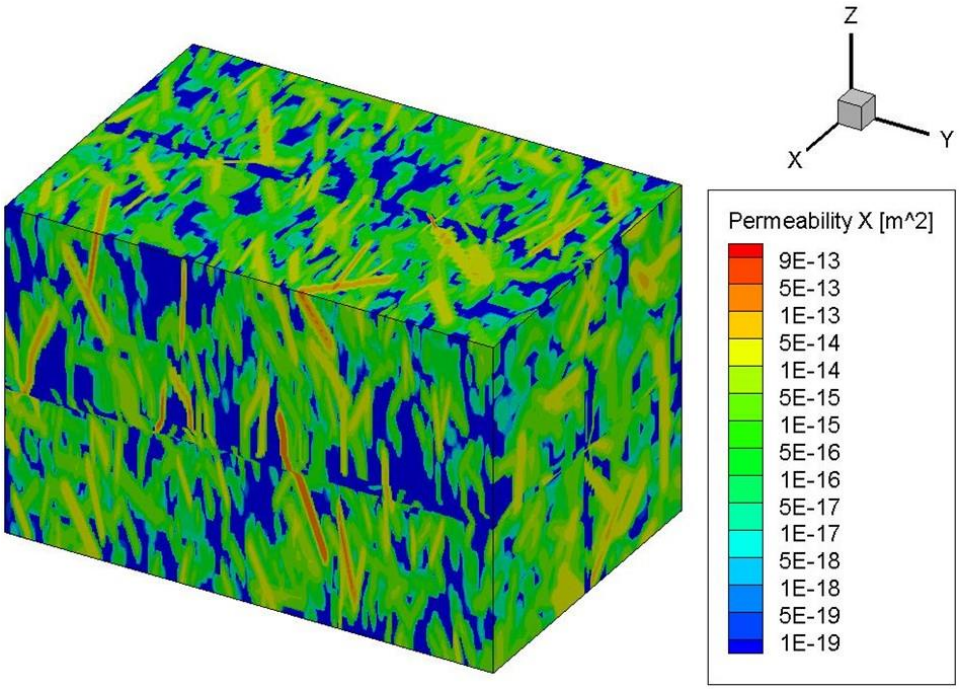

Figure 290. 3D domain representation of upscaled permeability field for DFN Realization 2.

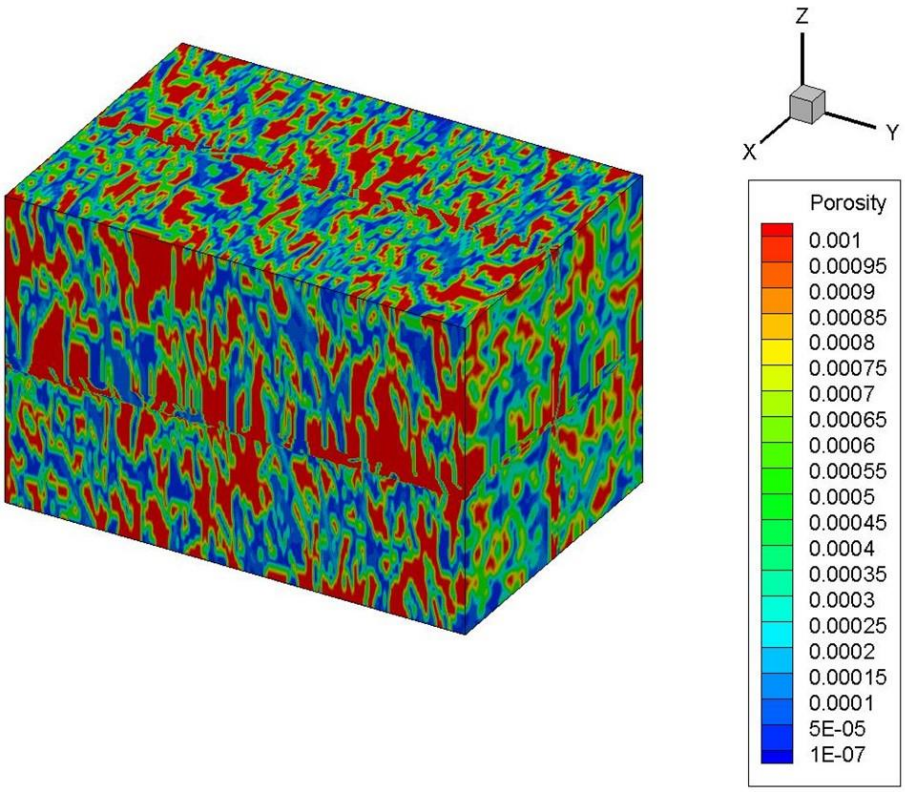

Figure 291. 3D domain representation of upscaled porosity field for DFN Realization 2.

The 3D reactive-transport model implementation is done in PFLOTRAN using similar parameters (e.g., material properties) to those adopted previously in the 1D evaluation of EBS material interactions (Jové Colón et al., 2016). The PFLOTRAN simulations were conducted in T-H mode (coupled thermal-hydrological flow) assuming full saturation. Thermodynamic data for cementitious (CSH (1.6), portlandite ($Ca(OH)_2$), C_3AH_6, C_3FH_6, Friedel's salt, ettringite) and mineral phases were obtained from the THERMODDEM database (Blanc et al., 2012; Blanc et al., 2006). The relative composition (volume fractions of phases) of the shotcrete domain is based on ordinary Portland cement (OPC) composition given in the data sets provided in the GREET website (https://www.jaea.go.jp/04/tono/miu/dataset/greet/greet.html). The model considers a Cl-bearing phase (Friedel's salt) and a Mg-bearing solid (brucite) as part of the cementitious phase assemblage. The reason for adding these phases is to have a shotcrete composition close to that consider by GREET and to evaluate their effect on solution chemistry, particularly on Cl concentration. The aggregate in the shotcrete is assumed to be composed of quartz and K-Na feldspars based on the analyses provided in the GREET website. Similar to the reactive transport simulations of the 12MI33 monitoring borehole, initial groundwater chemistry in the host rock above and below the CTD were constrained according to Iwatsuki et al. (2015).

Dissolution rates of cementitious solids were obtained from various sources as described in Jové Colón et al. (2016). The length of water-filled domain is about 47 m with a height of 5 m closely resembling the CTD dimensions. The cement plug thickness is 2 m and the shotcrete liner is 0.1 m thick. The flooded CTD domain is represented by a porous medium having a porosity of almost unity and a very high permeability. The initial groundwater in the flooded domain is assumed to have a similar chemistry to that of the host granitic rock. This groundwater also represents the starting solution chemistry of the water-filled CTD. The simulations were performed over a period of 300 - 600 days. Many PFLOTRAN simulations were carried out to assess the spatiotemporal trends of pH and solutes in the CTD and shotcrete.

Figure 293 shows four time-snapshots (0, 60, 150, 300 days) of the pH mapping to represent the evolution of the reactive front from the shotcrete liner domain. In this case, Ca concentration is constrained to be in equilibrium with CSH(1.6). As expected, pH increases with time from the interface into the water-filled CTD region and the host rock. After ~300 days of simulation time, the increase in pH because of the advancing front reaches ~0.5 m from the shotcrete interface into flooded CTD. About 1 m into the CTD, the pH remains close to the starting pH 8.9 for the remainder of the simulation.

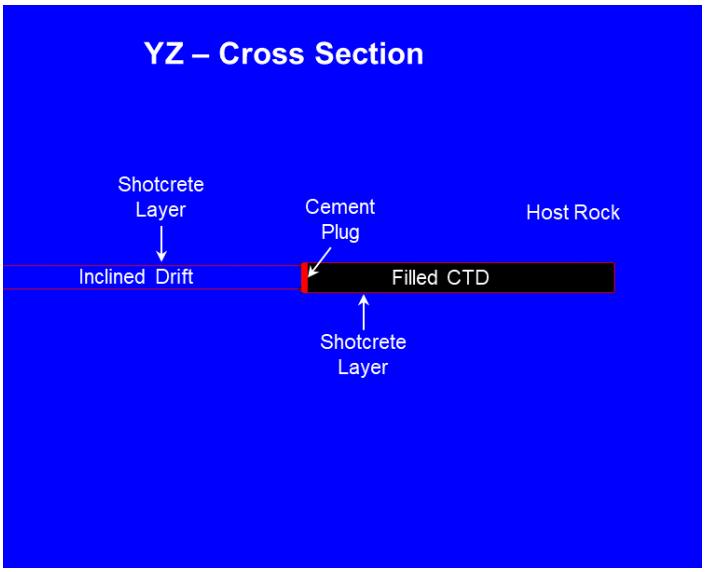

Figure 292. Schematic figure showing a YZ of the model domain in the PFLOTRAN reactive transport simulation of the CTD. Red areas delineate the shotcrete liner and cement plug. Observation points (not shown) are positioned at the tunnel length midpoint starting from the shotcrete-water interface up to a meter inside the water-filled tunnel.

The overall behaviour of the reaction front described in these snapshots is very similar to that shown in Jové Colón et al. (2018).

Figure 294 (upper panel) shows the pH predictions from the PFLOTRAN reactive-transport model and the measured pH data constraining Ca to be equilibrium with CSH(1.6). The measured pH (purple dots connected by a line) show a rapid monotonic increase early in time then progressing towards a pH~10. It's inferred that this rapid initial increase in pH is mainly due portlandite leaching in shotcrete. Notice the measured pH data after ~150 days (3/2016) show more variation with time (i.e., deviations from a monotonic increase) but still trending towards pH~10. The PFLOTRAN simulation results (solid curves) are shown for four observation points at a distance from the shotcrete interface (at the shotcrete interface, 0.4 m, 0.7 m, and 1 m) into the water-filled CTD. Notice that pH predictions at the observation point close to the shotcrete interface are in very good agreement with the measured data at t<~50 days. However, it then underestimates the measured data at the interval of ~50 - ~100 days. After 100 days, the model result is still in good agreement with the measured pH trend progressing towards pH~10. As in previous results, predictions at 0.45 m show a slower pH increase due to limited transport from the shotcrete interface into the water-filled CTD. This increase reaches pH~10 towards the end of the simulation at 600 days within the range of measured pH. Predictions of pH at 1 m from the shotcrete interface show a relatively small increase with time indicating the limited effect of the reaction front on groundwater pH towards the tunnel central axis.

The measured pH data was used to constrain the parameters in the transition state theory (TST) rate law in PFLOTRAN and adopted for portlandite and brucite dissolution kinetics (see Lichtner, 2016). The adjusted parameters are related to the primary chemical species (H^+, Ca^{++}, and Mg^{++}) in the prefactor term of the rate law for the mineral dissolution reaction of portlandite and brucite. The overall agreement in the representation of the observed pH trend from the PFLOTRAN simulation suggests portlandite is the primary contributor to this change. This is expected as the main leaching phase in the shotcrete interaction with groundwater. More sensitivity analyses on kinetic parameters are needed to evaluate the potential for other phases contributing to the overall temporal variation in pH.

Figure 294 shows the measured Na^+ concentration (lower panel) decreasing with time with some level of scatter. The PFLOTRAN predictions at the shotcrete interface indicate a sudden decrease of Na^+ concentration with time with a subsequent increase at t>100 days. This initial dip in the simulation prediction is off trend with the measured data even when it recovers at subsequent times. The subsequent increase in Na^+ concentration with time is consistent with initial porewater Na^+ concentrations in the

rock below the CTD region. This is indicative of the effects of groundwater mixing between the CTD and the host-rock through the shotcrete liner. Other simulations with different constrains have shown better agreement with the overall measured Na concentrations but at the compromise of not having a good representation of the measured pH trend at early times. The predictions of temporal changes in Na^+ concentration with distance from the shotcrete interface show similar decreasing profiles but with the expected effect of a slow moving front away from the shotcrete surface in the flooded CTD. It is inferred that simulation predictions obtained at a distance between the shotcrete interface and 0.4m would produce a trend that should be in better agreement with at least part of the data. However, the mesh cell discretization in these domains is not sufficiently fine to sample observation points at such intervals. Finer mesh discretizations were attempted but the large computational burden and memory size limitations prevented from having successful simulations within a reasonable period of time – even when using high performance computing (HPC) platforms.

Figure 295 shows the temporal evolution of Ca^{++} and Cl^- measured concentrations in the CTD. Notice that both aqueous component concentrations show an initial ($t \leq$ ~150 days) sharp decrease to subsequently attain a nearly steady-state concentration. The PFLOTRAN simulation does produce an initial decrease in both Ca^{++} and Cl^- at the shotcrete interface observation point. However, similar to the Na^+ concentration profile, the Ca^{++} and Cl^- dips initially with a subsequent increase towards the end of the simulation. Such an initial large decrease is caused by groundwater mixing and/or Cl^- uptake by precipitation of a Cl-bearing cementitious phase. The subsequent increase in Cl^- concentration by the mixing influence of the porewaters in the host-rock below the CTD through the shotcrete liner. It should be noted that calcite is predicted to form in the shotcrete liner but in relatively small amounts and could also contribute in controlling Ca^{++} concentration in the porewater. The formation of calcite in shotcrete has been reported by the GREET project. These observations need further evaluation through monitoring and phase characterization activities, along with reactive transport simulations, for example, focusing on evaluating the effects of hydrological characteristics (porosity and permeability) in shotcrete and host rock.

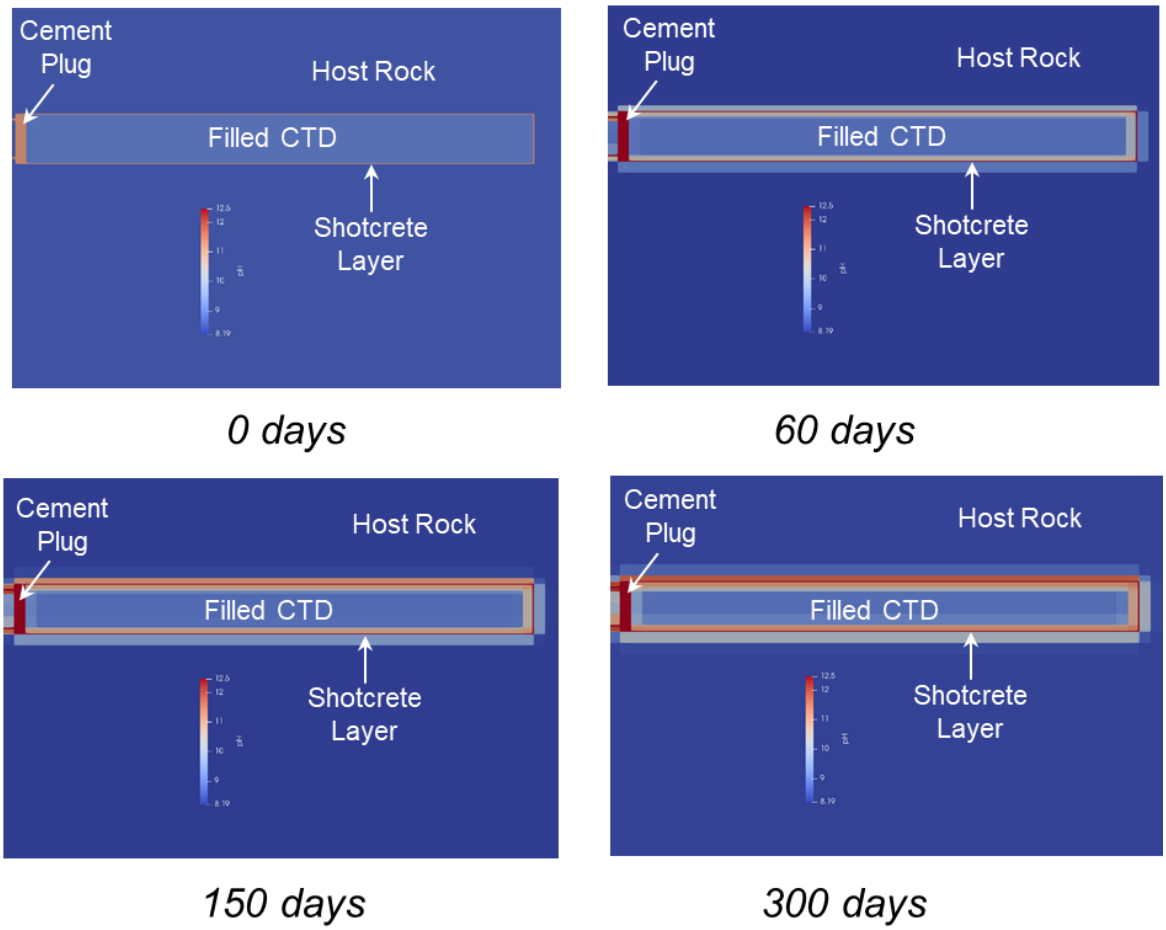

Figure 293. Predicted pH of the PFLOTRAN 3D reactive transport model of the CTD and surrounding host rock. The reaction front diffuses into the CTD and into host rock. pH colour map scale ranges from 8.19 to 12.5.

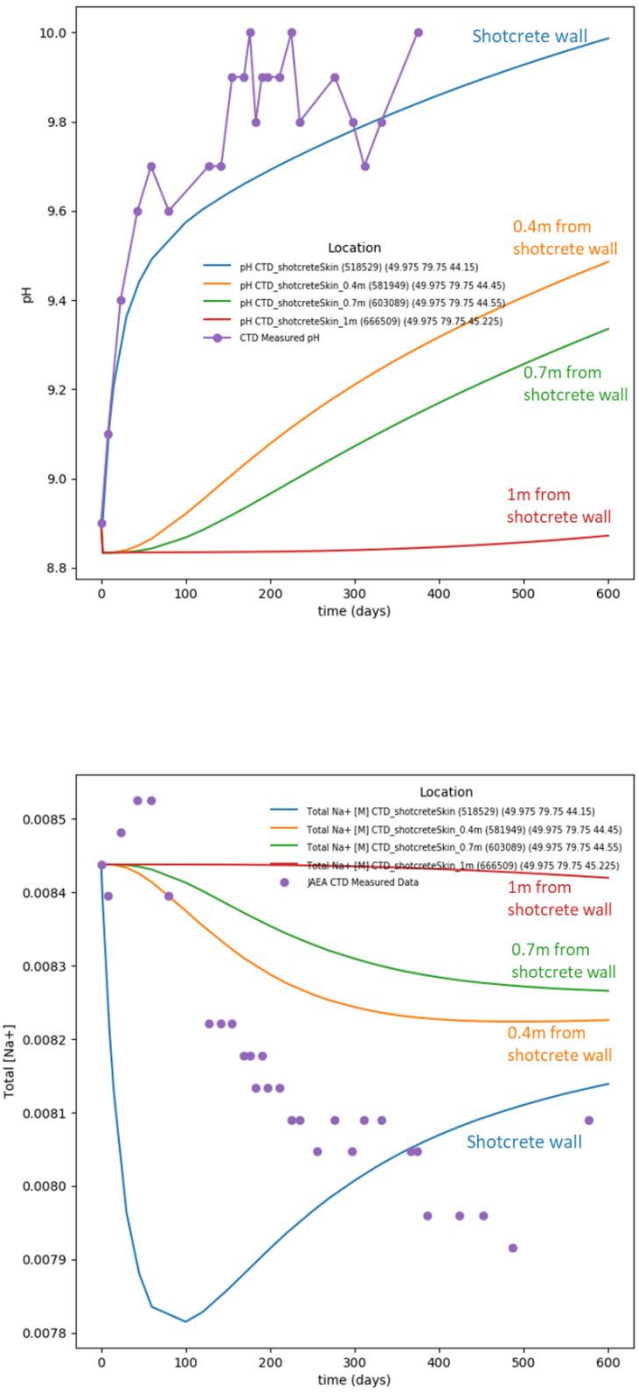

Figure 294. Measured and predicted pH (upper panel) and Na^+ concentration (lower panel) in moles/L profiles at the midpoint region of the CTD.

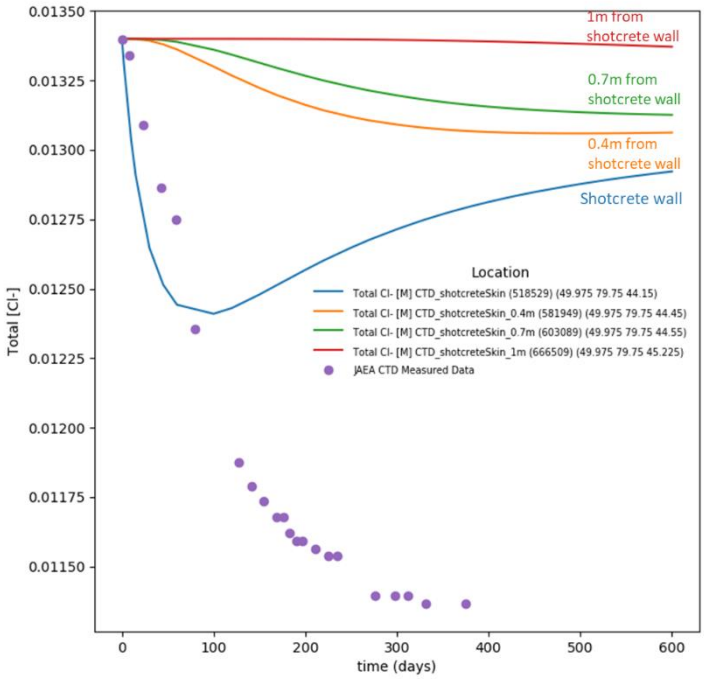

Figure 295. Measured and predicted Ca^{++} (upper panel) and Cl^{-} concentration (lower panel) profiles in moles/L at the midpoint region of the CTD.

14.3 Conclusions

Geochemical modelling has been applied to the analysis of dilution trends observed in monitoring borehole through simulation of groundwater mixing. Applications of this modelling methodology to simulate the extent of fluid mixing is useful in the analysis of groundwater compositions and their potential interactions with other phases such as gases and minerals. It also provides a consistent geochemical evaluation methodology to exploit the extensive hydrochemical field data relevant to site characterization. Moreover, in the case of the Mizunami site, it provides the opportunity to evaluate the effects of hydrological and chemical disruption due to excavation and site construction activities.

The 3D reactive transport model was also used to model groundwater interactions in six zones of the monitoring borehole 12MI33. This borehole lies parallel to the CTD and near the inclined drift. PFLOTRAN pH predictions of zones 1-5 in the monitoring borehole show overall consistency with the measured data suggesting the control of the granitic

host-rock on the groundwater chemistry. The high pH observed in zone 6 appears to be influenced by interactions with the nearby cement liner and could not be predicted by the current model. To test the possibility of enhanced mixing at this zone, simulations were made with shotcrete in neighboring mesh cells producing the observed pH trend at this zone.

3D reactive transport modelling of shotcrete liner interactions was implemented on a hydrological model of the site domain comprising the CTD. PFLOTRAN predictions of pH, Na^{+}, Ca^{++}, and Cl^{-} at the shotcrete interface in the midpoint length of the CTD showed some general agreement with measured data trends although with deviations. The predicted pH at the shotcrete interface is in good agreement with measured data at early times but it is slightly underestimated at later times. Predicted Na^{+}, Ca^{++}, and Cl^{-} concentrations show an initial decrease between 50 – 100 days with a subsequent increase afterwards. Such behavior could be explained by mixing effects from groundwater chemistries in the CTD with those of the host-rock interacting through the shotcrete liner.

This modelling effort provides the groundwork for future assessment of the observed data to explain deviations reactive transport model predictions in the evaluation of kinetic rate law, water chemistries, and transport parameter/model constrains to better represent the temporal changes in pH and water chemistries.

15 Results of Step 3 modelling (TUL)

The geochemical mixing model from Section 10.5 can be also extended for a partial understanding of the long-term behaviour of the groundwater ion composition. The calculation is based on chemical equilibrium and therefore does not considers time as a variable. Under the assumption of no reaction with natural rock (resulting from the fact the interaction is slow with respect to the experiment time scale and so the water-rock interaction process cannot be detected during the site observation), it determines a set of possible states, without regard to the temporal scale. The two processes are included, one is the mixing of higher and lower mineralized endmembers described in Section 10.5 and second is the reaction with shotcrete on the tunnel wall, which is added in the section below and within the next section, 15.2, the overall model is expressed.

15.1 Influence of shotcrete on groundwater parameters

Groundwaters, which deviate from the main trend of groundwater development in the rock environment of the CTD, comes, with some exceptions, from zones that are in direct contact with CTD, whose walls are covered with shotcrete. According to the phase analysis, it contains a relatively reactive phases as portlandite [$Ca(OH)_2$], calcite [$CaCO_3$], ettringite [$Ca_6Al_2(SO_4)_3(OH)_{12}\times 26H_2O$], and calcium silicate hydrate [C-S-H]. When the groundwater interacts with these shotcrete components, the pH value is significantly increased, while individual components are released into the groundwater. An example of development is the interaction of portlandite with typical groundwater from borehole 12MI33 with a total mineralization of 714 mg/L. Dissolving portlandite by equation

$$Ca(OH)_2 \text{ (portlandite)} \rightarrow Ca^{2+} + 2\ OH^-$$

the pH value increases, the concentration of Ca ions increases, the relative ratio of Ca ions and the total groundwater mineralization increases. As a result of the increase in pH, some groundwater components can in turn precipitate in the form of insoluble phases. An example is the precipitation of magnesium ions in the form of brucite [$Mg(OH)_2$]. The concentrations of components that are not part of the interacting phases and do not precipitate due to pH change remain unchanged. Similarly, ettringite and calcite affect groundwater. Both phases of the interaction with groundwater increase its pH values, Ca ion concentrations and their relative proportion to other cations. Examples of development when interacting with groundwater with portlandite are shown at Figure 296.

The development of pH values during interaction with portlandite is in very good agreement with the observed values, similarly for some other components such as Cl or Mg ions. A similar trend can be observed for other components, but satisfactory agreement of the observed concentrations is not achieved.

In principle, the model trend of groundwater development corresponds to the interaction with portlandite in the shotcrete. However, a more precise modeling of the processes of groundwater interaction with shotcrete is facing several serious problems:

1. In the interaction of shotcrete with water and solidification of shotcrete, hydrosilicates of the general formula $mCaO \times nSiO_2.pH_2O$, which are identified as minerals e.g. tobermorite-9A [$Ca5Si_6O_{17} \times 3H_2O$], afwillite [$Ca_3Si_2O_4(OH)_6$], hillebrandite [$Ca_2SiO_3(OH)_2 \times 0.17H_2O$], and xonotlite [$Ca_6Si_6O_{17}(OH)_2$]. However, often are generated gels with variable proportions of CaO, SiO_2, and H_2O, collectively referred to as CSH gels. Their thermodynamic properties depend, inter alia, on the aggregate state or degree of hydration. For example, other phases such as $Ca_2Si_3O_8 \times 5/2H_2O$, $Ca_2SiO_4 \times 7/6H_2O$, $Ca_4Si_3O_{10} \times 3/2H_2O$, $Ca_5Si_6O_{17} \times 11/2H_2O$, $Ca_5Si_6O_{17} \times 21/2H_2O$, $Ca_5Si_6O_{17}$^$3H_2O$, and $Ca_6Si_6O_{18} \times H_2O$ are given in thermodynamic databases.
2. In addition to the Ca-Si hydrated phases, the solidification process also produces phases containing aluminium and iron, such as $Ca_4Al_2O_7 \times 13H_2O$, $Ca_4Al_2O_7 \times 19H_2O$, $Ca_3Fe_2O_6 \times 6H_2O$, and several their modifications.
3. The process of shotcrete solidification has several phases, during which phase transitions occur at intervals from hours to several years.

The degree of influence of groundwater by interaction with the shotcrete can be characterized by the total dissolved species concentration. The greater the influence, the higher the dissolved species concentration is achieved. Basically, the parameters and components of the groundwater can be divided into three groups according to the interaction influence:

1. Parameters and concentrations of components that are not affected by interaction and with increasing mineralization do not change: oxidation-reduction potential, concentration of Br^- and Cl^-.
2. Parameters and concentrations of components that increase or decrease during interaction and are independent on water mineralization: Ca^{2+}, Mg^{2+}, Mn^{2+}, Na^+, and SO_4^{2-}.
3. Parameters and concentrations of components affected by the interaction and increase or decrease with increasing mineralization: pH, $B(OH)_3$, F^-, K^+, and SiO_2.

15.2 Conceptual model of groundwater development around CTD

The evaluation of groundwater geochemical development around the CTD can be simplified down to a conceptual model of development from before or at the beginning of CTD building to opening and dewatering CTD.

The geochemical evolution of groundwater around the CTD (shotcrete interaction analysis above together with previous evaluation of mixing in section 10.5) can then be expressed in the conceptual model shown in Figure 297. The groundwater's initial composition is marked by a green ellipse. It corresponds to the total dissolved species concentration of 700-800 mg/L. The groundwater is almost only Cl, with about 60 eq. % alkali metal and 40 eq. % of Ca^{2+}. They are practically free of Mg^{2+}.

In the period of construction, watering, opening and dewatering of CTD, the major part of groundwaters move along the endmember groundwater mixing line, which is marked by a red line. In zone 5 of boreholes 12MI33 and 13MI38, the total concentration of dissolved species is significantly increased, and the relative proportion of Ca ions is increased to 50 eq. %. On the contrary, in zone 4 of both boreholes, the total concentration of dissolved species decreases, and, at the same time, the relative proportion of alkali metals increases to 80 eq. %. With total mineralization below ~ 500 mg/L, groundwaters begin to deviate from the main mixing trend and move into groundwater development, which is characteristic of shallower water from depths of 200 to 400 m below the surface.

In addition, in groundwaters from zone 4 of boreholes 13MI39, 13MI40 and 13MI41, which are adjacent to CTD walls (and partly from waters of zone 6 of borehole 12MI33), there is a shift from the main mixing trend towards a higher relative proportion of Ca ions, with the overall trend of development of these waters parallel to the main mixing trend. This is a consequence of the groundwater interaction in these zones with the CTD shotcrete. These waters also have very high pH values (are strongly alkaline).

To illustrate the differences in the composition of the end members of the mixed groundwaters, the Stiff diagrams of these waters are also included. The endmember with the lowest total dissolved species concentration is typically sodium-chloride groundwater, the endmember with the highest total dissolved species concentration is high-Cl groundwater with a balanced content of Ca and alkali metals ions. For groundwaters which are affected by the interaction with the CTD shotcrete, there is a clearly higher concentration of Ca ions. At the highest total dissolved species concentrations in influenced groundwaters, Ca ions even prevail over the alkali metals.

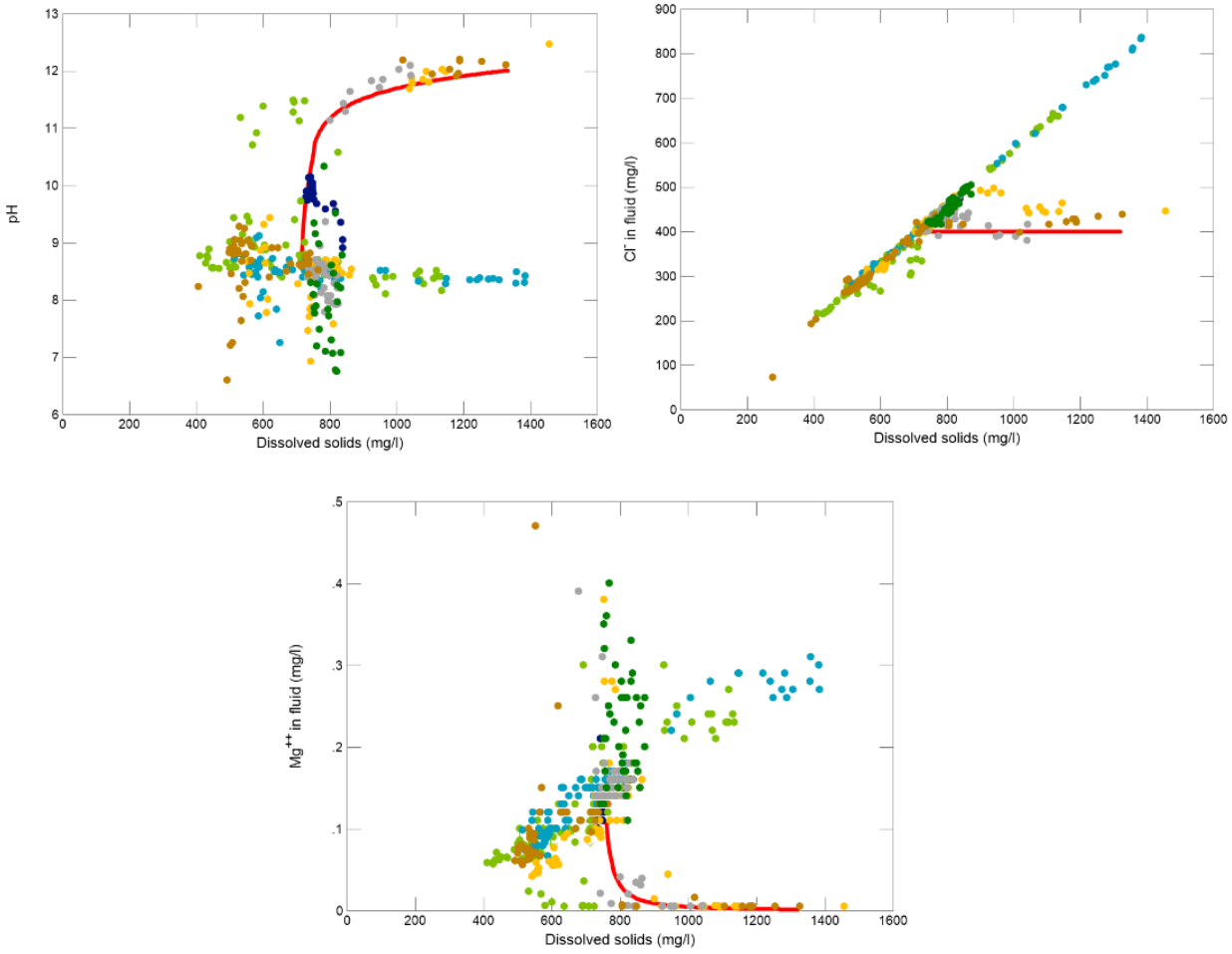

Figure 296. Evolution of conditions and selected components concentrations during the interaction of 1 liter of groundwater from borehole 12MI33 with total mineralization of 714 mg/L with 650 mg of portlandite (red line) and its comparison with the actually found values for waters around CTD. Color coding corresponds to individual boreholes according to the legend on Figure 249.

The development of groundwater in the rock environment around CTD is simplified as follows:

1. In the zone 4 of boreholes 12MI33 and 13MI38 there is a decrease in total mineralization and decrease of Cl concentration during the monitored period, which can be attributed to the penetration of groundwater from shallower levels.
2. In the zone 5 of boreholes 12MI33 and 13MI38, there is a significant increase in total mineralization and growth of Cl concentration in groundwater during the

period under monitoring, which can be attributed to groundwater penetration from deeper levels.

3. Groundwater that is sampled in zones adjacent to CTD walls with shotcrete are affected by the interaction with the shotcrete, and its pH increases significantly. These groundwaters are characterized by an increase in total mineralization and Ca ion concentration, Cl concentration remains unchanged.

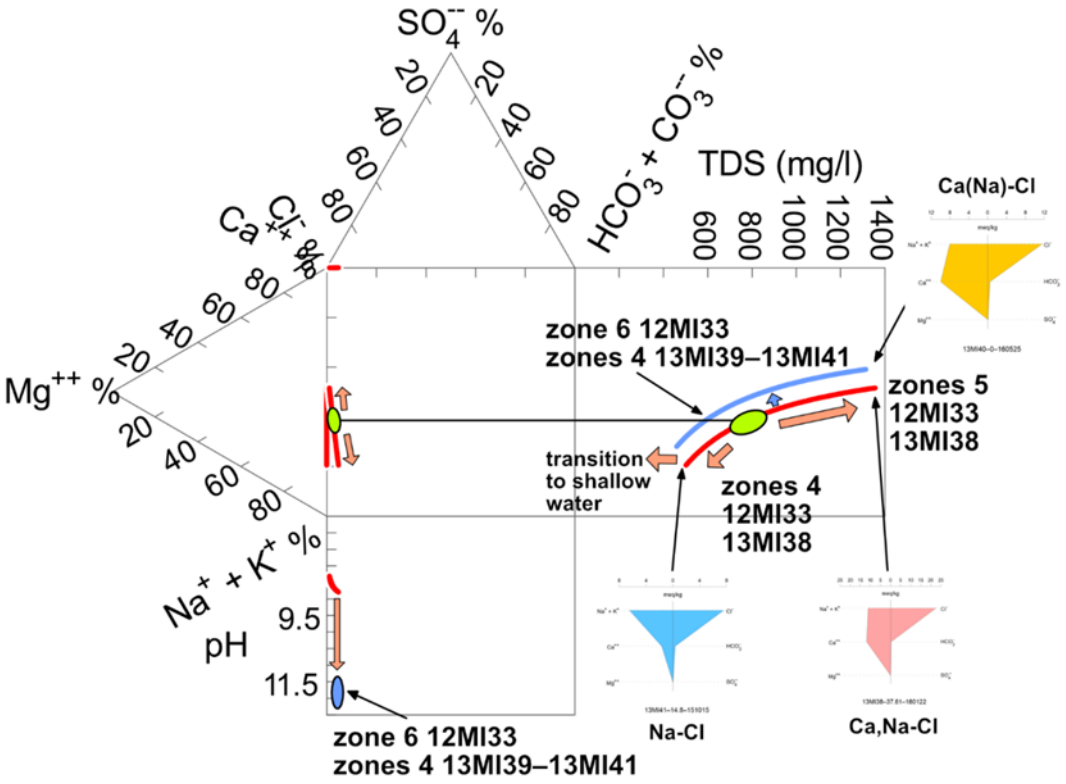

Figure 297. Conceptual model of groundwater chemical composition development around CTD. The red lines show the model development of the composition of the mixed groundwater 12MI33 and 13MI38. Green ellipse showing groundwater position at beginning of CTD building, orange arrows development during building, watering and after opening CTD. The blue line shows the shift in groundwater composition due to the interaction of groundwater with shotcrete.

16 The usefulness of knowledge in Task C for geological disposal project

16.1 The understanding of the environmental process around tunnel

In a series of experiments, we have understood the environmental disturbances after the excavation of the tunnel, their recovery process during the tunnel closure, and the stable environment after the tunnel closure. Based on the observations in and around the tunnel, features, events, and processes (FEPs) related to T-H-M-C-B during excavation, closing of the tunnel were conceptualized.

Excavation of the tunnel

The opening of the tunnel carries the atmosphere to underground. The temperature of rocks and water around the tunnel varies seasonally with air circulation. In the case of Mizunami, the unsaturated zone extends up to about 1 m from the tunnel wall, and groundwater drawdown and upconing occur at least within a few tens of meters from the tunnel depth. The water pressure change is apparently related to the heterogeneous hydrogeological region formed by the fracture network (Figure 298).

While no obvious rock deformation was observed. The drawdown and upconing of groundwater cause the mixing between chemically different waters such as high and low Cl concentration around the tunnel. The redox condition of the groundwater near the tunnel gradually changes to the oxidation state. As a result, anaerobic microbial habitats are transformed into aerobic microbial compositions.

Closure of the tunnel

The temperature after closing the tunnel becomes that of the groundwater filled in the tunnel (Figure 299). The water pressure will immediately return to the initial condition. The isolated water in the tunnel becomes alkaline water by interaction with cementitious material such as shotcrete over a period of several months. The redox state is restored to the reducing state by inflow of the reducing groundwater from the surrounding rock. Under such circumstances, natural analogue elements such as uranium tend to become immobile due to adsorption to the cementitious material in the tunnel.

Disturbed groundwater by mixing of chemically different water remains heterogeneous around the tunnel. Because fracture networks have different connectivity and continuity

in each hydrogeological region, the retention of chemically different groundwaters such as low salinity or high salinity water significantly reflects hydrogeological conditions. This means that a wide range of chemical data may need to be used for performance and safety assessments.

Event: Tunnel excavation

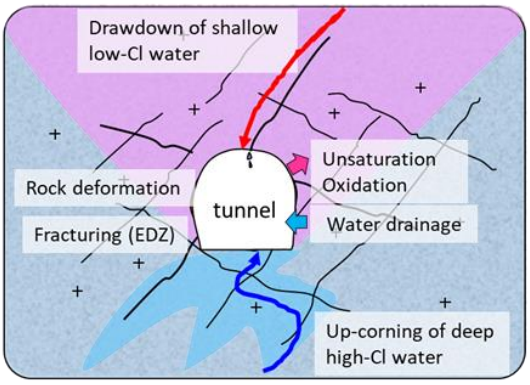

Main issues handled in simulation

	Process	Feature
T	Vary to temperature of ventilation air	Seasonal change (10-35 degree C)
H	Unsaturation (~1m) Drawdown/Up-corning of GW to tunnel	• 4 MPa -> 1.5 Mpa • Inherently inhomogeneous hydrogeological domains • Different water pressure at each domain • Preferential flow path along tunnel (EDZ)
M	Deformation	Less than 0.01mm
C	Oxidation Mixing among chemically-distinct waters	• pH: 8.6 • ORP: 0 ~ -100mV • Different Cl conc. at each domain (200-600mg/L)
B	Aerobic bacteria dominant habitat	α–γ Proteobacteria, etc

Figure 298. FEPs in and around the tunnel during excavation

Event: Tunnel closure

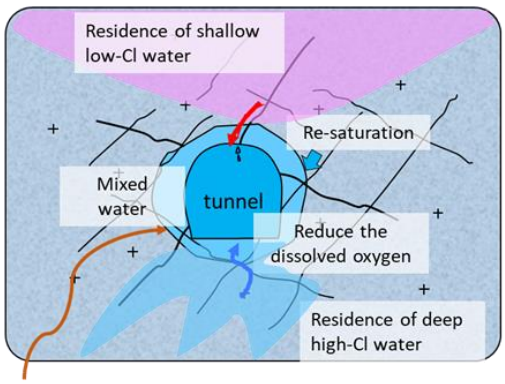

Main issues handled in simulation

	Process	Feature
T	Natural geothermal gradient	28 degree C
H	Different water pressure recovers to baseline	1.5MPa -> ~4 Mpa
M	Re-deformation	Less than 0.01mm
C	Replacement by reducing water Mixing among chemically-distinct waters Cement dissolution (alkalization)	pH: 8.6 -> 10 ORP: -100 -> -150mV Cl: 200-600mg/L
B	Anaerobic bacteria dominant habitat	Vercomicrobia, etc

Figure 299. FEPs in and around the tunnel during the closure

Steady state after the tunnel closure

A long time after the tunnel closure, the temperature will be that of the geothermal gradient. In addition, the flow of groundwater is controlled by the natural hydraulic gradient at each depth (Figure 300). The alkaline groundwater in the tunnel spreads in the fractures and pores in rock matrix around the tunnel by the groundwater flow. The chemical pH buffering process by rock minerals is unclear, it is a future research task.

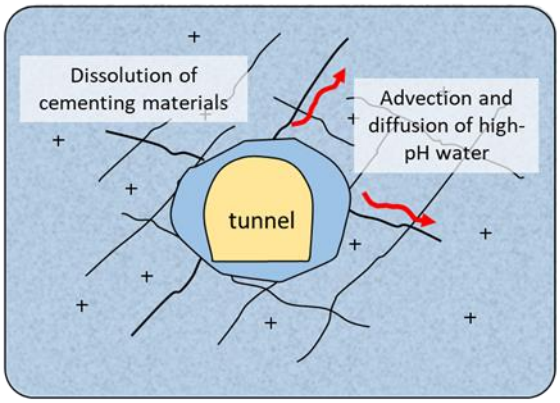

Main issues handled in simulation

	Process	Feature
T	Natural geothermal gradient	28 degree C
H	Very slow flow depending on the natural hydraulic gradient	~ 4 MPa 0.03~3 mm/yr.
M	Sub-stable	Less than 0.01mm
C	Chemical evolution by cement-water interaction and its spreading	pH: 10 ~ 12 ? ORP-SHE: ~ -150mV Cl: 200-600mg/L
B	Anaerobic and high-pH proof bacteria dominant habitat	Vercomicrobia, etc

Figure 300. Long-term FEPs in and around the tunnel after the closure

16.2 Applicability of modelling and simulation techniques

Throughout Decovalex-2019, Task C aimed to develop modelling and simulation methods and clarify the applicability of the various methods used in each phase of the HLW geological disposal project.

One important piece of information regarding the construction of underground facilities is the amount of water flowing into the tunnel. Project implementers will need to predict an expected groundwater inflow and prepare treatment facilities for groundwater drainage in the planning. In Step 1, the three teams attempted to predict groundwater inflows at the CTD and inclined gallery based on the hydrogeological data such as fracture mapping, etc. Various settings in the DFN model such as fracture frequency, hydraulic conductivity in fractures and skin effect of shotcrete, etc. were attempted by

each team to predict the inflow rate and calibrate into observed data. Consequently, it was confirmed that the current modelling and simulation technology can estimate the inflow rate of groundwater into the excavated tunnel with an estimation error of tens metric tons/day. Furthermore, the Sandia team suggested that an iterative approach based on multiple realization cases and domain sizes in DFN modelling considering the high permeable fractures would be an effective means to show the uncertainty (variation range) of groundwater inflow rate prediction. During the facility construction phase, pilot borehole surveys from the ground surface and tunnels need to be planned to collect information on fracture frequency and the hydrogeological characteristics, etc. and to construct the DFN models of the site with the larger domain.

As another important aspect regarding safety assessment around the tunnel, the environmental conditions after closing the tunnel are essential input parameters to assess solute transport, so the applicability of modelling and simulation techniques to predict it must also be confirmed.

Groundwater drawdown and recovery were distinctly dependent on the fracture distribution in granite. During the tunnel closure experiment, the water pressure response in the fracture connecting to the CTD directly synchronized the change of the water pressure in CTD. CTD water pressure was affected by water leakage around the plug so that the water pressure in some fractures would be also likely to be affected by water leaks.

Initially, each team's prediction of water pressure recovery after the tunnel closure indicated a similar value to the baseline water pressure before tunnelling. If the entire gallery will be backfilled, there will be no water leakage from tunnel, so the water pressure drawdown in the fracture connecting to the tunnel will probably recover to the baseline water pressure after tunnel closure. Therefore, the initial prediction results of each team are considered reasonable.

On the other hand, fractures that show a hydraulic response synchronized with the groundwater in the tunnel are considered important solute transport path in the performance and safety assessments of the geological isolation system. Therefore, showing the reproducibility of environmental changes in such hydrogeological structures is worthwhile to show the applicability of modelling and simulation methodologies.

Stochastic approach (DFN modelling and the calibration) considering the high permeable fractures by JAEA, SNL teams, and deterministic approach with inverse modelling by TUL team suggested that both methodologies are applicable to reproduce and predict water pressure recovery even in a fracture which has higher connectivity.

Moreover, the monitoring of hydraulic response using pilot boreholes during tunnel excavation and closure is an effective means to create the concept of fracture network (e.g. Fracture frequency, connectivity and continuity of channelling structure, etc.) for modelling and simulation of the hydrogeological environment in crystalline rock.

Regarding the chemical environment, we simulated Cl concentration in groundwater around the tunnel and pH, redox conditions and the chemical composition in CTD. Because Cl is a non-reactive chemical component, the concentration in groundwater around the tunnel is controlled primarily by the mixing of chemically different waters, not by the interaction of water and minerals. Cl concentrations varied greatly by mixing with groundwater derived from shallow or deep depths.

The ECPM model converted from the DFN model by JAEA and SNL teams and deterministic model by TUL team were applied to capture the wide variation in observed Cl concentration. Model domain size, mesh size, fracture continuity to the shallow and deep domain, the depth profile of Cl concentration disturbed by upconing around the shafts, etc. were considered in their model calibration, but the concentration in each monitoring point could not be simultaneously reproduced.

As a practical approach to estimate the wide variation range of Cl concentration, the JAEA team proposed the boundary condition settings in which the Cl concentration profile is controlled by a large hydrogeological compartment around the CTD. They showed a wide variation of Cl concentration could be formed by intense draw of shallow or deep groundwater in a small domain surrounded by low permeability faults. Channelization through fracture networks would be an important concept in modelling for the simulation relevant to Cl concentration. Precise Cl variation in each hydrogeological structure can only be reproduced qualitatively, but it is possible to present the range of Cl concentration variation by current methodology.

The chemical evolution of CTD groundwater was theoretically analysed by thermodynamic-only calculations at first. The inverse modelling by assuming various water-mineral interactions to reproduce chemical change of the isolated groundwater presented dominant minerals in shotcrete and granite which contribute the groundwater evolution. Reactive transport modelling including these minerals has not completed yet, but the spread of alkaline groundwater from CTD to rock was inferred to be retained in the vicinity of shotcrete. In order to predict long-term hydrochemical evolution, it is necessary to enter realistic advection rates after facility closure into reactive transport simulation. The simulation of the long-term advection or diffusion of chemically distinct water is a theme to be studied in the future.

17 Planned and Completed Publications

Table 53 gives the planned and completed publications under this task.

Table 53. Planned and completed journal and conference papers for Task C.

Author(s)	Title	Journal/ Conference	Status
Kalinina, E.A., Teklu, H., Wang, Y. and Iwatsuki, T.	Developing a Fracture Model of the Granite Rocks Around the Research Tunnel at the Mizunami Underground Research Laboratory in Central Japan.	AGU 2017– Conference Paper (2014)	Published
Kalinina, E.A., Teklu, H., Wang, Y., Ozaki, Y. and Iwatsuki, T.	Development and Validation of a Fracture Model f or the Granite Rocks at Mizunami Underground Research Laboratory, Japan	DFNE2018 – Conference Paper (2018)	Published
Hadgu, T., Kalinina, E.A., Wang, Y., Ozaki, Y. and Iwatsuki, T.	Investigations of Fluid Flow in Fractured Crystalline Rocks at the Mizunami Underground Research Laboratory	DFNE2018 – Conference Paper (2018)	Published
Ozaki, Y., Ishibashi, M., Onoe, H. and Iwatsuki, T.	Hydro-Mechanical-Chemical (HMC) simulation of Groundwater REcovery Experiment in Tunnel (GREET).	ARMS10 – Conference Paper (2018)	Published
Y. Ozaki, T. Iwatsuki and H. Onoe	Mock-up tunnel closure test and the hydro-chemical coupling simulation of environmental condition as a basis of solute transport analysis	Migration2019 – Conference Paper (2019)	Published
Y. Ozaki, H. Matsui, A. Kohashi, H. Onoe	Hydro-Mechanical (HM) response during compression and decompression of hydraulic pressure	YSRM2019 – Conference Paper (2019)	Published
H. Onoe et al.	Characterization of hydrogeological heterogeneity using Discrete Fracture model	Journal of Hydrology or Int. J. Rock Mech. Min. Sci. (TI DECOVALEX)	In review
Y. Ozaki et al.	Development of reactive-transport simulation method for environmental recovery after the drift closure	Journal of Hydrology or Int. J. Rock Mech. Min. Sci. (TI DECOVALEX)	In review

Hadgu, T. et al.	Evaluation of the hydrology of a fractured crystalline rock using in-situ experimental data.	Journal of Hydrology	In review
Hokr, M., Balvin, A.	Inverse hydraulic and transport model of groundwater recovery experiment using mixed-dimensional concept	Int. J. Rock Mech. Min. Sci. (TI DECOVALEX)	In review
Zeman J. et al	Geochemical groundwater background field and its disturbations during the construction of a large-scale underground facility at the Mizunami underground research laboratory (MIU)	Applied Geochemistry	In review

18 Acknowledgements

DECOVALEX is an international research project comprising participants from industry, government and academia, focusing on development of understanding, models and codes in complex coupled problems in sub-surface geological and engineering applications; DECOVALEX-2019 is the current phase of the project. The authors appreciate and thank the DECOVALEX-2019 Funding Organisations Andra, BGR/UFZ, CNSC, US DOE, ENSI, JAEA, IRSN, KAERI, NWMO, RWM, SÚRAO, SSM and Taipower for their financial and technical support of the work described in this report. The statements made in the report are, however, solely those of the authors and do not necessarily reflect those of the Funding Organisations.

Sandia National Laboratories is a multi-mission laboratory managed and operated by National Technology and Engineering Solutions of Sandia LLC, a wholly owned subsidiary of Honeywell International Inc., for the U.S. Department of Energy's National Nuclear Security Administration under contract DE-NA0003525. SAND2019-8670 R.

19 References

Adler, M., Mäder, U. and Waber, H. N. 1999. High pH alteration of argillaceous rocks: an experimental study, Scheiz. Mineral. Petrogr. Mitt., Vol. 79, pp. 445-454.

Ando, K., Tanaka, T., Hashimoto, S., Saegusa, H., Onoe, H. 2012. Study for establishment of the methodology for hydrogeological modeling using hydraulic discrete fracture networks (study on hydrogeology in crystalline fractured rock), JAEA-Research 2012-022, 60 p.

Atkins, M., Glasser, F. P., Kindness, A. 1992. Cement hydrate phase: solubility at 25°C, Cement Concrete Research, Vol. 22, pp. 241-246.

Baecher, G. B., Lanney, N. A., Einstein, H. H. 1977. Statistical description of rock properties and sampling, Proceedings, 18th US Symposium on Rock Mechanics, 1-8 (5C1).

Bethke, C. M., Yeakel S. 2018. The Geochemist's Workbench®, Release 11. GWB Essentials Guide. Aqueous Solutions, LLC, Champaign, Illinois. 190 p.

Birkholzer, J., Faybishenko, B., Zheng, L., Rutqvist, J., Dobson, P., Fox, P.M., Reimus, P., Viswanathan, H., Jove-Colon, C.F., Wang, Y., Kuhlman, K., McMahon, K. and Zavarin, M. 2017. International Collaboration Activities in Different Geologic Disposal Environments (SFWD-SFWST-2017-000013), Prepared for US Department of Energy, Spent Fuel and Waste Disposition Campaign (SFWD-SFWST-2017-000013). (National Laboratory Report No. LBNL-2001063), Berkeley, California, pp. 236 pp.

Blanc, P., Lassin, A., Piantone, P., Azaroual, M., Jacquemet, N., Fabbri, A. and Gaucher, A. 2012. Thermoddem: A geochemical database focused on low temperature water/rock interactions and waste materials. Applied Geochemistry, 27: 2107-2116.

Blanc, P., Piantone, P., Lassin, A. and Burnol, A. 2006. Thermochimie : Sélection de constantes thermodynamiques pour les éléments majeurs, le plomb et le cadmium, Rapport final BRGM/RP-54902-FR. BRGM, France, pp. 157.

Brezina J., Hokr, M. 2011. Mixed-hybrid formulation of multidimensional fracture flow, In: Numerical methods and applications (Lecture notes in computer science), 6046, pp. 125-132.

Bruines, P., Tanaka, T., Abumi, K., Hashimoto, S., Saegusa, H., Onoe, H., Ishibashi, M. 2014. Development and Application of the GeoDFN and HydroDFN at the Mizunami

Underground Research Laboratory, 8th Asian Rock Mechanics Symposium, October 14-16, Sapporo, Japan.

Butscher, C. 2012. Steady-State Groundwater Inflow into a Circular Tunnel, Tunnelling and Underground Space Technology, 32, pp. 158-167.

Dixon, D.A., Martino, J.B., Onagi, D.P. 2009. Enhanced Sealing Project (ESP): Design, Construction and Instrumentation Plan, APM-REP-01601-0001, Atomic Energy of Canada Limited.

Follin, S., Levén, J., Hartley, L., Jackson, P., Joyce, S., Roberts, D., Swift, B. 2007. Hydrogeological characterization and modelling of deformation zones and fracture domains, Forsmark modeling stage 2.2., SKB R-07-48.

Geuzaine, C. and Remacle J.-F. 2009. GMSH: a three-dimensional finite element mesh generator with built-in pre- and post-processing facilities. International Journal for Numerical Methods in Engineering 79(11), pp. 1309-1331.

Golden Software, 2018. https://www.goldensoftware.com/products/voxler.

Golder Associates, Inc. 2017. Interactive Discrete Feature Data Analysis, Geometric Modeling and Exploration Simulation, FracMan® Manual, April 6.

Hammond, G. E., Lichtner, P. C., and Mills, R. T. 2014. Evaluating the Performance of Parallel Subsurface Simulators: An Illustrative Example with PFLOTRAN, Water Resources Research, 50 (1), pp. 208-228.

Hodgkinson, E. S. and Hughes, C. R. 1999. The mineralogy and geochemistry of cement/rock reactions: high-resolution studies of experimental and analogue materials. In: Chemical Containment of Waste in the Geosphere, Metcalfe, R. and Rochelle, C. A. eds., The Geological Society, London, pp. 195-211.

Hong, S. Y. and Glasser, F. P. 1999. Alkali binding in cement pastes Part I. The C-S-H phase, Cement and Concrete Research, Vol. 29, pp.1893-1903.

Ishibashi, M., Sasao, E. 2015. Data on Fractures in the Toki Granite Based on the Deep Borehole Investigations. JAEA-Data/Code 2015-004, 8 p.

Ishibashi, M., Yoshida, H., Sasao, E., Yuguchi, T., 2016. Long term behavior of hydrogeological structures associated with faulting: an example from the deep crystalline rock in the Mizunami URL, Central Japan, Engineering Geology, 208, pp.114-127.

Iwatsuki, T., Furue, R., Mie, H., Ioka, S., Mizuno, T. 2005. Hydrochemical baseline condition of groundwater at the Mizunami underground research laboratory (MIU). Applied Geochemistry, 20, pp. 2283-2302.

Iwatsuki, T., Hagiwara, H., Ohmori, K., Munemoto, T., Onoe, H. 2015. Hydrochemical disturbances measured in groundwater during the construction and operation of a large-scale underground facility in deep crystalline rock in Japan. Environmental Earth Sciences, 74, pp. 3041-3057.

Iwatsuki, T. Munemoto, T., Kubota, M., Hayashida, K. and Kato, T. 2017. Characterization of rare earth elements (REEs) associated with suspended particles in deep granitic groundwater and their post-closure behavior from a simulated underground facility, Applied Geochemistry, Vol. 82, pp.134-145.

Jové Colón, C.F., J.A. Greathouse, S. Teich-McGoldrick, R.T. Cygan, T. Hadgu, J.E. Bean, M.J. Martinez, P.L. Hopkins, J.G. Argüello, F.D. Hansen, F.A. Caporuscio, M. Cheshire. 2012. Evaluation of Generic EBS Design Concepts and Process Models: Implications to EBS Design Optimization (FCRD-USED-2012-000140), U.S. Department of Energy, p.250.

Jové Colón, C.F., P.F. Weck, D.C. Sassani, L. Zheng, J. Rutqvist, C.I. Steefel, K. Kim, S. Nakagawa, J. Houseworth, J. Birkholzer, F.A. Caporuscio, M. Cheshire, M.S. Rearick, M.K. McCarney, M. Zavarin, A. Benedicto-Cordoba, A.B. Kersting, M. Sutton, J.L. Jerden, K.E. Frey, J.M. 2014. Copple, and W.L. Ebert., Evaluation of Used Fuel Disposition in Clay-Bearing Rock (FCRD-UFD-2014-000056), Sandia National Laboratories, SAND2014-18303 R: Albuquerque, NM, p. 434.

Jové Colón, C.F., Hammond, G.E., Kuhlman, K., Zheng, L., Kim, K., Xu, H., Rutqvist, J., Caporuscio, F.A., Norskog, K.E., Maner, J., Palaich, S., Cheshire, M., Zavarin, M., Wolery, T.J., Atkins-Duffin, C., Jerden, J.L., Copple, J.M., Cruse, T. and Ebert, W.L., 2016. Evaluation of Used Fuel Disposition in Clay-Bearing Rock (FCRD-UFD-2016-000074), Sandia National Laboratories, Albuquerque, NM. SAND2016-10311 R.

Jové Colón, C.F., C. Payne, A. Knight, T.A. Ho, J. Rutqvist, K. Kim, H. Xu, Y. Guglielmi, J. Birkholzer, F.A. Caporuscio, K.B. Sauer, M.J. Rock, L.M. Houser, J.L. Jerden, V.K. Gattu, and W.L. Ebert, 2018. Evaluation of Used Fuel Disposition in Clay-Bearing Rock in Spent Fuel Waste Science and Technology (SFWST) Deliverable M2SF-18SN010301051 (SAND2018-12044 R), Sandia National Laboratories: Albuquerque, NM USA. p. 396.

Klint, K. E. S., Gravesen, P., Rosenbom, A., Laroche, C., Trenty, L., Lethiez, P., Sanchez, F., Molinelli, L., Tsakiroglou, C. D. 2004. Multi-Scale Characterization of Fractured Rocks Used as a Means for the Realistic Simulation of Pollutant Migration Pathways in Contaminated Sites: A Case Study, Water, Air, and Soil Pollution: Focus 4: pp. 201-214.

Kobayashi, A. and Ohnishi, Y. 1986. Effects of non-linearity of material properties on the coupled mechanical-hydraulic-thermal behavior in rock mass. In: Collected Papers of Japan Society of Civil Engineers, Tokyo, Japan Society of Civil Engineers, pp. 101-110, (in Japanese).

Koyama, T., Chijimatsu, M., Shimizu, H., Nakama, S., Fujita T., Kobayashi, A., Ohnishi, Y. 2013. Numerical modeling for the coupled thermo-mechanical processes and spalling phenomena in Äspö Pillar Stability Experiment (APSE), Journal of Rock Mechanics and Geotechnical Engineering, 5 (1), pp. 58-72.

La Pointe, R.P. 2002. Derivation of parent fracture population statistics from trace length measurements of fractal fracture populations, International Journal of Rock Mechanics & Mining Sciences, 39 (3), pp. 381-388.

Lichtner, P. C., Hammond, G. E., Lu, C., Karra, S., Bisht, G., Andre, B., Mills, R. T., Kumar, J., 2013, PFLOTRAN User Manual: http://www.pflotran.org.

Lichtner, P.C., 2016. Kinetic rate laws invariant to scaling the mineral formula unit. American Journal of Science, 316(5): p. 437-469.

Long, J. C. S., Billaux, D., Hestir, K., Majer, E.L., Peterson, J. 1989. Characterization of fracture networks for fluid flow analysis, Lawrence Berkeley Lab., LBL-26868.

Mizuno, T. Aosai, D., Shingu, S., Hagiwara, H., Yamamoto, Y., Fukuda, A., 2013. Hydrochemical changes associated with construction of Mizunami Underground Research Laboratory, Transactions of the Atomic Energy Society of Japan, 12, pp. 89-102.

Nishigaki, M., Hishiya, T., Hashimoto, N. 2001. Density dependent groundwater flow with mass transport in saturated-unsaturated porous media, Proceedings of the First Asian-Pacific Congress on Computational Mechanics, pp. 1375-1380.

Oda, M. 1985. Permeability tensor for discontinuous rock masses, Geotechnique, 35(4), pp. 483-495.

Ohnishi, Y., Shibata, H., Kobayashi, A. 1987. Development of finite element code for the analysis of coupled thermo-hydro-mechanical behaviors of a saturated-unsaturated medium. In: Tsang CF, editor. Coupled Processes Associated with Nuclear Waste Repositories, Orlando, Academic Press, p. 551.

Onoe, H., Iwatsuki, T., Saegusa, H., Ohnuki, K., Takeuchi, R., Sanada, H., Ishibashi, M., Sato, T. 2014. Groundwater recovery experiment using an underground gallery in fractured crystalline rock, Proc. 8th Asian Rock Mechanics Symposium. Int. Soc. Rock Mech., Lisbon, Portugal, ISBN 978-4-907430-03-0.

Poeter, E.P., Hill, M.C. 1998. Documentation of UCODE, A Computer Code for Universal Inverse Modeling, USGS, 122 p.

Rochelle, C. A., Bateman, K., Milodowski, A. E., Noy, D. J., Pearce J. and Savage, D. 1992. Reaction of cement pore fluids with rock: Implications for the migration of radionuclides, Water-Rock Interaction, Khara and Maest Eds., Balkema, Rotterdam, pp. 423-426.

Saegusa H. and Matsuoka T. 2011. Final report on the surface-based investigation (phase I) at the Mizunami Underground Research Laboratory Project, JAEA-Research 2010-067, 377p.

SALOME, 2018. The Open Source Integration Platform for Numerical Simulation: http://www.salome-platform.org

Savage, D., Bateman, K., Hill, P., Hughes, C., Milodowski, A., Pearce, J., Rae, E. and Rochelle, C. A. 1992. Rate and mechanism of the reaction of silicates with cement pore fluids, Applied Clay Science, Vol. 7, pp. 33-45.

Savage, D., Hughes, C., Milodowski, A. E., Bateman, K., Pearce, J. M., Rae, E. and Rochelle, C. A. 1998 a. The evaluation of chemical mass transfer in the disturbed zone of a deep geological disposal facility for radioactive wastes. I. Reaction of silicates with calcium hydroxide fluids, Safety Studies Nirex Radioactive Waste Disposal, NSS/R244.

Savage, D., Bateman, K., Hill, P., Milodowski, A., Pearce, J., Rae, E. and Rochelle, C. A. 1998 b. The evaluation of chemical mass transfer in the disturbed zone of a deep geological disposal facility for radioactive wastes. II; Reaction of silicates with Na-K-Ca hydroxide fluids, Safety Studies Nirex Radioactive Waste Disposal, NSS/R283.

Sawada A. and Sakamoto K. 2016. An influence of the conceptualization between host rock and buffer on nuclide migration in host rock, JAEA-Research 2015-020, 21p.

Shibata, K., Ishihara, S. 1979. Rb - Sr whole-rock and K-Ar mineral ages of granitic rocks of the Komagane district, Nagano Prefecture, Central Japan. Geochemical Journal, 13, pp. 133-119.

Shikazono, N., Nakata, M. 1999. Compositional variation of pyrite, diagenetic alteration and genesis of Tono sandstone-type uranium deposits in Japan. Research Geology Special Issue. 20, pp. 55-64.

Shimono M, Suzuki S, Taguchi Y, Kamemura K, Sato T, Mikake S. 2004. Risk assessment approach for underground research laboratory. Proc. ISRM International Symposium: 3rd Asian Rock Mechanics Symposium, pp. 359-365.

Snow, D. 1969. Anisotropic Permeability of Fractured Media, Water Resources Research, 5 (6), pp. 1273-1289.

TUL 2017. Flow123d version 2.1.0, Documentation of file formats and brief user manual, NTI TUL, Online: http://flow123d.github.io/.

Vaněk, P., Mandel, J., Brezina, M. 1996. Algebraic multigrid by smoothed aggregation for second and fourth order elliptic problems, Computing, 56 (3), pp. 179-196.

Wang, X. 2005. Stereological interpretation of rock fracture traces on borehole wall and other cylindrical surfaces, Ph. D. dissertation, Virginia Polytechnic Institute and State University.

Wang, Y., T. Hadgu, E. Matteo, J.N. Kruichak, M.M. Mills, J.L. Jerden, J.M. Copple, T. Cruse, W.L. Ebert, R. Tinnacher, J.A. Davis, H. Visnawathan, S. Chu, T. Dittrich, F. Hyman, S. Karra, P. Makedonska, P. Reimus, M. Zavarin, P. Zhao, C. Joseph, J. Begg, Z. Dai, and A.B. Kersting, 2015. Used Fuel Disposal in Crystalline Rocks: FY15 Progress Report (FCRD-UFD-2015-000125), Sandia National Laboratories: Albuquerque, NM. USA (SAND2015-10687 R).

Wang, Y., T. Hadgu, E. A. Kalinina, J. Jerden, J. M. Copple, T. Cruse, W. Ebert, E. Buck, R. Eittman, R. Tinnacher, C. Tournassat, J. Davis, H. Viswanathan, S. Chu, T. Dittrich, F. Hyman, S. Karra, N. Makedonska, P. Reimus, M. Zavarin, C. Joseph. 2016. Used Fuel Disposition in Crystalline Rocks: FY16 Progress Report, Fuel Cycle Research and Development, FCRD-UFD-2016-000076, SAND2016-9297 R. September 21.

Wang, Y., T. Hadgu, E. A. Kalinina, J. Jerden, V. K. Gattu, W. Ebert, H. Viswanathan, J. Hyman, S. Karra, N., Knapp, N. Makedonska, P. Reimus, K. Telfeyan, P. M. Fox, P. S. Nico, M. Zavarin, E. Balboni, and C. Atkins-Duffin. 2017. Evaluation of Spent Fuel Disposition in Crystalline Rocks: FY17 Progress Report, Spent Fuel and waste Disposition, SFWD-SFWST-2017-000007.

Whiteley, J., P., K. Gillow, S. J. Tavener and A. C. 2011. Walter, Error bounds on block Gauss-Seidel solutions of couple Multiphysics problems, International Journal of Numerical methods in Engineering, 88(12), pp. 1219-1237.

Yamasaki, S., Umeda, K. 2012. Cooling history of the Cretaceous Toki granite in the eastern Sanyo Belt, Central Japan. Japanese Magazine of Mineralogical and Petrological Sciences, 41: p. 39-46.

Yeckel, A., Lun, L., Derby, J. 2009. An approximate block Newton method for coupled iterations of nonlinear solvers: Theory and conjugate heat transfer applications, Journal of Computer Physics, 228 (23), pp. 8566-8588.

Zhang, H.H. Einstein, Dershowitz, W.S. 2002. Stereological relationship between trace length and size distribution of elliptical discontinuities, Geotechnique, 52 (6), pp. 419-433.

Appendix A: Datasets used in Task C

Following data were provided from JAEA and used by three teams in each Step.

A.1 Data set of Step 1

Basic information

- Coordinate of URL
- Coordinate of boreholes
- Hydrogeological model data
- Hydraulic parameters of each hydrogeological unit
- Groundwater sampling methods

Geology

- Result of borehole investigations (core logging, BTV observation) from surface
- Result of borehole investigations (core logging, BTV observation) during facility construction
- Mineralogy of fracture fillings and wall rock
- Fracture map of -500 Access gallery wall

Hydrogeology

- Results of hydraulic test
- Long-term hydraulic pressure monitoring data
- Electric conductivity logging data
- Flow rate of water ring in shafts

Chemistry

- Groundwater chemistry in facility scale
- pH-ORP data at 200-400m (-201609)

Rock mechanics

- Initial stress
- hydromechanical property (Result of core sample experiment at MIZ-1)

Pilot Borehole (12MI33) data

- Geology: core logging, BTV observation, etc.
- Hydrogeology: hydraulic packer test (T, K, Ss, Hydraulic pressure), Flow-meter logging
- Chemistry: groundwater chemistry
- Rock mechanics: initial stress, elastic property
- pH-ORP data (-2013)

A.2 Data set of Step 2

Outline of CTD

- Time records of GREET
- Excavation progress of shafts and drift
- Generic composition of OPC
- Preliminary observation of shotcrete
- Fracture map of CTD wall

Monitoring data of 12MI33

Hydrogeology

- Hydraulic pressure response during excavation of the CTD in 12MI33
- Inflow rate into drifts at -500 Access/Research Gallery-North

Chemistry

- Groundwater chemistry in 12MI33 after the drift excavation
- pH-ORP data in 12MI33(-201506)

Boreholes (13MI38 - 13MI48) in and around CTD

Geology & Mineralogy

- 3D shape data of CTD
- Geology of 13MI38-13MI44 including mineralogical data of fracture fillings

Hydrogeology

- Result of Flow-meter logging and hydraulic packer test (T, K, Ss, Hydraulic pressure)
- Hydraulic response during cross-hole pumping test in 13MI38
- Hydraulic pressure monitoring after CTD excavation (until 20150731)

Chemistry

- Groundwater chemistry in 12MI33-48 after the drift excavation
- Precise analysis of shotcrete

A.3 Data set of Step 3

Monitoring in CTD and boreholes (13MI33 - 13MI48)

Geology

- Geophysical exploration in and around CTD

Hydrogeology

- Hydraulic pressure monitoring data (Hydraulic response during re-saturation around the CTD)
- Measurement data of inflow rate into each drift at -500 Access/Research Gallery-North

Chemistry

- Chemical variation of groundwater during water-filling

Data set of Step 3+

- Chemical variation of groundwater in a series of experiments
- Groundwater chemistry at Main shaft
- Groundwater chemistry at Ventilation shaft

Appendix B: Geochemical diagrams

The figures here are additional outputs to those presented in Chapter 5 and Chapter 10 as evaluation of geochemical analyses.

B.1 Main shaft data

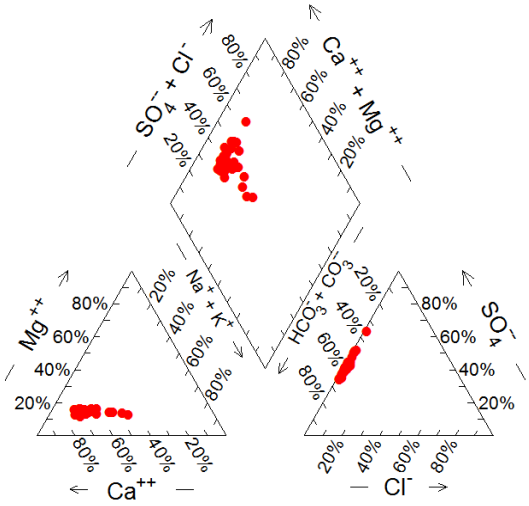

A-WR water collection ring 1 - 10,0 m

Alluvium

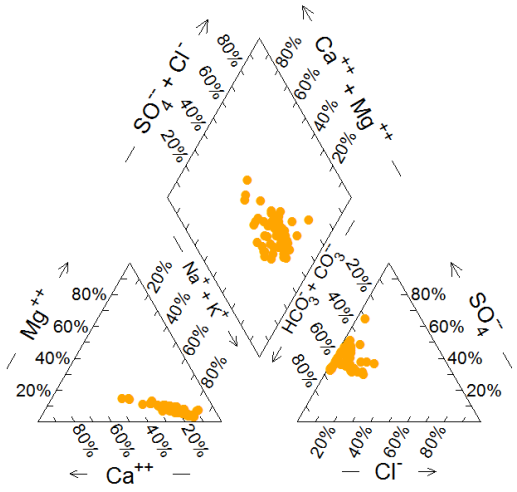

A-WR water collection ring 3 - 77,0 m

Conglomerate

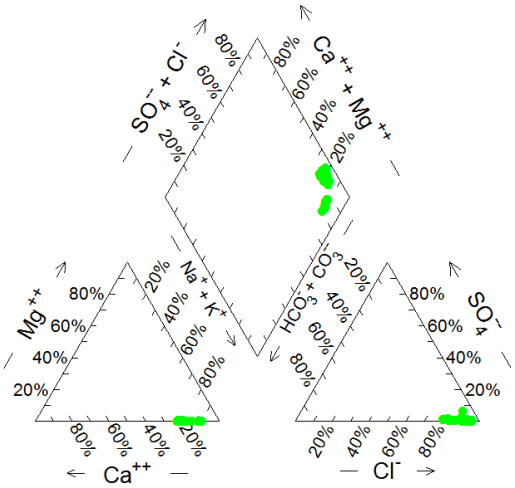

A-WR water collection ring 7 - 167,4 m

Basal conglomerate

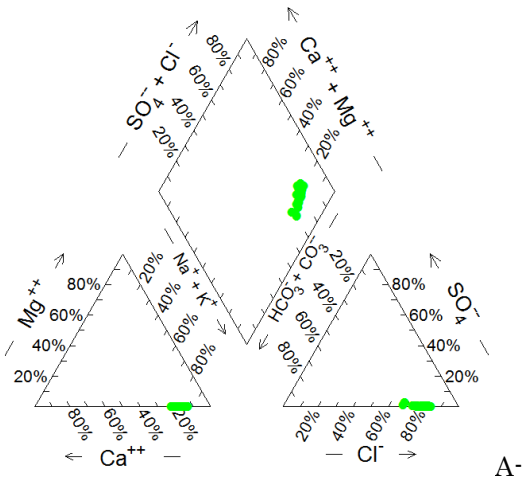

A-WR water collection ring 8 - 194,4 m

Toki granite (UHFD: Upper Highly Fractured Domain)

Figure 301. Relationships of groundwater composition to the rock type in A-WR depth zones (ring 1 to ring 18). (1/3)

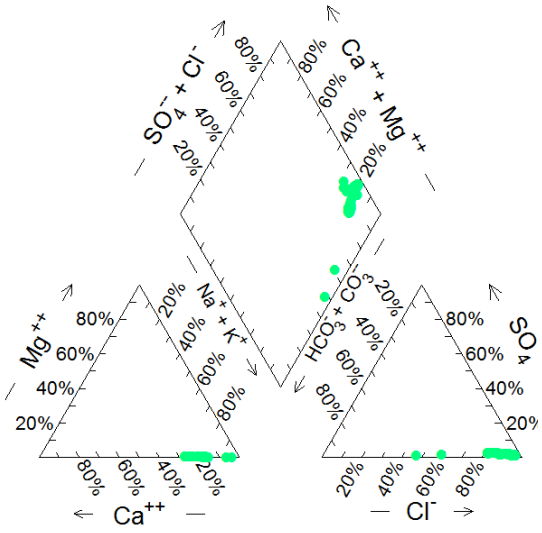

A-WR water collection ring 9 - 202,6 m

Toki granite (LAFZ: Low Angle Fractured Zone)

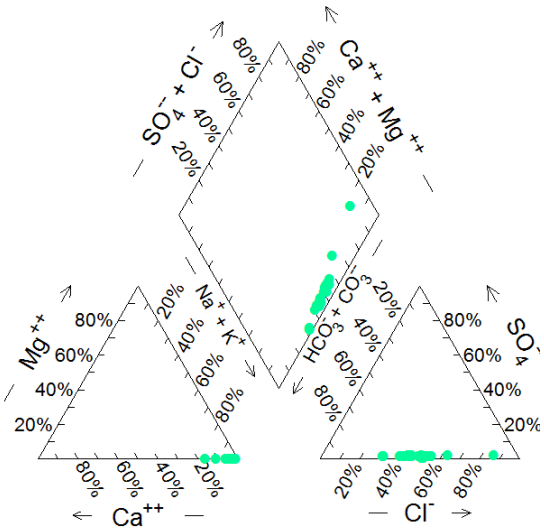

A-WR water collection ring 10 - 236,2 m

Toki granite (LAFZ)

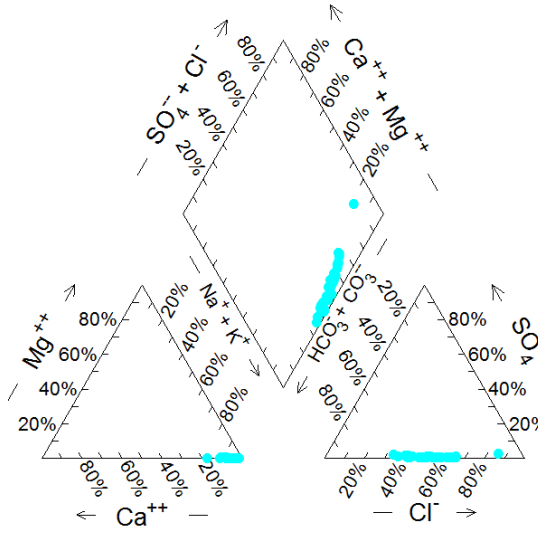

A-WR water collection ring 11 - 264,8 m

Toki granite (UHFD)

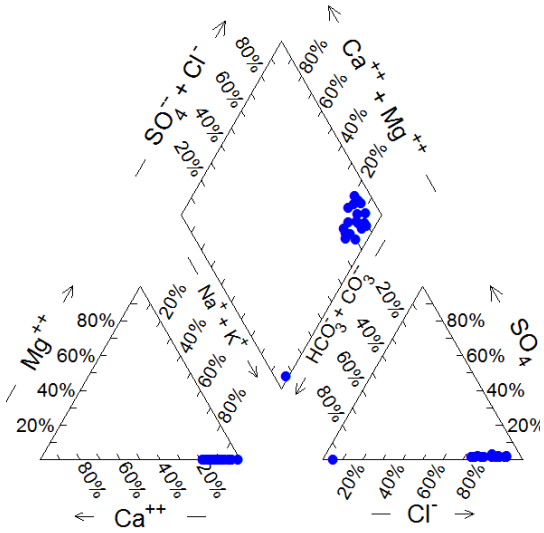

A-WR water collection ring 13 - 302,6 m

Toki granite (UHFD)

Figure 302. Relationships of groundwater composition to the rock type in A-WR depth zones (ring 1 to ring 18). (2/3)

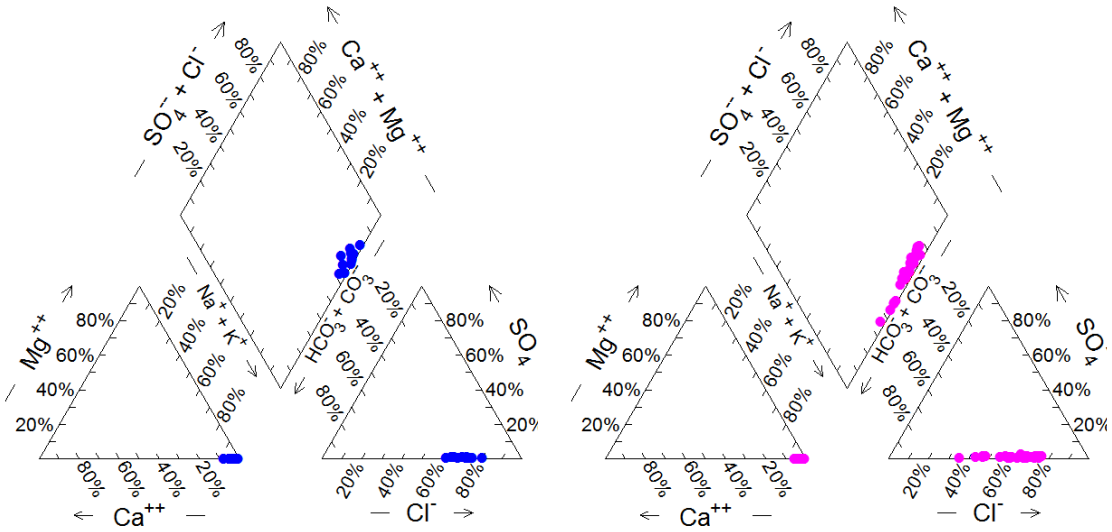

Figure 303. Relationships of groundwater composition to the rock type in A-WR depth zones (ring 1 to ring 18). (3/3)

B.2 CTD area data

Overall, the composition of groundwater is relatively stable, with the anions being almost exclusively Cl, the main cations being 30-40 eq. % calcium, 60-70 eq. % is alkali metal, Mg is almost absent (Figure 304). Since the start of sampling on January 25, 2016, the total mineralization of groundwater has been clearly decreasing over half a year from 840 to 740 mg/L (Figure 305). Since mid-2016, concentrations have been relatively stable. The positional points of the relationship between the TDS and the relative cation ratio in the Durov diagram create a compact group of data with little variance.

In the first half of the year, the pH values rose significantly to 9.8, and their growth continued to values oscillating around 10.0 (Figure 305). The oxidation-reduction potential in the first half of 2016 dropped steeply from nearly 300 mV to around –180 mV. The ratio of major anions and cations has changed very little during this development.

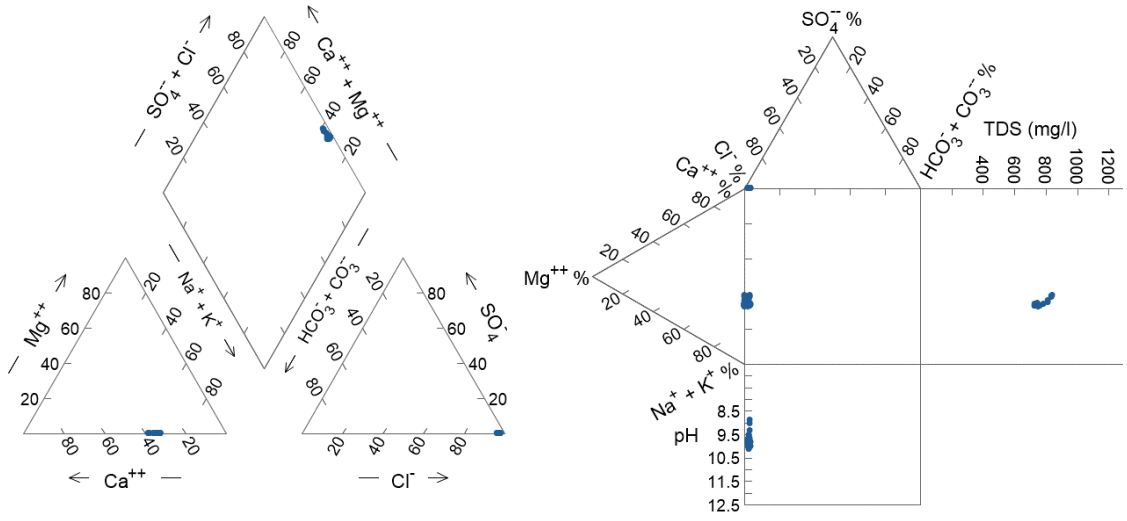

Figure 304. Piper (left) and Durov (right) diagram for groundwater composition sampled in CTD.

Borehole 12MI33

The horizontal borehole 12MI33 is located parallel to the CTD at approximately the same depth level, its length is 107.5 m and is monitored from March 8, 2013 ((the exact position of the borehole 12MI33 with respect to the CTD is shown in Figure 6)). For monitoring purposes, it is divided into 6 zones, their positions and dimensions are shown in Figure 306.

Overall, groundwater from individual zones is comparable to groundwater sampled in CTD, only the Cl are practically present in anions, the major cations are characterized by negligible concentrations of Mg ions, in comparison with groundwater from CTD, the range of calcium to alkali metals ratio has increased significantly, for calcium to 20-50 eq. %, for alkali metals 50-80 eq. % (Figure 307). The physico-chemical parameters and concentrations of the individual groundwater components have undergone a relatively complex and different development in the individual borehole zones, which indicates the inflow of water from different parts of rocks.

The initial concentrations of total dissolved solids in each zone are around 700 mg/L before the CTD build-up, and the Cl concentration is about 400 mg/L. During the construction of the CTD, the concentration of TDS in zone 5 rises to values of about 1,100 mg/L, while in zone 4 it decreases to values of approximately 400 mg/L (Figure 309). In the subsequent period of CTD filling they then fluctuate around these values. After opening and dewatering the CTD, concentrations in zones 4 and 5 slightly decrease and slightly increase in zones 1 and 2.

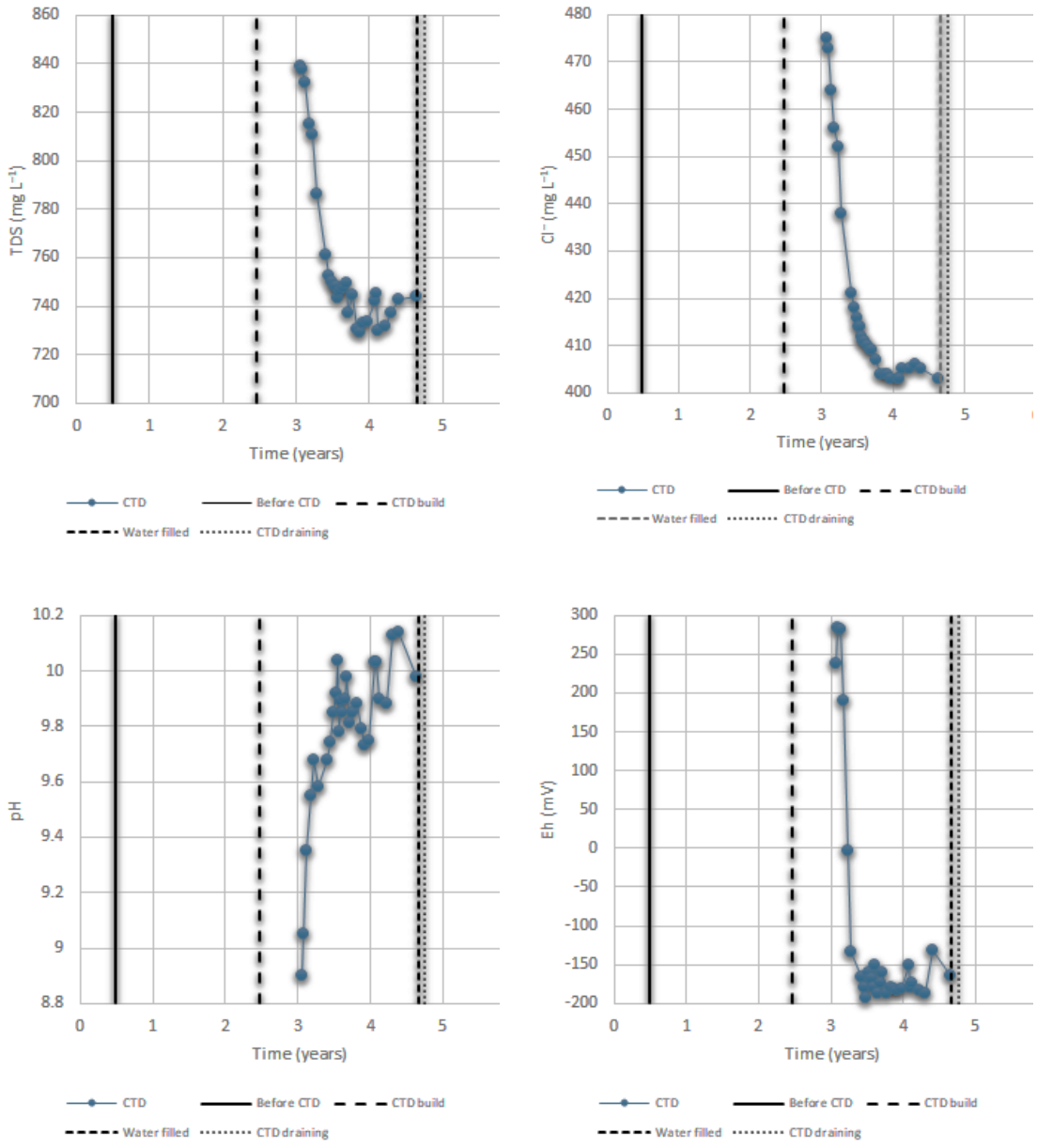

Figure 305. Time evolution of total dissolved solids, Cl, pH, and oxidation-reduction potential in the CTD. The vertical lines indicate the stages of building the CTD.

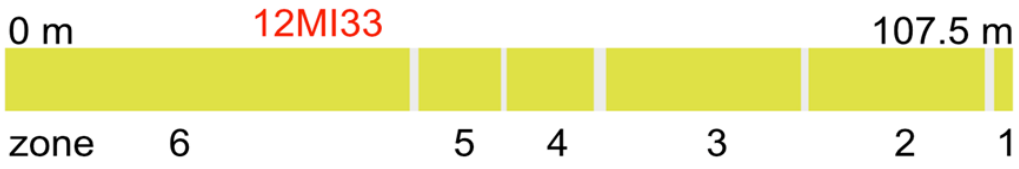

Figure 306. Position and dimensions of individual monitoring zones in borehole 12MI33.

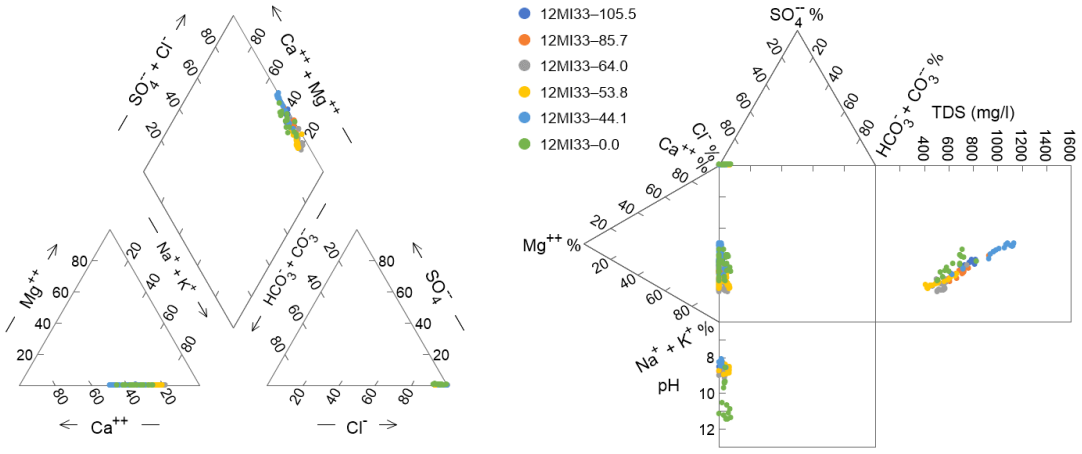

Figure 307. Piper (left) and Durov (right) diagrams for the composition of groundwater sampled in individual zones of the borehole 12MI33. The numbers in the legend indicate the beginning of the sampled zone.

Changes in the groundwater chemical composition of the 12MI33 borehole range between waters with a strong predominance of alkali metals (the lowest mineralized water) and groundwaters with roughly comparable levels of alkali metals and Ca ions. In all cases, they are saline waters with a negligible concentration of Mg ions. From this trend of changes in chemical composition it can be seen that the groundwater from zone 6 differs from the remainder, in which Ca ion concentrations are higher than the overall trend of change. At the same time, unlike groundwater from other borehole zones, these groundwaters are characterized by a significantly alkaline pH of up to 11.5 (Figure 309). The pH of groundwater in other zones ranges from 8 to 9.

Borehole 13MI38

Borehole 13MI38 is a horizontal borehole parallel to the CTD, located at approximately the same depth level, but on the opposite side of the CTD to borehole 12MI33 (the exact position of the borehole 13MI38 with respect to the CTD is shown in Figure 6). Its length is 102.1 m and is sampled from March 7, 2014. For monitoring purposes, it is divided into 6 zones, their positions and dimensions are evident from Figure 309.

The chemical composition of groundwater from individual zones of 13MI38 borehole is generally very similar to groundwater from individual zones of 12MI33 borehole. Again, they are saline waters with a minimum of other anions, the relative ratio of alkali metals to Ca ions is within the same range (Figure 309). Compared to groundwater of borehole 12MI33, higher maximum values of the total dissolved species concentration are reached, up to 1,400 mg/L, and the Cl concentration exceeding 800 mg/L. From the

continuous trend of correlation between total mineralization and relative cationic concentrations, some groundwaters from zones 2 and 4 deviated only slightly (Figure 309. Compared to borehole 12MI33, the time evolution of physico-chemical parameters and groundwater concentrations are much smoother.

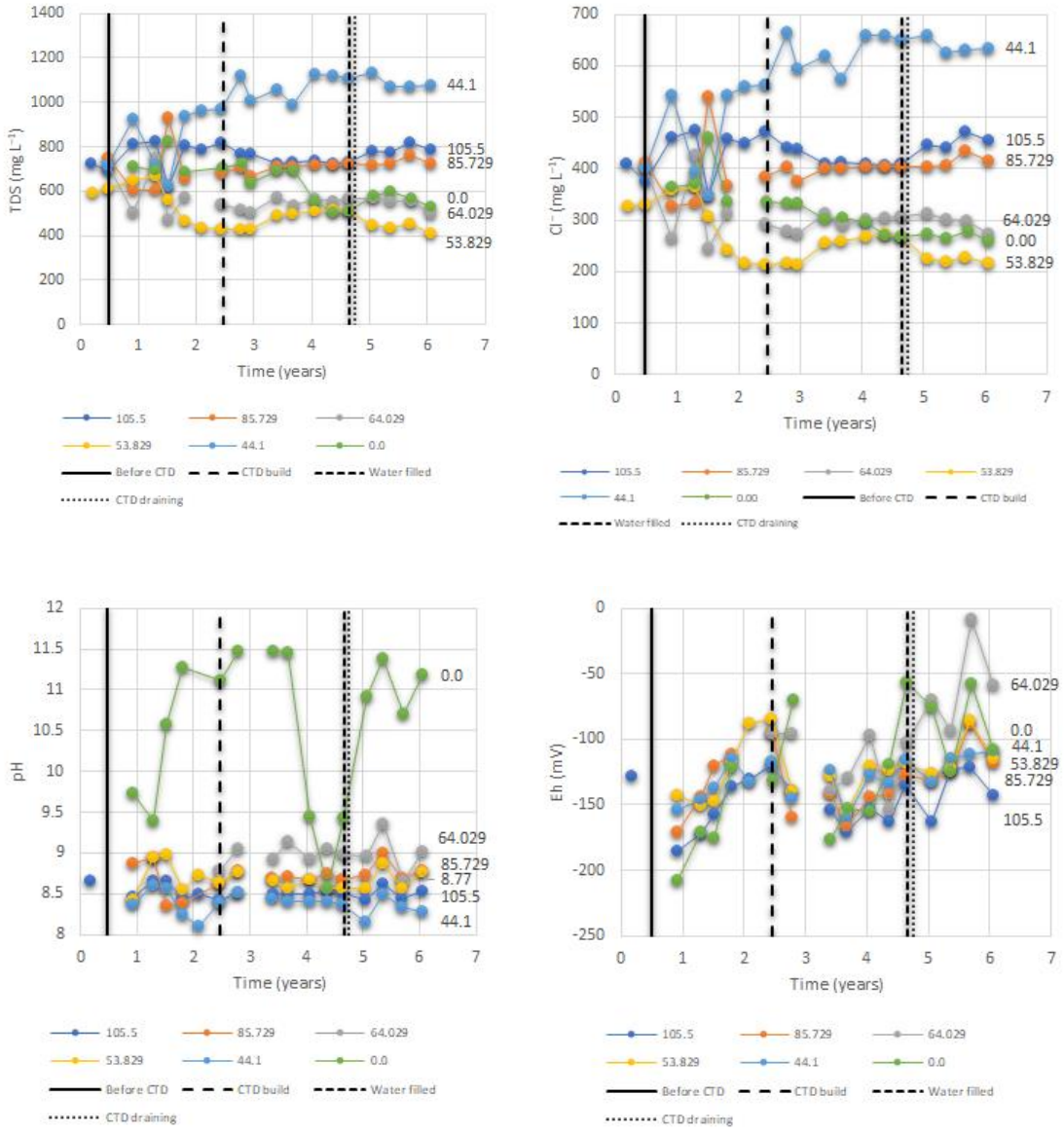

Figure 308. Time evolution of total dissolved solids concentration, Cl, pH, and oxidation-reduction potential in individual zones of borehole 12MI33. The vertical lines indicate the stages of building a CTD.

From the beginning of monitoring until the completion of CTD, there was a slight decrease in pH from about 8.6 to about 8.4 and a slight increase in oxidation-reduction potential (Figure 309). During the CTD filling with groundwater, the pH values were relatively stable, except for pH values in zone 3, which dropped randomly, exceptionally to 7.2. After dewatering of CTD, there was a distinct pH fluctuation and in zone 2 pH 9.0 was exceeded. Values of oxidation-reduction potential slightly decreased during watering, increased significantly after CTD drainage.

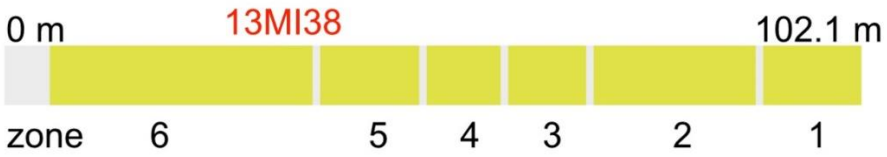

Figure 309. Position and dimensions of individual monitoring zones in borehole 13MI38.

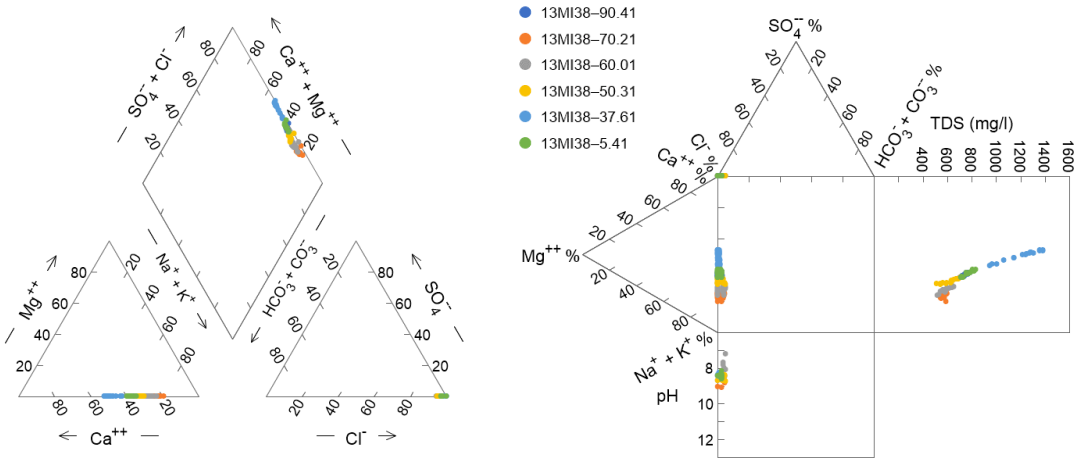

Figure 310. Piper (left) and Durov (right) diagrams for the composition of groundwater sampled in individual zones of borehole 13MI38. The numbers in the legend indicate the beginning of the sampled zone.

In terms of longitudinal development, the 13MI38 borehole zones can be divided into two groups. Zones 1–4 (50.3–102.1 m) form one group of continuous values and Zones 5–6 a second group (5.4–49.4 m). At the beginning of 2014, the total dissolved species concentrations in the borehole outer zones, i.e. zone 1 and zone 6, were around 700–750 mg/L. In a line of 1-4 zones concentrations decreased from 750 to 700 mg/L. In the

course of further development, the changes in individual zones differ significantly. Concentrations remained stable in the outer zones. In Zone 5, adjacent to the CTD plug from the outside, concentrations rose significantly until the beginning of 2016, followed by growth until the beginning of 2019 at a slower pace.

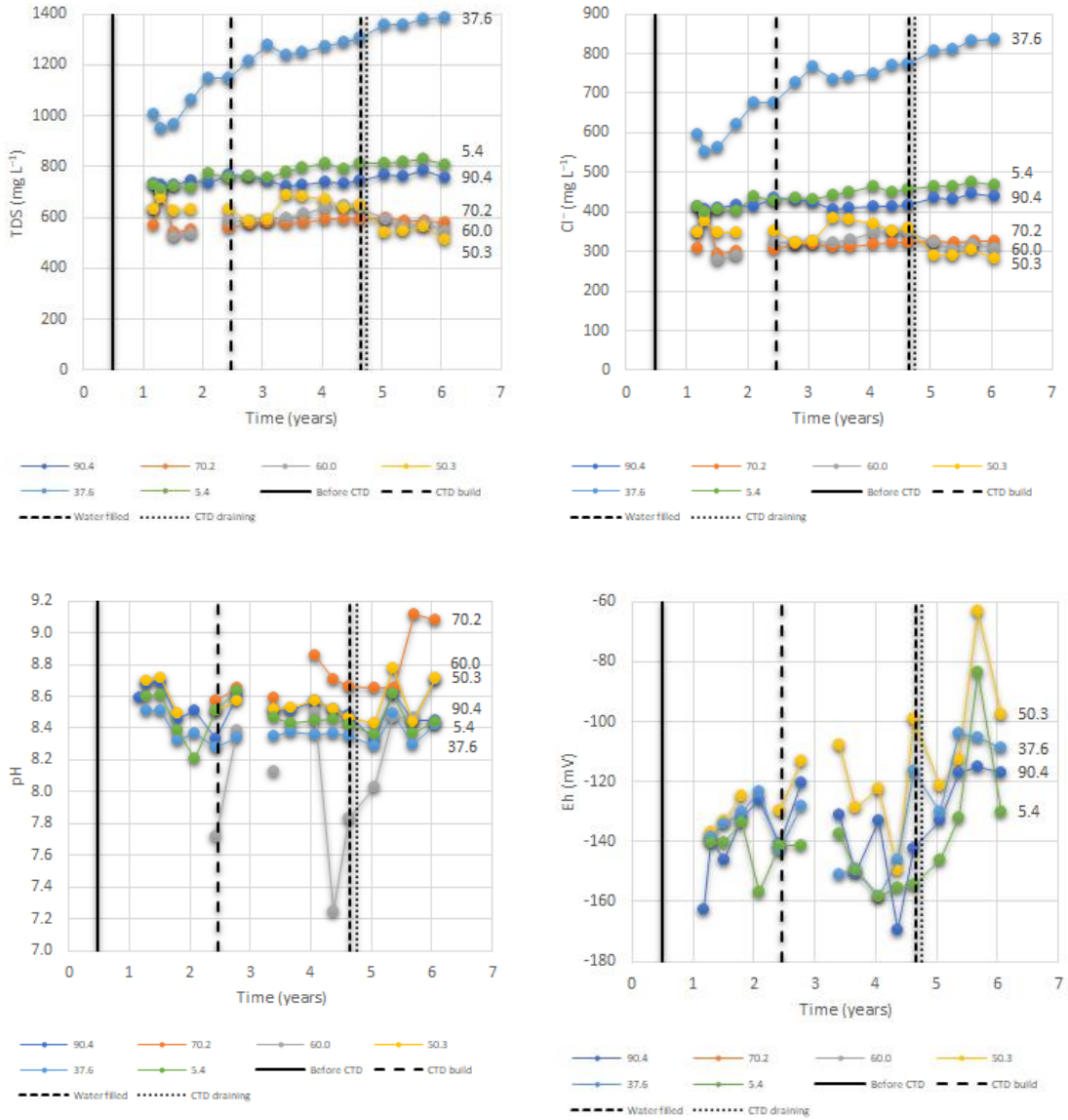

Figure 311. Time evolution of total dissolved species, Cl, pH and oxidation-reduction potentials in individual zones of 13MI38 borehole. The vertical lines indicate the stages of building a CTD.

The total dissolved species concentrations initially varied between 700–750 mg/L in individual zones of 13MI38 borehole, decreasing between zones 1–4 in this interval. The

exception was zone 5, where the concentration reached 1,000 mg/L at the beginning of sampling. In another, there was a significant increase in concentrations in zone 5 to nearly 1,400 mg/L, concentrations in zones 1–4 created a “bathtub” from the second half of 2014, which was modified by the increase in concentration in the zone 4 since mid-2016. After opening and draining the CTD, the concentrations in the individual zones remained relatively stable except for zone 4, in which concentrations decreased significantly. This behavior also applies to Cl concentrations.

Borehole 13MI39

Borehole 13MI39 is a vertical borehole from the floor of CTD in depth at position of zone 2 of boreholes 13MI40 and 13MI41. It has a total length of 16.2 m, the start of groundwater monitoring was on March 5, 2014. For monitoring purposes, it was divided into 4 zones whose position is listed on Figure 312.

Again, these are high-Cl groundwaters with very low concentrations of bicarbonate and without sulphates (Figure 313). In the composition of the main cations, the ratio between alkali metals and Ca ions varies similarly to the groundwater of boreholes 12MI33 and 13MI38, however, the proportion of Ca ions reaches up to 60 eq. % and corresponds to groundwaters with the highest mineralization. They are practically free of Mg ions. From the trend of correlation between total dissolved species concentrations and the relative proportions of the major cations, groundwaters from zone 4 and some samples from zone 2 lie off the trend.

Initially, the total dissolved species concentration ranged from 720 to 940 mg/L, with the concentration systematically increasing from zone 1 to zone 4 i.e. toward CTD (lowest in the deepest zone), see Figure 314. At the second sample campaign, one month after the start, total concentrations of dissolved species in each zone decreased significantly by up to 200 mg/L. From mid-2014 to mid-2016 concentrations in zones 2 and 4 grew, in zones 1 and 3 they were relatively stable. Since mid-2016, concentrations have been relatively stable. After the opening and dewatering of the CTD, the concentrations of total dissolved species in zones 1 and 4 decreased, while in zones 2 and 3 they increased.

Boreholes 13MI40-13MI41

The 13MI40 and 13MI41 horizontal boreholes are located at the depth of CTD and oriented perpendicular to CTD. Their position corresponds to zone 2 of boreholes 12MI33 and 13MI38. They are 13.3 meters long and each is divided into 4 zones (Figure 315). Their evaluation was performed simultaneously to see the profile perpendicular to the CTD. For evaluation purposes, the zones position of 13MI41 borehole was taken with a negative sign. Groundwater monitoring in boreholes started on March 4, 2014.

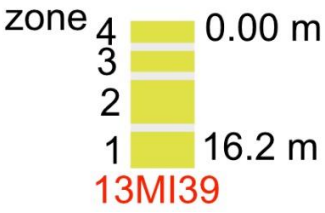

Figure 312. Position and dimensions of individual monitoring zones in borehole 13MI39.

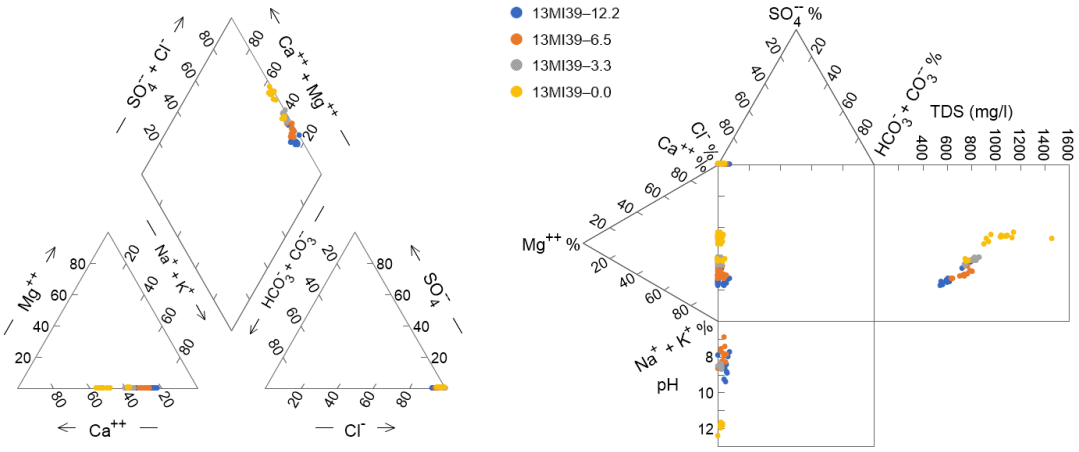

Figure 313. Piper (left) and Durov (right) diagrams for groundwater composition sampled in individual zones of 13MI39 borehole. The numbers in the legend indicate the beginning of the sampled zone.

The physico-chemical parameters and chemical composition of groundwater from individual zones of both boreholes are very similar to groundwater from previous boreholes 12MI33, 13MI38, and 13MI39. Again, these are groundwater with concentrations of bicarbonates (up to 10 eq. %), and without sulphates. Alkali metals and Ca ions ratio varies in wide range (20-60 eq. % of Ca^{2+}), groundwaters are almost free of Mg. In relation to the total dissolved species concentration and the cation ratio in the Durov diagram (Figure 316), most of the samples lie on the same line, except for samples from zones 4 of both boreholes, i.e., the zones adjacent to the CTD. These two zones also differ significantly in pH values. Most pH values in the zones of both boreholes range from 7.5 to 9.5, and at zones 4 of both boreholes it reaches a strongly alkaline environment up to a pH of around 12.

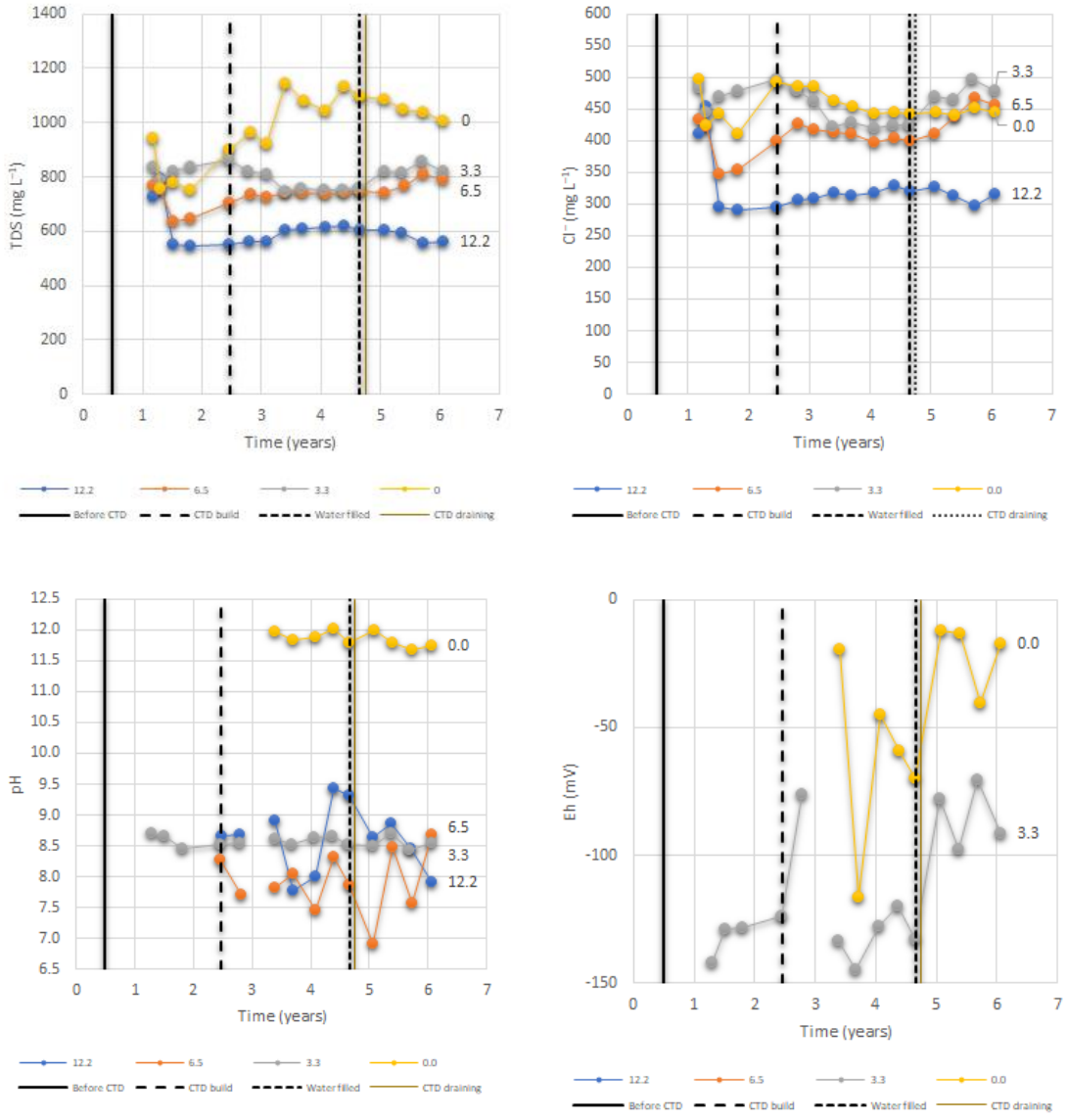

Figure 314. Time evolution of total dissolved species, Cl, pH and oxidation-reduction potentials in individual zones of 13MI39 borehole. The vertical lines indicate the stages of building a CTD.

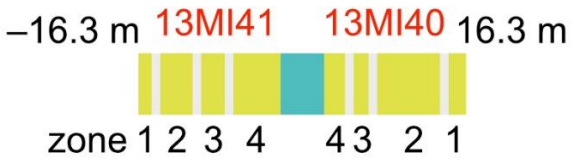

Figure 315. Position and dimensions of individual monitoring zones in boreholes 13MI40 and 13MI41. The green zone indicates the CTD position.

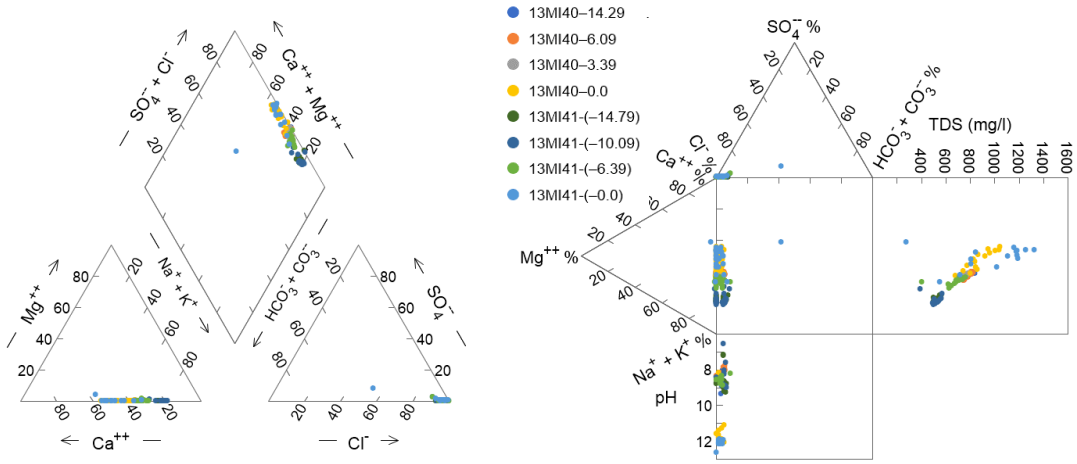

Figure 316. Piper (left) and Durov (right) diagram for groundwater composition sampled in individual zones of boreholes 13MI40 and 13MI41. The numbers in the legend indicate the beginning of the sampled zone, for the 13MI41 borehole with negative signs.

Time evolution of the groundwater of both boreholes is somewhat different (Figure 317). In borehole 13MI40, the initial total dissolved species concentration is around 800 mg/L and does not change much except for zone 4 until the beginning of 2019. In Zone 4, on May 25, 2016, the mineralization increased by 300 mg/L and then gradually decreased, but at the beginning of 2019 it was still about 100 mg/L higher than in the other zones.

In the longitudinal profile of the boreholes 13MI40 and 13MI41, which cross the CTD, there is a significant concentration gradient of the total dissolved species and Cl. Low concentrations are in zone 1 and 2 of borehole 13MI41, high in zones 1-3 of borehole 13MI40. These concentrations remain relatively constant after the initial development in the next period (TDS ~500 and ~800 mg/L). The total concentrations of dissolved species in the zones are significantly increased, in zone 4 of borehole 13MI40 is

concentration about 900 mg/L achieved, in zone 4 of borehole 13MI41 up to 1,300 mg/L (Figure 317). A similar development can be observed in the time evolution of Cl concentration. In gradual development, zones 1–4 of 13MI40 borehole and zones 3–4 of 13MI41 borehole have a Cl concentration about 430 mg/L, in zones 1–2 of borehole 13MI41 about 275 mg/L. There is significant difference between the development of total dissolved species and the Cl concentration. Concentration of Cl in zones 4 of both boreholes does not increase during monitoring unlike concentrations of total dissolved species.

Figure 317. Time evolution of total dissolved species, Cl, pH and oxidation-reduction potential values in individual zones of boreholes 13MI40 and 13MI41. The vertical lines indicate the stages of building a CTD.

Boreholes 13MI45-13MI48

These are four 1.5 m vertical bores made at the end of the CTD. Their monitoring began on 18 November 2014. These are high-Cl groundwaters with a relatively constant proportion of alkali metals and Ca ions (35-40 eq. % of Ca^{2+}) – Figure 318. The total dissolved species concentration is around 800 mg/L. During CTD watering, there was a slight decrease in concentrations. Conversely, after the opening and dewatering of the CTD, the dissolved species concentrations increased until the second half of 2018 (Figure 319). Trends in changes in Cl concentration follow the trends of changes in total dissolved species concentration. Differences between individual boreholes are insignificant.

However, there are significant differences in pH values and significant differences in time changes. Overall, the pH values vary in a wide range from 6.8 to 10.3.

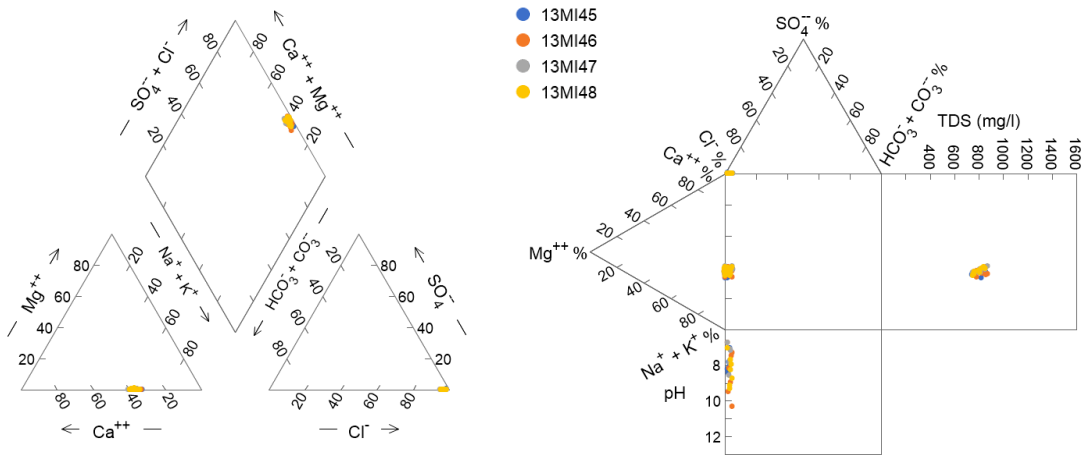

Figure 318. Piper (left) and Durov (right) diagrams for the composition of groundwater sampled in boreholes 13MI45–13MI48.

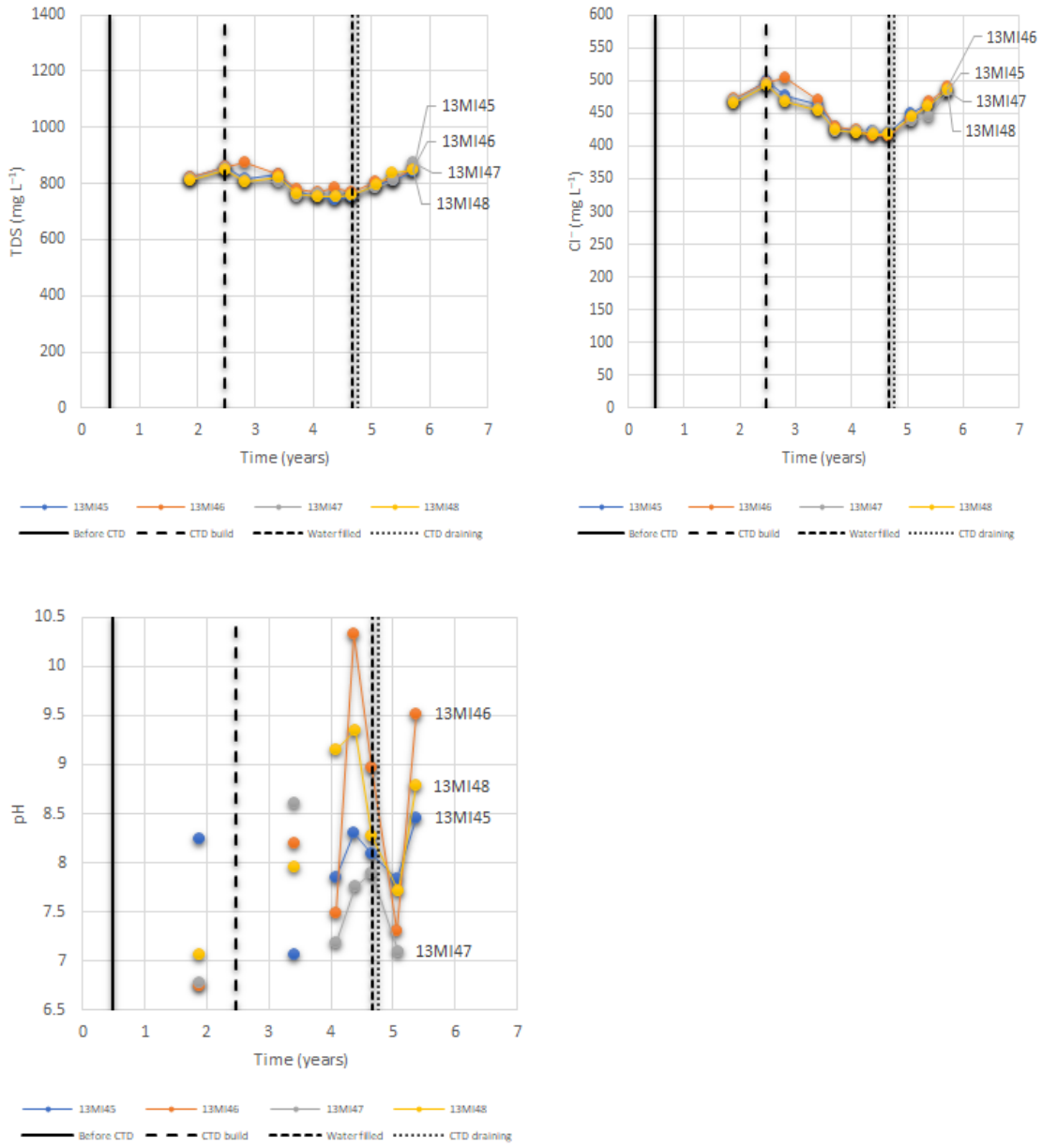

Figure 319. Time evolution of total dissolved species, Cl and pH values in boreholes 13MI45-13MI48. The vertical lines indicate the stages of building a CTD.

Overall characterization of groundwater around the CTD

The assessment of the physico-chemical parameters and chemical composition of groundwater in the CTD area shows that groundwater parameters form a continuous series in development. These are groundwaters with low concentrations of bicarbonate (up to 10 eq. %) and without sulphates. Alkali metals (Na^+, K^+) replaced with calcium ions in the range of 20-60 eq. % Ca^{2+}.

In relation to the total dissolved species concentration and the relative ratio of the major cations, most of the sampled waters lie on one line (see Durov diagram in Figure 320, TDS field). Most of the samples, which lie outside the main trend of development, come from the zones adjacent to the CTD, at borehole 12MI33 adjacent to the main shaft.

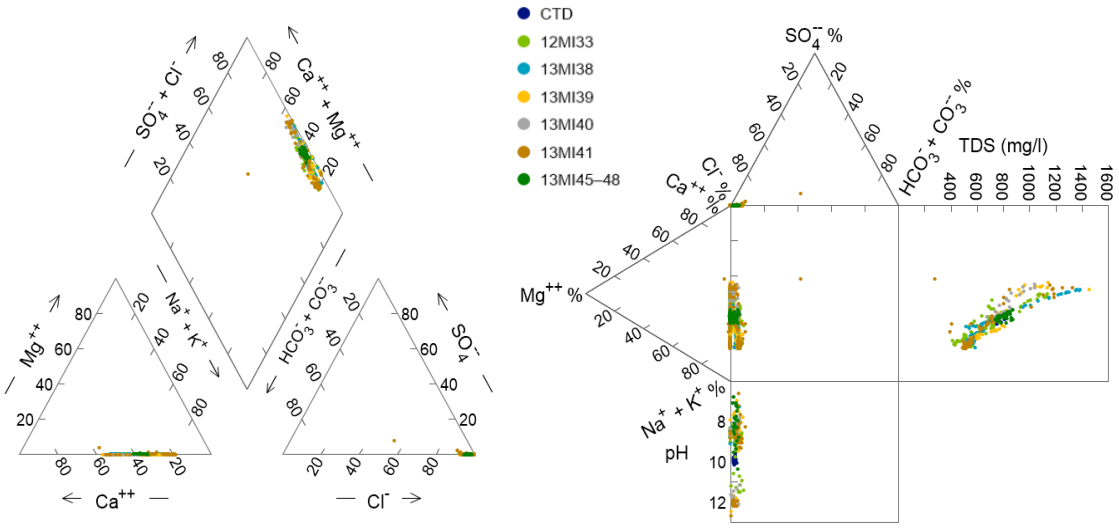

Figure 320. Piper (left) and Durov (right) diagrams for groundwater composition sampled in CTD and boreholes 12MI33-13MI48.

Samples that lie on the main line of trends in groundwater chemical composition are shown in Figure 321a, and Figure 321b, samples that lie outside the trend line on Figure 321c, and Figure 321d. Samples that lie outside the main trend of changes in groundwater chemical composition around CTD differ from the main trend by having a higher relative Ca ion concentrations at the expense of alkali metals, and at the same time they are characterized by high pH. The only exception is a few samples whose positions are completely outside the above trends and the whole deviated group consists of samples from zone 2 of borehole 13MI39.

a – without zones 4 and 6

b – without zones 4 and 6

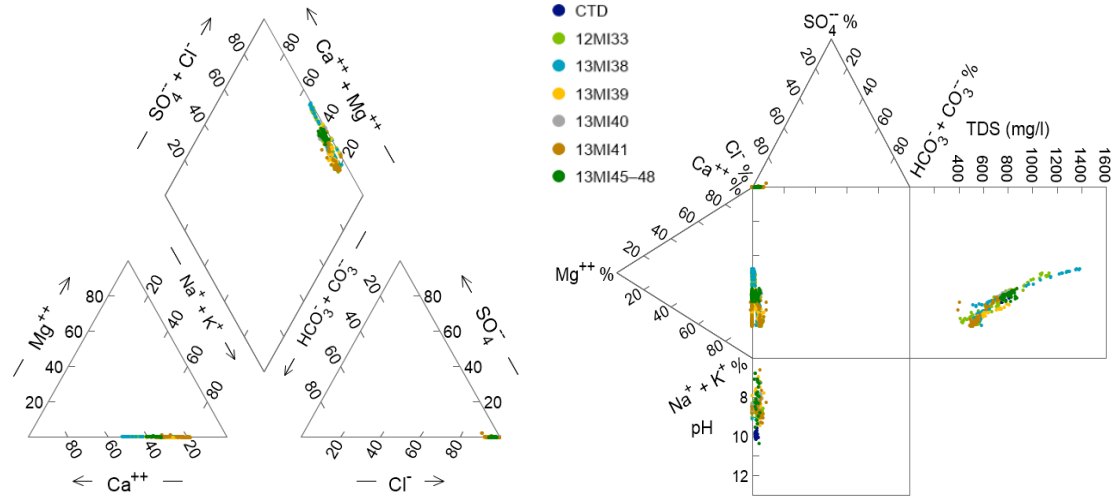

c – zones 4 and 6

d – zones 4 and 6

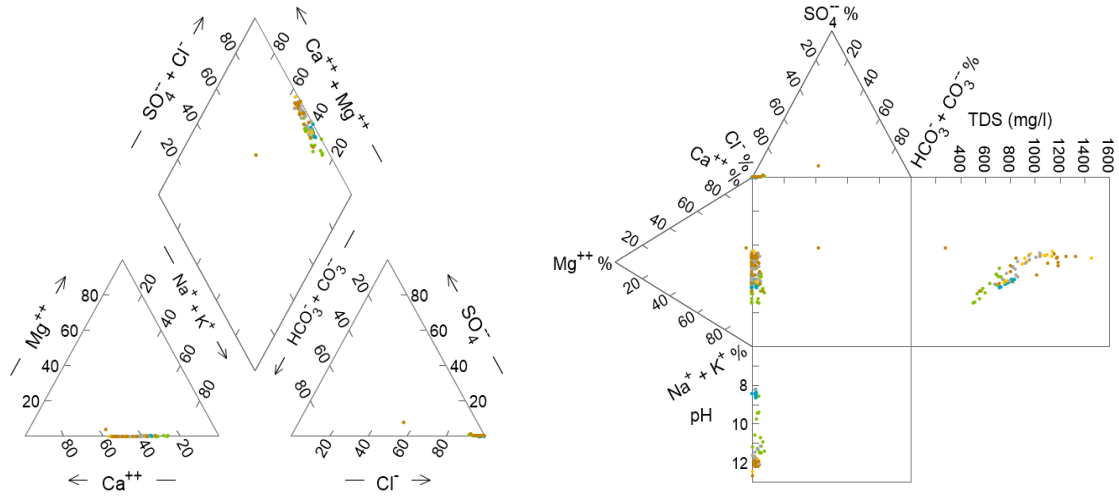

Figure 321. Piper and Durov diagrams for groundwater composition sampled in CTD and boreholes 12MI33–13MI48: (a) and (b) without groundwater from zones 4 (boreholes 13MI39–13MI41) and 6 (boreholes 12MI33 and 13MI38), (c) and (d) groundwater from zones 4 (boreholes 13MI39-13MI41) and 6 (boreholes 12MI33 and 13MI38).